Engineering Magnetic Anisotropy in Mononuclear Cobalt(II) Complexes and Lanthanide-based Metallacrowns

Feng Shao

NNT : 2017SACLS126

THESE DE DOCTORAT
DE
L'UNIVERSITE PARIS-SACLAY
PREPAREE A
L'UNIVERSITE PARIS-SUD

ECOLE DOCTORALE N° 571
Sciences Chimiques : Molécules, Matériaux, Instrumentation et Biosystèmes

Spécialité de doctorat : CHIMIE

Par

M. Feng SHAO

Ingénierie de l'anisotropie magnétique dans les complexes mononucléaires de cobalt(II) et les métallacrowns à base de lanthanides

Thèse présentée et soutenue à Orsay, le 4 juillet 2017 :

Composition du Jury :

Mme. DOLBECQ Anne	Directeur de Recherche, Université de Versailles Saint-Quentin	Présidente
M. LUNEAU Dominique	Professeur, Université Claude Bernard Lyon 1	Rapporteur
M. ROGEZ Guillaume	Chargé de Recherche, Université de Strasbourg	Rapporteur
M. SORACE Lorenzo	Professeur, Université de Florence	Examinateur
M. JOURNAUX Yves	Directeur de Recherche, Université Pierre et Marie Curie 6	Examinateur
M. MALLAH Talal	Professeur, Université Paris-Sud 11	Directeur de thèse
Mme. CAMPBELL Victoria	Chargé de Recherche, Université Paris-Sud 11	Co-directeur de thèse

ENGINEERING MAGNETIC ANISOTROPY IN MONONUCLEAR COBALT(II) COMPLEXES AND LANTHANIDE-BASED METALLACROWNS

BY FENG SHAO

A DISSERTATION PRESENTED TO THE GRADUATE SCHOOL OF THE UNIVERSITY OF PARIS SACLAY IN PARTIAL FULFILLMENT OF THE REQUIREMENTS FOR THE DEGREE OF DOCTOR OF PHILOSOPHY

UNIVERSITY OF PARIS-SACLAY

2017

Acknowledgements

I love brevity, so I'll keep this short and sweet. Firstly, I deeply thank Victoria and Talal for giving me a chance at continuing my graduate career. They have given me the freedom to explore different areas of research and I am a better scientist for it. I am pretty grateful for their encouragement, understanding, support, invaluable guidance and constructive criticism all these years. And Talal gave me a great opportunity to work in United States, where I met Vincent L. Pecoraro, who has been tremendously helpful in learning matallacrowns. I also warmly thank the rest of my committee – Prof. Lorenzo Sorace, Prof. Dominique Luneau, Dr. Yves Journaux, Dr. Guillaume Rogez and Dr. Anne Dolbecq for their insight and feedback.

Many deep thanks go to the great magnetic engineer, Eric Rivière and distinguished crystallographer, Régis Guillot. I've learned a great deal about magnetic measurements, treatments, and crystallography from them, the skills that have been quite useful and necessary for this dissertation. A special thank for Benjamin Cahier who worked hard on the theoretical part that allowed getting insight into the structural and geometric parameters that influence the nature and the magnitude of magnetic anisotropy in trigonal bipyramidal Co^{II} complexes.

I'd also like to thank the rest of the ICMMO staffs (too many to name) for making things run so smoothly. I owe a debt of gratitude to the collaborators I've had the good fortune to work with including Dr. Nathalie Guihéry, Dr. Anne-Laure Barra, Dr. Wolfgang Wernsdorfer, Dr. Svetlana Eliseeva, Dr. José J. Baldoví and Dr. Hélène Bolvin.

Furthermore, I would like to thank the entire LCI group (past and present) in ICMMO, especially Marta, Virgile, Monica, Olga, Christian, Nathalie, Stéphanie, Mauricio, Charlotte, Georges, Gabriella, Baptiste, Jérôme, Robinson, Clémence, Alice, Salomé, Fatima, Marie, Iréne, Khaled, Antoine, Lucile, Guillaume, Arnaud, Yiting, Luqiong, Fenglei, Lâm, Tâm and Linh, for their friendship and support; meanwhile, many warm thanks to all the permanent staffs, special thanks go to Ally, Sandra, Pei, Laure, Marie-Laure, Frédéric, Anne Bleuzen, Anne Léaustic, Amélie, Giulia, Jean-Jacques, Vincent, Zakaria, Jean-Noël, Katell, and Marie for their guidance and help. Also warm thanks go to the members in the group of Prof. Vincent Pecoraro, Jake, Tu, Leela, Karl, Tyler, Audrey, and Cathy, for their friendship

and support, and my special thanks go to my Chinese landlord family in Ann Arbor, Yinbin, Yao, and their little children Coco and Chris.

During my time in France, whenever I was nostalgic of the home that was thousands of miles from here, my Chinese friends (Xiaohua Guo, Qi Guo, Ruifang Ma, Jing Cao, Yaqiong Wang, Zixian Jia, Zhiqiang Deng, Lin Li, Jiangchao Liu, Jingfang Hao, Shuiyan Cao, Men Su, Jinjin Zhao ect…, especially the buddies in La Pacaterie, Zheng Chen, Zhaojie Yu, Zhengpeng Cui and Zhimin Song) here have made life a lot more fun and interesting for me, and I am thankful for all the laughter, the dinners, the parties, the Chinese food they cooked, the opportunities to talk for hours in my mother tongue — they played no small part in keeping me going. It has been my privilege to get to know you all.

I greatly thank the Collaborative Program between China Scholarship Council and Université Paris-Sud (No. 201306310014), and Marie Curie International Research Staff Exchange Scheme Fellowship within the 7th European Community Framework Program, studying in aboard is a dream come true for me, meanwhile a little sacrifice by my family, last but not least, I'd like to thank my family: my little brother Ming and my parents. Ming — many thanks for taking care of our parents while I am away from home; Mom — thanks for all of your love and encouragement all of these years. Dad — thanks for teaching me the value of hard work and to always strive to be the best I can be. To my good friends back home — Jiaping, Mingguang, Xiaofeng, Jihui and Songqian — you've always been a source of support and encouragement.

床前明月光，疑是地上霜。举头望明月，低头思故乡。— 李白
俱往矣，数风流人物，还看今朝。— 毛泽东
有志者，事竟成，破釜沉舟，百二秦关终属楚；
苦心人，天不负，卧薪尝胆，三千越甲可吞吴。

Feng SHAO
July 2017, Orsay
邵锋
二零一七年夏

Table of Contents

List of Figures

List of Tables

Résumé

Comme nous le savons, les applications sont déterminées par des propriétés, qui sont essentiellement déterminées par la structure. L'interaction entre la forme (structure moléculaire) et la fonction (propriétés physiques) peut être exploitée par le ligand, l'ion métallique, l'approche métallacrown et ainsi de suite. Les travaux de cette thèse portent sur la synthèse et l'étude du comportement magnétique de complexes mononucléaires de cobalt(II) de géométrie bipyramide trigonale et sur l'étude de complexes mononucléaires de lanthanides possédant une structure de type métallacrown.

Pour les complexes de cobalt(II), l'objectif a été de modifier l'anisotropie magnétique en modifiant la nature du ligand organique tétradenté et du ligand terminal en gardant, autant que faire se peut, la géométrie et même la symétrie des complexes. Presque tous ces complexes se comportent comme des molécules-aimants avec une barrière énergétique à l'inversion de l'aimantation qui peut être liée à leur anisotropie magnétique et donc à la nature des ligands. Et les complexes métallacrown à base de lanthanides étant hautement symétriques, permet de les utiliser comme modèles pour effectuer une corrélation entre la nature de l'ion lanthanide et leurs propriétés d'aimants.

La thèse est composée de 6 chapitres. Le chapitre 1 présente l'état de l'art du magnétisme, des molécules-aimants (SMMs et SIMs) en se basant sur quelques exemples importants de la littérature. Le chapitre 2 se concentre sur une famille de complexes de géométrie bipyramide trigonale de formule générale [Co(Me_6tren)X]Y avec le ligand axial (X) et le contre-ion (Y) induisant le comportement SMM. Dans cette série de composés, l'influence du ligand axial X sur la nature et l'amplitude de l'anisotropie magnétique a été étudiée. Nous avons montré que, pour la série des halogénures, l'anisotropie la plus forte est obtenue pour le ligand axial fluorure (F^-). L'effet du cation Y qui influence l'interaction entre les molécules et affecte légèrement le comportement d'aimant moléculaire a aussi été étudié. Au chapitre 3, on étudie l'influence du changement du ligand tétradenté. Le remplacement des trois atomes d'azote qui se trouvent en position équatoriale dans la sphère de coordination de cobalt(II) par des atomes de soufre induit une augmentation des distances Co–L dans le plan équatorial qui conduit à une plus forte anisotropie. Les calculs théoriques effectués sur

Feng SHAO: 0000-0001-8606-8628

ces complexes permettent de rationaliser les résultats expérimentaux et surtout de prévoir les propriétés de nouveaux complexes. Les chapitres 4 et 5 concernent deux séries de SMM de structure métallacrown de formule $LnGa_4$ (Ln = Tb^{III}, Dy^{III}, Ho^{III}, Er^{III}, Yb^{III}) avec les ligands basés sur l'acide salicylhydroxamique (H_3shi) et l'acide 3-hydroxy-2-naphtohydroxamique (H_3nha). Les calculs théoriques préliminaires permettent de rationaliser la différence entre les propriétés des magnétiques dues aux différents ions lanthanide. Enfin, une conclusion générale avec des perspectives sont récapitulées au chapitre 6.

Feng SHAO: 0000-0001-8606-8628

Abstract

As we know, the applications are determined by properties, which are essentially determined by structure. The interplay between form (molecular structure) and function (physical properties) can be exploited engineering by the ligand, the metal ion, the metallacrown (MC) approach and so on. The work focuses on the synthesis and the study of the magnetic behavior of mononuclear cobalt(II) complexes with trigonal geometry and on the study of mononuclear lanthanide complexes that possess a metallacrown structure.

For the cobalt(II) complexes, the aim was to tune the magnetic anisotropy by changing the nature of the tetradentate organic ligand and the terminal ligand. Almost all these complexes behave as Single Molecule Magnets (SMMs) with an energy barrier to the reversal of the magnetization that can be linked to their magnetic anisotropy and thus to the nature of the organic ligands. The lanthanide containing metallacrown complexes are highly symmetric, which allows performing a correlation between the nature of the lanthanide ion and their SMM properties.

The dissertation will be composed of 6 chapters. Chapter 1 introduces the background of the magnetism, SMMs, Single Ion Magnets (SIMs), and some important SIMs. Chapter 2 focuses on a family of trigonal bipyramidal complexes [Co(Me_6tren)X]Y (Me_6tren = Tris(2-(dimethylamino)ethyl)amine). We show that the axial ligand affects the SMM behavior allowing us to prepare a complex with a magnetic bistability at T = 2 K. In Chapter 3, we examine the effect of changing the coordinated atoms (sulfur instead of nitrogen) in the equatorial coordination sphere of cobalt(II). We demonstrate that this slight change improves the SMM behavior. Chapters 4 and 5, which concern two series of 12-MC-4 SMMs based on $LnGa_4$ (Ln = Tb^{III}, Dy^{III}, Ho^{III}, Er^{III}, Yb^{III}) with the ligands salicylhydroxamic acid (H_3shi) and 3-hydroxy-2-naphthohydroxamic acid (H_3nha), respectively, where we correlate the nature of the lanthanide ion to its magnetic behavior using *ab initio* calculations. At last, the understanding gained from this dissertation research, along with future research directions will be recapitulated in Chapter 6.

Feng SHAO: 0000-0001-8606-8628

List of Abbreviations

AC	Alternating Current
CASSCF	Complete Active Space Self-Consistent Field
DC	Direct Current
DFT	Density Functional Theory
HFEPR	High Frequency/Field Electron Paramagnetic Resonance
H_3shi	Salicylhydroxamic acid
H_3nha	3-hydroxy-2-naphthohydroxamic acid
Ipa	Isophathalic acid
IR	InfraRed
LF	Ligand Field
MCs	Metallacrowns
Me_6tren	Tris(2-(dimethylamino)ethyl)amine
NS^{iPr}	Tris(2-(isopropylthio)ethyl)amine
NS^{tBu}	2-(tert-butylthio)-N-(2-(tert-butylthio)ethyl)-N((neopentylthio)methyl)ethan-1-amine
Py	Pyridine
QTM	Quantum Tunneling of Magnetization
SMMs	Single Molecule Magnets
SIMs	Single Ion Magnets
SOC	Spin-Orbit Coupling
SO-RASSI	Spin-Orbit Restricted Active Space-State Interaction
SO-SI	Spin-Orbit State-Interaction
SQUID	Superconducting QUantum Interference Device
UV-Vis	UltraViolet-Visble
ZFS	Zero-Field Splitting

Feng SHAO: 0000-0001-8606-8628

CHAPTER 1 General Introduction

1.1 Historical Background of Magnetism

Magnetism, which is derived from Magnesia, a city in Greece where lodestone (magnetite), a naturally magnetic iron ore, was most probably first found by the Greek philosopher Thales of Miletus (625-547 BC) in the 6th century BC.[1] Actually the oldest manuscript that mentions the existence of lodestone is the work of Guan Zhong (720-645 BC), a famous chancellor and reformer of the Qi State during the Spring and Autumn period of China, but the objects made from magnetic materials have been found in archaeological sites dating from much further back in China.[2, 3] In ancient Chinese civilization, lodestones were called "soft stones". This is the general name of all strongly magnetic oxides existing in nature and having a permanent magnetic character. Now we know that they are the magnetic minerals based on iron: γ-Fe_2O_3, FeO-TiO_2-Fe_2O_3, sometimes also FeS_{1+x} and especially magnetite Fe_3O_4.[2]

The Chinese writings of Gui Guzi (400-320 BC) and Han Fei (280-233 BC), showed that the orientation of natural lodestone towards the earth's poles had also been known for a very long time.[2] Additionally, the remarkable physical properties of this material were used as the first compass that was invented during the period of 3rd and 4th century BC during the Han Dynasty of China.[1] The oldest "directional tool" (called Sinan in Chinese, means Directing South) known was made: it was a natural lodestone sculpted and polished into the form of a spoon. This "directional spoon", the ancestor of the compass, was described by Wang Chong (27-97) in Lun Heng: "This instrument resembles a spoon, and when it is placed on a plate on the ground, the handle points to the south". On an etching dating from the Han period, we see a spoon placed on a small square tray (Figure 1.1), it is commonly accepted that this is a painting of a directional instrument.

During the following centuries, the magnetic compasses were further refined but the origin of magnetism was not understood until the early 17th century, when English scientist William Gilbert (1540-1603) wrote in his book, *De Magnete*, that the Earth is itself a weak giant magnet. The following, early theoretical investigations into the nature of the Earth's magnetism were carried out by the German scientist Carl Friedrich Gauss (1777-1855).[1]

Feng SHAO: 0000-0001-8606-8628

Meanwhile, Gilbert still interpreted the attraction phenomenon with the soul concept: "Magnetic attraction arises because the loadstone has a soul".[4]

Figure 1.1. The "directional tool" Sinan in Han Dynasty of China.

In 1795, a breakthrough came rather unexpectedly by joining magnetism and molecules, when French scientist Charles de Coulomb (1736-1806), tried to imagine how a molecule could become polarized in the process of magnetization. He established the inverse square law of force, which states that the attractive force between two magnetized objects is directly proportional to the product of their individual fields and inversely proportional to the square of the distance between them.[1, 4] Shortly afterwards, Denis Poisson (1781-1840) introduced the notion of a magnetic field, as the force acting on a unit magnetic charge at all points in space. However, in contrast to electric charges, magnetic charges seem to only exist in pairs, constituting "magnetic dipoles".[5-8]

In 1820, another key-experiment by Danish physicist Hans Christian Ørsted (1777-1851) opened new perspectives in the understanding of magnetism by showing that a magnetic field could be created by the circulation of an electric current in a conducting wire (Figure 1.2). This experiment demonstrated the relationship between electricity and magnetism. Following experiments involving the effects of magnetic and electric fields on one another were then carried on by French scientist André-Marie Ampère (1775-1836) who showed that a current carrying a circular coil generates a magnetic field identical to that created by a magnetic dipole, and suggested that the magnetism of matter could be due to small electrical current loops circulating on the atomic scale. English scientist Michael Faraday (1791-1869) constructed the first dynamo and French scientist Pierre-Simon de

 Feng SHAO: 0000-0001-8606-8628

Laplace (1749-1827) established the expression for the force acting on a current carrying conductor in a magnetic field.[4] But it was the Scottish scientist, James Clerk Maxwell (1831-1879), who provided the mathematical frame finally that allowed the description of electromagnetism by showing, in the 19th century, that electricity and magnetism represent different aspects of the same fundamental force field.[9]

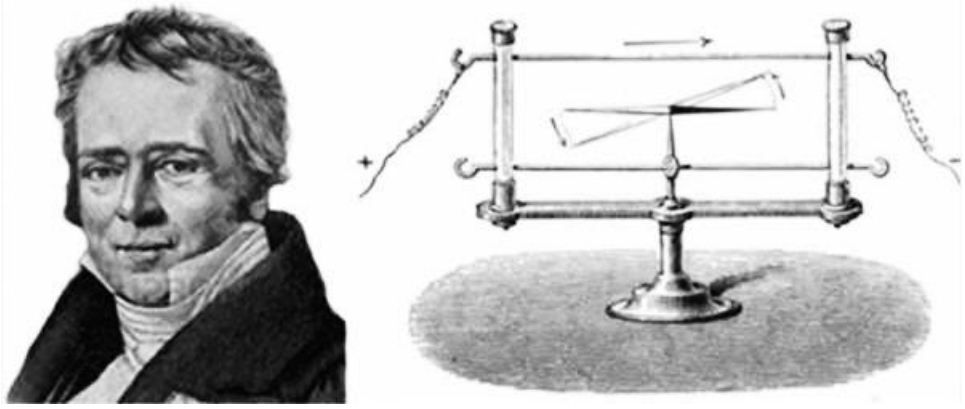

Figure 1.2. Danish physicist Hans Christian Ørsted and his historic experiment.

The modern understanding of magnetic phenomena originates from the work of two French scientists: Pierre Curie (1859-1906), and Pierre Weiss (1865-1940) who investigated the temperature dependence of the magnetization, discovering the law that carries their name. The discovery of the electron in 1897 by English physicist Joseph John Thomson (1856-1940)[10] and the ensuing refinement of the theory through quantum mechanics would usher in a new era of scientific discovery in the 20th century. Some major discoveries range from the advent of magnetic refrigeration[11] to superparamagnetism[12] to high temperature superconductors[13]. The present day understanding of magnetism based on the theory of the motion and interactions of electrons in atoms (quantum electrodynamics) stems from the work and theoretical models of two German scientists, Ernest Ising (1900-1998)[14] and Werner Karl Heisenberg (1901-1976)[15]. Werner Karl Heisenberg was also one of the founding fathers of modern quantum mechanics, which provided the tools for describing the magnetic properties, starting a revolution that we are still observing. Many new concepts were introduced, and some of them have had a fundamental impact on magnetism, most important among them spin and exchange.[4]

With the improvement of structural, magnetic characterization techniques and quantum mechanics approaching, coordination chemists began to study magnetic properties of compounds, which gave rise to the field of molecular magnetism.[16, 17] Actually,

molecular magnetism is an essentially multidisciplinary field, which involves synthetic chemistry, coordination chemistry, theoretical chemistry, solid state physics, and so on, with chemists, physicists, and material scientists (including some biologists) working to advance the field.[17] Molecular magnetism has the potential applications to unlock novel spintronic devices,[18, 19] to supply high-density storage devices, to act as qubits,[20, 21] to probe physical phenomena at the boarder of the classical and quantum regimes, and to serve as magnetic refrigerants.[11] This potential provides the motivation to probe these molecules. Indeed, Olivier Kahn (1942-1999)[22] in our laboratory is considered to be the father of molecular magnetism by many chemists, and has contributed in a crucial manner to the understanding of the exchange coupling phenomenon in coordination complexes, promoting the Goodenough-Kanamori rules using combined theoretical and experimental approaches.[17, 23-25] Thus, it became possible to engineer molecular magnetic materials to obtain predictable magnetic behavior, which was the birth of the field of Molecular Magnetism. In 1991, the field saw a revolution due to the discovery, by Dante Gatteschi (University of Florence), of what was then called Single Molecule Magnets (SMMs).[26-28] Magnetic anisotropy was the main physical phenomenon to study in order to deeply understand the magnetic behavior of SMMs. Herein, my research thesis is focused on the synthesis of mononuclear SMM complexes with the objective of understanding the origin of magnetic anisotropy using mainly an experimental approach; theoretical calculations are also used to provide a rationalization and more importantly as a predictive tool.

1.2 Fundaments of Single Molecule Magnets

Before introducing molecule-based SMM materials, it is essential to first discuss, briefly, some fundamental theory of magnetism at the microscopic level.

Magnetism originates from the presence of the spin and orbital angular momenta of unpaired electrons, which generate a magnetic moment.[29] Within a magnetic material, there can be several atoms that have unpaired electrons, generating a magnetic moment within the molecules. To minimize the magnetic energy in magnets, there are regions of space where all the magnetic moments align parallel or antiparallel with each other, known as domains. Basically, the energy of a d^n atom or ion due to various electronic and nuclear interactions is calculated by means of the following Hamiltonian[30]:

$$\hat{H} = \hat{H}_{EL} + \hat{H}_{CF} + \hat{H}_{LS} + \hat{H}_{SS} + \hat{H}_{ZE} + \hat{H}_{HF} + \hat{H}_{ZN} + \hat{H}_{II} + \hat{H}_{Q} \qquad (1.1)$$

the meaning of each term is given in Table 1.1.

Here we concentrate on magnetic and electronic interactions of intermediate magnitude, namely spin-orbit coupling, Zeeman effect and spin-spin interaction, which laid the foundation for the discussion of SMMs. Furthermore, if you are interested in in-depth examination of theory of molecular magnetism, please refer to several books on the topic.[16, 17, 30, 31]

Table 1.1. Atomic/electronic representation of Hamiltonians and their corresponding spectroscopic technique.

Hamiltonian	Representation	Energy magnitude (cm^{-1})[30, 32]	Spectroscopic technique
$\hat{H}_{EL}$	Electronic energy and electron repulsion energy	$10^4 – 10^5$	Electronic spectroscopy
$\hat{H}_{CF}$	Crystal field	$10^4 – 10^5$	Electronic spectroscopy
$\hat{H}_{LS}$	Spin-orbit coupling	$0 – 10^2$ for transition metals; 10^3 for lanthanides	Magnetism and electronic spectroscopy
$\hat{H}_{SS}$	Spin-spin interaction	$0 – 10^2$	Magnetism and electron paramagnetic resonance
$\hat{H}_{ZE}$	Electronic Zeeman effect	0 – 1	Magnetism and electron paramagnetic resonance
$\hat{H}_{HF}$	Hyperfine interaction	—	Electron paramagnetic resonance
$\hat{H}_{ZN}$	Nuclear Zeeman effect	—	Nuclear magnetic resonance
$\hat{H}_{II}$	Internuclear interaction	—	Nuclear magnetic resonance
$\hat{H}_{Q}$	Nuclear quadrupole effect	10^{-7}	Nuclear magnetic resonance, nuclear quadrupole resonance and Mössbauer spectroscopy

1.2.1 Spin-Orbit Coupling and Zeeman Effect

Spin-Orbit Coupling (SOC) is due to the interaction between the spin and the orbital angular momenta of unpaired electrons.[29] The coupling splits the electron's energy levels due to electromagnetic interaction between the electron's spin and the magnetic field generated by the electron's orbit around the nucleus. This, together with the non-cubic crystal field generated by the ligands, is responsible of the lift of the degeneracy of the spin levels in the absence of an applied magnetic field and leads to what is called Zero-Field Splitting (ZFS). ZFS is responsible of the magnetic anisotropy in transition metal ions and has profound effects on the magnetic properties.

An energy level diagram which illustrates the phenomenon of ZFS is presented in

Figure 1.3, in the case where the ground state is not orbitally degenerate (L = 0) for an S = 3/2 (represents 3d transition metals) system. In this case, the effect of SOC is said to be of second order because the lift of the degeneracy of the spin ground state is due to its coupling with the excited states via the spin-orbit operator. In an axial crystal field, the four-fold degeneracy, m_s = ±1/2, ±3/2, is partially resolved with the ±3/2 states separated an amount 2D (in units of energy, usually cm^{-1}) from the ±1/2 states. The nature of the ground m_s state (±1/2 or ±3/2) depends on several parameters and particularly on the magnitude and the symmetry of the crystal field. The influence of these parameters will be discussed in this work.

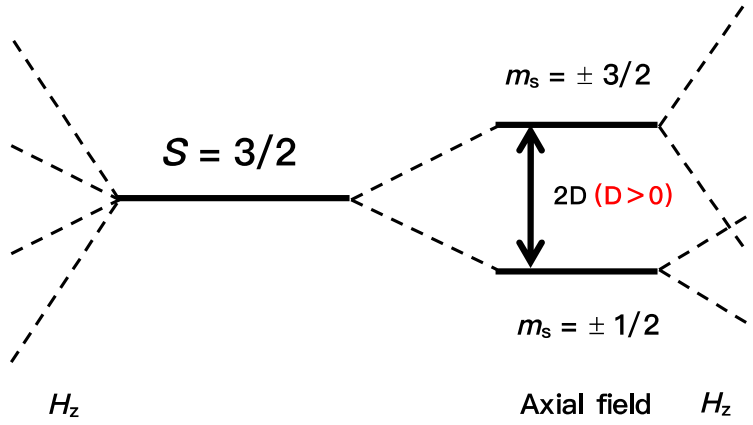

Figure 1.3. The behavior of an S = 3/2 state (center). The usual Zeeman splitting is illustrated on the left, while on the right the effect of ZFS is illustrated. The degeneracies are partially resolved before the magnetic field affects the levels.

The population of the levels then depends, by the Boltzmann principle, on the relative values of the ZFS parameter D and the thermal energy, k_BT. The fact that D not only has magnitude but also sign (see equation 1.3 below) is of large consequence for many magnetic systems. If D > 0, the ground levels have the lowest m_s values (Figure 1.3); while if D < 0, the ±3/2 levels have the lowest energy.[16]

The Zeeman effect depicts the removal of the degeneracy of the m_s levels in the presence of an applied direct-current (dc) magnetic field. In Figure 1.3, an S = 3/2 metal ion in an applied dc magnetic field, the energy of the m_s = –3/2 level is stabilized, whereas the energy of the m_s = +1/2 level is destabilized. In the absence of ZFS, when the dc magnetic field is applied parallel the anisotropy axis or when the applied field is much larger that ZFS, the energy of the m_s sub-levels is expressed by

$$E = g\mu_B m_s H \qquad (1.2)$$

where g is the Landé-factor, μ_B is the Bohr magneton, and H is the applied dc magnetic field.

1.2.2 Exchange Interactions

In polynuclear systems, there is an exchange interaction between neighboring metal atoms via the bridging ligands or organic radicals known as exchange coupling, which is expressed by the coupling parameter, *J*. Generally, there are two types of coupling, ferromagnetic ($J > 0$), where the electron spins are aligned parallel in the ground state, and antiferromagnetic ($J < 0$), where the spins are oriented antiparallel in the ground state. Goodenoug and Kanamori established rules that allows predicting the ferro- or antiferromagnetic nature of the exchange interaction knowing the geometrical structure between two metal ions, their rules were applied mainly on oxides but they have, of course, a general character.[23, 24] Later, Kahn[17] introduced formally the idea of overlap and orthogonality between magnetic orbitals that allowed chemists to simply predict the nature of the exchange coupling interaction in molecular systems; Anderson had already mentioned the same idea with a less formal development.[33] For lanthanides, the exchange coupling is quite weak (< 1 cm^{-1}) because the f-orbitals are contracted,[34] but they possess a very large SOC that leads to large magnetic anisotropy and thus to interesting mononuclear complexes that behave as SMMs.

1.2.3 Total Spin Hamiltonian

The ZFS within a $^{2S+1}\Gamma$ state without first-order angular momentum can be expressed by the phenomenological Hamiltonian:

$$\hat{H}_{ZFS} = \hat{S} \cdot \hat{D} \cdot \hat{S} \qquad (1.3)$$

where $\hat{D}$ is a symmetric and traceless tensor. In matrix notation, the total spin Hamiltonian considering the Zeeman perturbation is then

$$\hat{H} = \mu_B \hat{S} \cdot \boldsymbol{g} . \vec{H} + \hat{S} \cdot \hat{D} \cdot \hat{S} \qquad (1.4)$$

$\boldsymbol{g}$ being the *g*-tensor. Assuming the $\hat{D}$ and $\boldsymbol{g}$ tensors colinear, equation 1.4 could be rewritten as

$$\hat{H} = g_u \mu_B \hat{S}_u \cdot H_u + D\left[\hat{S}_z^2 - \frac{S_T(S_T+1)}{3}\right] + E(\hat{S}_x^2 - \hat{S}_y^2) \qquad (1.5)$$

If we consider the isotropic magnetic coupling, equation 1.5 becomes

$$\hat{H} = -J_{12}\hat{S}_1 \cdot \hat{S}_2 + D\left[\hat{S}_z^2 - \frac{S_T(S_T+1)}{3}\right] + E(\hat{S}_x^2 - \hat{S}_y^2) + g_u \mu_B \hat{S}_u \cdot H_u \qquad (1.6)$$

where J_{12} is the exchange coupling parameter; $\hat{S}_1$ and $\hat{S}_2$ are the corresponding spin operators; S_T is the total spin state; $\hat{S}_x$, $\hat{S}_y$, $\hat{S}_z$ and $\hat{S}_u$ are the corresponding spin operators; *H* is the magnetic field along direction u = x, y, z. *D* and *E* are the axial and rhombic ZFS

parameters, respectively, and, if we assume that $D_{xx} + D_{yy} + D_{zz} = 0$, they are related to the principal values D_{uu} (u = x, y, z) of the *D*-tensor through[17]

$$D = 3D_{zz}/2 \qquad (1.7)$$

$$E = |D_{xx} - D_{yy}|/2 \qquad (1.8)$$

1.2.4 Single Molecule Magnets

SMMs are a class of bistable metal-organic compounds that display superparamagnetic behavior below a certain blocking temperature (T_B). In this temperature range, SMMs may exhibit magnetic hysteresis of purely molecular origin. (see Figure 1.4) This hysteresis has its origin in the slow relaxation of the magnetization of the isolated molecules. The slow relaxation of the magnetization is due to the presence of an energy barrier *U* to the reorientation of the magnetization resulting from to the large spin value of the ground state and its Ising-type magnetic anisotropy, as depicted in Figure 1.4 for the most studied family of complexes: $Mn_{12}(OAc)$.

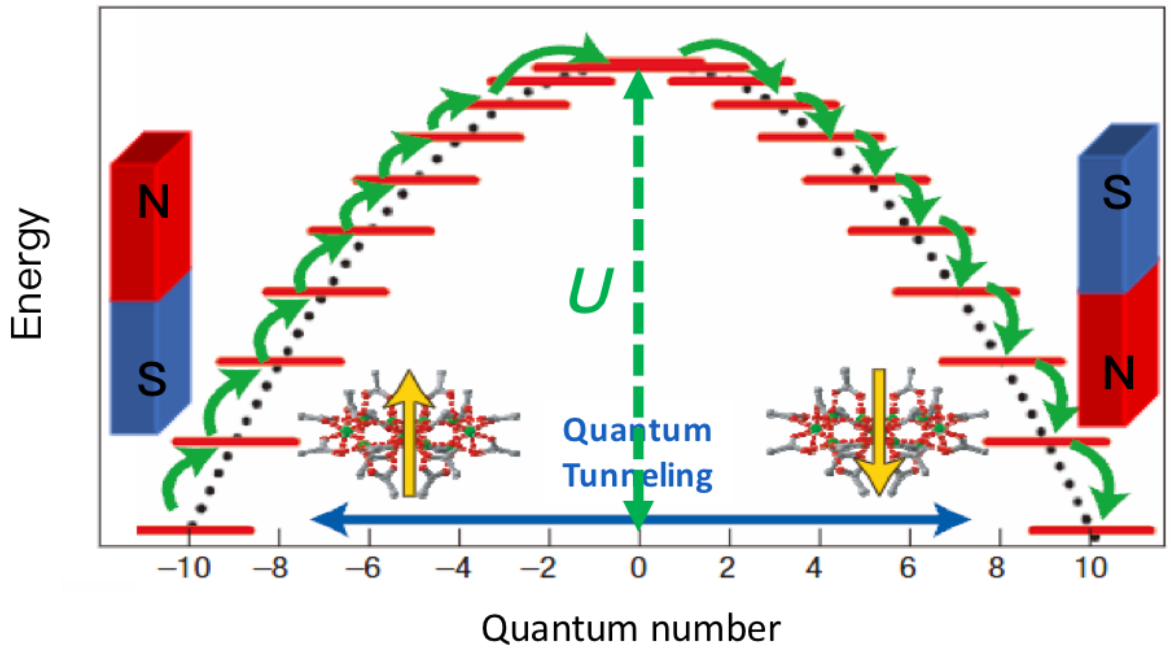

Figure 1.4. Heuristic depiction of dynamics of the magnetization for SMMs. Schematic representation of the energy landscape of a SMM with a spin ground state $S = 10$. The magnetization reversal can occur via quantum tunneling between energy levels (blue arrow) when the energy levels in the two wells are in resonance. Phonon absorption (green arrows) can also excite the spin up to the top of the potential energy barrier (U) with the quantum number $M = 0$, and phonon emission descends the spin to the second well.[19]

At low temperatures, the degeneracy (21) of the spin ground state S (10 in the case on $Mn_{12}(OAc)$) of the molecule is lifted at zero dc magnetic field by the axial anisotropy into its m_s components with $m_s = \pm S$ as the ground levels due to the Ising-type anisotropy of these complexes that is the result of the presence of a four-fold principle symmetry axis for the molecule. The height of the barrier U corresponds to the energy gap between the lowest level $m_s = \pm S$ and the top level $m_s = 0$. The energy barrier U is equal to $|D|S^2$ ($|D|(S^2–1/4)$ for half-integer spin systems), where S is the ground-state spin and D is the axial ZFS parameter.[35] There are two diagnostic methods to probe the relaxation of the magnetization of SMMs, one is the frequency-dependence of the alternating-current (ac) magnetic susceptibility, and the other is the magnetic hysteresis loop of the magnetization *vs.* applied dc magnetic field. It is important to note that the definition of a SMM is not straightforward because the slow relaxation of the magnetization is a property that is time-dependent. One strict definition is the opening of a magnetic hysteresis at zero dc magnetic field. However, the quantum nature of the isolated molecules leads in most cases to a tunneling of the magnetization at zero dc magnetic field precluding an opening of the loop, in most cases. Another less strict definition is the mere presence of a relatively slow relaxation of the magnetization observed in the ac data at a frequency weaker than 1500 Hz, provided that the relaxation is mainly due to an Orbach mechanism (relaxation over an energy barrier) in an Ising-type molecule and not to other mechanisms such as the Raman one.

1.2.5 Alternating-Current Magnetic Susceptibilities

In the ac studies, a small ac magnetic field (3.0 Oe) is applied, oscillating at a frequency range of 0.1 – 1500 Hz. Out-of-phase (or the imaginary part of the susceptibility) ac peaks (χ'') as well as a decrease in the in-phase (real part) ac susceptibility signal (χ') are observed when the magnetic moment of the molecule cannot relax fast enough to keep in-phase with the oscillating field (Figure 1.5).

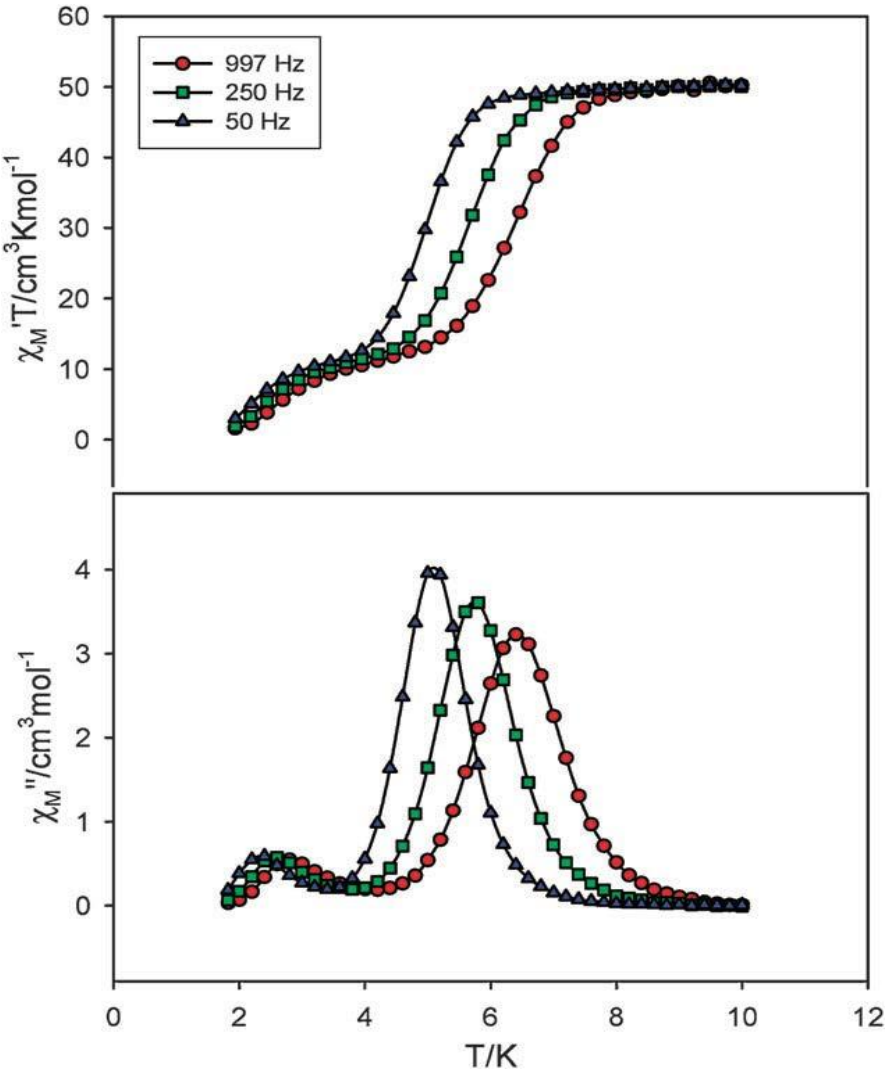

Figure 1.5. In-phase (χ', top) and out-of-phase (χ'', bottom) ac susceptibility signals for $[Mn_{12}O_{12}(O_2CR)_{16}(H_2O)_4]$ at different oscillation frequencies. Reprinted with permission from reference[36]. Copyright 2009 Royal Society of Chemistry.

At the χ'' peak maximum, the magnetization relaxation rate ($1/\tau$) should be equal to the angular frequency (ω) of the oscillating field: $\omega = 1/\tau = 2\pi\nu$, where τ is the relaxation time and ν is the frequency of oscillating field. At high temperatures, the magnetization relaxation rate ($1/\tau$) also obeys the Arrhenius equations:

$$1/\tau = (1/\tau_0)\exp(-U_{eff}/k_BT) \qquad (1.9)$$

$$\ln(1/\tau) = \ln(1/\tau_0) - U_{eff}/k_BT \qquad (1.10)$$

where τ_0 is the relaxation time at an infinite temperature (to be determined), U_{eff} is the effective energy barrier ($\leq U$ usually, because of the presence of other relaxation pathways), and k_B is the Boltzmann constant (1.380658×10^{-23} J/K or 0.69503877 cm^{-1}). The relaxation rate and the blocking temperature at each frequency can be extracted from the ac

measurements at variable frequencies of the oscillating field, which allows determining U_{eff} and τ_0. The ac susceptibility data are analyzed for different temperatures in terms of the Cole-Cole formalism, such analysis provides information on the nature of the magnetization relaxation processes. It represents the magnetic analog of the Debye theory, which was originally developed to describe the low frequency dependence of the dielectric constant in polar liquids.[37] Casimir and Du Pré proposed the first thermodynamic model for relaxation of a magnetic system in an oscillating magnetic field.[38] This model was further modified in order to take into account the presence of more than one relaxation time, or a distribution of relaxation times, obtaining the following expression for magnetic susceptibility:

$$\chi(\omega) = \chi_S + \frac{\chi_0 - \chi_S}{1+(i\omega\tau_c)^{1-\alpha}} \qquad (1.11)$$

where τ_c represents the characteristic relaxation time while the parameter α ranges from 0 to 1, represents the width of the relaxation time distribution (α is equal to zero in the case of one relaxation time). The parameter χ_0 represents the isothermal susceptibility (susceptibility in the limit of zero frequency of the applied magnetic field, obeys the Curie law). χ_s is the adiabatic susceptibility (susceptibility at a high frequency of the applied ac oscillating field, very slow relaxation, the system has no time to exchange energy with the external world).

Decomposing of equation (1.11) gives the expressions for in-phase $\chi'(\omega)$ and out-of-phase $\chi''(\omega)$ susceptibilities:

$$\chi'(\omega) = \chi_S + \frac{\chi_0 - \chi_S}{2} \times \left(1 - \frac{\sinh[(1-\alpha)\ln(\omega\tau_c)]}{\cosh[(1-\alpha)\ln(\omega\tau_c)] + \cos[(1/2)(1-\alpha)\pi]}\right) \qquad (1.12)$$

$$\chi''(\omega) = \frac{\chi_0 - \chi_S}{2} \times \left(1 - \frac{\sin[(1/2)(1-\alpha)\pi]}{\cosh[(1-\alpha)\ln(\omega\tau_c)] + \cos[(1/2)(1-\alpha)\pi]}\right) \qquad (1.13)$$

The experimental data are usually plotted in the complex plane as χ'' *vs.* χ' for different temperatures and fitted to the equation of a semi-circular arc (Cole-Cole or Argand plot):

$$\chi''(\chi') = -\frac{\chi_0 - \chi_S}{2\tan\left[(1-\alpha)\left(\frac{\pi}{2}\right)\right]} + \sqrt{(\chi' - \chi_S)(\chi_0 - \chi') + \frac{(\chi_0 - \chi_S)^2}{4\tan^2\left[(1-\alpha)\left(\frac{\pi}{2}\right)\right]}} \qquad (1.14)$$

with three adjustable parameters χ_0, χ_s and α.[37, 39]

An example of Cole-Cole plots (plot of χ_M'' *vs.* χ_M' at a given temperature) shows weakly flattened semi-circles (Figure 1.6). Fitting the Cole-Cole plots allows extracting the relaxation time at a given temperature and the corresponding α value.[40] Actually, many SMMs do not show a full peak in the out-of-phase ac magnetic susceptibility, above 1.8 K; therefore, it is not possible to determine U_{eff} and τ_0 by the above method. Bartolomé *et al.*,[41]

assuming that there is only one characteristic relaxation process of the Debye type with one energy barrier and one time constant, suggested to use equation 1.15 to evaluate roughly the energy barrier and τ_0:

$$\ln(\chi''/\chi') = \ln(\omega\tau_0) - U_{eff}/k_BT \qquad (1.15)$$

and this method has already been applied earlier in the determination of τ_0 in $Mn_{12}(OAc)$[41] and U_{eff} and τ_0 in Fe_3Ln.[42]

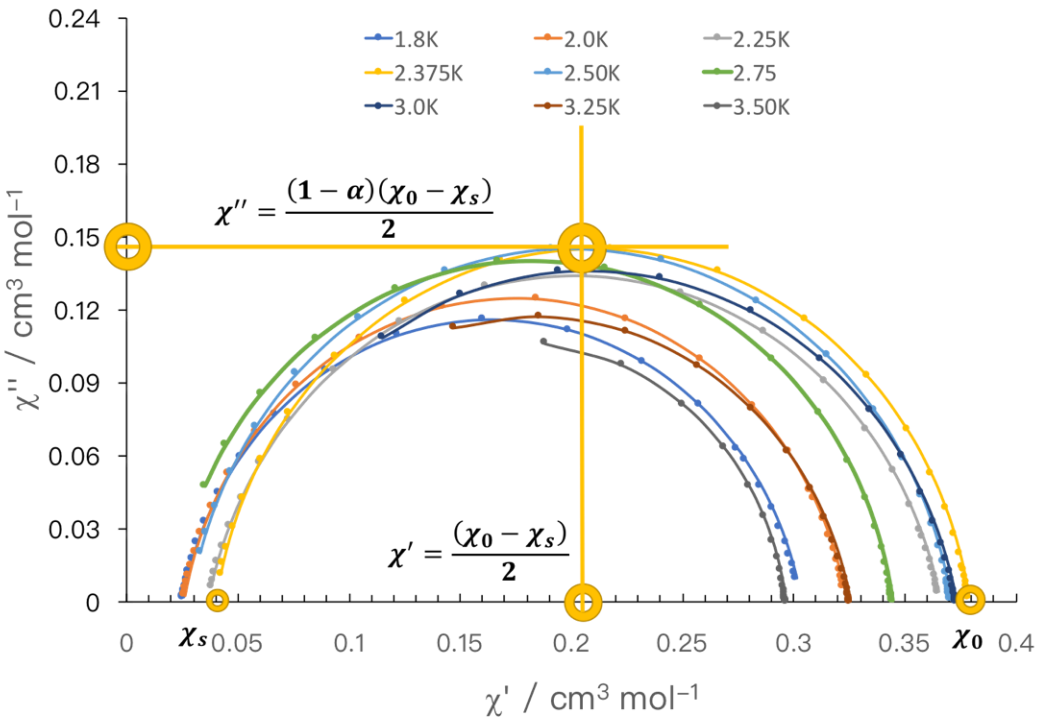

Figure 1.6. Heuristic depiction of for Cole-Cole plots of $[Co(NS_3^{iPr})Cl](BPh_4)$ for the slower relaxation processes. Reprinted with permission from reference[40]. Copyright 2015 Royal Society of Chemistry.

If the Cole−Cole plots suggest the coexistence of multiple relaxation pathways, the relaxation data should be modeled accounting for contributions from direct, Quantum Tunneling of the Magnetization (QTM), Raman, and Orbach relaxation processes. Those can be described by four consecutive terms in the following equation:

$$\tau^{-1} = AH^2T + \frac{B_1}{1+B_2H^2} + CT^n + \tau_0^{-1}\exp(-U/k_BT) \qquad (1.16)$$

where A, B_1, B_2, C, and n are coefficients, H is the applied dc magnetic field, T is the temperature, U is the thermal barrier of Orbach relaxation process, τ_0 is the attempt time, and k_B is the Boltzmann constant.[43]

1.2.6 Hysteresis and Quantum Tunneling of the Magnetization

SMMs may display hysteresis in the plot of magnetization *vs.* applied dc magnetic field (Figure 1.7) with an opening at zero dc magnetic field if the QTM pathway is not present. It is showed that the hysteresis loops of SMMs are marked differently from those of bulk traditional magnets in which coercive field increases with decreasing temperature and with increasing field sweep rate.[36] Owing to the molecular nature, SMMs exhibit some striking quantum effects that affect the magnetization reversal mechanism, and the most prominent is QTM,[31, 44-49] which produces the characteristic steps at the resonance fields in the hysteresis curve of SMMs, and these are different from the traditional superparamagnets.[19] The QTM phenomenon is the ability to reverse magnetic moment without going over the energy barrier (it tunnels through the barrier) between suitable sub-levels.[48] Because QTM only occurs when there is a coincidence of the energy of the m_s levels, the QTM steps only occur at some critical magnetic fields ($H = nD/g\mu_B$, $n = 1, 2 \ldots$) (Figure 1.8).

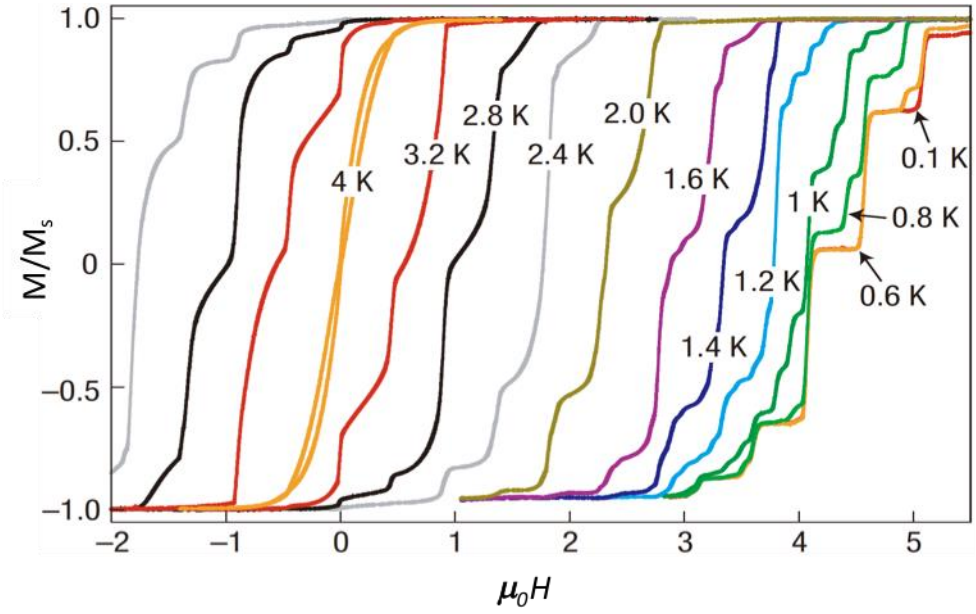

Figure 1.7. Heuristic depiction of dynamics of the magnetization. The Hysteresis loops of single crystals of $[Mn_{12}O_{12}(O_2CCH_2C(CH_3)_3)_{16}(CH_3OH)_4]$ SMM at different temperatures and a constant field sweep rate of 2 mT/s (data from reference[50]). The loops exhibit a series of steps, which are due to resonant quantum tunneling between energy levels. As the temperature is lowered, there is a decrease in the transition rate due to reduced thermally assisted tunneling. The hysteresis loops become temperature-independent below 0.6 K, demonstrating quantum tunneling at the lowest energy levels. Reprinted with permission from reference[19]. Copyright 2008 Nature Publishing Group.

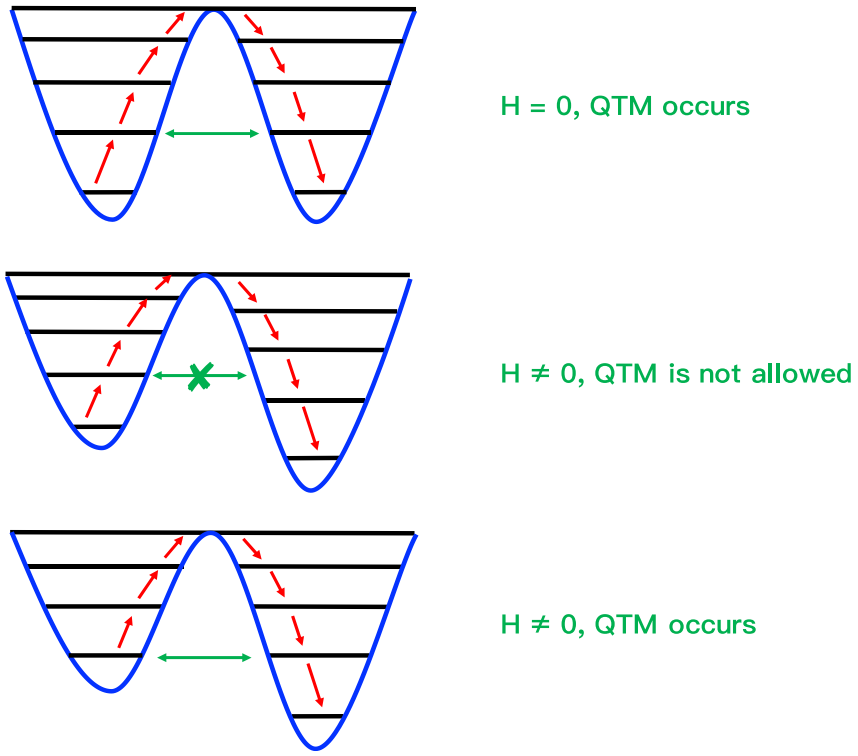

Figure 1.8. Heuristic schematic representation of the change in energy of m_s sublevels as the magnetic field is swept from zero to a non-zero value. Resonant magnetization tunneling occurs when the m_s sublevels are aligned between the two halves of the diagram.

1.2.7 Advantages and Outlook

SMMs have several advantages over traditional magnetic nanoparticles:

i) Easy Design and Synthesis. Chemically they could be synthesized with ease under mild reaction conditions, *i.e.* in solution at ambient temperature, in contrast to many traditional nanomagnets where high temperatures are usually not required.

ii) Good Solubility. They are truly soluble in organic solvents and water, not forming colloidal solutions as nanoparticles do, which allows deposition of the molecules evenly on a surface for potential applications.

iii) Easy Characterization. They can be crystallized, thus providing ordered arrays with (usually) a single orientation that can be well defined by single-crystal X-ray crystallography.

iv) Nanoscale Dimensions. They are a collection of truly monodisperse objects of nanoscale dimensions, even though interaction with a substrate may lead to some distortion from the crystallographic structure.

v) Well-Resolved Quantum Effects. Magnetically, they possess a single, well-defined ground-state spin and often display well-resolved quantum effects (*vide infra*).

SMMs have been proven to have intriguing properties and need to be explored further. At present, there are several research approaches employed in the SMM field:

i) Design synthesis of new SMMs with high energy barriers and blocking temperatures.[40, 51-56]

ii) Eliminating quantum tunneling.[57] Common strategies to reduce quantum tunneling include limiting rhombic anisotropy[58] and increasing the strength of magnetic coupling that act as a bias to avoid tunnelling.[54, 59, 60]

iii) Synthesis of SMMs in a controlled fashion to investigate different ideas of magnetism and quantum physics.[60-62]

iv) Achieving large coercive fields at high temperatures in the magnetic hysteresis experiments.[52]

v) Grafting of SMM on surfaces to study the possibility of using them for applications such as memories for ultra-dense devices.[19, 63, 64]

1.2.8 Magnetic Measurements and Data Analysis

To characterize the SMM behavior, several experiments need to be performed. Typically, since the source of SMM behavior is molecular, the crystal structure of the material should be collected via X-ray diffraction firstly. Secondly, magnetic susceptibility and magnetization data should be collected to attempt to determine the magnetic coupling parameter *J* between magnetic centers in the case of polynuclear complexes, and the spin state populations. And more importantly, it is necessary to measure the magnetic anisotropy: its magnitude and nature.

A Superconducting QUantum Interference Device (SQUID) is a very sensitive magnetometer used to measure extremely weak magnetic moments, based on superconducting loops containing Josephson junctions. In our laboratory, it's the SQUID XL7, which could measure the magnetic moment of a well-ground sample down to 1.8 K. By varying and extracting experimental parameters, we can obtain valuable information on the corresponding magnetic properties of a material.

Magnetization studies on a single crystal at very low temperatures using an array of Micro-SQUIDs[65, 66] give valuable information on the relaxation processes. They also allow for the hysteresis loop along the easy axis of magnetization to be measured at low temperature (down to 40 mK). This is a key-experiment for determining axial anisotropy and thus true SMM behavior.[31]

The magnetization *vs.* field and the susceptibility *vs.* temperature give also important information on the magnetic properties and particularly on the magnetic anisotropy of the compounds. It is not easy to have analytical expression for the magnetization when a molecule possesses magnetic anisotropy and when the measurement is carried out on a powder, because one must evaluate the magnetization for a statistical orientation of the anisotropy axes. This is usually done numerically. We will, however, give below the expression of the magnetization in the case of an isotropic sample, the Brillouin function.

In classical mechanics, when a sample is perturbed by an external magnetic field, its magnetization is related to its energy variation through

$$M = -\frac{\partial E}{\partial H} \qquad (1.17)$$

The molar magnetization weighted according to Boltzmann distribution laws which leads to[17]

$$M = \frac{N_A \sum_n (\partial E_n/\partial H) e^{-E_n/k_B T}}{\sum_n e^{-E_n/k_B T}} \qquad (1.18)$$

where M is the magnetization, N_A is Avogadro's number, E_n is the energy of quantum state $|n\rangle$, H is dc magnetic field, k_B is the Boltzmann constant. Equation (1.18) is considered the fundamental equation of molecular magnetism, as it does not lean on any approximations.[17] Although it is general, it is often difficult to apply. Indeed, it requires knowledge on the $E_n = f(H)$ variations for all thermally populated states to calculate the $\partial E_n/\partial H$ derivatives. To simplify the use of this equation, many of the equations described below are derived from equation (1.18) based on various assumptions and approximations,[17] such as the Van Vleck formula (equations (1.19, 1.20)) and the Brillouin function (equations (1.21-1.22)):

$$M = \frac{N_A H \sum_n (\frac{E_n^{(1)^2}}{k_B T} - E_n^{(2)}) e^{-E_n^{(0)}/k_B T}}{\sum_n e^{-E_n^{(0)}/k_B T}} \qquad (1.19)$$

$$\chi = \frac{N_A \sum_n (\frac{E_n^{(1)^2}}{k_B T} - E_n^{(2)}) e^{-E_n^{(0)}/k_B T}}{\sum_n e^{-E_n^{(0)}/k_B T}} \qquad (1.20)$$

$$M = N_A g \mu_B S[B_S(x)] \qquad (1.21)$$

$$B_S(x) = \frac{1}{S}[(S+\frac{1}{2})\coth\left(S+\frac{1}{2}\right)x - \frac{1}{2}\coth\left(\frac{x}{2}\right)] \qquad (1.22)$$

$$x = \frac{g\mu_B SH}{k_B T} \qquad (1.23)$$

where M is the magnetization, N_A is Avogadro's number, $E_n^{(0)}$ is the energy of level n in zero dc magnetic field, $E_n^{(1)}$ and $E_n^{(2)}$ are first- and second-order Zeemann coefficients, respectively,

k_B is the Boltzmann constant, g is the Landé-factor, μ_B is the Bohr magneton, S is the spin state and $B_S(x)$ is the Brillouin function proper and H is the dc magnetic field.

Now,

$$\coth(y) = \frac{1+\frac{1}{2}y^2+\cdots}{y+\frac{1}{6}y^3+\cdots} \cong \frac{\left(1+\frac{1}{2}y^2\right)\left(\frac{1}{y}\right)}{1+\frac{1}{6}y^2} \cong \left(\frac{1}{y}\right)\left(1+\frac{1}{2}y^2\right)\left(1-\frac{1}{6}y^2\right) \cong (\frac{1}{y})(1+\frac{1}{3}y^2)$$

or for small y,

$$\coth(y) = \frac{1}{y}+\frac{y}{3}$$

Thus, in the two cases, the limiting behaviors of the Brillouin function are:

i) For $x >> 1$, which is usually the case at large applied dc magnetic fields or low temperatures, the magnetization can be simplified

$$B_S(x) = \frac{1}{S}[(S+\frac{1}{2})-\frac{1}{2}] = 1$$

$$M = N_A g \mu_B S \qquad (1.24)$$

which corresponds to when the magnetic signal is saturated.

i) For $x << 1$,

$$B_S(x) = \frac{1}{S}[(S+\frac{1}{2})\frac{1}{\left(S+\frac{1}{2}\right)x}+\frac{1}{3}\left(S+\frac{1}{2}\right)x] - \frac{1}{2}(\frac{2}{x}+\frac{x}{6})]$$

$$= \frac{1}{S}[\frac{1}{3}\left(S+\frac{1}{2}\right)^2 x - \frac{1}{12x}] = \frac{x}{3S}\left(S^2+S+\frac{1}{4}-\frac{1}{4}\right) = \frac{x(S+1)}{3}$$

In fact, $g\mu_B H/k_B T << 1$,

$$M = N_A g \mu_B S \frac{x(S+1)}{3} = N_A g \mu_B S \frac{g\mu_B H(S+1)}{3k_B T} = \frac{N_A g^2 \mu_B{}^2 S(S+1)}{3k_B T} H \qquad (1.25)$$

$$\chi = \frac{M}{H} = \frac{N_A g^2 \mu_B{}^2 S(S+1)}{3k_B T} = \frac{g^2 S(S+1)}{8T} \qquad (1.26)$$

$$\chi T = \frac{M}{H} T = \frac{N_A g^2 \mu_B{}^2 S(S+1)}{3k_B} \qquad (1.27)$$

which is commonly the situation when the Curie law is observed.[16] Actually, equation (1.25) is the simplified Van Vleck equation[30] at low applied dc magnetic fields and high temperatures, in general, it can be used to describe the dc susceptibility data for well isolated single-spin paramagnets or for polynuclear complexes at high temperatures.

 Feng SHAO: 0000-0001-8606-8628

1.2.9 The First SMM: $Mn_{12}(OAc)$

The first studied SMM is the $Mn^{III}_8Mn^{IV}_4O_{12}(O_2C_2H_3)_{16}(H_2O)_4$ complex (Figure 1.9), commonly called $Mn_{12}(OAc)$.[31] Lis *et al*. synthesized this molecule in 1980.[67] The main structural features of this complex are eight Mn^{III} ions surrounding a Mn^{IV}-oxo cubane core (Figure 1.9).

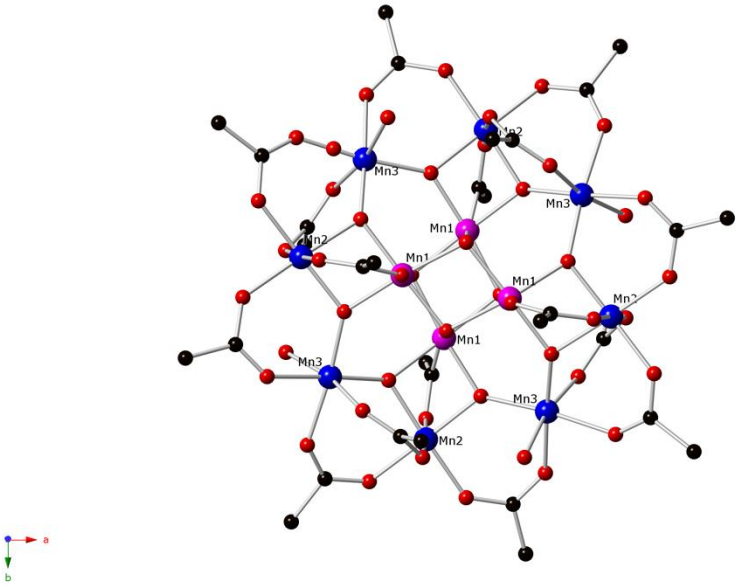

Figure 1.9. Crystal structure of $Mn^{III}_8Mn^{IV}_4O_{12}(O_2C_2H_3)_{16}(H_2O)_4$. Mn^{IV} – purple; Mn^{III} – blue; O – red; C – black; H atoms were omitted for clarity. The figure was reproduced from a crystal structure from reference[67]. Copyright 1980 International Union of Crystallography.

In 1991, Caneschi *et al.* studied the magnetic properties that revealed a ground spin state S = 10 and frequency dependence in the ac susceptibility plot (Figure 1.10).[26] A maximum of χ_M" was found at 7 K at a frequency of 500 Hz.

In 1993, a follow-up paper in Nature by Sessoli *et al*. discovered that the complex displayed a magnetic hysteresis, like a bulk ferromagnet (Figure 1.11). In ferromagnets, hysteresis originates from moving Bloch walls.[27] However, in the case of $Mn_{12}(OAc)$, the source of this hysteresis was different from that of bulk ferromagnets.[27]

In 1998, Hill *et al*. did the single crystal Electron Paramagnetic Resonance (EPR) measurements of $Mn_{12}(OAc)$. They found that the D value was –0.47 cm^{-1}, thus confirming that D was negative and supporting the ground spin state spin sub-levels was ±10, The energy barrier was determined to be 44.5 cm^{-1}.[68]

Feng SHAO: 0000-0001-8606-8628

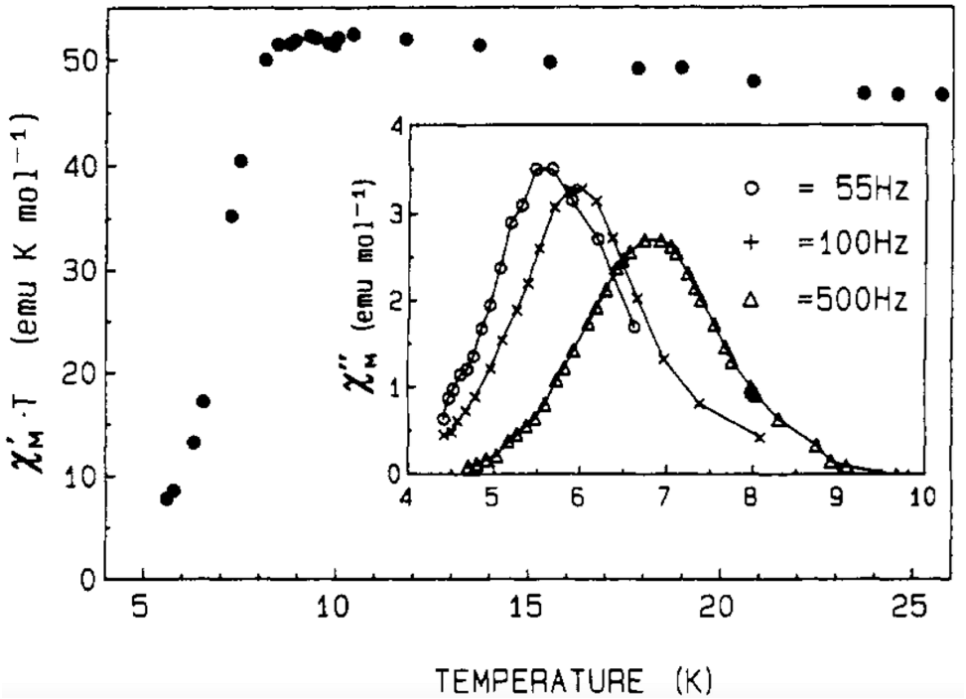

Figure 1.10. The ac magnetic susceptibility data for Mn_{12}(OAc) is shown. The inset features the out-of-phase magnetic susceptibility, indicating frequency dependence. Taken directly from reference[26]. Copyright 1993 American Chemical Society.

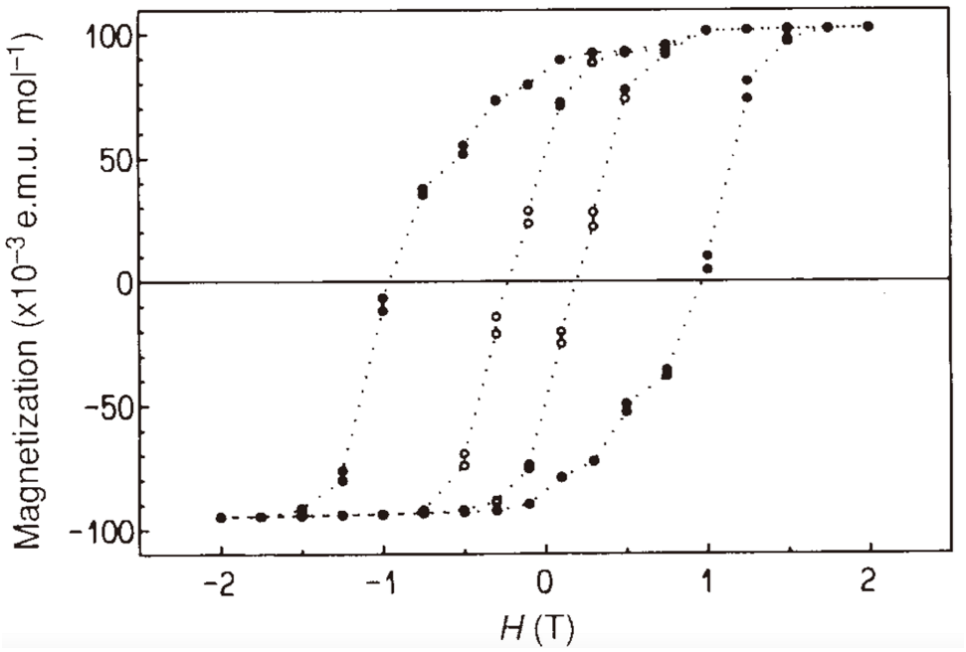

Figure 1.11. The dc magnetic hysteresis of Mn_{12}(OAc) is shown. The data was collected along the crystal *c* axis. The closed circles represent data collected at 2.2 K, and the open circles for data collected at 2.8 K. Taken directly from reference[27]. Copyright 1993 Nature Publishing Group.

1.3 Single Ion Magnets:

Single Ion Magnets (SIMs) are SMMs made from mononuclear complexes rather than polynuclear one. Alternatively, they can be called Mononuclear Single-Molecule Magnets (MSMMs).[69, 70] Monometallic SMM is probably better but herein, we have chosen to use the SIM acronym rather than e.g. MSMM, which is more awkward.[69]

1.3.1 Why the focus shift from SMMs to SIMs?

Since the birth of SMMs, more and more scientists focus on increasing the effective energy barrier (U_{eff}) and the blocking temperature (T_B). Early studies that focused on obtaining high ground spin state S led to a vast effort towards building complexes with the highest possible nuclearity in order to maximize the effective energy barrier. However, several theoreticians pointed out that the stumbling block encountered was that D itself was found to be inversely proportional to S^2.[71-73] In other words, incorporating large numbers of paramagnetic centers into a molecule is probably counterproductive in terms of generating large cluster anisotropies ($D_{cluster}$).[74] Another issue is that the anisotropy axis for a given ion within a polymetallic complex is not aligned with that of another ion within the same complex, leading to a diminished overall anisotropy.[69, 75] For example, even in the approximately isostructural $[Mn^{III}_3O(Rsao)_3(X)(sol)_{3–4}]$ (where R = H, Me, ^{t}Bu; X = O_2CR (sao = salicylaldoxime, R = H, Me, Ph etc.); sol = py and/or H_2O) family of SMMs, $D_{cluster}$ values of the ferromagnetically coupled S = 6 analogues are measurably smaller than the antiferromagnetically coupled S = 2 ones.[74, 76]

By employing a single ion, this scenario would be avoided providing the chemist is able to generate large anisotropy within the mononuclear complexes that would lead to high values of both U_{eff} and T_B.[74] However, because the spin will be lower than in polynuclear complexes, quantum effect may dominate. There are many nice reports of SIMs based on lanthanide systems since the properties of $[LnPc_2](NBu_4)$, (Pc = pthalocyanine; Ln = Tb, Dy; NBu_4 = tetrabutylammonium), were reported by Ishikawa and co-workers in 2003 (*vide infra*).[77] The origin of the large blocking temperatures in lanthanide based SIMs is the large magnetic anisotropy due to the large spin orbit coupling. The drawback in lanthanide molecules is the contraction the f electrons that preclude controlling their anisotropy by the ligand fields. While for the transition metal ions based complexes the symmetry can be better controlled even though their anisotropy is not as large as for lanthanides.

1.3.2 Important Transition Metal SIMs

The first 3d SIM: K[(tpa^{Mes})Fe^{II}]

The first transition metal SIM was the four-coordinated trigonal pyramidal high spin Fe^{II} compound K[(tpa^{Mes})Fe] (H_3tpa^{Mes} = Tris((5-mesityl-1*H*-pyrrol-2-yl)methyl)amine).[78] The Fe^{II} ion lies in a trigonal pyramidal geometry, with an N_4 coordination sphere (Figure 1.12). Magnetization measurements and fits at different temperatures led to D = –39.6 cm^{-1}, together with a small rhombic contribution, E = –0.4 cm^{-1}. This transverse contribution arises from a small structural distortion around the Fe^{II} ion, which reduces the three-fold symmetry. No out-of-phase signal for the ac magnetic susceptibility could be detected under an applied zero dc magnetic field. When a dc magnetic field of 1500 Oe was applied, a blocking of the magnetization was observed leading to U_{eff} = 42 cm^{-1} (Figure 1.13). This value was much lower than the theoretical energy barrier value $U = S^2|D|$ = 4 × 39.6 = 158 cm^{-1} due to tunneling and direct pathways for the relaxation of the magnetization. Several derivatives of tpa (tpa = tris(2-pyridylmethyl)amine) with similar geometries of Fe^{II} were reported later.[79]

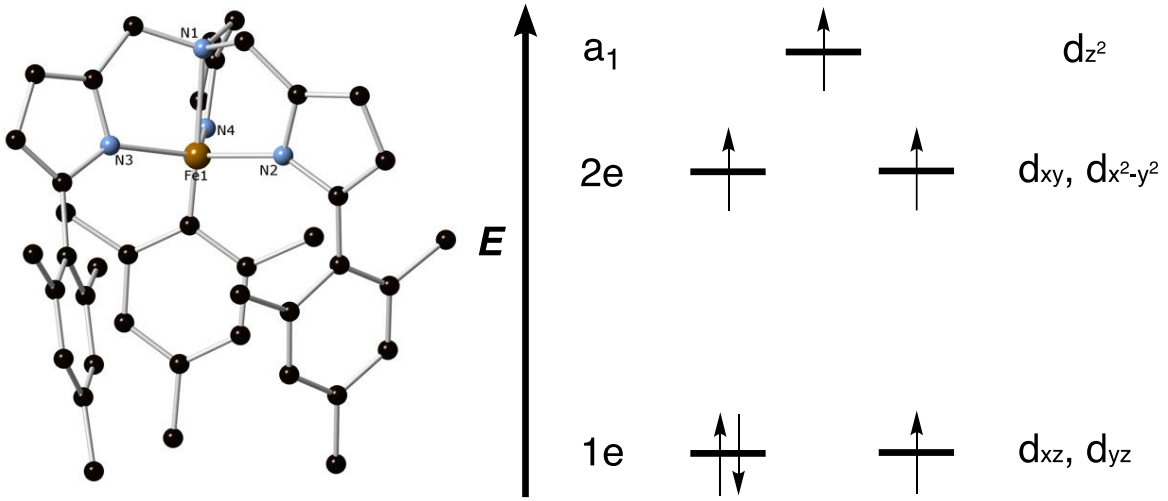

Figure 1.12. A view of the anion [(tpaMes)Fe]$^-$ (left). C – black; H atoms were omitted for clarity; a simplified view of the orbital splitting (right). Reprinted with permission from reference[78]. Copyright 2010 American Chemical Society.

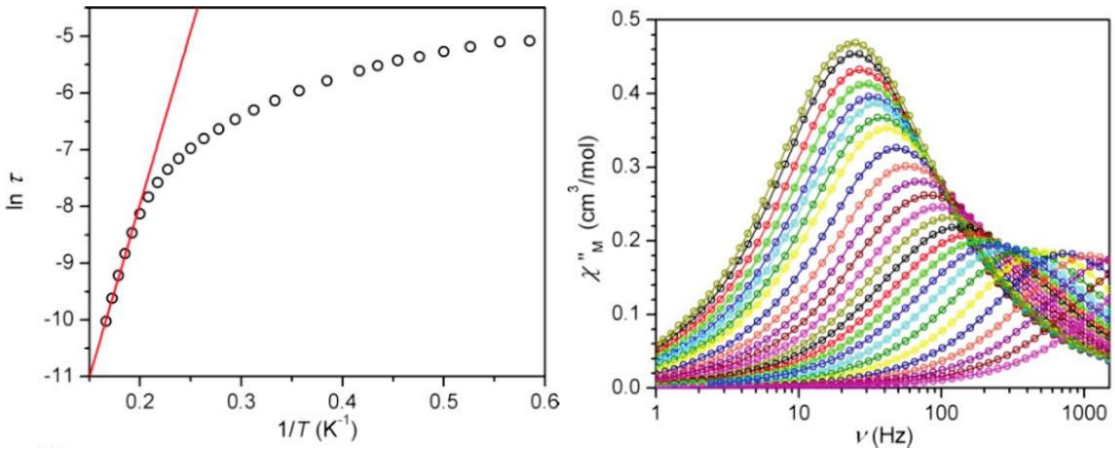

Figure 1.13. Arrhenius plot constructed from data obtained under an applied dc magnetic field of 1500 Oe. The solid red line corresponds to a linear fit to the thermally activated region(left); Variable-frequency out-of-phase ac susceptibility data K[(tpa^{Mes})Fe] (right). Reprinted with permission from reference[78]. Copyright 2010 American Chemical Society.

(Ph$_4$P)[Mn^{III}(opbaCl$_2$)(py)$_2$]

The (Ph$_4$P)[Mn(opbaCl$_2$)(py)$_2$] complex, where H$_4$opbaCl$_2$ = N,N'-3,4-dichloro-o-phenylenebis-(oxamic acid), py = pyridine, and Ph$_4$P = tetraphenylphosphonium, was reported by Vallejo and co-workers in 2013,[80] it exhibits a SIM behavior under an applied dc magnetic field. The complex contains an axially elongated Mn^{III} ion, with a mixed N_2O_2 donor set in the equatorial positions, provided by the ligand, and two axial N atoms provided by pyridine molecules (Figure 1.14). A high field/frequency EPR (HFEPR) powder study was performed yielding a value for the ZFS of D = 3.421(2) cm^{-1} and a transverse component E of 0.152(2) cm^{-1}, and the fit of the dc magnetization data gave D = 3.27 cm^{-1}, E = 0.11 cm^{-1} (E/D almost equal 0.33) and for g = 1.99. Ac magnetic susceptibility measurements revealed SIM behavior under an applied dc magnetic field of 1000 Oe, with a calculated effective barrier for magnetization orientation, U_{eff} = 18 K (12.5 cm^{-1}) (Figure 1.15 left). Measurements of a single crystal using a Micro-SQUID (Figure 1.15 right) reveal closed hysteresis loops at zero dc magnetic field, due to the fast QTM, consistent with the absence of out-of-phase signals at zero dc magnetic field. The absence of an opening of the hysteresis loop at zero dc magnetic field is due, among other things, to the presence of the transverse anisotropy E that mixes the m_s sub-levels wave functions and create a pathway for relaxation by quantum tunneling.

Feng SHAO: 0000-0001-8606-8628

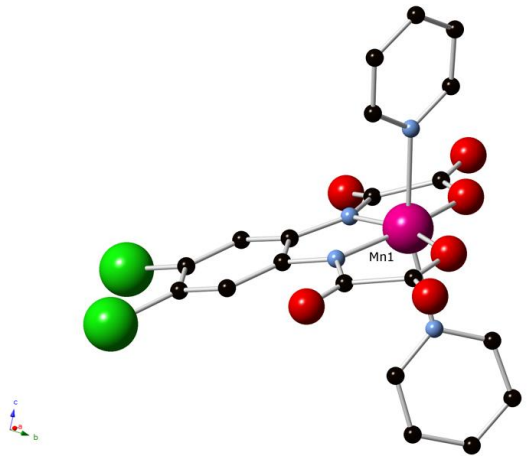

Figure 1.14. A view of the complex $[Mn(opbaCl_2)(py)_2]^-$. N – blue; O – red; Cl – green; C – black; H atoms were omitted for clarity. Reprinted with permission from reference[80]. Copyright 2013 Wiley-VCH Verlag GmbH & Co. KGaA, Weinheim.

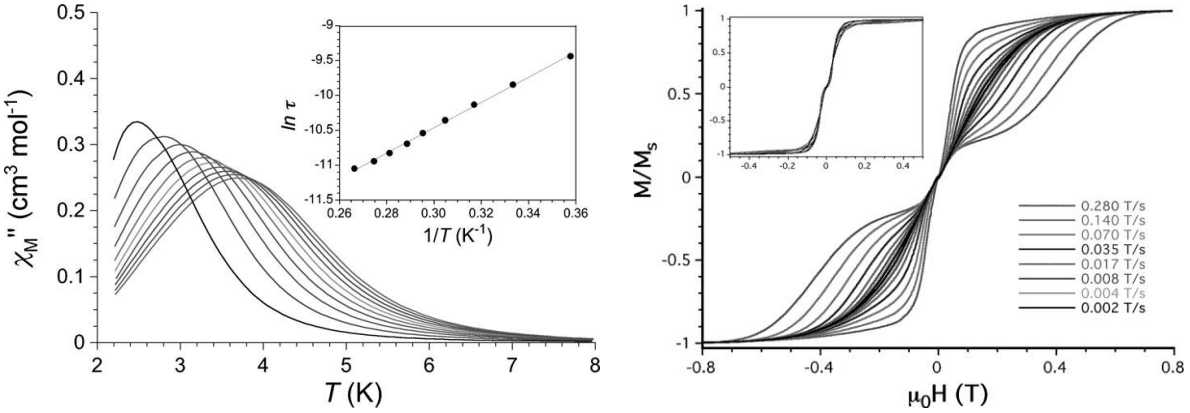

Figure 1.15. Temperature dependence of the out-of-phase magnetic susceptibility under an applied dc magnetic field of 1000 Oe and 4 Oe oscillating field (left, inset: Arrhenius plot), and, the sweep rate dependence of the magnetization at 0.5 K (right, inset: at 0.03 K). Reprinted with permission from reference[80]. Copyright 2013 Wiley-VCH Verlag GmbH & Co. KGaA, Weinheim.

[K(crypt-222)][Fe^{I}(C(SiMe$_3$)$_3$)$_2$]

The two-coordinated linear Fe^{I} complex [K(crypt-222)][Fe(C(SiMe$_3$)$_3$)$_2$] was reported by Zadrozny and co-workers in 2013 (Figure 1.16).[81] Fe^{I} has a half-integer spin of S = 3/2 the same as for Co^{II}. According to Kramers' theorem, QTM should be minimized in such half-integer systems, which should show slow relaxation of the magnetization, even in the absence of an applied dc magnetic field. *Ab initio* calculations confirmed the success of the strategy that consists in reducing the ligand field around the metal center, as well as indicating large energy splitting of the m_s sublevels, which should lead to a significant energy barrier. Ac alternating current magnetic susceptibility measurements reveal slow magnetic relaxation

below 29 K at zero dc magnetic field (Figure 1.17 left) and an effective spin-reversal barrier of U_{eff} = 226(4) cm^{-1} (Figure 1.17 right), pretty large observed for a SMM based on a transition metal. The blocking of the magnetization is observed below 4.5 K and the hysteresis loops (Figure 1.18) collected at an average sweep rate of 50 Oe/s is open only in the presence of an applied magnetic field. This feature results from the presence of tunneling pathways for the magnetization despite the large energy barrier values (Figure 1.17 left).

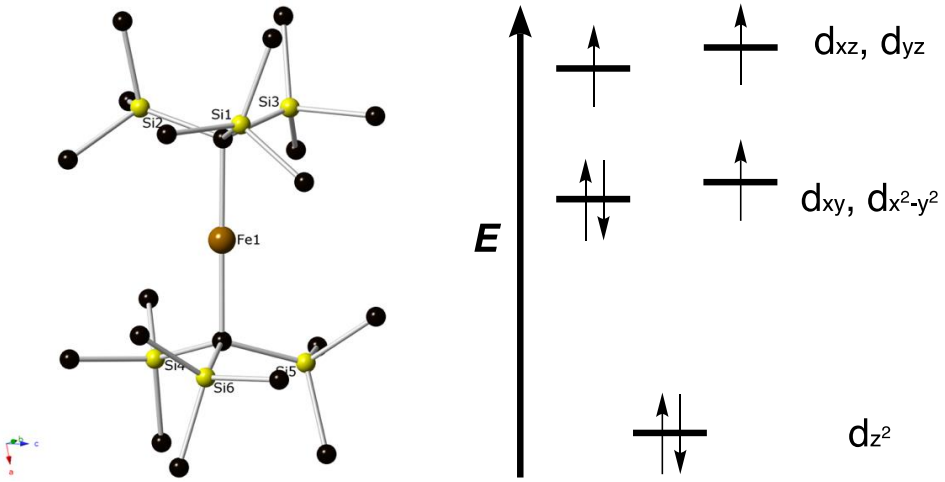

Figure 1.16. A view of the complex $[Fe(C(SiMe_3)_3)_2]^-$ (left). C – black; H atoms were omitted for clarity. Energies of the 3d orbitals extracted from an *ab initio* computational analysis of $[Fe(C(SiMe_3)_3)_2]^-$ (right). Reprinted with permission from reference[81]. Copyright 2013 Nature Chemistry, Macmillan Publishers Ltd.

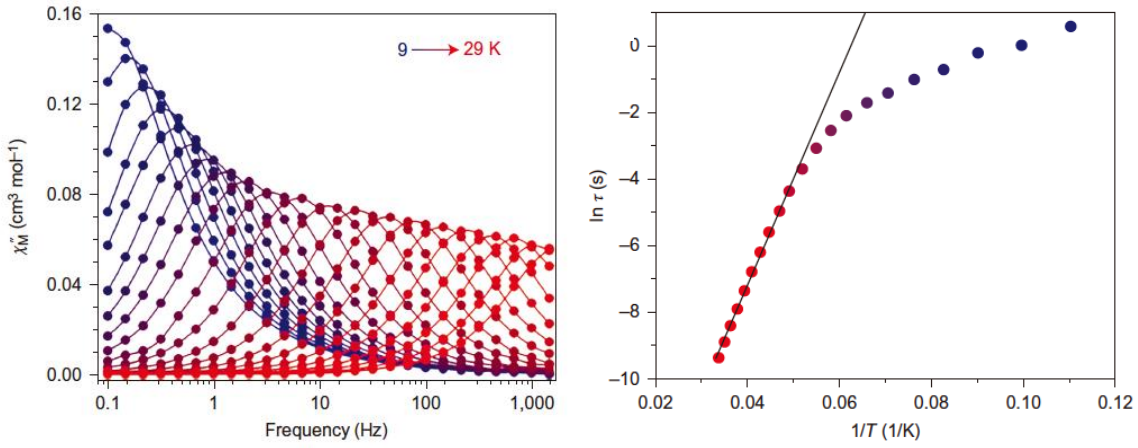

Figure 1.17. Dynamic magnetic susceptibility data for the complex [K(crypt-222)][Fe(C(SiMe$_3$)$_3$)$_2$], measured under an applied zero dc magnetic field (left); Arrhenius plot of the natural logarithm of the relaxation time, τ, *vs.* the inverse temperature (right). Reprinted with permission from reference[81]. Copyright 2013 Nature Chemistry, Macmillan Publishers Ltd.

Feng SHAO: 0000-0001-8606-8628

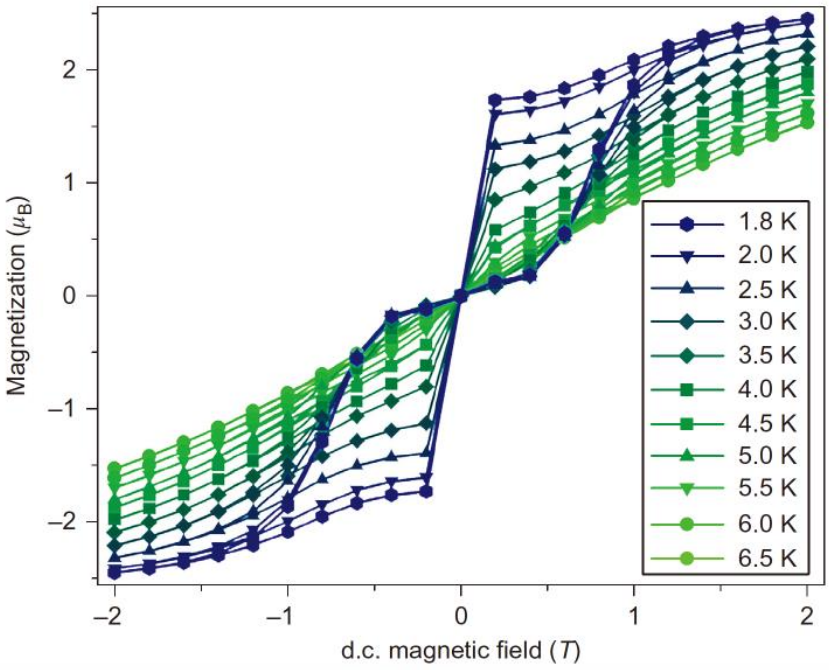

Figure 1.18. Variable-field magnetization data for the complex [K(crypt-222)][Fe(C(SiMe$_3$)$_3$)$_2$. Reprinted with permission from reference[81]. Copyright 2013 Nature Chemistry, Macmillan Publishers Ltd.

[Fe^{II}(1-ptz)$_6$](BF$_4$)$_2$

An interesting application recently proposed for a specific polymorph of the compound [Fe(1-ptz)$_6$](BF$_4$)$_2$ (where ptz is propyltetrazole, Figure 1.19) complex, which is a classic spin crossover (SCO) compound that behaves as an SMM when driven from the diamagnetic Low Spin (LS, S = 0) state to the paramagnetic High Spin (HS, S = 2) state at low temperature upon light irradiation in the solid state.[82] The local symmetry of the Fe^{II} ions gives rise to an axial magnetic anisotropy: HFEPR data gives D = –14.8 cm^{-1}, together with a transverse component of E = –0.95 cm^{-1}. The effective barrier to reorientation of the magnetization under an applied dc magnetic field of 2000 Oe, is 15 cm^{-1} extracted according to the Arrhenius law (Figure 1.20). The ability to turn the SIM behavior on and off by photo-switching between the HS and LS states is a way to address them (Figure 1.21).[69, 83]

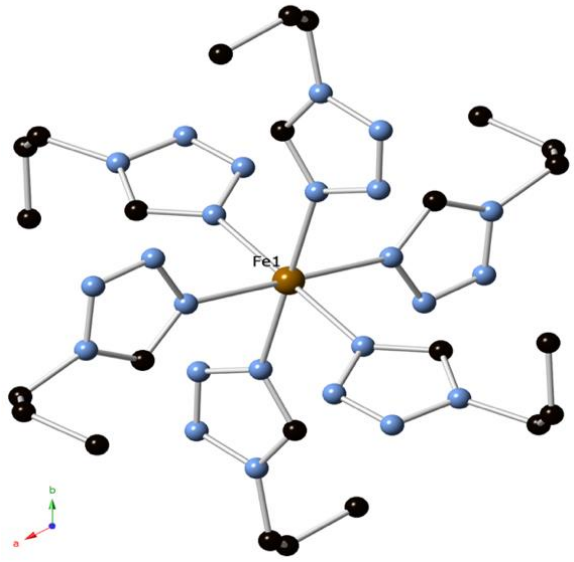

Figure 1.19. A view of the complex $[Fe(1\text{-ptz})_6]^{2+}$. N – blue; C – black; H atoms were omitted for clarity. Reprinted with permission from reference[83]. Copyright 2013 American Chemical Society.

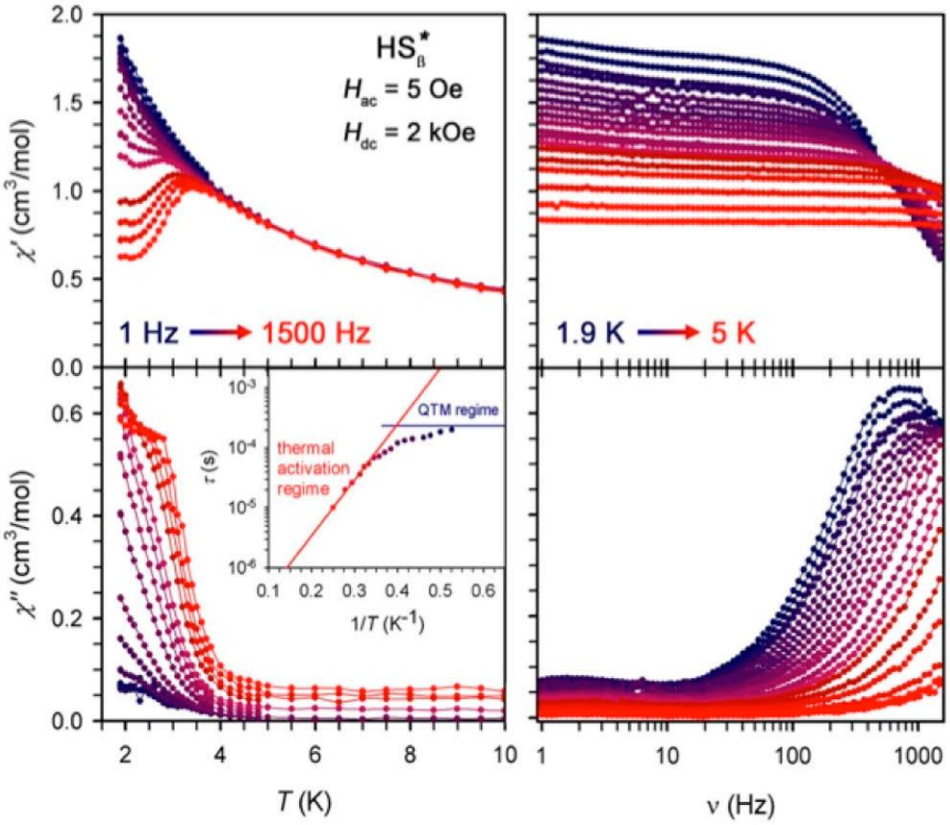

Figure 1.20. Dynamic magnetic susceptibility data for the complex $[Fe(1\text{-ptz})_6](BF_4)_2$, for HS_β* at oscillating frequencies between 1 and 1500 Hz and temperatures between 1.9 and 5 K. Arrhenius plot of the natural logarithm of the relaxation time, τ, *vs.* the inverse temperature (inset). Taken directly from reference[83]. Copyright 2013 American Chemical Society.

 Feng SHAO: 0000-0001-8606-8628

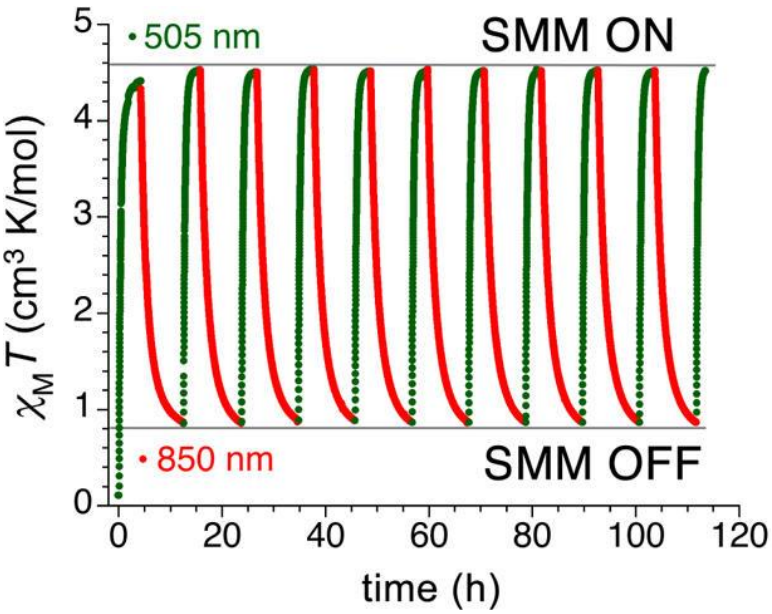

Figure 1.21. Excitation and de-excitation cycling between the HS and LS configuration of $[Fe(1\text{-ptz})_6](BF_4)_2$, represented as a variation in the $\chi_M T$ product at 10 K, under a 5000 Oe dc magnetic field. Taken directly from reference[83]. Copyright 2013 American Chemical Society.

[(PNP)Fe^{III}Cl$_2$]

The $[(PNP)FeCl_2]$ (PNP = N[2-P(CHMe$_2$)$_2$-4-methylphenyl]$_2$, Figure 1.22) complex which also exhibits a thermal SCO transition from S = 5/2 to 3/2 was reported in 2012 by Mossin and co-workers.[84] The ac SQUID data (Figure 1.23), at zero dc magnetic field and between frequencies 10 and 1042 Hz, clearly reveal that $[(PNP)FeCl_2]$ have frequency dependence of the out-of-phase signal and thus a SMM behavior with a thermally activated barrier of U_{eff} = 32 – 36 cm^{-1}.[84]

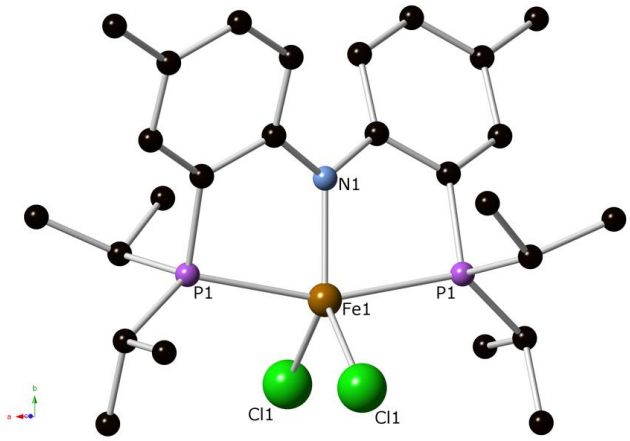

Figure 1.22. A view of the complex $[(PNP)FeCl_2]$. C – black; H atoms were omitted for clarity. Reprinted with permission from reference[85]. Copyright 2012 American Chemical Society.

Feng SHAO: 0000-0001-8606-8628

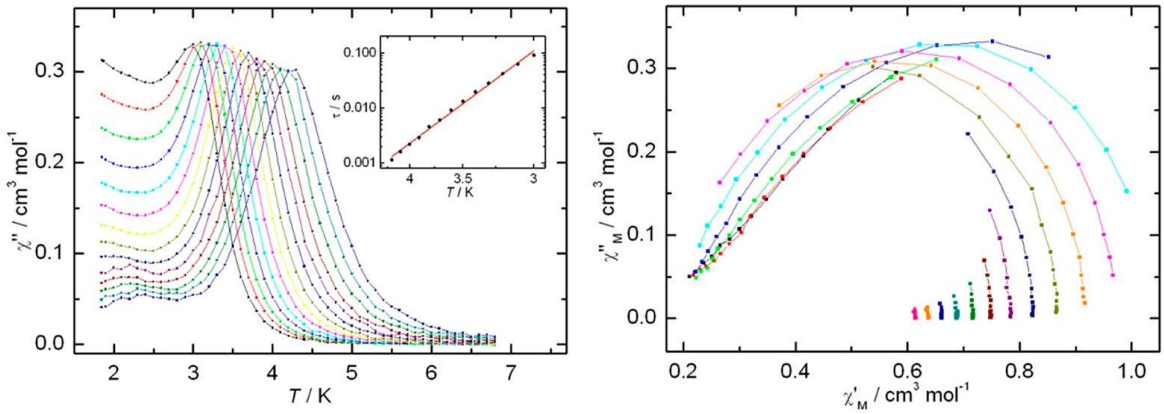

Figure 1.23. Dynamic magnetic susceptibility (left) and Cole-Cole plots (right) data for the complex [(PNP)$FeCl_2$] under an applied zero dc magnetic field, and Arrhenius plot of the natural logarithm of the relaxation time, τ, *vs.* the inverse temperature (inset). Reprinted with permission from reference[85]. Copyright 2012 American Chemical Society.

[Co^{I}(IMes)$_2$](BPh$_4$)

The [Co^{I}(IMes)$_2$](BPh$_4$) (IMes: 1,3-dimesitylimidazol-2-ylidene, Figure 1.24) complex represents an example of less reported d^8 SIM. It bears nearly linear C(carbene)–Co–C(carbene) alignment mode. The SIM behavior was observed under a 2000 Oe dc magnetic field with the effective energy barrier U_{eff} = 21.3 cm^{-1} (Figure 1.25). Magnetic anisotropy analysis indicates an easy plane of magnetization. It was, thus, concluded that the Raman process is probably responsible of the observed blocking of the magnetization instead of the Orbach one, as expected for genuine SIMs.[86, 87]

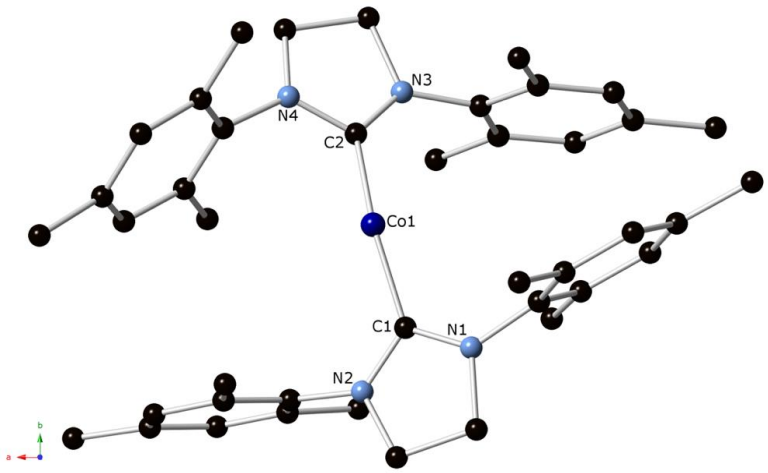

Figure 1.24. A view of the complex [Co(IMes)$_2$]$^+$. C – black; H atoms were omitted for clarity. Reprinted with permission from reference[87]. Copyright 2015 The Royal Society of Chemistry.

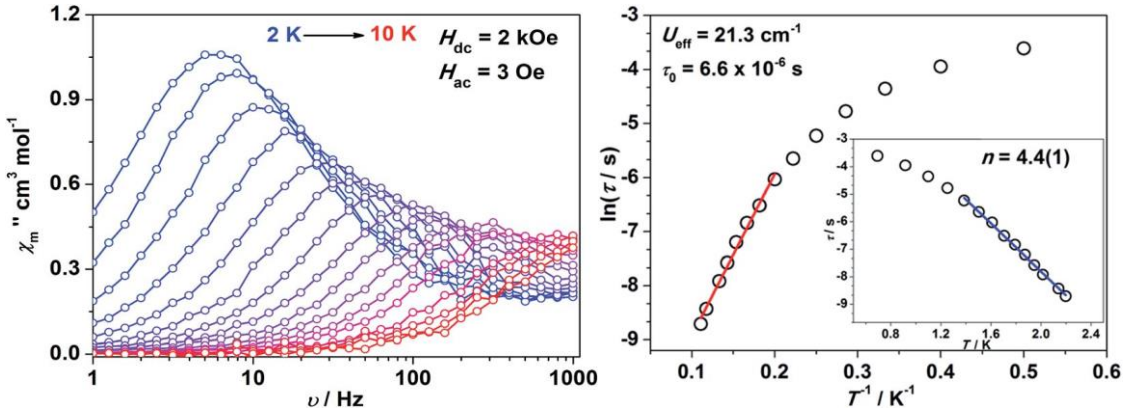

Figure 1.25. Dynamic magnetic susceptibility data for the complex[Co(IMes)$_2$](BPh$_4$) (left), and Arrhenius plot of the natural logarithm of the relaxation time, τ, *vs.* the inverse temperature (right). Reprinted with permission from reference[87]. Copyright 2015 The Royal Society of Chemistry.

[Co^{II}(terpy)Cl$_2$] and [Co^{II}(terpy)(NCS)$_2$]

[Co(terpy)Cl$_2$] and [Co(terpy)(NCS)$_2$] (terpy = terpyridine, Figure 1.26) were reported by Habib and co-workers in 2013.[74, 88] These systems have the tridentate terpy ligand coordinated to Co^{II}, with the remaining two coordination sites occupied by monodentate Cl or NCS ligands. Ac susceptibility measurements (Figure 1.27) under an applied dc magnetic field for both [Co(terpy)Cl$_2$] and [Co(terpy)(NCS)$_2$] leads to U_{eff} = 28 K (600 Oe), 4K (5600 Oe) and 17 K (600 Oe), 3K (5600 Oe), respectively, according to the Arrhenius law.

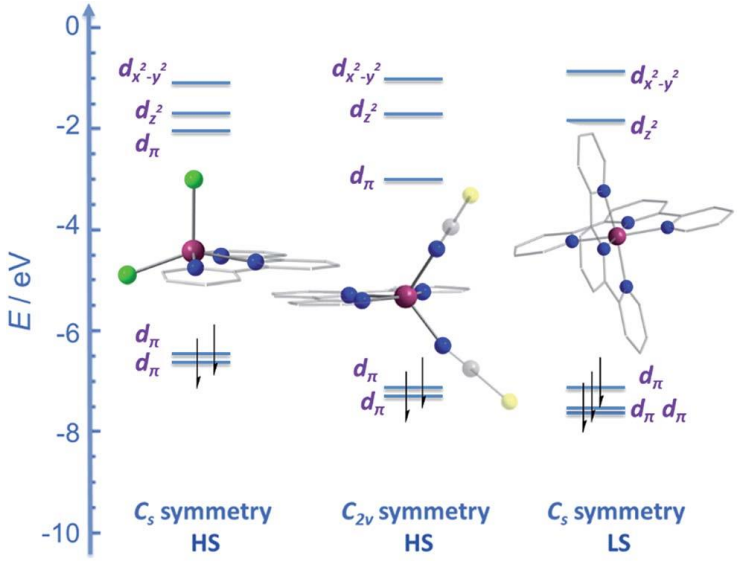

Figure 1.26. Energy level diagram depicting selected β-spin frontier molecular orbitals of [Co(terpy)Cl$_2$] and [(Co(terpy)(NCS)$_2$)] and [Co(terpy)$_2$]$^{2+}$. The increase in the number of β-spins for [Co(terpy)$_2$]$^{2+}$ comes at the cost of an α-spin, resulting in an overall decrease in the molecular spin state. Taken directly from reference[74]. Copyright 2016 The Royal Society of Chemistry.

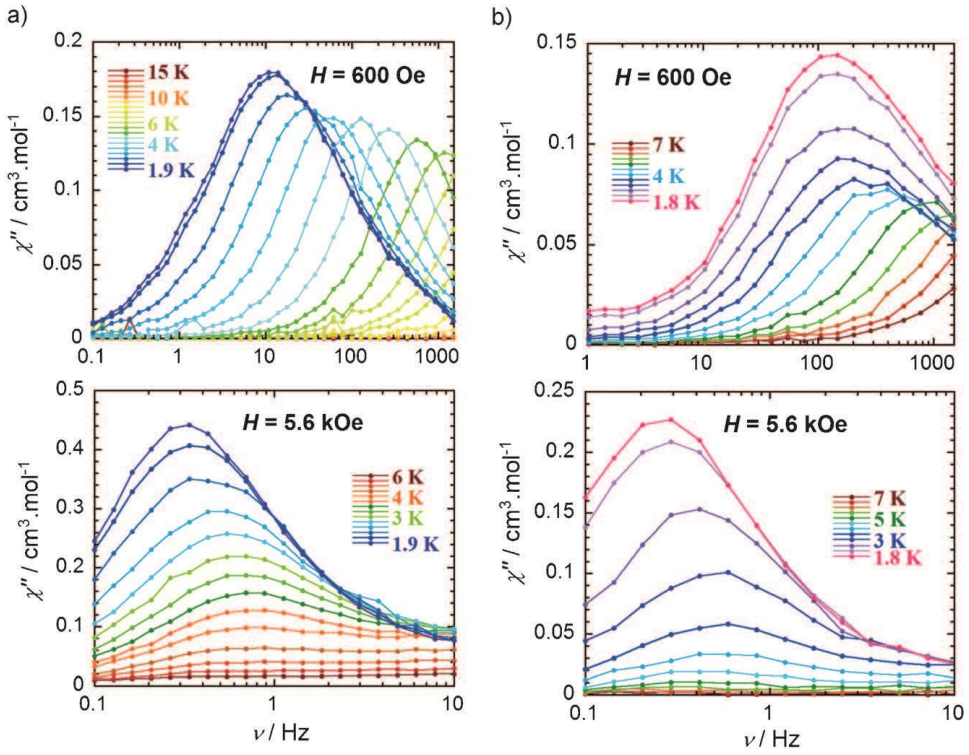

Figure 1.27. Dynamic magnetic susceptibility data for the complexes [Co(terpy)Cl_2] (left) and [(Co(terpy)$(NCS)_2$)] (right). Taken directly from reference[88]. Copyright 2013 Wiley-VCH Verlag GmbH & Co. KGaA, Weinheim.

[Co^{II}(12C4)$_2$](I_3)$_2$(12C4)

Intriguingly, an eight-coordinated Co^{II} ([Co^{II}(12C4)$_2$](I_3)$_2$(12C4)) (12C4 = 12-Crown-4, Figure 1.28) complex has been reported to exhibit SIM properties in 2014 by Chen and co-workers.[89] The Co^{II} ion is coordinated to four oxygen atoms from the two crown molecules, leading to a distorted square anti-prismatic geometry, which is the first eight-coordinated 3d mononuclear complex to show a slow relaxation of the magnetization. The fits of the magnetic data give values of D = –37.6 cm^{-1} and E = 0.1 cm^{-1}, with a rather modest U_{eff} = 17 cm^{-1} (under an applied dc magnetic field of 500 Oe, Figure 1.29). Single-crystal dc magnetization measurements were performed using a Micro-SQUID (Figure 1.30), a field sweep rate and a temperature-dependent hysteresis loops were observed, suggesting the complex is a real SMM. An opening of the hysteresis loop was observed below 1 K when the magnetic field was different from zero, the loop width increases with increasing sweep rate and decreasing temperature. However, the loop at 0.03 K is smaller than those at 0.1 − 0.5 K, which poses questions about the genuine SIM nature of this complex.[89]

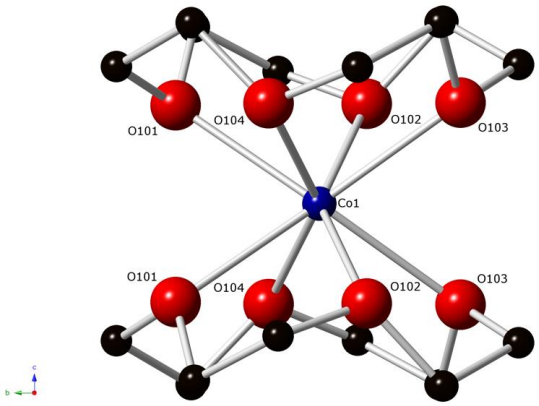

Figure 1.28. A view of the complex $[Co(12C4)_2](I_3)_2$. C – black; and H atoms were omitted for clarity. Reprinted with permission from reference[89, 90]. Copyright 2011 American Chemical Society.

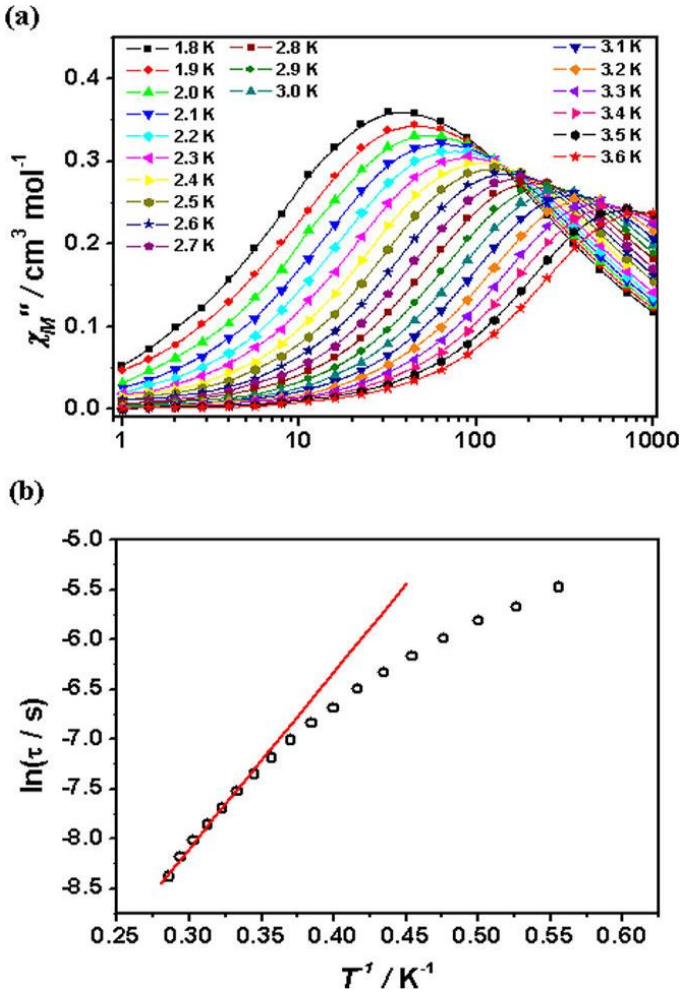

Figure 1.29. Dynamic magnetic susceptibility data for the complex $[Co(12C4)_2](I_3)_2]$ (12C4) (top), and Arrhenius plot of the natural logarithm of the relaxation time, τ, *vs.* the inverse temperature (bottom). Taken directly from reference[89]. Copyright 2014 American Chemical Society.

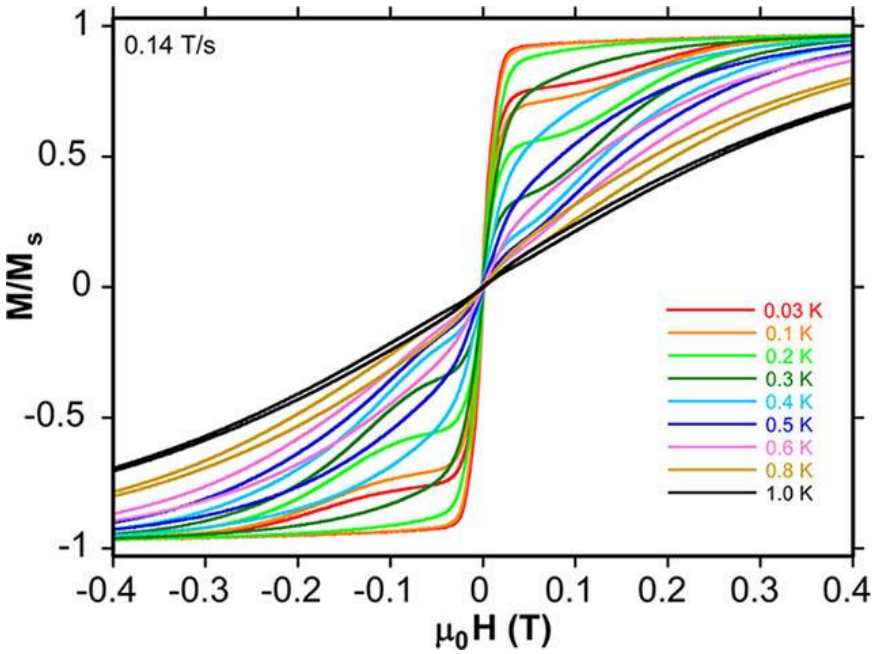

Figure 1.30. Field dependence of the normalized magnetization in the temperature range 0.03 – 1 K at field sweep rate 0.14 T/s for the complex $[Co(12C4)_2](I_3)_2]$ (12C4), Taken directly from reference[89]. Copyright 2014 American Chemical Society.

$[Co^{II}(SPh)_4](Ph_4P)_2$

$[Co(SPh)_4](Ph_4P)_2$ is notable example of a system showing slow relaxation in the absence of an applied dc magnetic field, reported by Long and co-workers in 2011.[91] The tetrahedral complex (Figure 1.31), has an $S = 3/2$ ground state with an axial ZFS of $D = –70$ $cm^{–1}$, and relatively low rhombicity with $E/D < 0.09$. It displays an out-of-phase susceptibility signal in the absence of an applied dc magnetic field (Figure 1.32), which is quite rare for mononuclear transition ion complexes. At very low temperatures, ac magnetic susceptibility data show the magnetic relaxation time, τ, to be temperature-independent, while above 2.5 K thermally activated Arrhenius behavior is apparent with $U_{eff} = 21(1)$ $cm^{–1}$ and $\tau_0 = 1.0(3) \times 10^{–7}$ s (Figure 1.32). Under an applied dc magnetic field of 1000 Oe, τ more closely approximates an Arrhenius behavior over the entire temperature range.[91]

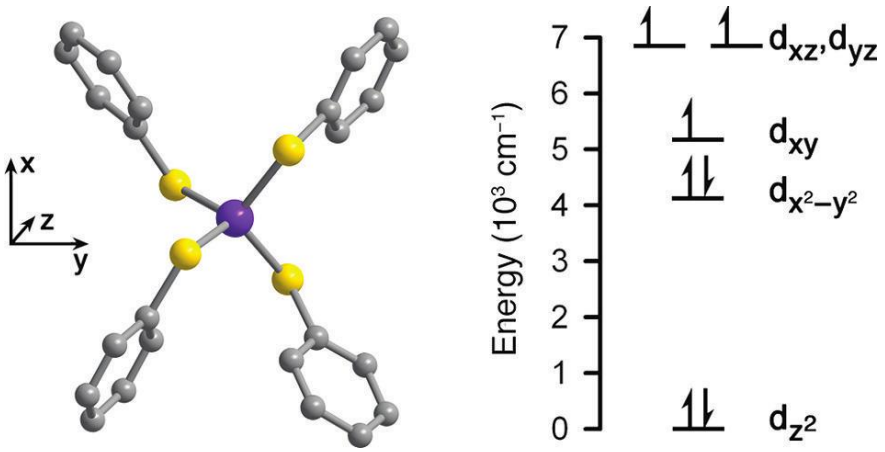

Figure 1.31. A view of the complex $[Co(SPh)_4]^{2-}$. Co – purple; S – yellow; C – grey; H atoms were omitted for clarity (left). Electronic configuration and d-orbital energy level splitting for the molecule, with energies derived using the angular overlap model (right). Taken directly from reference[91]. Copyright 2011 American Chemical Society.

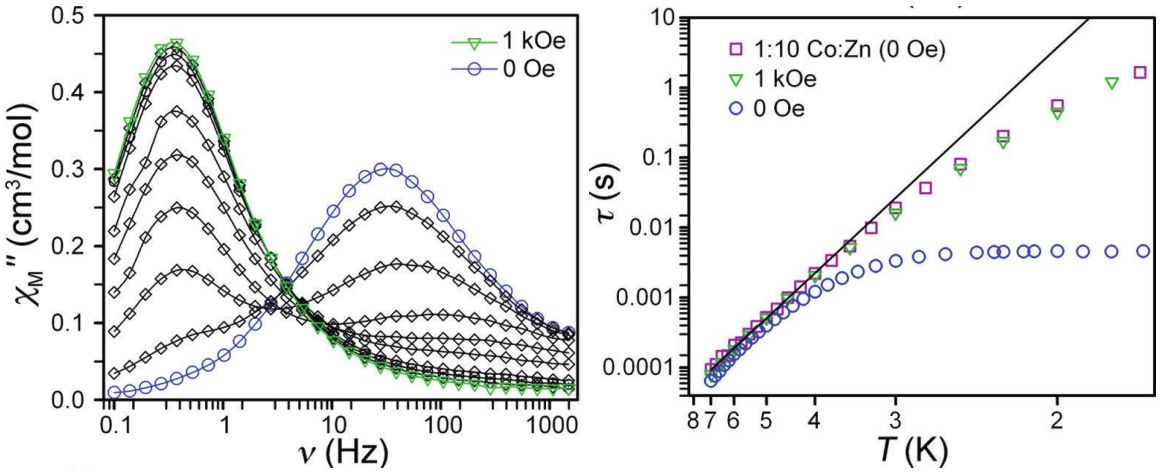

Figure 1.32. Molar out-of-phase ac susceptibility collected at 2 K under applied dc magnetic fields from 0 to 1 kOe in 100 Oe increments for the complex $[Co(SPh)_4](Ph_4P)$ (left), and Arrhenius plot of the natural logarithm of the relaxation time, τ, *vs.* the inverse temperature (right). Reprinted with permission from reference[91]. Copyright 2011 American Chemical Society.

$(HNEt_3)_2[Co^{II}(bmsab)_2]$

$(HNEt_3)_2[Co(bmsab)_2]$ (bmsab = 1,2-bis(methanesulfonamido)benzene, Figure 1.33) is also a notable SIM example, which was reported by Rechkemmer and co-workers in 2016.[92] The complex has also a tetrahedral (Figure 1.33), with an axial parameter D = –115 cm^{-1}. It also displays a single molecule magnet behavior in the absence of an applied dc magnetic field (Figure 1.34). Ac magnetic susceptibility was performed and an energy barrier of U_{eff} = 118 cm^{-1} was derived from a straight-line fit of the 10 highest temperature relaxation points, according to the Arrhenius law whereas the theoretical energy barrier

calculated from the *D* value, $|2D|$ is 230 cm^{-1}.

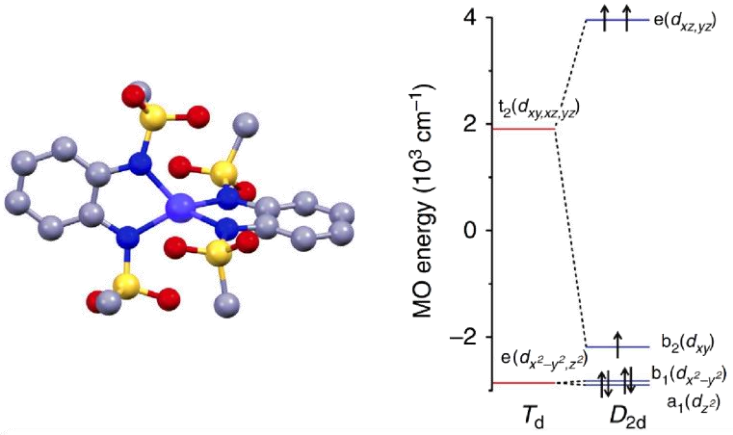

Figure 1.33. A view of the complex $[Co(bmsab)_2]^{2-}$. Co – violet; N – blue; O – red; S – yellow; C – grey; H atoms were omitted for clarity (left). Molecular orbital diagram showing the calculated d-orbital splitting for $(HNEt_3)_2[Co(bmsab)_2]$. Horizontal lines depict orbital energies while arrows pointing up or down stand for single electron spins (right). Taken directly from reference[92]. Copyright 2016 Nature Publishing Group.

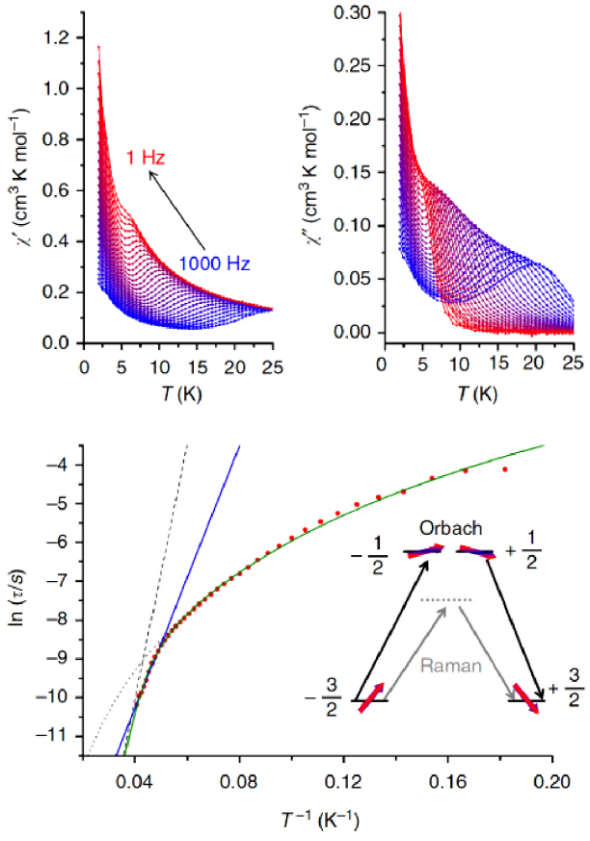

Figure 1.34. Dynamic magnetic susceptibility data for the complex $(HNEt_3)_2[Co(bmsab)_2]$ (top), and Arrhenius plot of the natural logarithm of the relaxation time, τ, *vs.* the inverse temperature (bottom). Taken directly from reference[92]. Copyright 2016 Nature Publishing Group.

$[Co^{II}(tbta)N_3](ClO_4)$

The coordination sphere of $[Co(tbta)N_3](ClO_4)$ (tbta = tris[(1-benzyl-1H-1,2,3-triazol-4-yl)methyl]amine, Figure 1.35) can be roughly described as a distorted CoN_5 trigonal bipyramid geometry with one long axial bond to the tertiary amine nitrogen atom of the tetradentate ligand. Static and dynamic magnetic data show that the slow relaxation of the magnetization is present in an applied dc magnetic field of 3000 Oe. The ZFS parameters deduced from magnetization studies (D = –10.7 cm^{-1}, E/D = 0.22) are in excellent agreement with the value of D inferred from the fit of the relaxation time *vs.* the temperature, with an extracted energy barrier of U_{eff} = 19.7 cm^{-1} (Figure 1.36).[93] Nevertheless, the excellent agreement between the two values is surprising because the rather large rhombic parameter E that usually reduces the theoretical energy barrier due to quantum tunneling and direct relaxation pathways. Probably, the rather large applied dc magnetic field quenches completely the QTM, but in this case relaxation by the direct process that depends on the square of the applied dc magnetic field should be active and thus reduce the magnitude of the energy barrier.

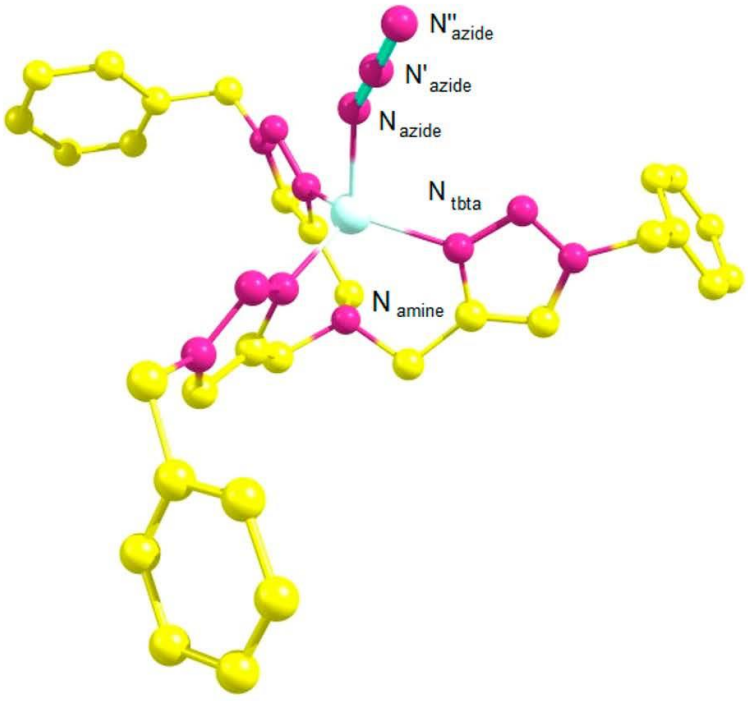

Figure 1.35. A view of the complex $[Co(tbta)N_3]^+$. Co – light green; B – violet; C – yellow; H atoms were omitted for clarity. Reprinted with permission from reference[93]. Copyright 2015 American Chemical Society.

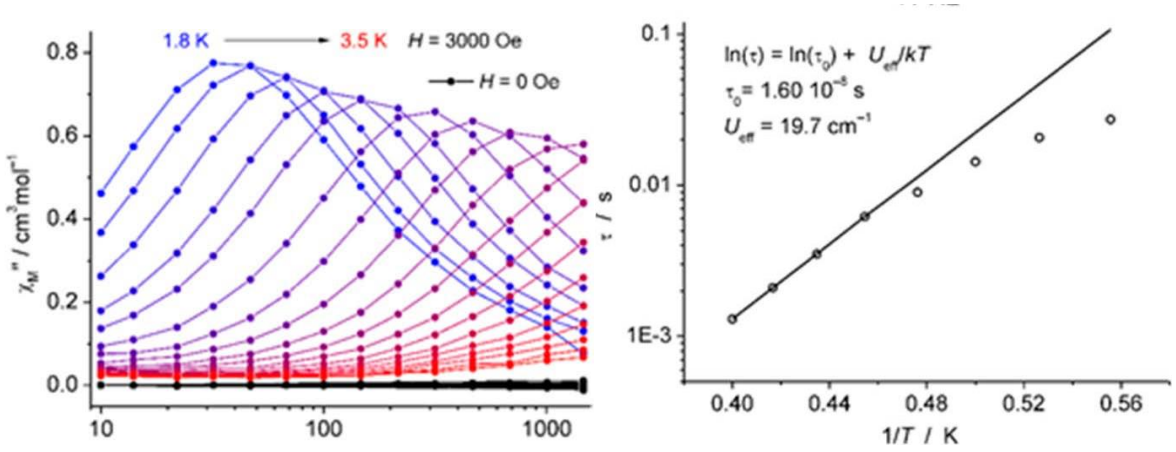

Figure 1.36. Dynamic magnetic susceptibility data for the complex $[Co(tbta)N_3](ClO_4)$ (left), and Arrhenius plot of the natural logarithm of the relaxation time, τ, *vs.* the inverse temperature (right). Reprinted with permission from reference[93]. Copyright 2015 American Chemical Society.

[Co^{II}(TPMA)Cl](Cl)

[Co(TPMA)Cl](Cl) (TPMA = tris(2-pyridylmethyl)amine, Figure 1.37) where the Co^{II} ion resides in a trigonal bipyramidal environment with the axial ligand Cl was reported by Woods and co-workers in 2016.[94] Static and dynamic magnetic data show a slow relaxation of the magnetization in an applied dc magnetic field of 2000 Oe. The ZFS parameters deduced from static susceptibility and magnetizations (D = –8.49 cm^{-1}, E = 0). In this case, U_{eff} was found equal to 16.4 cm^{-1}, which corresponds to the theoretical barrier (Figure 1.38).[94] The main difference with the preceding complex is the absence of transverse anisotropy because the exact C_{3v} of the complex. Despite the strict axial symmetry, a dc magnetic field was necessary to observe the blocking of the magnetization by ac susceptibility studies, while one would have expected a blocking at zero dc magnetic field because the wavefucntions of the ±3/2 sub-levels cannot mix with the ±1/2 ones and no QTM would be expected. There are two possible explanations to presence of QTM: i) the hyperfine interaction between the electronic and the I = 7/2 nuclear spin of Co^{II} and/or ii) the Raman process that cannot be neglected at temperatures higher than 1 or 2 K.

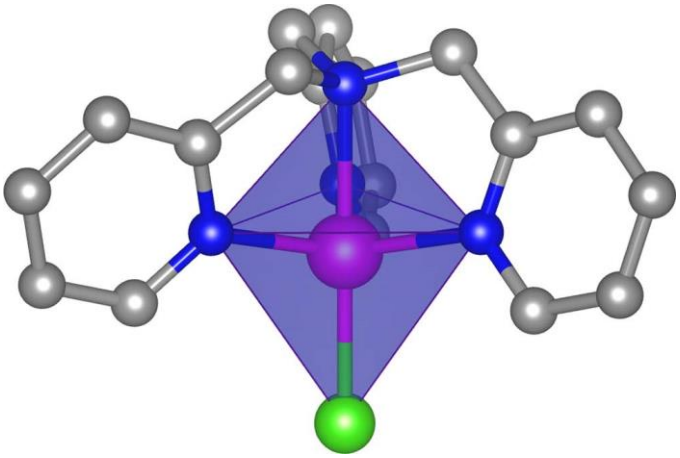

Figure 1.37. A view of the complex $[Co(TPMA)Cl]^+$. Co – purple; N – blue; Cl – green; C – grey; H atoms were omitted for clarity. Taken directly from reference[94]. Copyright 2016 American Chemical Society.

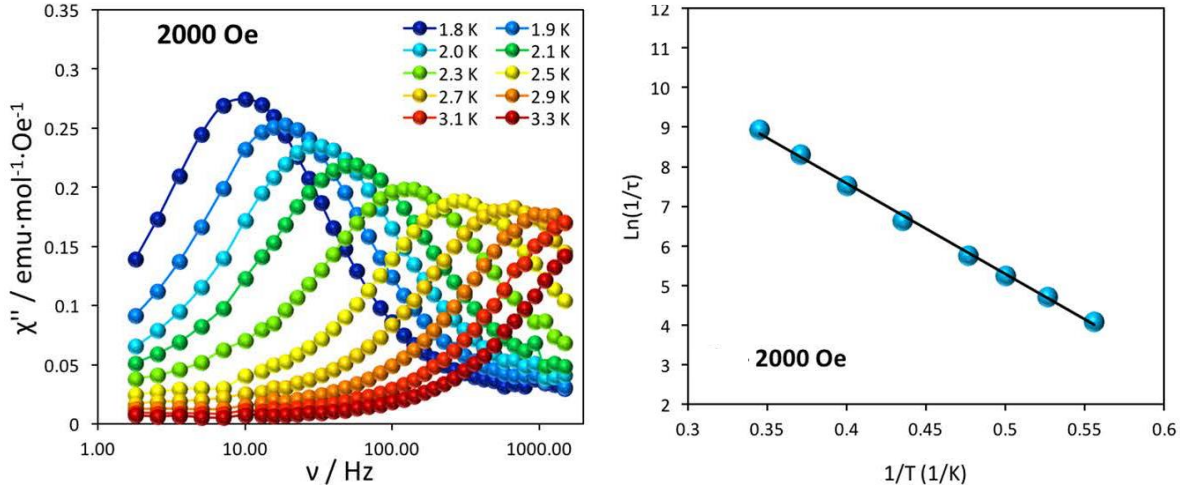

Figure 1.38. Dynamic magnetic susceptibility data for the complex [Co(TPMA)Cl](Cl) (left), and Arrhenius plot of the natural logarithm of the relaxation time, τ, *vs.* the inverse temperature (right). Reprinted with permission from reference[94]. Copyright 2016 American Chemical Society.

[(sIPr)Co^{II}N(Dmp)]

For the [(sIPr)CoN(Dmp)] (Dmp = 2,6-dimesitylphenyl, Figure 1.39) complex, the Co^{II} ion resides in a linear environment as reported by Gao and co-workers in 2016.[95] The two-coordinated cobalt(II) imido complexes featuring highly covalent Co=N cores exhibit slow relaxation of magnetization under an applied zero dc magnetic field (Figure 1.40) with a high effective relaxation barrier of 413 cm^{-1} (Figure 1.40), a new record for transition metal based SMMs till now.[95]

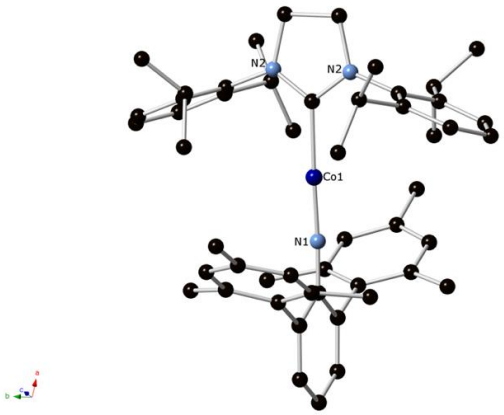

Figure 1.39. A view of the complex [(sIPr)CoN(Dmp)]. C – black; H atoms were omitted for clarity. Reprinted with permission from reference[95]. Copyright 2016 American Chemical Society.

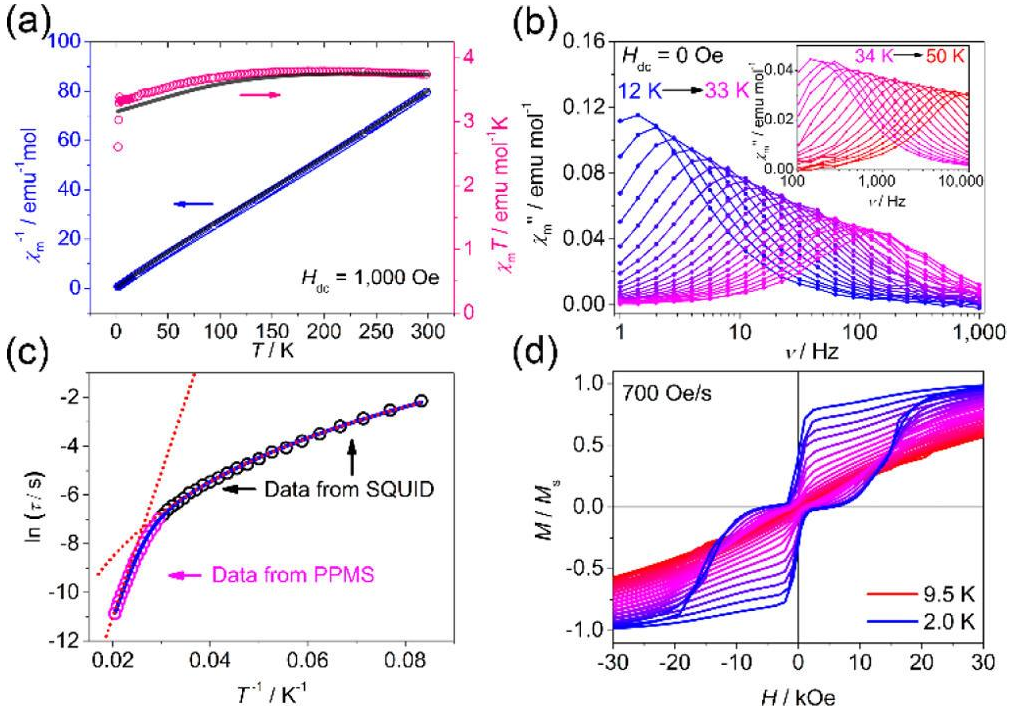

Figure 1.40. Static (a) and dynamic (b) magnetic susceptibility data for the complex [(sIPr)CoN(Dmp)]; (c) Arrhenius plot of the natural logarithm of the relaxation time, τ, *vs.* the inverse temperature; (d) Variable-field magnetization data at the sweep rate of 700 Oe/s under 2 – 9.5 K. Taken directly from reference[96]. Copyright 2016 American Chemical Society.

[Ni^{I}(6-Mes)$_2$](Br)

[Ni(6-Mes)$_2$](Br) (6-Mes = 1,3-bis(2,4,6-trimethylphenyl)-3,4,5,6-tetrahydropyrimidin-2-ylidene, Figure 1.41) is the only case of a Ni^{II} complex, reported in 2013, to have a slow relaxation of the magnetization.[97] But since it is a Ni^{I}, it has one single

electron. When S = 1/2, the magnetization cannot be blocked and the concept of SMM is meaningless. The slow relaxation of the magnetization observed in the presence of an applied magnetic field (Figure 1.42), must thus, have another origin as a Raman process for example. And the "energy barrier" extracted is probably not due to an Orbach process.

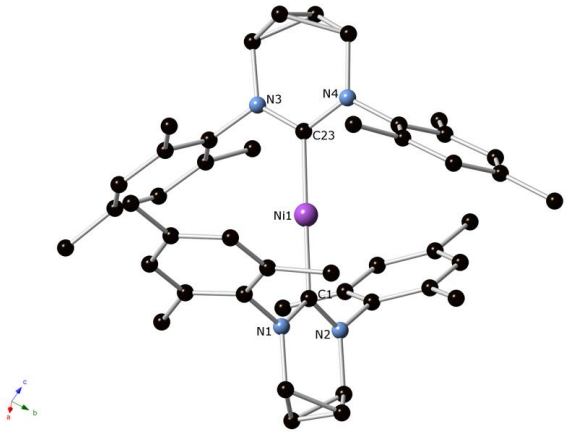

Figure 1.41. A view of the complex $[Ni(6\text{-}Mes)_2]^+$. C – black; H atoms were omitted for clarity. Reprinted with permission from reference[97]. Copyright 2013 American Chemical Society.

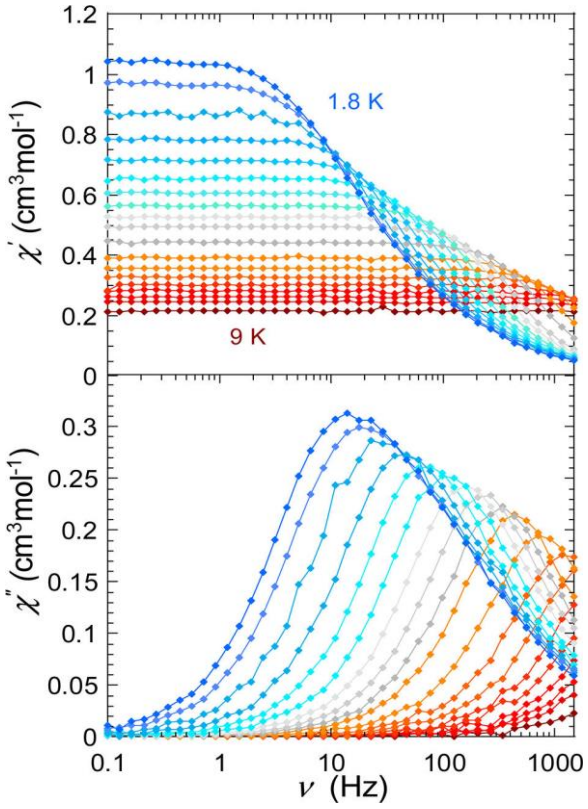

Figure 1.42. Dynamic magnetic susceptibility data under a 600 Oe dc magnetic field for the complex $[Ni(6\text{-}Mes)_2](Br)$. Taken directly from reference[97]. Copyright 2013 American Chemical Society.

[Ni^{II}(Me$_6$tren)Cl](ClO$_4$)

For the [Ni(Me$_6$tren)Cl](ClO$_4$) (Me$_6$tren = Tris(2-(dimethylamino)ethyl)amine, Figure 1.43) complex, the symmetry is C_{3v} and the geometry trigonal bipyramid. It was reported by our group, with a D value estimated to be between –120 and –180 cm^{-1} and E = 1.6 cm^{-1} from HFEPR measurements.[98] No experimental demonstration of slow relaxation of the magnetization during the dynamic magnetic susceptibility measurements was observed, which is not surprising because the m_s = ±1 ground level are mixed by the weak rhombic term (transverse anisotropy) activating the relaxation by QTM and precluding its blocking.[98]

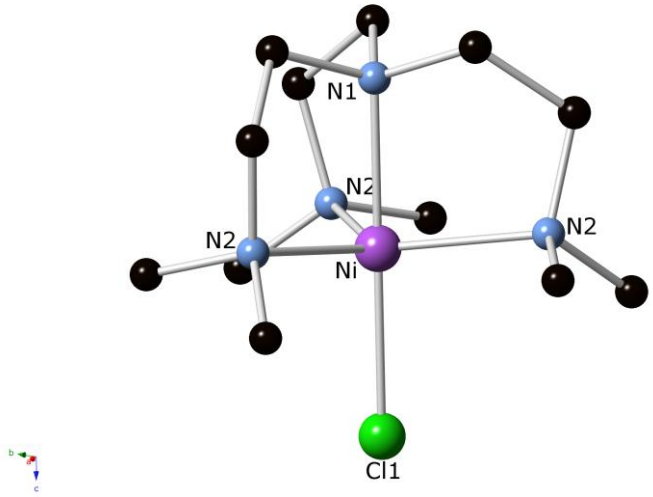

Figure 1.43. A view of the complex [Ni(Me$_6$tren)Cl]$^+$. C – black; H atoms were omitted for clarity. Reprinted with permission from reference[98]. Copyright 2013 American Chemical Society.

[Ni^{II}(MDABCO)$_2$Cl$_3$](ClO$_4$)

[Ni(MDABCO)$_2$Cl$_3$](ClO$_4$) (MDABCO$^+$ = 1-methyl-4-aza-1-azoniabicyclo[2.2.2] octanium cation, Figure 1.44 left) was reported by Murrie and co-workers in 2015.[99] The complex only exhibits slow relaxation behavior (Figure 1.45) in the presence of a dc magnetic field, with energy barriers of 25.2, 27.1 and 27.8 K in dc magnetic fields of 500, 1000 and 2000 Oe respectively (Figure 1.46). The most notable feature of this complex though, is the fact that the authors suggest a D value of –535 cm^{-1} based on HFEPR studies, with a corresponding E value of < 0.18 cm^{-1}. Again here, the slow relaxation of the magnetization cannot be due to an Orbach process but rather to a Raman type relaxation, so that the complex cannot be said to have a SIM behavior.

Feng SHAO: 0000-0001-8606-8628

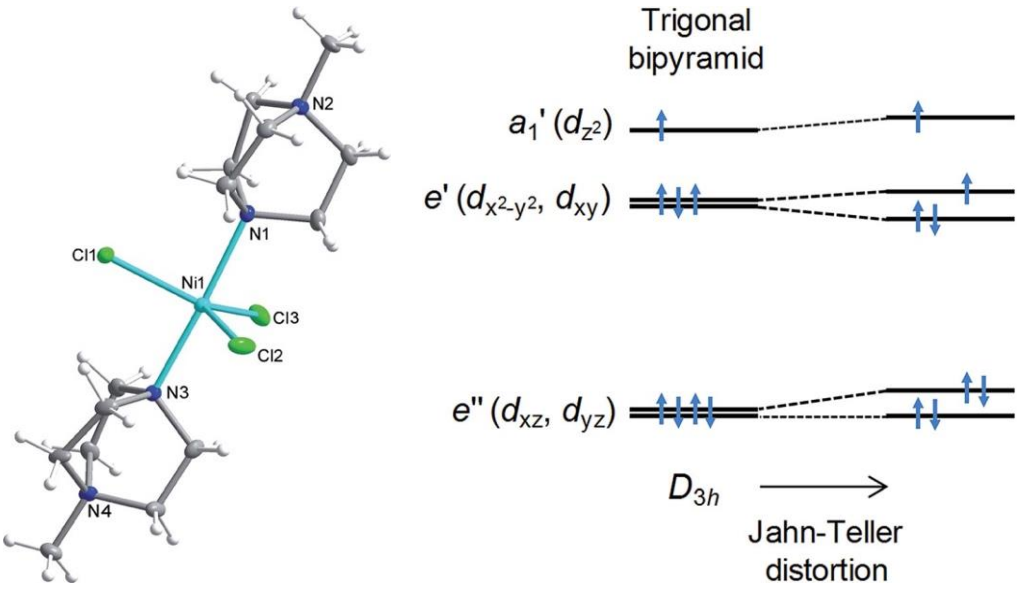

Figure 1.44. A view of the complex $[Ni(MDABCO)_2Cl_3]^+$. C – grey; H atoms were omitted for clarity. d-orbital splitting for high-spin Ni^{II} in an ideal trigonal bipyramidal environment and the effect of a symmetry-lowering Jahn-Teller distortion that removes the orbital degeneracy. Reprinted with permission from reference[99]. Copyright 2015 The Royal Society of Chemistry.

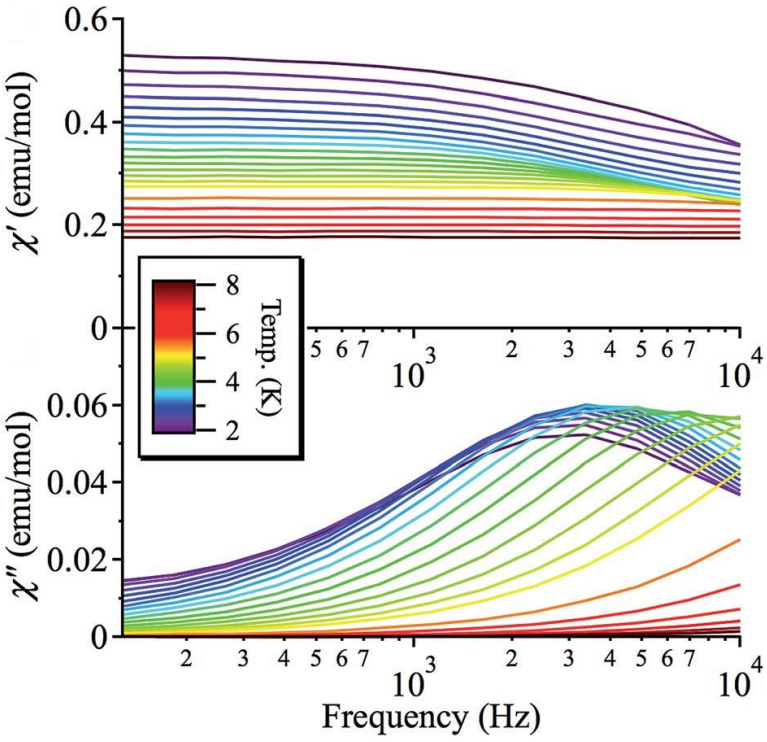

Figure 1.45. Dynamic magnetic susceptibility data under a 2000 Oe dc magnetic field for the complex $[Ni(MDABCO)_2Cl_3](ClO_4)$. Taken directly from reference[99]. Copyright 2015 The Royal Society of Chemistry.

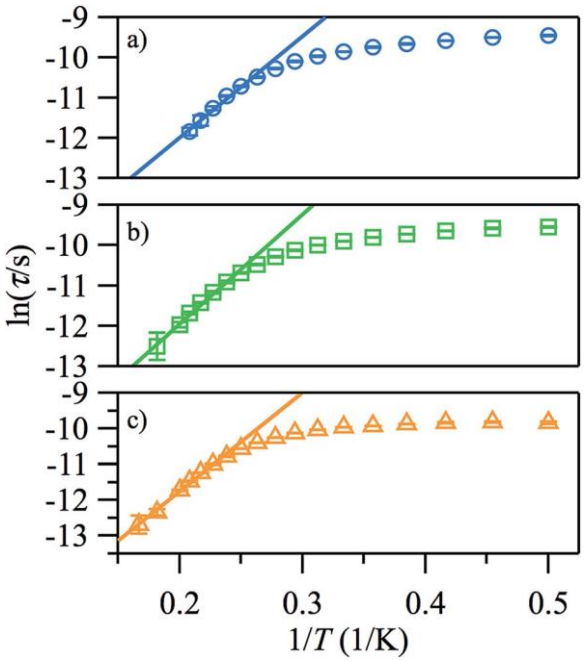

Figure 1.46. Arrhenius plot of the natural logarithm of the relaxation time, τ, *vs.* the inverse temperature for the complex $[Ni(MDABCO)_2Cl_3](ClO_4)$ under different dc magnetic fields 500 Oe (a), 1000 Oe (b), 2000 Oe (c). Taken directly from reference[99]. Copyright 2015 The Royal Society of Chemistry.

1.3.3 Lanthanide Magnetism and Important SIMs

Lanthanide ions possess magnetic properties different from 3*d* ions due to the intrinsic nature of 4*f* orbitals. The characters of lanthanide ions are summarized as follows:

i) The 4*f* electrons are screened by 5*d* and 6*s* orbitals so that the orbital momentum is largely conserved in the crystal field other than Eu^{III} ($^7F_0$), Gd^{III} ($^8S_{7/2}$), and Lu^{III} ($^1S_0$).

ii) The SOC of lanthanide ions is much stronger than that of the transition metal ions.

iii) The $^{2S+1}L_J$ multiplet pattern of Ln^{III} ions is derived from Pauli Principle and Hund's rule by taken the Coulombic interaction and the SOC into consideration. The crystal field effect acts as a much weaker interaction on 4*f* ions that further splits the $^{2S+1}L_J$ multiplet (Figure 1.47). For simplicity, the Russell-Saunders coupling approach is most commonly used to describe the energy levels for free lanthanide ions.[100] The energy levels are then further split by the crystal field. The cumulative effect of SOC and crystal field splitting for a Dy^{III} ion is shown in Figure 1.48.[101] The crystal field splitting varies with the coordination environments and determines the magnetic anisotropy and spin-lattice relaxation behavior of Ln-SIMs.[86]

iv) The orbital angular momentum of the lanthanide ions is generally not quenched by the crystal field. The Landé-factor g_J has the form:

$$g_J = \frac{3J(J+1)+S(S+1)-L(L+1)}{2J(J+1)} \qquad (1.28)$$

and for the molar magnetic susceptibility of free lanthanide ions:

$$\chi_M = \frac{N_A g_J{}^2 \mu_B{}^2}{3k_B T} J(J+1) \qquad (1.29)$$

The magnetization:

$$M = N_A g_J \mu_B J[B_J(x)] \qquad (1.30)$$

where S is replaced by J in the equation 1.20, and the saturated magnetization for free lanthanide ions is also similar:

$$M = N_A g_J \mu_B J \qquad (1.31)$$

where J is the total quantum number ($J = L + S$), L is the total angular quantum number, S is the total spin quantum number, M is the magnetization, N_A is Avogadro's number, k_B is the Boltzmann constant, μ_B is the Bohr Magneton, and $B_J(x)$ is the Brillouin function proper and H is the dc magnetic field.

Table 1.2. Summary of experimental spin-orbit interaction parameters, electronic configuration, spectroscopic terms of the ground states and first excited states and their separation together with the magnetic parameters for the tripositive lanthanide ions.[17]

Tripositive lanthanide ion	Ionic configuration	Ground state term	Excited state term	Energy separation (cm^{-1})	Spin orbital experimental (cm^{-1})	g_J	$\chi_M T$ (cm^3 K mol^{-1})	Saturated magnetization
Ce	$4f^1$	$^2F_{5/2}$	$^2F_{7/2}$	2200	643	6/7	0.81	2.14
Pr	$4f^2$	$^3H_4$	$^3H_5$	2100	800	4/5	1.60	3.20
Nd	$4f^3$	$^4I_{9/2}$	$^4I_{11/2}$	1900	900	8/11	1.64	3.27
Pm	$4f^4$	$^5I_4$	$^5I_5$	1600	—	3/5	0.90	2.40
Sm	$4f^5$	$^6H_{5/2}$	$^6H_{7/2}$	1000	1200	2/7	0.09	0.71
Eu	$4f^6$	$^7F_0$	$^7F_1$	400	1415	5	0.00	0.00
Gd	$4f^7$	$^8S_{7/2}$	^6P	30000	—	2	7.88	7.00
Tb	$4f^8$	$^7F_6$	$^7F_5$	2000	1620	3/2	11.82	9.00
Dy	$4f^9$	$^6H_{15/2}$	$^6H_{13/2}$	—	1820	4/3	14.14	10.00
Ho	$4f^{10}$	$^5I_8$	$^5I_7$	—	2080	5/4	14.06	10.00
Er	$4f^{11}$	$^4I_{15/2}$	$^4I_{13/2}$	6500	2360	6/5	11.46	9.00
Tm	$4f^{12}$	$^3H_6$	$^3H_5$	—	2800	7/6	7.28	7.00
Yb	$4f^{13}$	$^2F_{7/2}$	$^2F_{5/2}$	10000	2940	8/7	2.53	4.00

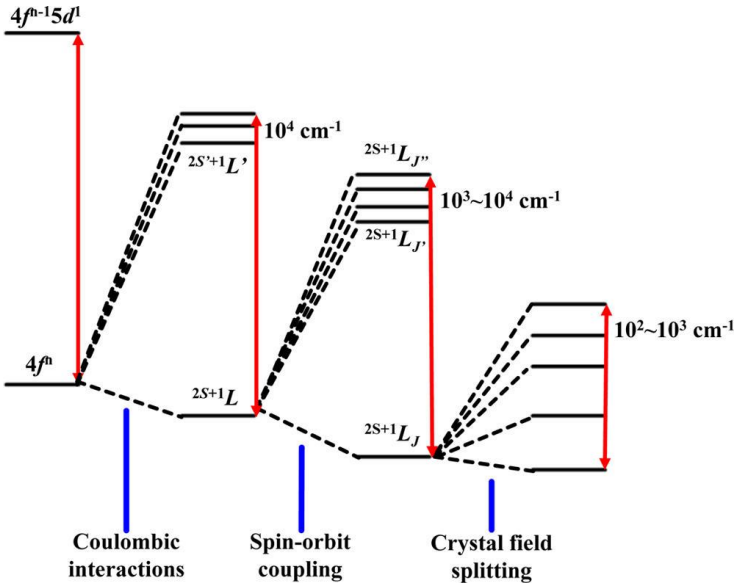

Figure 1.47. Energy splitting schematic diagram of the electronic structures of lanthanide ions in logarithmic energy scale. Reprinted with permission from reference[86]. Copyright 2016 American Chemical Society.

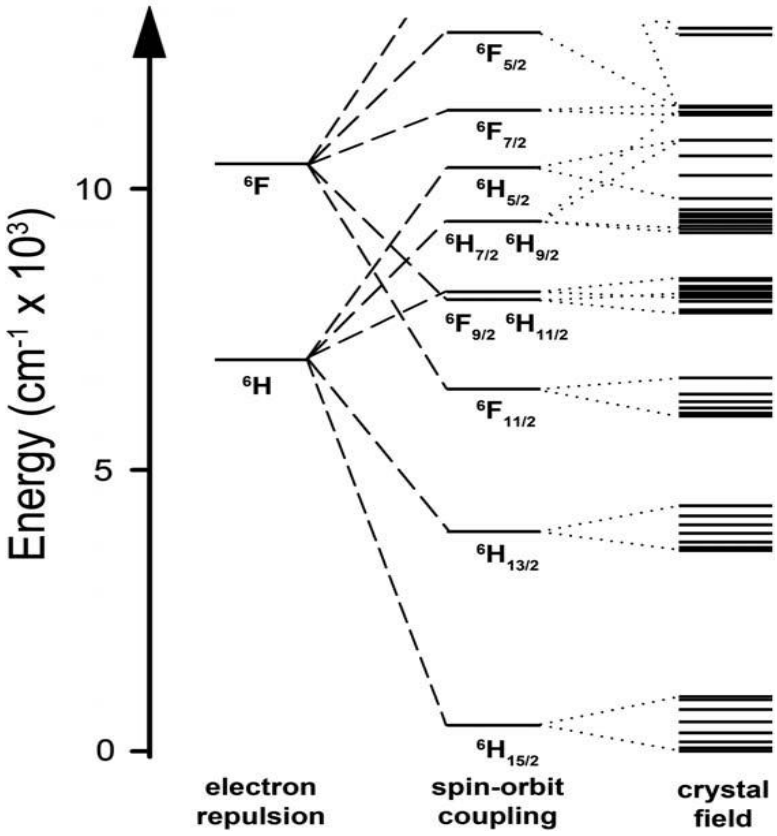

Figure 1.48. Low energy electronic structure of the Dy^{III} ion with sequential perturbations of electron-electron repulsions, spin-orbit coupling, and the crystal field. Reprinted with permission from reference[101]. Copyright 2011 Royal Society of Chemistry.

Understanding magnetic anisotropy is vital for the rational design of Ln-SIMs, which can be viewed from the asphericity of the 4*f* electron density.[102] The 4*f*-shell electron cloud shape of the Ising limit states and the shape of the 4f shell for Dy^{III} varies from prolate to oblate when the ground state differs from $|\pm 1/2\rangle$ to $|\pm 15/2\rangle$ are plotted in the Figure 1.49 bottom.[86, 101, 103]

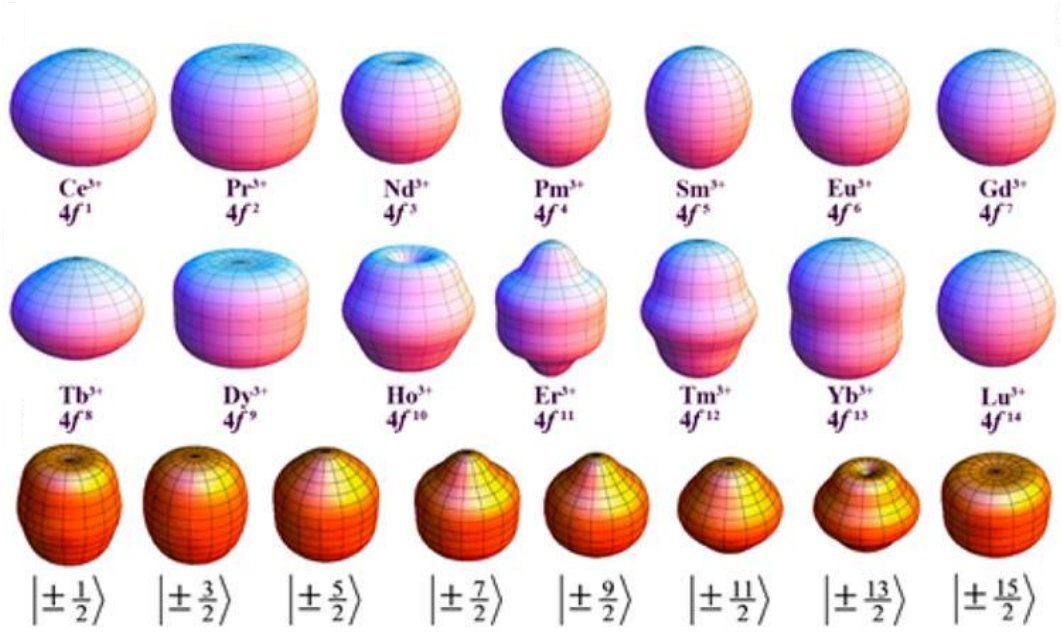

Figure 1.49. 4f electron density distribution of corresponding Ln^{III} ions in their Ising limit state (top & middle); electron density distribution of Dy^{III} ion in corresponding M_J state (bottom). Reprinted with permission from reference[86]. Copyright 2016 American Chemical Society.

$LnPc_2$ series: $[TbPc_2](NBu_4)$ — the First Lanthanide SIM

Ln-SMMs containing ligands derived from phthalocyanine are among the most important SMMs ever reported.[77, 104-107] The most common molecular structural motif is the double-decker, or sandwich, structure containing $[Pc'_2Ln]^{\pm/0}$ units, usually with a D_{4d} symmetry, and a square-antiprismatic coordination geometry. Pc' can be the parent phthalocyaninate ligand or a substituted analogue, and the complex can be a cation, an anion, or uncharged by virtue of the redox non-innocence of Pc ligands.

The magnetic behavior of the phthalocyanine based complexes $[TbPc_2](NBu_4)$ and $[DyPc_2](NBu_4)$ (H_2Pc = phthalocyanine, Figure 1.50) were reported by Ishikawa and co-workers in 2003 to exhibit slow magnetization relaxation (Figure 1.51) together with large tunneling effects.[77] The ac susceptibility data of the diluted samples were fitted to the Arrhenius law to give the barrier heights for the reversal of the magnetic moment of 230 and

28 cm^{-1} for $[TbPc_2](NBu_4)$ and $[DyPc_2](NBu_4)$, respectively. Their low-lying electronic structure was determined by the simultaneous least squares fit of paramagnetic NMR shifts and magnetic susceptibility data (Figure 1.52).[105]

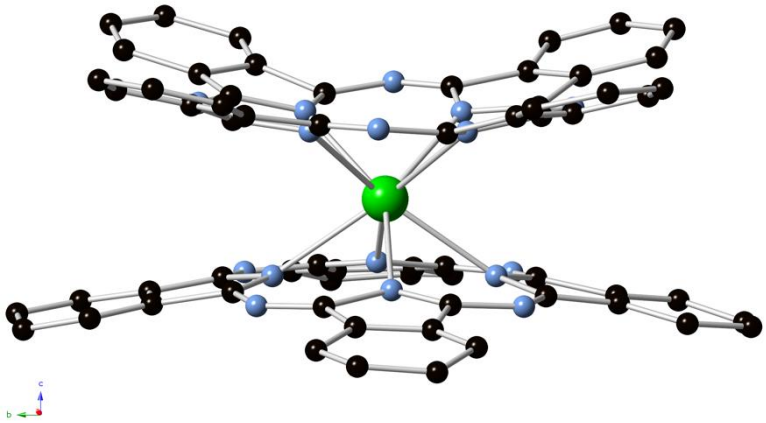

Figure 1.50. A view of the complex $[LnPc_2]^-$. Ln – green; N – blue; C – black; H atoms were omitted for clarity. Reprinted with permission from reference[108]. Copyright 1996 American Chemical Society.

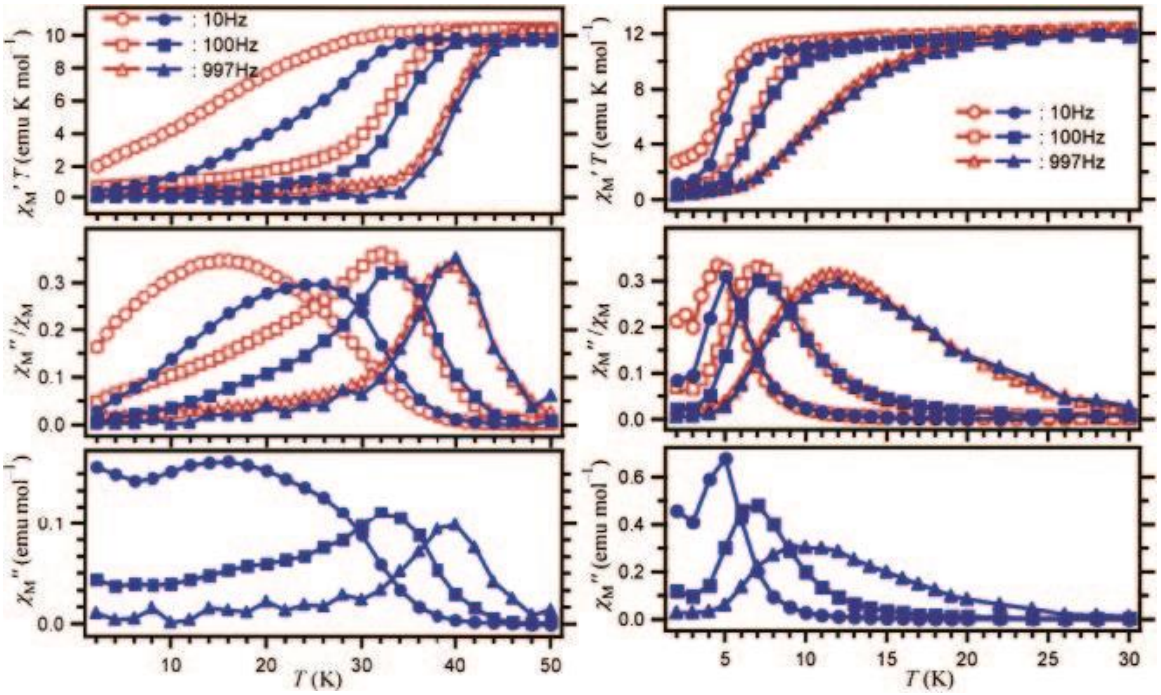

Figure 1.51. Dynamic magnetic susceptibility data for the complexes $[TbPc_2](NBu_4)$ (left, open marks) and $[DyPc_2](NBu_4)$ (right, open marks) and their diluted complexes (filled marks). Taken directly from reference[77]. Copyright 2003 American Chemical Society.

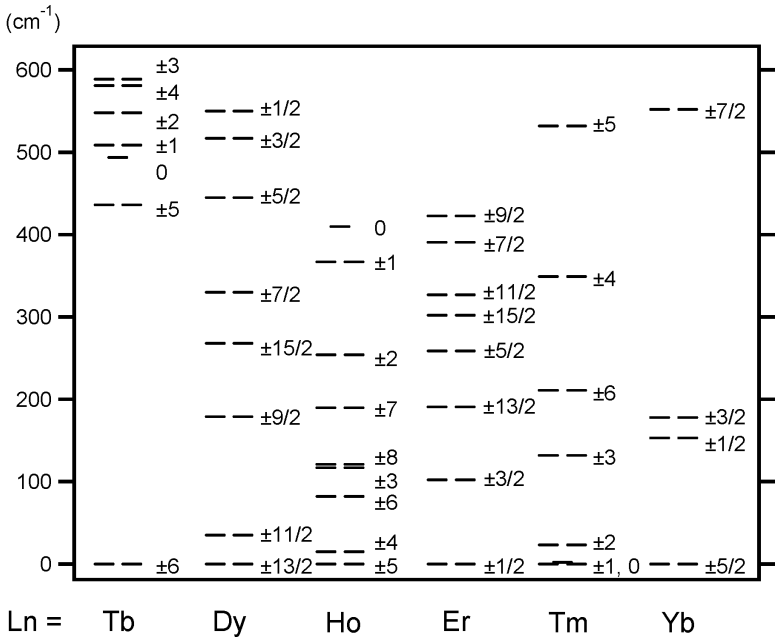

Figure 1.52. Splitting of the spin-orbit coupled (*J*) ground state by the crystal field for $[LnPc_2]^-$ complexes.[105, 106] Taken directly from reference[105]. Copyright 2004 American Chemical Society.

Ln-POM (Ln-based Polyoxometallates) series: $[ErW_{10}O_{36}]^{9-}$ — the First Ln-POM SIM.

The sodium(I) salt of $[ErW_{10}O_{36}]^{9-}$ polyanion was reported by AlDamen and co-workers in 2008.[109] The complex is formed by two anionic $[W_5O_{18}]^{6-}$ moieties sandwiching the Er^{III} ion (Figure 1.53). These anionic clusters are surrounded by sodium(I) cations, to balance the charge, which are octahedrally coordinated by water molecules. The coordination geometry of this complex is similar to those of bis(phthalocyaninato) lanthanide complexes. Low-temperature ac magnetic susceptibility measurements (Figure 1.54) reveal the typical features associated with the SMM behavior. Analysis of the frequency dependence of the out-of-phase peaks through an Arrhenius plot allows estimation of the magnetization relaxation parameters in this system (Figure 1.54). It afforded an energy barrier height (U_{eff}/k_B) of 55.2 K with a pre-exponential factor (τ_0) of 1.6×10^{-8} s. And then, several Ln-POM complexes replacing Er^{III} by other lanthanides were reported subsequently.[110-113] The main difference between the $[LnPc_2]$ and Ln-POM series is the more compressed D_{4d} symmetry of the Ln-POMs. In the former, the Tb^{III} (and the Dy^{III}) complex is a SMM, while in the latter the Er^{III} one is a SMM, which corresponds to the expected behavior inferred from the model presented in Figure 1.53.

 Feng SHAO: 0000-0001-8606-8628

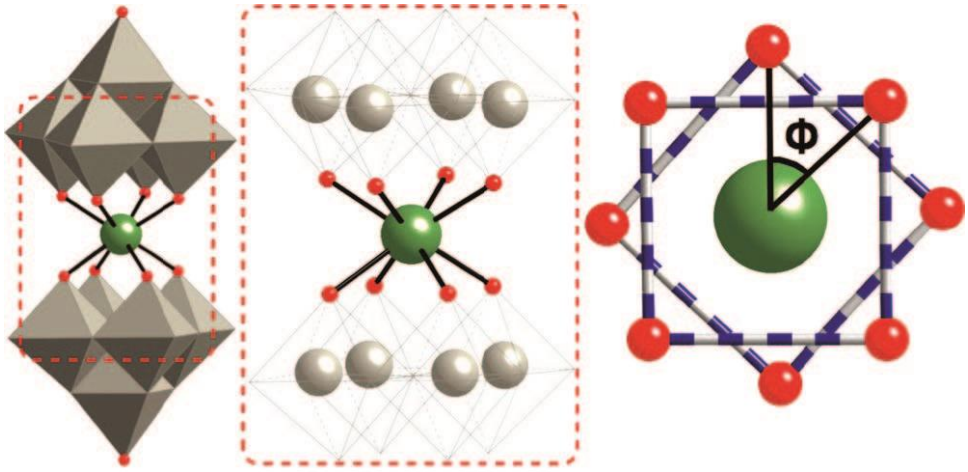

Figure 1.53. A view of the complex $[ErW_{10}O_{36}]^{9-}$ POM and projection showing the Er^{III} ion square-antiprismatic coordination. Taken directly from reference[109]. Copyright 2008 American Chemical Society.

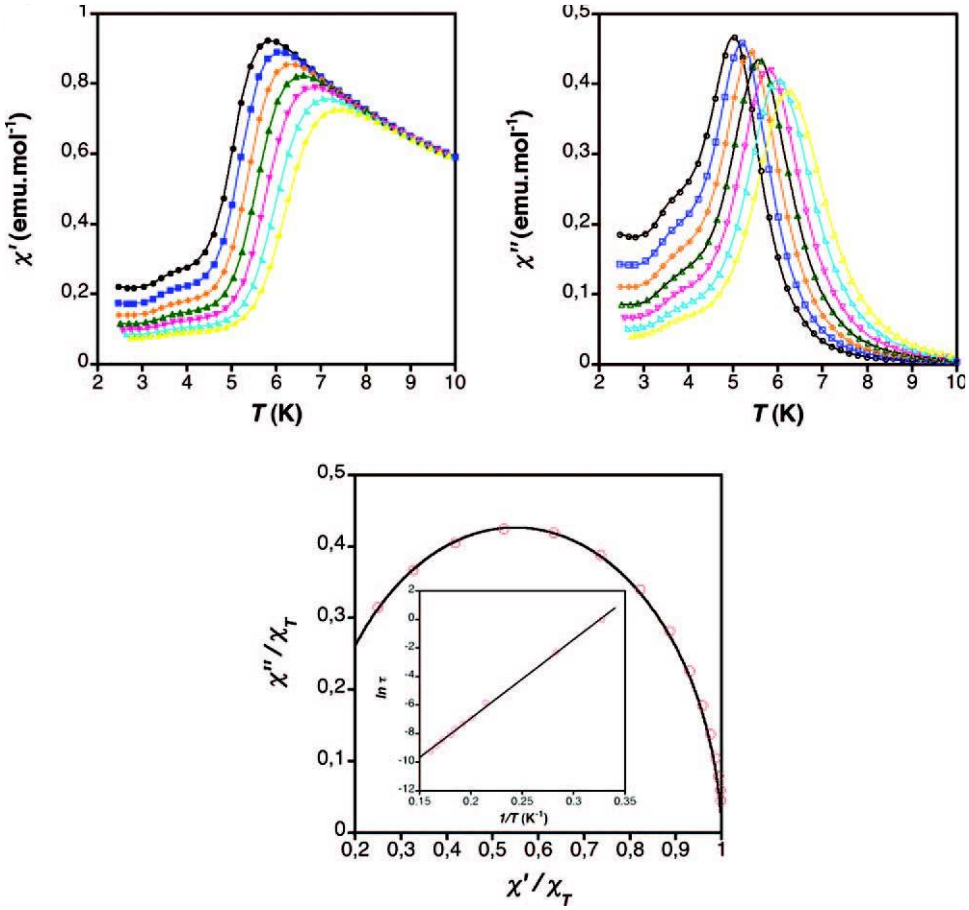

Figure 1.54. Dynamic magnetic susceptibility data, and Arrhenius plot of the natural logarithm of the relaxation time, τ, *vs.* the inverse temperature for the complexes $[ErW_{10}O_{36}]^{9-}$ POM. Taken directly from reference[109]. Copyright 2008 American Chemical Society.

$[Gd(W_5O_{18})_2]^{9-}$ and $[Gd(P_5W_{30}O_{110})_2]^{12-}$

We take the Gd^{III} POM as the example, because, Gd^{III} as a free ion, it has an isotropic electronic ground state with $L = 0$ and $S = 7/2$. It is therefore a model crystal-field probe: its magnetic anisotropy is almost exclusively determined by the Coulomb interaction with nearby ions.[114]

The potassium(I) salts of $[Gd(W_5O_{18})_2]^{9-}$ and $[Gd(P_5W_{30}O_{110})_2]^{12-}$ were studied by Martínez-Pérez in 2012.[111] Their ac susceptibility measurements have been extended down to 13 mK using a Micro-SQUID susceptometer, which show that the complexes behave as SMMs at low temperatures with an energy barrier U_{eff} = 2.22 K for $[Gd(W_5O_{18})_2]^{9-}$, which agrees with the theoretical anisotropy energy barrier U_{calc} = 2.15 K calculated from the D value found for this complex.[111]

[Dy(bbpen)Br]

The first SMM with effective energy barrier over 1000 K, which is the complex [Dy(bbpen)Br] (H_2bbpen = N,N'-bis(2-hydroxybenzyl)-N,N'-bis(2methylpyridyl)ethylenediamine, Figure 1.55) reported by Liu and co-workers in 2016.[53] The Dy^{III} ion has a pentagonal bipyramidal local geometry. The investigation of the dynamic magnetic susceptibility (Figure 1.56) reveals an effective energy barrier (U_{eff} = 1025 K) for the relaxation of magnetization and a pronounced magnetic hysteresis (loops up to 14 K).[53]

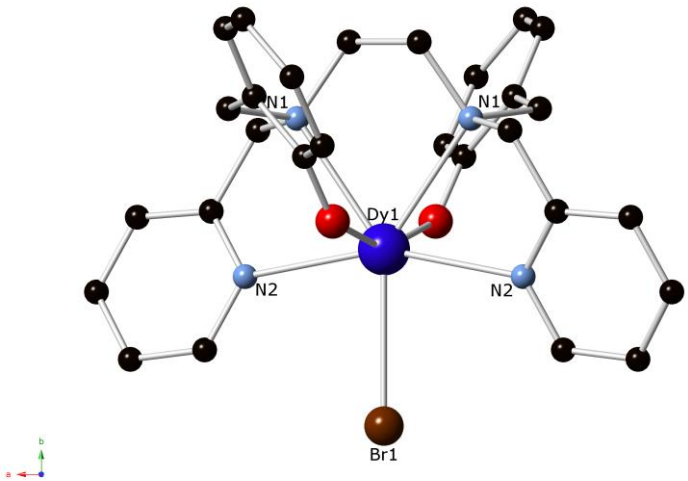

Figure 1.55. A view of the complex [Dy(bbpen)Br]. O – red; C – black; H atoms were omitted for clarity. Reprinted with permission from reference[53]. Copyright 2016 American Chemical Society.

Feng SHAO: 0000-0001-8606-8628

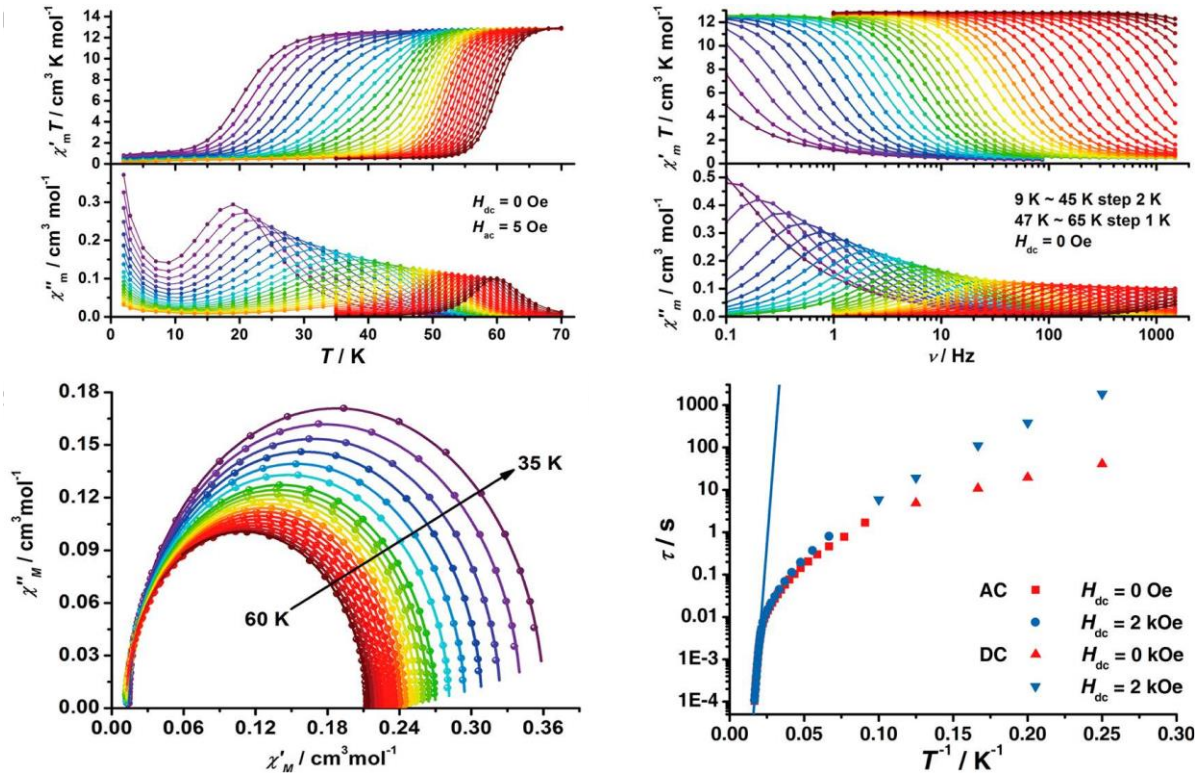

Figure 1.56. Dynamic magnetic susceptibility data and Arrhenius plot of the natural logarithm of the relaxation time, *τ*, *vs.* the inverse temperature for the [Dy(bbpen)Br]. Reprinted with permission from reference[53]. Copyright 2016 American Chemical Society.

[Dy(O^{t}Bu)$_2$(py)$_5$](BPh$_4$)

To date, the largest effective energy barrier SMM is the complex [Dy(O^{t}Bu)$_2$(py)$_5$](BPh$_4$) (py = pyridine, Figure 1.57), was reported by Ding and co-workers in 2016.[55] The massive magnetic anisotropy is due to bis-trans-disposed tertbutoxide ligands with weak equatorial pyridine donors, approaching the proposed schemes for high-temperature Dy^{III} SMM, where the axial electron donation must be larger than the equatorial one in order to enhance the axial anisotropy and thus the energy barrier. The alternating current susceptibility studies give out-of-phase peaks above 100 K (Figure 1.58), with the peaks showing a strong frequency and temperature dependence. And the effective energy barrier U_{eff} = 1815 K (Figure 1.59) entirely consistent with *ab initio* prediction.[55] The blocking temperature, T_B, that corresponds to the temperature where the zero field cooled (ZFC) magnetization is maximum was found equal to 14 K (Figure 1.60).

Feng SHAO: 0000-0001-8606-8628

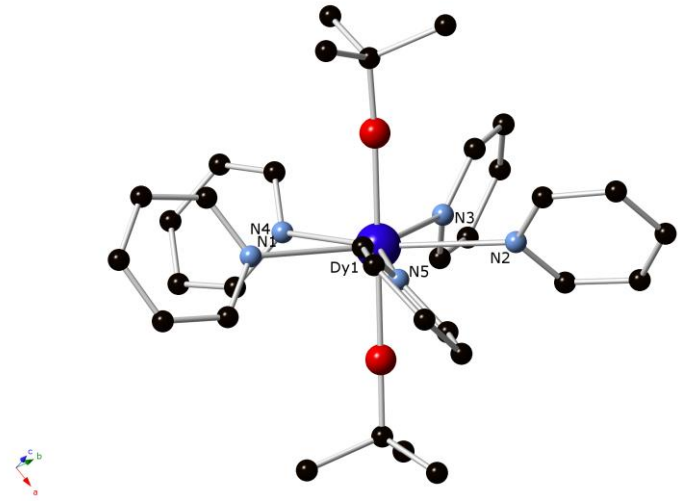

Figure 1.57. A view of the complex $[Dy(O^tBu)_2(py)_5](BPh_4)$. O – red; C – balck; H atoms were omitted for clarity. Reprinted with permission from reference[55]. Copyright 2016 Wiley-VCH Verlag GmbH & Co. KGaA, Weinheim.

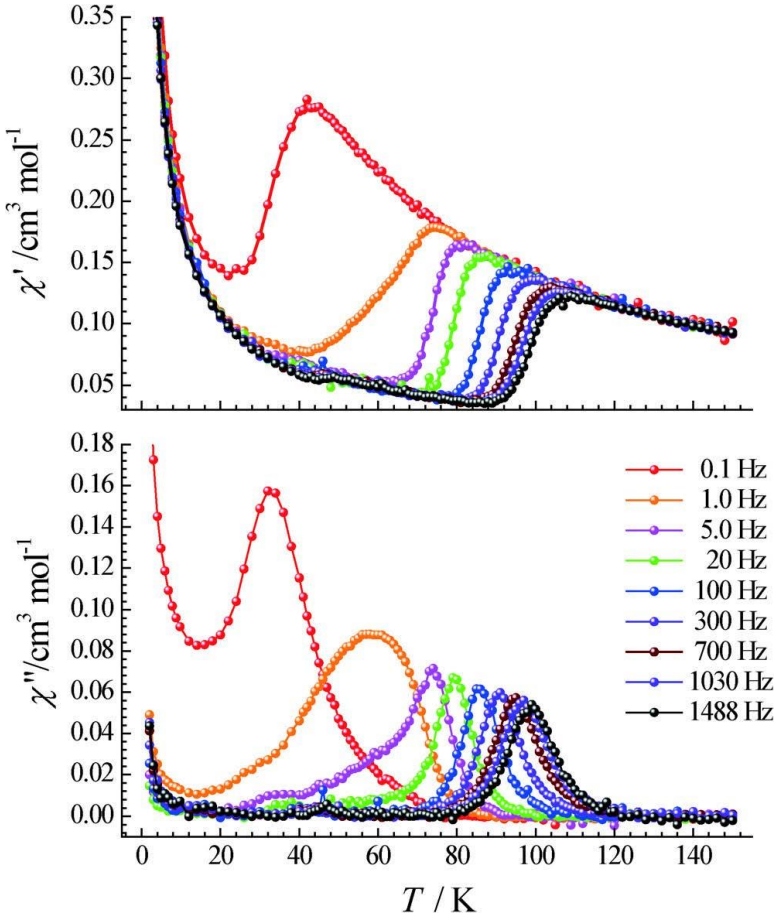

Figure 1.58. Dynamic magnetic susceptibility data for the complex $[Dy(O^tBu)_2(py)_5](BPh_4)$. Reprinted with permission from reference[55]. Copyright 2016 Wiley-VCH Verlag GmbH & Co. KGaA, Weinheim.

Feng SHAO: 0000-0001-8606-8628

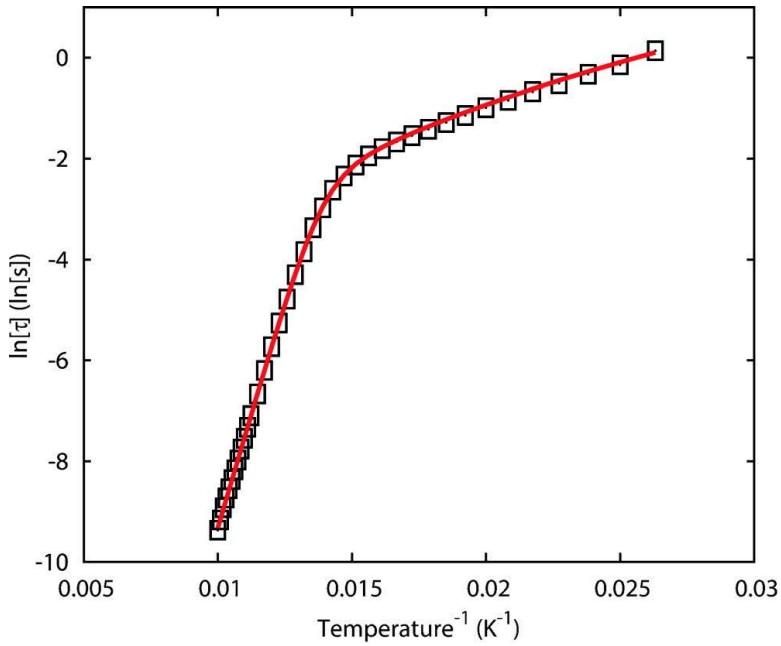

Figure 1.59. Arrhenius plot of the natural logarithm of the relaxation time, τ, *vs.* the inverse temperature for the $[Dy(O^tBu)_2(py)_5](BPh_4)$. Reprinted with permission from reference[55]. Copyright 2016 Wiley-VCH Verlag GmbH & Co. KGaA, Weinheim.

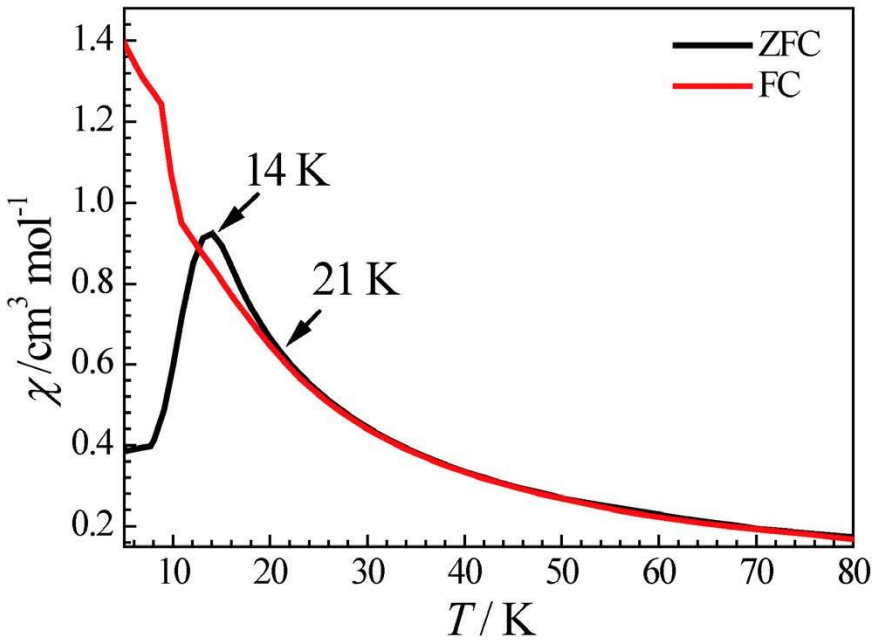

Figure 1.60. Variable-temperature magnetic susceptibility for the $[Dy(O^tBu)_2(py)_5](BPh_4)$, under Field Cooled (FC) and Zero-Field-Cooled (ZFC) conditions with a dc magnetic field of 2000 Oe. The ZFC measurements were made with increasing temperature. Taken directly from reference[55]. Copyright 2016 Wiley-VCH Verlag GmbH & Co. KGaA, Weinheim.

Feng SHAO: 0000-0001-8606-8628

1.4 Metallacrowns

Part of this dissertation is devoted to the preparation, the study of the magnetic properties and the preliminary luminescence study at low temperature of Ln-containing complexes based on metallacrowns (MCs). We will, thus, introduce the structural features of MCs here. We will also mention the only case of a MC based mononuclear lanthanide complex to present a SMM behavior where luminescence was investigated. Many polynuclear MC based complexes were reported.[115, 116]

The MC complexes are an exceptional class of coordination compounds as they have proven to combine a variety of beneficial synthetic and structural features in a most singular way, since their discovery in 1989 by Pecoraro and Lah.[116-118]

MCs are the crown ether analog of coordination complexes. The traditional definition of a MC is a repeat unit of –[M–N–O]– in a cyclic arrangement where the ring metal and nitrogen atom replace the methylene carbon atoms of a crown ether (Figure 1.61). As in crown ethers, MCs are named on the basis of the ring size and the number of donating oxygen atoms. The preferred nomenclature also includes the bound central metal, the ligand, and any bound or unbound ions. The typical MC nomenclature abides by the following scheme: MX[ring size-MC$_{M'Z(L)}$-ring oxygens]Y, where M is the bound central metal and its oxidation state; X is any bound anions; M' is the ring metal and its oxidation state; Z is the third heteroatom of the ring, usually N; L is the organic ligand used in the complex and Y is any unbound anions.[119]

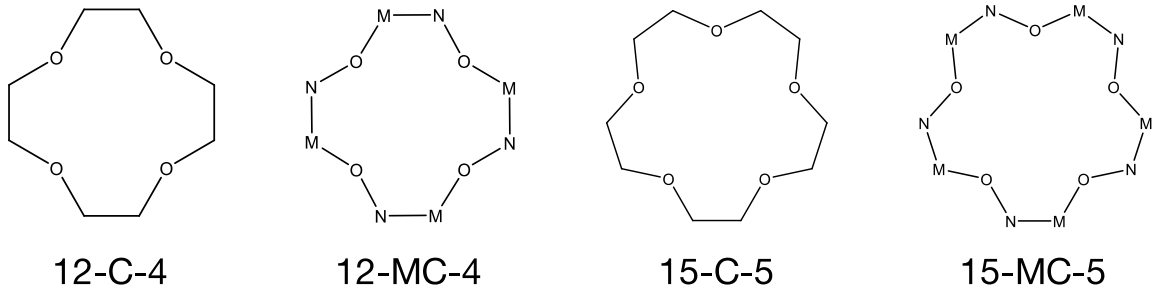

Figure 1.61. Examples of the analogy between organic crown ethers and metallacrowns.

The two most common MCs are of the 12-MC-4 and 15-MC-5 type (Figure 1.62). It should be noted that Figure 1.62 represents the idealized planar structures; X-ray crystallography reveals that actual structures may deviate from planarity. By following the simple design principles, many hydroxamic acid based ligands have been used to generate

various MCs. For instance, the ligand salicylhydroxamic acid (H_3shi) has the correct ligand geometry to prefer the 12-MC-4 topology (Figure 1.62). These ligands form a subunit with an idealized 90° internal angle between the lines bisecting the alternating 5- and 6-membered fused chelate rings, which repeat four times to form the square 12-MC-4 structure. Correspondingly, ligands such as picoline hydroxamic acid (H_2picHA) prefer the 15-MC-5 structure type by forming subunits with idealized 108° internal angles that propagate five times to form the pentagonal structure (Figure 1.62). Due to the structural adaptability of these ligands and the capacity of lanthanides to serve as ring metals, other complex structure types can be achieved. For instance, with H_3shi, alternative motifs deviating from the 12-MC-4 structure type such as the 9-MC-3,[120] 14-MC-5[121] and 15-MC-5[122] structures can also be synthesized depending on the choice of metal and reaction conditions. Actually, the synthesis of MCs requires considerations of several aspects including choice of ligand, metal, solvent, counter-ion, stoichiometry, and crystallization conditions.

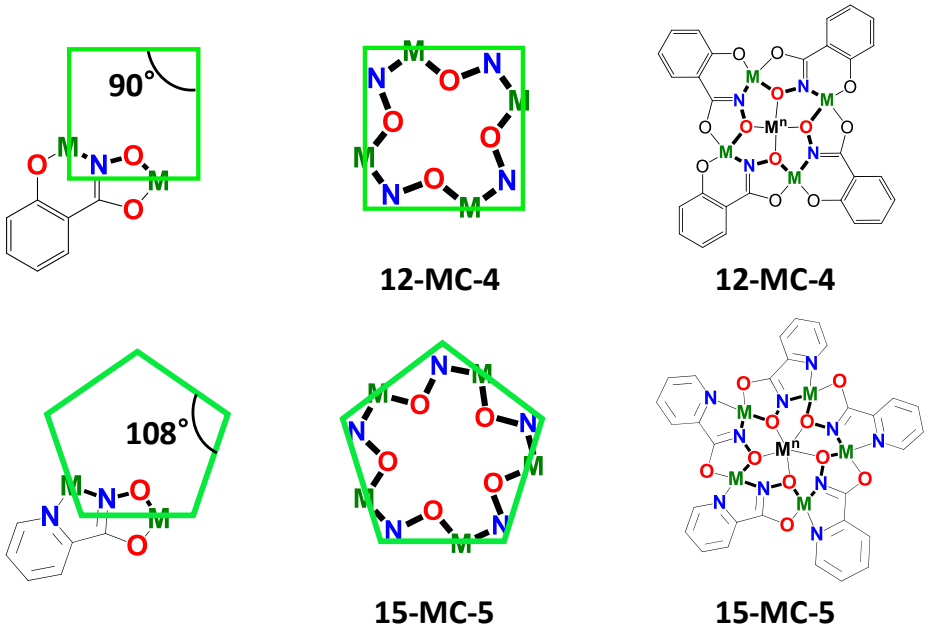

Figure 1.62. Diagrams displaying the design strategy for MCs based on the chelate ring geometry. The square shaped 12-MC-4 is generated from ligands which form a 90° internal angle between the lines bisecting the alternating 5- and 6-membered rings. The deprotonated form of H_3shi is pictured (top); The pentagonal 15-MC-5 is generated from ligands which form a 108° internal angle between the lines bisecting the fused 5-membered rings. The deprotonated form of H_2picHA is pictured (bottom). The MC ring structure is highlighted in bold. Reprinted with permission from reference[123]. Copyright 2014 American Chemical Society.

A typical serial MCs are the Ln^{III}[12-MC-4]$_2$⊂[24-MC-8] complexes, with the ring metal ion — Zn^{II} and the ligand can be picolinehydroxamic acid (picHA),[124]

quinolinehydroxamic acid (quinHA)[125] and so on. The Zn^{II} ion is d^{10} that does not have visible d-d transitions that would interfere with optical applications. The luminescent properties of Ln^{III}[12-MC$_{Zn^{II},\ N,\ pyzHA}$-4]$_2$⊂[24-MC$_{Zn^{II},\ N,\ pyzHA}$-8] complexes (pyzHA = Pyrazinehydroxamic acid, Figure 1.63 and Figure 1.64) were found to be exceptional with very large quantum yield because the Ln^{III} ions are deeply encapsulated and are far from the organic part limiting the quenching pathways.

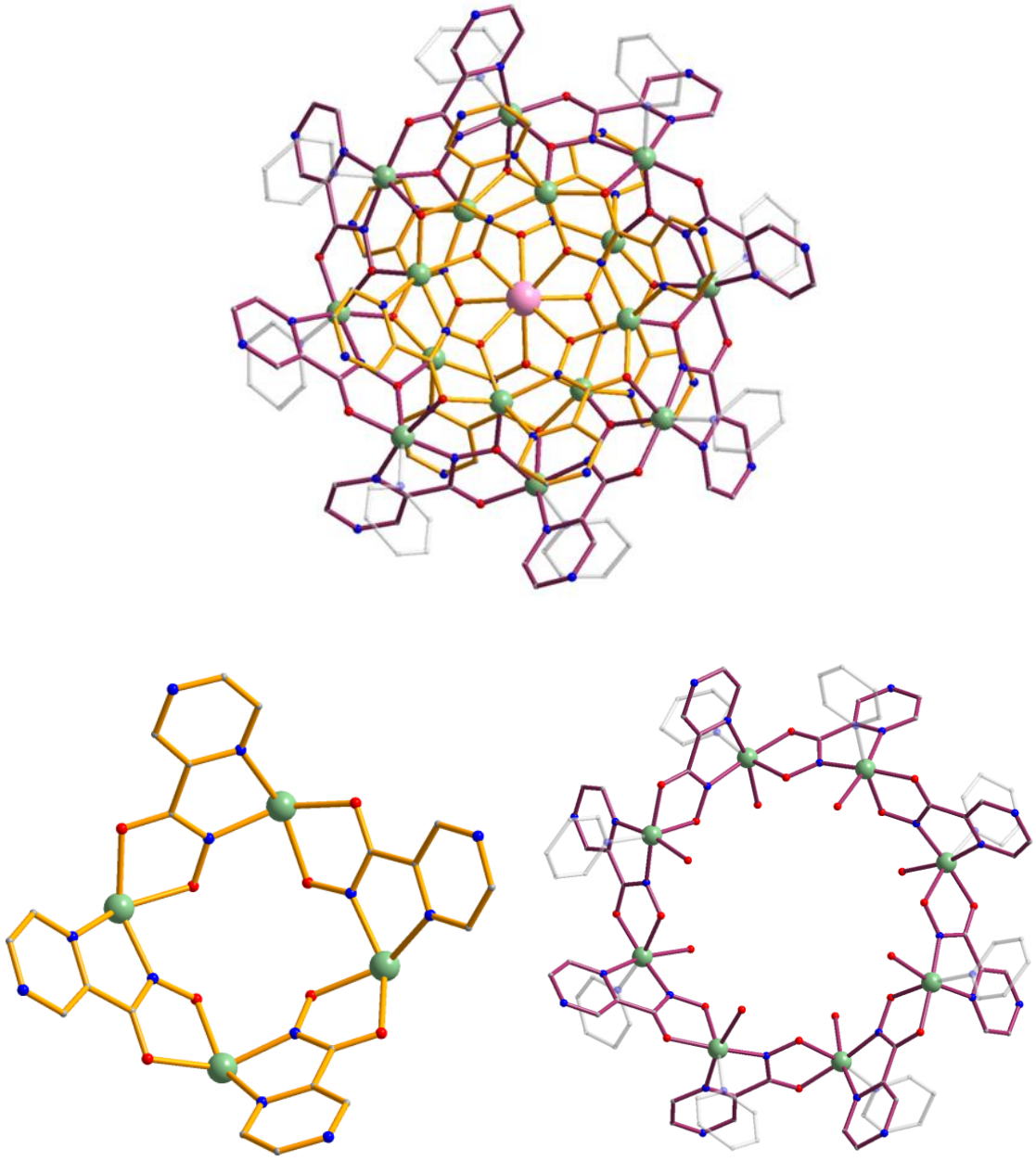

Figure 1.63. A top view of the complex Ln^{III}[12-MC$_{Zn^{II},\ N,\ pyzHA}$-4]$_2$⊂[24-MC$_{Zn^{II},\ N,\ pyzHA}$-8]. [12-MC-4] – bronze; [24-MC-8] – purple; Ln^{III} – pink; Pyridine ligands are displayed as thin grey-white lines; and H atoms were omitted for clarity.

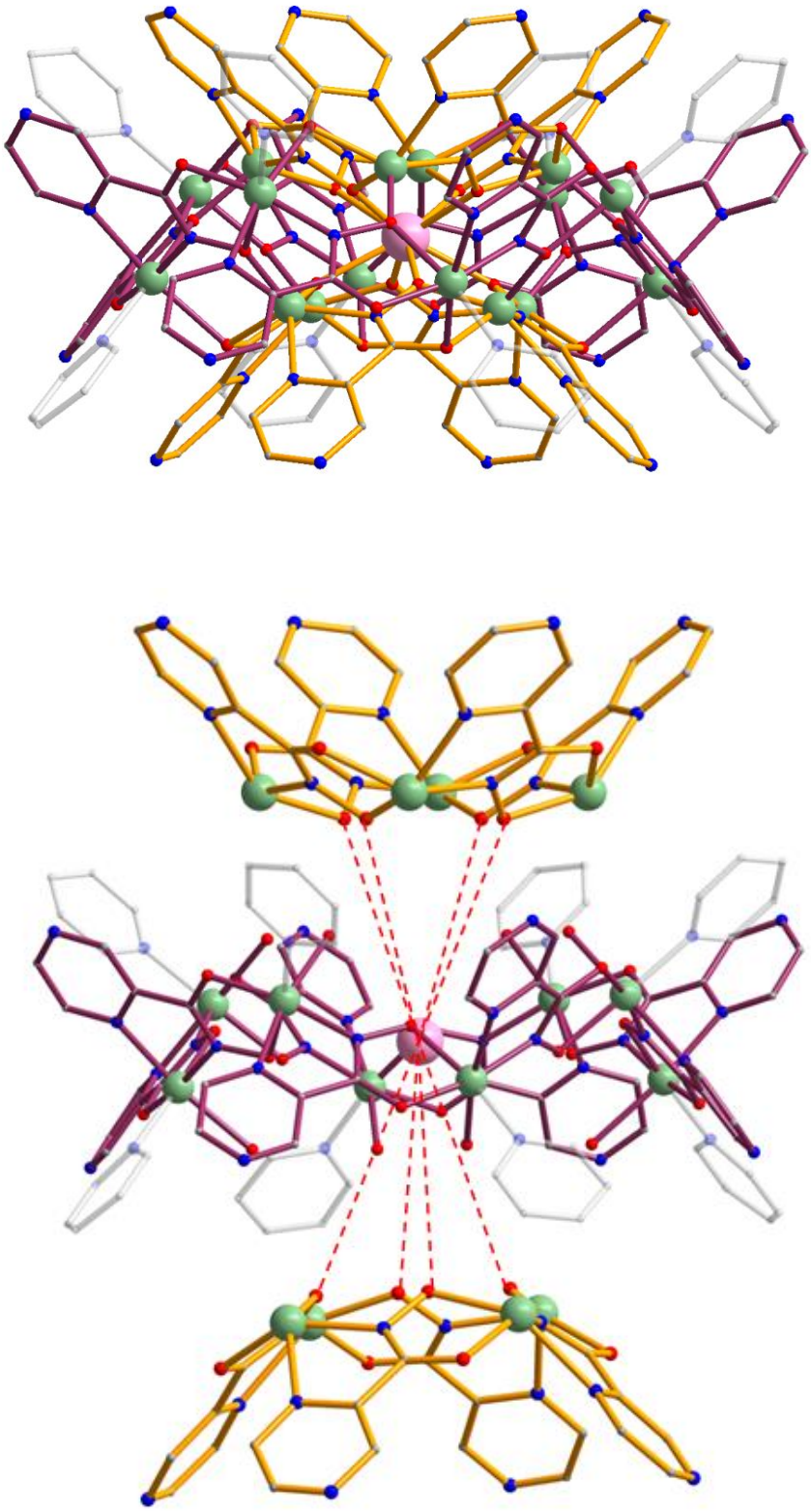

Figure 1.64. A side view of the complex Ln^{III}[12-$MC_{Zn^{II}, N, pyzHA}$-4]$_2$⊂[24-$MC_{Zn^{II}, N, pyzHA}$-8]. [12-MC-4] – bronze; [24-MC-8] – purple; Ln^{III} – pink; Pyridine ligands are displayed as thin grey-white lines; and H atoms were omitted for clarity.

1.5 Lanthanide Luminescence

Lanthanide complexes have been known for their luminescent optical properties before chemists discover their SMM properties. The f-f emission transitions in the trivalent rare earth ions are characterized by narrow line widths and long luminescence lifetimes.[126] These sharp transitions can range from the near-infrared (NIR) region for Pr^{III}, Nd^{III}, Ho^{III}, Er^{III}, Tm^{III} and Yb^{III}, visible region for Pr^{III}, Sm^{III}, Eu^{III}, Tb^{III}, Dy^{III} and Ho^{III} and the ultraviolet (UV) region for Gd^{III} (Figure 1.65 top).[126] These luminescence properties found new applications in material science for OLEDs,[127-130] telecommunications,[131] solar energy conversion,[132] sensing,[133-135] time-resolved luminescent immuno-assay,[136, 137] or time-resolved microscopy,[138, 139] bio-imaging.[140-142] Additionally, the longer wavelengths of the NIR emission allows for greater sensitivity of detection and tissue penetration depth in biological imaging applications.[125]

Energy levels and emission spectra

The ground and excited states of the Ln^{III} ions are shown in Figure 1.65 (bottom). While the metal ions on the periphery (Ce^{III} – Pm^{III}, Ho^{III} – Yb^{III}) have relatively small energy gaps between adjacent levels, the central metals (Sm^{III} – Dy^{III}) display larger gaps, particularly for Gd^{III}. Hence, for the former, non-radiative deactivation processes such as coupling to solvent vibrational modes are more efficient, and these ions are only weakly emissive. For the central group, the luminescent electronic transitions also involve a change in spin multiplicity. As a result, their luminescence is particularly long-lived (microseconds to milliseconds).

Feng SHAO: 0000-0001-8606-8628

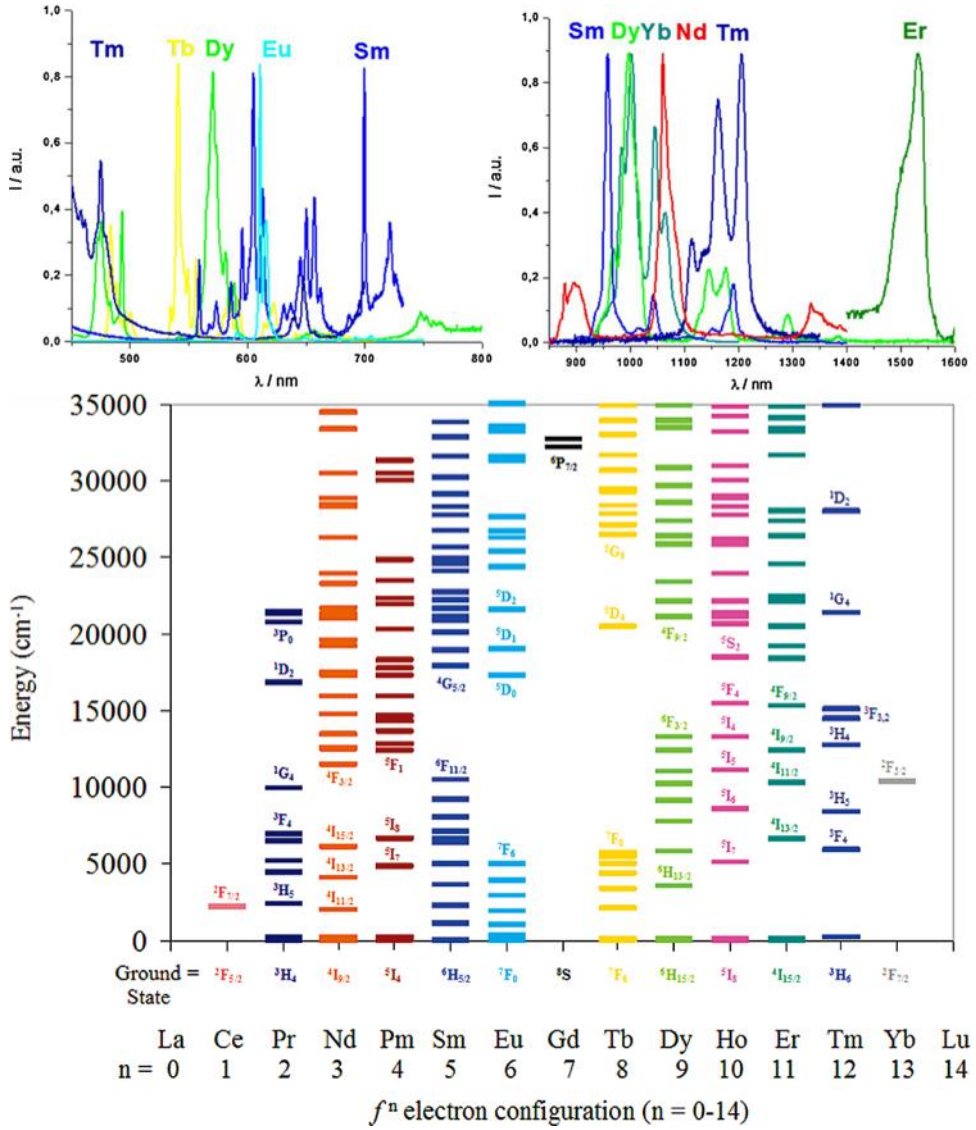

Figure 1.65. Luminescence spectra of some lanthanide complexes in the visible (top left) and NIR (top right) spectroscopic range and corresponding lanthanide(III) ion partial energy diagram (bottom). Taken directly from reference[136]. Copyright 2009 American Chemical Society.

Lanthanide MC-SIM Example: $[YbZn_4(quinha)_4(iqn)_4(DMF)_4](CF_3SO_3)_3$

$[YbZn_4(quinha)_4(iqn)_4(DMF)_4](CF_3SO_3)_3$, (Hquinha = quinaldichydroxamic acid iqn = isoquinoline, Figure 1.66), the first 'half-sandwich' Yb^{III} SIM based on [12-$MC_{Zn^{II}}$-4] was reported by Li and co-workers in 2015,[143] in which the central Yb^{III} ion is coordinated by YbO_8 geometry in D_{4d} symmetry. The anisotropic barrier (Figure 1.68) is extracted from the analysis of static, dynamic magnetism (Figure 1.67) and emission spectrum (Figure 1.69) offering an insight into the magneto-optical correlation.

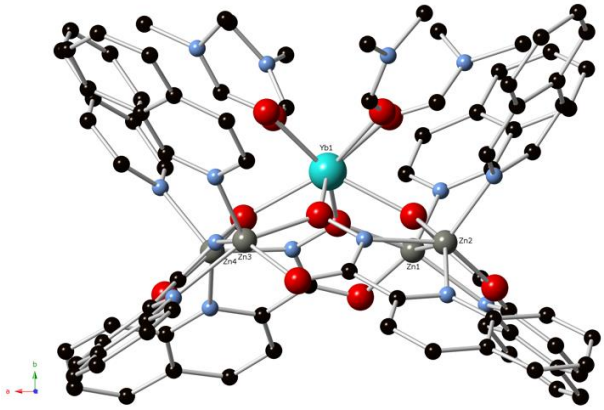

Figure 1.66. A view of the complex $[YbZn_4(quinha)_4(iqn)_4(DMF)_4](CF_3SO_3)_3$. O – red; N – blue; C – black; and H atoms were omitted for clarity. Reprinted with permission from reference[143]. Copyright 2015 The Royal Society of Chemistry.

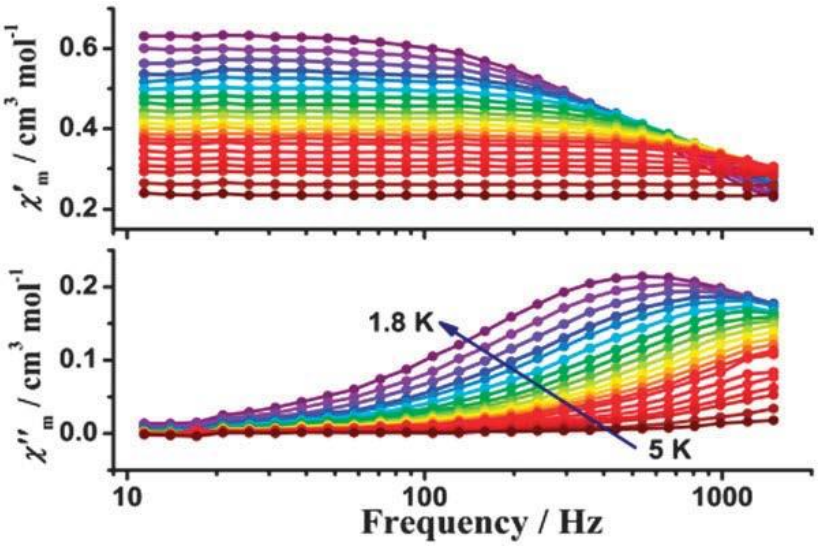

Figure 1.67. Dynamic magnetic susceptibility data for the complex $[YbZn_4(quinha)_4(iqn)_4(DMF)_4](CF_3SO_3)_3$. Reprinted with permission from reference[143]. Copyright 2015 The Royal Society of Chemistry.

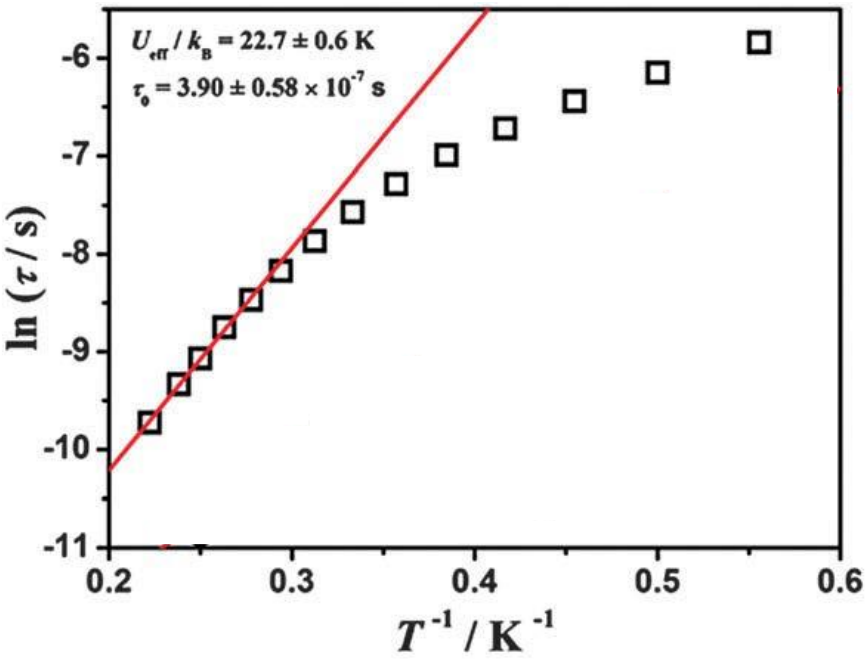

Figure 1.68. Arrhenius plot of the natural logarithm of the relaxation time, τ, *vs.* the inverse temperature for the $[YbZn_4(quinha)_4(iqn)_4(DMF)_4](CF_3SO_3)_3$. Reprinted with permission from reference[143]. Copyright 2015 The Royal Society of Chemistry.

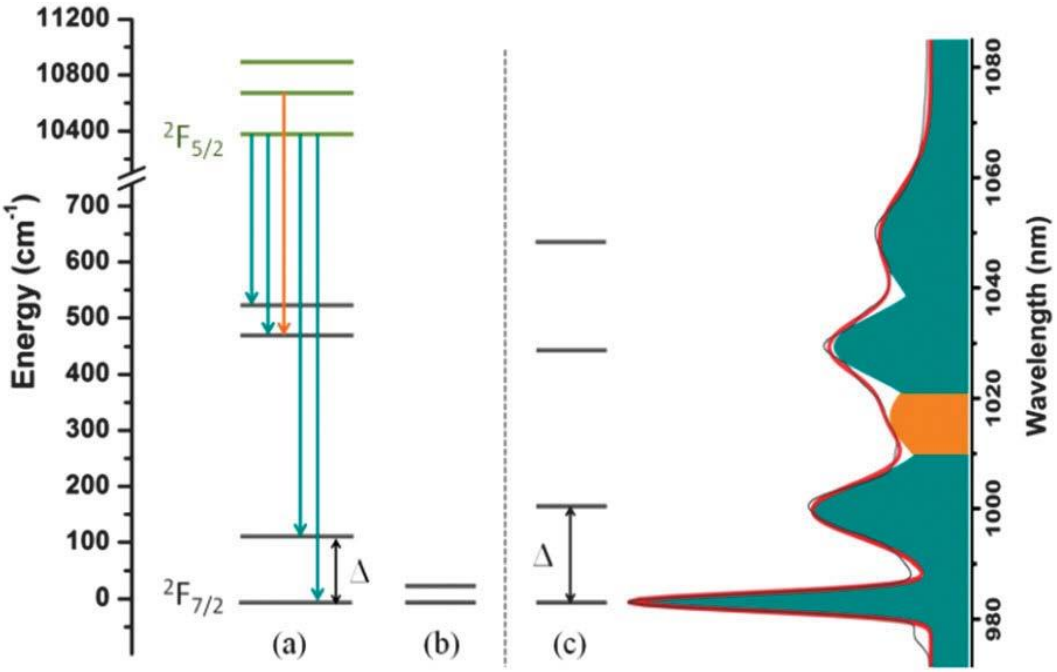

Figure 1.69. Energy levels of the $^2F_{7/2}$ ground state multiplet determined from the (a) dc fit (Δ = 116 cm^{-1}), (b) ac fit (U_{eff}/k_B = 16 cm^{-1}), and (c) the luminescence spectrum (Δ = 169 cm^{-1}). The area of Gaussian deconvolution corresponding to the four Kramers doublets (dark cyan) and one hot transition (orange). Taken directly from reference[143]. Copyright 2015 The Royal Society of Chemistry.

1.6 Thesis Aims

This work comprises two main parts. The first part focuses on the synthesis and the study of the magnetic behavior of mononuclear Co^{II} complexes with trigonal bipyramidal geometry and the second part on the study of mononuclear lanthanide complexes that possess a MC structure.

For the Co^{II} complexes, the aim was to tune the magnetic anisotropy by changing the nature of the tetradentate organic ligand and the terminal ligand. Almost all these complexes behave as SMMs with an energy barrier to the reversal of the magnetization that can be linked to their magnetic anisotropy and thus to the nature of the organic ligands. For the lanthanide complexes, we chose the MC structure because of their high symmetry, which allows performing a correlation between the nature of the lanthanide ion and their SMM properties.

The dissertation will be composed of 6 chapters. The present Chapter 1 introduces the background of the magnetism, SMMs, SIMs, and some important SIMs. Chapter 2 focuses on a family of trigonal bipyramidal complexes [Co(Me_6tren)X]Y (Me_6tren = tris(2-(dimethylamino)ethyl)amine, Figure 1.70, left) with the axial ligand (X) and counter-ion (Y). In Chapter 3, the tetradentate ligand Me_6tren has been replaced by two similar tetradentate ligands with three sulfur atoms (Figure 1.70, middle and right).

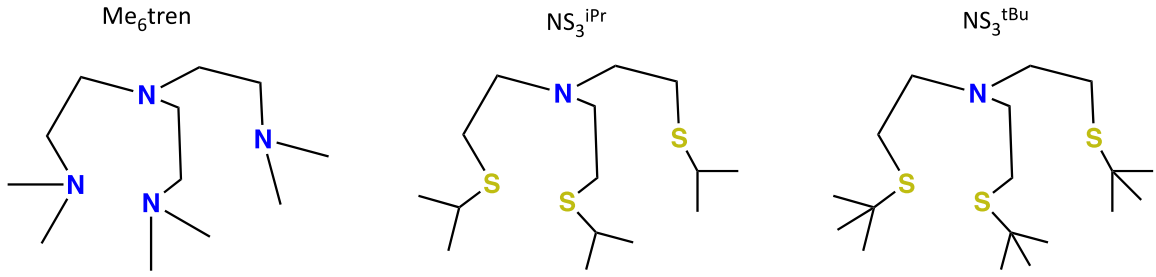

Figure 1.70. Schematic of the Me_6tren (left), NS_3^{iPr} (middle) and NS_3^{tBu} (right).

Chapter 4 and 5, which concern two series of 12-MC-4 SMMs based on $LnGa_4$ (Ln = Tb^{III}, Dy^{III}, Ho^{III}, Er^{III}, Yb^{III}) with the ligands salicylhydroxamic acid (H_3shi) and 3-hydroxy-2-naphthohydroxamic acid (H_3nha), respectively. At last, the understanding gained from this dissertation research, along with future research directions will be recapitulated in Chapter 6.

1.7 References

1. J. F. Keithley, *The Story of Electrical and Magnetic Measurements: From 500 BC to the 1940s*, Wiley-IEEE Press: New York, 1999.
2. D. Song and G. Li, *History of Electromagnetism: Observation and Utilization of electrical and magnetic Phenomena*, Popular Press Publishers: Guangxi, 1987.
3. S. Michel, *L'Asie, source de sciences et de techniques*, Presses Universitaires de Grenoble, 1995.
4. C. Benelli and D. Gatteschi, *Introduction to Molecular Magnetism*, Wiley-VCH Verlag GmbH & Co. KGaA: Weinheim, 2015.
5. B. C. Barish, *The search for magnetic monopoles*, Editions Frontieres, France, 1983.
6. T. Vachaspati, *Physical Review Letters*, 2016, **117**, 181601.
7. R. B. Griffiths, *Physical Review*, 1968, **176**, 655-659.
8. C. Pierre Auger, A. Aab, P. Abreu, M. Aglietta, I. Al Samarai, I. F. M. Albuquerque, I. Allekotte, A. Almela, J. Alvarez Castillo, J. Alvarez-Muñiz, M. Ambrosio, G. A. Anastasi, L. Anchordoqui, B. Andrada, S. Andringa, C. Aramo, F. Arqueros, N. Arsene, H. Asorey, P. Assis, J. Aublin, G. Avila, A. M. Badescu, A. Balaceanu, R. J. Barreira Luz, C. Baus, J. J. Beatty, K. H. Becker, J. A. Bellido, C. Berat, M. E. Bertaina, X. Bertou, P. L. Biermann, P. Billoir, J. Biteau, S. G. Blaess, A. Blanco, J. Blazek, C. Bleve, M. Boháčová, D. Boncioli, C. Bonifazi, N. Borodai, A. M. Botti, J. Brack, I. Brancus, T. Bretz, A. Bridgeman, F. L. Briechle, P. Buchholz, A. Bueno, S. Buitink, M. Buscemi, K. S. Caballero-Mora, L. Caccianiga, A. Cancio, F. Canfora, L. Caramete, R. Caruso, A. Castellina, G. Cataldi, L. Cazon, R. Cester, A. G. Chavez, J. A. Chinellato, J. Chudoba, R. W. Clay, R. Colalillo, A. Coleman, L. Collica, M. R. Coluccia, R. Conceição, F. Contreras, M. J. Cooper, S. Coutu, C. E. Covault, J. Cronin, S. D'Amico, B. Daniel, S. Dasso, K. Daumiller, B. R. Dawson, R. M. de Almeida, S. J. de Jong, G. De Mauro, J. R. T. de Mello Neto, I. De Mitri, J. de Oliveira, V. de Souza, J. Debatin, O. Deligny, C. Di Giulio, A. Di Matteo, M. L. Díaz Castro, F. Diogo, C. Dobrigkeit, J. C. D'Olivo, A. Dorofeev, R. C. dos Anjos, M. T. Dova, A. Dundovic, J. Ebr, R. Engel, M. Erdmann, M. Erfani, C. O. Escobar, J. Espadanal, A. Etchegoyen, H. Falcke, K. Fang, G. Farrar, A. C. Fauth, N. Fazzini, B. Fick, J. M. Figueira, A. Filipčič, O. Fratu, M. M. Freire, T. Fujii, A. Fuster, R. Gaior, B. García, D. Garcia-Pinto, F. Gaté, H. Gemmeke, A. Gherghel-Lascu, P. L. Ghia, U. Giaccari, M. Giammarchi, M. Giller, D. Głas, C. Glaser, H. Glass, G. Golup, M.

Gómez Berisso, P. F. Gómez Vitale, N. González, B. Gookin, A. Gorgi, P. Gorham, P. Gouffon, A. F. Grillo, T. D. Grubb, F. Guarino, G. P. Guedes, M. R. Hampel, P. Hansen, D. Harari, T. A. Harrison, J. L. Harton, Q. Hasankiadeh, A. Haungs, T. Hebbeker, D. Heck, P. Heimann, A. E. Herve, G. C. Hill, C. Hojvat, E. Holt, P. Homola, J. R. Hörandel, P. Horvath, M. Hrabovský, T. Huege, J. Hulsman, A. Insolia, P. G. Isar, I. Jandt, S. Jansen, J. A. Johnsen, M. Josebachuili, A. Kääpä, O. Kambeitz, K. H. Kampert, P. Kasper, I. Katkov, B. Keilhauer, E. Kemp, J. Kemp, R. M. Kieckhafer, H. O. Klages, M. Kleifges, J. Kleinfeller, R. Krause, N. Krohm, D. Kuempel, G. Kukec Mezek, N. Kunka, A. Kuotb Awad, D. LaHurd, M. Lauscher, P. Lebrun, R. Legumina, M. A. Leigui de Oliveira, A. Letessier-Selvon, I. Lhenry-Yvon, K. Link, L. Lopes, R. López, A. López Casado, Q. Luce, A. Lucero, M. Malacari, M. Mallamaci, D. Mandat, P. Mantsch, A. G. Mariazzi, I. C. Mariş, G. Marsella, D. Martello, H. Martinez, O. Martínez Bravo, J. J. Masías Meza, H. J. Mathes, S. Mathys, J. Matthews, J. A. J. Matthews, G. Matthiae, E. Mayotte, P. O. Mazur, C. Medina, G. Medina-Tanco, D. Melo, A. Menshikov, S. Messina, M. I. Micheletti, L. Middendorf, I. A. Minaya, L. Miramonti, B. Mitrica, D. Mockler, L. Molina-Bueno, S. Mollerach, F. Montanet, C. Morello, M. Mostafá, G. Müller, M. A. Muller, S. Müller, I. Naranjo, L. Nellen, J. Neuser, P. H. Nguyen, M. Niculescu-Oglinzanu, M. Niechciol, L. Niemietz, T. Niggemann, D. Nitz, D. Nosek, V. Novotny, H. Nožka, L. A. Núñez, L. Ochilo, F. Oikonomou, A. Olinto, D. Pakk Selmi-Dei, M. Palatka, J. Pallotta, P. Papenbreer, G. Parente, A. Parra, T. Paul, M. Pech, F. Pedreira, J. Pękala, R. Pelayo, J. Peña-Rodriguez, L. A. S. Pereira, L. Perrone, C. Peters, S. Petrera, J. Phuntsok, R. Piegaia, T. Pierog, P. Pieroni, M. Pimenta, V. Pirronello, M. Platino, M. Plum, C. Porowski, R. R. Prado, P. Privitera, M. Prouza, E. J. Quel, S. Querchfeld, S. Quinn, R. Ramos-Pollan, J. Rautenberg, D. Ravignani, D. Reinert, B. Revenu, J. Ridky, M. Risse, P. Ristori, V. Rizi, W. Rodrigues de Carvalho, G. Rodriguez Fernandez, J. Rodriguez Rojo, D. Rogozin, M. Roth, E. Roulet, A. C. Rovero, S. J. Saffi, A. Saftoiu, F. Salamida, H. Salazar, A. Saleh, F. Salesa Greus, G. Salina, J. D. Sanabria Gomez, F. Sánchez, P. Sanchez-Lucas, E. M. Santos, E. Santos, F. Sarazin, B. Sarkar, R. Sarmento, C. A. Sarmiento, R. Sato, M. Schauer, V. Scherini, H. Schieler, M. Schimp, D. Schmidt, O. Scholten, P. Schovánek, F. G. Schröder, A. Schulz, J. Schulz, J. Schumacher, S. J. Sciutto, A. Segreto, M. Settimo, A. Shadkam, R. C. Shellard, G. Sigl, G. Silli, O. Sima, A. Śmiałkowski, R. Šmída, G. R. Snow, P. Sommers, S.

Sonntag, J. Sorokin, R. Squartini, D. Stanca, S. Stanič, J. Stasielak, P. Stassi, F. Strafella, F. Suarez, M. Suarez Durán, T. Sudholz, T. Suomijärvi, A. D. Supanitsky, J. Swain, Z. Szadkowski, A. Taboada, O. A. Taborda, A. Tapia, V. M. Theodoro, C. Timmermans, C. J. Todero Peixoto, L. Tomankova, B. Tomé, G. Torralba Elipe, D. Torres Machado, M. Torri, P. Travnicek, M. Trini, R. Ulrich, M. Unger, M. Urban, J. F. Valdés Galicia, I. Valiño, L. Valore, G. van Aar, P. van Bodegom, A. M. van den Berg, A. van Vliet, E. Varela, B. Vargas Cárdenas, G. Varner, J. R. Vázquez, R. A. Vázquez, D. Veberič, I. D. Vergara Quispe, V. Verzi, J. Vicha, L. Villaseñor, S. Vorobiov, H. Wahlberg, O. Wainberg, D. Walz, A. A. Watson, M. Weber, A. Weindl, L. Wiencke, H. Wilczyński, T. Winchen, D. Wittkowski, B. Wundheiler, S. Wykes, L. Yang, D. Yelos, A. Yushkov, E. Zas, D. Zavrtanik, M. Zavrtanik, A. Zepeda, B. Zimmermann, M. Ziolkowski, Z. Zong and F. Zuccarello, *Physical Review D*, 2016, **94**, 082002.

9. G. Hall, *Philosophical Transactions of the Royal Society A: Mathematical, Physical and Engineering Sciences*, 2008, **366**, 1849-1860.
10. H. Kragh, *The Physics Teacher*, 1997, **35**, 328-332.
11. W. F. Giauque, *Journal of the American Chemical Society*, 1927, **49**, 1864-1870.
12. C. Kittel, J. K. Galt and W. E. Campbell, *Physical Review*, 1950, **77**, 725-725.
13. J. G. Bednorz and K. A. Müller, *Zeitschrift für Physik B Condensed Matter*, 1986, **64**, 189-193.
14. S. Kobe, *Brazilian Journal of Physics*, 2000, **30**, 649-654.
15. W. Heisenberg, *Physics and Philosophy: The Revolution in Modern Science*, Prometheus Books, 1958.
16. R. L. Carlin, *Magnetochemistry*, Springer-Verlag: Berlin, 1986.
17. O. Kahn, *Molecular Magnetism*, VCH Publishers, Inc.: New York, 1993.
18. S. A. Wolf, D. D. Awschalom, R. A. Buhrman, J. M. Daughton, S. von Molnár, M. L. Roukes, A. Y. Chtchelkanova and D. M. Treger, *Science*, 2001, **294**, 1488-1495.
19. L. Bogani and W. Wernsdorfer, *Nature Materials*, 2008, **7**, 179-186.
20. R. E. P. Winpenny, *Angewandte Chemie International Edition*, 2008, **47**, 7992-7994.
21. C. Davide, *Nature*, 2017, **541**, 9-10.
22. M. Verdaguer, *Polyhedron*, 2001, **20**, xxix-xxxi.
23. J. B. Goodenough, *Journal of Physics and Chemistry of Solids*, 1958, **6**, 287-297.
24. J. Kanamori, *Journal of Physics and Chemistry of Solids*, 1959, **10**, 87-98.

25. J. Goodenough, *Scholarpedia*, 2008, **3**, 7382.
26. A. Caneschi, D. Gatteschi, R. Sessoli, A. L. Barra, L. C. Brunel and M. Guillot, *Journal of the American Chemical Society*, 1991, **113**, 5873-5874.
27. R. Sessoli, D. Gatteschi, A. Caneschi and M. A. Novak, *Nature*, 1993, **365**, 141-143.
28. R. Sessoli, H. L. Tsai, A. R. Schake, S. Wang, J. B. Vincent, K. Folting, D. Gatteschi, G. Christou and D. N. Hendrickson, *Journal of the American Chemical Society*, 1993, **115**, 1804-1816.
29. G. I. Likhtenshtein, J. Yamauchi, S. i. Nakatsuji, A. I. Smirnov and R. Tamura, in *Nitroxides*, Wiley-VCH Verlag GmbH & Co. KGaA, 2008, DOI: 10.1002/9783527621743.ch1, pp. 1-45.
30. G. J. Ribas, *Coordination Chemistry*, WILEY-VCH Verlag GmbH & Co. KGaA: Weinheim, 2008.
31. D. Gatteschi, R. Sessoli and J. Villain, *Molecular Nanomagnets*, Oxford University Press: New York, 2006.
32. J. A. S. Smith, *Journal of Chemical Education*, 1971, **48**, 39.
33. J. C. Anderson, *Magnetism and magnetic materials*, CHAPMAN AND HALL, London, 1968.
34. C. Simon, *Lanthanide and Actinide Chemistry*, John Wiley & Sons Ltd.: West Sussex, 2006.
35. V. E. Campbell, H. Bolvin, E. Rivière, R. Guillot, W. Wernsdorfer and T. Mallah, *Inorganic Chemistry*, 2014, **53**, 2598-2605.
36. R. Bagai and G. Christou, *Chemical Society Reviews*, 2009, **38**, 1011-1026.
37. M. Perovic, V. Kusigerski, V. Spasojevic, A. Mrakovic, J. Blanusa, M. Zentkova and M. Mihalik, *Journal of Physics D: Applied Physics*, 2013, **46**, 165001.
38. H. B. G. Casimir and F. K. du Pré, *Physica*, 1938, **5**, 507-511.
39. K. S. Cole and R. H. Cole, *The Journal of Chemical Physics*, 1941, **9**, 341-351.
40. F. Shao, B. Cahier, N. Guihery, E. Riviere, R. Guillot, A.-L. Barra, Y. Lan, W. Wernsdorfer, V. E. Campbell and T. Mallah, *Chemical Communications*, 2015, **51**, 16475-16478.
41. J. Bartolomé, G. Filoti, V. Kuncser, G. Schinteie, V. Mereacre, C. E. Anson, A. K. Powell, D. Prodius and C. Turta, *Physical Review B*, 2009, **80**, 014430.
42. F. Luis, J. Bartolomé, J. F. Fernández, J. Tejada, J. M. Hernández, X. X. Zhang and R. Ziolo, *Physical Review B*, 1997, **55**, 11448-11456.

43. V. V. Novikov, A. A. Pavlov, Y. V. Nelyubina, M.-E. Boulon, O. A. Varzatskii, Y. Z. Voloshin and R. E. P. Winpenny, *Journal of the American Chemical Society*, 2015, **137**, 9792-9795.
44. L. Thomas, F. Lionti, R. Ballou, D. Gatteschi, R. Sessoli and B. Barbara, *Nature*, 1996, **383**, 145-147.
45. J. R. Friedman, M. P. Sarachik, J. Tejada, J. Maciejewski and R. Ziolo, *Journal of Applied Physics*, 1996, **79**, 6031-6033.
46. J. R. Friedman, M. P. Sarachik, J. Tejada and R. Ziolo, *Physical Review Letters*, 1996, **76**, 3830-3833.
47. D. Gatteschi and R. Sessoli, *Angewandte Chemie International Edition*, 2003, **42**, 268-297.
48. G. Christou, D. Gatteschi, D. N. Hendrickson and R. Sessoli, *MRS Bulletin*, 2000, **25**, 66-71.
49. W. Wernsdorfer and R. Sessoli, *Science*, 1999, **284**, 133-135.
50. N. E. Chakov, S.-C. Lee, A. G. Harter, P. L. Kuhns, A. P. Reyes, S. O. Hill, N. S. Dalal, W. Wernsdorfer, K. A. Abboud and G. Christou, *Journal of the American Chemical Society*, 2006, **128**, 6975-6989.
51. M. Hołyńska, D. Premužić, I.-R. Jeon, W. Wernsdorfer, R. Clérac and S. Dehnen, *Chemistry – A European Journal*, 2011, **17**, 9605-9610.
52. Y. C. Chen, J. L. Liu, L. Ungur, J. Liu, Q. W. Li, L. F. Wang, Z. P. Ni, L. F. Chibotaru, X. M. Chen and M. L. Tong, *Journal of the American Chemical Society*, 2016, **138**, 2829-2837.
53. J. Liu, Y. C. Chen, J. L. Liu, V. Vieru, L. Ungur, J. H. Jia, L. F. Chibotaru, Y. Lan, W. Wernsdorfer, S. Gao, X. M. Chen and M. L. Tong, *Journal of the American Chemical Society*, 2016, **138**, 5441-5450.
54. J. D. Rinehart, M. Fang, W. J. Evans and J. R. Long, *Journal of the American Chemical Society*, 2011, **133**, 14236-14239.
55. Y.-S. Ding, N. F. Chilton, R. E. P. Winpenny and Y.-Z. Zheng, *Angewandte Chemie International Edition*, 2016, **55**, 16071-16074.
56. D. Schweinfurth, J. Krzystek, M. Atanasov, J. Klein, S. Hohloch, J. Telser, S. Demeshko, F. Meyer, F. Neese and B. Sarkar, *Inorganic Chemistry*, 2017, **56**, 5253-5265.
57. L. Torlina, F. Morales, J. Kaushal, I. Ivanov, A. Kheifets, A. Zielinski, A. Scrinzi, H.

G. Muller, S. Sukiasyan, M. Ivanov and O. Smirnova, *Nat Phys*, 2015, **11**, 503-508.

58. F. Shao, B. Cahier, E. Rivière, R. Guillot, N. Guihéry, V. E. Campbell and T. Mallah, *Inorganic Chemistry*, 2017, **56**, 1104-1111.
59. J. D. Rinehart, M. Fang, W. J. Evans and J. R. Long, *Nature Chemistry*, 2011, **3**, 538-542.
60. W. Wernsdorfer, N. Aliaga-Alcalde, D. N. Hendrickson and G. Christou, *Nature*, 2002, **416**, 406-409.
61. S. Hill, R. S. Edwards, N. Aliaga-Alcalde and G. Christou, *Science*, 2003, **302**, 1015-1018.
62. R. Bagai, W. Wernsdorfer, K. A. Abboud and G. Christou, *Journal of the American Chemical Society*, 2007, **129**, 12918-12919.
63. S. Alex, J. B. Andrew, T. Nassiba, G.-L. Maria del Carmen, R. C. Neil, H. B. Peter and N. O. S. James, *Nanotechnology*, 2011, **22**, 075704.
64. M. Mannini, F. Pineider, C. Danieli, F. Totti, L. Sorace, P. Sainctavit, M. A. Arrio, E. Otero, L. Joly, J. C. Cezar, A. Cornia and R. Sessoli, *Nature*, 2010, **468**, 417-421.
65. W. Wernsdorfer, N. E. Chakov and G. Christou, *Physical Review B*, 2004, **70**, 132413.
66. W. Wernsdorfer, *Superconductor Science and Technology*, 2009, **22**, 064013.
67. T. Lis, *Acta Crystallographica Section B*, 1980, **36**, 2042-2046.
68. S. Hill, J. A. A. J. Perenboom, N. S. Dalal, T. Hathaway, T. Stalcup and J. S. Brooks, *Physical Review Letters*, 1998, **80**, 2453-2456.
69. G. A. Craig and M. Murrie, *Chemical Society Reviews*, 2015, **44**, 2135-2147.
70. S. Gomez-Coca, D. Aravena, R. Morales and E. Ruiz, *Coordination Chemistry Reviews*, 2015, **289**, 379-392.
71. O. Waldmann, *Inorganic Chemistry*, 2007, **46**, 10035-10037.
72. E. Ruiz, J. Cirera, J. Cano, S. Alvarez, C. Loose and J. Kortus, *Chemical Communications*, 2008, DOI: 10.1039/B714715E, 52-54.
73. F. Neese and D. A. Pantazis, *Faraday Discussions*, 2011, **148**, 229-238.
74. J. M. Frost, K. L. M. Harriman and M. Murugesu, *Chemical Science*, 2016, **7**, 2470-2491.
75. P. Parois, S. A. Moggach, J. Sanchez-Benitez, K. V. Kamenev, A. R. Lennie, J. E. Warren, E. K. Brechin, S. Parsons and M. Murrie, *Chemical Communications*, 2010, **46**, 1881-1883.
76. S. Hill, S. Datta, J. Liu, R. Inglis, C. J. Milios, P. L. Feng, J. J. Henderson, E. del

Barco, E. K. Brechin and D. N. Hendrickson, *Dalton Transactions*, 2010, **39**, 4693-4707.

77. N. Ishikawa, M. Sugita, T. Ishikawa, S.-y. Koshihara and Y. Kaizu, *Journal of the American Chemical Society*, 2003, **125**, 8694-8695.
78. D. E. Freedman, W. H. Harman, T. D. Harris, G. J. Long, C. J. Chang and J. R. Long, *Journal of the American Chemical Society*, 2010, **132**, 1224-1225.
79. W. H. Harman, T. D. Harris, D. E. Freedman, H. Fong, A. Chang, J. D. Rinehart, A. Ozarowski, M. T. Sougrati, F. Grandjean, G. J. Long, J. R. Long and C. J. Chang, *Journal of the American Chemical Society*, 2010, **132**, 18115-18126.
80. J. Vallejo, A. Pascual-Álvarez, J. Cano, I. Castro, M. Julve, F. Lloret, J. Krzystek, G. De Munno, D. Armentano, W. Wernsdorfer, R. Ruiz-García and E. Pardo, *Angewandte Chemie International Edition*, 2013, **52**, 14075-14079.
81. J. M. Zadrozny, D. J. Xiao, M. Atanasov, G. J. Long, F. Grandjean, F. Neese and J. R. Long, *Nature Chemistry*, 2013, **5**, 577-581.
82. A. Hauser, *Chemical Physics Letters*, 1986, **124**, 543-548.
83. X. Feng, C. Mathonière, I.-R. Jeon, M. Rouzières, A. Ozarowski, M. L. Aubrey, M. I. Gonzalez, R. Clérac and J. R. Long, *Journal of the American Chemical Society*, 2013, **135**, 15880-15884.
84. S. Mossin, B. L. Tran, D. Adhikari, M. Pink, F. W. Heinemann, J. Sutter, R. K. Szilagyi, K. Meyer and D. J. Mindiola, *Journal of the American Chemical Society*, 2012, **134**, 13651-13661.
85. S. Mossin, B. L. Tran, D. Adhikari, M. Pink, F. W. Heinemann, J. Sutter, R. K. Szilagyi, K. Meyer and D. J. Mindiola, *Journal of the American Chemical Society*, 2012, **134**, 13651-13661.
86. Y.-S. Meng, S.-D. Jiang, B.-W. Wang and S. Gao, *Accounts of Chemical Research*, 2016, **49**, 2381-2389.
87. Y.-S. Meng, Z. Mo, B.-W. Wang, Y.-Q. Zhang, L. Deng and S. Gao, *Chemical Science*, 2015, **6**, 7156-7162.
88. F. Habib, O. R. Luca, V. Vieru, M. Shiddiq, I. Korobkov, S. I. Gorelsky, M. K. Takase, L. F. Chibotaru, S. Hill, R. H. Crabtree and M. Murugesu, *Angewandte Chemie International Edition*, 2013, **52**, 11290-11293.
89. L. Chen, J. Wang, J.-M. Wei, W. Wernsdorfer, X.-T. Chen, Y.-Q. Zhang, Y. Song and Z.-L. Xue, *Journal of the American Chemical Society*, 2014, **136**, 12213-12216.

90. C. Fiolka, I. Pantenburg and G. Meyer, *Crystal Growth & Design*, 2011, **11**, 5159-5165.
91. J. M. Zadrozny and J. R. Long, *Journal of the American Chemical Society*, 2011, **133**, 20732-20734.
92. Y. Rechkemmer, F. D. Breitgoff, M. van der Meer, M. Atanasov, M. Hakl, M. Orlita, P. Neugebauer, F. Neese, B. Sarkar and J. van Slageren, *Nature Communications*, 2016, **7**.
93. D. Schweinfurth, M. G. Sommer, M. Atanasov, S. Demeshko, S. Hohloch, F. Meyer, F. Neese and B. Sarkar, *Journal of the American Chemical Society*, 2015, **137**, 1993-2005.
94. T. J. Woods, M. F. Ballesteros-Rivas, S. Gómez-Coca, E. Ruiz and K. R. Dunbar, *Journal of the American Chemical Society*, 2016, **138**, 16407-16416.
95. X.-N. Yao, J.-Z. Du, Y.-Q. Zhang, X.-B. Leng, M.-W. Yang, S.-D. Jiang, Z.-X. Wang, Z.-W. Ouyang, L. Deng, B.-W. Wang and S. Gao, *Journal of the American Chemical Society*, 2017, **139**, 373-380.
96. X.-N. Yao, J.-Z. Du, Y.-Q. Zhang, X.-B. Leng, M.-W. Yang, S.-D. Jiang, Z.-X. Wang, Z.-W. Ouyang, L. Deng, B.-W. Wang and S. Gao, *Journal of the American Chemical Society*, 2016, DOI: 10.1021/jacs.6b11043.
97. R. C. Poulten, M. J. Page, A. G. Algarra, J. J. Le Roy, I. López, E. Carter, A. Llobet, S. A. Macgregor, M. F. Mahon, D. M. Murphy, M. Murugesu and M. K. Whittlesey, *Journal of the American Chemical Society*, 2013, **135**, 13640-13643.
98. R. Ruamps, R. Maurice, L. Batchelor, M. Boggio-Pasqua, R. Guillot, A. L. Barra, J. Liu, E.-E. Bendeif, S. Pillet, S. Hill, T. Mallah and N. Guihéry, *Journal of the American Chemical Society*, 2013, **135**, 3017-3026.
99. K. E. R. Marriott, L. Bhaskaran, C. Wilson, M. Medarde, S. T. Ochsenbein, S. Hill and M. Murrie, *Chemical Science*, 2015, **6**, 6823-6828.
100. J.-C. G. Bünzli and S. V. Eliseeva, in *Lanthanide Luminescence: Photophysical, Analytical and Biological Aspects*, eds. P. Hänninen and H. Härmä, Springer Berlin Heidelberg, Berlin, Heidelberg, 2011, DOI: 10.1007/4243_2010_3, pp. 1-45.
101. J. D. Rinehart and J. R. Long, *Chemical Science*, 2011, **2**, 2078-2085.
102. J. Sievers, *Zeitschrift für Physik B Condensed Matter*, 1982, **45**, 289-296.
103. S.-D. Jiang and S.-X. Qin, *Inorganic Chemistry Frontiers*, 2015, **2**, 613-619.
104. N. Ishikawa, M. Sugita and W. Wernsdorfer, *Journal of the American Chemical*

Society, 2005, **127**, 3650-3651.

105. N. Ishikawa, M. Sugita, T. Ishikawa, S.-y. Koshihara and Y. Kaizu, *The Journal of Physical Chemistry B*, 2004, **108**, 11265-11271.
106. N. Ishikawa, M. Sugita, T. Okubo, N. Tanaka, T. Iino and Y. Kaizu, *Inorganic Chemistry*, 2003, **42**, 2440-2446.
107. N. Ishikawa, *Journal of Physical Chemistry A*, 2003, **107**, 5831-5835.
108. N. Koike, H. Uekusa, Y. Ohashi, C. Harnoode, F. Kitamura, T. Ohsaka and K. Tokuda, *Inorganic Chemistry*, 1996, **35**, 5798-5804.
109. M. A. AlDamen, J. M. Clemente-Juan, E. Coronado, C. Martí-Gastaldo and A. Gaita-Ariño, *Journal of the American Chemical Society*, 2008, **130**, 8874-8875.
110. S. Ghosh, S. Datta, L. Friend, S. Cardona-Serra, A. Gaita-Arino, E. Coronado and S. Hill, *Dalton Transactions*, 2012, **41**, 13697-13704.
111. M. J. Martínez-Pérez, S. Cardona-Serra, C. Schlegel, F. Moro, P. J. Alonso, H. Prima-García, J. M. Clemente-Juan, M. Evangelisti, A. Gaita-Ariño, J. Sesé, J. van Slageren, E. Coronado and F. Luis, *Physical Review Letters*, 2012, **108**, 247213.
112. J. J. Baldovi, Y. Duan, C. Bustos, S. Cardona-Serra, P. Gouzerh, R. Villanneau, G. Gontard, J. M. Clemente-Juan, A. Gaita-Arino, C. Gimenez-Saiz, A. Proust and E. Coronado, *Dalton Transactions*, 2016, **45**, 16653-16660.
113. M. A. AlDamen, S. Cardona-Serra, J. M. Clemente-Juan, E. Coronado, A. Gaita-Ariño, C. Martí-Gastaldo, F. Luis and O. Montero, *Inorganic Chemistry*, 2009, **48**, 3467-3479.
114. B. Bleaney, H. E. D. Scovil and R. S. Trenam, *Proceedings of the Royal Society of London. Series A. Mathematical and Physical Sciences*, 1954, **223**, 15-29.
115. C. M. Zaleski, E. C. Depperman, J. W. Kampf, M. L. Kirk and V. L. Pecoraro, *Inorganic Chemistry*, 2006, **45**, 10022-10024.
116. M. S. Lah and V. L. Pecoraro, *Journal of the American Chemical Society*, 1989, **111**, 7258-7259.
117. V. L. Pecoraro, *Inorganica Chimica Acta*, 1989, **155**, 171-173.
118. P. Happ, C. Plenk and E. Rentschler, *Coordination Chemistry Reviews*, 2015, **289–290**, 238-260.
119. G. Mezei, C. M. Zaleski and V. L. Pecoraro, *Chemical Reviews*, 2007, **107**, 4933-5003.
120. M. S. Lah, M. L. Kirk, W. Hatfield and V. L. Pecoraro, *Journal of the Chemical*

Society, Chemical Communications, 1989, DOI: 10.1039/C39890001606, 1606-1608.

121. T. T. Boron, J. W. Kampf and V. L. Pecoraro, *Inorganic Chemistry*, 2010, **49**, 9104-9106.
122. D. P. Kessisoglou, J. Kampf and V. L. Pecoraro, *Polyhedron*, 1994, **13**, 1379-1391.
123. J. Jankolovits, J. W. Kampf and V. L. Pecoraro, *Inorganic Chemistry*, 2014, **53**, 7534-7546.
124. J. Jankolovits, C. M. Andolina, J. W. Kampf, K. N. Raymond and V. L. Pecoraro, *Angewandte Chemie International Edition*, 2011, **50**, 9660-9664.
125. E. R. Trivedi, S. V. Eliseeva, J. Jankolovits, M. M. Olmstead, S. Petoud and V. L. Pecoraro, *Journal of the American Chemical Society*, 2014, **136**, 1526-1534.
126. S. V. Eliseeva and J.-C. G. Bunzli, *Chemical Society Reviews*, 2010, **39**, 189-227.
127. K. Junji, N. Katsutoshi and O. Yutaka, *Chemistry Letters*, 1990, **19**, 657-660.
128. J. Kido and Y. Okamoto, *Chemical Reviews*, 2002, **102**, 2357-2368.
129. A. de Bettencourt-Dias, *Dalton Transactions*, 2007, DOI: 10.1039/B702341C, 2229-2241.
130. G. Zucchi and #235, *International Journal of Inorganic Chemistry*, 2011, **2011**.
131. J.-C. G. Bünzli and S. V. Eliseeva, *Journal of Rare Earths*, 2010, **28**, 824-842.
132. S. F. H. Correia, V. de Zea Bermudez, S. J. L. Ribeiro, P. S. Andre, R. A. S. Ferreira and L. D. Carlos, *Journal of Materials Chemistry A*, 2014, **2**, 5580-5596.
133. J.-C. G. Bünzli, *Chemical Reviews*, 2010, **110**, 2729-2755.
134. R. M. Duke, E. B. Veale, F. M. Pfeffer, P. E. Kruger and T. Gunnlaugsson, *Chemical Society Reviews*, 2010, **39**, 3936-3953.
135. C. P. Montgomery, B. S. Murray, E. J. New, R. Pal and D. Parker, *Accounts of Chemical Research*, 2009, **42**, 925-937.
136. E. G. Moore, A. P. S. Samuel and K. N. Raymond, *Accounts of Chemical Research*, 2009, **42**, 542-552.
137. J. Yuan and G. Wang, *TRAC Trends in Analytical Chemistry*, 2006, **25**, 490-500.
138. J. Yuan and G. Wang, *Journal of Fluorescence*, 2005, **15**, 559-568.
139. A. Beeby, S. W. Botchway, I. M. Clarkson, S. Faulkner, A. W. Parker, D. Parker and J. A. G. Williams, *Journal of Photochemistry and Photobiology B: Biology*, 2000, **57**, 83-89.
140. E. G. Moore, J. Xu, S. C. Dodani, C. J. Jocher, A. D'Aléo, M. Seitz and K. N. Raymond, *Inorganic Chemistry*, 2010, **49**, 4156-4166.

141. P. Verwilst, S. V. Eliseeva, L. Vander Elst, C. Burtea, S. Laurent, S. Petoud, R. N. Muller, T. N. Parac-Vogt and W. M. De Borggraeve, *Inorganic Chemistry*, 2012, **51**, 6405-6411.

142. S. Comby, D. Imbert, A.-S. Chauvin and J.-C. G. Bünzli, *Inorganic Chemistry*, 2006, **45**, 732-743.

143. Q.-W. Li, J.-L. Liu, J.-H. Jia, Y.-C. Chen, J. Liu, L.-F. Wang and M.-L. Tong, *Chemical Communications*, 2015, **51**, 10291-10294.

CHAPTER 2 Engineering the Ising-type Anisotropy in Trigonal Bipyramidal Co^{II} Complexes Based on Me_6tren

2.1 Introduction

The first SMM was polynuclear transition metal cluster with large spin ground state (*S*) and relatively moderate ZFS value (*D*) associated to the ground state.[1, 2] More recently, research efforts have focused on building mononuclear SMMs with the intent to better control and tune the magnetic anisotropy, on one hand, and on the other hand to have complexes with a better stability that can be manipulated in solution. The interest in mononuclear complexes started with the discovery of the SMM behavior in the double-decker lanthanide complexes family.[3-17] These complexes benefit from the large SOC of the *f*-block elements inherent to the single ion, which induces large magnetic anisotropy in the presence of the crystal field of the ligands. The nature of magnetic anisotropy that may induce an Ising or planar magnetization is intimately related to the symmetry imposed by the ligands. But, for lanthanides the *f* orbitals are deeply buried beneath the valence shell, and the control of the symmetry of the molecules by the ligands is difficult in most cases. This is not the case for transition metal ions where the effect of the ligand crystal field on the metal electrons is larger, thus allowing a better control of the symmetry and thus of the magnetic anisotropy. It is important to note that for transition metal ions the SOC effect is weaker than for lanthanides leading, generally, to magnetic anisotropy with weaker magnitude. Despite this drawback, the magnitude of the magnetic anisotropy may be large enough in transition metal mononuclear complexes to observe the SMM behavior. The most notable examples are a linear Fe^{I} complex, a tetrahedral Co^{II} complex, and a trigonal bipyramidal Co^{II} complex.[18-24] As mentioned above, mononuclear complexes present clear advantages over polynuclear clusters, as they can be easily manipulated in solution and on surfaces, which is a requirement if one wants to employ them as single quantum bits for quantum information applications.[25] The interest in mononuclear transition metal SMMs stems, thus, from the possibility to more easily control their coordination geometry and in turn tune and shape their magnetic anisotropy.

Our group has previously shown that imposing a trigonal bipyramidal symmetry around Co^{II} and Ni^{II} cations leads to Ising-type magnetic anisotropy (negative *D* value) that is very large for the Ni^{II} complex.[18, 19] The anisotropy arises from the axial symmetry imposed by the organic ligand Tris(2-(dimethylamino)ethyl)amine (Me_6tren). The [Ni(Me_6tren)Cl](ClO_4) complex has a *D* value close to –200 cm^{-1}, due to the quasi first-order SOC.[19] Blocking of the magnetization was not observed because QTM is usually large in *S* = 1 systems due to the presence of a tiny transverse anisotropy resulting from a dynamic Jahn-Teller effect, which leads to fast relaxation of the magnetization. Slow relaxation of the magnetization and an opening of the hysteresis loop (both parameters are indicative of SMM behavior) were observed in the Co^{II} analog ([Co(Me_6tren)Cl](ClO_4), *S* = 3/2), which has a strict C_{3v} symmetry, even though its anisotropy is much weaker than the isostructural Ni^{II} complex.[18] It was found that the ZFS parameter *D* changes when the Cl^- is replaced by Br^- (from 8.1 to 4.6 cm^{-1}, respectively). The difference in magnitude was rationalized in terms of the σ/π donating effects of the ligands and the arrangements of the packing between molecules. Building upon these results we designed the study reported below. We explored the effect of the counter anion on the magnetic anisotropy of the $[Co(Me_6tren)Cl]^+$ complex and the effect of substituting the chloride axial ligand by the fluoride and the iodide anions.

2.2 Experimental Section

2.2.1 Syntheses

All starting materials were obtained commercially and were used without further purification unless otherwise stated. The ligand Me_6tren and all reported cobalt(II), zinc(II) complexes were synthesized according to literature procedures or minor alterations thereof.[18, 26-28] And the new complexes were synthesized similarly.

Tris(2-(dimethylamino)ethyl)amine: Me_6tren

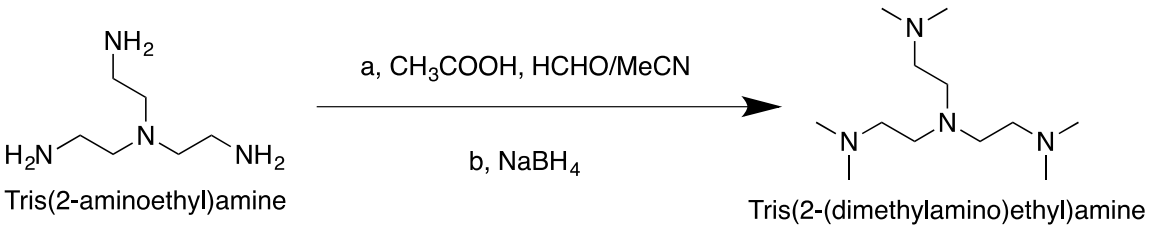

Scheme 2.1. Synthesis of Tris(2-(dimethylamino)ethyl)amine.

Aqueous formaldehyde (49.0 mL, 660 mmol, 37 wt%) was added to a solution of 3.00

mL (19.9 mmol) of tris(2-aminoethyl)amine and 135 mL of acetic acid in acetonitrile (600 mL) and allowed to stir for 1 h. Subsequently, the reaction mixture was cooled to 0 °C and 10.0 g (26.4 mmol) of sodium borohydride slowly added. After being stirred for 48 h, all solvents were removed, the residue was made strongly basic with 3 M aqueous sodium hydroxide, and extracted several times with DCM. The DCM extracts were combined, dried ($MgSO_4$), and the solvent removed. The residue was dissolved in pentane, filtered, and the filtrate reduced to dryness to give **Me$_6$tren** as pale yellow oil (4.32 g, 94%). ^{1}H NMR ($CDCl_3$, 300 MHz, ppm from TMS): δ 2.56 (m, 6H, C*H*$_2$N(CH$_3$)$_2$), 2.32 (m, 6H, NC*H*$_2$CH$_2$N(CH$_3$)$_2$), 2.19 (s, 18H, NC*H*$_3$).

[Co(Me$_6$tren)Cl](ClO$_4$) (2-1)

$CoCl_2 \cdot 6H_2O$ (200 mg, 0.84 mmol) was dissolved in EtOH (20 mL) at 55 °C. Me$_6$tren (214 mg, 0.92 mmol) dissolved in EtOH (10 mL) was added dropwise with stirring, forming a blue solution that was stirred overnight at room temperature. $NaClO_4$ (103 mg, 0.84 mmol) *(*Cautions: *Perchlorates are dangerous chemical species with unpredictable behavior; they can produce violent explosions. A maximum of 150 mg of the starting material must be used in one preparation. The final material must not be heated nor scratched)* was added with stirring inducing precipitation of pale blue **2-1** (336 mg, 95%), which was isolated by filtration and dried in air. Crystals suitable for X-ray analysis were formed upon cooling a hot MeOH solution of **2-1**. Elem Anal. Calcd: C, 34.03; H, 7.15; N, 13.24. Found: C, 33.81; H, 7.08; N, 13.05. IR(KBr) ν/cm^{-1}: 3431 (w), 2983 (m), 2903 (m), 2852 (m), 2795 (w), 2017 (w), 1486 (s), 1475 (s), 1461 (s), 1435 (m), 1359 (w), 1300 (s), 1248 (w), 1174 (m), 1091 (s), 1053 (s), 1023 (m), 1006 (m), 938 (m), 913 (m), 807 (m), 778 (m), 742 (w), 622 (s), 602 (m), 573 (w), 486 (m), 411 (w), 382 (w) cm^{-1}. Single-crystal unit cell: trigonal, space group *R*3*c*, *a* = 9.891(5) Å, *b* = 9.891(5) Å, *c* = 33.183(5) Å, $\alpha = 90°$, $\beta = 90°$, $\gamma = 120°$, *V* = 2811(2) Å^3.

[Co(Me$_6$tren)Cl](PF$_6$) (2-2)

To a solution of $CoCl_2 \cdot 6H_2O$ (118.97mg, 0.5 mmol) in EtOH (5 mL), Me$_6$tren (138.24 mg, 0.6 mmol) in EtOH (3 mL) were added dropwise with stirring, followed by tetrabutylammonium hexafluorophosphate (193.72 mg, 0.5 mmol) was added portionwise, which inducing precipitation isolated by filtration and dried in air. X-ray quality crystals **2-2** were obtained by vapor diffusion of diethyl ether into MeOH solution. Yield, 86.43%, 203 mg. Elem Anal. Calcd: C, 30.68; H, 6.44; N, 11.93. Found: C, 30.84; H, 6.32; N, 11.77.

Single-crystal unit cell: Trigonal, space group *R*3*H*, *a* = 10.2778(8) Å, *b* = 10.2778(8) Å, *c* = 16.0130(13) Å, $\alpha = 90°$, $\beta = 90°$, $\gamma = 120°$, *V* = 1464.9(3) Å^3.

[Co(Me$_6$tren)Cl](Cl) (2-3)

To a solution of $CoCl_2 \cdot 6H_2O$ (118.97mg, 0.5 mmol) in EtOH (5 mL), Me$_6$tren (138.24 mg, 0.6 mmol) in EtOH (3 mL) were added dropwise with stirring for 3 h, X-ray quality crystals **2-3** were obtained by vapor diffusion of diethyl ether into abovementioned solution. Yield, 77.72%, 140 mg. Elem Anal. Calcd: C, 40.01; H, 8.39; N, 15.55. Found: C, 39.69; H, 68.53; N, 15.44. Single-crystal unit cell: Cubic, space group *P*2$_1$3, *a* = 11.8163(4) Å, *b* = 11.8163(4) Å, *c* = 11.8163(4) Å, $\alpha = 90°$, $\beta = 90°$, $\gamma = 90°$, *V* = 1649.85(17) Å^3.

[Co(Me$_6$tren)Br](ClO$_4$) (2-4)

To a solution of $CoBr_2 \cdot H_2O$ (118.38 mg, 0.5 mmol) in EtOH (10 mL), Me$_6$tren (138.24 mg, 0.6 mmol) in EtOH (5 mL) were added dropwise with stirring, followed by $NaClO_4$ (157.76 mg, 0.5 mmol) was added portionwise, which inducing precipitation isolated by filtration and dried in air. X-ray quality crystals **2-4** were obtained by vapor diffusion of diethyl ether into MeOH solution. Yield, 76.81%, 180 mg. Elem Anal. Calcd: C, 30.75; H, 6.45; N, 11.95. Found: C, 28.07; H, 5.96; N, 10.93. Single-crystal unit cell: Cubic, space group *P*2$_1$3, *a* = 12.4738(4) Å, *b* = 12.4738(4) Å, *c* = 12.4738(4) Å, $\alpha = 90°$, $\beta = 90°$, $\gamma = 90°$, *V* = 1940.87(19) Å^3.

[Co(Me$_6$tren)I](ClO$_4$) (2-5)

To a solution of CoI_2 (156.37 mg, 0.5 mmol) in EtOH (10 mL), Me$_6$tren (138.24 mg, 0.6 mmol) in EtOH (5 mL) were added dropwise with stirring, followed by $NaClO_4$ (157.76 mg, 0.5 mmol) was added portionwise, which inducing precipitation isolated by filtration and dried in air. X-ray quality crystals **2-5** were obtained by vapor diffusion of diethyl ether into MeOH solution. Yield, 81.45%, 210 mg. Elem Anal. Calcd: C, 27.95; H, 5.86; N, 10.86. Found: C, 28.07; H, 5.96; N, 10.93. IR (KBr) ν/cm^{-1}: 3436 (w), 3010 (w), 2981 (w), 2913 (w), 2876 (w), 1643 (w), 1481 (m), 1473 (m), 1295 (m), 1108 (s), 1084 (s), 1035 (m), 1015 (m), 998 (m), 934 (m), 773 (m), 624 (m) cm^{-1}. Single-crystal unit cell: Cubic, space group *P*2$_1$3, *a* = 12.6169(7) Å, *b* = 12.6169(7) Å, *c* = 12.6169(7) Å, $\alpha = 90°$, $\beta = 90°$, $\gamma = 90°$, *V* = 2008.4(3) Å^3.

[Co(Me6tren)F](ClO4) (2-6)

To a hot solution of $Co(ClO_4)_2 \cdot 6H_2O$ (182.96 mg, 0.5 mmol) in EtOH (5 mL), Me_6tren (138.24 mg, 0.6 mmol) in EtOH (3 mL) were added dropwise with stirring, followed by tetrabutylammoniumfluoride trihydrate (157.76 mg, 0.5 mmol) was added portionwise. Then the stirred solution was cooled down to room temperature at ambient condition. X-ray quality crystals **2-6·0.5H2O** were obtained by vapor diffusion of diethyl ether into cooled solution. Yield, 76.78%, 160 mg. Elem Anal. Calcd: C, 34.58; H, 7.50; N, 13.44. Found: C, 34.50; H, 7.78; N, 13.32. IR (pure) ν/cm^{-1}: 3611 (w), 3322 (w), 2989 (w), 2900 (w), 2856 (w), 2813 (w), 1633 (w), 1472 (m), 1294 (m), 1105 (s), 1067 (s), 939 (m), 779 (m), 624 (m) cm^{-1}. Single-crystal unit cell: Monoclinic, space group $P2_1/n$, a = 9.6785(5) Å, b = 14.8653(8) Å, c = 13.1096(7) Å, α = 90°, β = 91.074(2)°, γ = 90°, V = 1885.80(17) Å^3.

[Zn(Me6tren)F](ClO4) (2-7)

To a hot solution of $Zn(ClO_4)_2 \cdot 6H_2O$ (186.20 mg, 0.5 mmol) in EtOH (5 mL), Me_6tren (138.24 mg, 0.6 mmol) in EtOH (3 mL) were added dropwise with stirring, followed by Tetrabutylammoniumfluoride trihydrate (157.76 mg, 0.5 mmol) was added portionwise. Then the stirred solution was cooled down to room temperature at ambient condition. X-ray quality crystals **2-7·0.5H2O** were obtained by vapor diffusion of diethyl ether into cooled solution. Yield, 61.43%, 130 mg. Elem Anal. Calcd: C, 34.05; H, 7.38; N, 13.24. Found: C, 33.68; H, 7.57; N, 13.09. IR (pure) ν/cm^{-1}: 3610 (w), 3300 (w), 3210 (w), 3017 (w), 2987 (w), 2883 (w), 2853 (w), 1625 (w), 1473 (m), 1294 (m), 1099 (s), 937 (m), 777 (m), 622 (m) cm^{-1}. Single-crystal unit cell: Monoclinic, space group $P2_1/n$, a = 9.6596(4) Å, b = 14.8339(6) Å, c = 13.1289(6) Å, α = 90°, β = 91.251(2)°, γ = 90°, V = 1880.79(14) Å^3.

[Co0.12Zn0.88(Me6tren)F](ClO4) (2-8)

To a hot solution of $Co(ClO_4)_2 \cdot 6H_2O$ (18.30 mg, 0.05 mmol) and $Zn(ClO_4)_2 \cdot 6H_2O$ (167.58 mg, 0.45 mmol) in EtOH (5 mL), Me_6tren (138.24 mg, 0.6 mmol) in EtOH (3 mL) were added dropwise with stirring, followed by tetrabutylammoniumfluoride trihydrate (157.76 mg, 0.5 mmol) was added portionwise. Then the stirred solution was cooled down to room temperature at ambient condition. X-ray quality crystals **2-8·0.5H2O** were obtained by vapor diffusion of diethyl ether into cooled solution. Yield, 66.28%, 140 mg. Elem Anal. Calcd: C, 34.11; H, 7.40; N, 13.26. Found: C, 33.60; H, 7.51; N, 13.18. IR (pure) ν/cm^{-1}: 3611 (w), 3306 (w), 3208 (w), 2986 (w), 2896 (w), 2854 (w), 1633 (w), 1472 (m), 1294 (m),

1108 (s), 1067 (s), 939 (m), 783 (m), 623 (m) cm^{-1}. Single-crystal unit cell: Monoclinic, space group $P2_1/n$, a = 9.6651(5) Å, b = 14.8493(7) Å, c = 13.1275(6) Å, α = 90°, β = 91.232(2)°, γ = 90°, V = 1883.62(16) Å^3.

2.2.2 Physical Measurements

General procedures

Elemental analyses for C, H, N were performed on a Thermo Scientific Flash analyzer. IR spectra were recorded on a Bruker TENSOR-27 FT-IR spectrometer equipped with an attenuated total reflectance (ATR) sample holder in the 4000 − 500 cm^{-1} range. NMR spectra were recorded on a Bruker Aspect 300 NMR spectrometer. X-ray diffraction data were collected by using a Bruker Kappa VENTURE PHOTON 100 diffractometer with graphite-monochromatic Mo K$_\alpha$ radiation (λ = 0.71073 Å). Magnetic data were collected using a Quantum Design MPMS XL7 SQUID magnetometer. Electron Paramagnetic Resonance (EPR) data were collected on the standard Bruker ELEXSYS 500 spectrometer and the standard HFEPR Grenoble spectrometer.

X-ray Crystallography

X-ray diffraction data were collected by using a Kappa VENTURE PHOTON 100 Bruker diffractometer with IμS microfocus graphite-monochromated MoK$_\alpha$ radiation (λ = 0.71073 Å). Crystals were mounted on a CryoLoop (Hampton Research) with Paratone-N (Hampton Research) as cryoprotectant and then flash frozen in a nitrogen-gas stream at 100 K. The temperature of the crystal was maintained at the selected value (100 K) by means of a 700 series Cryostream cooling device to within an accuracy of ±1 K. The data were corrected for Lorentz polarization, and absorption effects. The structures were solved by direct methods using SHELXS-97[29, 30] and refined against F^2 by full-matrix least-squares techniques using SHELXL-97[29, 30] or SHELXL-2014[31] with anisotropic displacement parameters for all non-hydrogen atoms. Hydrogen atoms were located on a difference Fourier map and introduced into the calculations as a riding model with isotropic thermal parameters. All calculations were performed by using the crystal structure crystallographic software package WINGX.[32, 33] The crystal data collection and refinement parameters are given in Table 2.1, Table 2.3 and Table 2.5.

Magnetic Measurements

The direct-current (dc) and alternating-current (ac) magnetic susceptibility measurements were performed on powdered samples that were mulled in eicosane to prevent torqueing of the samples in high applied magnetic fields on a Quantum Design MPMS-XL7 SQUID magnetometer operating with a working temperature range of 1.8 – 300 K and dc-applied fields ranging from –7 to 7 T. Polycrystalline samples were ground using a small mortar and pestle, transferred to a gelatin capsule of known mass, and weighed. A small amount of melted eicosane was added and left to solidify. The entire capsule was then weighed, and a piece of brown tape was applied to hold the capsule together. The capsule was then inserted into a clear plastic drinking straw. Holes were punched into the straw to allow air to escape. Diamagnetic corrections were applied for the sample holder from previous direct measurements, and molar diamagnetic susceptibilities were calculated from Pascal's constants. Ac susceptibility measurements were carried out under an oscillating-drive field of 3 Oe and ac frequencies ranging between 0.1 and 1500 Hz within an optimum dc magnetic field.

Micro-SQUID Measurements

The magnetization studies on an oriented single crystal using a Micro-SQUID array were performed by Wolfgang Wernsdorfer (Insitut Néel, CNRS, Université Grenoble Alpes, France).[34] The field aligned parallel to the easy-axis of magnetization by the transversal field method.[35] Measurements were performed at a temperature range from 0.03 to 5 K in fields up to 1.1 T with sweep rates between 0.008 and 0.280 T/s, and exhibits field stability of better than 1 μT. The time resolution is approximately 1 ms. The field can be applied in any direction of the Micro-SQUID plane with precision greater than 0.1° by separately driving three orthogonal coils. In order to ensure good thermalization, the single crystal was fixed with apiezon grease.

Electron Paramagnetic Resonance (EPR) Measurements

High Field/Frequency Electron Paramagnetic Resonance (HFEPR) spectra were collected on the standard HFEPR Grenoble spectrometer[36-40] at the Laboratoire National des Champs Magnétiques Intenses by Anne-Laure Barra, who recorded the spectra and helped us to analyze them.

Computational Details

Theoretical calculations were performed by Benjamin Cahier in the group in order to analyze the relation between the structure and the value of the ZFS in the different complexes. Experimental structures were used for calculations. The position of the hydrogen atoms was optimized using DFT calculations (UB3LYP/6-311g). The *ab initio* calculations were done using the two-step approach implemented in the MOLCAS code.[41-45] The first step consists in calculating the non-relativistic Born-Oppenheimer Hamiltonian using complete active space self-consistent field (CASSCF) methods.[46] The second step takes into account the SOC using the Spin-Orbit Restricted Active Space-State Interaction (SO-RASSI) method.[47, 48] For CASSCF calculations, the active space contains seven electrons in 10 orbitals (five 3*d* orbitals plus five diffuse 4*d* orbitals).[42, 44, 45] The ground electronic state was described by a state-specific calculation while excited states (nine quartets and 40 doublets) were obtained using state-average calculations. ANO-RCC basis set was used with the following contraction scheme: 6*s*5*p*4*d*2*f*1*g* for Co^{II}, 5*s*5*p*3*d*1*f* for Cl and S, 6*s*3*p*2*d*1*f* for N, 6*s*3*p* for C and 2*s* for H. All the calculated electronic states were included in the SO-RASSI calculations.[45, 49] The *D* values are reported in Table 2.23 and are in good agreement with the experimental values.

2.3 Results and Discussion

2.3.1 Syntheses

In the direct approach, the reaction can occur between the ligands and simple metal salts. In our case, different reactions between Me$_6$tren, and a series of cobalt(II) and zinc(II) salts were screened under different conditions such as a variety of solvents, chemical ratios, or the use of different counter ions, etc…

The formation of complexes **2-1** to **2-8** are summarized in equations 2.1 to 2.8, respectively.

$CoCl_2 + Me_6tren + NaClO_4 \longrightarrow [Co(Me_6tren)Cl]ClO_4 + NaCl$ (2.1)

$CoCl_2 + Me_6tren + [n\text{-}Bu_4N]PF_6 \longrightarrow [Co(Me_6tren)Cl]PF_6 + [n\text{-}Bu_4N]Cl$ (2.2)

$CoCl_2 + Me_6tren \longrightarrow [Co(Me_6tren)Cl]Cl$ (2.3)

$CoBr_2 + Me_6tren + NaClO_4 \longrightarrow [Co(Me_6tren)Br]ClO_4 + NaBr$ (2.4)

$CoI_2 + Me_6tren + NaClO_4 \longrightarrow [Co(Me_6tren)I]ClO_4 + NaI$ (2.5)

$Co(ClO_4)_2 + Me_6tren + [n\text{-}Bu_4N]F_3 \longrightarrow [Co(Me_6tren)F]ClO_4 + [n\text{-}Bu_4N]ClO_4$ (2.6)

$Zn(ClO_4)_2 + Me_6tren + [n\text{-}Bu_4N]F_3 \longrightarrow [Zn(Me_6tren)F]ClO_4 + [n\text{-}Bu_4N]ClO_4$ (2.7)

$0.12\ Co(ClO_4)_2 + 0.88\ Zn(ClO_4)_2 + Me_6tren + [n\text{-}Bu_4N]F_3 \longrightarrow [Co_{0.12}Zn_{0.88}(Me_6tren)F]ClO_4 + [n\text{-}Bu_4N]ClO_4$ (2.8)

The complex **2-1** was synthesized using the same procedure reported by our group.[18] During the synthesis, the ligand Me$_6$tren was used in slight excess which leads to an increase of the yield of the reaction. Ethanol is essential in the reactions since it helps to completely dissolve all the reactants and more importantly leads to the precipitation of the complex **2-1**.

For the synthesis of complexes **2-2** to **2-8**, the ligand Me$_6$tren was also used in slight excess increasing the yield of the final compounds. It should be mentioned that no precipitate is obtained for the reactions of complexes **2-3**, **2-6** to **2-8**. The X-ray quality crystals were obtained by vapor diffusion of diethyl ether into the corresponding reaction mother solutions. For the reactions 2.6 to 2.8, we cannot use the CoF_2 because it is insoluble in organic solvents. An alternative solution consists in using cobalt(II) perchlorate and tetrabutylammonium fluoride hydrate to do the reactions.

2.3.2 Description of Structures

Partially labeled structure of complexes **2-1** to **2-8** are shown in the figures below. The general structure of the cations for complexes **2-1** to **2-8** consists in the transition metal ion five-coordinated by four amino nitrogen atoms from the neutral Me$_6$tren ligand and one halide ion as an axial ligand. The geometry is trigonal bipyramid and the symmetry of the complexes is strictly C_3 (C_{3v} if only the first coordination sphere is taken into account) apart when the axial ligand is F^- where a small distortion is observed. The charge balance is provided by a perchlorate, hexafluorophosphate or halide anion.

Some important interatomic distances and angles of these eight complexes are listed in Table 2.2, Table 2.4 and Table 2.6.

Complexes 2-1, 2-2 and 2-3

The complexes **2-1**, **2-2** and **2-3**, which have the same cation $[Co(Me_6tren)Cl]^+$ (Figure 2.1), but with three different counter-ions, ClO_4^-, PF_6^-, Cl^-, respectively. They crystallize in the space groups *R*3*c*, *R*3*H*, *P*2$_1$3, respectively (Table 2.1). We will detail the description of the complex **2-1** because it was the first complex of the series; the structure of the other complexes is similar. The Co^{II} ion lies 0.327 Å below the equatorial plane of the three nitrogen atoms with an equatorial $N_2\widehat{CoCl}_1$ angle of 98.74°. The Co–N$_1$ axial bond length (2.176 Å) is slightly longer than the equatorial ones (2.152 Å). The Co–Cl$_1$ distance is equal to 2.282 Å. The $N_2\widehat{CoN}_2'$ and the $N_1\widehat{CoN}_2$ angles are equal to 117.73° and 81.26°, respectively. More details can be found in the paper published in Chemical Science.[18] The comparison of the parameters of the three complexes (**2-1**, **2-2** and **2-3**) is shown in Table 2.1 and Table 2.2. The main structural difference among the three complexes concerns the cobalt(II) ligand bond lengths. The Co–N$_e$ distances decreases when going from complexes **2-1** to **2-3**, while the axial bond lengths increase. We will see below whether these differences do or do not have an impact on the magnetic anisotropy.

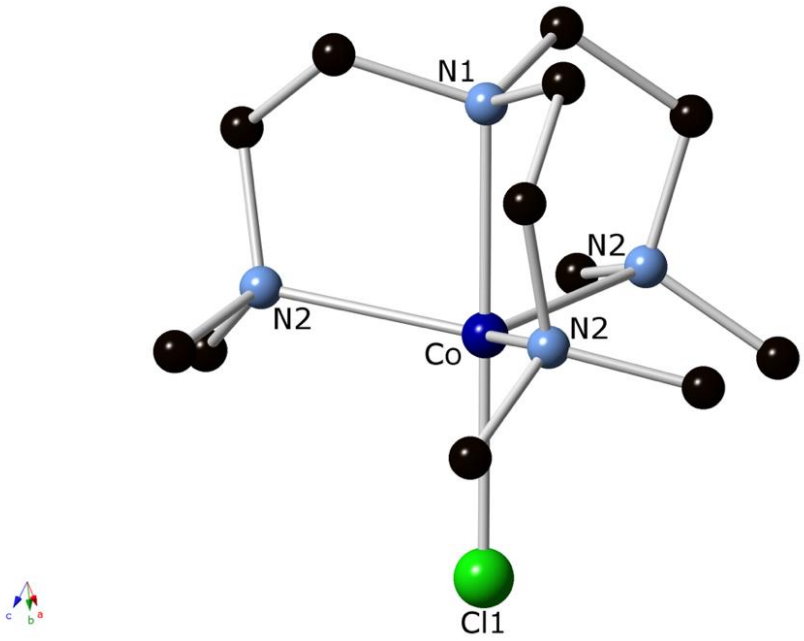

Figure 2.1. A view of the molecular structure for complex **2-1**. C – black; H atoms and counter-ions were omitted for clarity.

Table 2.1. Crystallographic data structure refinement for complexes **2-1** to **2-3**.

Complexes	**2-1**	**2-2**	**2-3**
formula	$C_{12}H_{30}N_4CoCl_2O_4$	$C_{12}H_{30}N_4CoClPF_6$	$C_{12}H_{30}N_4CoCl_2$
M_r	424.23	469.75	360.23
cryst syst	Trigonal	Trigonal	Cubic
space group	*R*3*c*	*R*3*H*	$P2_13$
a, Å	9.891(5)	10.2778(8)	11.8163(4)
b, Å	9.891(5)	10.2778(8)	11.8163(4)
c, Å	33.183(5)	16.0130(13)	11.8163(4)
α, deg	90	90	90
β, deg	90	90	90
γ, deg	120	120	90
cell volume, Å^3	2811(2)	1464.9(3)	1649.85(2)
Z	6	3	4
T, K	100(1)	293(1)	100(1)
F_{000}	1338	729	764
μ, mm^{-1}	1.22	1.10	1.36
reflns collected	13201	6273	19327
reflns unique	2790	2300	2370
R_1	0.032	0.063	0.026
wR_2 (all data)	0.080	0.141	0.045
GOF	1.05	1.06	1.02

Table 2.2. Relevant Co^{II}–ligand bond distances (Å) and angles (°) for complexes **2-1** to **2-3**.

Complexes	**2-1**	**2-2**	**2-3**
[b] d_{CoN_a}	2.176	2.209	2.220
[b] d_{CoN_e}	2.152	2.143	2.133
[b] d_{CoX}	2.282	2.284	2.306
[b] $d_{Co-N_eN'_eN''_e}$	0.327	0.338	0.332
[c] $\widehat{N_eCoN_e}$	117.73	117.57	117.62
[c] $\widehat{N_eCoX}$	98.74	99.08	98.97
[c] $\widehat{N_aCoX}$	180	180	180
[c] $\widehat{N_aCoN_e}$	81.26	80.91	81.03
[d] θ	8.74	9.09	8.97

[a] means axial; [b] in Angstrom (Å); [c] in degree (°); [d] $\theta = 180° - \widehat{N_aCoN_e}$; in degree (°); [e] means equatorial.

Complexes 2-4 and 2-5

The two complexes possess the same counter-ion (ClO_4^-) and a different axial ligand (Br^-, I^- for complexes **2-4** and **2-5** respectively; Figure 2.2; Table 2.3 and Table 2.4).

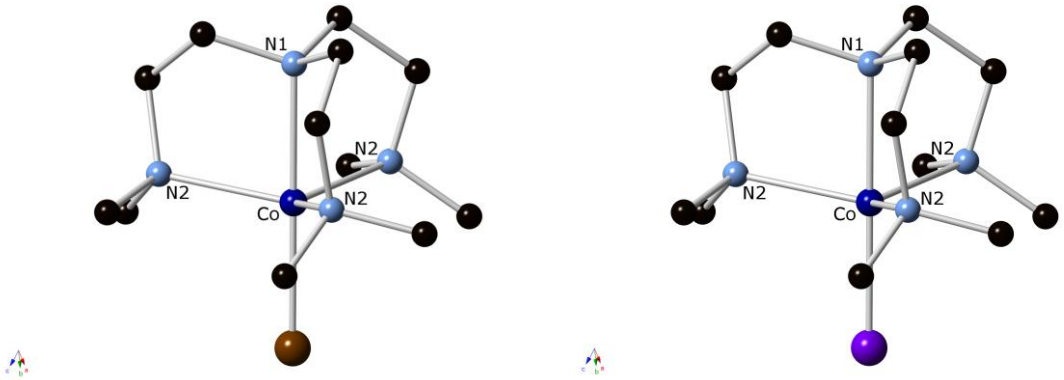

Figure 2.2. A view of the molecular structure for complexes **2-4** (left) and **2-5** (right); C – black; Br – brown; I – violet; H atoms and counter-ions were omitted for clarity.

Table 2.3. Crystallographic data structure refinement for complexes **2-1**, **2-4** to **2-6**.

Complexes	**2-1**	**2-4**	**2-5**	**2-6**
formula	$C_{12}H_{30}N_4CoCl_2O_4$	$C_{12}H_{30}N_4CoBrClO_4$	$C_{12}H_{30}N_4CoIClO_4$	$C_{12}H_{32}N_4CoFClO_5$
M_r	424.23	468.69	515.68	425.79
cryst syst	Trigonal	Cubic	Cubic	Monoclinic
space group	*R*3*c*	$P2_13$	$P2_13$	$P2_1/n$
a, Å	9.891(5)	12.4738 (4)	12.6169(7)	9.6785(5)
b, Å	9.891(5)	12.4738 (4)	12.6169(7)	14.8653(8)
c, Å	33.183(5)	12.4738 (4)	12.6169(7)	13.1096(7)
α, deg	90	90	90	90
β, deg	90	90	90	91.074(2)
γ, deg	120	90	90	90
cell volume, Å^3	2811(2)	1940.87(19)	2008.4(3)	1885.80(2)
Z	6	4	4	4
T, K	100(1)	100(1)	100(1)	100(1)
F_{000}	1338	964	1036	900
μ, mm^{-1}	1.22	3.10	2.40	1.09
reflns collected	13201	34624	72315	115911
reflns unique	2790	3260	2054	5775
R_1	0.032	0.041	0.020	0.049
wR_2 (all data)	0.080	0.082	0.041	0.084
GOF	1.05	1.02	1.08	1.09

Table 2.4. Relevant Co^{II}–ligand bond distances (Å) and angles (°) for complexes **2-1**, **2-4** to **2-6**.

Complexes	2-1	2-4	2-5	2-6
[b] d_{CoN_a}	2.176	2.210	2.201	2.203
[b] d_{CoN_e}	2.152	2.137	2.141	2.132; 2.134; 2.149
[b] d_{CoX}	2.282	2.459	2.666	1.906
[b] $d_{Co-N_eN_e'N_e''}$	0.327	0.333	0.321	0.322
[c] $\widehat{N_eCoN_e}$	117.73	117.61	117.79	116.93; 117.26; 119.15
[c] $\widehat{N_eCoX}$	98.74	98.97	98.63	97.15; 99.32; 99.50
[c] $\widehat{N_aCoX}$	180	180	180	178.74
[c] $\widehat{N_aCoN_e}$	81.26	81.03	81.37	80.75; 81.56; 81.74
[d] θ	8.74	8.97	8.63	9.25; 8.44; 8.26

[a] means axial; [b] in Angstrom (Å); [c] in degree (°); [d] $\theta = 180° - \widehat{N_aCoN_e}$; in degree (°); [e] means equatorial.

Complexes 2-6, 2-7 and 2-8

Complexes **2-6**, **2-7** and **2-8** are isostructural. The main difference between the complexes that have the axial F^- ligand and all the others is the presence of a water molecule that interacts with the fluoride via a hydrogen bond (Figure 2.3). This leads to a distortion of the $\widehat{N_1CoF_1}$ that is equal to 170.8° instead of 180° in the other complexes. The effect is also present in the coordination sphere of the metal ions for bond lengths and angles as shown in Table 2.5 and Table 2.6. **2-6** crystallizes in the space group $P2_1/n$. The Co^{II} ion lies 0.322 Å below the equatorial plane of the three nitrogen atoms with three different inequatorial $\widehat{N_eCoF_1}$ angles of 97.15°, 99.32°, 99.50°. The Co–N_1 bond length (2.203 Å) is slightly longer than the equatorial ones (2.132, 2.134, 2.149 Å respectively). The Co–F_1 distance is equal to 1.906 Å, much shorter than the other Co^{II}–halide distances. The $\widehat{N_eCoN_e'}$ and the $\widehat{N_aCoN_e}$ angles are equal to 116.93°, 117.26°, 119.15° and 80.75°, 81.56°, 81.74°, respectively (Table 2.5 and Table 2.6).

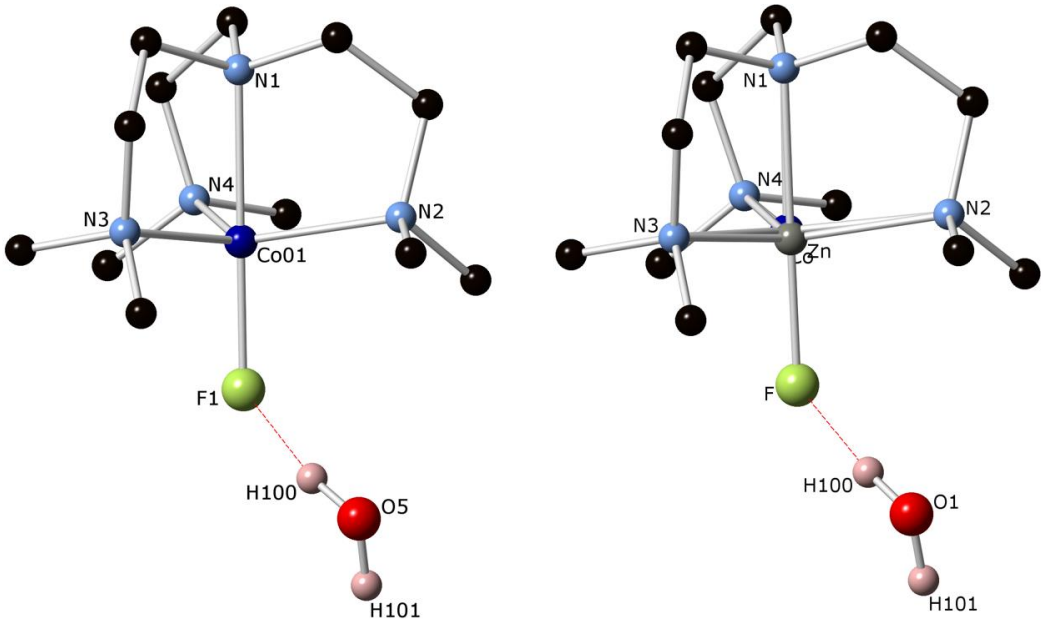

Figure 2.3. A view of the molecular structure for complexes **2-6** (left) and **2-8** (right). F – light green; Co – blue; Zn – grey; C – black; most H atoms and counter-ions were omitted for clarity.

Table 2.5. Crystallographic data structure refinement for complexes **2-6** to **2-8**.

Complexes	**2-6**	**2-7**	**2-8**
formula	$C_{12}H_{32}N_4CoFClO_5$	$C_{12}H_{32}N_4ZnFClO_5$	$C_{12}H_{32}N_4Co_{0.12}Zn_{0.88}FClO_5$
M_r	425.79	432.23	491.16
cryst syst	Monoclinic	Monoclinic	Monoclinic
space group	$P2_1/n$	$P2_1/n$	$P2_1/n$
a, Å	9.6785(5)	9.6596(4)	9.6651(5)
b, Å	14.8653(8)	14.8339(6)	14.8493(7)
c, Å	13.1096(7)	13.1289(6)	13.1275(6)
α, deg	90	90	90
β, deg	91.074(2)	91.251(2)	91.232(2)
γ, deg	90	90	90
cell volume, Å^3	1885.80(2)	1880.79(2)	1883.62(2)
Z	4	4	4
T, K	100(1)	100(1)	100(1)
F_{000}	900	912	1020
μ, mm^{-1}	1.09	1.49	2.34
reflns collected	115911	34584	84158
reflns unique	5775	6573	9163
R_1	0.049	0.036	0.049
wR_2 (all data)	0.084	0.092	0.061
GOF	1.09	1.10	1.03

Table 2.6. Relevant Co^{II}–ligand bond distances (Å) and angles (°) for complexes **2-6** to **2-8**.

Complexes	2-6	2-7	2-8(Co)	2-8(Zn)
[b] d_{CoN_a}	2.203	2.210	2.125	2.220
[b] d_{CoN_e}	2.132; 2.134; 2.149	2.130; 2.131; 2.148	2.073; 2.120; 2.187	2.143; 2.129; 2.139
[b] d_{CoX}	1.906	1.919	2.006	1.909
[b] $d_{Co-N_eN'_eN''_e}$	0.322	0.282	0.210	0.297
[c] $\widehat{N_eCoN_e}$	116.93; 117.26; 119.15	117.59; 117.68; 119.58	116.06; 120.47; 120.85	117.55; 117.36; 119.41
[c] $\widehat{N_eCoX}$	97.15; 99.32; 99.50	96.19; 97.97; 98.63	94.24; 96.25; 95.68	98.52; 98.95; 96.46
[c] $\widehat{N_aCoX}$	178.74	178.64	176.95	178.54
[c] $\widehat{N_aCoN_e}$	80.75; 81.56; 81.74	81.73; 82.67; 82.83	82.73; 84.80; 86.20	81.53; 82.29; 82.27
[d] θ	9.25; 8.44; 8.26	8.27; 7.23; 7.17	7.27; 5.20; 3.80	8.47; 7.71; 7.73

[a] means axial; [b] in Angstrom (Å); [c] in degree (°); [d] $\theta = 180° - \widehat{N_aCoN_e}$; in degree (°); [e] means equatorial.

2.3.3 Magnetic Studies

2.3.3.1 Direct current magnetic susceptibility studies

The thermal variation of the molar magnetic susceptibility ($\chi_M T$) for complexes **2-1** to **2-8** (except for the diamagnetic Zn^{II} complex **2-7**), are plotted from Figure 2.4 to Figure 2.7, respectively. $\chi_M T$ has the same behavior for the seven complexes. It is constant between room temperature and ca. 40 K with values in the range 2.37 – 2.26 $cm^3mol^{-1}K$ for all the complexes, which is expected for a S = 3/2 spin moment with a g-value in the range 2.24 – 2.17. For the complex **2-8** diluted in the diamagnetic Zn^{II} matrix (Table 2.7), the $\chi_M T$ value at room temperature is 0.253 $cm^3mol^{-1}K$, which is very close to the dilution used during the synthesis *i.e.* 12%.

Below 40 K, $\chi_M T$ decreases and reaches values close to 1.2 cm^3mol^{-1} K for complexes **2-1** to **2-6** and 0.145 cm^3mol^{-1} K for the diluted complex **2-8**. This decrease can be qualitatively assigned to a ZFS of the S = 3/2 manifold. The fit of the susceptibility data with the spin Hamiltonian that includes the ZFS part allows extracting the axial ZFS parameter D and the g value for all complexes. It is not possible to discriminate between negative and positive D values from these data. The fit results are presented in Table 2.7.

Table 2.7. ZFS parameters D and Landé g-factor from $\chi_M T$ fit for complexes **2-1** to **2-8**.

Complexes	**2-1**	**2-2**	**2-3**	**2-4**	**2-5**	**2-6**	**2-7**	**2-8**
[a] $\lvert D \rvert$	8.2	8	6.8	8	6	11	N/A	11
g	2.24	2.23	2.17	2.25	2.20	2.25	N/A	2.25

[a] in wavenumbers (cm^{-1}), the sign (+/–) cannot be confirmed here.

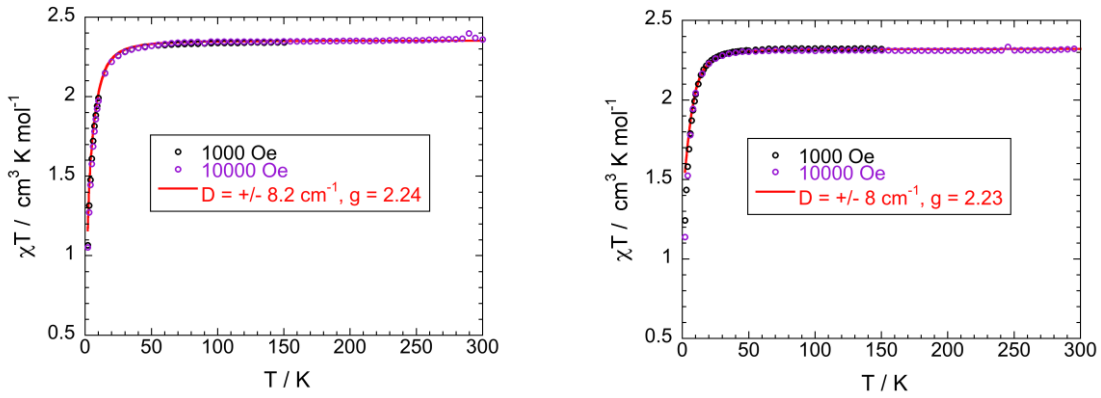

Figure 2.4. Temperature dependence of the χT product (○ (exp), — (best fit)) for complexes **2-1** (left) and **2-2** (right).

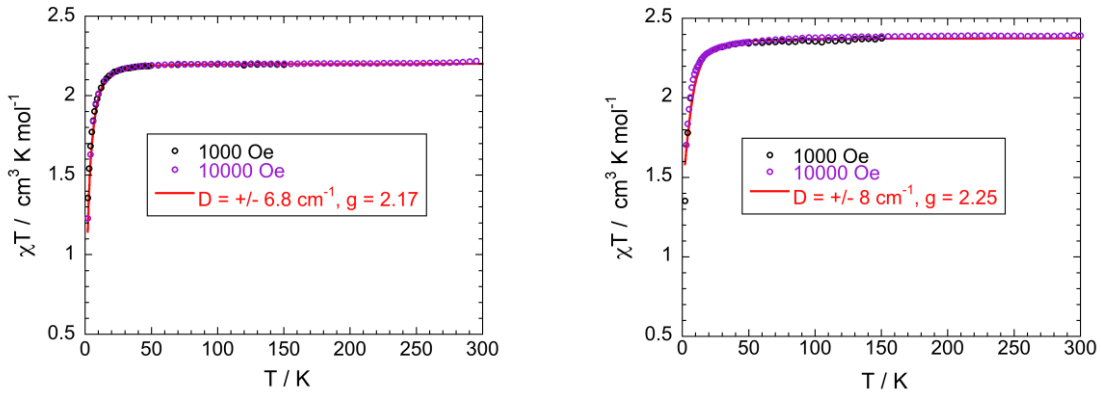

Figure 2.5. Temperature dependence of the χT product (○ (exp), — (best fit)) for complexes **2-3** (left) and **2-4** (right).

 Feng SHAO: 0000-0001-8606-8628

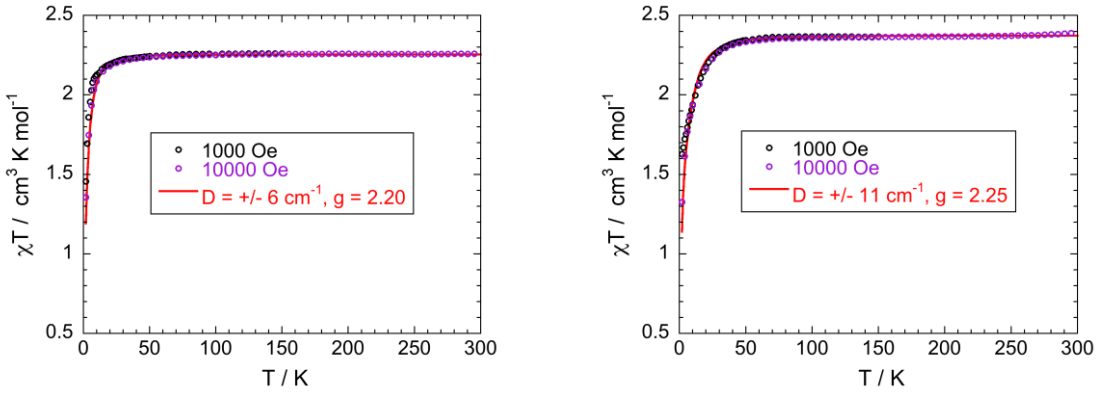

Figure 2.6. Temperature dependence of the χT product (○ (exp), — (best fit)) for complexes **2-5** (left) and **2-6** (right).

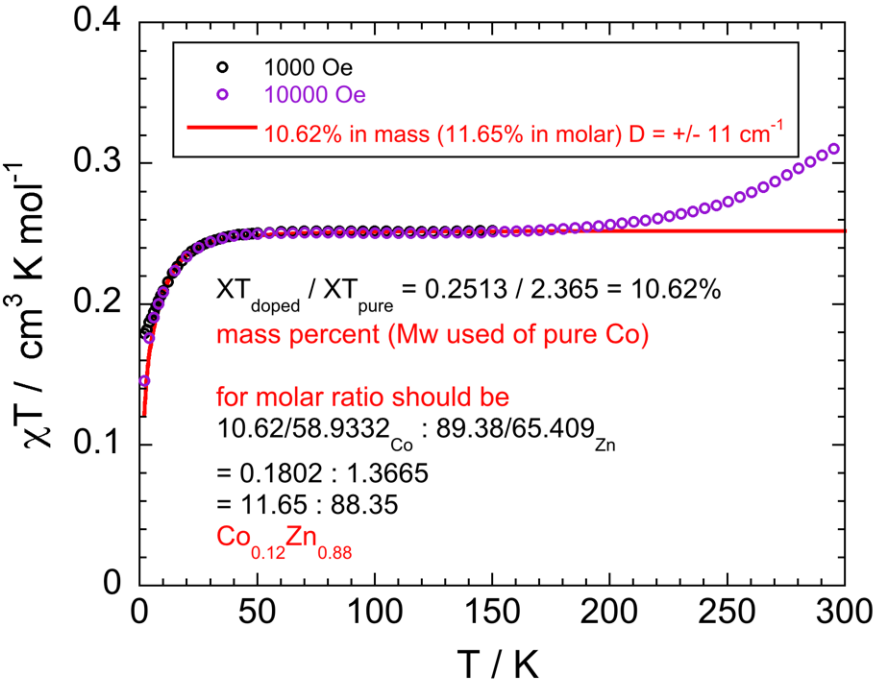

Figure 2.7. Temperature dependence of the χT product (○ (exp), — (best fit)) for complex **2-8**.

2.3.3.2 Magnetization versus dc magnetic field

The magnetization *vs.* the applied dc magnetic field for complexes **2-1** to **2-8** (except for the diamagnetic Zn^{II} complex **2-7**), are plotted in Figure 2.8 to Figure 2.14 in the form of $M = f(\mu_0 H)$ and $M = f(\mu_0 H/T)$. They have a similar behavior for the seven complexes. We comment one of the curves (Figure 2.8). The magnetization does not reach saturation at the highest field available. Its value at T = 2 K and $\mu_0 H$ = 5.5 T (around 2.5 Bohr Magneton) is well below that corresponding to S = 3 and g = 2.3 (3.45 Bohr Magneton). The $M = f(\mu_0 H/T)$ curves at different temperatures do not superimpose on one master curve. All these characteristics are consistent with the presence of a ZFS of the four degenerate S = 3/2 states.

To quantify the magnitude of the ZFS parameter, we fitted the magnetic data using the spin Hamiltonian $\hat{H} = g\mu_B \hat{S} \cdot \vec{H} + D\left[\hat{S}_z^2 - \frac{S_T(S_T+1)}{3}\right] + E(\hat{S}_x^2 - \hat{S}_y^2)$ for S = 3/2 where $\hat{S}, \hat{S}_x, \hat{S}_y, \hat{S}_z$ are spin operators, $\vec{H}$ is the applied dc magnetic field vector, g is the Landé factor that was assumed to be scalar, μ_B is the Bohr Magneton, D and E are the axial and rhombic ZFS parameters respectively. The rhombic parameter E is zero for complexes **2-1** to **2-5** because of the presence of a three-fold principal symmetry axis, but for complexes **2-6** and **2-8**, the parameter E is non-zero, even though it was assumed to be the case in order to avoid overparametrization during the fit procedure. The magnetization data were fitted leaving the g and the D values free during the fit and leading to the parameters presented in Table 2.8 for complexes **2-1** to **2-8** (except for the diamagnetic Zn^{II} complex **2-7**). These data suggest that the magnetic anisotropy is the Ising-type *i.e.* the $M_S = \pm 3/2$ sub-levels lie lower in energy than the ±1/2 ones and there is an easy axis of magnetization. It is not possible to obtain a fit with positive D values. Note that R in the figures corresponds to the agreement factor between the calculated and experimental data.

Table 2.8. ZFS parameters D and Landé g-tensor from $M = f(\mu_0 H)$ fit for complexes **2-1** to **2-8**.

Complexes	2-1	2-2	2-3	2-4	2-5	2-6	2-7	2-8
[a] D	–6.20	–5.37	–5.11	–3.51	–2.09	–16.67	N/A	–19.62
g	2.24	2.33	2.17	2.22	2.15	2.39	N/A	2.41

[a] in wavenumbers (cm^{-1}).

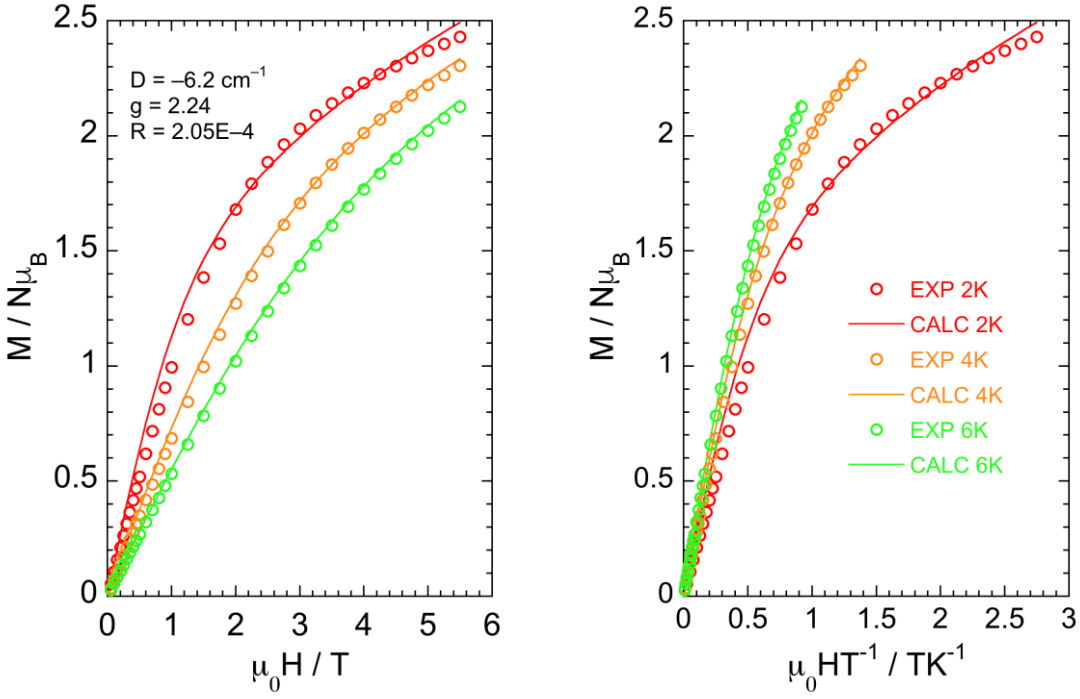

Figure 2.8. Magnetization *vs.* $\mu_0 H$ (left) and *vs.* $\mu_0 H/T$ (right) at variable temperatures (○ (exp), — (best fit)) for complex **2-1**.

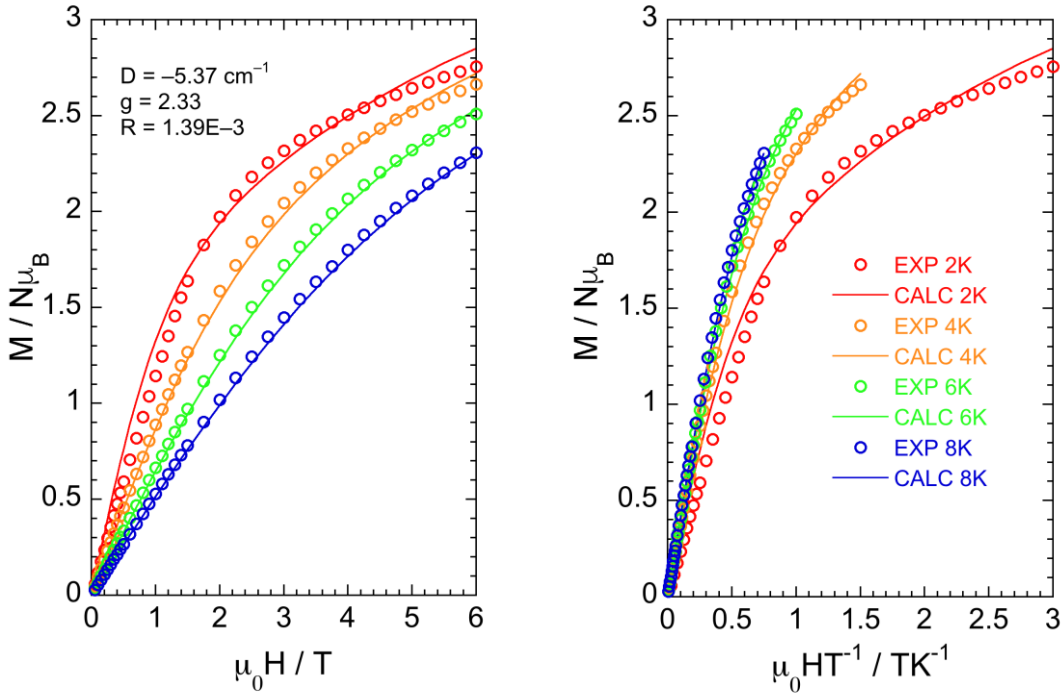

Figure 2.9. Magnetization *vs.* $\mu_0 H$ (left) and *vs.* $\mu_0 H/T$ (right) at variable temperatures (○ (exp), — (best fit)) for complex **2-2**.

 Feng SHAO: 0000-0001-8606-8628

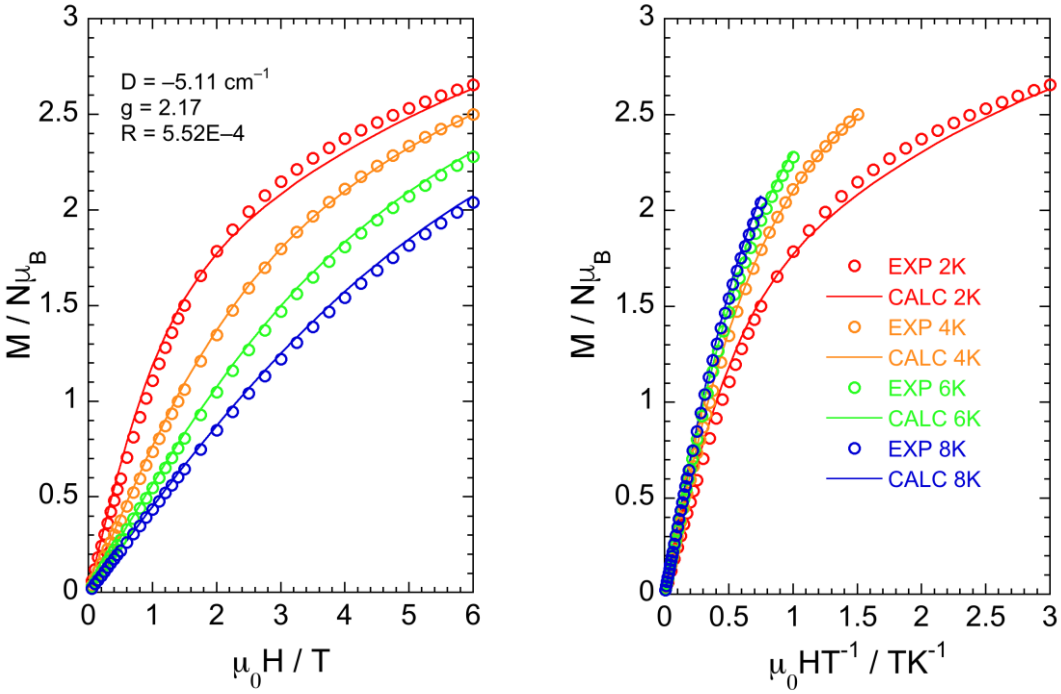

Figure 2.10. Magnetization *vs.* $\mu_0 H$ (left) and *vs.* $\mu_0 H/T$ (right) at variable temperatures (○ (exp), — (best fit)) for complex **2-3**.

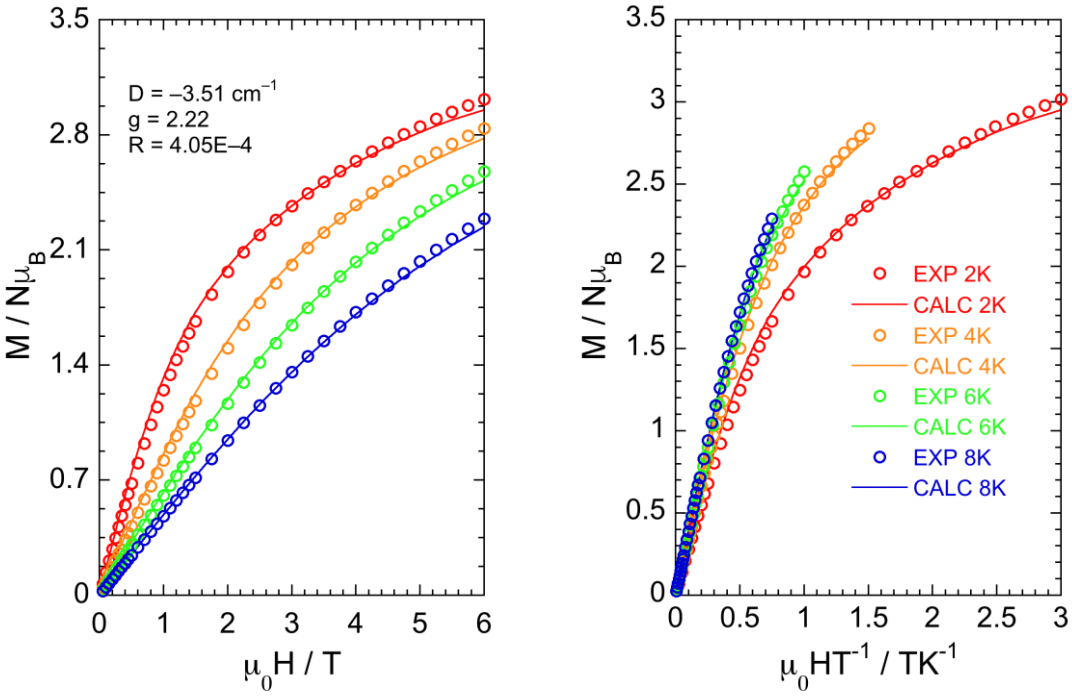

Figure 2.11. Magnetization *vs.* $\mu_0 H$ (left) and *vs.* $\mu_0 H/T$ (right) at variable temperatures (○ (exp), — (best fit)) for complex **2-4**.

 Feng SHAO: 0000-0001-8606-8628

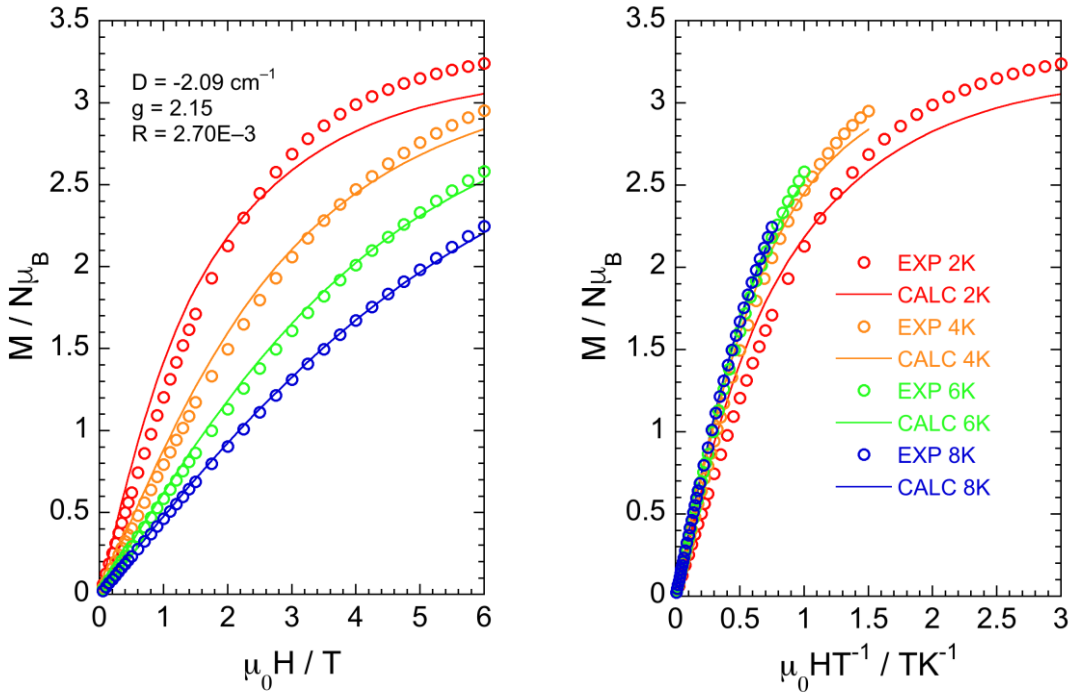

Figure 2.12. Magnetization *vs.* $\mu_0 H$ (left) and *vs.* $\mu_0 H/T$ (right) at variable temperatures (○ (exp), — (best fit)) for complex **2-5**.

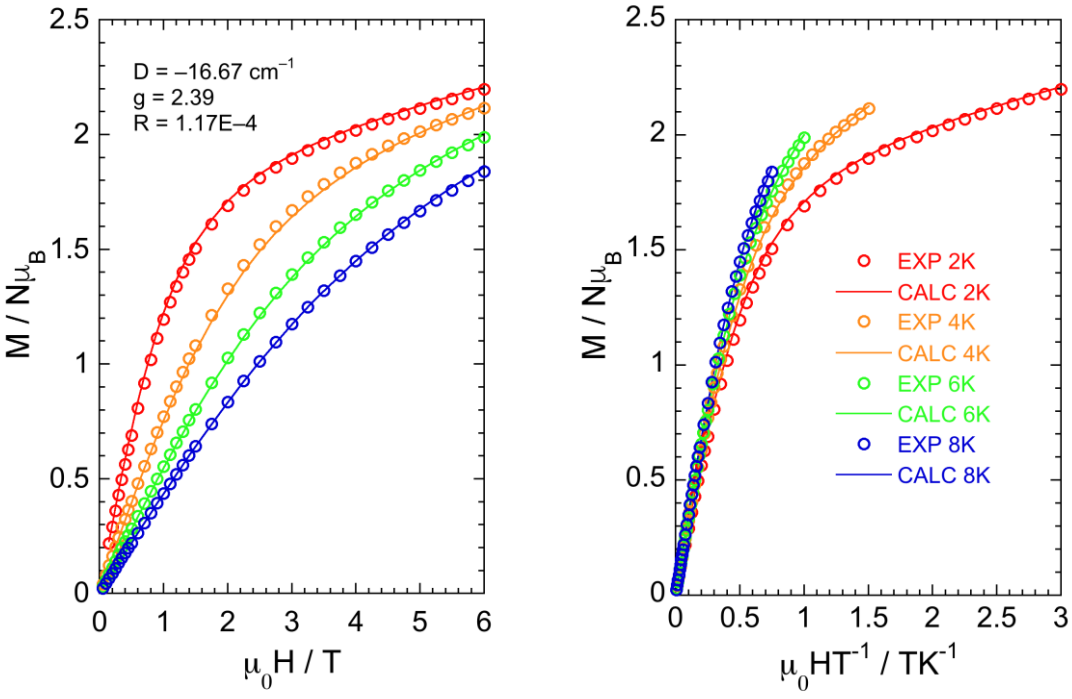

Figure 2.13. Magnetization *vs.* $\mu_0 H$ (left) and *vs.* $\mu_0 H/T$ (right) at variable temperatures (○ (exp), — (best fit)) for complex **2-6**.

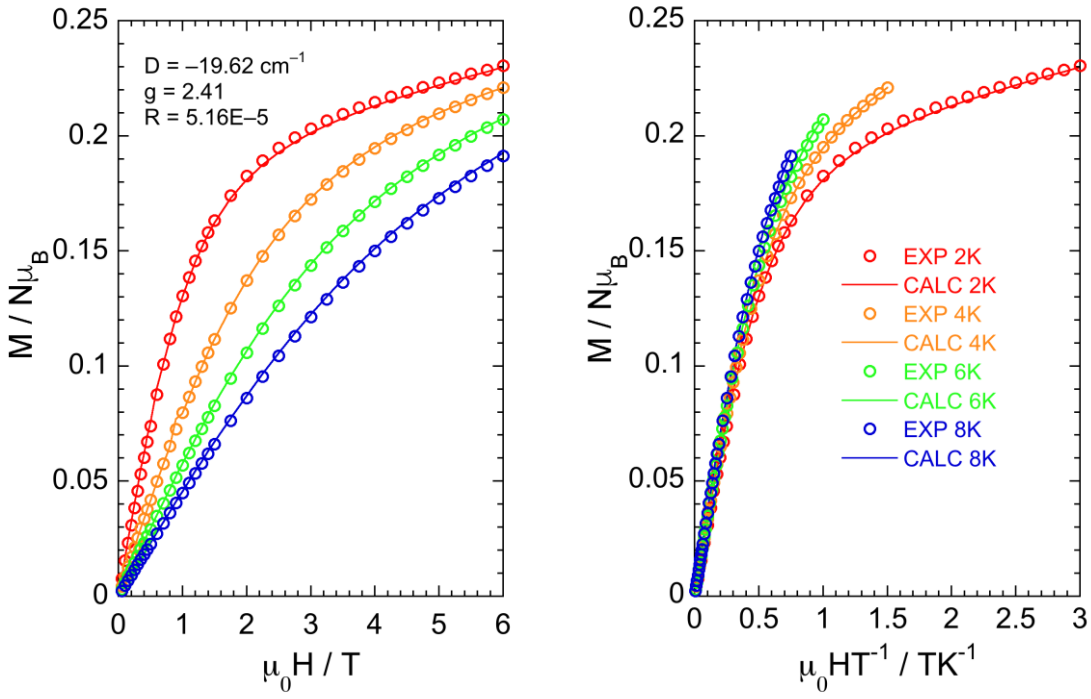

Figure 2.14. Magnetization *vs.* $\mu_0 H$ (left) and *vs.* $\mu_0 H/T$ (right) at variable temperatures (○ (exp), — (best fit)) for complex **2-8**.

2.3.3.3 High field/frequency electron paramagnetic resonance studies

In order to confirm the magnetization results and specifically the negative sign of *D*, HFEPR measurements were carried out at different frequencies and up to an applied dc magnetic field of 16 T for complexes **2-1** and **2-6**. The results for **2-1** were already reported; they confirm the negative *D* value that was found equal to –8.1 cm^{-1}.[18] For complex **2-6**, the spectra were recorded at 220.8, 331.2 and 662.4 GHz (Figure 2.15). A satisfactory simulation of all the spectra (Figure 2.16) was obtained with the following set of parameters g_x = 2.20, g_y = 2.12, g_z = 2.34, E = 0.08 cm^{-1} and D = –17.7 cm^{-1}. Thus, an accurate *D* value but less accurate *g* values, because of the masking effect of the large |*D*|, are obtained from these simulations. Whereas resonance positions in the experimental spectra are rather well reproduced in the simulated spectra, their relative intensities within each spectrum are less satisfactorily reproduced.

 Feng SHAO: 0000-0001-8606-8628

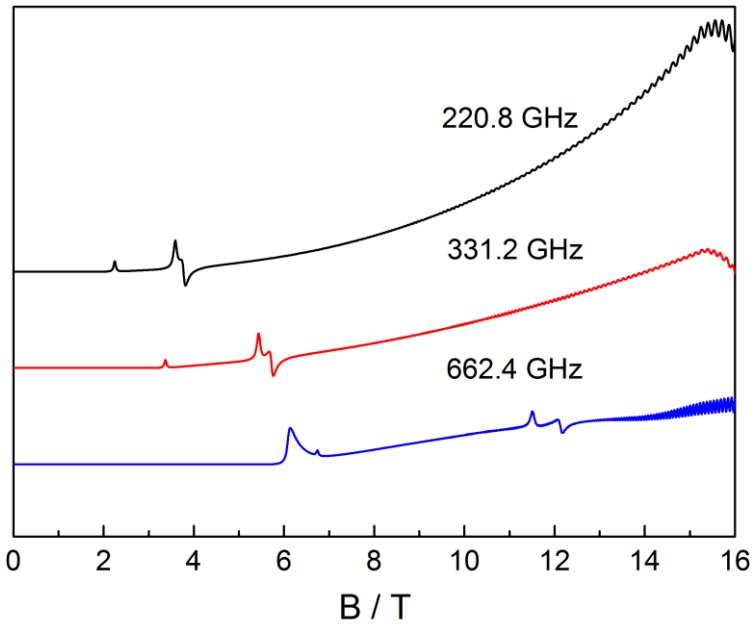

Figure 2.15. Experimental EPR spectra of complex **2-6** at 15 K with three frequencies.

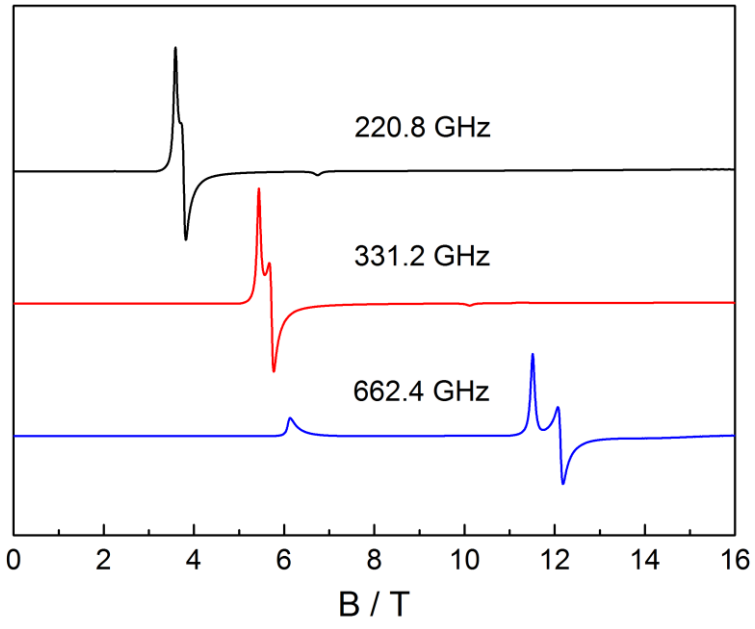

Figure 2.16. Calculated EPR spectra of complex **2-6** at 15 K with three frequencies.

2.3.3.4 Alternating current magnetic susceptibility studies

Ac susceptibility measurements may bring complementary information on the dynamics of the magnetization reversal at higher temperatures. And applying a dc magnetic field may slow down the QTM and make other processes more visible. We, first, measured the ac susceptibility at T = 2 K (or 2.3 K) for different frequencies and at different values of the applied dc magnetic field in order to find the optimum filed value where the relaxation is slower. This optimum field corresponds, normally, to the one where QTM is suppressed and where the direct mechanism is minimized.

Complexes 2-1, 2-2 and 2-3

The dynamic magnetic properties of these three complexes are similar, we describe the data of complex **2-1** in more details.

For complex **2-1**, field optimization experiment was studied at T = 2 K using an applied dc magnetic field in range 0 – 4000 Oe. Figure 2.17 top presents the plots of χ'' = f(ν) from $\mu_0 H$ = 0 to 4000 Oe. For $\mu_0 H$ = 0 Oe, the maximum of the curve is at a frequency value larger than 1500 Hz, cannot accessible with our SQUID magnetometer. Upon increasing the field, the maximum at high frequency seems to decrease in intensity, while another peak appears around 100 Hz, whose intensity increases when the field is increased. One can see the presence of a quasi isobestic point for the curves. This may correspond to two relaxation processes with contributions controlled by the applied dc magnetic field. Figure 2.17 bottom shows that the optimum field where the high frequency relaxation process has almost vanished in favor of the low frequency one is larger than 2800 Oe. We thus performed the ac measurements for $\mu_0 H$ = 2800 Oe. Figure 2.18 shows the variation of the in-phase and the out-of-phase components of the ac susceptibility *vs.* frequency at different temperatures. As expected for SMMs, the relaxation of the magnetization (maximum of the plots in Figure 2.18 left) slows down upon decreasing the temperature.

 Feng SHAO: 0000-0001-8606-8628

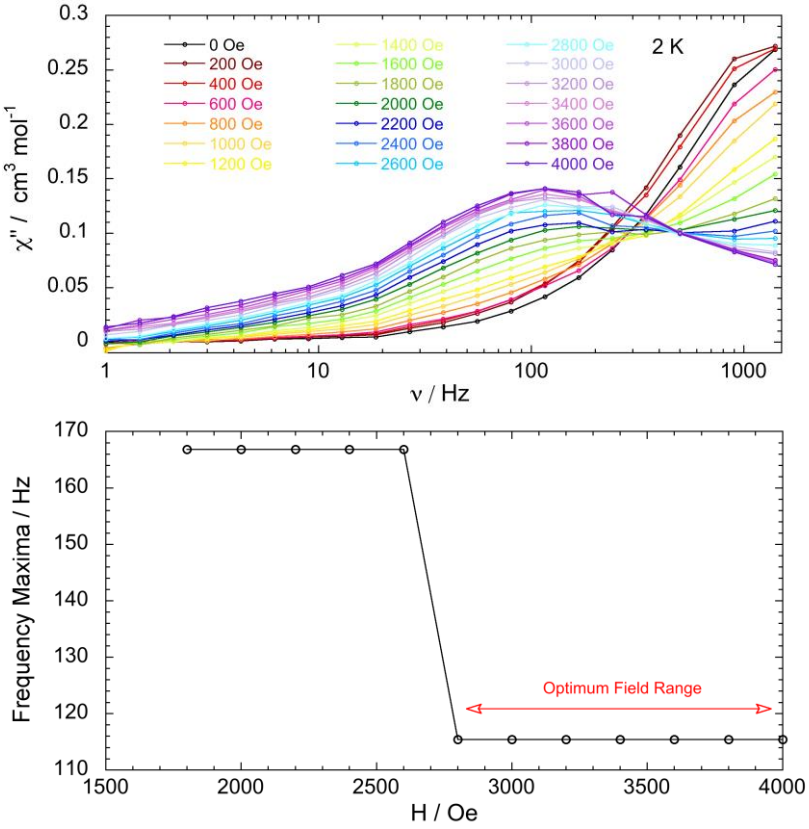

Figure 2.17. Out-of-phase susceptibility measurements at 2 K with a frequency range from 1 to 1500 Hz under various applied dc magnetic fields (top) and plot of frequency maxima *vs.* applied dc magnetic fields (bottom) for complex **2-1**.

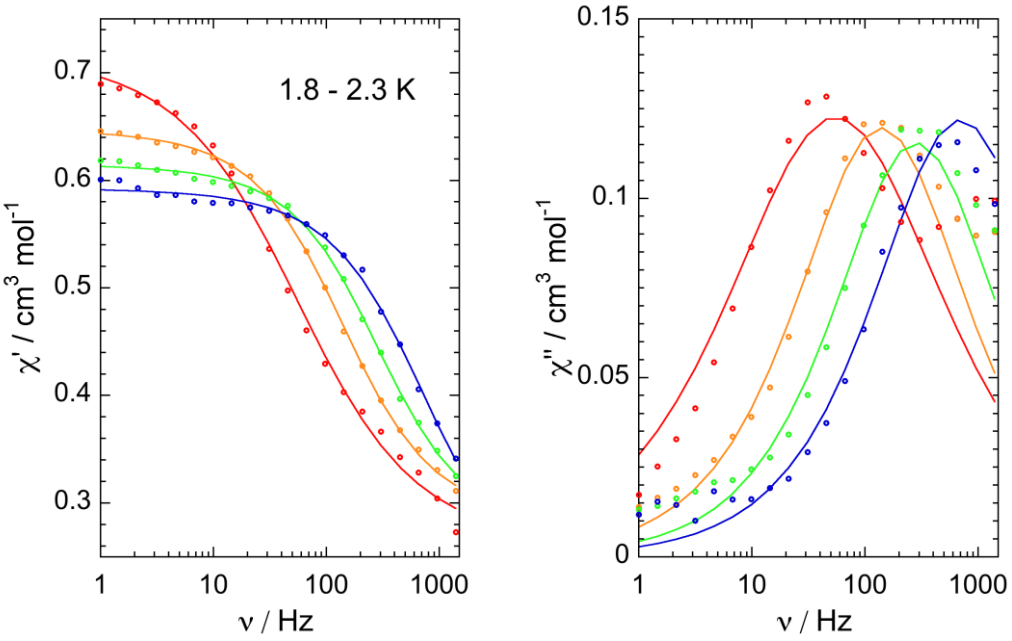

Figure 2.18. Frequency dependent in-phase and out-of-phase ac magnetic susceptibilities (○ (exp), — (fit)) for complex **2-1** under an applied dc magnetic field of 2800 Oe.

The Cole-Cole plots for complex **2-1** at 2800 Oe were obtained with a temperature range 1.8 – 2.3 K (Figure 2.19). They were fitted using a generalized Debye model[50, 51] which allows extracting the relaxation times (τ) and their distribution (α) for each temperature (Table 2.9).

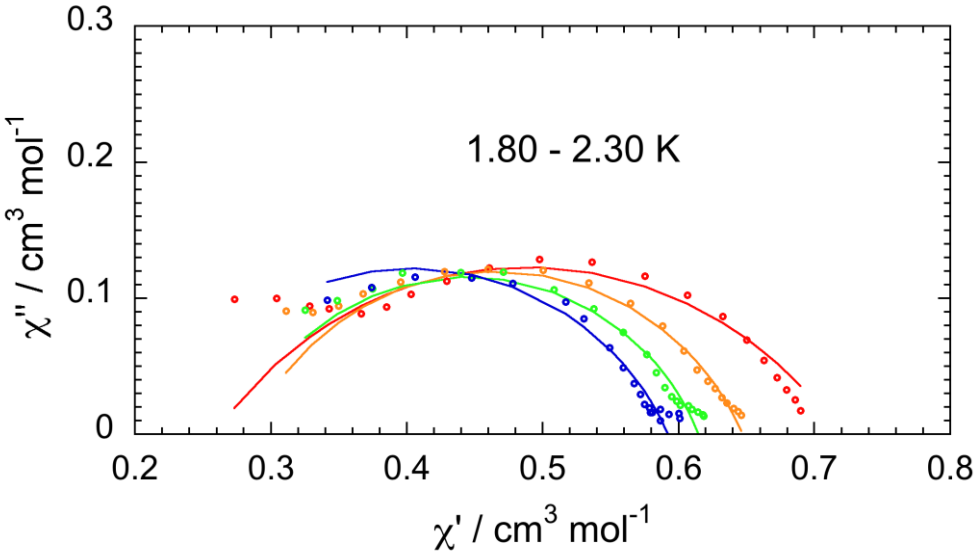

Figure 2.19. Cole-Cole plots (○ (exp), — (fit)) for complex **2-1** under an applied dc magnetic field of 2800 Oe.

Table 2.9. Cole-Cole fit parameters under an applied dc magnetic field of 2800 Oe for complexes **2-1** to **2-3**.

Complexes	Temperature	χ_0	χ_∞	α	τ
2-1	1.80 K	0.7176499292	0.2592461725	0.3743402040	0.0028940236
	2.00 K	0.6469177364	0.2845216884	0.2564638623	0.00113808160
	2.15 K	0.6145932696	0.2749628873	0.2396132294	0.0005603109
	2.30 K	0.5923126750	0.2167967583	0.2667213528	0.0002282341
2-2	1.80 K	0.8812986695	0.1774288328	0.2110747220	0.0019909085
	2.00 K	0.8082100679	0.17618355130	0.2098974452	0.0006971637
	2.20 K	0.7616431267	0.1248699307	0.2528865335	0.0002748907
	2.40 K	0.7153213588	0.1049990860	0.2507290400	0.0001158328
2-3	1.80 K	0.6997166352	0.4207985665	0.2863856124	0.0008501904
	2.00 K	0.6543275446	0.4121279778	0.2491465591	0.0003554725
	2.15 K	0.6256408531	0.3726950031	0.2332497920	0.0001541062
	2.30 K	0.6050046801	0.3727330695	0.2572216449	0.0000921729

The fit of the χ'= f(ν), χ''= f(ν) and χ'' = f(χ') were carried out using a home-made program:

$$\chi'(\nu_{ac}) = \chi_\infty + \frac{(\chi_0 - \chi_\infty)[1 + (2\pi\nu_{ac}\tau)^{1-\alpha}\sin(\frac{\alpha\pi}{2})]}{1 + 2(2\pi\nu_{ac}\tau)^{1-\alpha}\sin\left(\frac{\alpha\pi}{2}\right) + (2\pi\nu_{ac}\tau)^{2(1-\alpha)}}$$

$$\chi''(\nu_{ac}) = \chi_\infty + \frac{(\chi_0 - \chi_\infty)[(2\pi\nu_{ac}\tau)^{1-\alpha}\cos(\frac{\alpha\pi}{2})]}{1 + 2(2\pi\nu_{ac}\tau)^{1-\alpha}\sin\left(\frac{\alpha\pi}{2}\right) + (2\pi\nu_{ac}\tau)^{2(1-\alpha)}}$$

where χ_∞ is the adiabatic susceptibility (at $\nu_{ac} \to \infty$), χ_0 is the isothermal susceptibility (at $\nu_{ac} \to 0$) and τ is the average relaxation time of magnetization.

Then, the extracted relaxation times for each temperature were used to plot the ln(τ) = f(1/T) curve (Figure 2.20). Assuming that the relaxation is thermally activated *i.e.* only an Orbach process is responsible of the reorientation of the magnetization, it is possible to fit the ln(τ) = f(1/T) curve with a straight line that provides the magnitude of the effective energy barrier for the reorientation of the magnetization U_{eff} that is found equal to 20.6 K (14.3 cm^{-1}); the τ_0 value was found equal to 3.4 × 10^{-8} s. The U_{eff} value is very close to the theoretical value 2|D| (16.2 cm^{-1}). This is in line with mainly an Orbach process for the relaxation of the magnetization. The α value is found to be in the range 0.2 – 0.4, corresponding to a relatively weak distribution of the relaxation times. This may be due to tiny magnetic inhomogenoeties within the compounds due to the fact that all the molecules do not feel exactly the same applied dc magnetic field. In order to get a better insight and to detect small differences in the relaxation times among similar complexes, it is necessary to study the diluted ones, where the interaction between the molecules that may influence the relaxation processes are minimized.

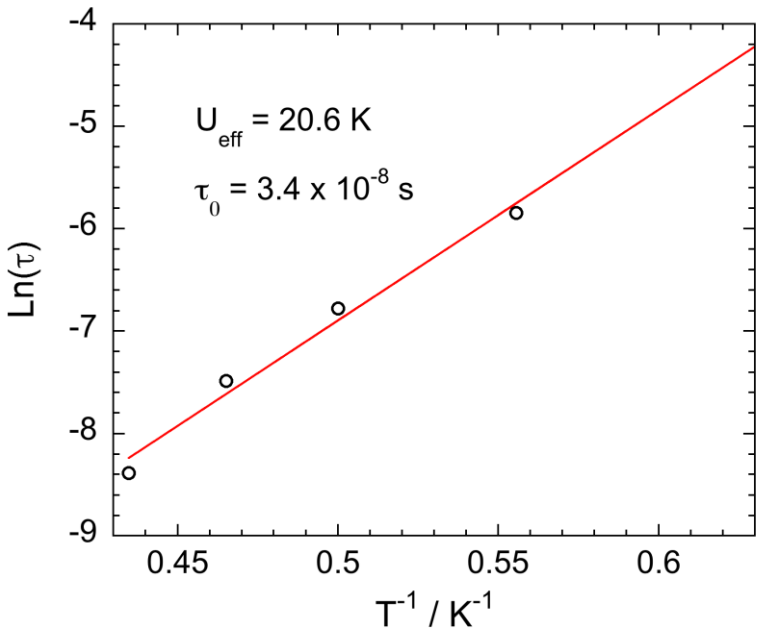

Figure 2.20. ln(τ) = f(1/T) plot (○ (exp), — (linear fit)) for the relaxation processes for complex **2-1** under an applied dc magnetic field of 2800 Oe.

Table 2.10. Magnetic parameters for complexes **2-1** to **2-3**.

Complexes	**2-1**	**2-2**	**2-3**
[a] D	–6.20	–5.37	–5.11
[b] g	2.24	2.33	2.17
[c] *OFR*	2600 – 4000	2400 – 3000	2600 – 3000
[d] U_{eff}	14.3	14.2	13.0
[e] τ_0	3.4×10^{-8}	2.5×10^{-8}	2.7×10^{-8}
[e] τ (1.8 K)	2.89×10^{-3}	1.99×10^{-3}	8.5×10^{-4}

[a] ZFS parameter D in wavenumbers (cm^{-1}); [b] Landé g-tensor; [c] Optimum Field Range in Ørsted (Oe); [d] effective energy barriers in wavenumbers (cm^{-1}). [e] pre-exponential factor in seconds (s).

To sum up, one can conclude that the three complexes possess very close local structure around the Co^{II} ion, but with small differences. These differences lead to slightly different D values (from the magnetization data) and to relaxation times of 3×10^{-3}, 2×10^{-3} and 8×10^{-4} s at T = 1.8 K for complexes **2-1**, **2-2** and **2-3** respectively, correlated with the magnitude of the axial magnetic anisotropy parameters (Table 2.10). We did not perform studies on the complexes diluted in the diamagnetic Zn^{II} matrix.

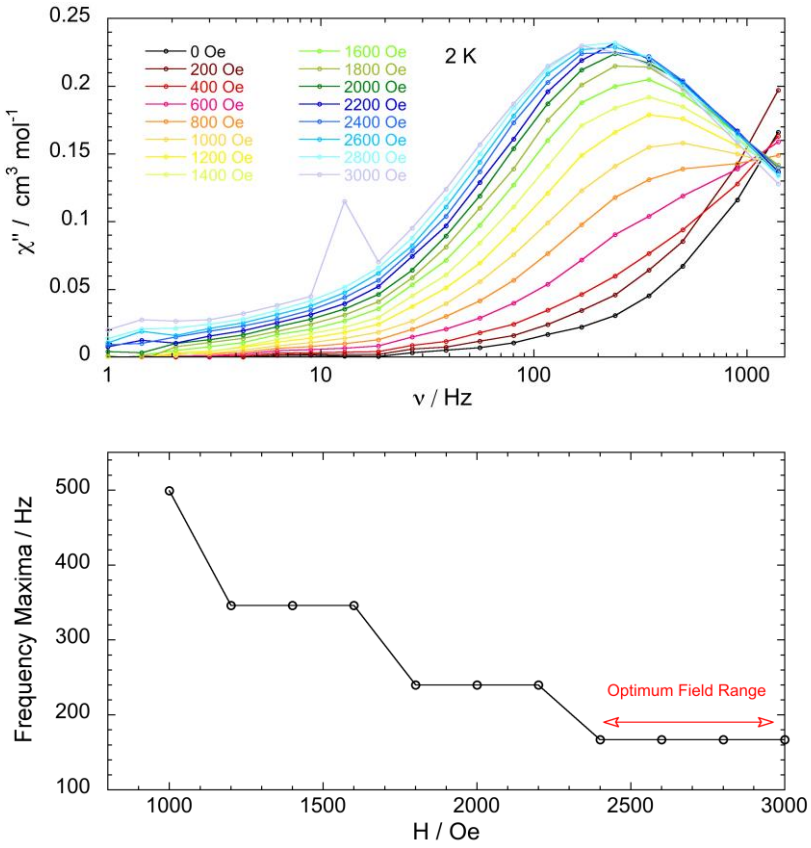

Figure 2.21. Out-of-phase susceptibility measurements at 2 K with a frequency range from 1 to 1500 Hz under various applied dc magnetic fields (top) and plot of frequency maxima *vs.* applied dc magnetic fields (bottom) for complex **2-2**.

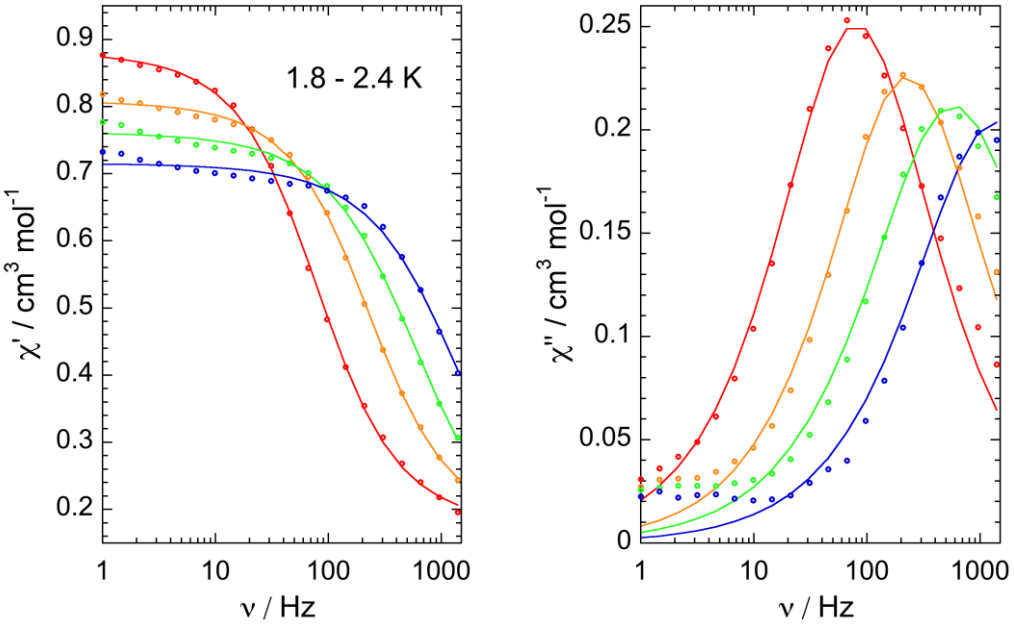

Figure 2.22. Frequency dependent in-phase and out-of-phase ac magnetic susceptibilities (○ (exp), — (fit)) for complex **2-2** under an applied dc magnetic field of 2800 Oe.

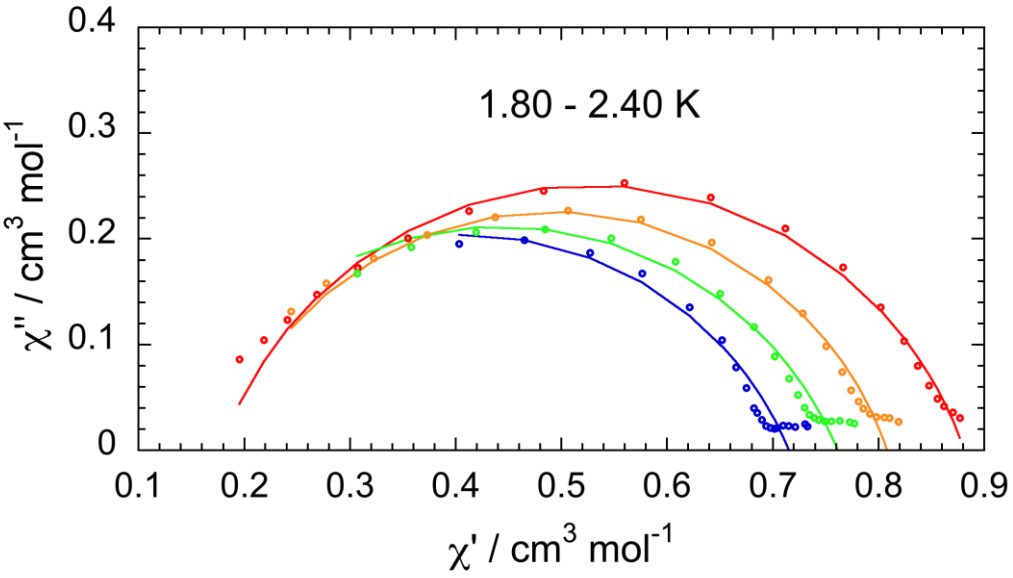

Figure 2.23. Cole-Cole plots (○ (exp), — (fit)) for complex **2-2** under an applied dc magnetic field of 2800 Oe.

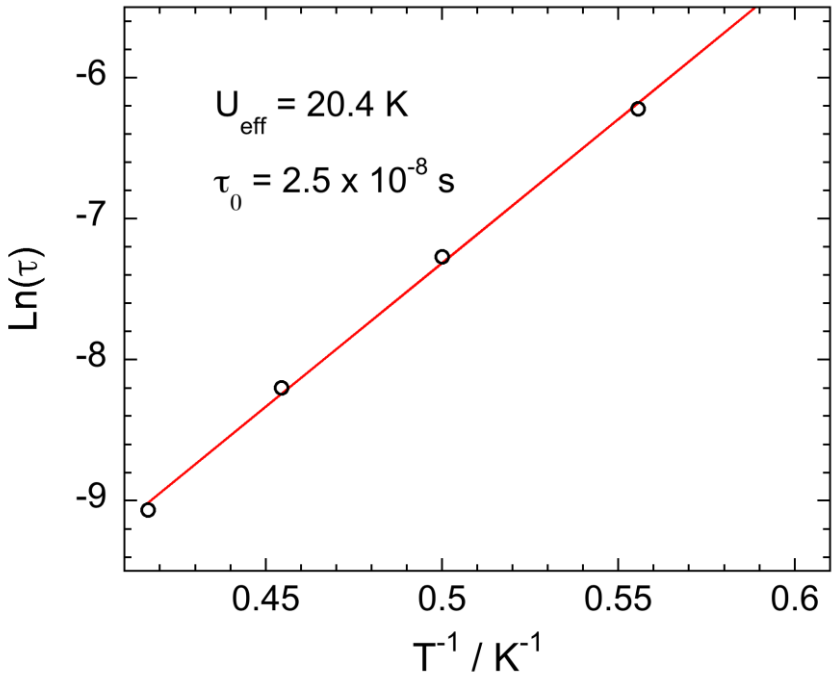

Figure 2.24. ln(τ) = f(1/T) plot (○ (exp), — (linear fit)) for the relaxation processes for complex **2-2** under an applied dc magnetic field of 2800 Oe.

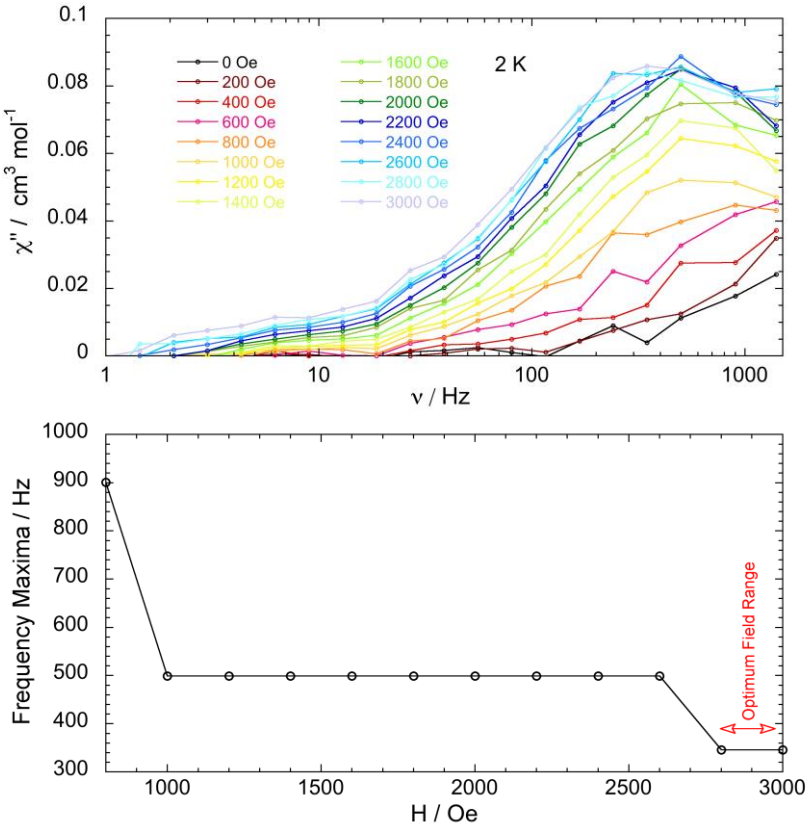

Figure 2.25. Out-of-phase susceptibility measurements at 2 K with a frequency range from 1 to 1500 Hz under various applied dc magnetic fields (top) and plot of frequency maxima *vs.* applied dc magnetic fields (bottom) for complex **2-3**.

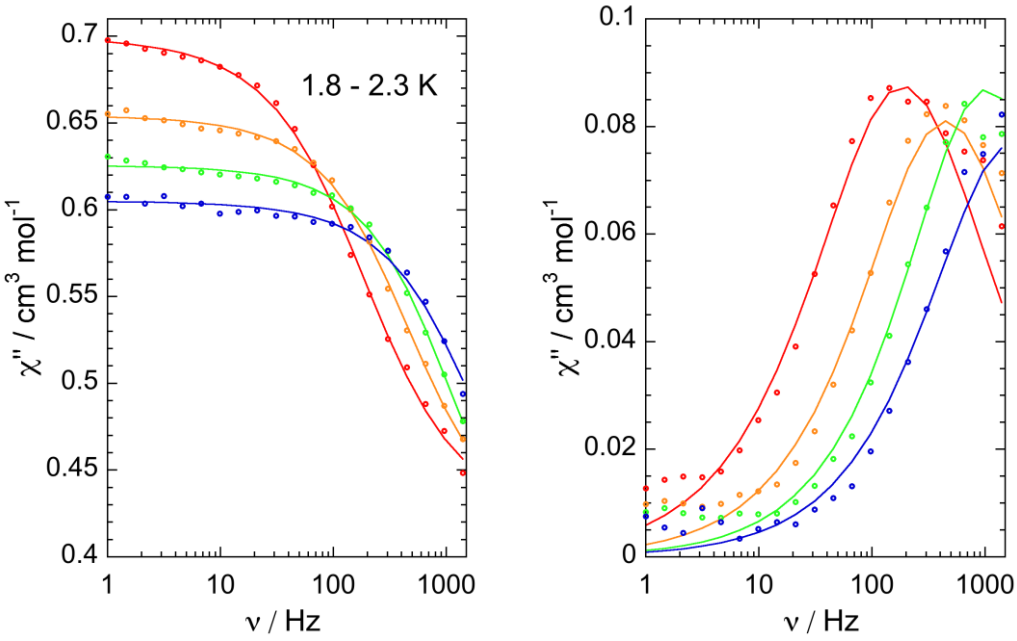

Figure 2.26. Frequency dependent in-phase and out-of-phase ac magnetic susceptibilities (○ (exp), — (fit)) for complex **2-3** under an applied dc magnetic field of 2800 Oe.

 Feng SHAO: 0000-0001-8606-8628

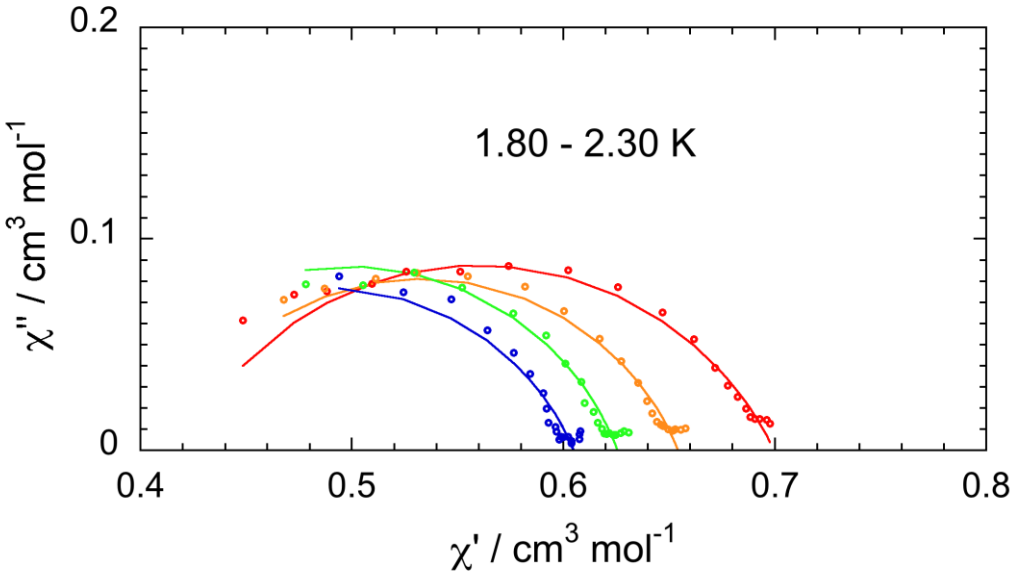

Figure 2.27. Cole-Cole plots (○ (exp), — (theoretical fit)) for complex **2-3** under an applied dc magnetic field of 2800 Oe.

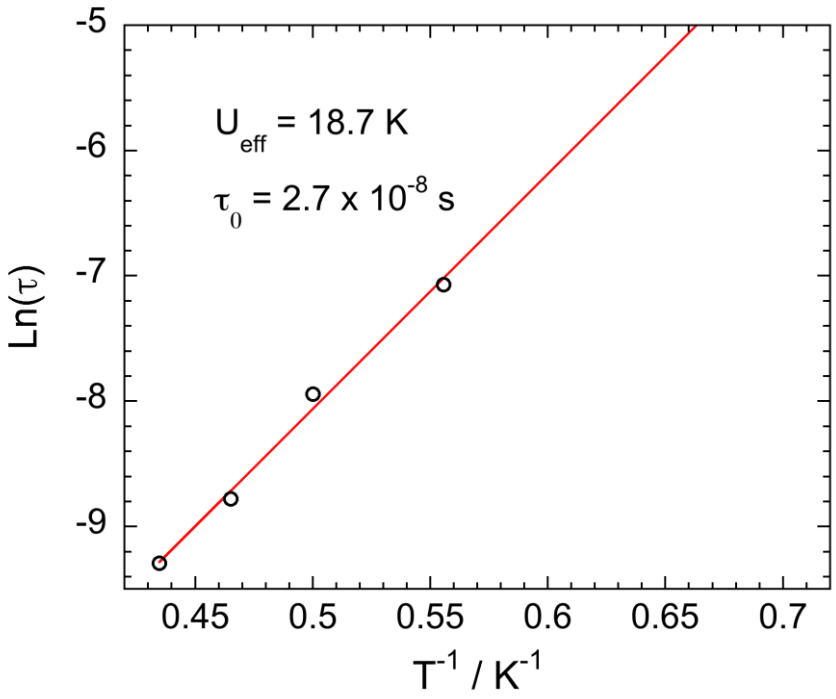

Figure 2.28. ln(τ) = f(1/T) plot (○ (exp), — (linear fit)) for the relaxation processes for complex **2-3** under an applied dc magnetic field of 2800 Oe.

Complexes 2-4 and 2-5

Field optimization experiment for complex **2-4** was carried out at T = 2 K with an applied dc magnetic field range 1000 – 10000 Oe (Figure 2.29 top), which reveals that the optimum applied dc magnetic field is 10000 Oe. (Figure 2.29 bottom). Below 1000 Oe field, no maxima in the frequency-dependent ac susceptibility plot could be observed. The out-of-phase and the in-phase susceptibilities were thus measured at 10000 Oe (Figure 2.30), but the data were not of enough good quality to go further in the analysis, to fit the data and extract the relaxation times and the energy barrier values. For complex **2-5**, applying the dc magnetic field in the range 0 – 4000 Oe (Figure 2.31) does not lead to an out-of-phase susceptibility response.

The absence of a blocking of the magnetization in the complex with iodide as the axial ligand (**2-5**) is not surprising because of the weak value of the ZFS parameter found from the magnetization studies. When the axial ligand is Br^- (**2-4**), it is possible to observe a blocking of the magnetization but when only applying a large field and at temperatures smaller than when the axial ligand is the chloride (complexes **2-1**, **2-2** and **2-3**). This is also due to the relatively weak magnetic anisotropy.

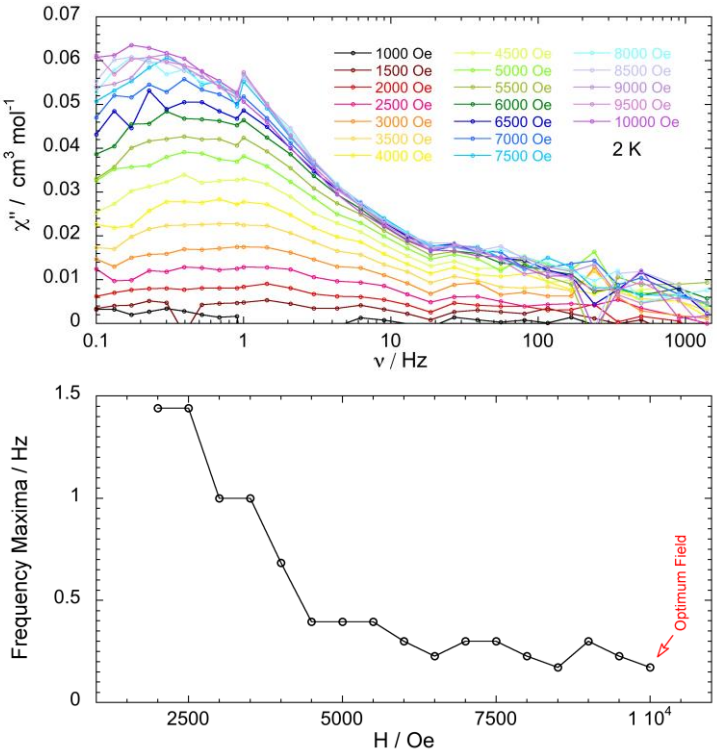

Figure 2.29. Out-of-phase susceptibility measurements at 2 K with a frequency range from 1 to 1500 Hz under various applied dc magnetic fields (top) and plot of frequency maxima *vs.* applied dc magnetic fields (bottom) for complex **2-4**.

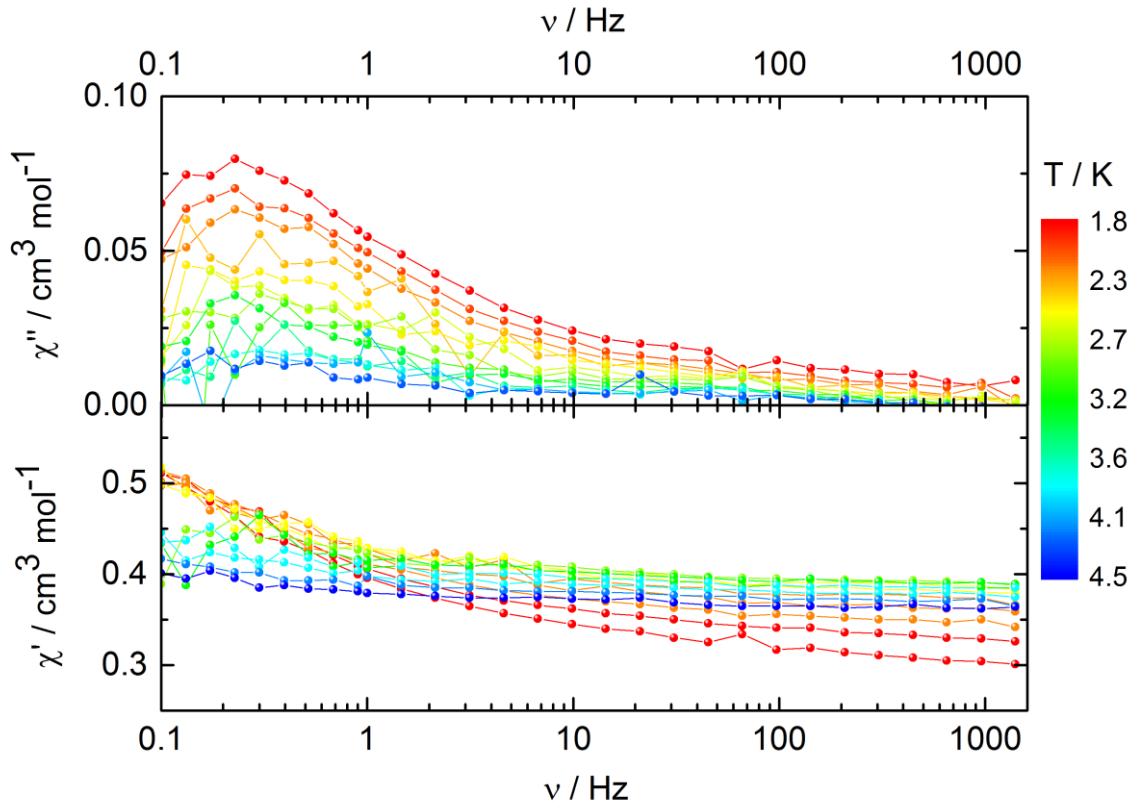

Figure 2.30. Frequency dependent in-phase and out-of-phase ac magnetic susceptibilities for complex **2-4** under an applied dc magnetic field of 10000 Oe.

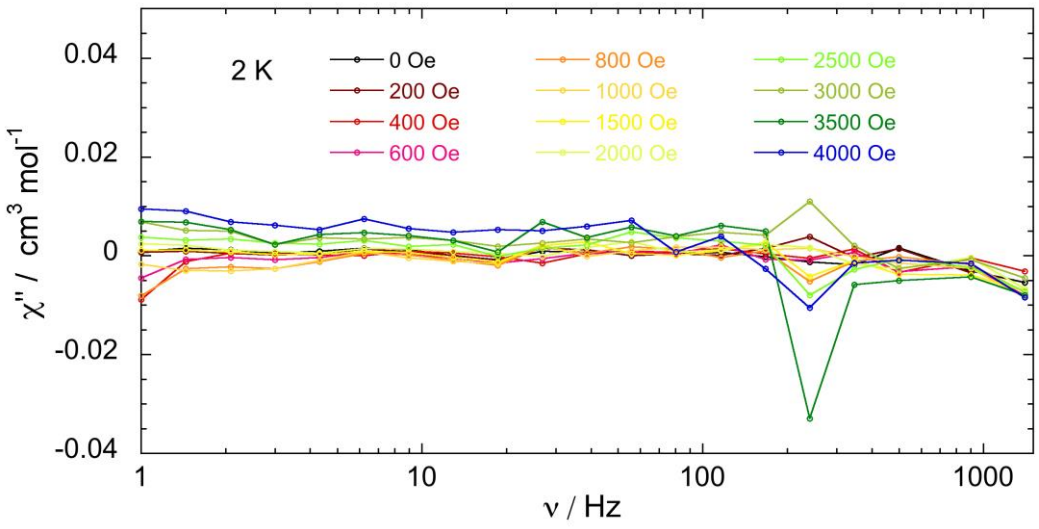

Figure 2.31. Out-of-phase susceptibility measurements at 2 K with a frequency range from 1 to 1500 Hz under various applied dc magnetic fields for complex **2-5**.

 Feng SHAO: 0000-0001-8606-8628

Complexes 2-6

Field optimization experiment was carried out at T = 2 K with an applied dc magnetic field range 0 – 3800 Oe for complex **2-6** (fluoride as the axial ligand) (Figure 2.32 top). For zero applied dc magnetic field, the maximum of the χ'' = f(ν) curve is above 1500 Hz (cannot thus be observed with our SQUID), which corresponds to a rather fast relaxation of the magnetization. One also notices the presence of a kink at around 50 Hz, suggesting the presence of a slower relaxation process. Upon applying a dc magnetic field of 200 Oe, the intensity of the kink around 50 Hz slightly increases. A further increase of the applied dc magnetic field leads to the disappearance of the maximum assumed to be at a frequency higher than 1500 Hz and the increase of the value of χ'' of the low frequency maximum with a shift towards low frequency. At dc magnetic field of 2200 Oe, the maximum of the χ'' = f(ν) is around 2 Hz. If the dc magnetic field is further increased, the frequency of the maximum of the curve stays constant until a value of 3200 Oe, and then shifts back towards high frequency (Figure 2.32). From these observations, one may conclude to the presence of two relaxation processes, one rather fast and the other slower.

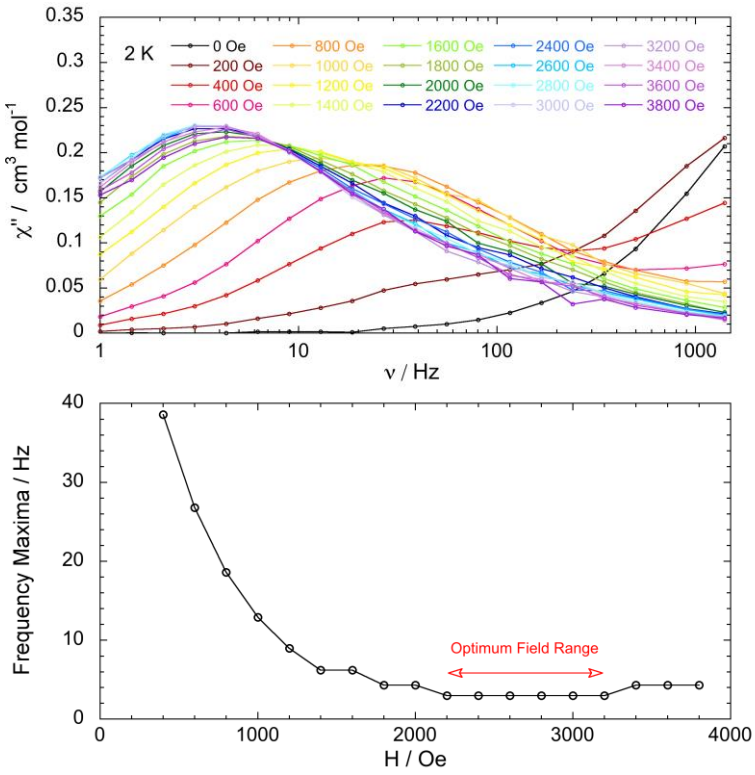

Figure 2.32. Out-of-phase susceptibility measurements at 2 K with a frequency range from 1 to 1500 Hz under various applied dc magnetic fields (top) and plot of frequency maxima *vs.* applied dc magnetic fields (bottom) for complex **2-6**.

The fast one can be assigned to molecules with predominant QTM relaxation, while the slower to molecules that undergo relaxation with a predominant Orbach mechanism. Upon increasing the field, the number of molecules with a fast relaxation process decreases, while the number of those with the slower process increases. The increase of the frequency of the maximum of the χ'' = f(ν) plots when the dc magnetic field becomes larger than 3200 Oe is due to the direct relaxation mechanism that depends on the magnitude of the applied dc magnetic field. These observations lead to the conclusion that the slow relaxation process is probably the result of several mechanisms including the Orbach, the direct and may be the Raman one.

In order to get information on the dependence of the relaxation time with temperature, we measured the ac susceptibility as a function of the frequency at different temperatures using the optimum applied dc magnetic field $\mu_0 H$ = 2200 Oe (Figure 2.33). The χ'' = f(ν) plots (Figure 2.33 right) show that the maximum of the curves shifts towards low frequency upon cooling down as expected for a SMM behavior.

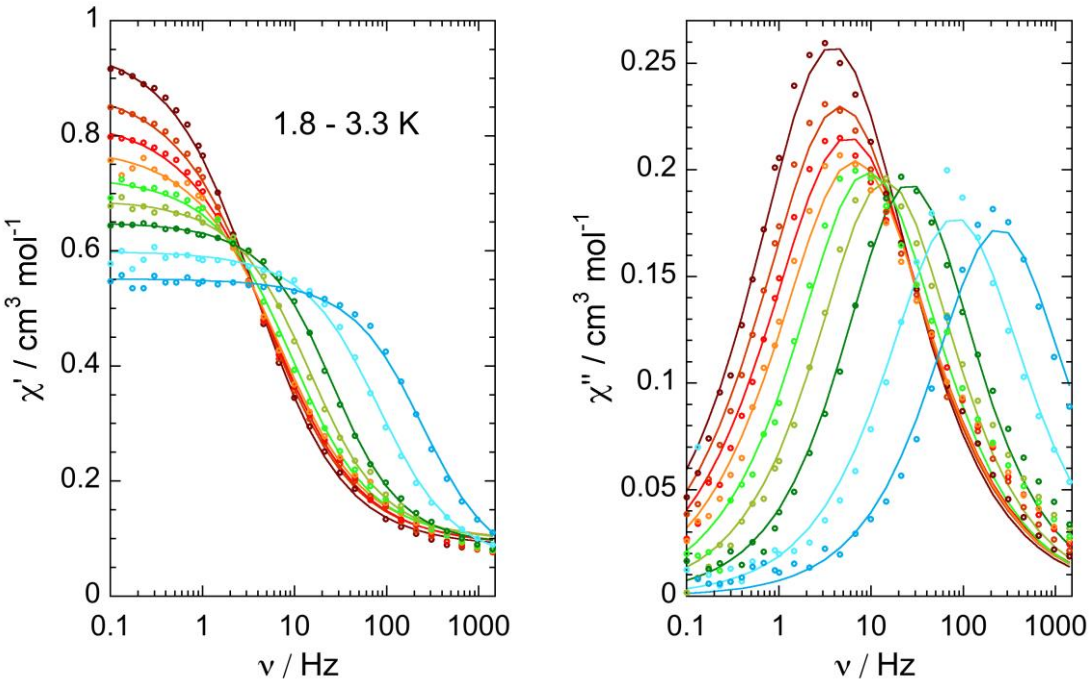

Figure 2.33. Frequency dependent in-phase and out-of-phase ac magnetic susceptibilities (○ (exp), — (fit)) for complex **2-6** under an applied dc magnetic field of 2200 Oe.

 Feng SHAO: 0000-0001-8606-8628

The χ'' = f(χ') plots in the 1.8 – 3.3 K temperature range (Cole-Cole, Figure 2.34) have the expected slightly flattened semi-circles. The fit of the different curves allows extracting the relaxation times and their distribution for each temperature (Table 2.11). The relaxation time speeds up from 4×10^{-2} to 6×10^{-4} s between 1.8 and 3.3 K but their distribution (α) does change much. It is worth noting that the relaxation time for complex **2-6** (4.1×10^{-2} s, fluoride as the axial ligand) is one order of magnitude larger than the complex **2-1** that the chloride as the axial ligand.

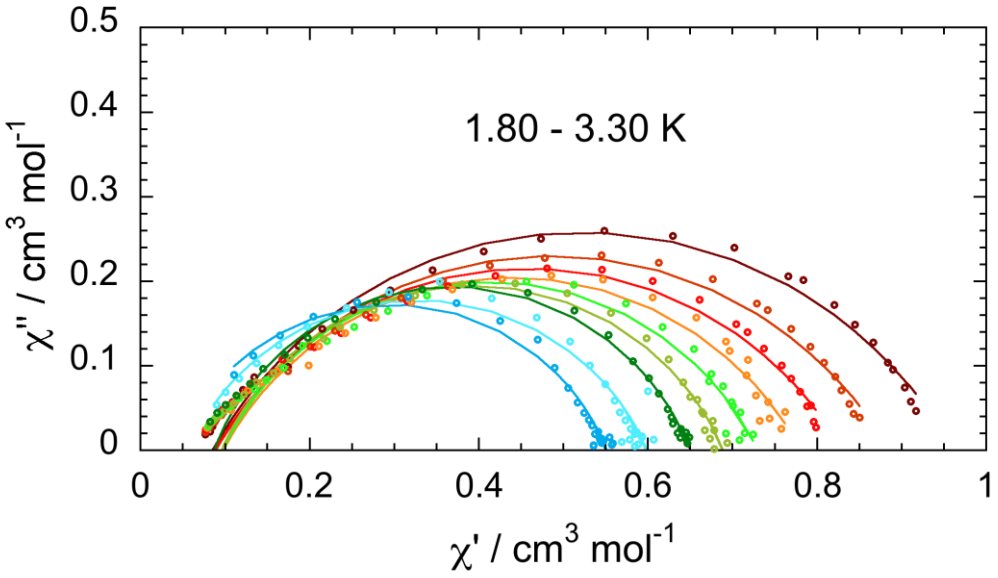

Figure 2.34. Cole-Cole plots (○ (exp), — (fit)) for complex **2-6** under an applied dc magnetic field of 2200 Oe.

Table 2.11. Cole-Cole fit parameters under an applied dc magnetic field of 2200 Oe for complex **2-6**.

Complex	Field	Temperature	χ_0	χ_∞	α	τ
2-6	2200 Oe	1.80 K	0.9607425460	0.0853909470	0.3218999380	0.0414665540
		2.00 K	0.8852336430	0.0892928340	0.3330568170	0.0340223460
		2.15 K	0.8301024940	0.0878521900	0.3310240500	0.0280583130
		2.30 K	0.7809503890	0.0977592420	0.3137109680	0.0237608600
		2.45 K	0.7294083200	0.0968522760	0.2844872310	0.0169017290
		2.60 K	0.6895133620	0.0957527030	0.2602714670	0.0111030450
		2.75 K	0.6497642920	0.0868766230	0.2329673270	0.0061708270
		3.00 K	0.5994955220	0.0559441000	0.2636517090	0.0019433420
		3.30 K	0.5515515270	0.0422502800	0.2427576550	0.0006559970

The ln(τ) = f(*1/T*) curve (Figure 2.35) has three parts: a linear one at high temperature corresponding mainly to an activated mechanism (Orbach), a more leveled part at low temperature where the relaxation time is almost temperature independent that may correspond mainly to a QTM and at intermediate temperature dependence. We, first, fitted only the linear part of the curve (Figure 2.35 left) in order to estimate the effective energy barrier U_{eff} that was found equal to 27.1 cm^{-1}, and a τ_0 value of 5 × 10^{-9} s. In order to fit the whole curve, one must consider all the relaxation mechanisms. We, thus, attempted to fit the dependence of the relaxation time using the following general expression:

$$\tau^{-1} = AH^2T + \frac{B_1}{1 + B_2H^2} + CT^n + \tau_0^{-1}\exp(-U/k_BT)$$

where AH^2T, $\frac{B_1}{1+B_2H^2}$, CT^n and $\tau_0^{-1}\exp(-U/k_BT)$, correspond to the direct, the QTM, the Raman and the Orbach processes respectively; *A*, B_1, B_2, *C*, and *n* are coefficients, *H* is the applied dc magnetic field, *T* is the temperature, *U* is the thermal barrier of the Orbach relaxation mechanism, τ_0 is the attempt time, and k_B is the Boltzmann constant.[52-54] Two fits were performed, one considering QTM of the magnetization and the other excluding this process. As shown in Figure 2.35, right and in Table 2.12, it is possible to obtain good fits in the two cases. The fit including the QTM gives parameters showing that this process is negligible (when the applied dc magnetic field is 2200 Oe). Thus, the shape of the ln(τ) =

f(1/*T*) plot can be explained by the presence of the direct and the Raman processes. The energy barrier is slightly larger (31 instead of 27 cm^{-1}) when these additional processes are considered. Finally, it is worth noting that the energy barrier is very close to that found from the EPR data ($2|D| = 34\ cm^{-1}$).

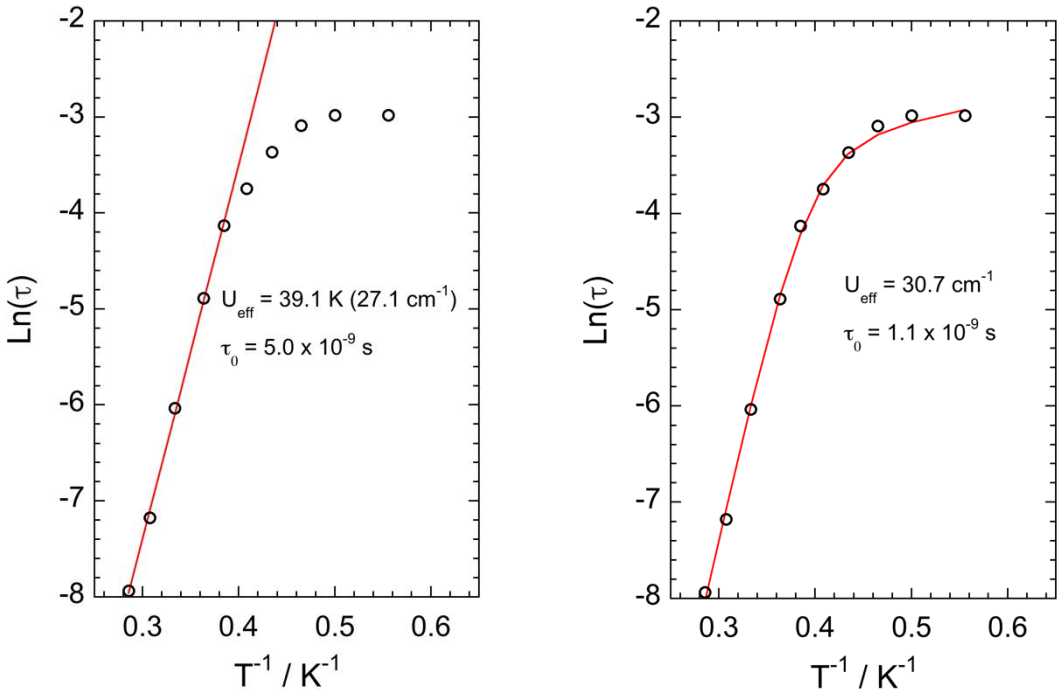

Figure 2.35. ln(τ) = f(1/*T*) plot (○ (exp), — (fit)) for the relaxation processes for complex **2-6** under an applied dc magnetic field of 2200 Oe. Left: only consider Orbach process; right: including Direct, QTM, Raman and Orbach processes.

Table 2.12. Fit parameters from ln(τ) = f(1/*T*) plot under an applied dc magnetic field of 2200 Oe for complex **2-6**.

Parameters	***H***	***A***	B_1	B_2	***C***	***n***	τ_0	U_{eff}	***R/GOF***
Units	***T***	$s^{-1}T^{-2}K^{-1}$	s^{-1}	T^{-2}	$s^{-1}K^{-5}$	—	***s***	cm^{-1}	—
	[a] 0.22^{Orbach}	—	—	—	—	—	5.1×10^{-9}	27.1	0.99937
2-6	[b] 0.22^{NoQTM}	200.56	—	—	0.038033	5	8.271×10^{-10}	31.298	1.98×10^{-4}
	[c] 0.22^{All}	200.56	11420	612180	0.037041	5	1.077×10^{-9}	30.741	1.88×10^{-4}

[a] relaxation fit only considering Orbach relaxation; [b] relaxation fit with Direct, Raman and Orbach relaxations, without considering QTM; [c] relaxation fit considering all relaxations (Direct, QTM, Raman and Orbach).

In order to get insights in the different relaxation processes, we performed the same studies and fits with applied dc magnetic fields $\mu_0 H$ = 400 and 1000 Oe. For $\mu_0 H$ = 400 Oe, the in-phase (Figure 2.36 left) and out-of-phase (Figure 2.36 right) susceptibilities plots show the presence of two relaxation processes, one fast with maxima of χ" at frequencies larger than 1500 Hz and the other slower at frequencies smaller than 100 Hz. The two processes are shown in the Cole-Cole plots (Figure 2.37).

It is, thus, possible to fit the ac data using the generalized Debye model considering the two relaxation processes and extract the parameters corresponding to the fast and the slow one (Table 2.13). Figure 2.38 and Figure 2.40 present ac theoretical data extracted from the experimental ones for the fast and the slow relaxation processes respectively. The corresponding Cole-Cole plots are depicted in Figure 2.39 and Figure 2.41. The α values for the two relaxation processes (0.059 and 0.112 for fast and the slow processes respectively at T = 1.8 K) are smaller than for the other complexes where it was not possible to separate two processes. This is in line with the presence of a dominant relaxation pathway for each process.

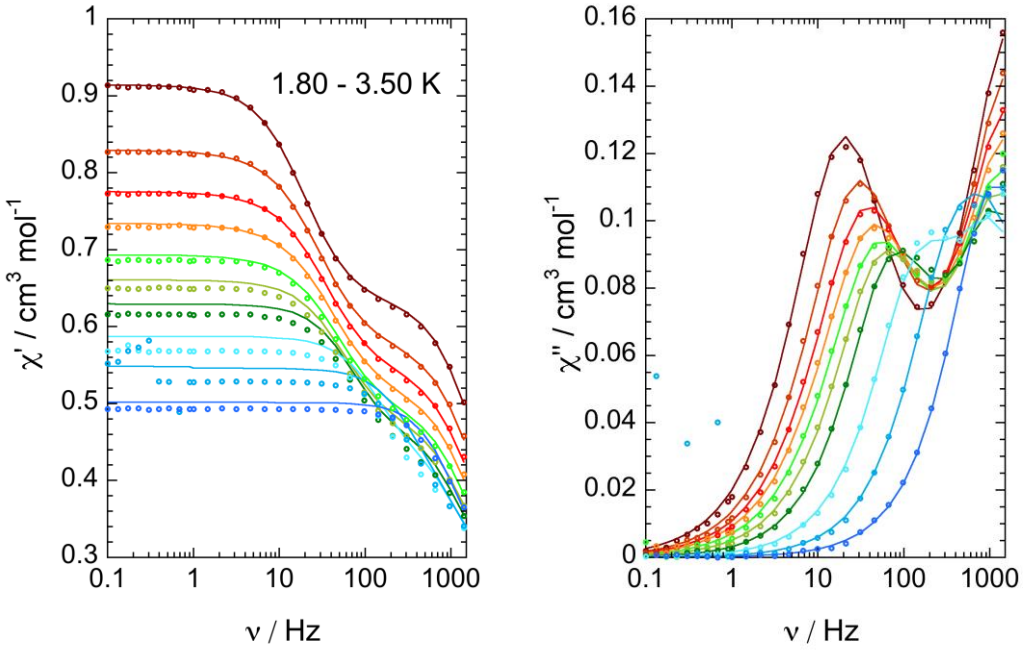

Figure 2.36. Frequency dependent in-phase and out-of-phase ac magnetic susceptibilities (○ (exp), — (fit)) for complex **2-6** under an applied dc magnetic field of 400 Oe.

 Feng SHAO: 0000-0001-8606-8628

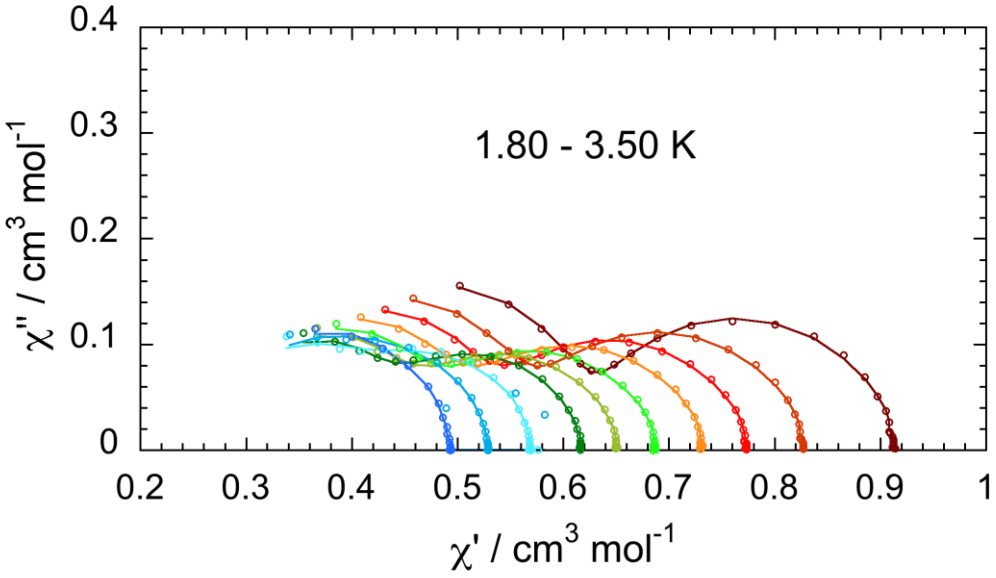

Figure 2.37. Cole-Cole plots (○ (exp), — (fit)) for complex **2-6** under an applied dc magnetic field of 400 Oe.

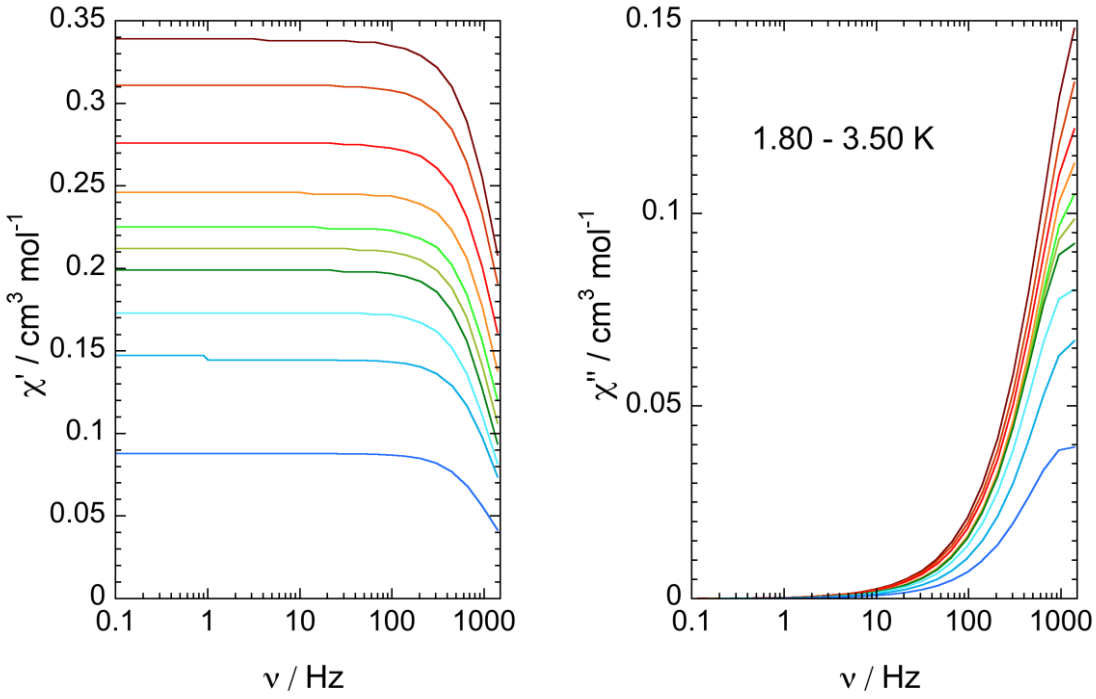

Figure 2.38. Deconvoluted frequency dependent in-phase and out-of-phase ac magnetic susceptibilities for complex **2-6** under an applied dc magnetic field of 400 Oe at difference temperatures for the fast processes.

 Feng SHAO: 0000-0001-8606-8628

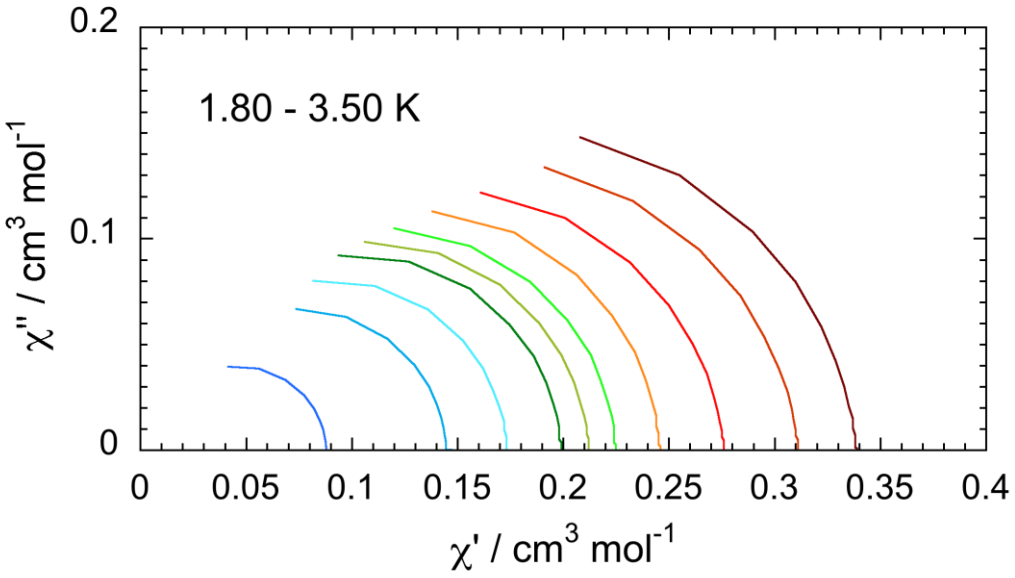

Figure 2.39. Deconvoluted Cole-Cole plots for complex **2-6** under an applied dc magnetic field of 400 Oe at difference temperatures for the fast processes.

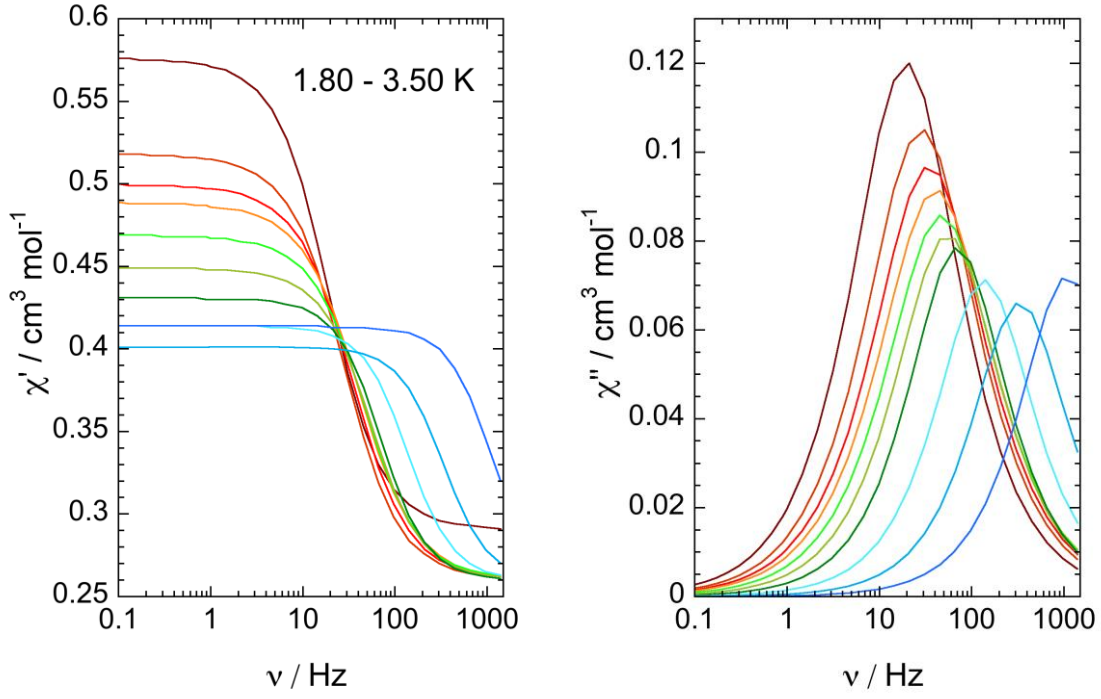

Figure 2.40. Deconvoluted frequency dependent in-phase and out-of-phase ac magnetic susceptibilities for complex **2-6** under an applied dc magnetic field of 400 Oe at difference temperatures for the slow processes.

 Feng SHAO: 0000-0001-8606-8628

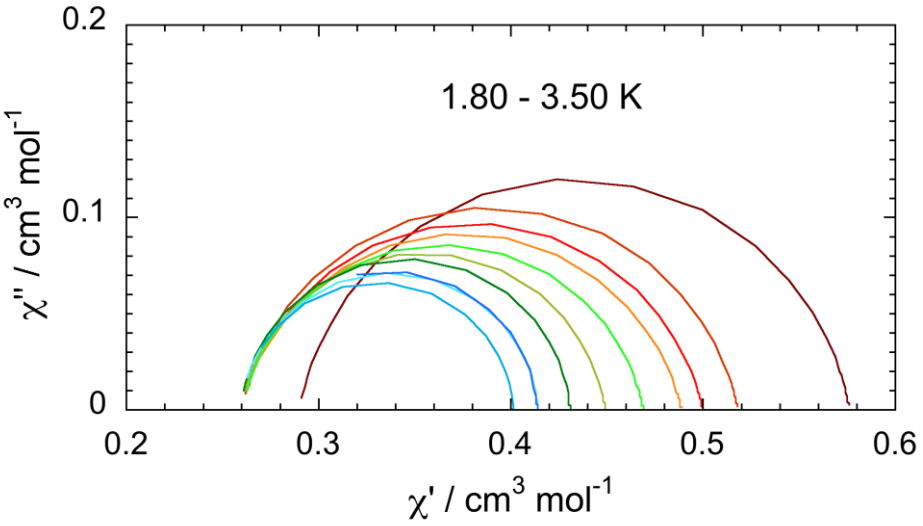

Figure 2.41. Deconvoluted Cole-Cole plots for complex **2-6** under an applied dc magnetic field of 400 Oe at difference temperatures for the slow processes.

Table 2.13. Cole-Cole fit parameters under an applied dc magnetic field of 400 Oe for complex **2-6**.

Complex	Field	Temperature	χ_0	χ_∞	α	τ
2-6	400 Oe (fast)	1.80 K	0.677187224	0.00990897	0.059148615	8.816×10^{-5}
		2.00 K	0.622550299	0.012784887	0.065836172	8.831×10^{-5}
		2.15 K	0.552007685	0.009817878	0.057593598	9.514×10^{-5}
		2.30 K	0.491239676	0.010285108	0.033919766	0.000101152
		2.45 K	0.449314947	0.009918687	0.0309097	0.000108595
		2.60 K	0.423785474	0.010021521	0.030992572	0.0001165
		2.75 K	0.397590245	0.010054009	0.02874303	0.000124777
		3.00 K	0.34661333	0.010010652	0.027168892	0.000125206
		3.25K	0.289207555	0.010004125	0.026970349	0.000115754
		3.50 K	0.175698621	0.009979225	0.026931362	0.000129356
	400 Oe (slow)	1.80 K	1.152501533	0.579997946	0.112494883	0.008226771
		2.00 K	1.036334845	0.519720857	0.128865903	0.005596696
		2.15 K	0.999790317	0.520024412	0.134657395	0.004582136
		2.30 K	0.977624854	0.51999241	0.140702389	0.003893391
		2.45 K	0.937909475	0.5200037	0.124084603	0.003360608
		2.60 K	0.898250974	0.519999675	0.094195111	0.002886900
		2.75 K	0.861472624	0.520005189	0.052865669	0.002265817
		3.00 K	0.828147707	0.519941939	0.049999821	0.001156978
		3.25 K	0.802741008	0.519906455	0.041660119	0.000477636
		3.50 K	0.827517923	0.520043838	0.040468818	0.000145091

 Feng SHAO: 0000-0001-8606-8628

In order the get a more quantitative analysis of the relaxation times, we plotted the ln(τ) = f(1/T) curves for the two processes and fitted them considering the different mechanisms. The linear part of the curve corresponding to the slow process was first fitted with only the Orbach mechanism and leads to U_{eff} = 30.1 cm^{-1} and τ_0 = 6.6 ×10^{-10} s (Figure 2.42 left). When considering all the other mechanisms with or without QTM, it is possible to fit the whole curve leading to a slight increase of the energy barrier value (Figure 2.42 right and Table 2.14). For the slow process, the contribution of the QTM mechanism is not a major one. While for the fast process, the ln(τ) = f(1/T) curve (Figure 2.43) is almost temperature independent. The slight dependence observed has no physical meaning because the large uncertainty on the extracted τ values due to the absence of maxima for the χ" = f(ν) curves (Figure 2.38 right); the maxima are at high frequencies and are not accessible with our apparatus as mentioned above.

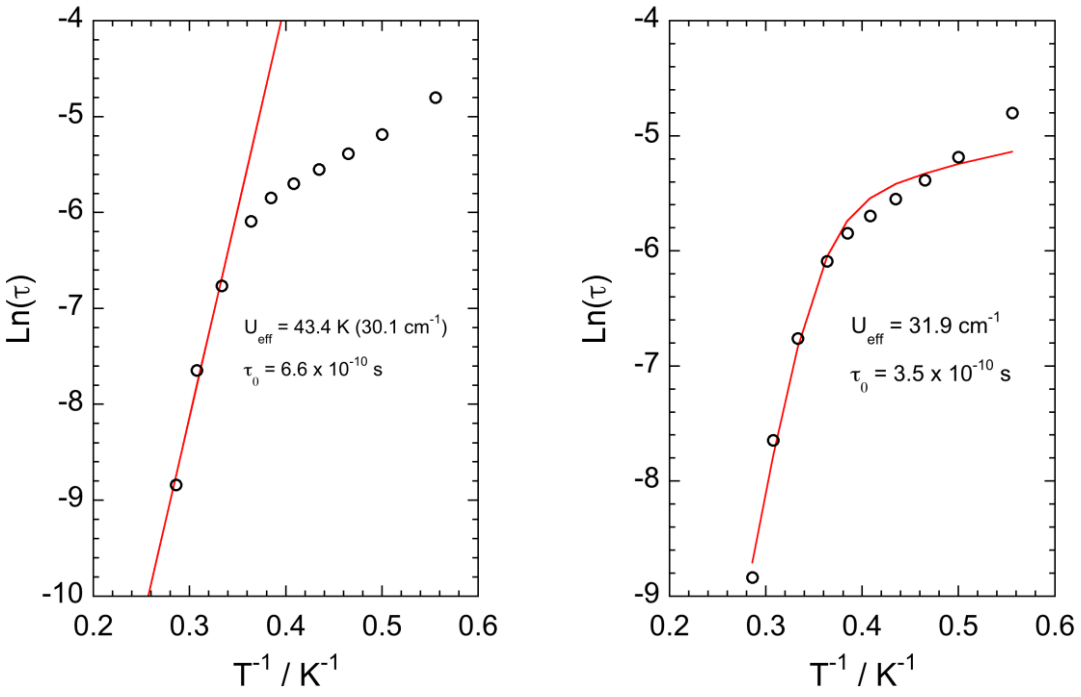

Figure 2.42. ln(τ) = f(1/T) plot (○ (exp), — (fit)) for the slow relaxation processes for complex **2-6** under an applied dc magnetic field of 400 Oe, only consider Orbach process (left) and all the processes (right).

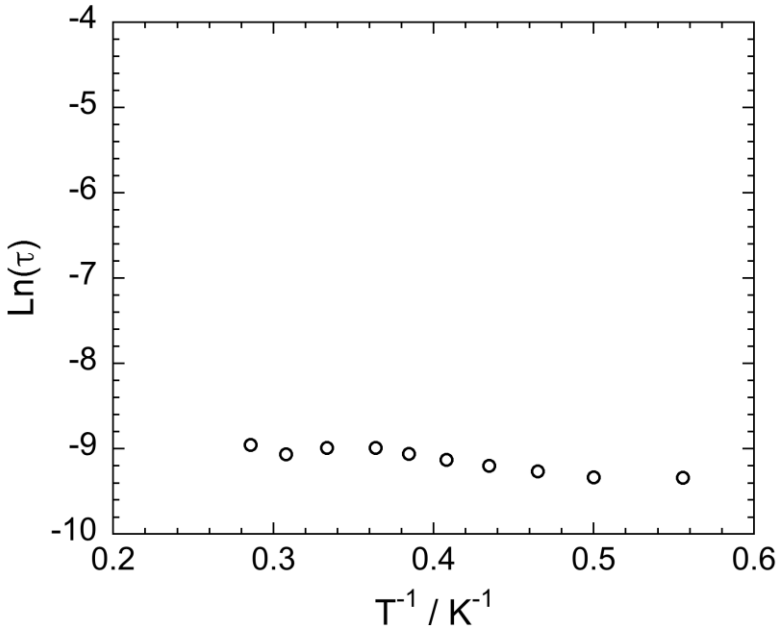

Figure 2.43. ln(τ) = f(1/T) plot for the fast relaxation process for complex **2-6** under an applied dc magnetic field of 400 Oe.

Table 2.14. Fit parameters from ln(τ) = f(1/T) plot under an applied dc magnetic field $\mu_0 H$ = 400 Oe for complex **2-6**.

Parameters	***H***	***A***	B_1	B_2	***C***	***n***	τ_0	U_{eff}	***R/GOF***
Units	***T***	$s^{-1}T^{-2}K^{-1}$	s^{-1}	T^{-2}	$s^{-1}K^{-5}$	—	***s***	cm^{-1}	—
	[a] 0.04^{slowOrbach}	—	—	—	—	—	1.6×10^{-10}	30.1	0.99163
2-6	[b] 0.04^{slowNoQTM}	49288	—	—	0.050437	5	1.71×10^{-9}	28.535	5.48×10^{-4}
	[c] 0.04^{slowAll}	58170	10153	384370	0.050437	5	3.54×10^{-10}	31.897	5.46×10^{-4}

[a] slow relaxation fit only considering Orbach relaxation; [b] slow relaxation fit with Direct, Raman and Orbach relaxations, without considering QTM; [c] slow relaxation fit considering all relaxations (Direct, QTM, Raman and Orbach).

The ac studies of complex **2-6** were also performed under an applied dc magnetic field of 1000 Oe. Only one relaxation process is visible at the difference to the two processes observed under an applied dc magnetic field of 400 Oe as depicted in Figure 2.44. The fit of the ac data and their plots in the form of a Cole-Cole curve provides the values of the relaxation times at different temperatures (Figure 2.45 and Table 2.15). The relaxation time, at T = 2 K, is slightly slower when the field is larger (1.2×10^{-2} s at 1000 Oe instead of 5.5×10^{-3} s at 400 Oe).

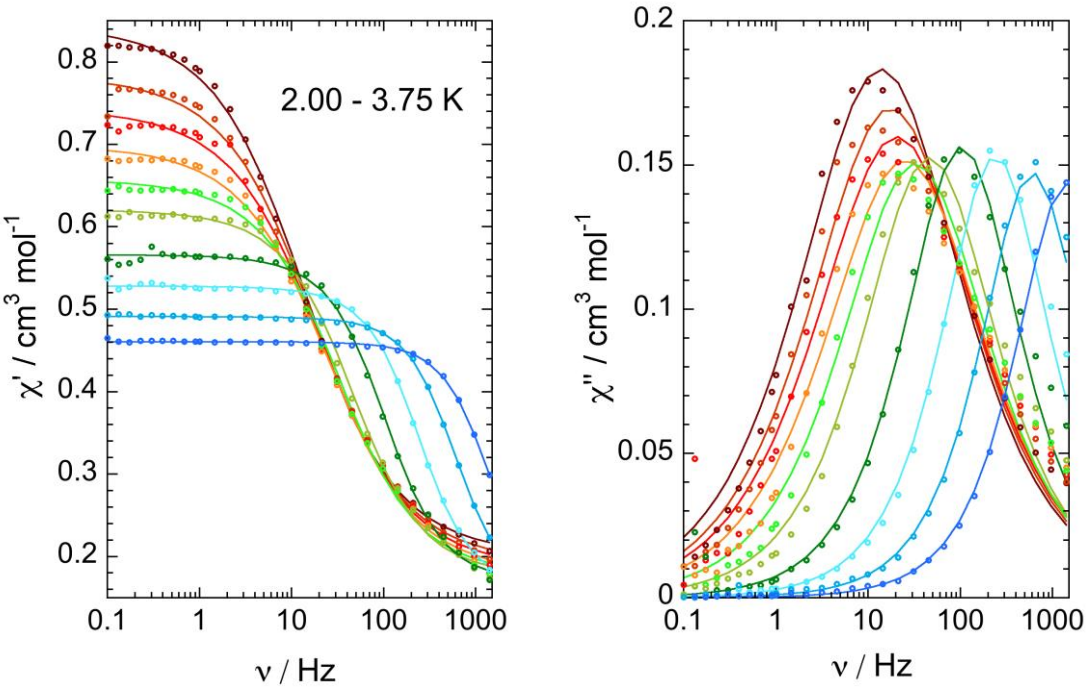

Figure 2.44. Frequency dependent in-phase and out-of-phase ac magnetic susceptibilities (○ (exp), — (fit)) for complex **2-6** under an applied dc magnetic field of 1000 Oe.

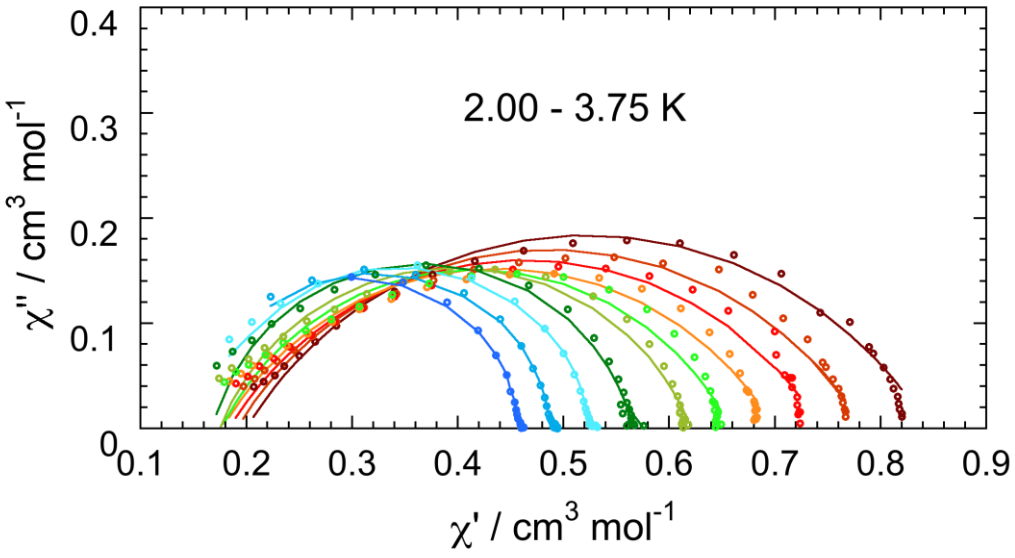

Figure 2.45. Cole-Cole plots (○ (exp), — (fit)) for complex **2-6** under an applied dc magnetic field of 1000 Oe.

Table 2.15. Cole-Cole fit parameters under an applied dc magnetic field of 1000 Oe for complex **2-6**.

Complex	Field	Temperature	χ_0	χ_∞	α	τ
2-6	1000 Oe	2.00 K	0.8449066893	0.2005028732	0.3415162549	0.0115420561
		2.15 K	0.7839641699	0.1915497740	0.3376821947	0.0090621669
		2.30 K	0.7436173463	0.1841489369	0.3388575113	0.0077273797
		2.45 K	0.6991172442	0.1778851518	0.3280177814	0.0063202860
		2.60 K	0.6575428483	0.1767335185	0.2872631769	0.0048887821
		2.75 K	0.6206910403	0.1748505104	0.2358063996	0.0034392616
		3.00 K	0.5661916002	0.1682975022	0.1517503316	0.0015378248
		3.25 K	0.5280423388	0.1597380085	0.1165292611	0.0006563167
		3.50 K	0.4910421935	0.1509775755	0.0911431046	0.0002626373
		3.75 K	0.4605690892	0.1387163393	0.0736908155	0.0001140000

The fit of the linear part of the $\ln(\tau) = f(1/T)$ plot leads to U_{eff} = 24.4 cm^{-1} and $\tau_0 = 1.1 \times 10^{-8}$ s. Fitting the whole curve using the general formula including all the mechanisms provides an effective energy barrier of 28.6 cm^{-1} (Figure 2.46 and Table 2.16). The U_{eff} value obtained is slightly lower than that corresponding to the slow process under an applied dc magnetic field of 400 Oe. However, the difference is too small to be able to make a conclusion on the effect of the applied magnetic field. The important point is that the value of the energy barrier is very close to the theoretical one of $2|D|$ determined from the EPR studies. It, thus, appears that the dominant mechanism of relaxation at high temperature is the Orbach mechanism. But even though the QTM mechanism is avoided at low temperature, the relaxation by the Raman and the direct mechanisms are still active at slightly higher temperature. The contribution of the direct mechanism increases when the applied dc magnetic field increases (see next section) because the better mixture between the wavefunctions of the $m_s = \pm 3/2$ sublevels.

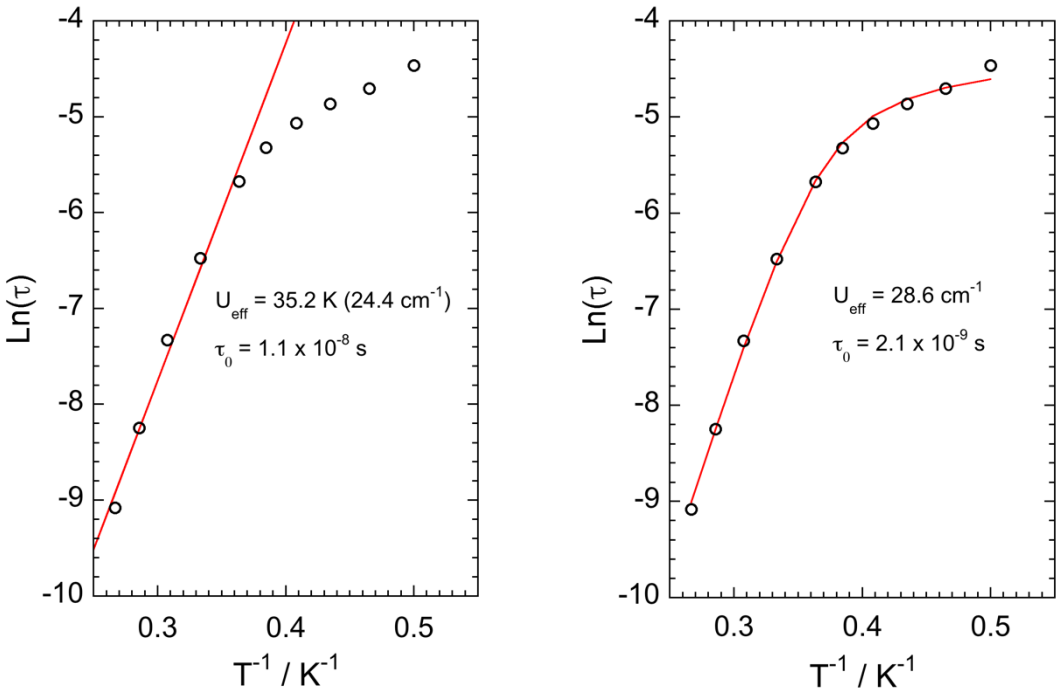

Figure 2.46. ln(τ) = f(1/T) plot (○ (exp), — (fit)) for the relaxation processes for complex **2-6** under an applied dc magnetic field of 1000 Oe. Left: only consider Orbach process; right: including Direct, QTM, Raman and Orbach processes.

Table 2.16. Fit parameters from ln(τ) = f(1/T) plot under an applied dc magnetic field $\mu_0 H$ = 1000 Oe for complex **2-6**.

Parameters	***H***	***A***	***B*$_1$**	***B*$_2$**	***C***	***n***	***τ*$_0$**	***U*$_{eff}$**	***R/GOF***
Units	***T***	***s*$^{-1}$*T*$^{-2}$*K*$^{-1}$**	***s*$^{-1}$**	***T*$^{-2}$**	***s*$^{-1}$*K*$^{-5}$**	—	***s***	***cm*$^{-1}$**	—
	[a] 0.1^{Orbach}	—	—	—	—	—	1.1×10^{-8}	24.4	0.99438
2-6	[b] 0.1^{NoQTM}	3544.7	—	—	0.63034	5	7.745×10^{-10}	31.298	2.07×10^{-5}
	[c] 0.1^{All}	4832.6	10456	650090	0.03701	5	2.146×10^{-9}	28.601	1.09×10^{-4}

[a] relaxation fit only considering Orbach relaxation; [b] slow relaxation fit with Direct, Raman and Orbach relaxations, without considering QTM; [c] slow relaxation fit considering all relaxations (Direct, QTM, Raman and Orbach).

Complexes 2-8 (~10% dilution of the complex **2-6** in the diamagnetic [Zn(Me$_6$tren)F]$^+$ matrix)

Field optimization experiment was carried out at T = 2 K by measuring the out-of-phase signal *vs.* frequency at different applied dc magnetic fields in the range 0 – 2200 Oe (Figure 2.47 top). Plotting the frequency of the maxima of the χ" = f(ν) curves *vs.* the applied field allowed determining the optimum field that corresponds to the minimum of the curve. As explained above, when a magnetic field is applied (200 Oe in this case), the value of the maximum present at high frequency decreases (or vanishes) and in the same time another maximum present at high frequency (around 200 Hz at μ_0H = 0 Oe in Figure 2.47 top) decreases and another maximum appears at lower frequency (around 0.6 Hz) corresponding to a slower relaxation process. Upon increasing the magnitude of the applied, the maximum shifts towards lower frequency and reaches a value around 0.1 Hz at μ_0H = 1000 Oe. Then it shifts back towards higher frequency, which is the signature of a speed-up of the relaxation time when the applied field is larger than 1000 Oe. The low frequency shift corresponds to decrease of the contribution of the QTM process that may be considered as negligible at μ_0H = 1000 Oe, and the re-increase of the frequency of the maximum is due to the larger contribution of the direct mechanism. The direct mechanism corresponds to a relaxation from an excited to the ground m_s level by the emission of a phonon. Thus, when the field becomes too large, this mechanism contributes to the relaxation of the magnetization and the frequency value of the maximum of the χ" = f(ν) shifts back to high frequency (Figure 2.47 top).

The comparison of the data χ" = f(ν) at T = 2 K for different values of the applied dc magnetic fields (Figure 2.32 top and Figure 2.47 top) highlights the effect of dilution on the relaxation behavior of the [Co(Me$_6$tren)F]$^+$ complex. The dilution allows observing an out-of-phase signal at μ_0H = 0 Oe. In addition, the dilution shifts the fast and the slow relaxation processes towards low frequencies, highlighting the effect of the interaction between the molecules on the relaxation processes and showing that one must not only consider the individual molecules when analyzing the relaxation of the magnetization. Even though the dilution does not avoid completely intermolecular interaction between the magnetic molecules, one may assume that the processes observed in the diluted compound are mainly due to the individual Co^{II} molecules.

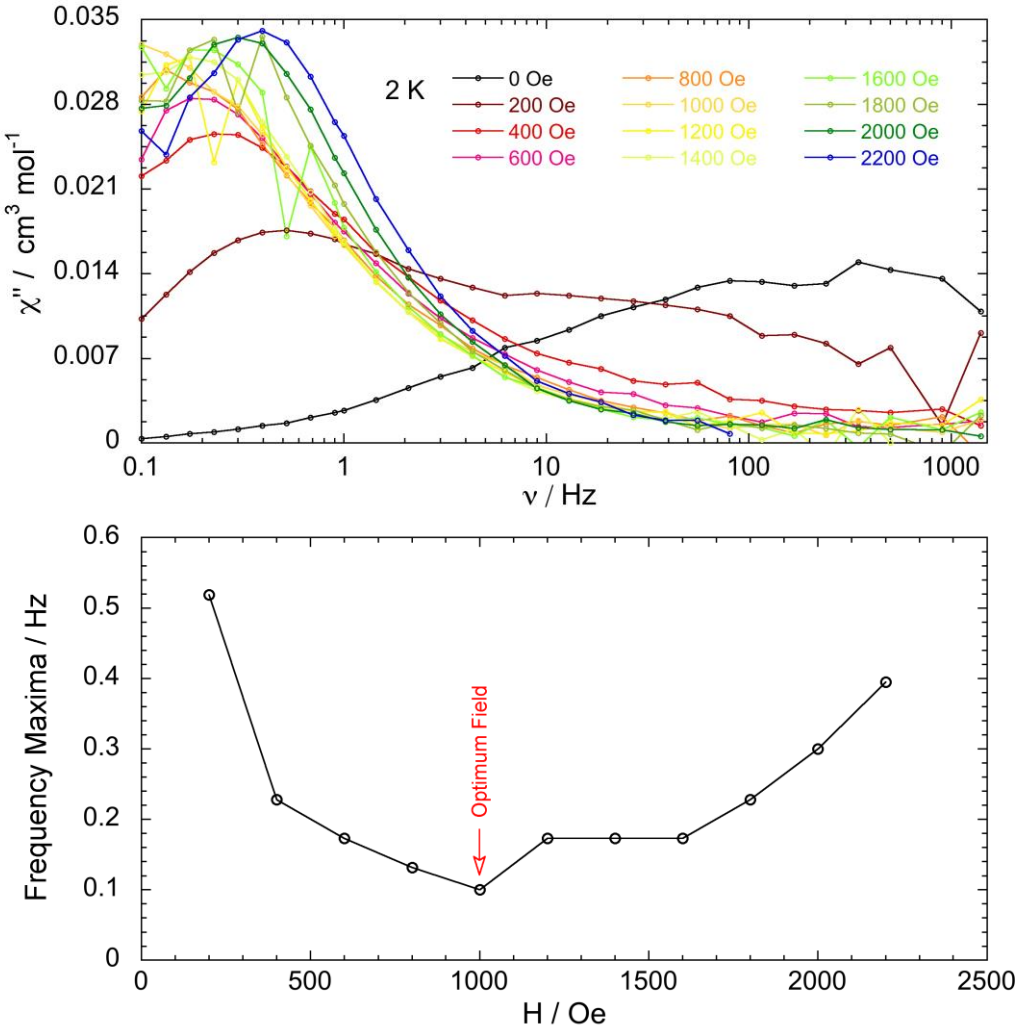

Figure 2.47. Out-of-phase susceptibility measurements at 2 K with a frequency range from 1 to 1500 Hz under various applied dc magnetic fields (top) and plot of frequency maxima *vs.* applied dc magnetic fields (bottom) for complex **2-8**.

It is possible to fit dependence of the inverse of the relaxation time with the applied magnetic field at T = 2.3 K assuming that the Raman and the Orbach processes negligible (Figure 2.48). The presence of a maximum in the zero dc magnetic field χ" curve allows determining the value of B_1 (1046.27 s^{-1}) and then fit A and B_2 by fixing B_1.

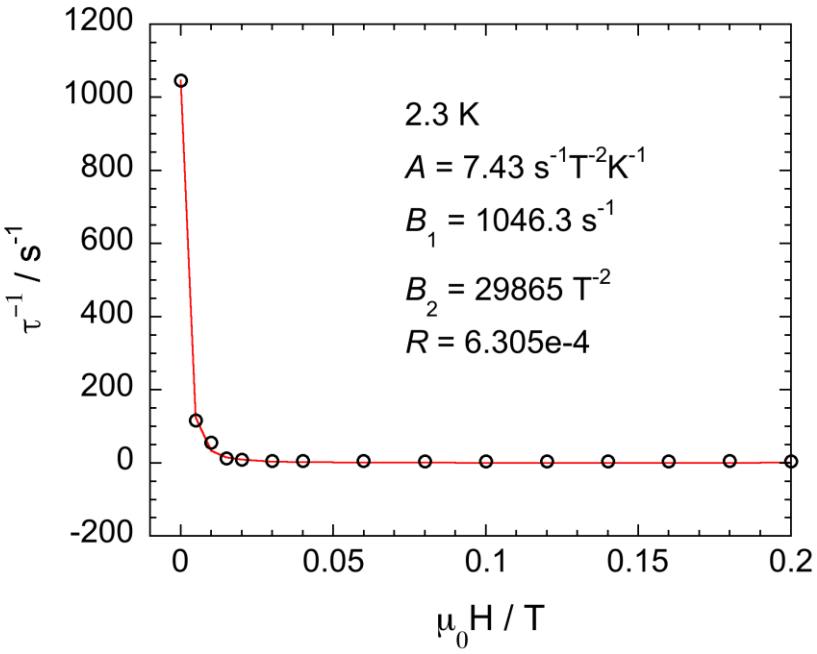

Figure 2.48. Fit of the inverse of τ *vs.* applied dc magnetic fields (○ (exp), — (fit)) for complex **2-8**.

We, then, measured the ac susceptibility in the absence of a dc magnetic field, fitted the data with the generalized Debye model (Figure 2.49, Figure 2.50 and Table 2.17) and extracted the dependence of the relaxation times with temperature. The relaxation time is almost temperature independent below 2.4 K (Table 2.17), which suggests that the QTM process is the dominant one. The fit of the ln(τ) = f(1/T) plot was performed for the linear part, and then for the whole curve as indicated in Table 2.18. The value obtained using the equation

$$\tau^{-1} = B_1 + CT^n + \tau_0^{-1}\exp(-U/k_BT)$$

are C = 0.0012781 $s^{-1}K^{-5}$, n = 5, τ_0 = 2.1 × 10^{-10} s and U_{eff} = 31.4 cm^{-1} with B_1 fixed at 1046.3 s^{-1}, where the direct process is not considered because the applied dc magnetic field is equal to zero. The exponent n of the Raman mechanism should be equal to 9 for a Kramers doublet but weaker values (n = 4 – 5) were reported.[53, 54] These values will be subsequently used to fit the data in the presence of an applied magnetic field. It is interesting to observe that the energy barrier values extracted from the two fits are almost the same and are very close to the theoretical value of 34 cm^{-1}.

 Feng SHAO: 0000-0001-8606-8628

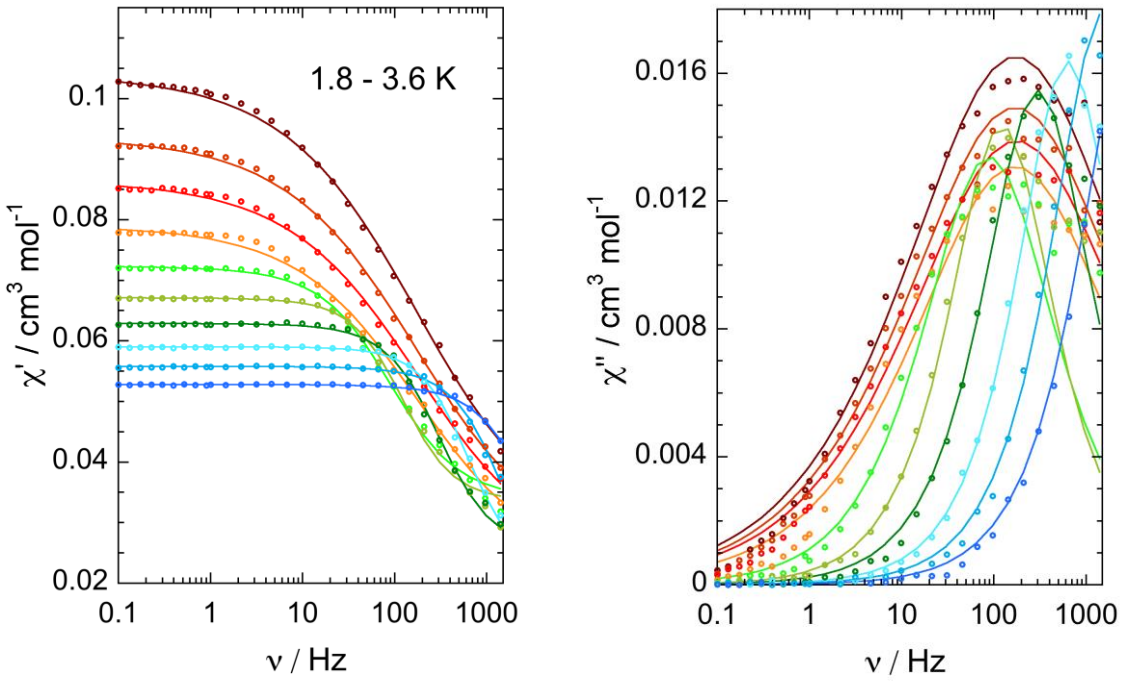

Figure 2.49. Frequency dependent in-phase and out-of-phase ac magnetic susceptibilities (○ (exp), — (fit)) for complex **2-8** under zero dc magnetic field.

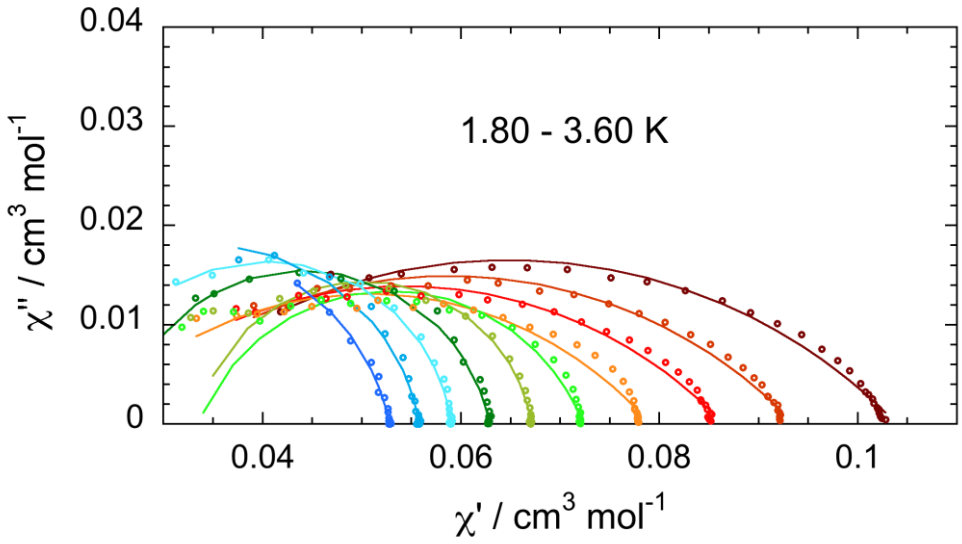

Figure 2.50. Cole-Cole plots (○ (exp), — (fit)) for complex **2-8** under an applied zero dc magnetic field.

Table 2.17. Cole-Cole fit parameters under zero dc magnetic field for complex **2-8**.

Complex	Field	Temperature	χ_0	χ_∞	α	τ
2-8	0 Oe	1.80 K	0.103991353	0.025738949	0.491116665	0.000924747
		2.00 K	0.093663147	0.023887468	0.484951892	0.000938302
		2.20 K	0.086473742	0.022219914	0.480627168	0.000900749
		2.40 K	0.079025932	0.022257653	0.449554986	0.000940478
		2.60 K	0.072309547	0.033593963	0.229566969	0.00179169
		2.80 K	0.067097114	0.033457145	0.099770221	0.001308191
		3.00 K	0.062881035	0.025512217	0.119508184	0.000528573
		3.20 K	0.059022292	0.02179594	0.081185378	0.00025027
		3.40 K	0.055788166	0.013465375	0.104879893	0.000100511
		3.60 K	0.052813628	0.008947568	0.1254518	4.56192E-05

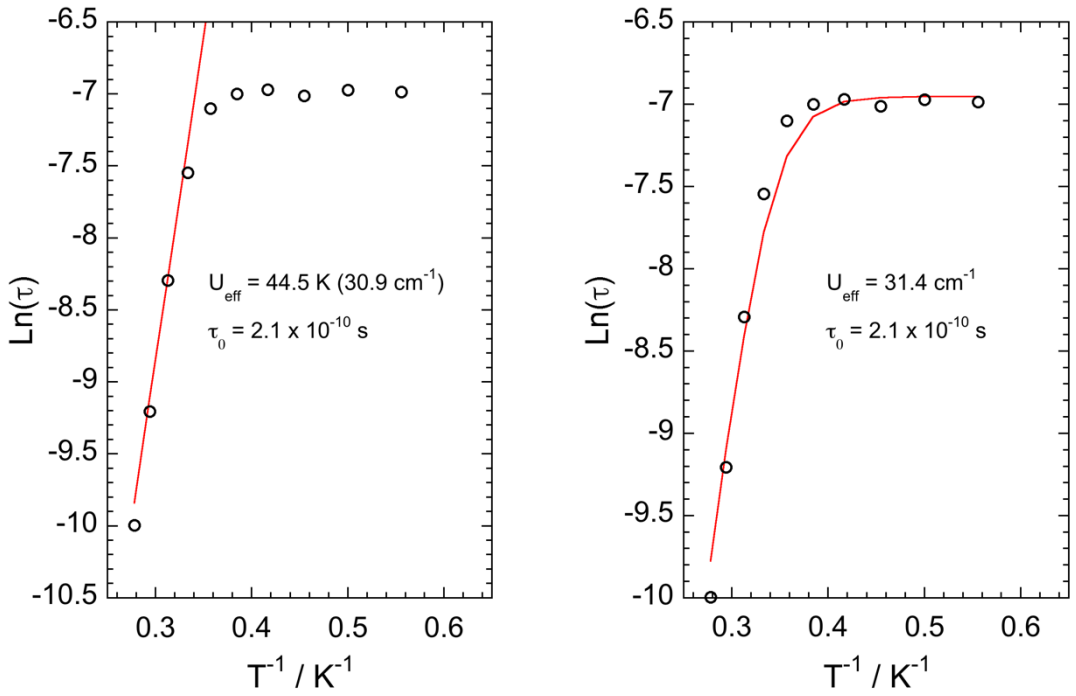

Figure 2.51. ln(τ) = f(1/T) plot (○ (exp), — (fit)) for the relaxation processes for complex **2-8** under zero dc magnetic field. Left: only consider Orbach process; right: including QTM, Raman and Orbach processes.

 Feng SHAO: 0000-0001-8606-8628

Table 2.18. Fit parameters from ln(τ) = f(1/T) plot under an applied dc magnetic field $\mu_0 H$ = 0 Oe for complex **2-8**.

Parameters	***H***	***A***	***B*$_1$**	***B*$_2$**	***C***	***n***	***τ*$_0$**	***U*$_{eff}$**	***R/GOF***
Units	***T***	***s*$^{-1}$*T*$^{-2}$*K*$^{-1}$**	***s*$^{-1}$**	***T*$^{-2}$**	***s*$^{-1}$*K*$^{-5}$**	**—**	***s***	***cm*$^{-1}$**	**—**
2-8	[a] 0^{Orbach}	—	—	—	—	—	2.1×10^{-10}	30.9	0.99716
	[b] $0^{NoDirect}$	—	1046.3	—	0.0012781	5	2.1×10^{-10}	31.4	3.05×10^{-4}

[a] relaxation fit only considering Orbach relaxation; [b] relaxation fit with QTM, Raman and Orbach relaxations without considering Direct relaxation.

In order to get insight in the different relaxation processes and the corresponding mechanisms, we carried out measurements of the ac data under several applied dc magnetic fields ($\mu_0 H$ = 200, 400 and 1000 Oe; 1000 Oe is the optimum magnetic field where the QTM and the direct mechanisms are minimized).

The ac data measured under an applied field of 200 Oe show the presence of two relaxation processes (Figure 2.52, Figure 2.53 and Table 2.19). The data were deconvoluted into a fast (Figure 2.54 and Figure 2.55) and a slow process (Figure 2.56 and Figure 2.57) in order to extract the parameters corresponding to the two processes. At T = 1.8 K, the relaxation time of the fast process is around 4 ms, while for the slow process it is around 750 ms. The ln(τ) = f(1/T) curves (Figure 2.58 and Figure 2.59) were fitted for the two processes considering different situations as indicated in Table 2.20. The parameters of the fits are coherent with the different processes: the B_2 parameter is weaker for the fast process than for the slow one indicating that the QTM mechanism contributes more to the fast process, while the A parameter is larger for the fast process suggesting a larger contribution of the direct mechanism to the fast process than to the slow one; the C parameter indicates that the contribution of the Raman relaxation mechanism is almost the same for the two processes and finally B_1 and n were fixed during the fit of the data. This analysis shows that the slow process is mainly due to the Orbach mechanism for the relaxation of the magnetization over the energy barrier, while the fast process is mainly dominated by the direct and the QTM mechanisms, the Raman mechanism contributing in the same manner for the two processes.

 Feng SHAO: 0000-0001-8606-8628

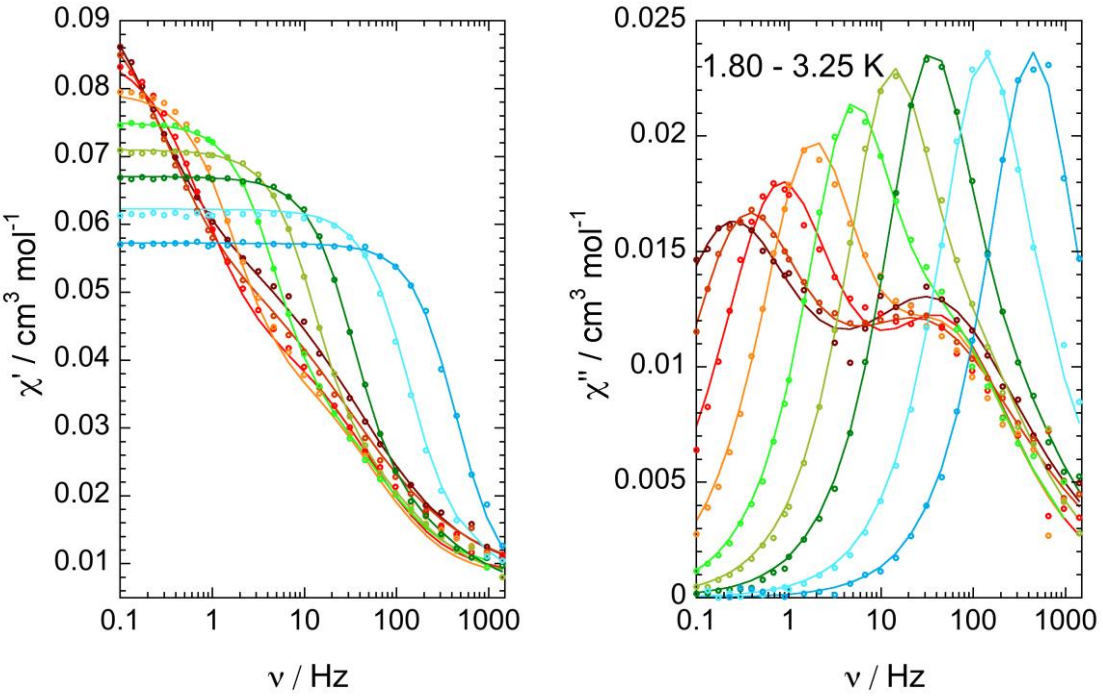

Figure 2.52. Frequency dependent in-phase and out-of-phase ac magnetic susceptibilities (○ (exp), — (fit)) for complex **2-8** under an applied dc magnetic field of 200 Oe.

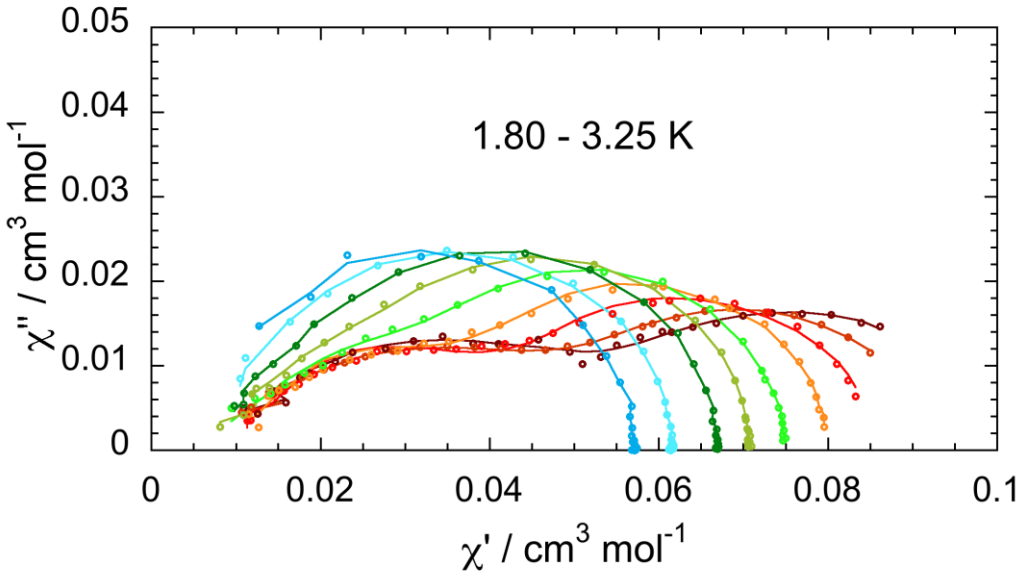

Figure 2.53. Cole-Cole plots (○ (exp), — (fit)) for complex **2-8** under an applied dc magnetic field of 200 Oe.

 Feng SHAO: 0000-0001-8606-8628

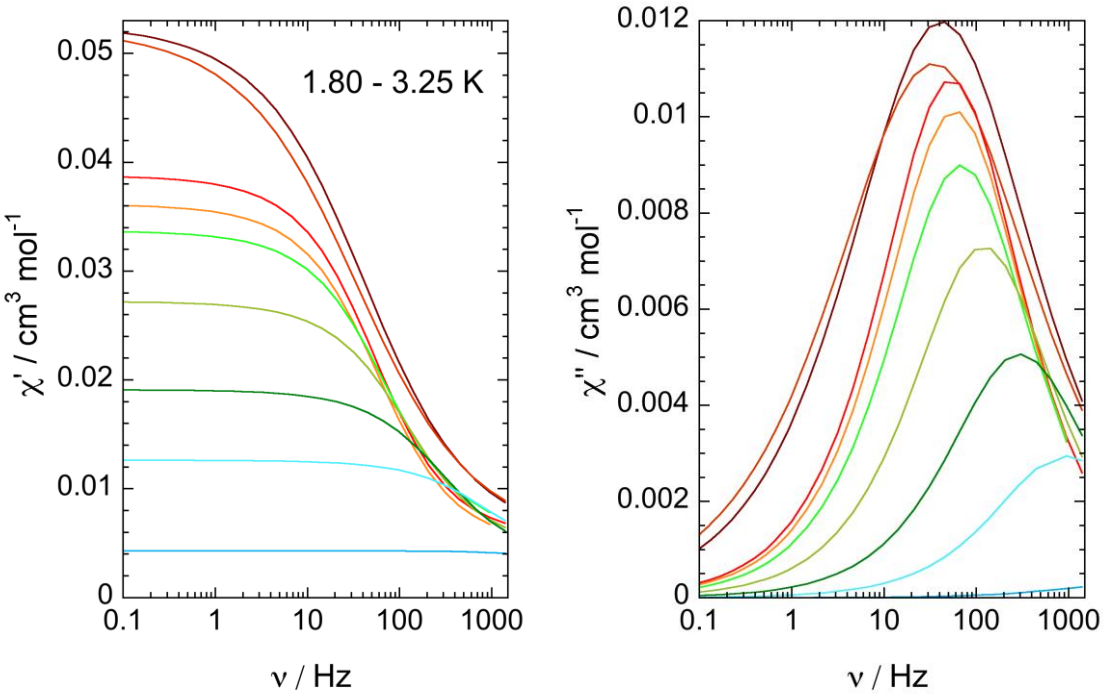

Figure 2.54. Deconvoluted frequency dependent in-phase and out-of-phase ac magnetic susceptibilities for complex **2-8** under an applied dc magnetic field of 200 Oe at different temperatures for the fast process.

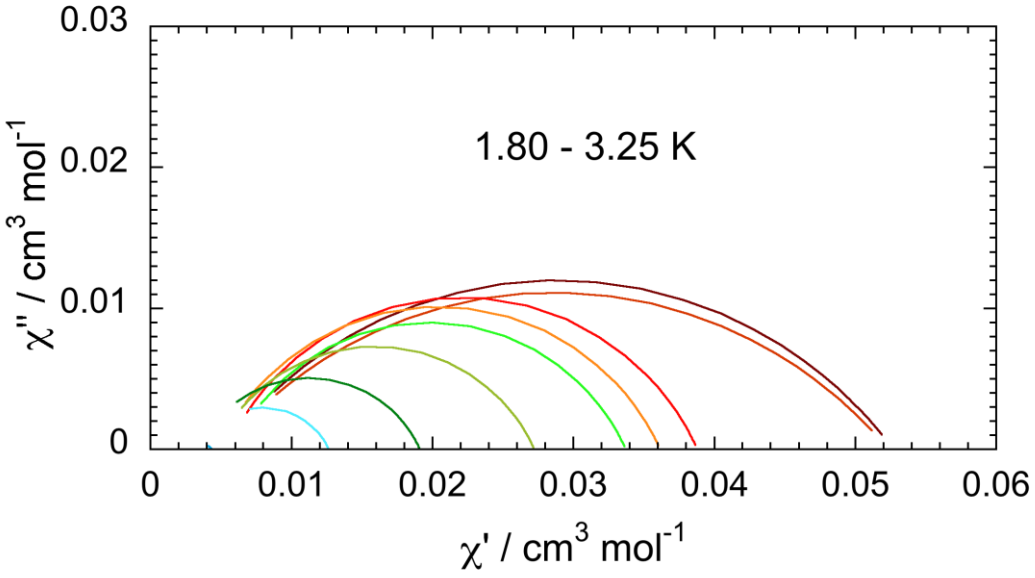

Figure 2.55. Deconvoluted Cole-Cole plots for complex **2-8** under an applied dc magnetic field of 200 Oe at different temperatures for the fast process.

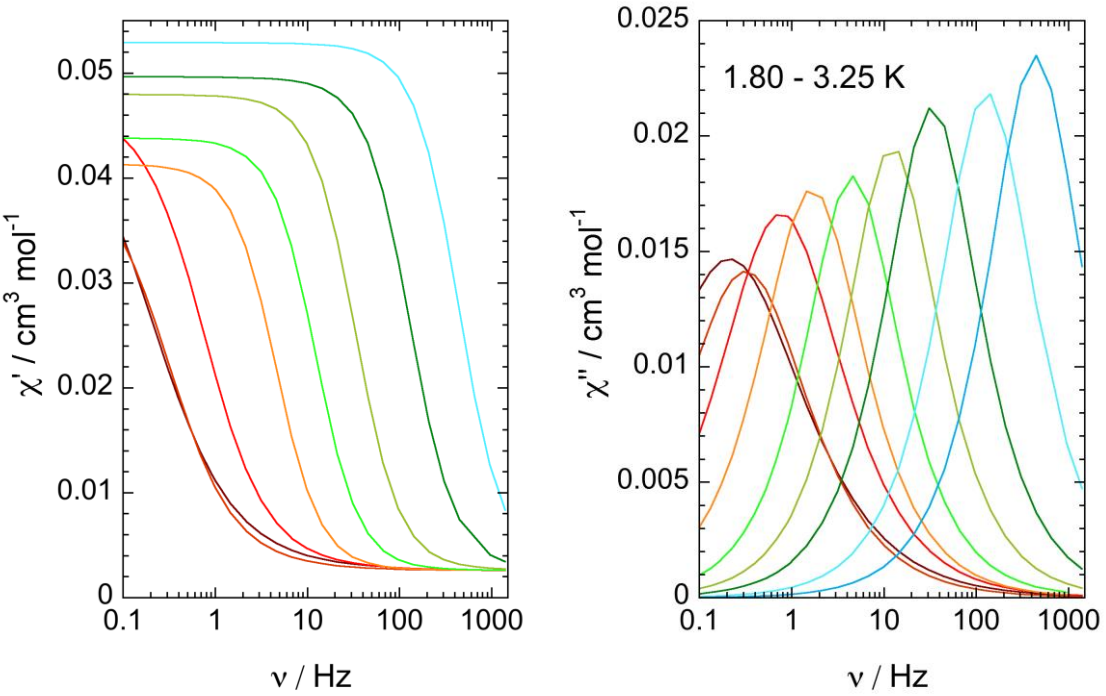

Figure 2.56. Deconvoluted frequency dependent in-phase and out-of-phase ac magnetic susceptibilities for complex **2-8** under an applied dc magnetic field of 200 Oe at different temperatures for the slow process.

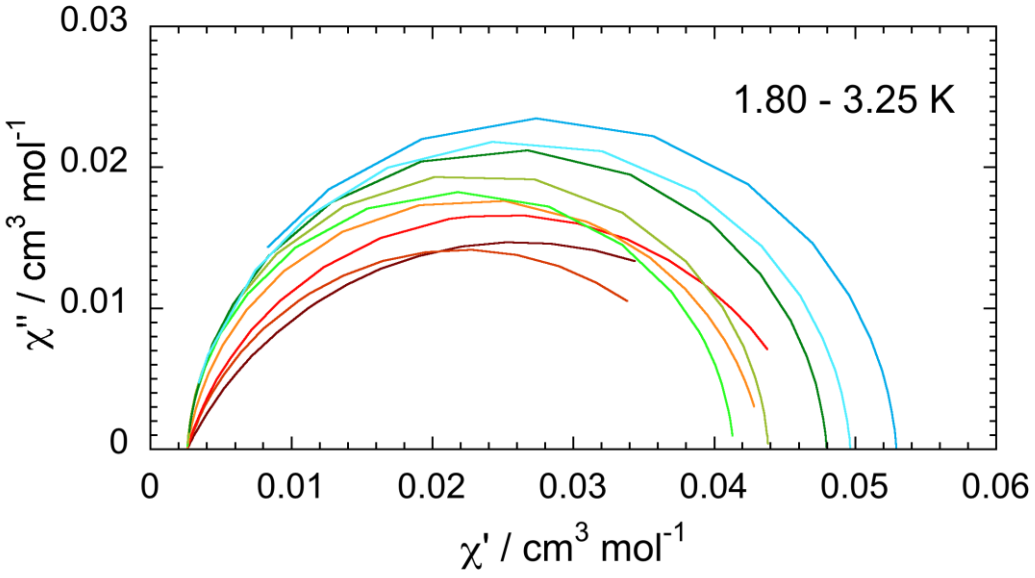

Figure 2.57. Deconvoluted Cole-Cole plots for complex **2-8** under an applied dc magnetic field of 200 Oe at different temperatures for the slow process.

 Feng SHAO: 0000-0001-8606-8628

Table 2.19. Cole-Cole fit parameters under an applied dc magnetic field of 200 Oe for complex **2-8**.

Complex	Field	Temperature	χ_0	χ_∞	α	τ
2-8	200 Oe (fast)	1.80 K	0.1053693061	0.0101718253	0.4058135365	0.0037896709
		2.00 K	0.1046406919	0.0100987421	0.4403829979	0.0046036815
		2.15 K	0.0775883180	0.0108012139	0.2698071799	0.0029652339
		2.30 K	0.0722911009	0.0095517691	0.2699016332	0.0027267009
		2.45 K	0.0674255346	0.0117196457	0.2693179640	0.0023280608
		2.60 K	0.0544494355	0.0092316429	0.2698753911	0.0013338666
		2.75 K	0.0382114896	0.0068129564	0.2704920844	0.0005357352
		3.00 K	0.0252635624	0.0069967429	0.2700005670	0.0001748762
		3.25 K	0.0086268194	0.0070594994	0.2699946663	0.0000473507
	200 Oe (slow)	1.80 K	0.0991848130	0.0991848130	0.2887430274	0.7525007613
		2.00 K	0.0833566439	0.0051786485	0.2019764850	0.5014596869
		2.15 K	0.0945656162	0.0051916804	0.1848167979	0.2074438160
		2.30 K	0.0869565691	0.0051996709	0.0903202514	0.0952469451
		2.45 K	0.0827248981	0.0052222738	0.0377493321	0.0349626986
		2.60 K	0.0876568384	0.0051971393	0.0335941653	0.0129891787
		2.75 K	0.0959511720	0.0052700086	0.0410379210	0.0047884214
		3.00 K	0.0993093075	0.0052002060	0.0456583534	0.0012275264
		3.25 K	0.1058468839	0.0051993747	0.0437241160	0.0003628333

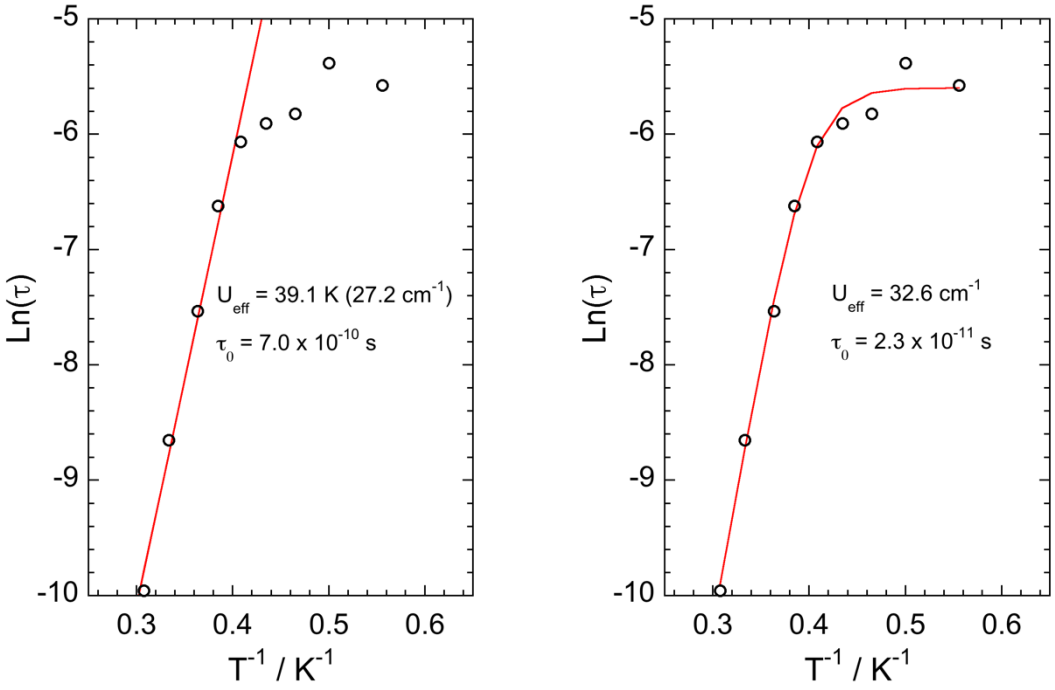

Figure 2.58. ln(τ) = f(1/T) plot (○ (exp), — (fit)) for the fast relaxation processes for complex **2-8** under an applied dc magnetic field of 200 Oe. Left: only consider Orbach process; right: including Direct, QTM, Raman and Orbach processes.

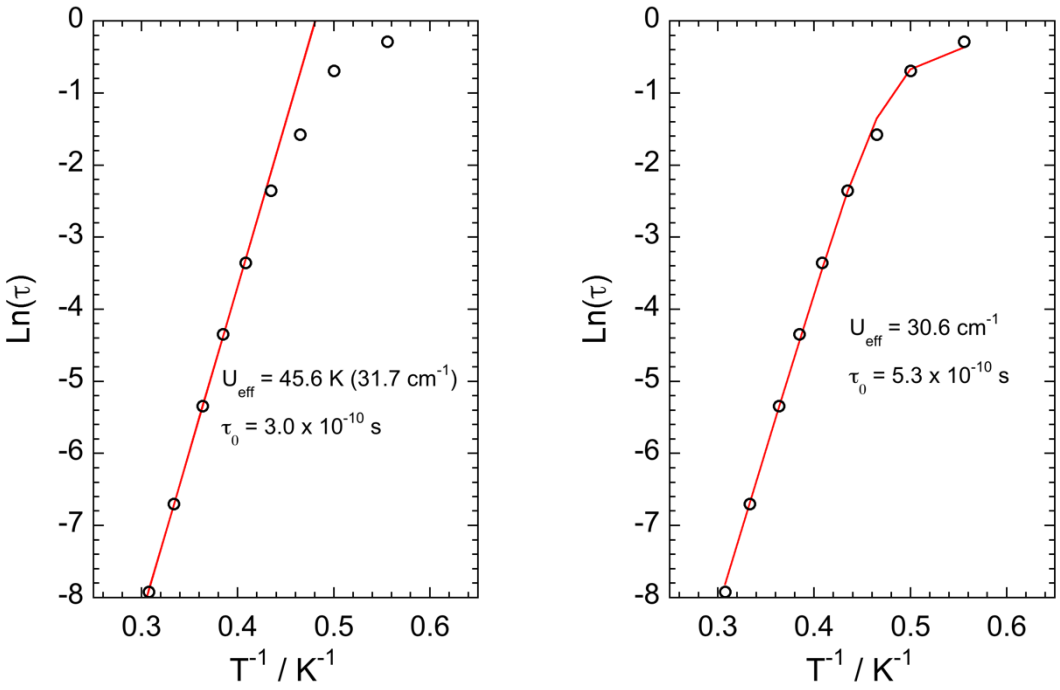

Figure 2.59. ln(τ) = f(1/T) plot (○ (exp), — (fit)) for the slow relaxation processes for complex **2-8** under an applied dc magnetic field of 200 Oe. Left: only consider Orbach process; right: including Direct, QTM, Raman and Orbach processes.

Table 2.20. Fit parameters from ln(τ) = f(1/T) plot under an applied dc magnetic field $\mu_0 H$ = 200 Oe for complex **2-8**.

Parameters	***H***	***A***	***B*$_1$**	***B*$_2$**	***C***	***n***	**τ_0**	**U_{eff}**	***R/GOF***
Units	***T***	$s^{-1}T^{-2}K^{-1}$	s^{-1}	T^{-2}	$s^{-1}K^{-5}$	—	*s*	cm^{-1}	—
2-8	[a] 0.02^{fastOrbach}	—	—	—	—	—	7.0×10^{-10}	27.2	0.99397
	[b] 0.02^{fastAll}	1181.6	1046.3	72440	0.00088044	5	2.257×10^{-11}	32.577	2.86×10^{-4}
	[c] 0.02^{slowOrbach}	—	—	—	—	—	3.0×10^{-10}	31.7	0.99982
	[d] 0.02^{slowAll}	7.43	1046.3	1924500	0.0018902	5	5.270×10^{-10}	30.591	4.91×10^{-4}

[a] fast relaxation fit only considering Orbach relaxation; [b] fast relaxation fit considering all relaxations (Direct, QTM, Raman and Orbach); [c] slow relaxation fit only considering Orbach relaxation; [d] slow relaxation fit considering all relaxations (Direct, QTM, Raman and Orbach).

The data measured under an applied field of 400 and 1000 Oe are similar (Figure 2.60, Figure 2.61, Figure 2.62, Figure 2.63 and Table 2.21). The two relaxation processes cannot be separated anymore because the magnetic field is now large enough to minimize the contribution of the QTM mechanism. The relaxation time, at T = 1.8 K, is now equal to 6 s under an applied field of 1000 Oe instead of 0.75 s for $\mu_0 H$ = 200 Oe. In addition, the distribution of relaxation times has decreased upon increasing the applied dc magnetic field value.

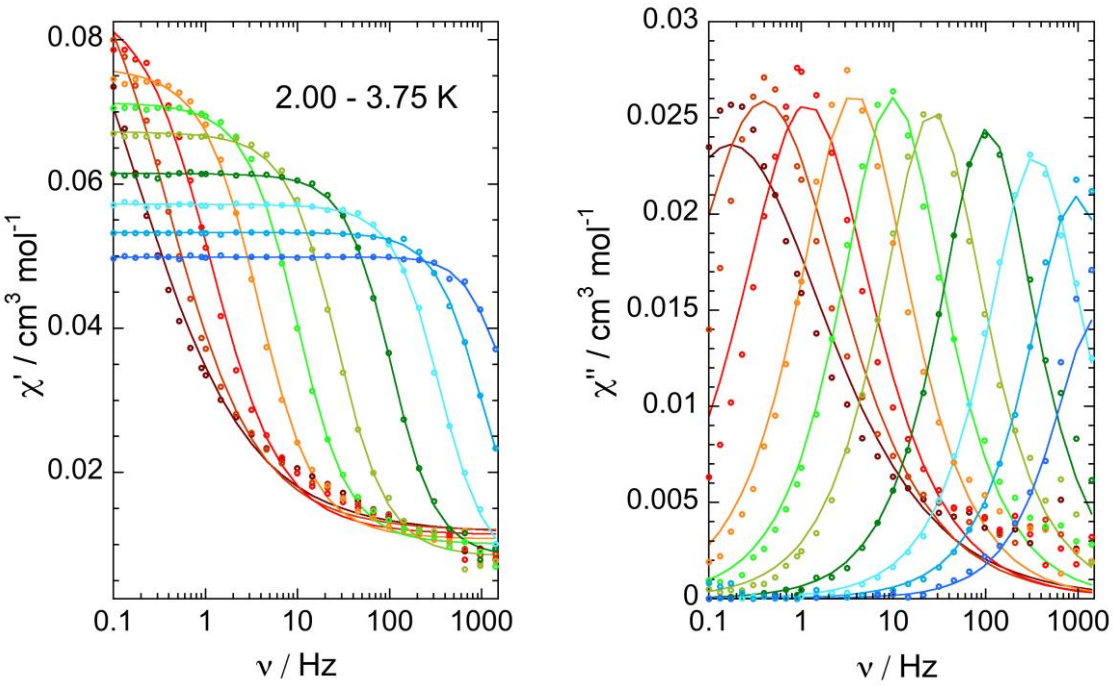

Figure 2.60. Frequency dependent in-phase and out-of-phase ac magnetic susceptibilities (○ (exp), — (fit)) for complex **2-8** under an applied dc magnetic field of 400 Oe.

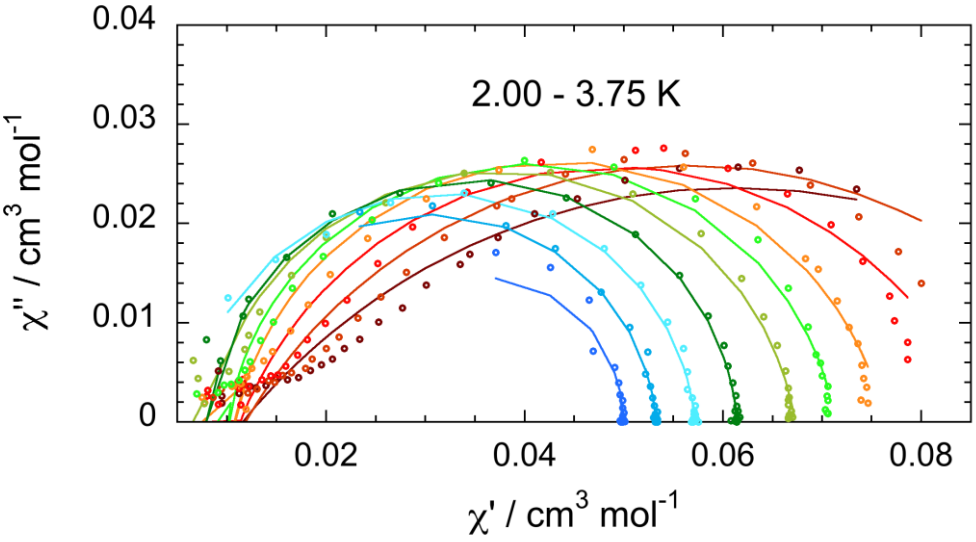

Figure 2.61. Cole-Cole plots (○ (exp), — (fit)) for complex **2-8** under an applied dc magnetic field of 400 Oe.

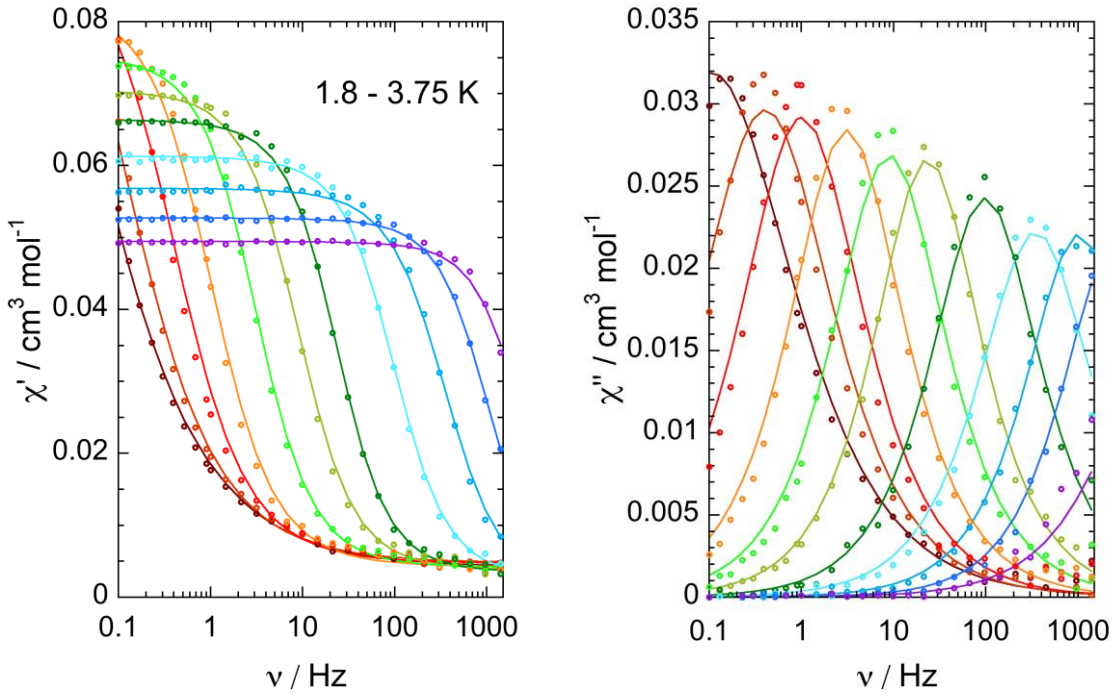

Figure 2.62. Frequency dependent in-phase and out-of-phase ac magnetic susceptibilities (○ (exp), — (fit)) for complex **2-8** under an applied dc magnetic field of 1000 Oe.

 Feng SHAO: 0000-0001-8606-8628

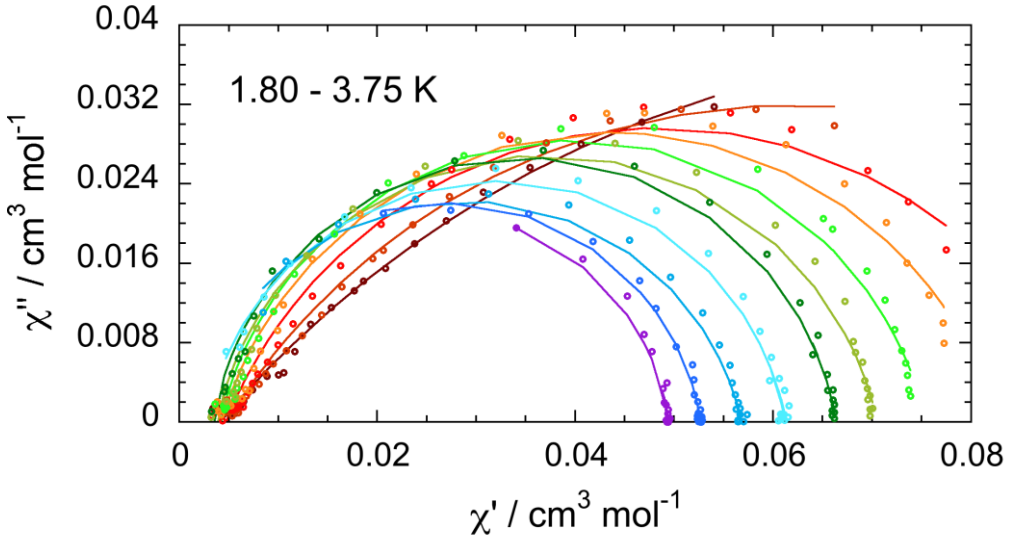

Figure 2.63. Cole-Cole plots (○ (exp), — (fit)) for complex **2-8** under an applied dc magnetic field of 1000 Oe.

Table 2.21. Cole-Cole fit parameters under an applied dc magnetic field of 400 and 1000 Oe for complex **2-8**.

Complex	Field	Temperature	χ_0	χ_∞	α	τ
2-8	400 Oe	2.00 K	0.1109060626	0.0116007919	0.4348404959	0.9190000000
		2.15 K	0.1014293433	0.0118865470	0.3329843991	0.4030000000
		2.30 K	0.0863270059	0.0113539413	0.2348324352	0.1369884413
		2.45 K	0.0763649903	0.0107536545	0.1400010283	0.0422238308
		2.60 K	0.0713553117	0.0100246980	0.1031926799	0.0160563432
		2.75 K	0.0672547039	0.0082507018	0.0964980706	0.0059052644
		3.00 K	0.0614674421	0.0082579547	0.0541269037	0.0015367548
		3.25 K	0.0571999480	0.0063078506	0.0632252271	0.0004549202
		3.50 K	0.0532882837	0.0079012647	0.0522145634	0.0001660000
		3.75 K	0.0499346478	0.0220086457	0.0145042206	0.0001010000
	1000 Oe	1.80 K	0.166515005	0.004122617	0.448888107	6.03585104
		2.00 K	0.119077176	0.004795673	0.351283817	1.504862281
		2.15 K	0.092498148	0.004712158	0.243749802	0.390003149
		2.30 K	0.08288002	0.004230792	0.187035206	0.155890432
		2.45 K	0.075466816	0.004119122	0.143704993	0.05114069
		2.60 K	0.070535482	0.0037415	0.136561841	0.017784526
		2.75 K	0.066405484	0.003420452	0.105765001	0.006799699
		3.00 K	0.061330789	0.0027536	0.11845071	0.001618378
		3.25 K	0.056844802	0.001147472	0.142298299	0.000457509
		3.50 K	0.052707365	0.001009424	0.1003784	0.000156653
		3.75 K	0.049450263	0.001002116	0.084382654	6.61029E-05

The dependence of the relaxation time with temperature is depicted in Figure 2.64 and Figure 2.65 for $\mu_0 H$ = 400 and 1000 Oe respectively. The experimental data show mainly a linear dependence of ln(τ) with 1/T suggesting that the Orbach mechanism is the dominating one. But since the relaxation time is slower for $\mu_0 H$ = 1000 Oe, this field is indeed the optimum one to minimize the effects of the direct and the QTM mechanisms to the relaxation of the magnetization. The parameters allowing to obtain the best fit of the data are presented in Table 2.22 for $\mu_0 H$ = 400 and 1000 Oe.

 Feng SHAO: 0000-0001-8606-8628

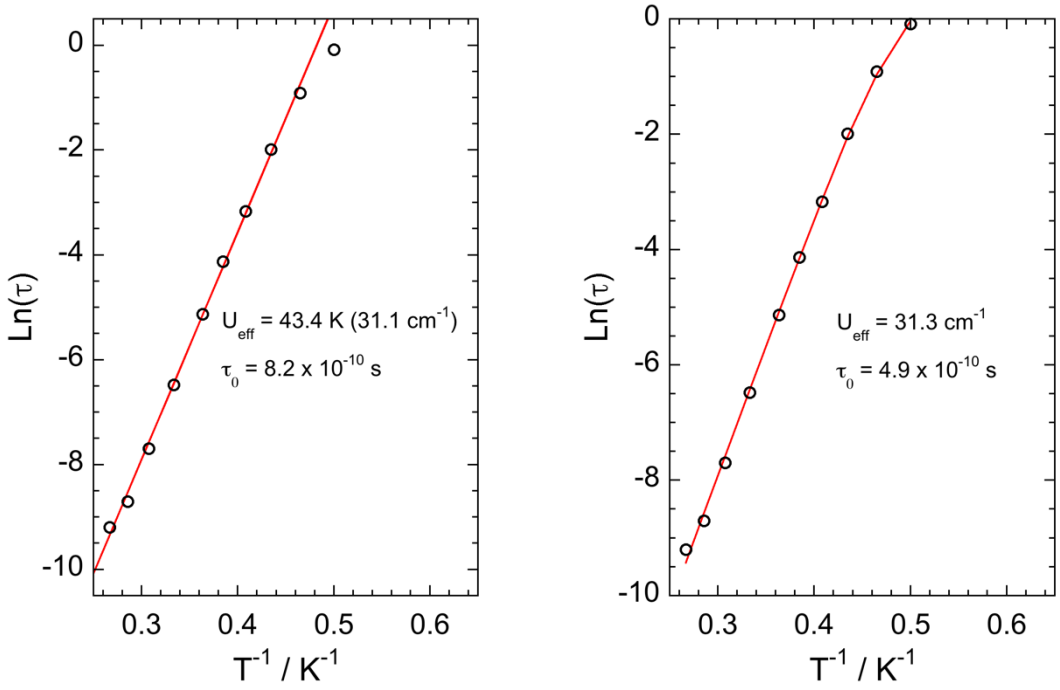

Figure 2.64. ln(τ) = f(1/T) plot (○ (exp), — (fit)) for the relaxation processes for complex **2-8** under an applied dc magnetic field of 400 Oe. Left: only consider Orbach process; right: including Direct, Raman and Orbach processes.

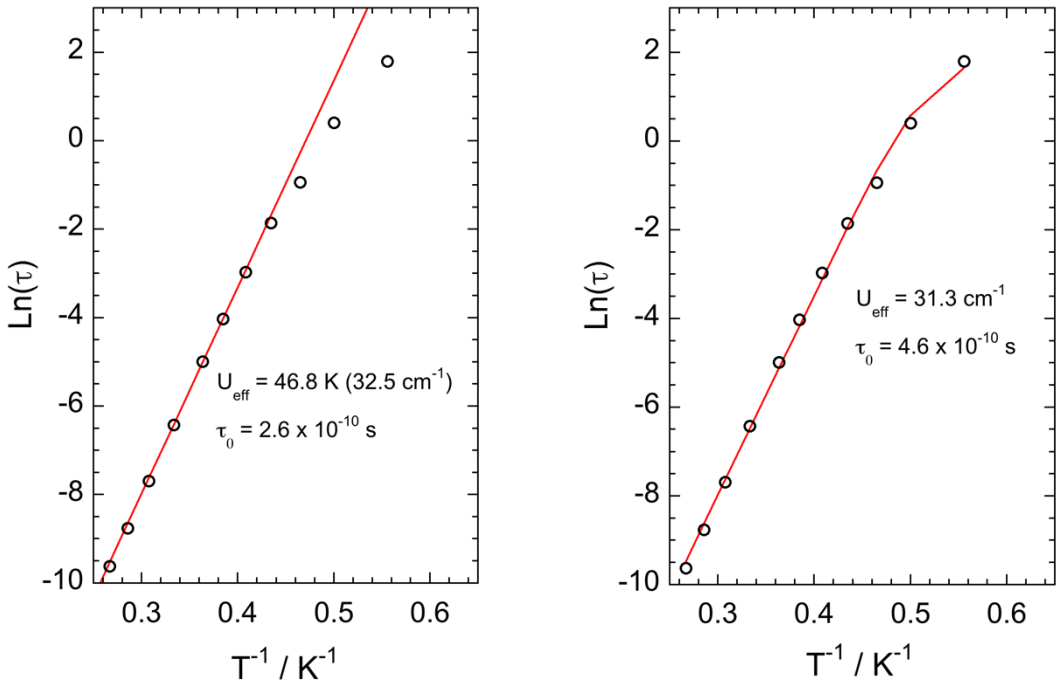

Figure 2.65. ln(τ) = f(1/T) plot (○ (exp), — (fit)) for the relaxation processes for complex **2-8** under an applied dc magnetic field of 1000 Oe. Left: only consider Orbach process; right: including Direct, Raman and Orbach processes.

Table 2.22. Fit parameters from ln(τ) = f(1/T) plot under an applied dc magnetic field $\mu_0 H$ = 400 and 1000 Oe for complex **2-8**.

Parameters	***H***	***A***	***B*$_1$**	***B*$_2$**	***C***	***n***	**τ_0**	***U*$_{eff}$**	***R/GOF***
Units	***T***	***s*$^{-1}$*T*$^{-2}$*K*$^{-1}$**	***s*$^{-1}$**	***T*$^{-2}$**	***s*$^{-1}$*K*$^{-5}$**	**—**	***s***	***cm*$^{-1}$**	**—**
2-8	[a] 0.04^{Orbach}	—	—	—	—	—	8.2×10^{-10}	31.1	0.99918
	[b] 0.04^{NoQTM}	7.43	—	—	0.020980	5	4.897×10^{-10}	31.292	3.23×10^{-4}
	[c] 0.04^{All}	7.43	1046.3	32111000	0.020980	5	4.807×10^{-10}	31.333	3.04×10^{-4}
	[a] 0.1^{Orbach}	—	—	—	—	—	2.6×10^{-10}	32.5	0.99973
	[b] 0.1^{NoQTM}	7.43	—	—	0.0014615	5	4.590×10^{-10}	31.298	7.32×10^{-4}
	[c] 0.1^{All}	7.43	1046.3	8890600	0.0014615	5	2.272×10^{-10}	32.531	1.56×10^{-3}

[a] relaxation fit only considering Orbach relaxation; [b] relaxation fit with Direct, Raman and Orbach relaxations, without considering QTM; [c] relaxation fit considering all relaxations (Direct, QTM, Raman and Orbach).

In conclusion of this experimental part, the dilution the Co^{II}-containing molecules in the diamagnetic Zn^{II} matrix has a large influence on the relaxation time. For the pure compound, an optimum applied field of 2200 Oe is necessary to reach a compromise allowing to decrease the contribution the QTM mechanism and limiting the effect of the relaxation by the direct mechanism leading to a relaxation time of 0.04 s at T = 1.8 K. While for the 10% diluted compound, the necessary optimum field is only 1000 Oe, which allows limiting the contribution of the direct mechanism and thus reaching a relaxation time value of 6 s at T = 1.8 K, two orders of magnitude larger than for the pure compound. The Raman mechanism that contributes to the relaxation of the magnetization was found to be almost independent form the value of the applied dc magnetic field for each compound. However, its contribution is almost one order of magnitude larger for the non-diluted compound (C = 0.04 and 0.01 for complexes **2-6** and **2-8** respectively, see Table 2.12 and Table 2.22), highlighting the role of the environment of this relaxation process.

2.3.3.5 Magnetization versus dc magnetic field hysteresis loops

In order to assess the field dependence of the magnetization for the isolated molecules, we used the Micro-SQUID set up where it is possible to measure a single crystal oriented with the magnetic field parallel to its easy magnetization axis.[34, 35] We will first present the published results obtained on the diluted **2-1** compound ([$Co_{0.1}Zn_{0.9}$(Me$_6$tren)Cl](ClO$_4$))[18] and then compare them with those of **2-8** ([$Co_{0.12}Zn_{0.88}$(Me$_6$tren)F](ClO$_4$)). It important to note that complex **2-1** crystallizes in the trigonal space group *R*3*c* where the molecules are aligned with their anisotropy axes along the crystallographic *c* axis. Furthermore, the molecules possess a threefold symmetry axis and a C_{3v} local symmetry. While complex **2-8** crystallizes in the monoclinic $P2_1/n$ space group, and the molecules do not have a strict three-fold symmetry axis. The molecules lie along the crystallographic *b* axis of the crystal making an angle of 147.4° between their pseudo threefold symmetry axis. This disposition leads to an experimental easy axis of magnetization not collinear with the local anisotropy axis of each molecule that is expected to be very close to the Co–F bond as it is along the Co–Cl bond in complex **2-1**. Such non-alignment may affect the hysteresis loop of the single crystal. The magnetization *vs.* field hysteresis loop at different temperatures with a sweep field rate equal to 0.07 T/s is depicted in Figure 2.66, for the diluted **2-1** complex. At T = 0.03 K, an opening of the hysteresis loop is observed when the magnetic field is different from zero and persists until T = 1 K. Two main steps are observed. One near zero magnetic field that corresponds to the reversal of the QTM and one at 0.39 T. The step at high magnetic field is not due to QTM because the avoided crossing between the m_s = –1/2 and the m_s = +3/2 is expected around 8.4 T for **2-1** because $|D|$ = 8.12 cm^{-1} and g_z = 2.22 for this complex. It is due to a reversal of the magnetization through the direct relaxation mechanism involving non-coherent tunneling events combined with the emission or absorption of phonons. The spin-lattice relaxation time for such a direct transition is essentially, limited by the phonon density of states at the spin resonance and the spin-phonon coupling.[55] As the temperature decreases from 1 K to 0.03 K, the number of molecules that undergo relaxation by thermal activation diminishes and those that undergo relaxation by tunneling increases. The result is a larger value for the plateau for the red curve (T = 0.03 K) than the green one (T = 1 K) because a larger number of molecules have already tunneled at the lowest temperature. To confirm that the reversal in due to tunneling, the magnetization was cycled at different sweep rates from 0.002 to 0.280 T/s at T = 0.03 K (Figure 2.67).

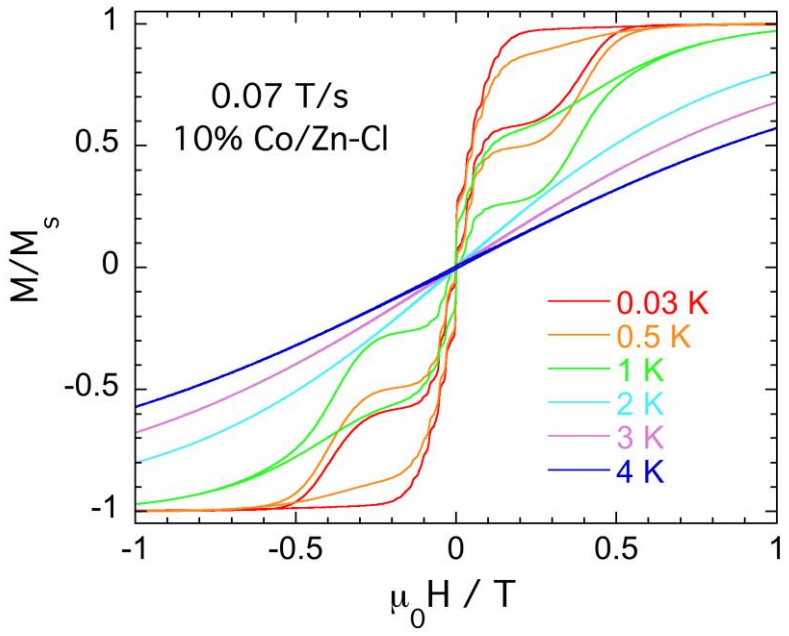

Figure 2.66. Magnetization *vs.* fields on a single crystal of **2-1** with its easy axis aligned with the fields at different temperatures.

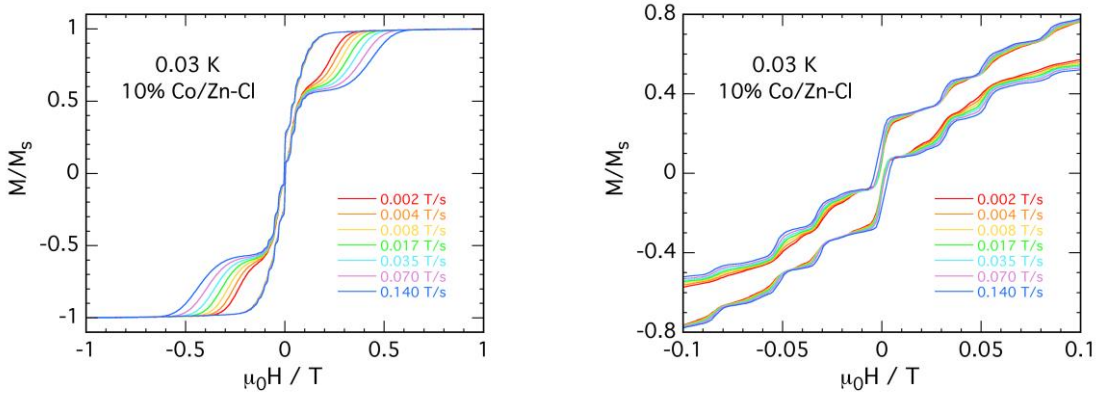

Figure 2.67. Magnetization *vs.* fields on a single crystal of **2-1** with its axis aligned with the fields at 0.03 K with different sweep rates (left) and together with a zoom in the –0.1 — 0.1 T region (right).

At $\mu_0 H$ = –1 T, all the molecules are in the m_s = +3/2 state. When the magnetic field reaches zero, there is resonance between the +3/2 and the –3/2 m_s levels and part of the molecules tunnel to m_s = –3/2 state, while the remaining stay in the m_s = +3/2 state. This is the origin of the step near zero magnetic field. The tunnel probability decreases when the sweep rate is increased,[56, 57] therefore, when the same experiment is carried out at higher

sweep rates, the number of molecules tunneling is less important and the hysteresis loop is slightly larger (Figure 2.67). There are 8 steps observed in the hysteresis loops, they have been assigned to the hyperfine interaction resulting from the coupling between electronic spin and the I = 7/2 nuclear spin of cobalt(II).[18]

The measurements carried out on complex **2-8** are similar to those made on the chloride-containing complex. But, in this case, the hysteresis loop persists at until T = 2 K (Figure 2.68), while it stayed open until T = 1 K for the former. The hysteresis loops were also measured for as a function of the sweep rate (Figure 2.69) showing the dependence of the width of the loops with the sweep rate that is a signature of the SMM behavior. When zooming in the –0.1 — 0.1 T range, a weak opening of the hysteresis is observed at zero dc magnetic field. However, one cannot see the steps due to the hyperfine interaction as for the diluted **2-1** complex. This is probably due to the non-alignment of the anisotropy axes of the molecules that leads to a weak broadening of the loops precluding the observation of the hyperfine structure.

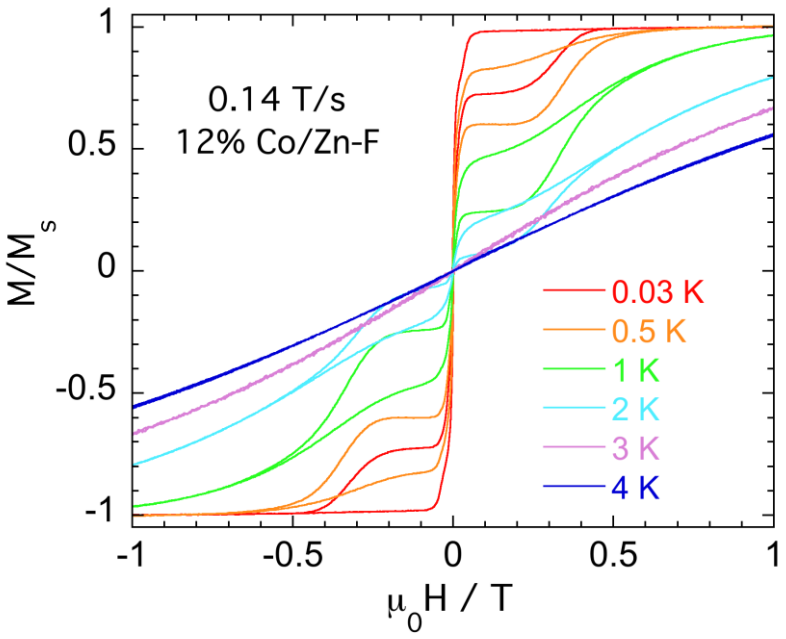

Figure 2.68. Magnetization *vs.* fields on a single crystal of complex **2-8** with its easy axis aligned with the fields at different temperatures.

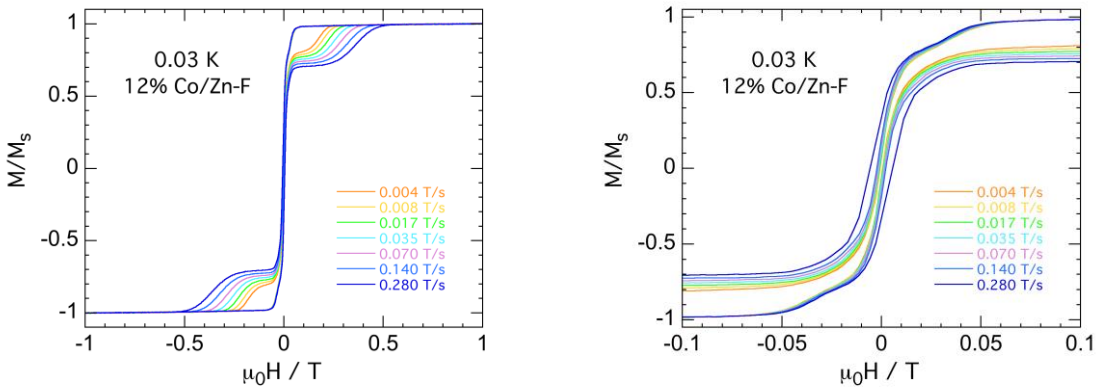

Figure 2.69. Magnetization *vs.* fields on a single crystal of complex **2-8** with its axis aligned with the fields at 0.03 K with different sweep rates (left) and together with a zoom in the –0.1 — 0.1 T region (right).

The main conclusion when comparing the results of the fluoride-containing complex to the chloride one is the slower relaxation of the former compared to the latter. Thus, a large axial anisotropy may lead to an opening of the hysteresis loop at higher temperature despite the presence of the transverse anisotropy. Of course, the opening occurs in the presence of a magnetic field, where the QTM is a precluded, but where the direct mechanism is active. Furthermore, the opening of the hysteresis loop at very low temperature and at zero dc magnetic field is very weak in the perfectly symmetric **2-1** complex. This is usually attributed to the QTM mechanism. However, the origin of this mechanism is not clear in this Kramers doublet where the $m_s = \pm 3/2$ wave functions are pure (do not mix with the ±1/2 ones). The hyperfine coupling may be invoked, but this hypothesis must be examined further. Another possibility is the coupling between the molecules through the lattice (spin lattice) despite the 10% dilution. We have examined this possibility by performing Mirco-SQUID measurements on a 5% diluted sample of complex **2-1** with no observable difference. One may need to isolate more efficiently the molecules to access the bistability at zero dc magnetic field and the work is in progress in this direction.

2.4 Theoretical Calculations and Tentative of Magneto-Structural Correlation

Experimental geometries were used for the theoretical study. The *ab initio* calculations have been performed using the two-step approach implemented in the ORCA code in which the SOC and spin-spin coupling (SSC) relativistic effects are included *a posteriori*.[58, 59] Because the SOC contribution to the ZFS parameters is more important than the SSC one, the rationalization of the magnitude and the sign of *D* only uses the spin-orbit operator (see equation 2.9) that couples the ground state m_s components with those of the excited states.

$$\hat{H}_{SO} = \sum_i \xi_i \hat{l}_i \cdot \hat{s}_i = \sum_i \xi_i (\hat{l}_{z_i} \cdot \hat{s}_{z_i} + \frac{1}{2}(\hat{l}_{+_i} \cdot \hat{s}_{-_i} + \hat{l}_{-_i} \cdot \hat{s}_{+_i})) \qquad (2.9)$$

The *D* values are reported in Table 2.23, *E* was systematically found to be equal to zero as expected from the C_{3v} symmetry of the complex except for the complex **2-6**. Comparing the values obtained at several levels of correlations, one may first notice that the inclusion of dynamic correlation, using the energies of the NEVPT2 method, reduces substantially the |*D*| values. At this level, the calculated values are in good agreement with the experimental data.[18] This allows us to perform a rationalization of the origin of negative *D* in these trigonal bipyramidal complexes.

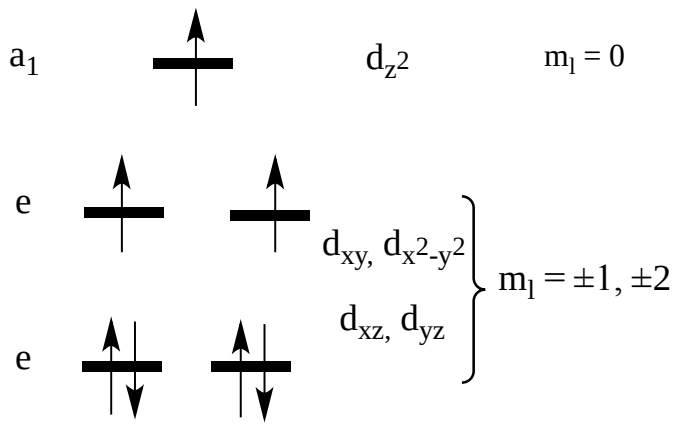

Figure 2.70. Removal of the degeneracy of the d orbitals in a trigonal bipyramidal (C_{3v}) crystal field.

In a trigonal bipyramid, the splitting of the d orbital by the ligand field leads usually the scheme depicted in Figure 2.70. The d_{xy}, d_{yz} orbitals have the lowest energy, the $d_{xy}, d_{x^2-y^2}$ orbitals have intermediate energy and the d_{z^2} one has the highest energy. However, when the symmetry is C_{3v}, this description is not strictly true because the four first

orbitals are base of the same irreducible representation (IRREP) *e* of the C_{3v} point group. The consequence is that the four orbitals are mixed and one cannot assign one pair of orbitals to one pair of levels. The calculations show that the two lowest energy levels can be expressed as a mixture of the four orbitals. This is also the case of the two other energy levels. The consequence is that the ground energy state $^4A_2$ coming from the $e^4e^2a_1^1$ electronic configuration and the first excited state $^4A_1$ coming from the $e^3e^3a_1^1$ configuration mix together via the spin-orbit operator in a way to give a negative contribution to the overall axial anisotropy parameter *D*. It is worth noting that if the symmetry were D_3 and not C_3, no mixing between the ground and the excited states exist and thus the main negative contribution to *D* vanishes. It is, thus, the C_3 symmetry that is mainly responsible of the large Ising-type anisotropy of these compounds as demonstrated by Cahier *et al.*[60]

We will not perform a detailed analysis of the relationship between the structure of the complexes and the anisotropy. We will only comment the results of the calculations and try to extract only general ideas on the effect of the axial ligands on the anisotropy.

The *ab initio* calculation results of the energy spectrum for the four complexes are depicted in Figure 2.71.

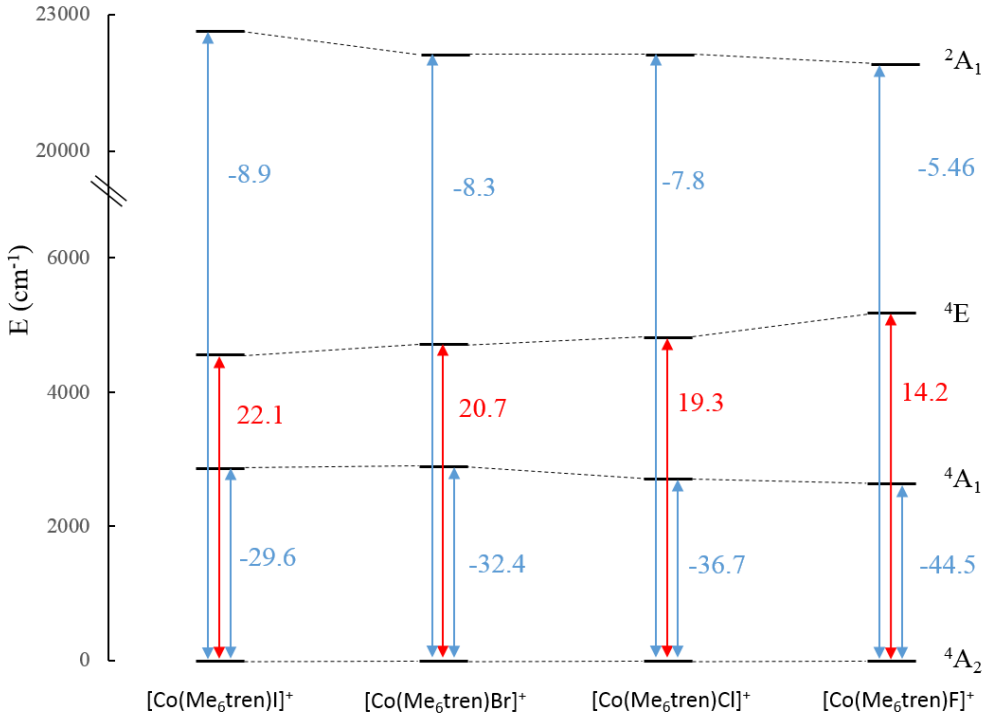

Figure 2.71. Energy spectrum of the $[Co(Me_6tren)X]^+$ complexes including only the states that have the largest contribution to *D*. The number indicates the contribution of a given state to the overall *D* value.

The evolution of the energy spectrum shows that the energy difference between the ground and the first excited state decreases when going from X = I^- to X = F^-. Since the |*D*| value is proportional to the inverse of the energy difference, the contribution of the first excited state is larger (in absolute value) for X = F^- than for X = I^-. Another feature of the energy spectra is the evolution of the energy of the second excited state (^{4}E) that increases when going from X = I^- to X = F^-, leading to weaker positive contribution to *D* for the latter than for the former.

It is important to note that the ^{4}E state is obtained by an excitation from the ground *e* orbitals to the a_1 orbital. It is thus the energy difference between the ground *e* orbitals and the a_1 orbital that determine the contribution of the ^{4}E state *i.e.* the positive contribution to *D*. In order to rationalize the effect of the ^{4}E state, we determined from calculations the energy of the d orbitals for the four complexes as depicted in Figure 2.72. The energy difference between the ground *e* orbitals and the a_1 orbital increases through the I^- to F^- series leading to an increase of the energy difference between the ground and the ^{4}E states and thus to an increase of the overall negative *D* value, as observed experimentally. This effect can be related to the Co–X bond length that is the weakest for X = F^-. The axial ligand F^- has thus a large crystal field effect along the *z* axis of the complex leading to a ^{4}E state with higher energy and thus to more negative *D* value. This relatively simple analysis allows rationalizing part of the origin of the larger |*D*| value for X = F^-.

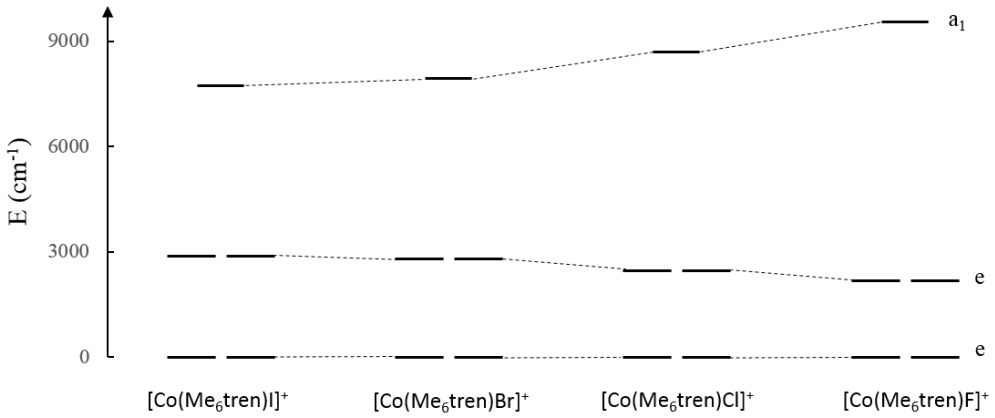

Figure 2.72. Energy spectrum of d orbitals for the [Co(Me$_6$tren)X]$^+$ complexes.

Table 2.23. Relevant Co^{II}–ligand bond distances and angles and anisotropy parameters for complexes **2-1** to **2-6**.

Complexes	**2-1**	**2-2**	**2-3**	**2-4**	**2-5**	**2-6**
Space group	*R*3*c*	*R*3*H*	$P2_13$	$P2_13$	$P2_13$	$P2_1/n$
[b] d_{CoN_a}	2.176	2.209	2.220	2.210	2.201	2.203
[b] d_{CoN_e}	2.152	2.143	2.133	2.137	2.141	2.132; 2.134; 2.149
[b] $d_{CoN_e}aveage$	2.152	2.143	2.133	2.137	2.141	2.1383
[b] d_{CoX}	2.282	2.284	2.306	2.459	2.666	1.906
[b] $d_{Co-N_eN_e'N_e''}$	0.327	0.338	0.332	0.333	0.321	0.322
[c] $\widehat{N_eCoN_e}$	117.73	117.57	117.62	117.61	117.79	116.93; 117.26; 119.15
[c] $\widehat{N_eCoX}$	98.74	99.08	98.97	98.97	98.63	97.15; 99.32; 99.50
[c] $\widehat{N_aCoX}$	180	180	180	180	180	178.74
[c] $\widehat{N_aCoN_e}$	81.26	80.91	81.03	81.03	81.37	80.75; 81.56; 81.74
[c] θ	8.74	9.09	8.97	8.97	8.63	9.25; 8.44; 8.26
$g_{\chi T}$	2.24	2.23	2.17	2.25	2.20	2.25
[d] $D_{\chi T}$	±8.2	±8	±6.8	±8	±6	±11
g_{MH}	2.24	2.33	2.17	2.22	2.15	2.39
[d] D_{MH}	–6.2	–5.4	–5.1	–3.5	–2.1	–16.7
[d] D_{HFEPR}	–8.12	—	—	—	—	–17.7
[d] D_{CALC}	–10.3	—	—	–5.5	–1.52	–20.23
[d] E_{CALC}	0	0	0	0	0	0.27
[d] U_{eff}	14.3	14.2	13.0	—	—	27.1

[a] means axial; [b] in Angstrom (Å); [c] in degree (°), $\theta = 180° - \widehat{N_aCoN_e}$; [d] in wavenumbers ($cm^{-1}$); [e] means equatorial.

2.5 Conclusions and Outlook

The main conclusion from this work is that we can engineer and tune the magnetic anisotropy and the barrier to the reorientation of the magnetization of trigonal bipyramidal Co^{II} complexes by chemical design. Despite the presence of a transverse anisotropy term in the F-containing complex, the effective energy barrier U_{eff} (32 cm^{-1}) was the largest in the series.

The theoretical calculations allow preliminary magneto-structural correlation that leads to the conclusion that the presence of a ligand with a large crystal field along the principal symmetry axis (*z*) leads contributes to a larger Ising-type anisotropy because its contribution decreases the positive contribution to *D*. The origin of the difference in energy between the ground and the first excited states that has a large influence on the *D* value is related to the energy difference between the two sets of *e* orbitals (Figure 2.72). The origin of this difference is not simple to analyze qualitatively without including the effect of electron repulsion. However, it appears clearly that an interesting way to increase the negative contribution to *D* is to reduce the energy difference between the two sets of *e* orbitals. One possibility to do so is to reduce the crystal field in the equatorial plane. This should lead to a reduction of the energy difference between the two sets of *e* orbitals and thus to a reduction of the energy difference between the ground and the first excited states leading to a larger negative contribution to *D*. The efforts in this direction are presented in the next chapter.

2.6 References

1. A. Caneschi, D. Gatteschi, R. Sessoli, A. L. Barra, L. C. Brunel and M. Guillot, *Journal of the American Chemical Society*, 1991, **113**, 5873-5874.
2. R. Sessoli, D. Gatteschi, A. Caneschi and M. A. Novak, *Nature*, 1993, **365**, 141-143.
3. N. Ishikawa, M. Sugita, T. Ishikawa, S.-y. Koshihara and Y. Kaizu, *Journal of the American Chemical Society*, 2003, **125**, 8694-8695.
4. D. N. Woodruff, R. E. P. Winpenny and R. A. Layfield, *Chemical Reviews*, 2013, **113**, 5110-5148.
5. J. D. Rinehart and J. R. Long, *Chemical Science*, 2011, **2**, 2078-2085.
6. N. Ishikawa, M. Sugita, T. Okubo, N. Tanaka, T. Iino and Y. Kaizu, *Inorganic Chemistry*, 2003, **42**, 2440-2446.
7. N. Ishikawa, M. Sugita, T. Ishikawa, S.-y. Koshihara and Y. Kaizu, *The Journal of Physical Chemistry B*, 2004, **108**, 11265-11271.

8. N. Ishikawa, M. Sugita and W. Wernsdorfer, *Journal of the American Chemical Society*, 2005, **127**, 3650-3651.
9. M. A. AlDamen, J. M. Clemente-Juan, E. Coronado, C. Martí-Gastaldo and A. Gaita-Ariño, *Journal of the American Chemical Society*, 2008, **130**, 8874-8875.
10. M. A. AlDamen, S. Cardona-Serra, J. M. Clemente-Juan, E. Coronado, A. Gaita-Ariño, C. Martí-Gastaldo, F. Luis and O. Montero, *Inorganic Chemistry*, 2009, **48**, 3467-3479.
11. S.-D. Jiang, B.-W. Wang, G. Su, Z.-M. Wang and S. Gao, *Angewandte Chemie*, 2010, **122**, 7610-7613.
12. S.-D. Jiang, B.-W. Wang, H.-L. Sun, Z.-M. Wang and S. Gao, *Journal of the American Chemical Society*, 2011, **133**, 4730-4733.
13. M. J. Martínez-Pérez, S. Cardona-Serra, C. Schlegel, F. Moro, P. J. Alonso, H. Prima-García, J. M. Clemente-Juan, M. Evangelisti, A. Gaita-Ariño, J. Sesé, J. van Slageren, E. Coronado and F. Luis, *Physical Review Letters*, 2012, **108**, 247213.
14. N. F. Chilton, S. K. Langley, B. Moubaraki, A. Soncini, S. R. Batten and K. S. Murray, *Chemical Science*, 2013, **4**, 1719-1730.
15. P. Zhang, L. Zhang, C. Wang, S. Xue, S.-Y. Lin and J. Tang, *Journal of the American Chemical Society*, 2014, **136**, 4484-4487.
16. A. J. Brown, D. Pinkowicz, M. R. Saber and K. R. Dunbar, *Angewandte Chemie*, 2015, **127**, 5962-5966.
17. Q.-W. Li, J.-L. Liu, J.-H. Jia, Y.-C. Chen, J. Liu, L.-F. Wang and M.-L. Tong, *Chemical Communications*, 2015, **51**, 10291-10294.
18. R. Ruamps, L. J. Batchelor, R. Guillot, G. Zakhia, A.-L. Barra, W. Wernsdorfer, N. Guihery and T. Mallah, *Chemical Science*, 2014, **5**, 3418-3424.
19. R. Ruamps, R. Maurice, L. Batchelor, M. Boggio-Pasqua, R. Guillot, A. L. Barra, J. Liu, E.-E. Bendeif, S. Pillet, S. Hill, T. Mallah and N. Guihéry, *Journal of the American Chemical Society*, 2013, **135**, 3017-3026.
20. J. M. Zadrozny, D. J. Xiao, M. Atanasov, G. J. Long, F. Grandjean, F. Neese and J. R. Long, *Nature Chemistry*, 2013, **5**, 577-581.
21. J. M. Zadrozny, J. Liu, N. A. Piro, C. J. Chang, S. Hill and J. R. Long, *Chemical Communications*, 2012, **48**, 3927-3929.
22. D. Schweinfurth, M. G. Sommer, M. Atanasov, S. Demeshko, S. Hohloch, F. Meyer, F. Neese and B. Sarkar, *Journal of the American Chemical Society*, 2015, **137**, 1993-

2005.

23. T. J. Woods, M. F. Ballesteros-Rivas, S. Gómez-Coca, E. Ruiz and K. R. Dunbar, *Journal of the American Chemical Society*, 2016, DOI: 10.1021/jacs.6b10154.
24. F. Shao, B. Cahier, N. Guihery, E. Riviere, R. Guillot, A.-L. Barra, Y. Lan, W. Wernsdorfer, V. E. Campbell and T. Mallah, *Chemical Communications*, 2015, **51**, 16475-16478.
25. G. A. Timco, S. Carretta, F. Troiani, F. Tuna, R. J. Pritchard, C. A. Muryn, E. J. L. McInnes, A. Ghirri, A. Candini, P. Santini, G. Amoretti, M. Affronte and R. E. P. Winpenny, *Nat Nano*, 2009, **4**, 173-178.
26. G. J. P. Britovsek, J. England and A. J. P. White, *Inorganic Chemistry*, 2005, **44**, 8125-8134.
27. S. Fu, Y. Liu, Y. Ding, X. Du, F. Song, R. Xiang and B. Ma, *Chemical Communications*, 2014, **50**, 2167-2169.
28. A. Galperin, T. J. Long, S. Garty and B. D. Ratner, *Journal of Biomedical Materials Research Part A*, 2013, **101A**, 775-786.
29. G. M. Sheldrick, University of Göttingen, Göttingen, Germany, 1997.
30. G. M. Sheldrick, University of Göttingen, Göttingen, Germany, 1997.
31. G. M. Sheldrick, *Acta Crystallographica Section A: Foundations of Crystallography*, 2008, **64**, 112-122.
32. L. J. Farrugia, *Journal of Applied Crystallography*, 1999, **32**, 837-838.
33. L. Farrugia, *Journal of Applied Crystallography*, 2012, **45**, 849-854.
34. W. Wernsdorfer, *Superconductor Science and Technology*, 2009, **22**, 064013.
35. W. Wernsdorfer, N. E. Chakov and G. Christou, *Physical Review B*, 2004, **70**, 132413.
36. F. Muller, M. A. Hopkins, N. Coron, M. Grynberg, L. C. Brunel and G. Martinez, *Review of Scientific Instruments*, 1989, **60**, 3681-3684.
37. A. L. Barra, L. C. Brunel and J. B. Robert, *Chemical Physics Letters*, 1990, **165**, 107-109.
38. A. L. Barra, D. Gatteschi and R. Sessoli, *Physical Review B*, 1997, **56**, 8192-8198.
39. D. Gatteschi, A. L. Barra, A. Caneschi, A. Cornia, R. Sessoli and L. Sorace, *Coordination Chemistry Reviews*, 2006, **250**, 1514-1529.
40. A.-L. Barra, A. Caneschi, A. Cornia, D. Gatteschi, L. Gorini, L.-P. Heiniger, R. Sessoli and L. Sorace, *Journal of the American Chemical Society*, 2007, **129**, 10754-10762.

41. R. Maurice, R. Bastardis, C. d. Graaf, N. Suaud, T. Mallah and N. Guihéry, *Journal of Chemical Theory and Computation*, 2009, **5**, 2977-2984.
42. F. Aquilante, L. De Vico, N. Ferré, G. Ghigo, P.-å. Malmqvist, P. Neogrády, T. B. Pedersen, M. Pitoňák, M. Reiher, B. O. Roos, L. Serrano-Andrés, M. Urban, V. Veryazov and R. Lindh, *Journal of Computational Chemistry*, 2010, **31**, 224-247.
43. B. O. Roos and P.-A. Malmqvist, *Physical Chemistry Chemical Physics*, 2004, **6**, 2919-2927.
44. G. Karlström, R. Lindh, P.-Å. Malmqvist, B. O. Roos, U. Ryde, V. Veryazov, P.-O. Widmark, M. Cossi, B. Schimmelpfennig, P. Neogrady and L. Seijo, *Computational Materials Science*, 2003, **28**, 222-239.
45. P. Å. Malmqvist, B. O. Roos and B. Schimmelpfennig, *Chemical Physics Letters*, 2002, **357**, 230-240.
46. B. O. Roos, P. R. Taylor and P. E. M. Si÷gbahn, *Chemical Physics*, 1980, **48**, 157-173.
47. R. Maurice, C. de Graaf and N. Guihéry, *Physical Review B*, 2010, **81**, 214427.
48. L. F. Chibotaru, L. Ungur, C. Aronica, H. Elmoll, G. Pilet and D. Luneau, *Journal of the American Chemical Society*, 2008, **130**, 12445-12455.
49. H. Bolvin, *ChemPhysChem*, 2006, **7**, 1575-1589.
50. K. S. Cole and R. H. Cole, *The Journal of Chemical Physics*, 1941, **9**, 341-351.
51. H. Miyasaka, R. Clérac, K. Mizushima, K.-i. Sugiura, M. Yamashita, W. Wernsdorfer and C. Coulon, *Inorganic Chemistry*, 2003, **42**, 8203-8213.
52. V. V. Novikov, A. A. Pavlov, Y. V. Nelyubina, M.-E. Boulon, O. A. Varzatskii, Y. Z. Voloshin and R. E. P. Winpenny, *Journal of the American Chemical Society*, 2015, **137**, 9792-9795.
53. Y. Rechkemmer, F. D. Breitgoff, M. van der Meer, M. Atanasov, M. Hakl, M. Orlita, P. Neugebauer, F. Neese, B. Sarkar and J. van Slageren, *Nature Communications*, 2016, **7**.
54. J. M. Zadrozny, M. Atanasov, A. M. Bryan, C.-Y. Lin, B. D. Rekken, P. P. Power, F. Neese and J. R. Long, *Chemical Science*, 2013, **4**, 125-138.
55. A. Abragam and B. Bleany, *Electron Paramagnetic Resonance of Transition Ions*, 1970.
56. W. Wernsdorfer and R. Sessoli, *Science*, 1999, **284**, 133-135.
57. M. Moragues-Cánovas, É. Rivière, L. Ricard, C. Paulsen, W. Wernsdorfer, G. Rajaraman, E. K. Brechin and T. Mallah, *Advanced Materials*, 2004, **16**, 1101-1105.

58. F. Weigend and R. Ahlrichs, *Physical Chemistry Chemical Physics*, 2005, **7**, 3297-3305.

59. C. Angeli, R. Cimiraglia, S. Evangelisti, T. Leininger and J.-P. Malrieu, *The Journal of Chemical Physics*, 2001, **114**, 10252-10264.

60. B. Cahier, R. Maurice, H. Bolvin, T. Mallah and N. Guihéry, *Magnetochemistry*, 2016, **2**, 31.

CHAPTER 3 Engineering the Ising-type Anisotropy in Trigonal Bipyramidal Co^{II} Complexes Based on Two Types of S-based Ligands

3.1 Introduction

The results obtained on the Co^{II} complexes with the Me$_6$tren series highlighted the effect of the axial ligand on the magnitude of the axial magnetic anisotropy and the relaxation times at 1.8 K. The analysis of the theoretical calculations demonstrated that changing the axial ligand X from I^- to F^- allowed increasing the $|D|$ value keeping the Ising-type anisotropy. As mentioned in Chapter 2, the Co–L bond distances in the equatorial plane may also influence the magnitude of the axial magnetic anisotropy. This distance is related to the difference in energy between the ground $^4A_2$ and the first excited $^4A_1$ states that contribute the most to the axial anisotropy. We thus reasoned that decreasing the energy difference between these two energy states will increase their mixing by the Spin-Orbital Operator and thus leads to a larger (in absolute value) *D* parameter. We, thus, used a tetradentate ligand with three sulfur atoms instead of three nitrogen atoms that may coordinate to Co^{II} in the equatorial plane assuming that the Co–S bond distances will be larger than the Co–N ones. Larger equatorial distances lead to less energy separation between the *e* orbitals and thus to larger axial magnetic anisotropy. We could obtain with Cl^-, as the axial ligand, *D* values as large as 23 cm^{-1} in absolute value.[1]

We prepared several complexes with two sulfur-containing tetradentate ligands depicted below:

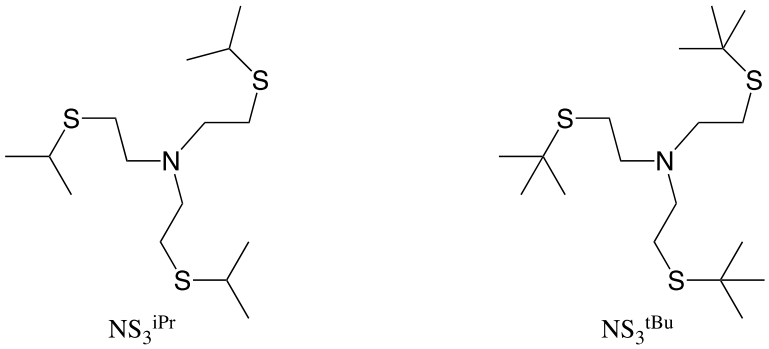

Scheme 3.1. Schematic view of the sulfur-containing tetradentate ligands.

3.2 Experimental Section

3.2.1 Syntheses

All starting materials were obtained commercially and were used without further purification unless otherwise stated. NS_3^{iPr}, NS_3^{tBu} and all cobalt(II), zinc(II) complexes were synthesized according to literature procedures or minor alterations thereof.[2-4] And the new complexes were synthesized similarly.

Tris(2-(isopropylthio)ethyl)amine: NS_3^{iPr}

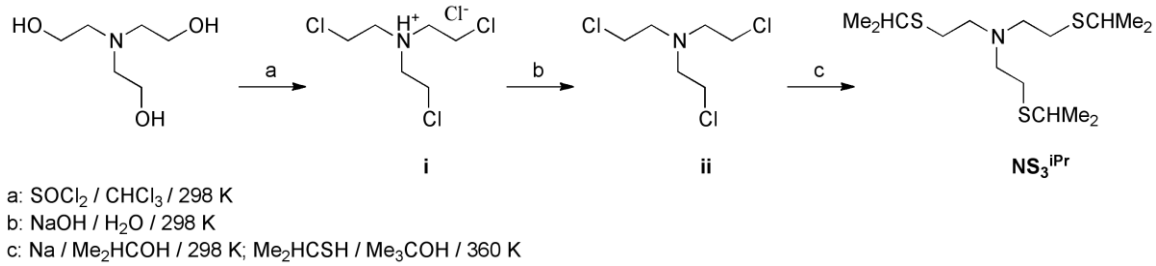

Scheme 3.2. Synthesis of tris(2-(isopropylthio)ethyl)amine.

Tris(2-chloroethyl)amine hydrochloride (i). A 250 mL two-necked round-bottom flask, which was fitted with a dropping funnel and a reflux condenser, was charged with thionyl chloride (52 mL, 0.70 mol) and chloroform (80 mL). A solution of triethanolamine (29.80 g, 0.20 mol) in 50 mL of chloroform was added dropwise to this solution. The addition was carried out at ambient temperature for 1 h. The reaction continued at room temperature until gas evolution stopped, and then the mixture was heated at reflux for 4 h. After cooling to room temperature, a white solid precipitate was formed, which was filtered and washed with $CHCl_3$ (50 × 3 mL) and dried overnight in a vacuum oven. Tris(2-chloroethyl)amine hydrochloride (**i**) was obtained in 80 % yield (38.56 g).

Tris(2-chloroethyl)amine (**ii**). Sodium hydroxide (2.00 g, 0.05 mol) was added portionwise to a solution of complex **i** (12.05 g, 0.05 mol) and 30 mL of water. The reaction was stirred for 1 h. The solution was extracted with $CHCl_3$ (20 × 3 mL) and the organic layer was further washed with (20 × 3 mL) distilled water, dried over anhydrous $MgSO_4$. The solvent was removed and the heavy oil product was obtained by vacuum-distillation (7.26 g, 71% yield).

Tris(2-(isopropylthio)ethyl)amine (**NS_3^{iPr}**). *(Cautions: The 2-Propanethiol used in this synthesis is a poisonous gas with an obnoxious odor. All procedures must be carried out*

in an efficient fume hood. The apparatus must be connected to a series of washing bottles charged with chromic acid mixture or other absorbing solutions.) All glassware must be previously dried. A two-necked flask was equipped with a reflux condenser topped with a drying tube ($CaCl_2$) and a 500-mL dropping funnel with external warming bath. With stirring, anhydrous 2-Propanol (200 mL) was added and refluxed at 360 K, followed by sodium (2.30 g, 0.10 mol) in small portions. Upon reaction of all the sodium, the flask was allowed to cool to room temperature. 2-Propanethiol (9.29 mL, 0.10 mol), and 50 mL of warm anhydrous 2-Propanol were poured into the dropping funnel, which was heated by warm water. The solution was added dropwise with stirring to the sodium iso-propoxide solution during a 1 h period. The warming bath was then drained off, and a solution of $N(CH_2CH_2Cl)_3$ (**ii**) (6.81 g, 0.033 mol) of dissolved in 20 mL of anhydrous 2-Propanol was placed in the dropping funnel. The sodium iso-propoxide solution was heated to 323 – 333 K, and slowly added over 4 h. The mixture was then refluxed for 1 h, and cooled to room temperature. The NaCl, which precipitates, was filtered, and the solution was concentrated under reduced pressure. The residue was diluted with diethyl ether, filtered, concentrated, and vacuum-distilled. The ligand was collected at 408 – 409 K / 2 torr to yield 7.91 g (0.023 mol) of **NS_3^{iPr}** (74.1% yield). ^{1}H NMR ($CDCl_3$, 300 MHz, ppm from TMS): 1.183 – 1.279 (18H, $(CH_3)_2CHS$–); 2.92 (3H, $(CH_3)_2CHS$–); 2.62 (6H, $Me_2CHSCH_2CH_2$–); 2.69 (6H, $Me_2CHSCH_2CH_2$–). MS-ESI: *m/z* calcd for $C_{18}H_{39}NS_3$: 323.2, found: 324.1.

2-(tert-butylthio)-N-(2-(tert-butylthio)ethyl)-N((neopentylthio)methyl)ethan-1-amine: NS_3^{tBu}.

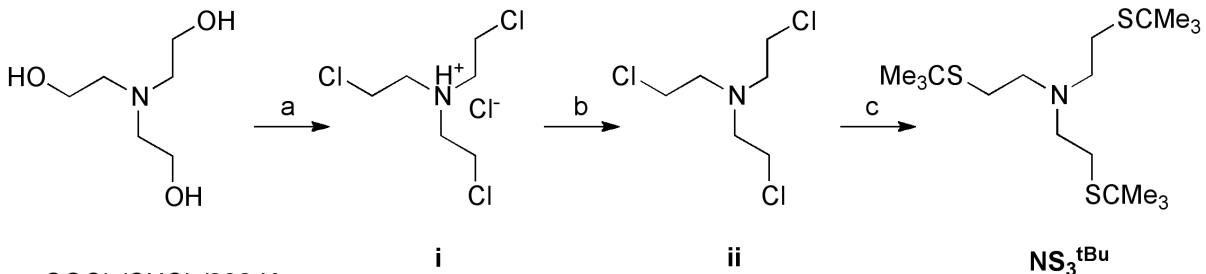

Scheme 3.3. Schematic representation of the synthesis of the ligand NS^{tBu}.

2-(tert-butylthio)-N-(2-(tert-butylthio)ethyl)-N((neopentylthio)methyl)ethan-1-amine (NS_3^{tBu}).

(Cautions: The tert-Butylmercaptan used in this synthesis is a poisonous gas with an obnoxious odor. All procedures must be carried out in an efficient fume hood. The apparatus must be connected to a series of washing bottles charged with chromic acid mixture or other absorbing solutions.) All glassware must be previously dried. A two-necked flask was equipped with a reflux condenser topped with a drying tube ($CaCl_2$) and a 500-mL dropping funnel with external warming bath. With stirring, anhydrous tert-Butyl alcohol (200 mL) was added and refluxed at 360 K, followed by sodium (2.30 g, 0.10 mol) in small portions. Upon reaction of all the sodium, the flask was allowed to cool to room temperature. 2-Methyl-2-propanethiol (11.28 mL, 0.10 mol), and 50 mL of warm anhydrous tert-Butyl alcohol were poured into the dropping funnel, which was heated by warm water. The solution was added dropwise with stirring to the sodium tert-butoxide solution during a 1 h period. The warming bath was then drained off, and a solution of $N(CH_2CH_2Cl)_3$ (**ii**) (6.81 g, 0.033 mol) of dissolved in 20 mL of anhydrous tert-Butyl alcohol was placed in the dropping funnel. The sodium tert-butoxide solution was heated to 323 – 333 K, and slowly added over 4 h. The mixture was then refluxed for 1 h, and cooled to room temperature. The NaCl, which precipitates, was filtered, and the solution was concentrated under reduced pressure. The residue was diluted with diethyl ether, filtered, concentrated, and vacuum-distilled. The ligand was collected at 427 – 429 K /2 torr to yield 8.45 g (0.023 mol) of product (70% yield). ^{1}H NMR ($CDCl_3$, 300 MHz, ppm from TMS): 1.185 – 1.266 (27H, $(CH_3)_3CS$–); 2.54 (6H, $Me_3CSCH_2CH_2$–); 2.62 (6H, $Me_3CSCH_2CH_2$–). MS-ESI: *m/z* calcd for $C_{18}H_{39}NS_3$: 365.3, found: 366.2291.

[Co(NS_3^{iPr})Cl](BPh_4) (3-1)

To a hot solution of $CoCl_2$ (65.1 mg, 0.5 mmol) in 1-butanol (3 mL), NS_3^{iPr} (194.2 mg, 0.6 mmol) in 1-butanol (1 mL) were added followed by $NaBPh_4$ (171.1 mg, 0.5 mmol) in1-butanol (2 mL). Then the solution was cooled down to room temperature at ambient condition. A purple precipitate was formed, it was filtered, washed with 1-butanol and petroleum ether, and dried in vacuum at room temperature. Yield, 78.7%, 290 mg. X-ray quality crystals were obtained by vapor diffusion of diethyl ether into an ethanol/acetone (v/v 1:1) solution of **3-1**. Elem Anal. Calcd: C, 62.77; H, 7.29; N, 1.8. Found: C, 62.33; H, 7.00; N, 1.76. IR (KBr) ν/cm^{-1}: 3468 (s), 3053 (s), 2981 (s), 1579 (w), 1477 (m), 1455 (m), 1423 (m),

1368 (w), 737 (s), 709 (s), 611 (m) cm^{-1}. Single-crystal unit cell: Triclinic, space group *P*–1, *a* = 11.5577(5) Å, *b* = 18.1837(8) Å, *c* = 18.2006(8) Å, α = 97.507(2)°, β = 92.728(2)°, γ = 92.840(2)°, *V* = 3782.0(3) $Å^3$.

[Co(NS_3^{tBu})Cl]ClO_4 (3-2)

To a hot solution of $CoCl_2$ (65.1 mg, 0.5 mmol) in 1-butanol (2 mL), NS_3^{tBu} (219.4 mg, 0.6 mmol) in 1-butanol (2 mL) were added followed by $[Bu_4N]ClO_4$ (170.6 mg, 0.5 mmol) in ethanol (1 mL). Then the stirred solution was cooled down to room temperature at ambient condition. A purple precipitate was formed, it was filtered, washed with 1-butanol and petroleum ether, and dried in vacuum at room temperature. Yield, 32%, 89.5 mg. X-ray quality crystals were obtained by vapor diffusion of diethyl ether into an ethanol/acetone (v/v 1:1) solution of **3-2**. Elem Anal. Calcd: C, 38.64; H, 7.02; N, 2.50. Found: C, 38.66; H, 7.14; N, 2.49. IR (KBr) ν/cm^{-1}: 3436 (m), 2960 (m), 2865 (w), 1464 (m), 1370 (m), 1162 (m), 1103 (s), 623 (m) cm^{-1}. Single-crystal unit cell: Monoclinic, space group $P2_1/c$, *a* = 15.2642(5) Å, *b* = 10.9170(3) Å, *c* = 17.0452(5) Å, α = 90°, β = 115.0890(10)°, γ = 90°, *V* = 2572.41(13) $Å^3$.

[Co(NS_3^{tBu})Br]ClO_4 (3-3)

To a hot solution of $CoBr_2 \cdot H_2O$ (118.4 mg, 0.5 mmol) in 1-butanol (2 mL), NS_3^{tBu} (219.4 mg, 0.6 mmol) in 1-butanol (2 mL) were added followed by $[Bu_4N]ClO_4$ (170.6 mg, 0.5 mmol) in ethanol (1 mL). Then the stirred solution was cooled down to room temperature at ambient condition. A purple precipitate was formed, it was filtered, washed with 1-butanol and petroleum ether, and dried in vacuum at room temperature. Yield, 29.8%, 90 mg. X-ray quality crystals were obtained by vapor diffusion of diethyl ether into an ethanol/acetone (v/v 1:1) solution of **3-3**. Elem Anal. Calcd: C, 35.79; H, 6.51; N, 2.32. Found: C, 35.81; H, 6.49; N, 2.22. IR (KBr) ν/cm^{-1}: 3436 (m), 2959 (m), 2865 (w), 1464 (m), 1370 (m), 1161 (m), 1102 (s), 623 (m) cm^{-1}. Single-crystal unit cell: Monoclinic, space group $P2_1/c$, *a* = 15.8788(13) Å, *b* = 28.594(2) Å, *c* = 11.7160(9) Å, α = 90°, β = 96.219(3)°, γ = 90°, *V* = 5288.3(7) $Å^3$.

[Co(NS_3^{tBu})NCS]ClO_4 (3-4)

To a hot solution of $Co(NCS)_2$ (88 mg, 0.5 mmol) in 1-butanol (2 mL), NS_3^{tBu} (219.4 mg, 0.6 mmol) in 1-butanol (2 mL) were added followed by $[Bu_4N]ClO_4$ (170.6 mg, 0.5

mmol) in ethanol (1 mL). Then the stirred solution was cooled down to room temperature at ambient condition. A purple precipitate was formed, it was filtered, washed with 1-butanol and petroleum ether, and dried in vacuum at room temperature. Yield, 5.1%, 15 mg. X-ray quality crystals were obtained by vapor diffusion of diethyl ether into an ethanol/acetone (v/v 1:1) solution of **3-4**. Elem Anal. Calcd: C, 39.20; H, 6.75; N, 4.81. Found: C, 39.08; H, 6.78; N, 4.80. IR (KBr) ν/cm^{-1}: 3436 (m), 2960 (m), 2863 (w), 2067 (s), 1457 (w), 1365 (w), 1159 (w), 1099 (w), 623 (m) cm^{-1}. Single-crystal unit cell: Cubic, space group $P2_13$, a = 14.1508(5) Å, b = 14.1508(5) Å, c = 14.1508(5) Å, $\alpha = 90°$, $\beta = 90°$, $\gamma = 90°$, V = 2833.6(3) Å^3.

3.2.2 Physical Measurements

Unless otherwise stated, all starting materials were obtained commercially and were used without further purification. General procedures, X-ray Crystallography, Magnetic Measurements, and Micro-SQUID Measurements are aforementioned in Chapter 2.

Electron Paramagnetic Resonance (EPR) Measurements

X-band EPR[5] spectra were recorded on a Bruker ELEXSYS 500 spectrometer equipped with a Bruker ER4119HS X band resonator, an Oxford Instrument continuous flow ESR 900cryostat and a temperature control system in the Laboratoire de Chimie Inorganique, Institut de Chimie Moléculaire et des Matériaux d'Orsay (ICMMO), Université Paris-Sud, Université Paris-Saclay, France. EPR samples were collected by Christian Herrero during the course of electrolysis and immediately frozen in liquid N_2. The EPR tubes were put through 5 cycles of vacuum/helium in order to purge oxygen from the samples before being entered into the EPR spectrometer.

The HFEPR was done in Grenoble at the Laboratoire de Champs Magnétiques Intenses in collaboration with Anne-Laure Barra, who recorded the spectra and helped us to analyze them.

Computational Details

Theoretical calculations have been performed in order to rationalize the values of the ZFS parameters that were determined experimentally. As these parameters are very sensitive to the geometrical features, the theoretical study was performed using experimental geometries obtained from the X-ray crystal data. *Ab initio* calculations were done using the two-step Complete Active Space Self Consistent Field (CASSCF) method followed by the Spin-Orbit State-Interaction (SO-SI)[6] method implemented in the MOLCAS code.[7] More

details see the Theoretical Calculations part in this chapter. The theoretical calculations were performed and analyzed by Benjamin Cahier.

3.3 Results and Discussion

3.3.1 Syntheses

In the direct approach, the reaction can occur between the ligands and simple metal salts. In our case, different reactions among NS_3^{iPr}, NS_3^{tBu} and a series of cobalt(II) and zinc(II) salts were screened under different conditions such as a variety of solvents, or chemical ratios, or the use of different counter-ions, etc…

The formation of complexes **3-1** to **3-4** are summarized in equations 3.1 to 3.4, respectively.

$$CoCl_2 + NS_3^{iPr} + NaBPh_4 \longrightarrow [Co(NS_3^{iPr})Cl]BPh_4 + NaCl \quad (3.1)$$

$$CoCl_2 + NS_3^{tBu} + [n\text{-}Bu_4N]ClO_4 \longrightarrow [Co(NS_3^{tBu})Cl]ClO_4 + [n\text{-}Bu_4N]Cl \quad (3.2)$$

$$CoBr_2 + NS_3^{tBu} + [n\text{-}Bu_4N]ClO_4 \longrightarrow [Co(NS_3^{tBu})Br]ClO_4 + [n\text{-}Bu_4N]Br \quad (3.3)$$

$$Co(NCS)_2 + NS_3^{tBu} + [n\text{-}Bu_4N]ClO_4 \longrightarrow [Co(NS_3^{tBu})NCS]ClO_4 + [n\text{-}Bu_4N]NCS \quad (3.4)$$

During the syntheses, the ligands NS_3^{iPr}, NS_3^{tBu} were used in slight excess leading to an increase of the yields. In addition, anhydrous cobalt(II) salts and solvents are essential in these reactions otherwise no product could be obtained. In equation 3.1, sodium tetraphenylborate can induce precipitation while the other counter-ions such as perchlorate do not work. But precipitates were obtained when the ligand NS_3^{tBu} was used (equations 3.2 to 3.4).

3.3.2 Description of Structures

Partially labeled structure of complexes **3-1** to **3-4** are shown in Figure 3.1 to Figure 3.3, respectively. Some important interatomic distances and angles of these four complexes are listed in Table 3.1 and Table 3.2. The cation structure for complexes **3-1** to **3-4** consists of a five-coordinated Co^{II} ion by one nitrogen atom and three sulfur atoms from the neutral NS_3^{iPr} or NS_3^{tBu} ligands and one halide/thiocyanate axial ligand. The ligands are distributed at the apices of a trigonal bipyramid with crystallographic pseudo C_3 symmetry apart from the **3-4** (NCS axial ligand) that has a strict C_3 symmetry with no distortion); the three equatorial sites are occupied by the sulfur atoms and the axial sites are occupied by the nitrogen and

the halide/thiocyanate ion. The charge balance is provided by a tetraphenylborate or perchlorate anion.

Complex 3-1

Complex **3-1** crystallizes in the space group *P*–1 (Table 3.1 and Table 3.2). The cation structure for complex **3-1** is depicted in Figure 3.1. Charge balance is provided by a tetraphenylborate anion. Complex **3-1** has two crystallographically independent molecules in the asymmetric unit, reference isomers **3-1(i)** and **3-1(ii)** below. For isomers **3-1(i)**, the Co^{II} ion lies 0.352 Å below the equatorial plane of the three sulfur atoms with an in-equatorial $\widehat{S_1CoCl_1}$ angles of 103.49°, 94.84°, 95.86° respectively. The Co–N_1 bond length is 2.263 Å. The Co–Cl_1 distance is equal to 2.255 Å. The $\widehat{S_1CoS_1'}$ and the $\widehat{N_1CoS_1}$ angles are equal to 122.08°, 124.02°, 108.25° and 82.87°, 81.94°, 81.54° respectively (Table 3.1 and Table 3.2). And for isomers **3-1(ii)**, the Co^{II} ion lies 0.415 Å below the equatorial plane of the three sulfur atoms with an in-equatorial $\widehat{S_1CoCl_1}$ angles of 103.82°, 99.40°, 96.98° respectively. The Co–N_1 bond length (2.408 Å) is larger than for isomer **3-1(i)**. The Co–Cl_1 distance is equal to 2.266 Å. The $\widehat{S_1CoS_1'}$ and the $\widehat{N_1CoS_1}$ angles are equal to 113.40°, 121.40°, 116.35° and 79.60°, 81.29°, 79.81° respectively. For more details, see the Table 3.1 and Table 3.2 or the paper published in Chemical Communication.[1]

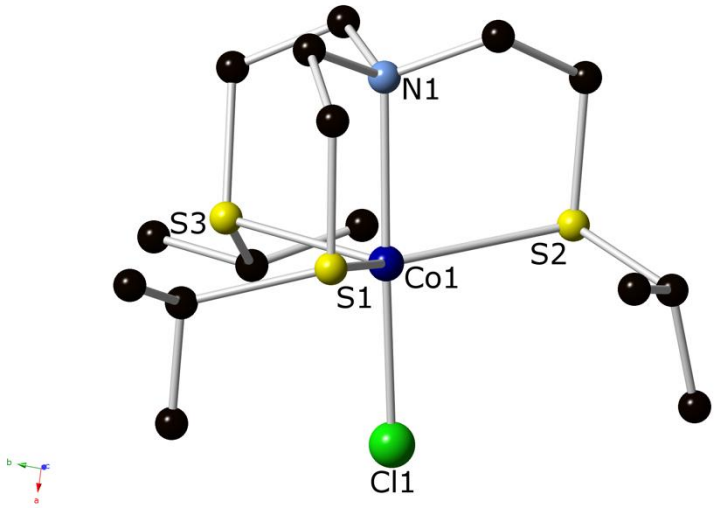

Figure 3.1. A view of the molecular structure for complex **3-1**. C – black; H atoms and counter-ions were omitted for clarity.

Table 3.1. Crystallographic data structure refinement for complexes **3-1** to **3-4**.

Complexes	3-1(Cl)	3-2(Cl)	3-3(Br)	3-4(NCS)
formula	$C_{39}H_{53}BNS_3CoCl$	$C_{18}H_{39}NS_3CoCl_2O_4$	$C_{18}H_{39}NS_3CoBrClO_4$	$C_{19}H_{39}N_2S_4CoClO_4$
M_r	737.19	559.51	603.97	582.14
cryst syst	Triclinic	Monoclinic	Monoclinic	Cubic
space group	*P*–1	$P2_1/c$	$P2_1/c$	$P2_13$
a, Å	11.5577(5)	15.2642(5)	15.8788(13)	14.1508(5)
b, Å	18.1837(8)	10.9170(3)	28.594(2)	14.1508(5)
c, Å	18.2006(8)	17.0452(5)	11.7160(9)	14.1508(5)
α, deg	97.507(2)	90	90	90
β, deg	92.728(2)	115.0890(10)	96.219(3)	90
γ, deg	92.840(2)	90	90	90
cell volume, Å^3	3782.0(3)	2572.41(13)		2833.6(3)
Z	4	4	4	4
T, K	100(1)	100(1)	100(1)	100(1)
F_{000}	1564	1180	2504	1228
μ, mm^{-1}	0.72	1.14	1.45	1.12
reflns collected	153139	65003	134662	43924
reflns unique	24980	7856	16248	2921
R_1	0.043	0.056	0.075	0.068
wR_2 (all data)	0.089	0.081	0.222	0.120
GOF	1.01	1.04	1.131	1.115

Table 3.2. Relevant Co^{II}–ligand bond distances (Å) and angles (°) for complexes **3-1** to **3-4**.

Complexes	3-1 (i)	3-1 (ii)	3-2	3-3 (i)	3-3 (ii)	3-4
[a] d_{CoN}	2.263	2.408	2.287	2.231	2.273	2.346
[a] d_{CoS}	2.412; 2.391; 2.388	2.365; 2.379; 2.362	2.404; 2.397; 2.389	2.435; 2.416; 2.385	2.412; 2.411; 2.407	2.380
[a] d_{CoX}	2.255	2.266	2.264	2.361	2.383	2.001
[a] d_{Co-SSS}	0.352	0.415	0.341	0.331	0.357	0.374
[b] $\widehat{SCoS}$	122.08; 124.02; 108.25	113.40; 121.40; 116.35	118.89; 116.50; 118.60	122.28; 122.81; 109.71	116.83; 114.07; 122.81	117.58
[b] $\widehat{SCoX}$	103.49; 94.84; 95.86	103.82; 99.40; 96.98	97.82; 97.32; 99.38	93.85; 101.18; 98.19	98.66; 97.24; 99.29	99.03
[b] $\widehat{NCoX}$	173.63	175.78	179.00	175.08	178.92	180
[b] $\widehat{NCoS}$	82.87; 81.94; 81.54	79.60; 81.29; 79.81	81.94; 81.97; 81.58	81.82; 83.31; 82.21	81.76; 81.69; 81.42	80.97
[b] θ	7.13; 8.06; 8.46	10.40; 8.71; 10.82	8.06; 8.03; 8.42	8.18; 6.69; 7.79	8.24; 8.31; 8.58	9.03

[a] in Angstrom (Å); [b] in degree (°), $\theta = 180° - \widehat{NCoS}$.

Complexes 3-2, 3-3 and 3-4

Complexes **3-2** and **3-3** (Figure 3.2) crystallize in the space group $P2_1/c$ (Table 3.1 and Table 3.2). Complexes **3-2** and **3-4** only have one crystallographically independent molecule in the asymmetric unit but complex **3-3** has two, reference isomers **3-3(i)** and **3-3(ii)**, as for complex **3-1**. More importantly, complex **3-4** (Figure 3.3) crystallizes in the cubic space group $P2_13$, which is the main difference from the other complexes, the molecules have strict C_3 symmetry. Similar crystallographic parameters can be found in the Table 3.1 and Table 3.2 or the paper published in Inorganic Chemistry.[8]

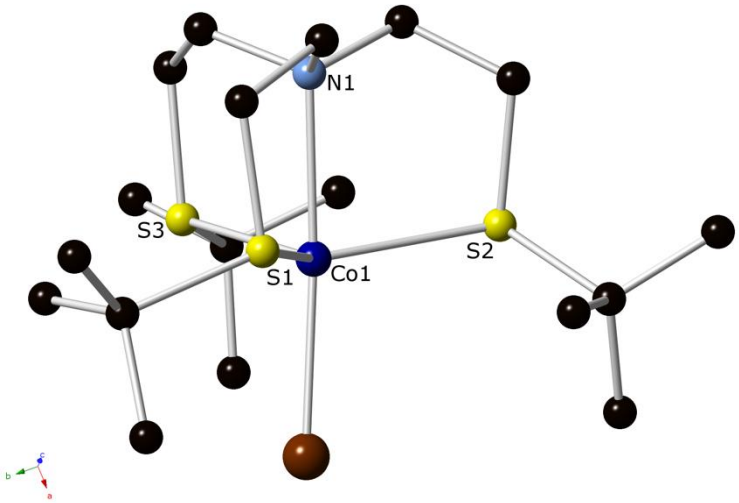

Figure 3.2. A view of the molecular structure for complexes **3-2** and **3-3**. Cl/Br – brown; C – black; H atoms and counter-ions were omitted for clarity.

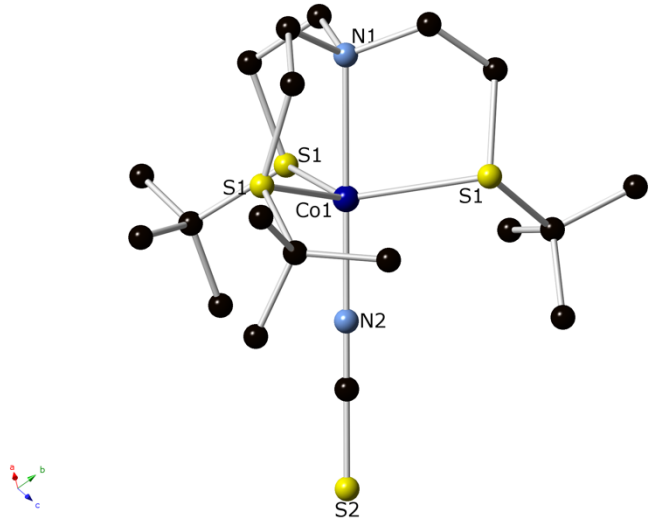

Figure 3.3. A view of the molecular structure for complex **3-4**. C – black; H atoms and counter-ions were omitted for clarity.

3.3.3 Magnetic Studies

3.3.3.1 Direct current magnetic susceptibility studies

The thermal variation of the molar magnetic susceptibility ($\chi_M T$) for complexes **3-1** to **3-4** are plotted in Figure 3.4 and Figure 3.5, respectively. $\chi_M T$ has the same behavior for the four complexes.

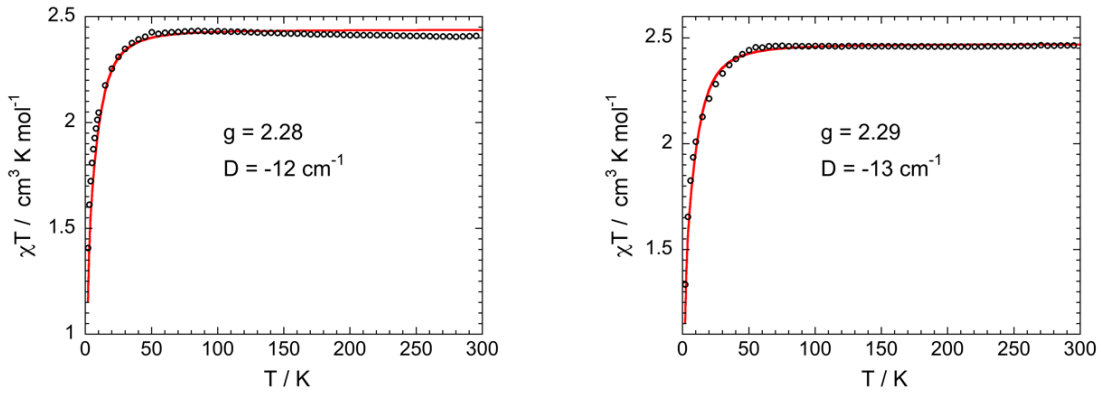

Figure 3.4. Temperature dependence of the χT product (○ (exp), — (best fit)) for complexes **3-1** (left) and **3-2** (right).

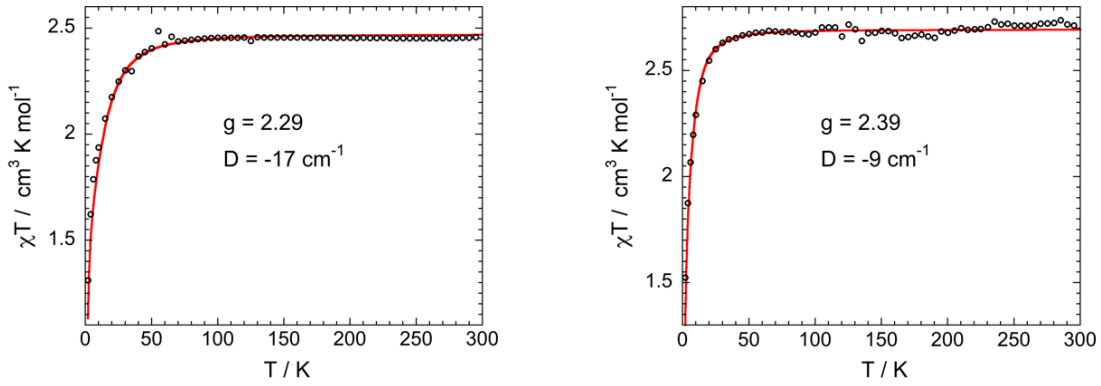

Figure 3.5. Temperature dependence of the χT product (○ (exp), — (best fit)) for complexes **3-3** (left) and **3-4** (right).

The χT product is constant between room temperature and ca. 50 K with values close to 2.44, 2.46, 2.46 and 2.69 $cm^3mol^{-1}K$ for complexes **3-1** to **3-4** respectively, as expected for a $S = 3/2$ spin moment with g-values (considered to be isotropic) equal to 2.28, 2.20, 2.20 and 2.39 (Table 3.3). Below 50 K, $\chi_M T$ collapses to 1.41, 1.34, 1.31, and 1.52 $cm^3mol^{-1}K$ for

complexes **3-1** to **3-4**, respectively indicating the presence of magnetic anisotropy (ZFS of the M_s = ±1/2 and ±3/2 sub-levels).

Table 3.3. ZFS parameters *D* and Landé *g*-factor from $\chi_M T$ fit for complexes **3-1** to **3-4**.

Complexes	3-1	3-2	3-3	3-4
[a] *D* (+/–)	12	13	17	9
g	2.28	2.29	2.29	2.39

[a] in wavenumbers (cm^{-1}), the sign (+/–) cannot be confirmed here.

3.3.3.2 Magnetization versus dc magnetic field studies

The magnetization *vs.* the applied magnetic field for complexes **3-1** to **3-4** are plotted in Figure 3.6 to Figure 3.9, respectively, in the form of M = f($\mu_0 H$) and M = f(($\mu_0 H/T$). They have similar behavior for the four complexes.

To quantify the magnitude of the ZFS parameter, we fitted the magnetic data using the spin Hamiltonian $\widehat{H} = g\mu_B \hat{S} \cdot \vec{H} + D\left[\hat{S}_z^2 - \frac{S_T(S_T+1)}{3}\right] + E(\hat{S}_x^2 - \hat{S}_y^2)$ for S = 3/2 where $\hat{S}, \hat{S}_x, \hat{S}_y, \hat{S}_z$ are spin operators, $\vec{H}$ is the applied magnetic field vector, g is the Landé factor that was assumed to be scalar, μ_B is the Bohr Magneton, D and E are the axial and rhombic ZFS parameters respectively. We assume that the rhombic parameter E is zero for complex **3-4** because of the presence of an exact C_3 principal symmetry axis, but for complexes **3-1**, **3-2** and **3-3**, their parameters of E are non-zero. We, however, assumed that E is zero when performing the fit in order to avoid overparametrezation. Then the magnetization data were fitted with the g and D values free leading to the parameters in Table 3.4 for complexes **3-1** to **3-4**. These data suggest that the magnetic anisotropy is of the Ising-type *i.e.* the M_s = ±3/2 sub-levels lie lower in energy than the ±1/2 ones and there is an easy axis of magnetization. It is not possible to obtain a good fit of the data with positive D values.

Table 3.4. ZFS parameters *D* and Landé *g*-tensor from M = f(($\mu_0 H$) fit for complexes **3-1** to **3-4**.

Complexes	3-1	3-2	3-3	3-4
[a] *D*	–19.9	–21.4	–20.2	–11.0
g	2.43	2.42	2.39	2.48

[a] in wavenumbers (cm^{-1}).

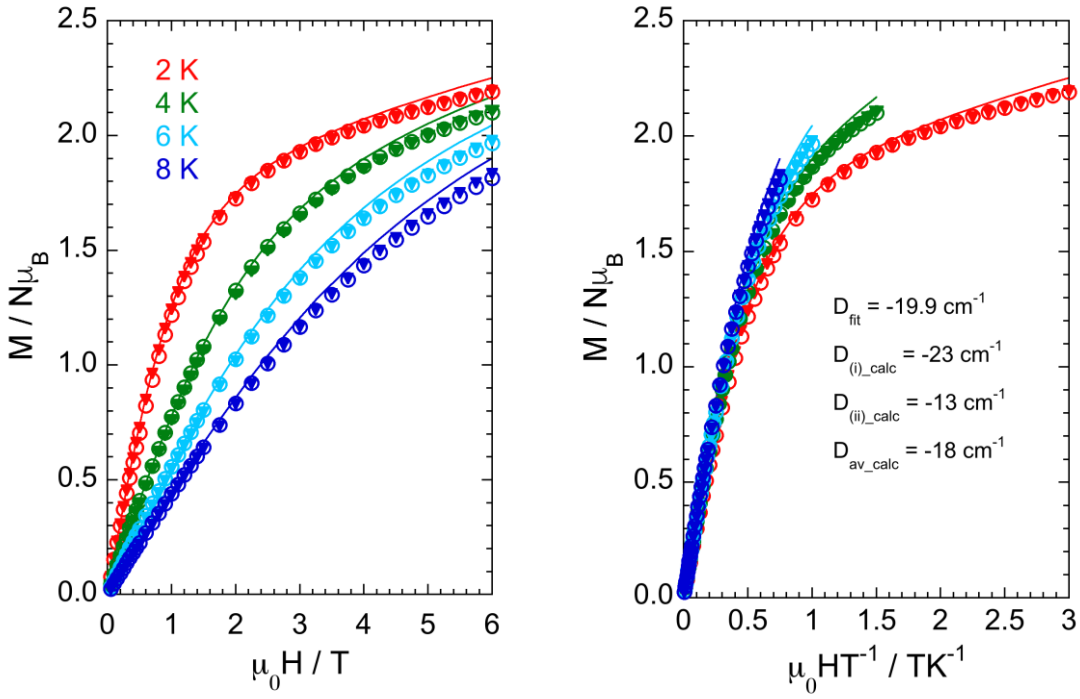

Figure 3.6. Field dependent magnetization at variable temperatures; (○) experimental data; (—) fit with the best *D* and *g* parameters; (▼) average of the calculated magnetization considering *D* values from *ab initio* calculations (see below) for complex **3-1**.

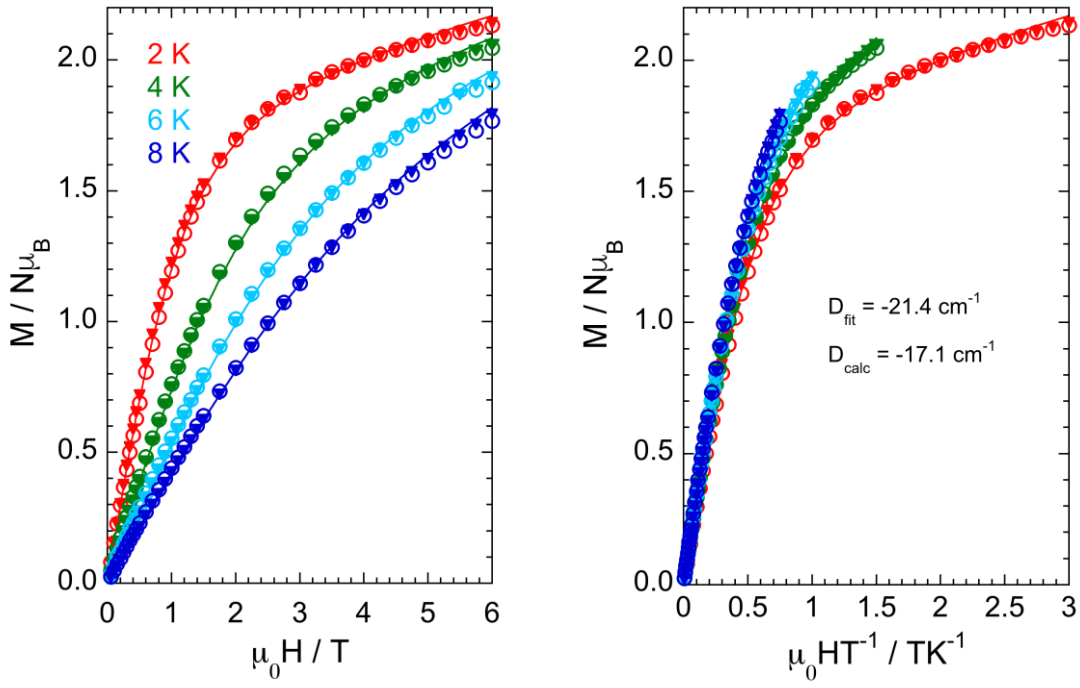

Figure 3.7. Field dependent magnetization at variable temperatures; (○) experimental data; (—) fit with the best *D* and *g* parameters; (▼) average of the calculated magnetization considering *D* values from *ab initio* calculations (see below) for complex **3-2**.

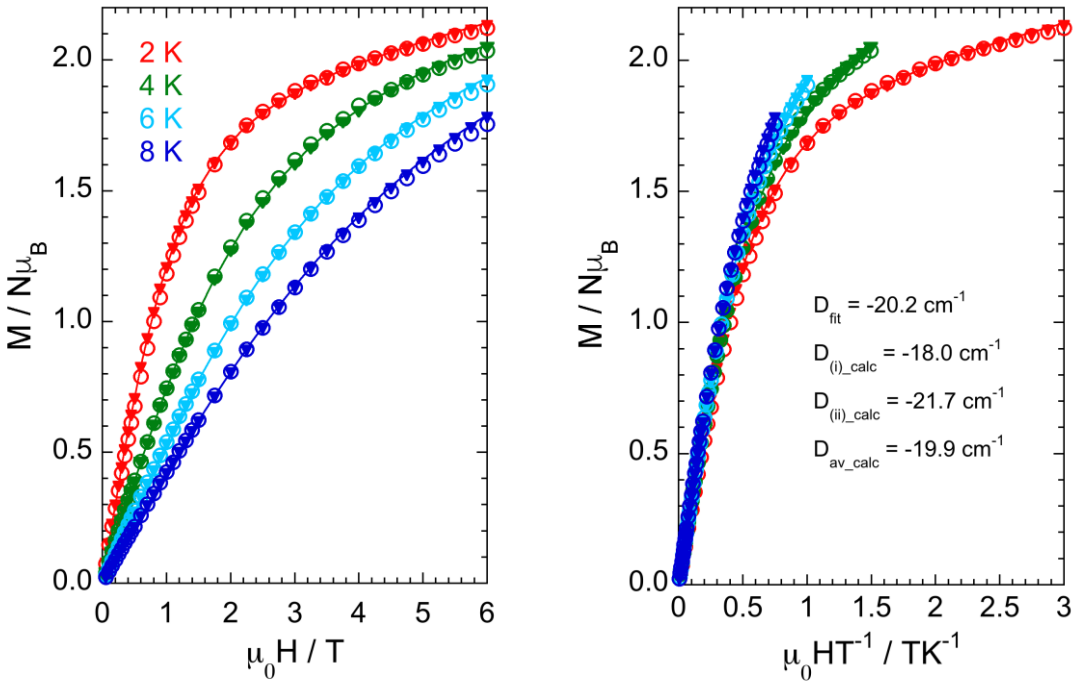

Figure 3.8. Field dependent magnetization at variable temperatures; (○) experimental data; (—) fit with the best *D* and *g* parameters; (▼) average of the calculated magnetization considering *D* values from *ab initio* calculations (see below) for complex **3-3**.

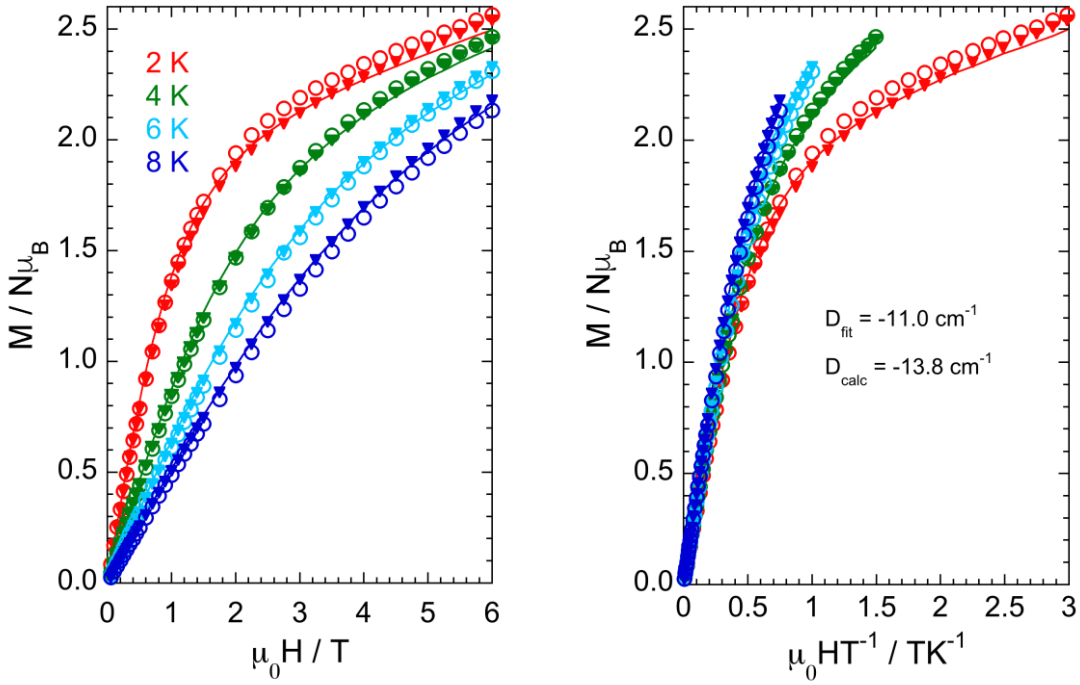

Figure 3.9. Field dependent magnetization at variable temperatures; (○) experimental data; (—) fit with the best *D* and *g* parameters; (▼) average of the calculated magnetization considering *D* values from *ab initio* calculations (see below) for complex **3-4**.

3.3.3.3 Electron paramagnetic resonance studies

In order to validate the magnetization results, we performed a powder EPR study at several frequencies, at different temperatures for the 460 GHz frequency for complex **3-1**. Unfortunately, the quality of the recorded spectra was rather poor. In addition, no spectra could be obtained for the other complexes, perhaps due to non-resonant absorption of the microwave power by the sulfur ligand. Thus, only a few transitions could be identified and the resulting information on the magnetic anisotropy of the system is limited. At the lowest temperature, only one signal is observed at low frequencies corresponding to an effective *g*-value of 7.05 (Figure 3.10). With the increase of the frequency, this signal splits in two components of comparable intensity, with effective *g*-values of $g_{1\text{eff}}$ = 7.14 and $g_{2\text{eff}}$ = 6.95 respectively. These two signals originate from the ground energy level (M_s = –3/2) as their intensity decreases with the increase of temperature. Conversely, another signal appears at temperature larger than 5 K; it corresponds to an effective *g*-value of $g_{3\text{eff}}$ = 3.18. From the rough temperature dependence performed (measurements at 5, 15, 25 and 40 K), the signal intensity goes through a maximum around 25 K with an uncertainty of ±10 K (Figure 3.11). This signal, coming from an excited level, is attributed to a transition inside the M_s = ±1/2 levels because it can be followed with an effective *g* description. As no other signal could be surely identified, it is not possible to extract the parameters governing the magnetic anisotropy directly from the EPR spectra. Thus, we limited the analysis to checking the compatibility with the resonances expected using the values obtained from *ab initio* calculations (see below). Fixing the *g*-values, according to the magnetic measurements, to g_x = g_y = 2.2 and g_z = 2.4, we find that $g_{1\text{eff}}$ corresponds to $|E/D|$ = 0.09, close to the values obtained from the *ab initio* calculations. Conversely, for the same set of fixed g-values, $g_{2\text{eff}}$ corresponds to $|E/D|$ = 0.18, far from the calculated values. However, both signals have comparable intensities, pointing towards signals associated to the different molecules present in the cell; this may correspond to the two different isomers **3-1(i)** and **3-1(ii)**. Finally, the HFEPR study allows determining a minimum value for the axial anisotropy parameter $|D|$, due to the absence of new signals (up to 662 GHz): $|D| > 15$ cm^{-1}.

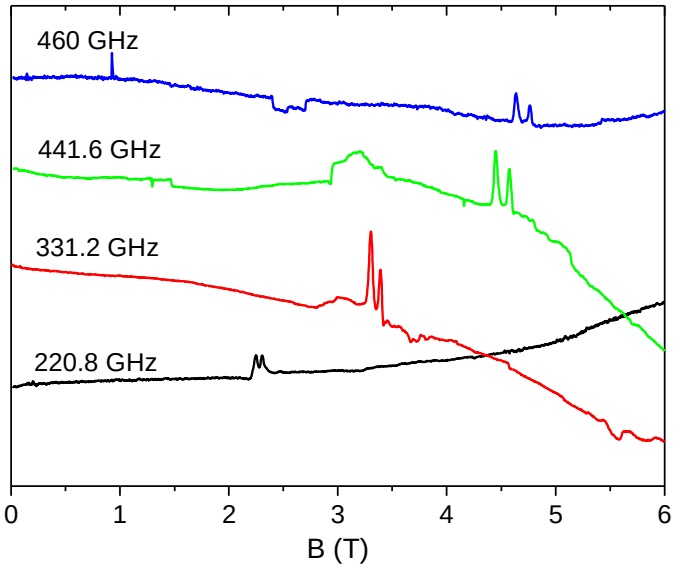

Figure 3.10. Powder EPR spectra of **3-1** recorded at 5 K with four frequencies, showing the signals corresponding to g_{1eff} and g_{2eff}.

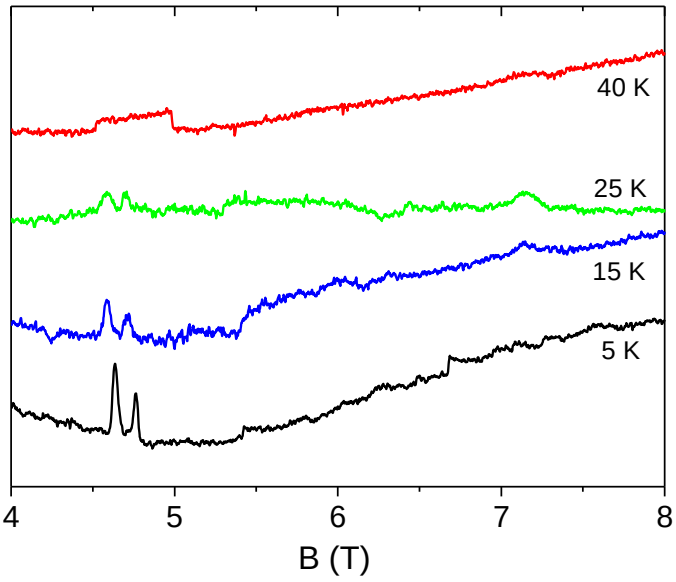

Figure 3.11. Powder EPR spectra of **3-1** recorded at 460 GHz with four different temperatures. At 5 K, only the signals corresponding to g_{1eff} and g_{2eff} are visible (at 4.7 and 4.8 T respectively). At higher temperature, a third signal can be followed, corresponding to g_{3eff} (at 7.2 T).

3.3.3.4 Alternating current magnetic susceptibility studies

Field optimization experiments at low temperature were carried out. The dynamic magnetic properties of these four complexes are similar, we describe the complexes **3-1** and **3-2** in more details. Some magnetic parameters extracted for these complexes can be found in Table 3.5, Table 3.6 and Table 3.7.

The fit of the $\chi' = f(\nu)$, $\chi'' = f(\nu)$ and $\chi'' = f(\chi')$ were carried out using a home-made program as aforementioned in Chapter 2.

Complex 3-1

Field optimization experiment was carried out at T = 2 K with an applied dc magnetic field range 0 – 2400 Oe for complex **3-1** (Figure 3.12 top). Under an applied zero dc magnetic field, no maximum in the frequency-dependent ac susceptibility plot could be observed. Upon increasing the field (200 Oe), a maximum appears around 50 Hz. It shifts towards low frequency when increasing the field up to 2400 Oe (Figure 3.12 top). The variation of the frequency value of the maximum of χ'' *vs.* $\mu_0 H$ shows that the optimum applied dc magnetic field is between 2000 and 2400 Oe (Figure 3.12 bottom). We thus performed the ac measurements for $\mu_0 H$ = 2000 Oe (Figure 3.13), which show the variation of the in-phase and the out-of-phase components of the ac susceptibility *vs.* frequency at different temperatures. As expected for SMMs, the relaxation of the magnetization (maximum of the plots, Figure 3.13 left) slows down upon decreasing the temperature. It is worth noting that the plots are wide and dissymmetric suggesting the presence of more than one relaxation process.

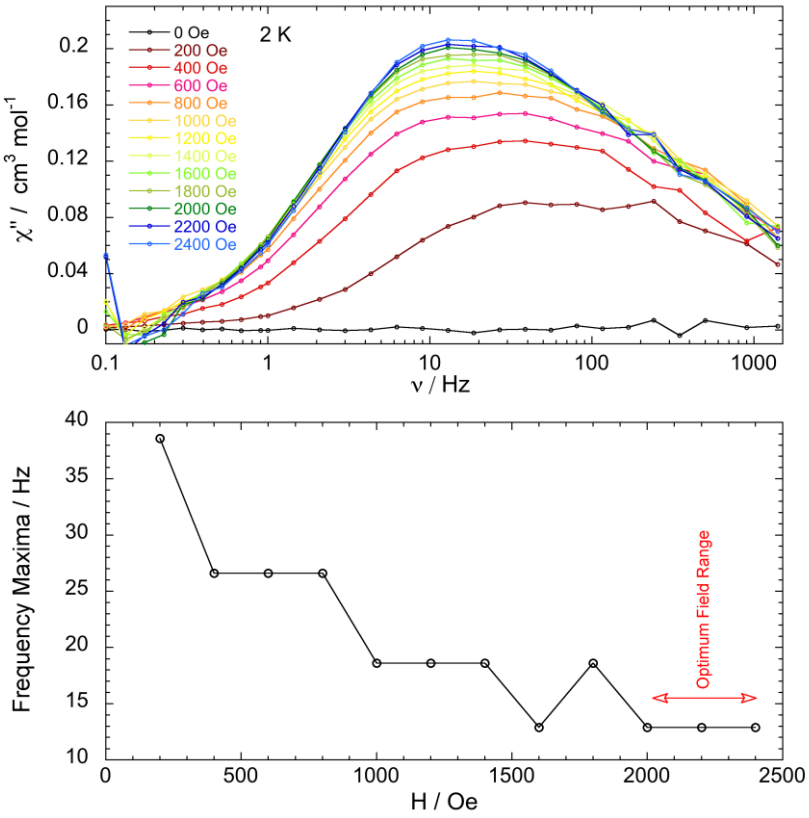

Figure 3.12. Out-of-phase susceptibility measurements at 2 K with a frequency range from 1 to 1500 Hz under various applied dc magnetic fields (top) and plot of frequency maxima *vs.* applied dc magnetic fields (bottom) for complex **3-1**.

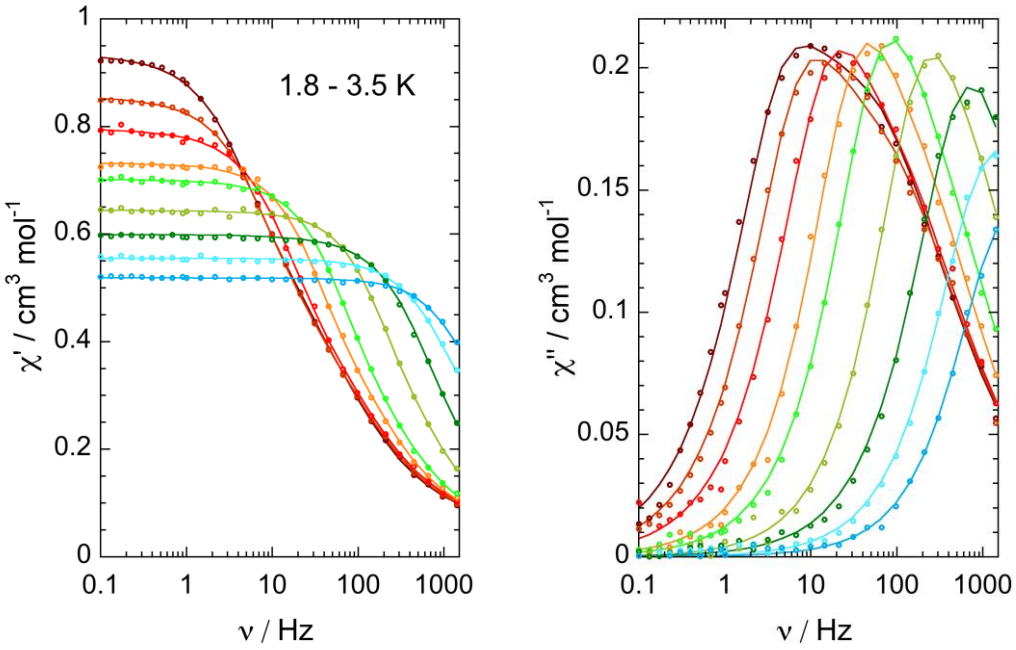

Figure 3.13. Frequency dependent in-phase and out-of-phase ac magnetic susceptibilities (○ (exp), — (fit)) for complex **3-1** under an applied dc magnetic field of 2000 Oe.

The Cole-Cole plots for complex **3-1** at 2000 Oe were obtained with a temperature range 1.80 – 3.50 K (Figure 3.14). Using the fit procedure of the generalized Debye model[9, 10], The ac data can be deconvoluted into two series of curves (Figure 3.15 and Figure 3.17) leading to two Cole-Cole plots associated to the two relaxation processes (Figure 3.16 and Figure 3.18). This allows extracting the relaxation times (τ) and their distribution (α) for each temperature (Table 3.5).

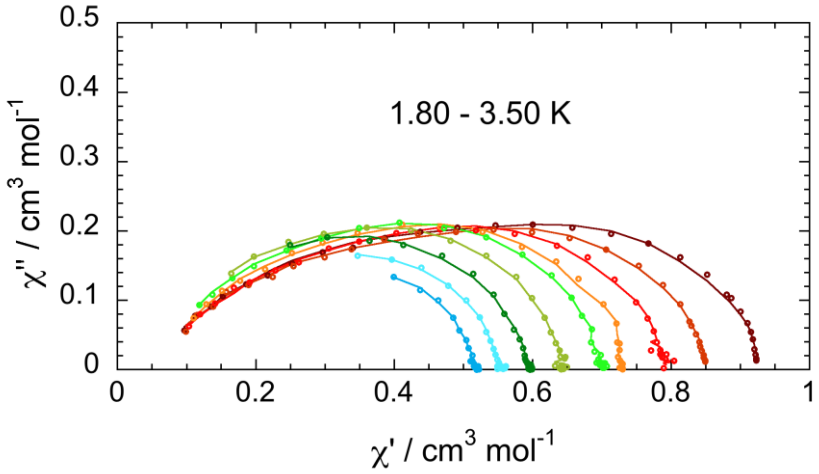

Figure 3.14. Cole-Cole plots (○ (exp), – (fit)) for complex **3-1** under an applied dc magnetic field of 2000 Oe.

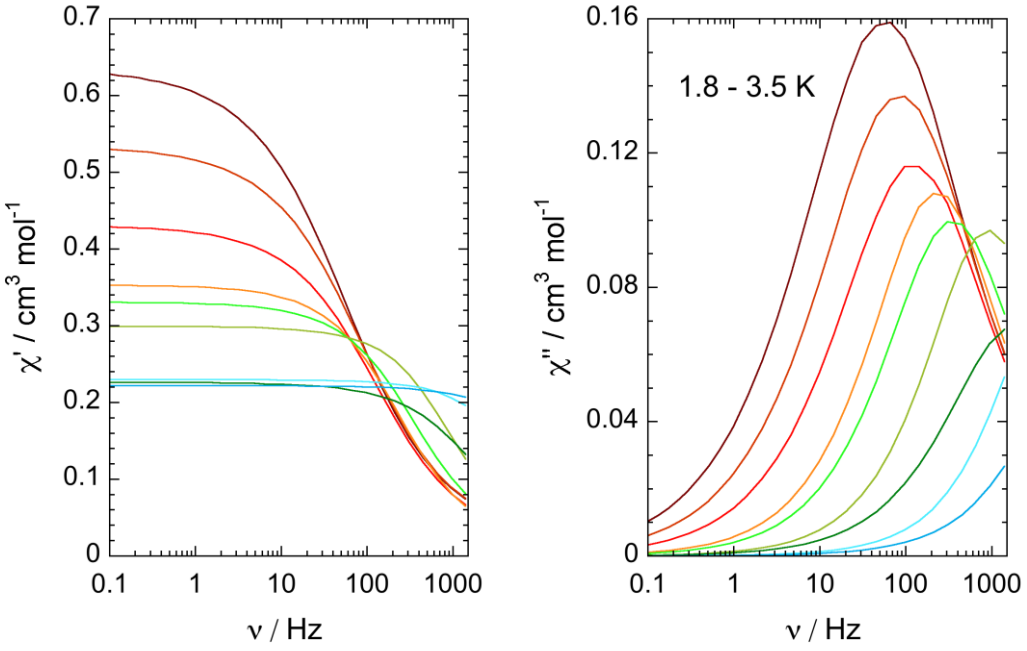

Figure 3.15. Deconvoluted frequency dependent in-phase and out-of phase ac magnetic susceptibilities for complex **3-1** under an applied dc magnetic field of 2000 Oe at difference temperatures for the fast processes.

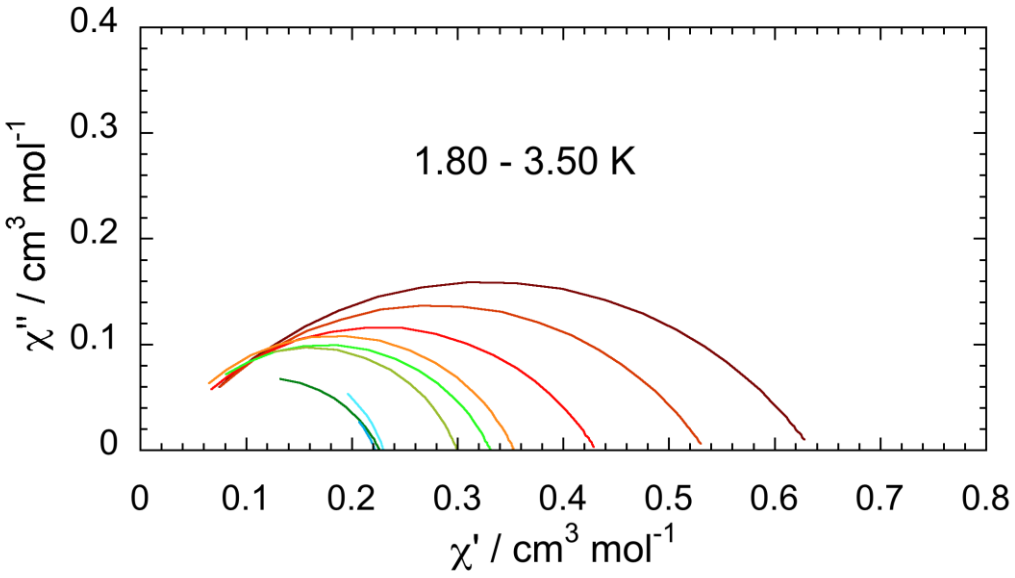

Figure 3.16. Deconvoluted Cole-Cole plots for complex **3-1** under an applied dc magnetic field of 2000 Oe at difference temperatures for the fast processes.

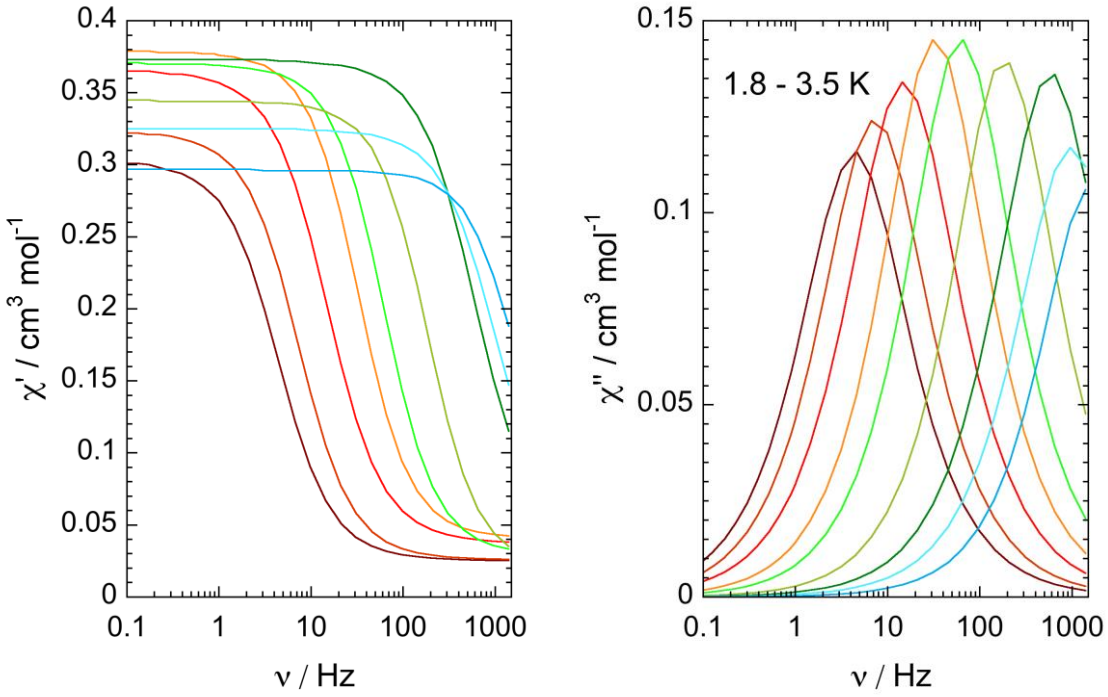

Figure 3.17. Deconvoluted frequency dependent in-phase and out-of phase ac magnetic susceptibilities for complex **3-1** under an applied dc magnetic field of 2000 Oe at difference temperatures for the slow processes.

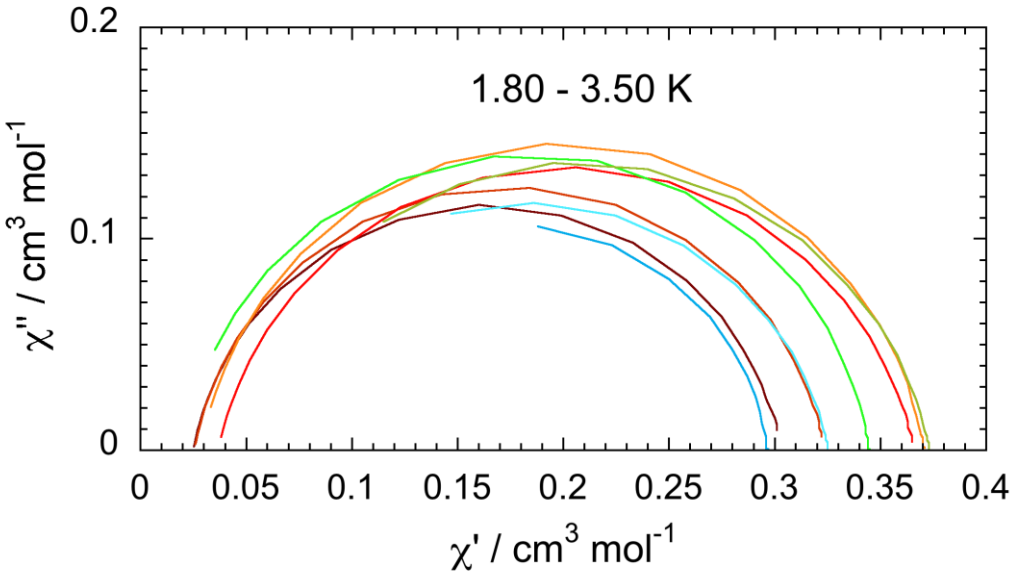

Figure 3.18. Deconvoluted Cole-Cole plots for complex **3-1** under an applied dc magnetic field of 2000 Oe at difference temperatures for the slow processes.

Table 3.5. Cole-Cole fit parameters under an applied dc magnetic field of 2000 Oe for complex **3-1**.

Complex	T / K	χ_0	χ_s	α	τ
	1.80	0.60655	0.04996	0.11613	0.035960405
	2.00	0.64742	0.05104	0.11311	0.021673529
	2.25	0.73203	0.07352	0.13037	0.010603178
	2.375	0.75822	0.08038	0.09804	0.004831523
3-1(slow)	2.50	0.74157	0.05737	0.10427	0.002552686
	2.75	0.68920	0.04134	0.09190	0.000862512
	3.00	0.74640	0.08366	0.12477	0.000271624
	3.25	0.65083	0.08264	0.12318	0.000162255
	3.50	0.59318	0.10883	0.08033	0.000100015
	1.80	1.27049	0.04323	0.39044	0.002806275
	2.00	1.06812	0.04504	0.37278	0.001863941
	2.25	0.86153	0.03648	0.34488	0.001275364
	2.375	0.70654	0.03464	0.27036	0.000690317
3-1(fast)	2.50	0.66204	0.03677	0.27586	0.000454918
	2.75	0.59858	0.04188	0.22443	0.000176098
	3.00	0.45248	0.01175	0.29063	8.39391E-05
	3.25	0.45978	0.00600	0.19207	2.74887E-05
	3.50	0.44403	0.01211	0.24820	9.30660E-06

Fitting the linear parts of the ln(τ) = f(1/T) plots (Figure 3.19) provides the magnitude of the effective energy barriers for the reorientation of the magnetization U_{eff} that is found equal to 46.1 K (32 cm^{-1}) and τ_0 is 2.1 × 10^{-11} s for the slow process and 30.0 K (20.8 cm^{-1}) and τ_0 is 2.1 × 10^{-8} s for the fast process (Table 3.6). The effective energy barrier is weaker for the fast process because one may reasonably assume that the QTM and/or the direct mechanisms contribute more than the Orbach one. The U_{eff} value for the slow process is probably not very accurate because there are only three points to fit, it is however larger than for the fast one. It is possible to assign the two relaxation processes to the two independent molecules in the unit cell, especially that, theoretical calculations give D values equal to –13 and –23 for the isomers **3-1(ii)** and **3-1(i)** respectively. However, the "optimum" applied dc magnetic field may not be optimum for the two independent molecules. For isomer **3-1(ii)** the field is probably not large enough to completely avoid the QTM mechanism to remain active. In such a case, the fast process may be the result of the relaxation of one of the molecules (isomer **3-1(ii)** that has the small |D| value), while the slow one is due to the contribution of the two molecules. This interpretation may explain why the slow process still has contribution that is temperature independent due to the fact that the applied dc magnetic field is not large enough for the molecule with the weak |D| value. We did not attempt to fit the data considering the other relaxation mechanisms.

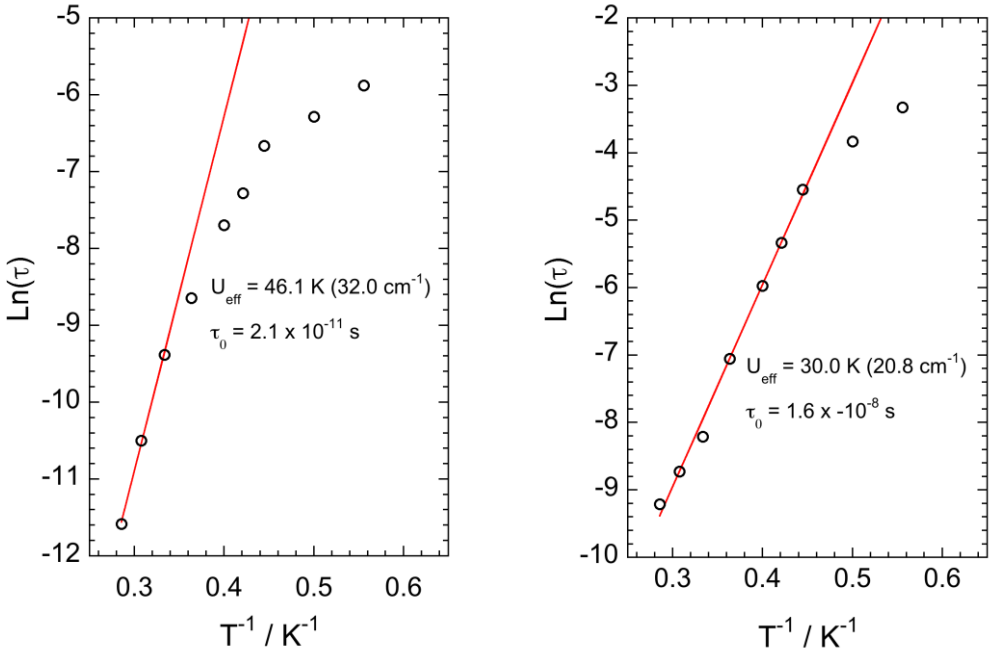

Figure 3.19. ln(τ) = f(1/T) plot (○ (exp), — (linear fit)) for the relaxation processes (left: slow; right: fast) for complex **3-1** under an applied dc magnetic field of 2000 Oe.

Table 3.6. Magnetic parameters for complexes **3-1** to **3-4**.

Complexes	3-1	3-2	3-3	3-4
[a] D	–19.9	–21.4	–20.2	–11.0
[b] g	2.43	2.39	2.39	2.48
[c] OFR	2000 – 2400	3000 – 3600	3000 – 4000	1000 – 1800
[d] U_{eff}	32	—	21.1	19.4
[e] τ_0	2.1×10^{-11}	—	4.5×10^{-8}	2.0×10^{-9}

[a] ZFS parameter D in wavenumbers (cm^{-1}); [b] Landé g-tensor; [c] Optimum Field Range in Ørsted (Oe); [d] effective energy barriers in wavenumbers (cm^{-1}). [e] pre-exponential factor in seconds (s).

Complexes 3-2, 3-3 and 3-4

The dynamic magnetic properties of these three complexes are similar, we describe the data of complex **3-2** in more details.

Field optimization experiment was carried out at T = 2 K with an applied dc magnetic field range 0 – 4000 Oe for complex **3-2** (Figure 3.20 top). Under zero dc magnetic field, no maximum in the frequency-dependent ac susceptibility plot could be observed, but upon increasing the field, the maximum appears, as shown in Figure 3.20 top. The variation of the frequency value of the maximum of χ'' *vs.* $\mu_0 H$ shows that the optimum applied dc magnetic field is between 3000 and 3400 Oe (Figure 3.20 bottom). We thus performed the ac measurements for $\mu_0 H$ = 3000 Oe (Figure 3.21). As expected for SMMs, the relaxation of the magnetization (maximum of the χ'' plots, Figure 3.21 right) slows down upon decreasing the temperature.

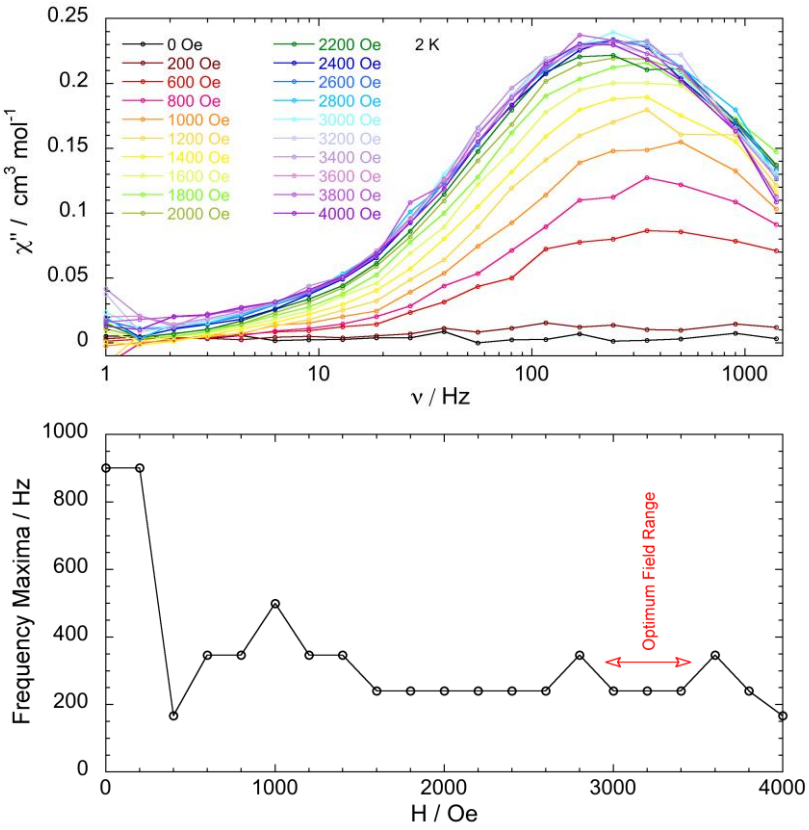

Figure 3.20. Out-of-phase susceptibility measurements at 2 K with a frequency range from 1 to 1500 Hz under various applied dc magnetic fields (top) and plot of frequency maxima *vs.* applied dc magnetic fields (bottom) for complex **3-2**.

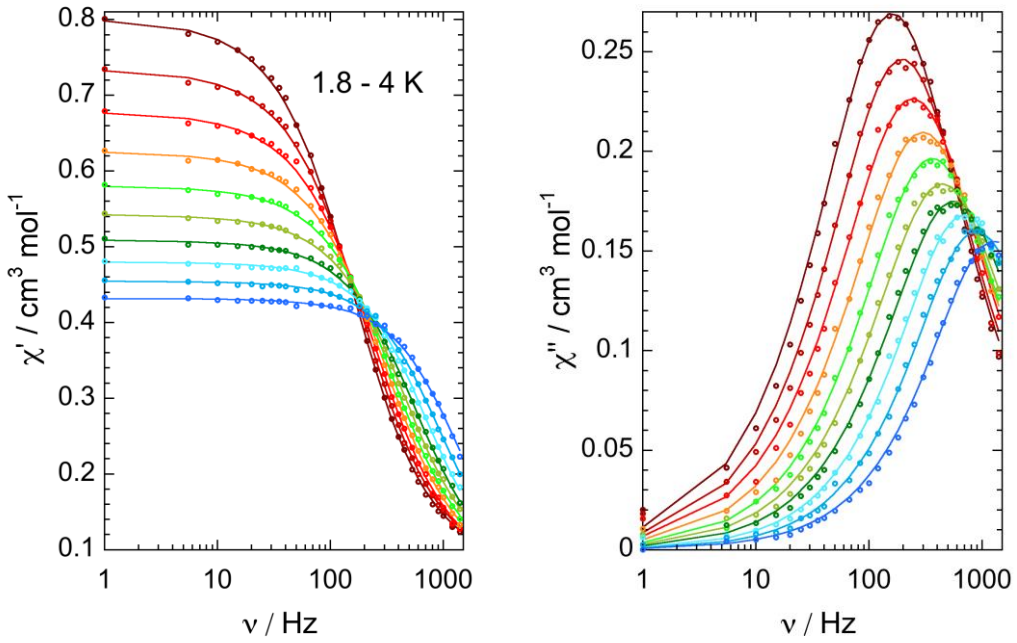

Figure 3.21. Frequency dependent in-phase and out-of-phase ac magnetic susceptibilities (○ (exp), — (fit)) for complex **3-2** under an applied dc magnetic field of 3000 Oe.

The Cole-Cole plots for complex **3-2** at 3000 Oe were obtained with a temperature range 1.80 – 4.00 K (Figure 3.22). They were fitted using a generalized Debye model[9, 10] which allows extracting the relaxation times (τ) and their distribution (α) for each temperature (Table 3.7).

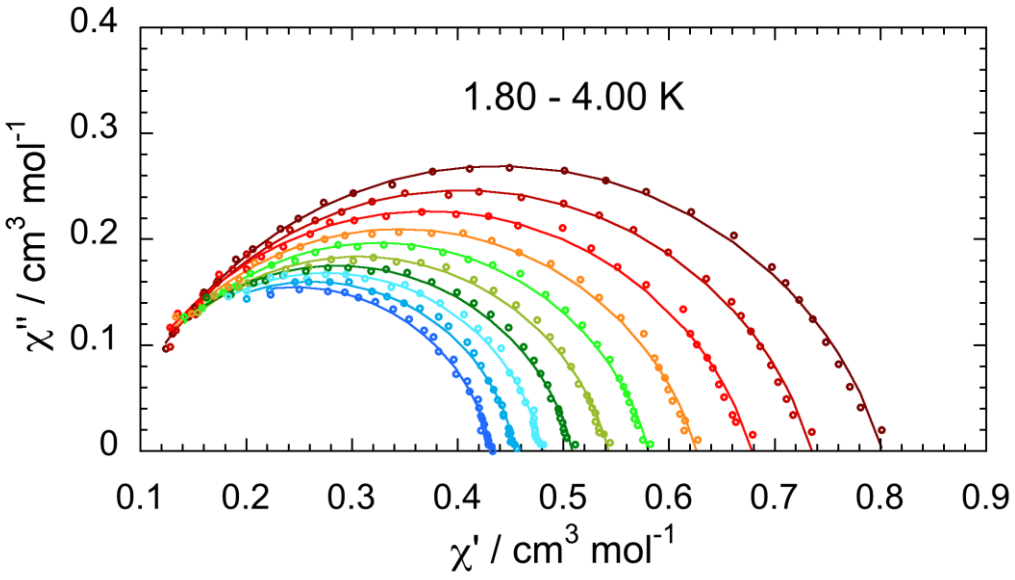

Figure 3.22. Cole-Cole plots (○ (exp), — (fit)) for complex **3-2** under an applied dc magnetic field of 3000 Oe.

Table 3.7. Cole-Cole fit parameters under an applied dc magnetic field of 3000, 3000 and 1600 Oe for complexes **3-2** to **3-4** respectively.

Complexes	T / K	χ_0	χ_s	α	τ
3-2	1.80	0.802019415	0.075391306	0.187801062	0.001003366
	2.00	0.735305411	0.073996102	0.184656074	0.000817578
	2.25	0.678669309	0.064270631	0.190685189	0.000653469
	2.50	0.626325808	0.066062582	0.181677628	0.000533317
	2.75	0.580800033	0.071138174	0.163385368	0.000441315
	3.00	0.542741505	0.069674761	0.159149990	0.000358516
	3.25	0.508934827	0.063853304	0.151311433	0.000282315
	3.50	0.479844332	0.071840615	0.122420071	0.000230888
	3.75	0.454514540	0.070289279	0.115851185	0.000177762
	4.00	0.431697651	0.058331282	0.117793690	0.000125724
3-3	1.80	0.828108381	0.103977443	0.298528199	0.001569637
	2.00	0.759930388	0.107651910	0.290507465	0.001352130
	2.25	0.692424449	0.121017605	0.254045335	0.001147989
	2.50	0.635029072	0.126932867	0.216448304	0.000931581
	2.75	0.588361244	0.137938498	0.159680125	0.000745154
	3.00	0.547282986	0.136508446	0.122685019	0.000544785
	3.25	0.510987074	0.132452132	0.087659721	0.000379869
	3.50	0.480294094	0.130926457	0.058723646	0.000261352
	3.75	0.453957836	0.108279505	0.055899585	0.000158243
	4.00	0.430627632	0.059220211	0.060070061	0.000087899
3-4	1.80	1.091520903	0.079200601	0.261360811	0.010142145
	2.00	0.935617913	0.112580386	0.130900252	0.002756536
	2.25	0.835310836	0.078552252	0.118864405	0.000546540
	2.50	0.746054140	0.055442273	0.033410814	0.000130196

It is worth noting that fitting the first three points of the ln(τ) = f(1/T) plot (Figure 3.23) for complex **3-2** provides the magnitude of the effective energy barriers for the reorientation of the magnetization U_{eff} that is found equal to 17.0 K (11.8 cm^{-1}) and τ_0 is 1.9 × 10^{-6} s (Table 3.6). Actually, there is no clear linear part showing that the relaxation in the 1.8 − 4 K temperature range has little contribution from an Orbach mecahnism and that other processes dominate such as the direct and the multiphonon Raman-like ones.[8, 11, 12]

It should be mentioned that for complex **3-4**, the ln(τ) = f(1/T) plot (Figure 3.31) is different from the complex **3-2** and **3-3**, probably because the rhombic ZFC parameter E = 0. The fit of the linear dependence leads to an effective energy barriers for the reorientation of the magnetization U_{eff} equal to 19.4 K (13.5 cm^{-1}) and τ_0 is 2.0 × 10^{-9} s (Table 3.6).

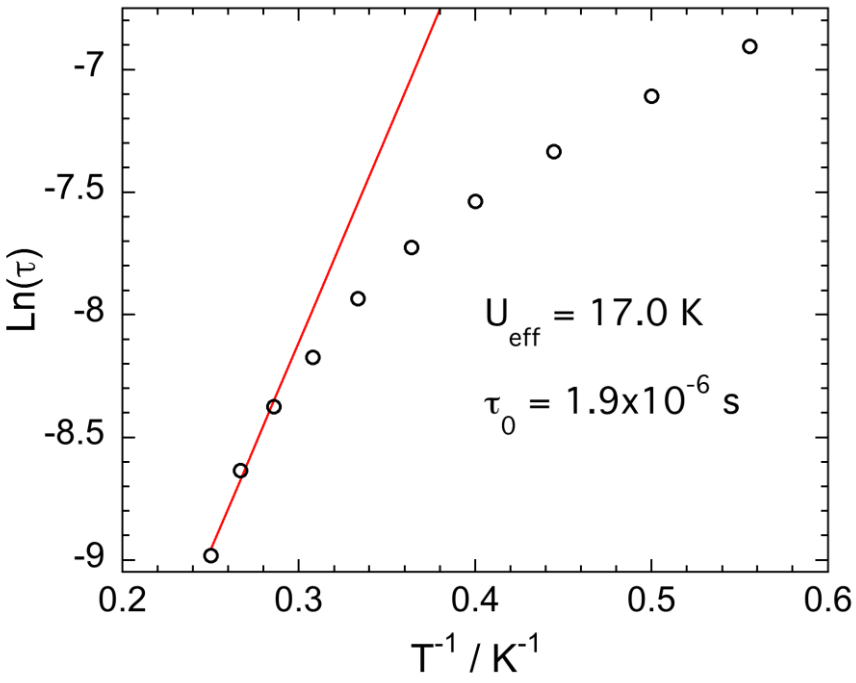

Figure 3.23. ln(τ) = f(1/T) plot (○ (exp), — (linear fit)) for the relaxation processes for complex **3-2** under an applied dc magnetic field of 3000 Oe.

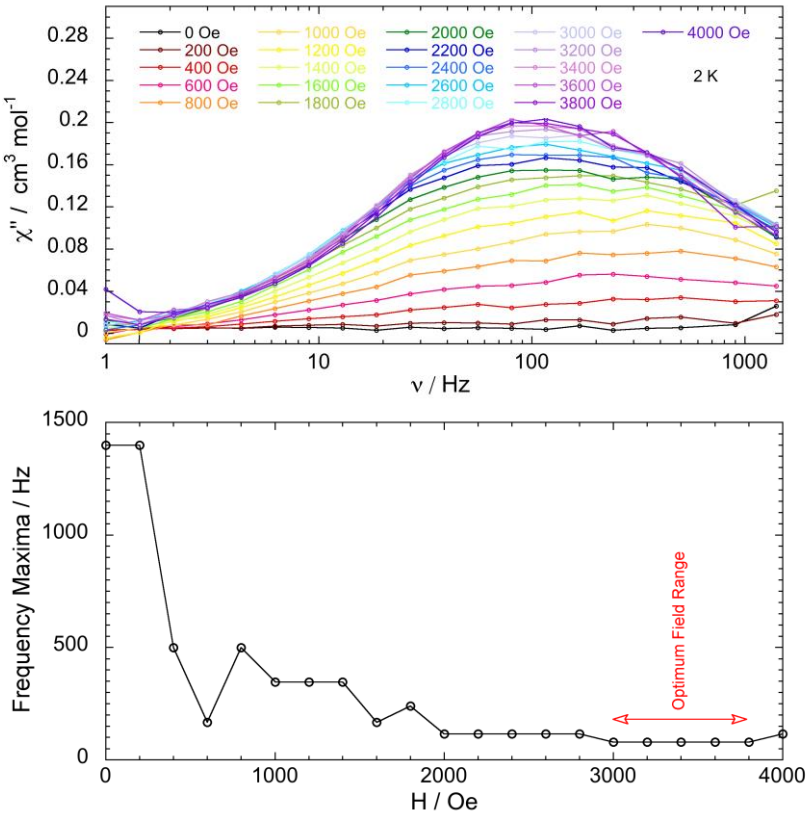

Figure 3.24. Out-of-phase susceptibility measurements at 2 K with a frequency range from 1 to 1500 Hz under various applied dc magnetic fields (top) and plot of frequency maxima *vs.* applied dc magnetic fields (bottom) for complex **3-3**.

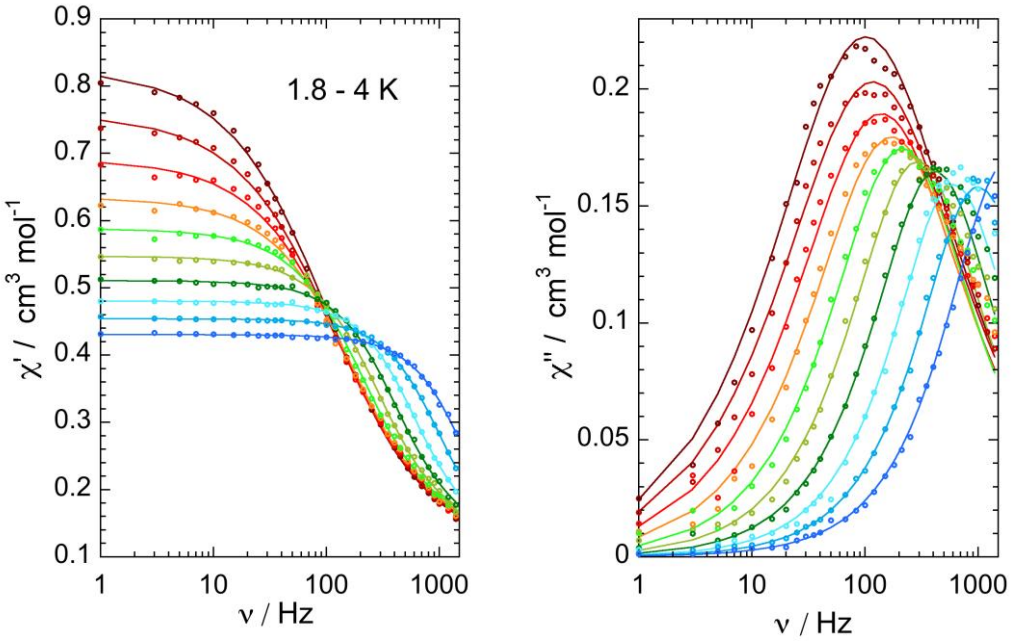

Figure 3.25. Frequency dependent in-phase and out-of-phase ac magnetic susceptibilities (○ (exp), — (fit)) for complex **3-3** under an applied dc magnetic field of 3000 Oe.

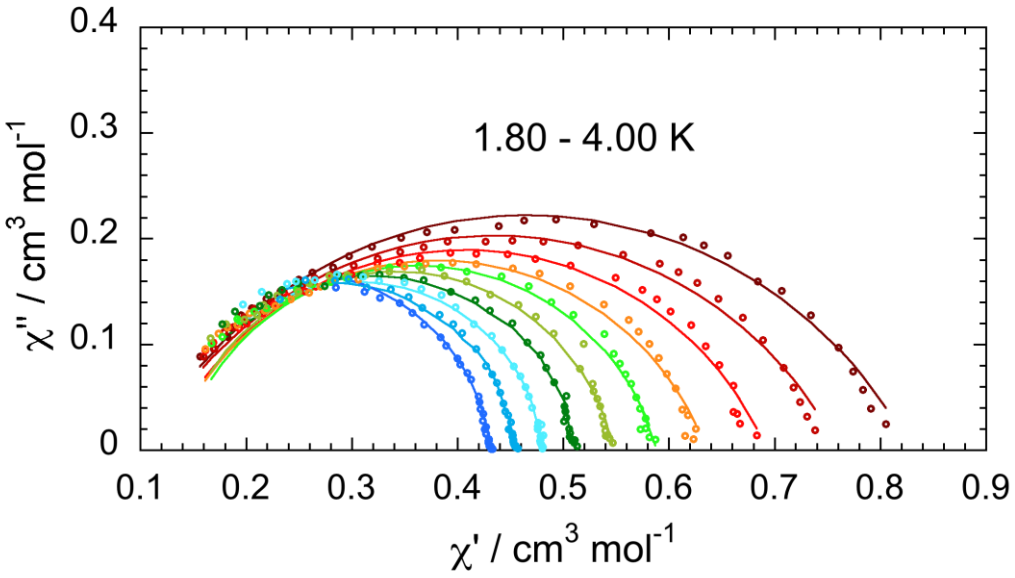

Figure 3.26. Cole-Cole plots (○ (exp), — (fit)) for complex **3-3** under an applied dc magnetic field of 3000 Oe.

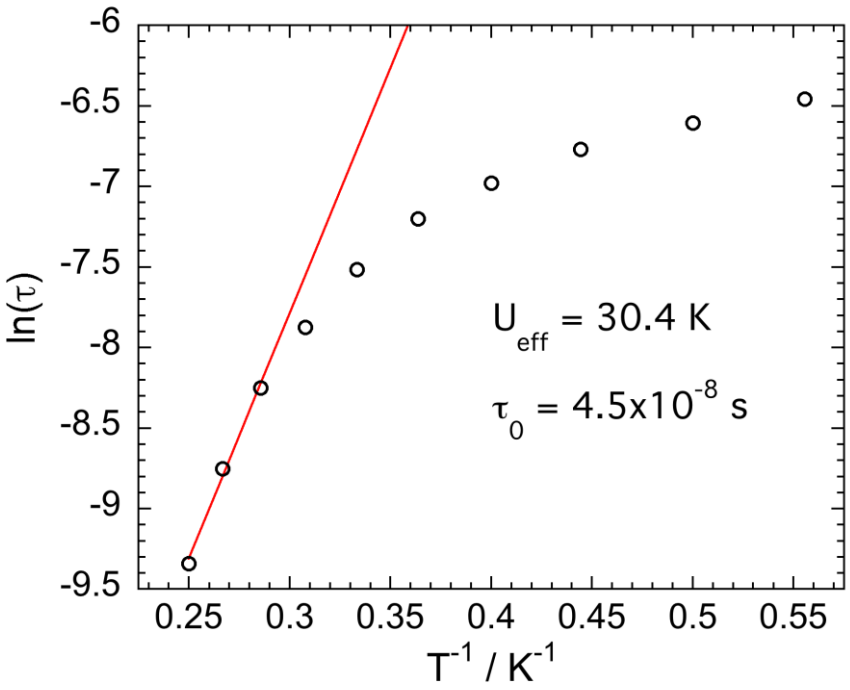

Figure 3.27. ln(τ) = f(1/T) plot (○ (exp), — (linear fit)) for the relaxation processes for complex **3-3** under an applied dc magnetic field of 3000 Oe.

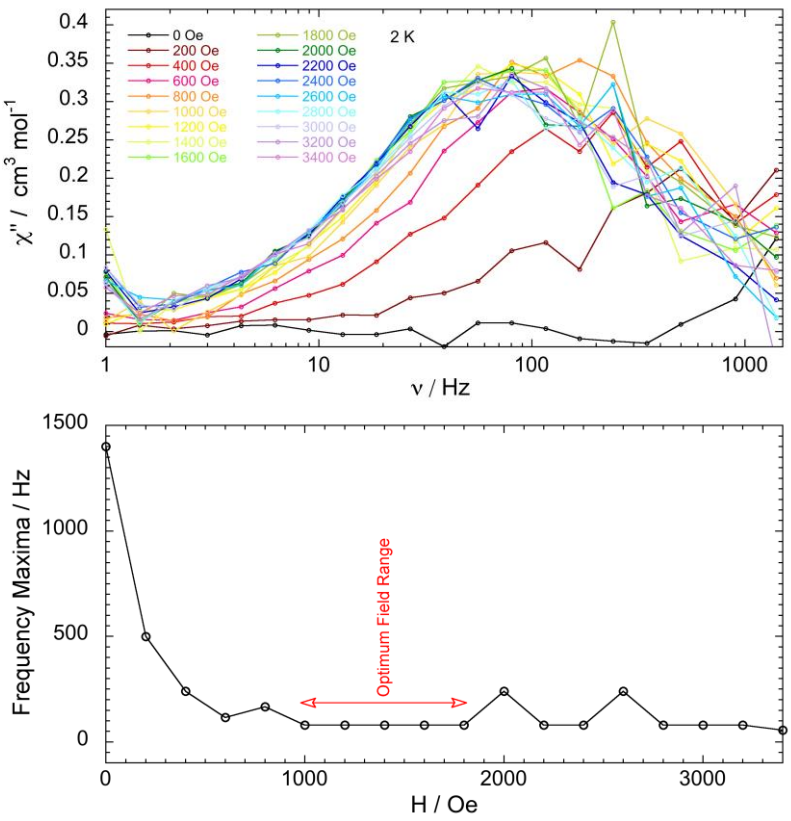

Figure 3.28. Out-of-phase susceptibility measurements at 2 K with a frequency range from 1 to 1500 Hz under various applied dc magnetic fields (top) and plot of frequency maxima *vs.* applied dc magnetic fields (bottom) for complex **3-4**.

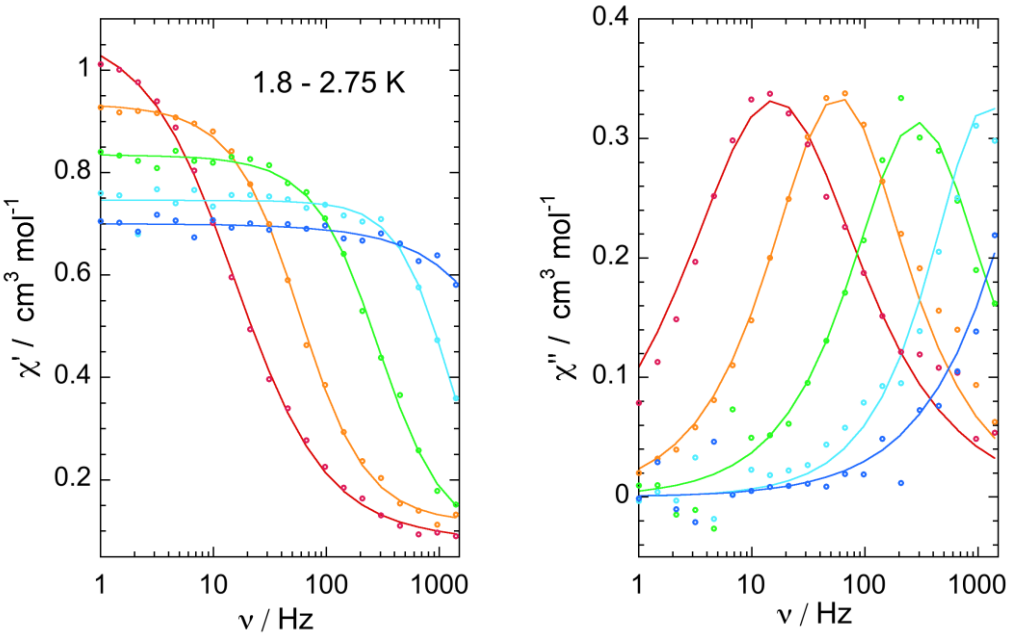

Figure 3.29. Frequency dependent in-phase and out-of-phase ac magnetic susceptibilities (○ (exp), — (fit)) for complex **3-4** under an applied dc magnetic field of 1600 Oe.

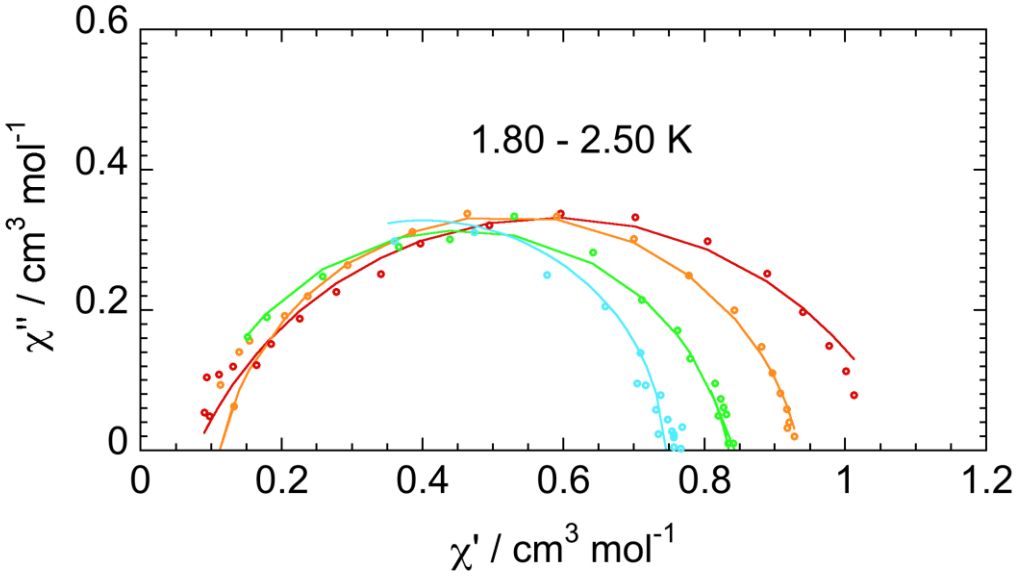

Figure 3.30. Cole-Cole plots (○ (exp), — (fit)) for complex **3-4** under an applied dc magnetic field of 1600 Oe.

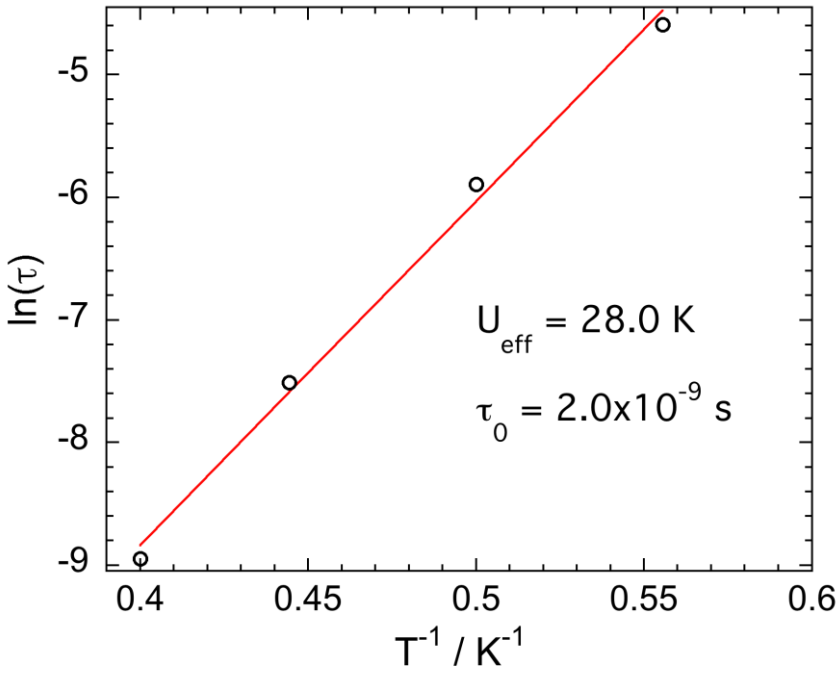

Figure 3.31. ln(τ) = f(1/T) plot (○ (exp), — (linear fit)) for the relaxation processes for complex **3-4** under an applied dc magnetic field of 1600 Oe.

3.3.3.5 Magnetization versus dc magnetic field hysteresis loops

To probe the SMM behavior of complex **3-1**, and to gain further insight into its low temperature behavior, single crystal magnetization measurements were performed using a Micro-SQUID[13, 14] instrument at temperatures ranging from 0.03 to 5 K. The field was aligned parallel to the easy axis of magnetization by using the transverse field method.[15] Opening of the hysteresis loops were observed below T = 2 K in the presence of a magnetic field (Figure 3.32 left), indicating that the complex exhibits slow relaxation of the magnetization. The effect of the QTM between the M_s = ±3/2 states is evidenced by the fast steps at zero dc magnetic field. The tunnel rate is very fast because even at the faster field sweep rate of 0.28 T/s the hysteresis loop remains closed at $\mu_0 H$ = 0 Oe, which is consistent with the results of the aforementioned ac studies. In order to see better the slow relaxation at non-zero dc magnetic field, we recorded hysteresis loops starting from M = 0, at 0.03 K, and with scan rates in the range of 0.004 – 0.280 T/s (Figure 3.32 right). As soon as a small field is applied, tunneling is blocked and a large amount of molecules are in the M_s = +3/2 state and this amount decreases slowly upon increasing the magnetic field, revealing a large SMM-type hysteresis. At higher fields, the M_s = +3/2 relaxes to the M_s = –3/2 state via the direct relaxation mechanism, emitting a phonon.

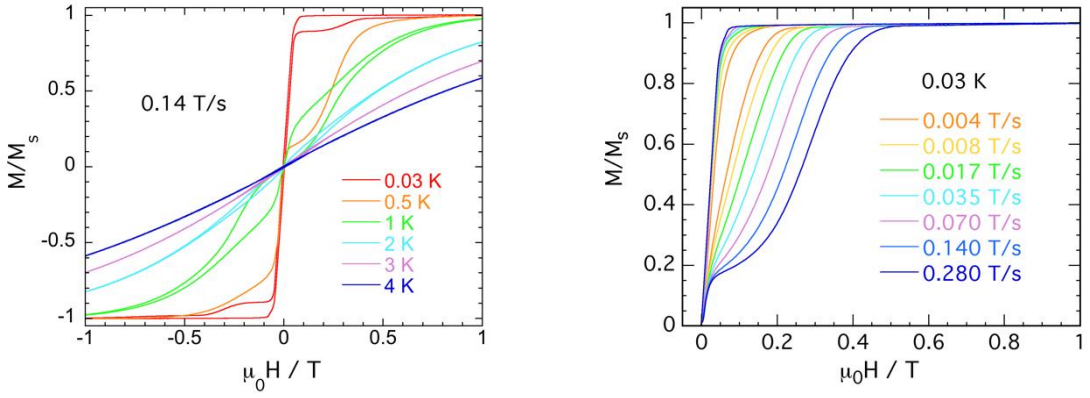

Figure 3.32. Magnetization *vs.* field on a single crystal of complex **3-1** with its easy axis aligned with the field at different temperatures (left) and at 0.03 K with different sweep rates (right).

3.4 Theoretical Calculations

Complex 3-1

Theoretical calculations were performed to validate the experimental values of *D* obtained, as it is not possible to distinguish between the magnetism of the two independent molecules. We used the experimental geometries for our study. The *ab initio* calculations were done using the two-step approach implemented in the MOLCAS code.[16-20] The values of *D* for the two isomers **3-1(i)** and **3-1(ii)** were found equal to –23.0 and –13.1 cm^{-1} respectively. The energy difference between the ground ($^4A_2$) and the first excited state ($^4A_1$) were found equal to 2719 and 3221 cm^{-1} for **3-1(i)** and **3-1(ii)** respectively. These energy gaps are coherent with a larger |*D*| value for isomer **3-1(i)**, as explained in the preceding chapter. The energy difference between $^4A_2$ and $^4A_1$ is mainly related to ΔE_1 (Figure 3.33), because the first excited state is obtained by an excitation between the two sets of degenerate orbitals separated by ΔE_1. This effect translated to a weaker energy difference in complexes that have larger equatorial metal-ligand (Co–S) distances. We, therefore, obtain a larger |*D*| value for [Co(NS$_3^{iPr}$)Cl]$^+$ (**3-1(i)**) than for [Co(NS$_3^{iPr}$)Cl]$^+$ (**3-1(ii)**) (–23.0 and –13.1 cm^{-1}, respectively). In addition to their size sulfur atoms possess π-donating character that reduces the energy differences between $^4A_2$ and $^4A_1$, bringing an additional negative contribution to *D*.

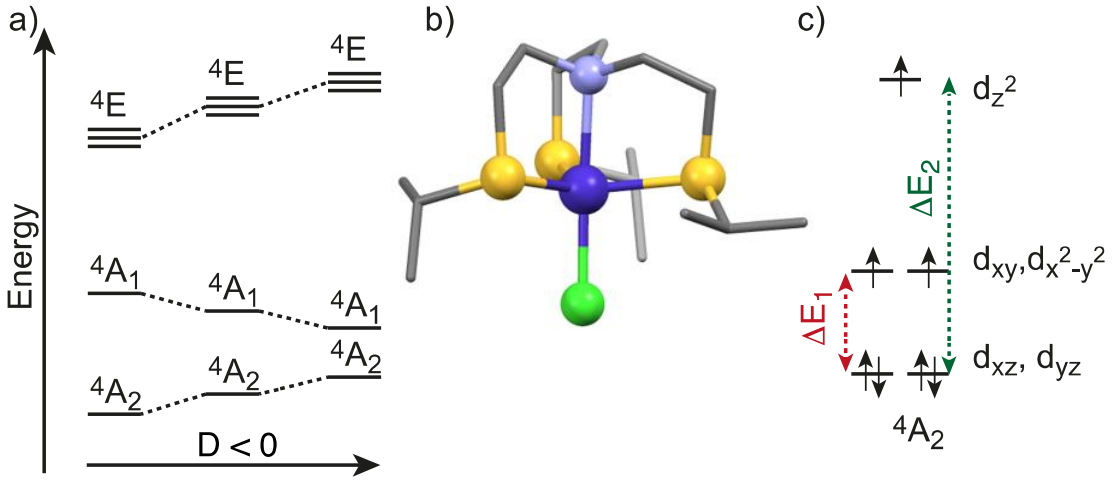

Figure 3.33. a) Schematic energy diagram of the lowest quadruplets for a trigonal bipyramidal Co^{II} complex; b) X-ray crystal structure of complex **3-1**: C – grey; N – lilac; S – yellow; Cl – green; H atoms and counter ions were removed for clarity; c) orbital energy diagram for a trigonal bipyramidal Co^{II} complex.

The difference in the magnitude of *D* for the two isomers is in line with the ac data of complex **3-1**, where two relaxation processes were observed. Indeed, as suggested in the magnetic section, isomer **3-1(ii)** is expected to have a slower relaxation time than isomer **3-1(i)** because of its larger axial anisotropy.

It is possible to compare the results of isomer **3-1(i)** to those of the $[Co(Me_6tren)Cl]^+$ complex. Comparing the Co–L equatorial bond lengths of isomer **3-1(i)** (average d_{Co-S} = 2.40 Å) to that of $[Co(Me_6tren)Cl]^+$ (d_{Co-N} = 2.15 Å) that both have the same axial Cl ligand but differ by the nature of the equatorial ligands (S instead of N) rationalize the difference in the *D* values that was found equal to –23 cm^{-1} for the former and –8 cm^{-1} for the latter. This result highlights the major effect of the equatorial ligands in tuning the magnetic anisotropy of trigonal bipyramidal Co^{II} complexes.

Finally, it is interesting to compare the relaxation times of the two complexes measured after applying an optimum dc magnetic field. Isomer **3-1(i)** has a relaxation time of 0.036 s at *T* = 1.8 K (Table 3.5), while the $[Co(Me_6tren)Cl]^+$ has a relaxation time of 2.9 × 10^{-3} s, The larger axial magnetic anisotropy leads to a slower relaxation time, as expected. It was unfortunately not possible to prepare the Zn^{II} analog of the sulfur-containing complexes to study the effect of dilution on their relaxation behavior.

Complexes 3-2 to 3-4

The values of *D* and *E*, for these three complexes, and their average for the crystallographically different molecules of complex **3-3** are reported in Table 3.8, and are in relatively good agreement with the values obtained from the fit of the magnetic data.

Table 3.8. *D* and *E* values obtained for CASPT2 calculations.

Complexes	3-2	3-3(i)	3-3(ii)	3-4
D (cm^{-1})	–17.1	–18.0	–21.7	–13.8
E (cm^{-1})	0.4	0.95	2.73	0

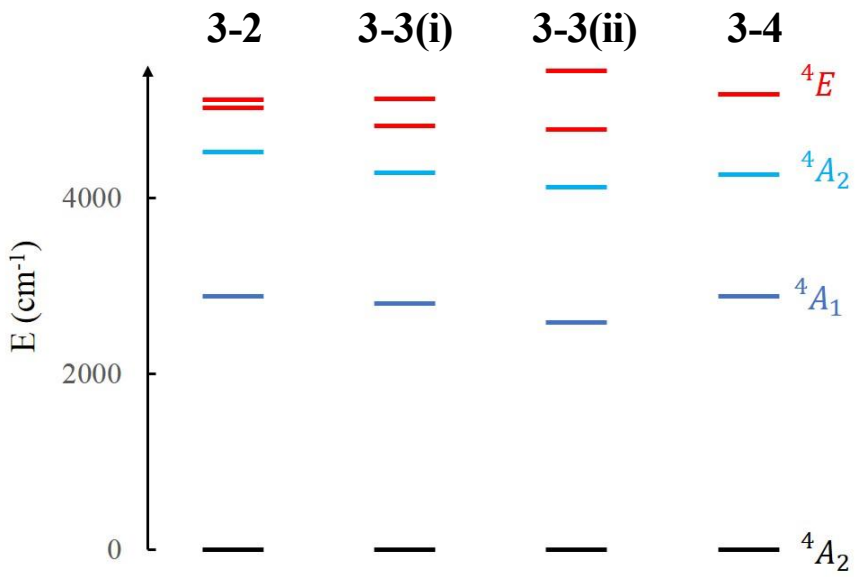

Figure 3.34. Calculated CASSCF energies for complexes **3-2**, **3-3(i)**, **3-3(ii)** and **3-4**.

The main contribution to the anisotropy parameters are primarily due to the two quadruplet excited states, $^4A_1$, and ^4E (Figure 3.34). The first excited state $^4A_1$ is responsible for the negative value of *D* while ^4E brings a positive but smaller contribution. Please note that there is another excited quadruplet state ($^4A_2$ in light blue in Figure 3.34) just above the excited $^4A_1$ state but this state does not contribute to *D*. As the symmetry of the molecules is not exactly C_3 for **3-2** and **3-3** — the Co–S bond lengths and $\widehat{SCoS}$ angles are different — there is a non-zero rhombic parameter *E*, which is due to the lift of degeneracy of the ^4E states. The energy difference between the ground state $^4A_2$ and the first excited state $^4A_1$ — that has a negative contribution to *D* — can be related to the energy difference between the (d_{xz}, d_{yz}) and ($d_{x^2-y^2}$, d_{xy}) orbitals (noted ΔE_1 in Figure 3.33c) because the state $^4A_1$ is obtained from a single excitation involving these orbitals. The state ^4E results from excitations between (d_{xz}, d_{yz}) and the d_{z^2} orbitals (noted ΔE_2 in Figure 3.33c). Therefore, the $^4A_2$–$^4A_1$ energy difference that brings a negative contribution to *D* is related to ΔE_1, and the $^4A_2$–^4E energy difference that brings a positive contribution to *D* is related to ΔE_2. As we have demonstrated above, complexes with longer equatorial Co–L distances (weaker equatorial σ-donating effect) decreases ΔE_1 and thus increases the negative contribution to *D*. While complexes with short axial Co–L distances increases ΔE_2 (weaker equatorial σ-donating effect) and thus decreases the positive contribution to *D*. It is important to note that the axial ligands also have an influence on ΔE_1 if they possess π-donor orbitals as for Cl^-, Br^- and NCS^- (Figure 3.35).

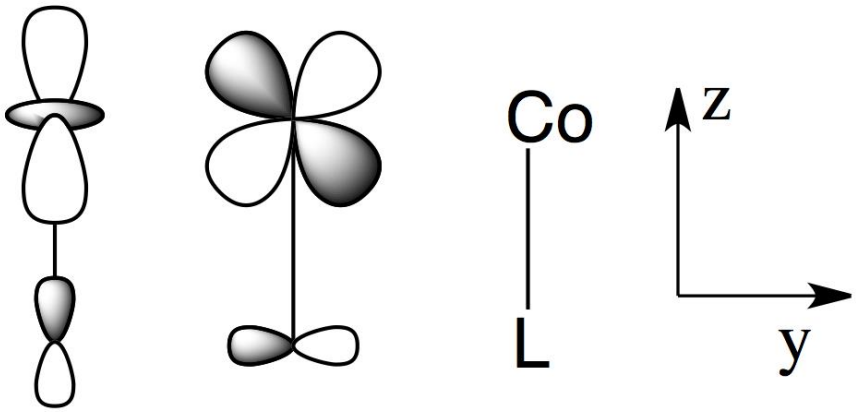

Figure 3.35. σ- and π-types overlap between the axial ligand and the symmetry related d orbitals.

There is a synergistic effect between the axial (π-donating) and equatorial (σ-donating) ligands on ΔE_1 that may, if they are complementary *i.e.* large axial π-donation and weak equatorial σ-donation, further increase the negative contribution to *D*. The influence of structural parameters on the magnetic properties of the three compounds were also analyzed. Complex **3-3** has the shortest Co–S bond lengths (Table 3.9), which induces a larger ΔE_1 value and thus decreases the negative contribution to *D*. Furthermore, the axial Co–N_a bond distance is the longest for **3-4** resulting in a weaker σ-donating effect of the axial amine that decreases ΔE_2 and therefore brings a larger positive contribution to *D*. The combination of these two effects is in line with an overall less negative *D* value for **3-4** than for **3-2** and **3-2**. The effect of the axial X ligands is more difficult to rationalize as they contribute by both their σ- and π-donating effects in addition to their distance to the metal ion that depends on their size. Br^- has a better π-donating effect than NCS^-, which decreases ΔE_1 and brings a larger negative contribution to *D* but its bond length with Co^{II} is longer, which has the opposite effect. In **3-3(ii)**, *D* is more negative than in the other compounds. One may assume that the π-donating effect of Br^- is the leading effect. From the spectrochemical series, Br^- is considered to induce a weaker ligand field than NCS^-, which is consistent with a smaller ΔE_1 and thus a larger negative contribution to *D*, as observed. In summary, the weaker σ-donation of sulfur (because of longer Co–S bond lengths) together with the larger π-donation of Br^- contribute to a weaker ΔE_1 for Br^- than for NCS^- and rationalize the largest negative *D* value in **3-3(ii)**.

Table 3.9. Relevant Co^{II}–ligand bond distances and angles and anisotropy parameters for complexes **3-1** to **3-4**.

Complexes	3-1 (i)	3-1 (ii)	3-2	3-3 (i)	3-3 (ii)	3-4
[a] d_{CoN}	2.263	2.408	2.287	2.231	2.273	2.346
[a] d_{CoS}	2.412; 2.391; 2.388	2.365; 2.379; 2.362	2.404; 2.397; 2.389	2.435; 2.416; 2.385	2.412; 2.411; 2.407	2.380
[a] d_{CoX}	2.255	2.266	2.264	2.361	2.383	2.001
[a] d_{Co-SSS}	0.352	0.415	0.341	0.331	0.357	0.374
[b] $\widehat{SCoS}$	122.08; 124.02; 108.25	113.40; 121.40; 116.35	118.89; 116.50; 118.60	122.28; 122.81; 109.71	116.83; 114.07; 122.81	117.58
[b] $\widehat{SCoX}$	103.49; 94.84; 95.86	103.82; 99.40; 96.98	97.82; 97.32; 99.38	93.85; 101.18; 98.19	98.66; 97.24; 99.29	99.03
[b] $\widehat{NCoX}$	173.63	175.78	179.00	175.08	178.92	180
[b] $\widehat{NCoS}$	82.87; 81.94; 81.54	79.60; 81.29; 79.81	81.94; 81.97; 81.58	81.82; 83.31; 82.21	81.76; 81.69; 81.42	80.97
[b] θ	7.13; 8.06; 8.46	10.40; 8.71; 10.82	8.06; 8.03; 8.42	8.18; 6.69; 7.79	8.24; 8.31; 8.58	9.03
$g_{\chi T}$	2.28		2.29	2.29		2.39
[c] $D_{\chi T}$	±12		±13	±17		±9
g_{MH}	2.43		2.39	2.39		2.48
[c] D_{MH}	–19.9		–21.4	–20.2		–11
[c] D_{HFEPR}	< –15		—	—		—
[c] D_{CALC}	–23.0	–13.1	–17.1	–21.7	–18.0	–13.8
[c] E_{CALC}	2.07	1.05	0.24	0.80	2.00	0
[c] U_{eff}	32	20.8	—	21		20

[a] in Angstrom (Å); [b] in degree (°), $\theta = 180° - \widehat{NCoS}$; [c] in wavenumbers ($cm^{-1}$)

Finally, the larger rhombic parameter *E* for **3-3** than for **3-2** is due to the larger deviation of the Co–S bond lengths and $\widehat{SCoS}$ angles from the average values in the former than in the latter. The fact that *E* is equal to zero for **3-4** is, of course, due to its C_3 symmetry. Finally, the "larger" π-donation effect of Br^- invoked above is not simple to rationalize, it is probably due to several structural parameters such as the Co–Br bond length and probably the $N_a\widehat{CoBr}$ angle that deviate from 180° leading to a non-negligible interaction of the π orbitals of Br^- with the metallic d orbitals. A more complete analysis taking into account these effects and based on the study of model complexes can be found in the Inorganic Chemistry paper recently published.[8]

3.5 Summary and Conclusions

Complex 3-1

The conclusion from this work is that we can engineer and tune the anisotropy and the barrier of the reorientation of the magnetization of trigonal bipyramidal Co^{II} complexes by chemical design. Despite the presence of a transverse anisotropy term in the sulfur based complexes, the effective energy barrier U_{eff} was increased from 16 cm^{-1} ($[Co(Me_6trenCl)]^+$) to 32 cm^{-1} in the present case. The reduction of the value of the energy barrier from the theoretical one (46 cm^{-1} corresponding the isomer with the largest $|D|$ value) is about 30%. It is usually ascribed to multiphonon mechanisms (Raman type) that are active at high temperatures.[21] At low temperature where the Micro-SQUID data were recorded, the multiphonon mechanisms are negligible.[22] At these temperatures only direct and quantum tunneling mechanisms are active. The fast relaxation at zero dc magnetic field observed in the $M = f(\mu_0 H)$ loops are mainly due to the nature of the wavefunctions within the Kramers low-lying doublet. The presence of a rhombic term due to the lack of the strict axial symmetry of the complexes mixes the M_s wavefunctions (–1/2 with +3/2 and +1/2 with –3/2). The degenerate ground state Kramers doublet is not a pure ±3/2 state but has contribution from the ±1/2 wavefunctions; this mixing increases the QTM when other processes are present, such as hyperfine interaction.

Complexes 3-2 to 3-4

We have shown the synthesis and characterization of three sulfur-containing trigonal bipyramidal Co^{II} complexes. We showed that it is possible to perform correlation between the geometrical structure of the complexes and the electronic structure of the ligands on the one

hand and the magnitude of the magnetic anisotropy on the other hand. We demonstrated that, in the low temperature range, the relaxation time of the complex with the weaker axial anisotropy (but with $E = 0$) is the slowest and that its energy barrier corresponds to what is expected if all other relaxation effects are absent. While for the complex with the largest axial anisotropy parameters (but with $E \neq 0$) the relaxation is much faster. The main reason behind the "better" properties of complex **3-4** is the absence of the rhombic term due to the C_{3v} symmetry point group that prevents tunneling between the low-lying ±3/2 sub-levels, while the ground levels of the other complexes are made from mixtures of the ±3/2 and ±1/2 wave functions allowing a pathway for quantum tunneling. Therefore, in order to design Co^{II} complexes with slow relaxation times and large barrier to the reorientation of the magnetization one needs not only to perform large axial anisotropy but the rhombic term must be strictly equal to zero. For large axial anisotropy terms to be obtained, the D_{2d} symmetry seems to be efficient as recently demonstrated,[12] but one must succeed to avoid small distortions that deviate from the strict symmetry, which is still a challenge.

3.6 References

1. F. Shao, B. Cahier, N. Guihery, E. Riviere, R. Guillot, A.-L. Barra, Y. Lan, W. Wernsdorfer, V. E. Campbell and T. Mallah, *Chemical Communications*, 2015, **51**, 16475-16478.
2. G. Fallani, R. Morassi and F. Zanobini, *Inorganica Chimica Acta*, 1975, **12**, 147-154.
3. P. Stavropoulos, M. C. Muetterties, M. Carrie and R. H. Holm, *Journal of the American Chemical Society*, 1991, **113**, 8485-8492.
4. A. H. Cowley, R. A. Jones, M. A. Mardones and C. M. Nunn, *Organometallics*, 1991, **10**, 1635-1637.
5. D. Gatteschi, A. L. Barra, A. Caneschi, A. Cornia, R. Sessoli and L. Sorace, *Coordination Chemistry Reviews*, 2006, **250**, 1514-1529.
6. P. A. Malmqvist and B. O. Roos, *Chemical Physics Letters*, 1989, **155**, 189-194.
7. F. Aquilante, J. Autschbach, R. K. Carlson, L. F. Chibotaru, M. G. Delcey, L. De Vico, I. F. Galvan, N. Ferre, L. M. Frutos, L. Gagliardi, M. Garavelli, A. Giussani, C. E. Hoyer, G. Li Manni, H. Lischka, D. X. Ma, P. A. Malmqvist, T. Muller, A. Nenov, M. Olivucci, T. B. Pedersen, D. L. Peng, F. Plasser, B. Pritchard, M. Reiher, I. Rivalta, I. Schapiro, J. Segarra-Marti, M. Stenrup, D. G. Truhlar, L. Ungur, A. Valentini, S. Vancoillie, V. Veryazov, V. P. Vysotskiy, O. Weingart, F. Zapata and R. Lindh,

Journal of Computational Chemistry, 2016, **37**, 506-541.

8. F. Shao, B. Cahier, E. Rivière, R. Guillot, N. Guihéry, V. E. Campbell and T. Mallah, *Inorganic Chemistry*, 2017, **56**, 1104-1111.
9. K. S. Cole and R. H. Cole, *The Journal of Chemical Physics*, 1941, **9**, 341-351.
10. H. Miyasaka, R. Clérac, K. Mizushima, K.-i. Sugiura, M. Yamashita, W. Wernsdorfer and C. Coulon, *Inorganic Chemistry*, 2003, **42**, 8203-8213.
11. V. V. Novikov, A. A. Pavlov, Y. V. Nelyubina, M.-E. Boulon, O. A. Varzatskii, Y. Z. Voloshin and R. E. P. Winpenny, *Journal of the American Chemical Society*, 2015, **137**, 9792-9795.
12. Y. Rechkemmer, F. D. Breitgoff, M. van der Meer, M. Atanasov, M. Hakl, M. Orlita, P. Neugebauer, F. Neese, B. Sarkar and J. van Slageren, *Nature Communications*, 2016, **7**.
13. W. Wernsdorfer, N. E. Chakov and G. Christou, *Physical Review B*, 2004, **70**, 132413.
14. W. Wernsdorfer, *Superconductor Science and Technology*, 2009, **22**, 064013.
15. N. Ishikawa, *Journal of Physical Chemistry A*, 2003, **107**, 5831-5835.
16. R. Maurice, R. Bastardis, C. d. Graaf, N. Suaud, T. Mallah and N. Guihéry, *Journal of Chemical Theory and Computation*, 2009, **5**, 2977-2984.
17. F. Aquilante, L. De Vico, N. Ferré, G. Ghigo, P.-Å. Malmqvist, P. Neogrády, T. B. Pedersen, M. Pitoňàk, M. Reiher, B. Roos, L. Serrano-Andrés, M. Urban, V. Veryazov and R. Lindh, *Journal of Computational Chemistry*, 2010, **31**, 224-247.
18. B. O. Roos and P.-A. Malmqvist, *Physical Chemistry Chemical Physics*, 2004, **6**, 2919-2927.
19. G. Karlstroem, R. Lindh, P.-A. Malmqvist, B. O. Roos, U. Ryde, V. Veryazov, P.-O. Widmark, M. Cossi, B. Schimmelpfennig, P. Neogrady and L. Seijo, *Computation Materials Science*, 2003, **28**, 222-239.
20. P. A. Malmqvist, B. O. Roos and B. Schimmelpfennig, *Chemical Physics Letters*, 2002, **357**, 230-240.
21. J. M. Zadrozny, D. J. Xiao, M. Atanasov, G. J. Long, F. Grandjean, F. Neese and J. R. Long, *Nature Chemistry*, 2013, **5**, 577-581.
22. A. Abragam and B. Bleaney, *Electron paramagnetic resonance of transition ions*, Oxford University Press, 2012.

CHAPTER 4 Single Molecule Magnet Behavior in Ln^{III}[12-$MC_{Ga^{III}shi}$-4] Complexes

4.1 Introduction

Single Molecule Magnets (SMMs)[1-3] have received increasing attraction because of their magnetic bistability, which could have potential applications in high density storage, spintronics[4] and quantum processing.[5] Towards this goal it is essential to design SMMs at high temperatures. Increasing the spin (*S*) value of the ground state[6] or/and the magnitude of the Ising-type magnetic anisotropy[7] (negative ZFS parameter *D*) are the two strategies that authors have focused on for transition metal ion based complexes.

Employing metal ions with strong unquenched orbital angular momentum, such as lanthanides and actinides, which possess large intrinsic anisotropy, turned out to be a rewarding strategy to obtain SMMs with potentially high blocking temperatures.[8-10] The interest for lanthanide-containing complexes started after the discovery by Ishikawa of the SMM behavior in the [$LnPc_2$] (pc = phtalocyanine) family of complexes, and pparticularly the Tb^{III} derivative.[11-13] Other lanthanide based complexes with larger energy barriers were reported, subsenquently.[14, 15]

In the same time, efforts were made to calculate the energy spectrum of the complexes in order to rationalize their magnetic behavior and to, eventually, predict the properties of new complexes.[16-19] This task is pursued by many groups. In order to be able to perform a magneto-structural correlation, it is necessary to carry out studies on a series of isostructural complexes with different lanthanide ions, which allows studying the effect of the nature of the lanthanide on the magnetic anisotropy. Such effort along this direction have been initiated by Gatteschi *et al.*[16] on the [$LnPc_2$] complexes. But there is still much work to do in order to get insights into the influence of the different parameters on the magnetic behavior, particularly correlating structure, theoretical calculation, magnetic behavior and luminescence.

To do so, it is easier to consider a series of complexes with well-defined symmetry as the pseudo D_{4d} one of [$LnPc_2$] complexes or the polyoxometallates reported by Coronado *et*

al.[20-24] Another series of lanthanide-containing complexes where the symmetry can be controlled is the metallacrown (MC) one discovered by Pecoraro in 1989.[25-36]

With this in mind, we focused on two new families of Ga^{III}/Ln^{III} MCs based on the ligand salicylhydroxamic acid (H_3shi), one is the mononuclear half-sandwich series with the formula $[LnGa_4(shi)_4(C_6H_5CO_2)_4(C_5H_5N)(CH_3OH)]\cdot C_5H_6N\cdot C_5H_5N\cdot CH_3OH$ (where Ln = Tb^{III} (**4-1**), Dy^{III} (**4-2**), Ho^{III} (**4-3**), Er^{III} (**4-4**), Yb^{III} (**4-5**)); and the other is the binuclear sandwich series with the formula $[Ln_2Ga_8(shi)_8(C_6H_2C_2O_4)_4(DMF)_6Na_2]\cdot(DMF)_x\cdot(H_2O)_y$ (where Ln = Tb^{III} (**4-6**), Dy^{III} (**4-7**), Ho^{III} (**4-8**), Er^{III} (**4-9**), Yb^{III} (**4-10**). The luminescence studies at room temperature of the mononuclear series was already reported by Pecoraro *et al.*, together with the structure of only the Dy^{III} derivative.[37] We prepared the whole series and succeeded to obtain single crystals that allowed studying their structure and their magnetic behavior and performing theoretical calculations. X-ray diffraction analysis demonstrates that within each series the complexes are isostructural: the half-sandwich with a [12-$MC_{Ga^{III}shi}$-4] core and four benzoate molecules bridging the central Ln^{III} ion to the Ga^{III} ring ions and the sandwich with two [12-$MC_{Ga^{III}shi}$-4] cores bridging four isophthalate molecules with the central Ln^{III} ion to the Ga^{III} ring metals. As analyzed below using the SHAPE program, the local structure of the lanthanide ions within these complexes is very close to a square antiprism with a pseudo D_{4d} local symmetry. However, slight deviation from the strict symmetry is enough to impact their magnetic behavior.

4.2 Experimental Section

4.2.1 Syntheses

All starting materials were obtained commercially and were used without further purification unless otherwise stated.

Half-sandwich $[LnGa_4(shi)_4(C_6H_5CO_2)_4(C_5H_5N)(CH_3OH)]\cdot C_5H_6N\cdot C_5H_5N\cdot CH_3OH$

The process was slightly modified from the previously reported method.[37]

H_3shi (153.1 mg, 1.0 mmol), $Ln(NO_3)_3\cdot xH_2O$ (0.25 mmol) (Ln^{III} = Tb^{III}, Dy^{III}, Ho^{III}, Er^{III}, Yb^{III}), and $Ga(NO_3)_3\cdot xH_2O$ (255.7 mg, 1.0 mmol) were dissolved in 40 mL (60 mL for Yb^{III}) of methanol. Sodium benzoate (576.4 mg, 4.0 mmol) was added to the solution and stirred overnight. The solution was filtered, followed by the addition of 2 mL (3 mL for Yb^{III}) pyridine. The resulting solution was stirred for 20 min and then filtered. The slow

evaporation of the solution yielded crystalline complex after 1 week.

$[TbGa_4(C_7H_4NO_3)_4(C_6H_5CO_2)_4(C_5H_5N)(CH_3OH)]\cdot C_5H_6N\cdot C_5H_5N\cdot CH_3OH$ (4-1). Yield: 98.7 mg (21.7%). ESI-MS, calc. for $[M]^-$, $C_{56}H_{36}N_4O_{20}TbGa_4$, 1522.8; found, 1522.8. IR (ν/cm^{-1}): 3436.45, 3065.67, 1599.23, 1574.48, 1529.10, 1490.79, 1476.07, 1448.29, 1407.60, 1323.93, 1262.55, 1250.36, 1104.38, 1067.80, 1039.79, 952.75, 864.11, 759.23, 723.89, 681.66, 580.77. Anal. Calc. for $DyGa_4C_{73}H_{60}N_7O_{22}$: C, 47.95; H, 3.31; N, 5.36. Found: C, 47.90; H, 2.55; N, 5.44. Single-crystal unit cell: monoclinic, space group $P2_1/n$, a = 17.1409 Å, b = 17.7668 Å, c = 24.1889 Å, α = 90°, β = 94.5902°, γ = 90°, V = 7094.98 Å^3.

$[DyGa_4(C_7H_4NO_3)_4(C_6H_5CO_2)_4(C_5H_5N)(CH_3OH)]\cdot C_5H_6N\cdot C_5H_5N\cdot CH_3OH$ (4-2). Yield: 96.5 mg (21.1%). ESI-MS, calc. for $[M]^-$, $C_{56}H_{36}N_4O_{20}DyGa_4$, 1525.8; found, 1525.8. IR (ν/cm^{-1}): 3436.94, 3063.64, 1599.02, 1573.70, 1525.20, 1490.14, 1475.09, 1447.53, 1407.89, 1324.15, 1261.06, 1250.18, 1104.36, 1062.96, 1038.82, 952.79, 864.40, 759.13, 724.03, 681.20, 579.92. Anal. Calc. for $DyGa_4C_{73}H_{60}N_7O_{22}$: C, 47.95; H, 3.31; N, 5.36. Found: C, 47.44; H, 2.92; N, 5.39. Single-crystal unit cell: monoclinic, space group $P2_1/n$, a = 17.1202 Å, b = 17.1515 Å, c = 24.2068 Å, α = 90°, β = 94.6057°, γ = 90°, V = 7085.15 Å^3.

$[HoGa_4(C_7H_4NO_3)_4(C_6H_5CO_2)_4(C_5H_5N)(CH_3OH)]\cdot C_5H_6N\cdot C_5H_5N\cdot CH_3OH$ (4-3). Yield: 158.6 mg (34.6%). ESI-MS, calc. for $[M]^-$, $C_{56}H_{36}N_4O_{20}HoGa_4$, 1528.8; found, 1528.8. IR (ν/cm^{-1}): 3436.61, 3064.42, 1599.11, 1573.91, 1525.83, 1490.32, 1475.22, 1447.75, 1407.90, 1324.76, 1261.32, 1250.45, 1104.26, 1063.01, 1039.00, 953.27, 864.67, 759.10, 723.98, 682.04, 580.66. Anal. Calc. for $DyGa_4C_{73}H_{60}N_7O_{22}$: C, 47.95; H, 3.31; N, 5.36. Found: C, 47.85; H, 2.63; N, 5.56. Single-crystal unit cell: monoclinic, space group $P2_1/n$, a = 17.0538 Å, b = 17.1687 Å, c = 24.2569 Å, α = 90°, β = 94.8692°, γ = 90°, V = 7076.64 Å^3.

$[ErGa_4(C_7H_4NO_3)_4(C_6H_5CO_2)_4(C_5H_5N)(CH_3OH)]\cdot C_5H_6N\cdot C_5H_5N\cdot CH_3OH$ (4-4). Yield: 150.3 mg (34.1%). ESI-MS, calc. for $[M]^-$, $C_{56}H_{36}N_4O_{20}ErGa_4$, 1529.8; found, 1529.8. IR (ν/cm^{-1}): 3436.46, 3064.57, 1599.15, 1573.89, 1526.06, 1490.29, 1475.21, 1447.39, 1407.95, 1324.90, 1261.24, 1250.52, 1104.21, 1062.93, 1038.90, 953.58, 864.76, 759.22, 723.99, 682.20, 580.95. Anal. Calc. for $DyGa_4C_{73}H_{60}N_7O_{22}$: C, 47.82; H, 3.30; N, 5.35. Found: C, 47.95; H, 2.75; N, 5.40. Single-crystal unit cell: monoclinic, space group $P2_1/n$, a = 17.0849 Å, b = 17.1267 Å, c = 24.2569 Å, α = 90°, β = 94.7302°, γ = 90°, V = 7067.1Å^3.

$[YbGa_4(C_7H_4NO_3)_4(C_6H_5CO_2)_4(C_5H_5N)(CH_3OH)]\cdot C_5H_6N\cdot C_5H_5N\cdot CH_3OH$ (4-5). Yield: 95.6 mg (20.8%). ESI-MS, calc. for $[M]^-$, $C_{56}H_{36}N_4O_{20}YbGa_4$, 1535.8; found, 1535.8. IR (ν/cm^{-1}): 3435.82, 3066.43, 1600.10, 1574.81, 1528.26, 1490.66, 1475.77, 1448.46, 1408.44, 1324.97, 1261.86, 1250.48, 1104.48, 1067.82, 1040.01, 954.65, 865.07, 758.85, 724.12, 685.94, 582.53. Anal. Calc. for $DyGa_4C_{73}H_{60}N_7O_{22}$: C, 47.67; H, 3.29; N, 5.33. Found: C, 47.78; H, 3.22; N, 5.36. Single-crystal unit cell: monoclinic, space group $P2_1/n$, a = 17.0584 Å, b = 17.1545 Å, c = 24.3343 Å, α = 90°, β = 94.8564°, γ = 90°, V = 7095.4 Å^3.

Sandwich $[Ln_2Ga_8(shi)_8(C_6H_2C_2O_4)_4(DMF)_6Na_2]\cdot(DMF)_x\cdot(H_2O)_y$

H_3shi (306.3 mg, 2.0 mmol), $Ln(NO_3)_3\cdot xH_2O$ (0.50 mmol) (Ln^{III} = Tb^{III}, Dy^{III}, Ho^{III}, Er^{III}, Yb^{III}), $Ga(NO_3)_3\cdot xH_2O$ (511.5 mg, 2.0 mmol) and isophthalic acid (166.1 mg, 1.0 mmol) were dissolved in 15 mL DMF. Sodium bicarbonate (672.08 mg, 8.0 mmol) was added to the solution and stirred overnight. The solution was filtered, slow evaporation of the solution yielded crystalline complex after 3 months.

$[Tb_2Ga_8(C_7H_4NO_3)_8(C_6H_2C_2O_4)_4(C_3H_7NO)_6Na_2]\cdot(C_3H_7NO)\cdot(H_2O)_2$ (4-6). Yield: 70.8 mg (8.5%). Elem Anal. Calc: C, 39.35; H, 3.06; N, 6.32. Found: C, 39.02; H, 3.04; N, 6.39. Single-crystal unit cell: monoclinic, space group $P2_1/n$, a = 14.6832(7) Å, b = 21.8429(11) Å, c = 21.7220(10) Å, α = 90°, β = 106.304(2)°, γ = 90°, V = 6686.6(6) Å^3.

$[Dy_2Ga_8(C_7H_4NO_3)_8(C_6H_2C_2O_4)_4(C_3H_7NO)_6Na_2]\cdot(C_3H_7NO)_3\cdot(H_2O)_8$ (4-7). Yield: 95.6 mg (10.7%). Elem Anal. Calc: C, 38.50; H, 3.57; N, 6.64. Found: C, 38.32; H, 3.51; N, 6.99. Single-crystal unit cell: monoclinic, space group $P2_1/n$, a = 14.6631(5) Å, b = 21.8204(7) Å, c = 21.7429(8) Å, α = 90°, β = 106.5260(10)°, γ = 90°, V = 6669.4(4) Å^3.

$[Ho_2Ga_8(C_7H_4NO_3)_8(C_6H_2C_2O_4)_4(C_3H_7NO)_6Na_2]\cdot(C_3H_7NO)_4\cdot(H_2O)_8$ (4-8). Yield: 60.6 mg (6.6%). Elem Anal. Calc: C, 38.66; H, 3.68; N, 6.88. Found: C, 38.45; H, 3.74; N, 7.10. Single-crystal unit cell: monoclinic, space group $P2_1/n$, a = 14.6517(14) Å, b = 21.848(2) Å, c = 21.770(2) Å, α = 90°, β = 106.425(4)°, γ = 90°, V = 6684.6(11) Å^3.

$[Er_2Ga_8(C_7H_4NO_3)_8(C_6H_2C_2O_4)_4(C_3H_7NO)_6Na_2]\cdot(C_3H_7NO)_4\cdot(H_2O)_6$ (4-9). Yield: 148 mg (16.3%). Elem Anal. Calc: C, 38.99; H, 3.61; N, 6.94. Found: C, 38.86; H, 3.71; N, 7.32. Single-crystal unit cell: monoclinic, space group $P2_1/n$, a = 14.6621(7) Å, b = 21.8274(11) Å, c = 21.7260(12) Å, α = 90°, β = 106.276(2)°, γ = 90°, V = 6674.4(6) Å^3.

$[Yb_2Ga_8(C_7H_4NO_3)_8(C_6H_2C_2O_4)_4(C_3H_7NO)_6Na_2]\cdot(C_3H_7NO)_4\cdot(H_2O)_6$ (4-10). Yield: 162 mg (17.8%). Elem Anal. Calc: C, 38.87; H, 3.59; N, 6.92. Found: C, 38.52; H, 3.52; N, 7.21. Single-crystal unit cell: monoclinic, space group $P2_1/n$, a = 14.6643(5) Å, b = 21.8542(7) Å, c = 21.7423(7) Å, α = 90°, β = 106.1650(10)°, γ = 90°, V = 6692.4(4) Å^3.

4.2.2 Physical Measurements

Unless otherwise stated, all starting materials were obtained commercially and were used without further purification. General procedures, X-ray Crystallography, and Magnetic Measurements are aforementioned in Chapter 2. Electron Paramagnetic Resonance (EPR) Measurements are aforementioned in Chapter 3.

4.3 Results and Discussion

4.3.1 Syntheses

Half-sandwich $[LnGa_4(shi)_4(C_6H_5CO_2)_4(C_5H_5N)(CH_3OH)]\cdot C_5H_6N\cdot C_5H_5N\cdot CH_3OH$

The one pot reaction H_3shi, $Ga(NO_3)_3\cdot xH_2O$, and sodium benzoate with the corresponding hydrated $Ln(NO_3)_3$ salt in CH_3OH/pyridine mixture afforded the MC-like structure complexes that adopt the half-sandwich 12-MC-4 topology. The complexes are negatively charged with one pyridinium as a cation. The yields range from 20 to 35%. (Scheme 4.1)

Sandwich $[Ln_2Ga_8(shi)_8(C_6H_2C_2O_4)_4(DMF)_6Na_2]\cdot(DMF)_x\cdot(H_2O)_y$

The one pot reaction H_3shi, $Ga(NO_3)_3\cdot xH_2O$, isophthalic acid, and sodium bicarbonate with the corresponding hydrated $Ln(NO_3)_3$ salt in DMF afforded MC-like structure complexes that adopt the sandwich 12-MC-4 topology; the negative charge of the complexes is counter-balanced by two sodium cations and the yields are ranging from 6.6 to 17.8% (Scheme 4.1).

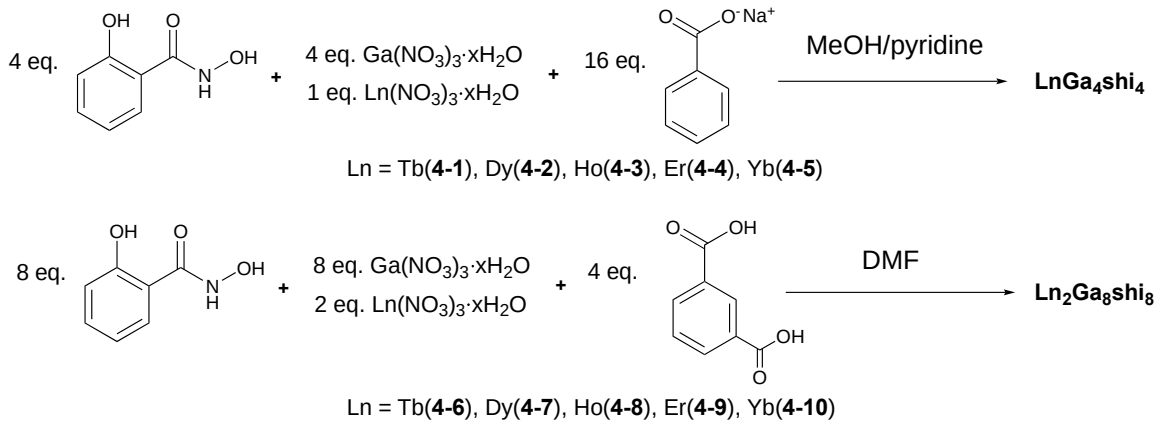

Scheme 4.1. Synthesis of **$LnGa_4shi_4$** and **$Ln_2Ga_8shi_4$** complexes.

4.3.2 Description of Structures

Half-sandwich $[LnGa_4(shi)_4(C_6H_5CO_2)_4(C_5H_5N)(CH_3OH)]\cdot C_5H_6N\cdot C_5H_5N\cdot CH_3OH$

Single crystal X-ray analysis of complexes **4-1** to **4-5** revealed that the mononuclear MC complexes have a slightly distorted D_{4d} symmetry, as noted in Table 4.1. They were isostructural and crystallized in the monoclinic $P2_1/n$ space group. Therefore, only the dysprosium(III) complex **4-2** will be described in detail. The four organic ligands shi^{3-} and bridges Ga^{III} ions form a $[12\text{-}MC_{Ga^{III}}\text{-}4]$ ring with –[Ga–N–O]– as the repeat unit. Two Ga^{III} ions are five-coordinated with shi^{3-} ligands and benzoate ligands. While the other two Ga^{III} ions are six-coordinated with one pyridine ligand and one methanol solvent bound axially. The central Dy^{III} ion is bridged to the $[12\text{-}MC_{Ga^{III}}\text{-}4]$ ring by four benzoates and four shi^{3-} ligands. The four hydroximate oxygen atoms (O_{MC}) present in a planar square, while the four oxygen atoms (O_{Bz}) of benzoate serve as another square, and adopts an eight-coordinated square antiprism geometry (quasi-double decker structure), which was confirmed by the continued shape measurements (CShM) SHAPE analysis,[38, 39] the results are listed in Table 4.7 for the five complexes. The smaller the value is, the closer the coordination geometry to the ideal model is. Regarding the lanthanide inner coordination sphere, the skew angle (ϕ) defined as the offset between the two squares defined by the mean planes through the coordinating oxygen atoms (O2, O5, O8, O11 and O101, O111, O121, O131) (Figure 4.1 left), is equal to 41.12°, 42.39°, 48.49° and 48.29°, and the ideal value of the D_{4d} symmetry (Table 4.2) is 45°. The minimum of the mean absolute deviation for ϕ (MAD_ϕ) in Table 4.3 indicates that the Dy^{III} coordination site can be described as a slightly distorted square antiprism. Dy–O distances also support this minor distortion because they range from 2.294

to 2.368 Å (average value 2.332 Å, Table 4.5). In addition, the ratio (0.915) between the interplanar distance d_{pp} = 2.527 Å (Figure 4.1 top left), calculated as the distance between the upper and lower planes containing the four oxygen atoms, and the average distance between the four neighboring oxygen atoms placed in each plane, d_{in} = 2.763 Å (Figure 4.1 top left), corresponds to a slight elongation of the square antiprism along the four-fold axis because the ideal ratio of d_{pp}/d_{in} is 0.841.[23, 24] It worth noting that the ratio of d_{pp}/d_{in} for the double-decker complexes [$DyPc_2$] and [$DyPc_2$](NBu_4) are 0.997 and 1.001 respectively corresponding to a large elongation.[40 41] The Ln-POM complex $DyMo_{10}$ (0.944)[20] is also more elongated than the metallacrown complex we obtained. All the **$LnGa_4shi_4$** compounds (Table 4.3 and Table 4.6) present a weak axial elongation of the square antiprism formed by the eight-coordinated oxygen ion. The planarity of the [12-$MC_{Ga^{III}}$-4] ring is closely similar to the $Mn^{II}(OAc)_2$[12-$MC_{Mn^{III}N}$-4][26] and slightly more planar than $Na^{I}Ln^{III}(benzoate)_4$[12-$MC_{Mn^{III}N}$-4][42] or $K^{I}Ln^{III}(benzoate)_4$[12-$MC_{Mn^{III}N}$-4][43]. The four Ga^{III} ions are crystallographically inequivalent; however, the molecule possesses a pseudo-C_4 symmetry. The negative charge of the 12-MC-4 metallacrown is balanced by one pyridinium cation, which was found to form a hydrogen bond with an adjacent pyridine solvent molecule. Meanwhile, the analysis of the packing arrangement reveals that there are some intermolecular forces between neighboring molecules, σ–π and π–π interactions (Figure 4.2 and Table 4.4).

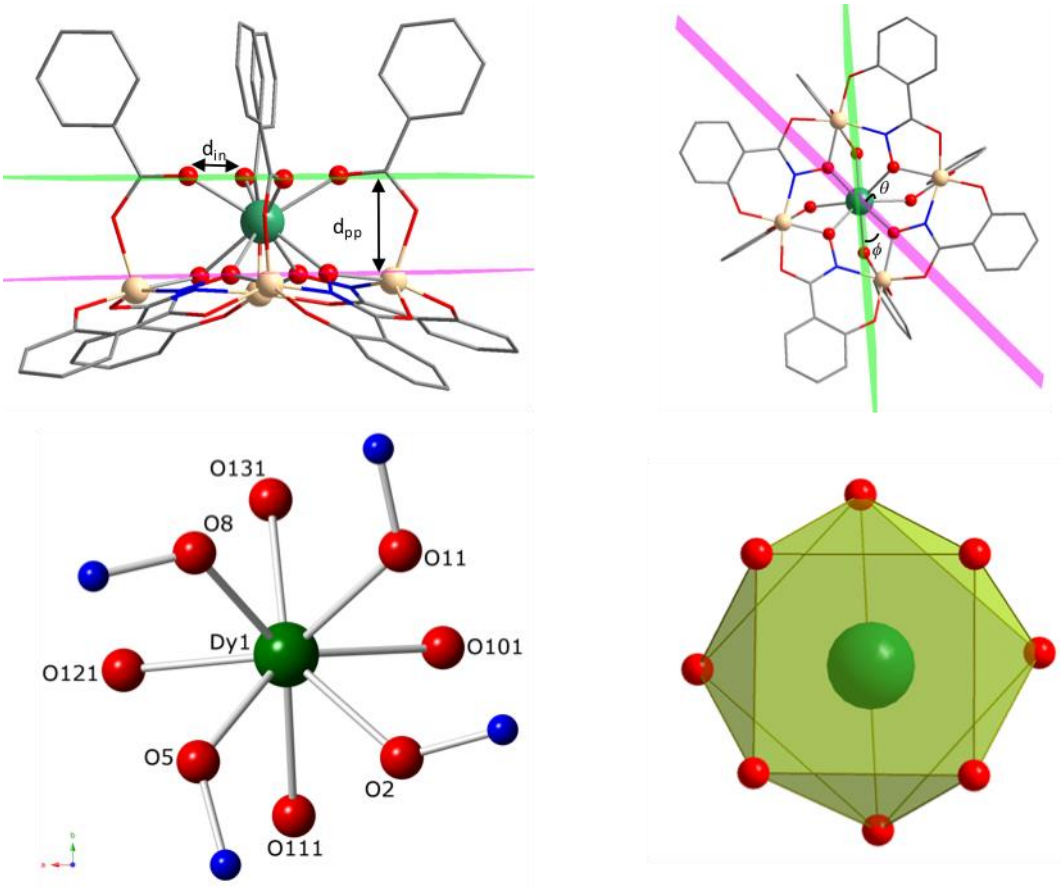

Figure 4.1. Molecular structure of complex **4-2** obtained from X-ray diffraction: (top left) side-view perspective showing d_{in} and d_{pp}; (top right) top-down view showing ϕ and θ structural features of the [12-$MC_{Ga^{III}}$-4] core; (bottom) square-antiprismatic coordination geometry around the central Dy^{III} ion. Dy – green; Ga – tan; O – red; N – blue; C – grey; H atoms and solvent molecules coordinated to Ga^{III} were omitted for clarity.

Table 4.1. Crystallographic data structure refinement for complexes **4-1** to **4-5**.

Complexes	**4-1(Tb)**	**4-2(Dy)**	**4-3(Ho)**	**4-4(Er)**	**4-5(Yb)**
formula	$C_{73}H_{60}N_7O_{22}Ga_4Tb$	$C_{73}H_{60}N_7O_{22}Ga_4Dy$	$C_{73}H_{60}N_7O_{22}Ga_4Ho$	$C_{73}H_{60}N_7O_{22}Ga_4Er$	$C_{73}H_{60}N_7O_{22}Ga_4Yb$
M_r	1825.08	1828.66	1831.09	1833.42	1839.20
cryst size, mm^3	0.07 × 0.06 × 0.03	0.20 × 0.19 × 0.06	0.13 × 0.10 × 0.04	0.12 × 0.07 × 0.02	0.09 × 0.08 × 0.05
cryst syst	Monoclinic	Monoclinic	Monoclinic	Monoclinic	Monoclinic
space group	$P2_1/n$	$P2_1/n$	$P2_1/n$	$P2_1/n$	$P2_1/n$
a, Å	17.1409(11)	17.1202(3)	17.0538(5)	17.0849 (4)	17.0584(19)
b, Å	17.1668(11)	17.1515(3)	17.1687(5)	17.1267 (4)	17.1545(19)
c, Å	24.1889(16)	24.2068(17)	24.2569(9)	24.2345 (8)	24.334(3)
α, deg	90	90	90	90	90
β, deg	94.590(2)	94.605(7)	94.869(2)	94.730(2)	94.856(4)
γ, deg	90	90	90	90	90
cell volume, $Å^3$	7094.9(8)	7085.1(5)	7076.6(4)	7067.1	7095.4
Z	4	4	4	4	4
T, K	100(1)	85(2)	100(1)	100(1)	100(1)
F_{000}	3648	3651	3656	3660	3668
μ, mm^{-1}	2.57	7.958	2.69	2.764	2.888
θ range, deg	2.3–29.7	3.1–68.3	2.3–22.2	2.3–25.3	2.3–30.1
reflns collected	204245	191116	134863	163019	238326
reflns unique	21823	12987	21661	21640	21762
R_{int}	0.0979	0.0660	0.1968	0.1021	0.0995
R_1	0.0442	0.0346	0.0930	0.0472	0.0982
wR_2 (all data)	0.0918	0.0869	0.2513	0.1190	0.2524
GOF	1.023	1.068	1.053	1.053	1.202
largest diff. peak and hole ($e·Å^{-3}$)	2.81, –0.80	2.57, –0.72	3.35, –2.41	2.50, –1.42	6.44, −3.51

Table 4.2. Characteristic parameters (θ, ϕ) of a square anti-prism geometry for complexes **4-1** to **4-5**.

Angle / °	**4-1(Tb)**		**4-2(Dy)**		**4-3(Ho)**		**4-4(Er)**		**4-5(Yb)**		**Ideal** D_{4d}[24, 44]
θ1	O2	52.32	O2	52.47	O1	53.84	O1	54.37	O1	54.50	57.23
θ2	O5	53.54	O5	53.62	O4	53.81	O4	53.81	O4	54.33	57.23
θ3	O8	53.93	O8	54.11	O7	52.48	O7	52.78	O7	53.08	57.23
θ4	O11	53.25	O11	53.44	O10	53.56	O10	54.08	O10	54.29	57.23
θ5	O13	60.56	O101	60.18	O15	60.92	O15	60.49	O15	60.12	57.23
θ6	O16	58.74	O111	58.29	O18	60.33	O18	59.61	O18	59.38	57.23
θ7	O18	63.59	O121	63.08	O19	58.06	O19	58.07	O19	57.30	57.23
θ8	O20	61.67	O131	61.41	O21	62.55	O21	62.31	O21	61.29	57.23
ϕ1	O2	41.36	O2	41.42	O1	41.23	O1	41.36	O1	41.15	45
ϕ2	O5	42.47	O5	42.39	O4	42.65	O4	42.37	O4	42.09	45
ϕ3	O8	48.41	O8	48.49	O7	48.51	O7	48.47	O7	48.60	45
ϕ4	O11	48.36	O11	48.29	O10	48.01	O10	48.29	O10	48.50	45

 Feng SHAO: 0000-0001-8606-8628

Table 4.3. Structural parameters of a square anti-prism geometry for complexes **4-1** to **4-5**.

Complexes	Ln–O_{ave} [a] / Å	MAD_ϕ [b] / °	d_{in} [c] / Å	d_{pp} [d] / Å	d_{pp}/d_{in} [e]
4-1(Tb)	2.339	3.235	2.775	2.525	0.910
4-2(Dy)	2.332	3.243	2.763	2.527	0.915
4-3(Ho)	2.311	3.160	2.735	2.514	0.919
4-4(Er)	2.309	3.258	2.733	2.513	0.920
4-5(Yb)	2.294	3.465	2.711	2.508	0.925

[a] The average values for bond lengths of Ln–O; [b] MAD = mean absolute deviation, skew angle ϕ for the ideal D_{4d} ligand field symmetry is 45°; [c] d_{in} means the average distance between the four neighboring atoms placed in each square; [d] d_{pp} means the distance between two centroids from the upper and lower planes respectively; [e] d_{pp}/d_{in} is 0.841 for the ideal square antiprism.[23, 44]

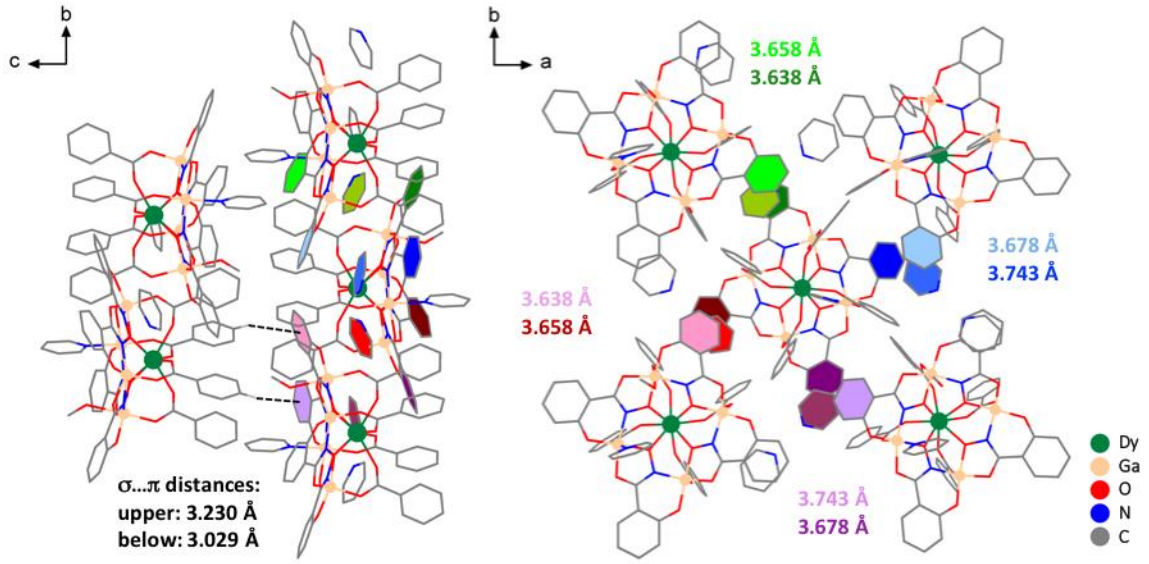

Figure 4.2. The packing arrangement of complex **4-2** with σ–π distances (Å) (left, shown as dashed line) and intermolecular π–π distances (right, shown as noted corresponding to different color to the middle pyridine). The shortest intermolecular Dy^{III}–Dy^{III} distances is 11.9314(3) Å.

Table 4.4 Interaction parameters for complexes **4-1** to **4-5**.

Complexes	$d_{Ln-Ln(min)}$	$d_{\sigma-\pi}$		$d_{\pi-\pi}$							
4-1(Tb)	11.9405(7)	3.2595(2)	3.0539(2)	3.6536(2)	3.6342(2)	3.6779(2)	3.7507(2)	3.6342(2)	3.6536(2)	3.7507(2)	3.6779(2)
4-2(Dy)	11.9314(3)	3.2302(2)	3.0288(2)	3.6575(2)	3.6375(3)	3.6784(2)	3.7432(3)	3.6375(3)	3.6575(2)	3.7432(3)	3.6784(2)
4-3(Ho)	11.9349(8)	3.2708(1)	3.0389(1)	3.6447(1)	3.6244(1)	3.7047(1)	3.7271(1)	3.6244(1)	3.6447(1)	3.7271(1)	3.7047(1)
4-4(Er)	11.9127(5)	3.2559(1)	3.0407(1)	3.6581(1)	3.6411(1)	3.6732(1)	3.7343(1)	3.6411(1)	3.6581(1)	3.7343(1)	3.6732(1)
4-5(Yb)	11.9320(11)	3.2623(4)	3.0623(3)	3.7039(4)	3.5330(4)	3.7018(4)	3.7326(3)	3.5330(4)	3.7039(4)	3.7326(3)	3.7018(4)

Table 4.5. Lanthanide center bonds with oxygen for complexes **4-1** to **4-5**.

Bond length / Å									
4-1(Tb)		**4-2(Dy)**		**4-3(Ho)**		**4-4(Er)**		**4-5(Yb)**	
Tb1–O2	2.347	Dy1–O2	2.340	Ho1–O1	2.291	Er1–O1	2.292	Yb1–O1	2.282
Tb1–O5	2.328	Dy1–O5	2.324	Ho1–O4	2.297	Er1–O4	2.307	Yb1–O4	2.284
Tb1–O8	2.323	Dy1–O8	2.315	Ho1–O7	2.321	Er1–O7	2.317	Yb1–O7	2.305
Tb1–O11	2.337	Dy1–O11	2.330	Ho1–O10	2.300	Er1–O10	2.299	Yb1–O10	2.292
Tb1–O13	2.376	Dy1–O101	2.367	Ho1–O15	2.312	Er1–O15	2.304	Yb1–O15	2.285
Tb1–O16	2.373	Dy1–O111	2.368	Ho1–O18	2.347	Er1–O18	2.340	Yb1–O18	2.320
Tb1–O18	2.300	Dy1–O121	2.294	Ho1–O19	2.345	Er1–O19	2.340	Yb1–O19	2.328
Tb1–O20	2.330	Dy1–O131	2.319	Ho1–O21	2.278	Er1–O21	2.273	Yb1–O21	2.255
Tb1–O_{ave}	2.339	Dy1–O_{ave}	2.332	Ho1–O_{ave}	2.311	Er1–O_{ave}	2.309	Yb1–O_{ave}	2.294

Table 4.6. The distance between the four neighboring atoms placed in each square for complexes **4-1** to **4-5**.

d_{in} / Å									
4-1(Tb)		**4-2(Dy)**		**4-3(Ho)**		**4-4(Er)**		**4-5(Yb)**	
O2–O5	2.617	O2–O5	2.614	O1–O4	2.602	O1–O4	2.626	O1–O4	2.617
O5–O8	2.673	O5–O8	2.670	O4–O7	2.632	O4–O7	2.630	O4–O7	2.620
O8–O11	2.645	O8–O11	2.643	O7–O10	2.584	O7–O10	2.601	O7–O10	2.605
O11–O2	2.644	O11–O2	2.643	O10–O1	2.639	O10–O1	2.655	O10–O1	2.647
O13–O16	2.887	O101–O111	2.870	O15–O18	2.894	O15–O18	2.859	O15–O18	2.834
O16–O18	2.893	O111–O121	2.870	O18–O19	2.838	O18–O19	2.822	O18–O19	2.791
O18–O20	2.907	O121–O131	2.889	O19–O21	2.832	O19–O21	2.829	O19–O21	2.781
O20–O16	2.932	O131–O101	2.907	O21–O15	2.858	O21–O15	2.843	O21–O15	2.796
O–O_{ave}	2.775	O–O_{ave}	2.763	O–O_{ave}	2.735	O–O_{ave}	2.733	O–O_{ave}	2.711

Table 4.7. SHAPE analysis of eight-coordinated geometry for complexes **4-1** to **4-5**.

Label Symmetry	OP D_{8h}	HPY C_{7v}	HPBY D_{6h}	CU O_h	SAPR D_{4d}	TDD D_{2d}	JGBF D_{2d}	JETBPY D_{3h}	JBTP C_{2v}	BTPR C_{2v}	JSD D_{2d}	TT T_d	ETBPY D_{3h}
4-1(Tb)	29.509	23.687	16.407	9.164	0.405	2.358	16.463	29.276	2.884	1.805	5.447	9.994	24.338
4-2(Dy)	29.692	23.661	16.362	9.107	0.395	2.331	16.470	29.310	2.896	1.856	5.443	9.940	24.364
4-3(Ho)	29.909	23.626	16.234	9.116	0.411	2.348	16.332	29.173	2.902	1.837	5.468	9.958	24.396
4-4(Er)	29.883	23.680	16.332	9.040	0.372	2.316	16.503	29.392	2.895	1.908	5.459	9.871	24.450
4-5(Yb)	30.125	23.583	16.129	8.889	0.366	2.287	16.451	29.422	2.919	1.977	5.472	9.723	24.560

Abbreviations: OP – Octagon, HPY – Heptagonal pyramid, HBPY – Hexagonal bipyramid, CU – Cube, SAPR – Square antiprism, TDD – Triangular dodecahedron, JGBF – Johnson – Gyrobifastigium (J26), JETBPY – Johnson Elongated triangular bipyramid (J14), JBTP – Johnson Biaugmented trigonal prism (J50), BTPR – Biaugmented trigonal prism, JSD – Snub disphenoid (J84), TT – Triakis tetrahedron, ETBPY – Elongated trigonal pyramid.

Sandwich $[Ln_2Ga_8(shi)_8(C_6H_2C_2O_4)_4(DMF)_6Na_2]\cdot(DMF)_x\cdot(H_2O)_y$

Single crystal X-ray analysis of complexes **4-6** to **4-10** revealed that the binuclear lanthanide MC complexes have also a distorted D_{4d} symmetry (Figure 4.3), as noted in Table 4.8. They are isostructural and crystallize in the monoclinic $P2_1/n$ space group. Therefore, only the dysprosium(III) complex **4-7** will be described in detail. The four organic ligands shi^{3-} bridge the Ga^{III} ions forming a [12-$MC_{Ga^{III}}$-4] ring with –[Ga–N–O]– as the repeat unit. Two Ga^{III} ions are five-coordinated with shi^{3-} ligands and isophthalate ligands. While the other two Ga^{III} ions are six-coordinated with one water molecule and one DMF solvents bound axially. The central Dy^{III} ion is bridged to the [12-$MC_{Ga^{III}}$-4] ring by four isophthalates and four shi^{3-} ligands, meanwhile, four isophthalates bridged two [12-$MC_{Ga^{III}}$-4] rings. The four hydroximate oxygen atoms (O_{MC}) form a planar square, while the four oxygen atoms (O_{iso}) of isophthalate serve as another square, and adopts an eight-coordinated square antiprism geometry (quasi-double deck structure), which was also confirmed by the continued shape measurements (CShM) SHAPE analysis,[38, 39] the results are listed in Table 4.13 for the five complexes. The skew angle (ϕ) defined as the offset between the two squares defined by the mean planes through the coordinating oxygen atoms (O1, O4, O18, O20 and O7, O10, O13, O16) (Figure 4.3) are equal to 39.98°, 49.07°, 48.80° and 42.16° (Table 4.9). In contrast to the ideal D_{4d} symmetry with ϕ = 45°, the minimum of the mean absolute deviation for ϕ (MAD_ϕ) in Table 4.10 indicates that the Dy^{III} coordination site can be described as a slightly distorted square antiprism. Dy–O distances also support this minor distortion because they range from 2.575 to 2.908 Å (average value 2.750 Å, Table 4.12). The distance d_{pp} (Figure 4.3 left) between the squares formed by the oxygen atoms is equal to 2.565 Å, and the average distance between the four neighboring oxygen atoms placed in each plane, d_{in} (Figure 4.3 left) is 2.750 Å. The local structure of Dy^{III} can be considered as an elongated square antiprism (Table 4.10 and Table 4.11). The four Ga^{III} ions are crystallographically inequivalent as in the preceding complexes. The negative charge of the 12-MC-4 metallacrown is balanced by one sodium cation, which was found to coordinate with one DMF and three shi^{3-} ligands. Meanwhile, the analysis of the packing arrangement reveals that one $Ln_2Ga_8shi_8$ molecule is arranged perpendicular to the others (Figure 4.4).

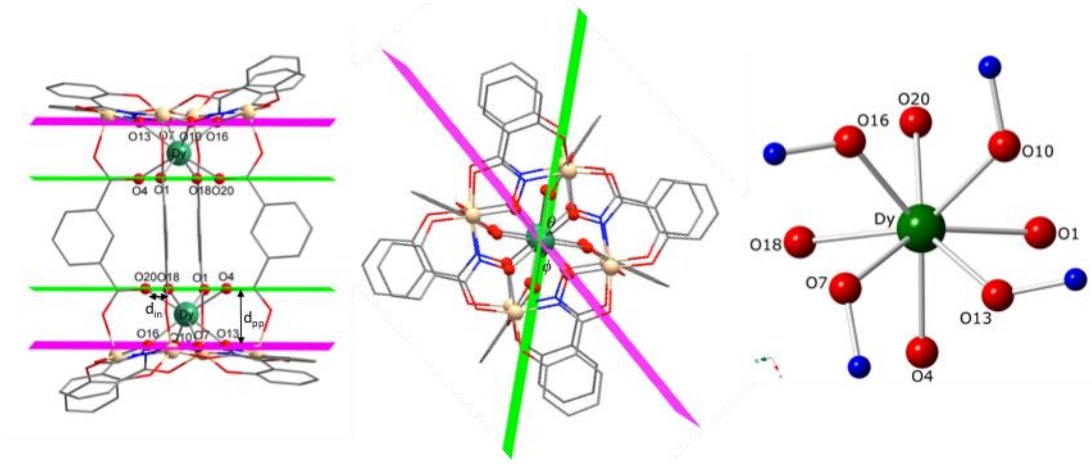

Figure 4.3. Molecular structure of complex **4-7** obtained from X-ray diffraction: (left) side-view perspective showing d_{in} and d_{pp}; (middle) top-down view showing ϕ and θ structural features of the [12-$MC_{Ga^{III}}$-4] core; (bottom) square-antiprismatic coordination geometry around the central Dy^{III} ion. Dy – green; Ga – tan; O – red; N – blue; C – grey; H atoms and solvent molecules coordinated to Ga^{III} were omitted for clarity.

Table 4.8. Crystallographic data structure refinement for complexes **4-6** to **4-10**.

Complexes	**4-6(Tb_2)**	**4-7(Dy_2)**	**4-8(Ho_2)**	**4-9(Er_2)**	**4-10(Yb_2)**
formula	$C_{118}H_{118}Ga_8N_{18}Na_2O_{56}Tb_2$	$C_{118}H_{130}Ga_8N_{18}Na_2O_{56}Dy_2$	$C_{118}H_{118}Ga_8N_{18}Na_2O_{56}Ho_2$	$C_{118}H_{118}Ga_8N_{18}Na_2O_{56}Er_2$	$C_{118}H_{118}Ga_8N_{18}Na_2O_{56}Yb_2$
M_r	3605.88	3625.15	3617.91	3622.56	3634.13
cryst size, mm^3	0.32 × 0.17 × 0.11	0.41 × 0.29 × 0.12	0.29 × 0.13 × 0.04	0.28 × 0.13 × 0.04	0.29 × 0.12 × 0.04
cryst syst	Monoclinic	Monoclinic	Monoclinic	Monoclinic	Monoclinic
space group	$P2_1/n$	$P2_1/n$	$P2_1/n$	$P2_1/n$	$P2_1/n$
a, Å	14.6832(7)	14.6631(5)	14.6517(14)	14.6621(7)	14.6643(5)
b, Å	21.8429(11)	21.8204(7)	21.848(2)	21.8274(11)	21.8542(7)
c, Å	21.722(1)	21.7429(8)	21.770(2)	21.7260(12)	21.7423(7)
α, deg	90	90	90	90	90
β, deg	106.304(2)	106.526(1)	106.425(4)	106.276(2)	106.165(1)
γ, deg	90	90	90	90	90
cell volume, $Å^3$	6686.6(6)	6669.4(4)	6684.6(11)	6674.4(6)	6692.4(4)
Z	2	2	2	2	2
T, K	100(1)	100(1)	100(1)	100(1)	100(1)
F_{000}	3600	3628	3608	3612	3620
μ, mm^{-1}	2.735	2.802	2.861	2.938	3.073
θ range, deg	2.4–30.5	2.2–31.5	2.2–30.2	2.2–30.5	2.3–30.5
reflns collected	100257	140882	126518	134772	109215
reflns unique	20244	22311	20499	20483	20156
R_{int}	0.0461	0.0321	0.0834	0.0386	0.0468
R_1	0.0531	0.0426	0.0601	0.0436	0.0500
wR_2 (all data)	0.1150	0.1183	0.1588	0.1175	0.1371
GOF	1.118	1.048	1.086	1.093	1.060
largest diff. peak and hole ($e·Å^{-3}$)	3.46, −1.40	4.68, −2.34	4.28, −1.96	4.44, −1.47	5.97, −1.87

Table 4.9. Characteristic parameters (θ, ϕ) of a square anti-prism geometry for complexes **4-6** to **4-10**.

Angle / °	4-6(Tb_2)		4-7(Dy_2)		4-8(Ho_2)		4-9(Er_2)		4-10(Yb_2)		Ideal D_{4d}[24, 44]
θ1	O1	61.64	O18	61.35	O1	60.80	O1	60.51	O1	59.88	57.23
θ2	O3	60.45	O4	60.20	O3	59.65	O3	59.35	O3	58.79	57.23
θ3	O7	61.50	O1	61.31	O7	60.44	O7	60.32	O7	59.58	57.23
θ4	O5	59.96	O20	59.69	O5	59.25	O5	58.87	O5	58.14	57.23
θ5	O11	52.97	O16	53.09	O11	53.17	O11	53.39	O11	53.69	57.23
θ6	O14	51.24	O7	51.31	O14	51.65	O14	51.98	O14	52.34	57.23
θ7	O20	52.20	O13	52.38	O20	52.55	O20	52.75	O20	53.06	57.23
θ8	O17	53.30	O10	53.41	O17	53.33	O17	53.66	O17	54.05	57.23
ϕ1	O1	40.69	O18	39.98	O1	40.04	O1	39.99	O1	40.05	45
ϕ2	O3	48.98	O4	49.07	O3	49.08	O3	49.06	O3	49.20	45
ϕ3	O7	48.66	O1	48.80	O7	48.74	O7	48.92	O7	48.91	45
ϕ4	O5	42.29	O20	42.16	O5	42.15	O5	42.04	O5	41.85	45

Table 4.10. Structural parameters of a square anti-prism geometry for complexes **4-6** to **4-10**.

Complexes	Ln–O_{ave} [a] / Å	MAD_ϕ [b] / °	d_{in} [c] / Å	d_{pp} [d] / Å	d_{pp}/d_{in} [e]
4-6(Tb_2)	2.349	3.665	2.768	2.575	0.930
4-7(Dy_2)	2.335	3.933	2.750	2.565	0.932
4-8(Ho_2)	2.327	3.908	2.734	2.573	0.941
4-9(Er_2)	2.319	3.988	2.726	2.565	0.941
4-10(Yb_2)	2.306	4.053	2.707	2.563	0.947

[a] The average values for bond lengths of Ln–O; [b] MAD = mean absolute deviation, skew angle ϕ for the ideal D_{4d} ligand field symmetry is 45°; [c] d_{in} means the average distance between the four neighboring atoms placed in each square; [d] d_{pp} means the distance between two centroids from the upper and lower planes respectively; [e] d_{pp}/d_{in} is 0.841 for the ideal square antiprism.[23, 44]

 Feng SHAO: 0000-0001-8606-8628

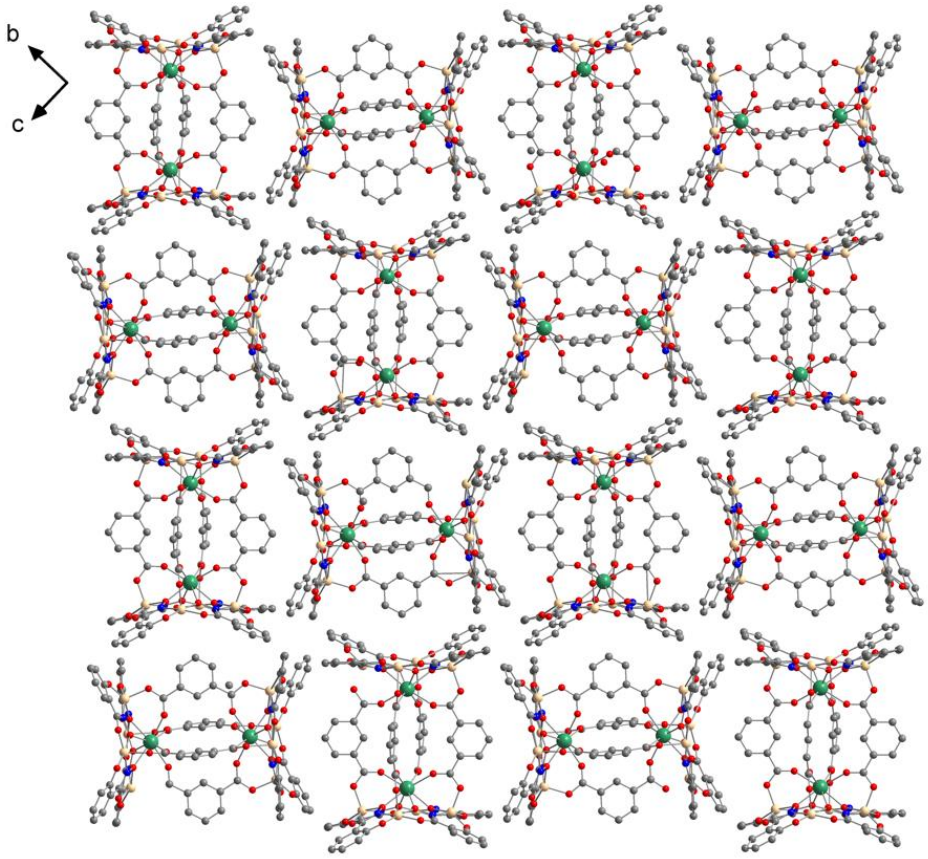

Figure 4.4. The packing arrangement of complex **4-7**. Dy – green; Ga – tan; O – red; N – blue; C – grey; H atoms and solvent molecules coordinated to Ga^{III} were omitted for clarity.

Table 4.11. Lanthanide center bonds with oxygen for complexes **4-6** to **4-10**.

Bond length / Å									
4-6(Tb_2)		**4-7(Dy_2)**		**4-8(Ho_2)**		**4-9(Er_2)**		**4-10(Yb_2)**	
Tb1–O1	2.358	Dy1–O18	2.348	Ho1–O1	2.336	Er1–O1	2.331	Yb1–O1	2.321
Tb1–O3	2.318	Dy1–O4	2.304	Ho1–O3	2.299	Er1–O3	2.291	Yb1–O3	2.276
Tb1–O7	2.380	Dy1–O1	2.367	Ho1–O7	2.361	Er1–O7	2.352	Yb1–O7	2.341
Tb1–O5	2.339	Dy1–O20	2.327	Ho1–O5	2.317	Er1–O5	2.312	Yb1–O5	2.300
Tb1–O11	2.323	Dy1–O16	2.308	Ho1–O11	2.301	Er1–O11	2.293	Yb1–O11	2.280
Tb1–O14	2.381	Dy1–O7	2.366	Ho1–O14	2.352	Er1–O14	2.342	Yb1–O14	2.330
Tb1–O20	2.348	Dy1–O13	2.331	Ho1–O20	2.325	Er1–O20	2.316	Yb1–O20	2.302
Tb1–O17	2.343	Dy1–O10	2.331	Ho1–O17	2.326	Er1–O17	2.316	Yb1–O17	2.301
$Tb1–O_{ave}$	2.349	$Dy1–O_{ave}$	2.335	$Ho1–O_{ave}$	2.327	$Er1–O_{ave}$	2.319	$Yb1–O_{ave}$	2.306

Table 4.12. The distance between the four neighboring atoms placed in each square for complexes **4-6** to **4-10**.

	d_{in} / Å								
4-6(Tb_2)		**4-7(Dy_2)**		**4-8(Ho_2)**		**4-9(Er_2)**		**4-10(Yb_2)**	
O1–O3	2.860	O18–O4	2.838	O1–O3	2.815	O1–O3	2.798	O1–O3	2.771
O3–O7	2.932	O4–O1	2.908	O3–O7	2.881	O3–O7	2.865	O3–O7	2.825
O7–O5	2.898	O1–O20	2.875	O7–O5	2.846	O7–O5	2.829	O7–O5	2.797
O5–O1	2.920	O20–O18	2.900	O5–O1	2.869	O5–O1	2.856	O5–O1	2.817
O11–O14	2.588	O16–O7	2.575	O11–O14	2.571	O11–O14	2.574	O11–O14	2.572
O14–O20	2.647	O7–O13	2.632	O14–O20	2.632	O14–O20	2.627	O14–O20	2.624
O20–O17	2.620	O13–O10	2.610	O20–O17	2.605	O20–O17	2.606	O20–O17	2.603
O17–O11	2.676	O10–O16	2.664	O17–O11	2.655	O17–O11	2.652	O17–O11	2.646
O–O_{ave}	2.768	O–O_{ave}	2.750	O–O_{ave}	2.734	O–O_{ave}	2.726	O–O_{ave}	2.707

Table 4.13. SHAPE analysis of eight-coordinated geometry for complexes **4-6** to **4-10**.

Label	OP	HPY	HPBY	CU	SAPR	TDD	JGBF	JETBPY	JBTP	BTPR	JSD	TT	ETBPY
Symmetry	D_{8h}	C_{7v}	D_{6h}	O_h	D_{4d}	D_{2d}	D_{2d}	D_{3h}	C_{2v}	C_{2v}	D_{2d}	T_d	D_{3h}
4-6(Tb_2)	30.450	22.959	16.296	8.826	0.522	2.295	16.611	29.219	2.989	1.877	5.410	9.688	24.589
4-7(Dy_2)	30.547	22.946	16.231	8.758	0.525	2.265	16.559	29.257	3.003	1.900	5.401	9.622	24.562
4-8(Ho_2)	30.898	22.985	16.189	8.691	0.525	2.261	16.654	29.320	3.042	1.970	5.426	9.958	24.751
4-9(Er_2)	30.885	22.999	16.120	8.642	0.509	2.234	16.590	29.333	3.034	2.019	5.401	9.495	24.763
4-10(Yb_2)	31.125	22.969	16.064	8.558	0.504	2.213	16.571	29.369	3.055	2.120	5.404	9.409	24.836

Abbreviations: OP – Octagon, HPY – Heptagonal pyramid, HBPY – Hexagonal bipyramid, CU – Cube, SAPR – Square antiprism, TDD – Triangular dodecahedron, JGBF – Johnson – Gyrobifastigium (J26), JETBPY – Johnson Elongated triangular bipyramid (J14), JBTP – Johnson Biaugmented trigonal prism (J50), BTPR – Biaugmented trigonal prism, JSD – Snub disphenoid (J84), TT – Triakis tetrahedron, ETBPY – Elongated trigonal pyramid.

4.3.3 Magnetic Studies

4.3.3.1 Direct current magnetic susceptibility studies

Half-sandwich $[LnGa_4(shi)_4(C_6H_5CO_2)_4(C_5H_5N)(CH_3OH)]\cdot C_5H_6N\cdot C_5H_5N\cdot CH_3OH$

The direct-current (dc) magnetic susceptibility measurements were carried out between 2 and 300 K at 1000 and 10000 Oe (Figure 4.5 – Figure 4.9 left; Table 4.14). At

room temperature, $\chi_M T$ = 11.56, 13.96, 13.80, 11.56 and 2.49 $cm^3mol^{-1}K$ for complexes **4-1** to **4-5**, respectively, which are in good agreement with the expected values for mononuclear Tb^{III} (S = 3, L = 3, $^7F_6$, g = 3/2, $\chi_M T_{free\ ion}$ = 11.81 $cm^3mol^{-1}K$), Dy^{III} (S = 5/2, L = 5, $^6H_{15/2}$, g = 4/3, $\chi_M T_{free\ ion}$ = 14.17 $cm^3mol^{-1}K$), Ho^{III} (S = 2, L = 6, $^5I_8$, g = 5/4, $\chi_M T_{free\ ion}$ = 14.48 $cm^3mol^{-1}K$), Er^{III} (S = 3/2, L = 6, $^4I_{15/2}$, g = 36/5, $\chi_M T_{free\ ion}$ = 11.48 $cm^3mol^{-1}K$), and Yb^{III} (S = 1/2, L = 3, $^2F_{7/2}$, g = 8/7, $\chi_M T_{free\ ion}$ = 2.53 $cm^3mol^{-1}K$) complexes (Table 4.14). The red lines in the Figure 4.5 – Figure 4.9 left, represent the calculation values from their corresponding structures. Due to the thermal depopulation of the Stark sublevels and to the presence of significant anisotropy, the $\chi_M T$ values decrease at low temperature.

Sandwich $[Ln_2Ga_8(shi)_8(C_6H_2C_2O_4)_4(DMF)_6Na_2]\cdot(DMF)_x\cdot(H_2O)_y$

For the complexes **4-6** to **4-10**, the magnetic coupling between the lanthanide ions can be ignored because of the large isophtalate bridge between the two $LnGa_4$ species. The dc magnetic susceptibility measurements were carried out between 2 and 300 K at 1000 and 10000 Oe (Figure 4.5 – Figure 4.9 right). At room temperature, $\chi_M T$ = 23.28, 28.96, 28.18, 23.54 and 4.96 $cm^3mol^{-1}K$ for complexes **4-6** to **4-10**, respectively (Table 4.14), which are in good agreement with the expected values of two non-interacting Ln^{III} ions.

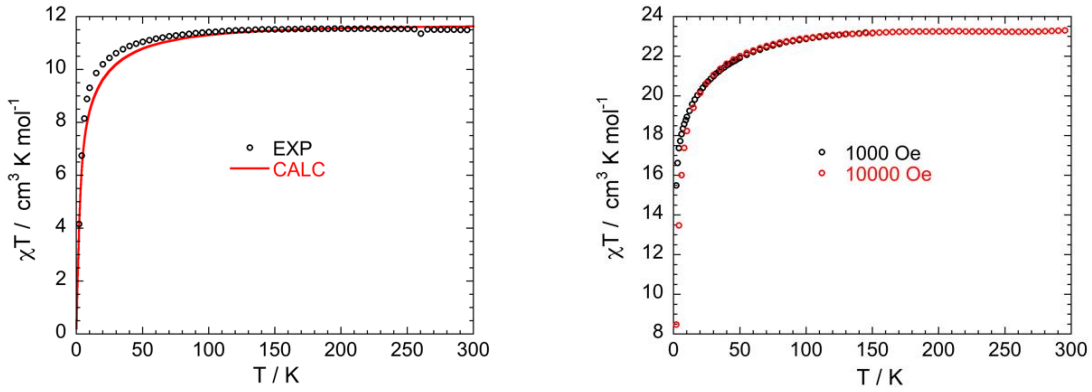

Figure 4.5. Temperature dependence of the χT product for complexes **4-1** (left, (○ (exp), – (calculated)) and **4-6** (right).

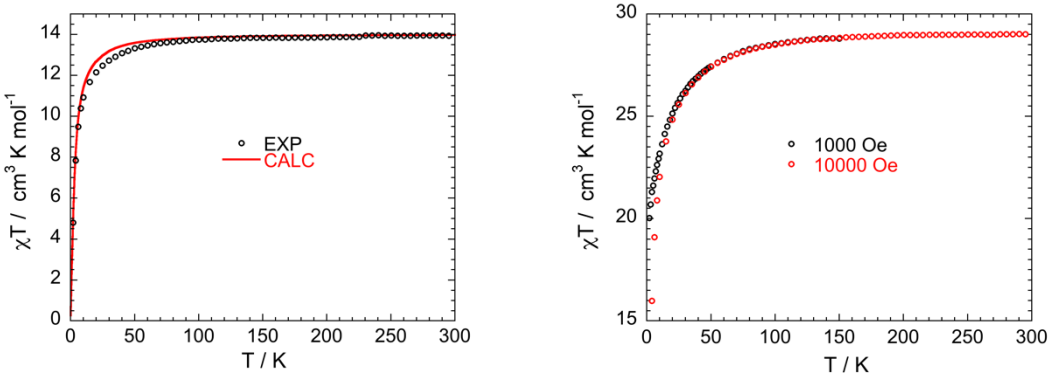

Figure 4.6. Temperature dependence of the χT product for complexes **4-2** (left, (○ (exp), – (calculated)) and **4-7** (right).

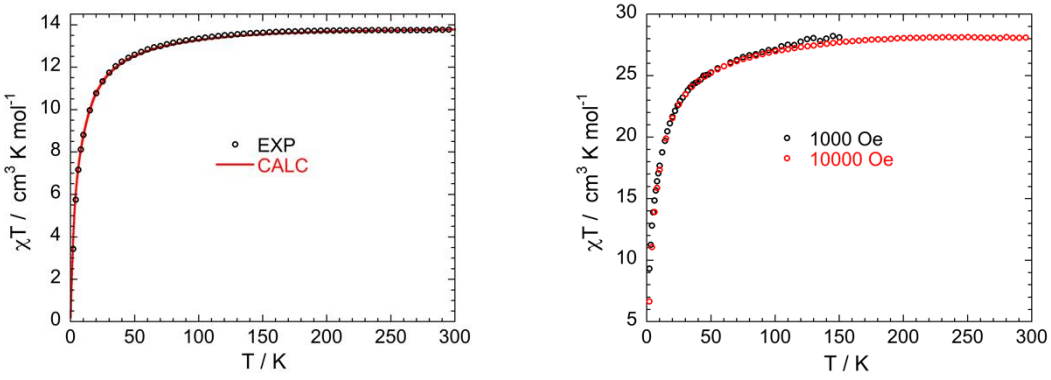

Figure 4.7. Temperature dependence of the χT product for complexes **4-3** (left, (○ (exp), – (calculated)) and **4-8** (right).

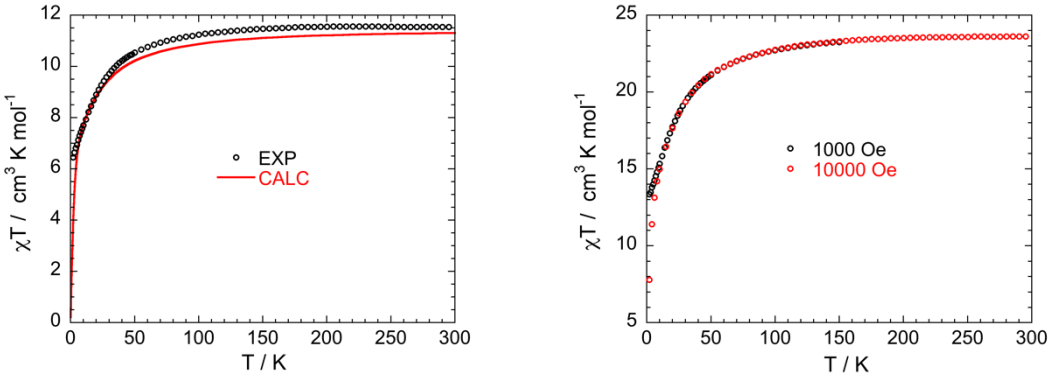

Figure 4.8. Temperature dependence of the χT product for complexes **4-4** (left, (○ (exp), – (calculated)) and **4-9** (right).

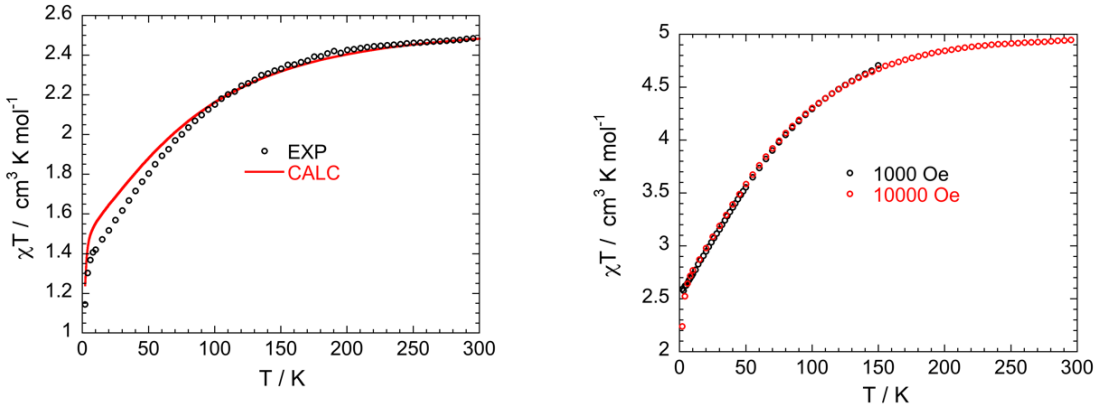

Figure 4.9. Temperature dependence of the χT product for complexes **4-5** (left, (○ (exp), – (calculated)) and **4-10** (right).

Table 4.14. Expected[a] and experimental[b] room temperature $\chi_M T$ values ($cm^3mol^{-1}K$) for complexes **4-1** to **4-10**.

Complexes	4-1(Tb)	4-2(Dy)	4-3(Ho)	4-4(Er)	4-5(Yb)	4-6(Tb_2)	4-7(Dy_2)	4-8(Ho_2)	4-9(Er_2)	4-10(Yb_2)
g_J	3/2	4/3	5/4	6/5	8/7	3/2	4/3	5/4	6/5	8/7
[a] $\chi_M T$	11.82	14.14	14.06	11.46	2.53	23.64	28.28	28.12	22.92	5.06
[b] $\chi_M T$	11.56	13.96	13.80	11.56	2.49	23.28	28.96	28.18	23.54	4.96

4.3.3.2 Magnetization versus dc magnetic field studies

The magnetization vs. the applied magnetic field M = f($\mu_0 H$) for complexes **4-1** to **4-10**, are plotted from Figure 4.10 to Figure 4.14, respectively. M = f($\mu_0 H$) has the similar behavior for the ten complexes, which does not saturate at high fields (up to 6 T) and at low temperatures. This behavior is indicative of highly magnetically anisotropic systems. The red lines in the Figure 4.10 – Figure 4.14 left, represent the theoretical values obtained from *ab initio* calculations (see below). It is worth noting that the apart from the Er^{III}-containing complex, the agreement between the calculated and the experimental magnetization is rather good. This aspect will be commented in the theoretical section.

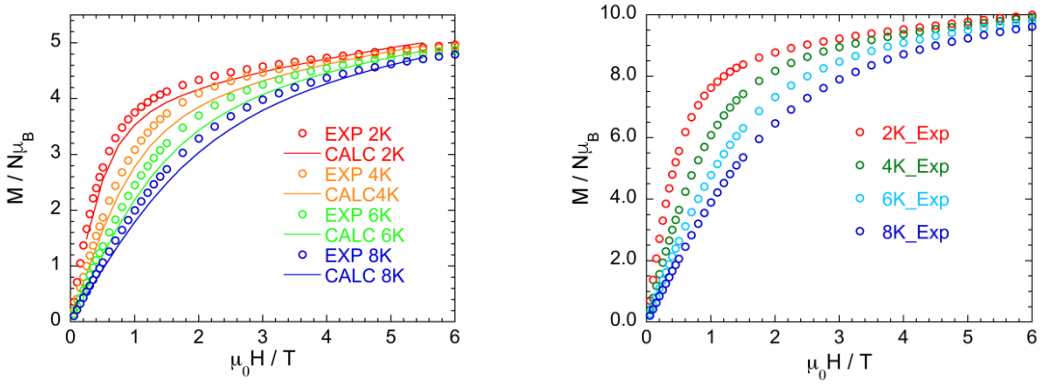

Figure 4.10. Magnetization *vs.* $\mu_0 H$ at variable temperatures for complexes **4-1** (left, (○ (exp), — (calculated)) and **4-6** (right).

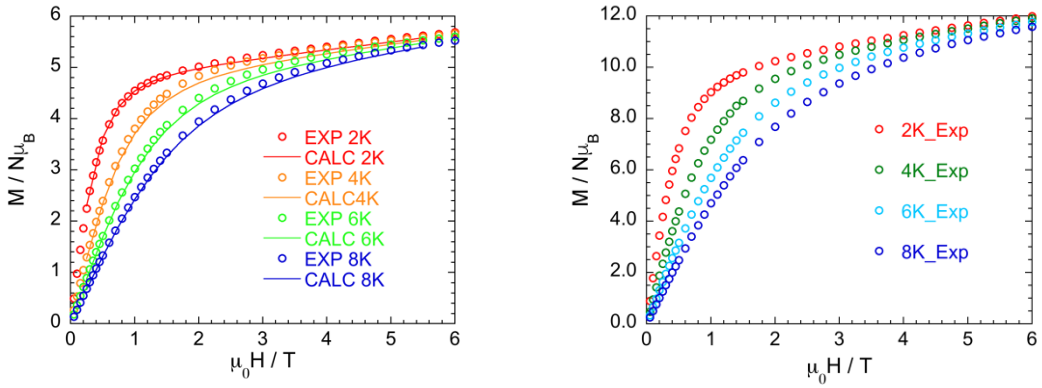

Figure 4.11. Magnetization *vs.* $\mu_0 H$ at variable temperatures for complexes **4-2** (left, (○ (exp), — (calculated)) and **4-7** (right).

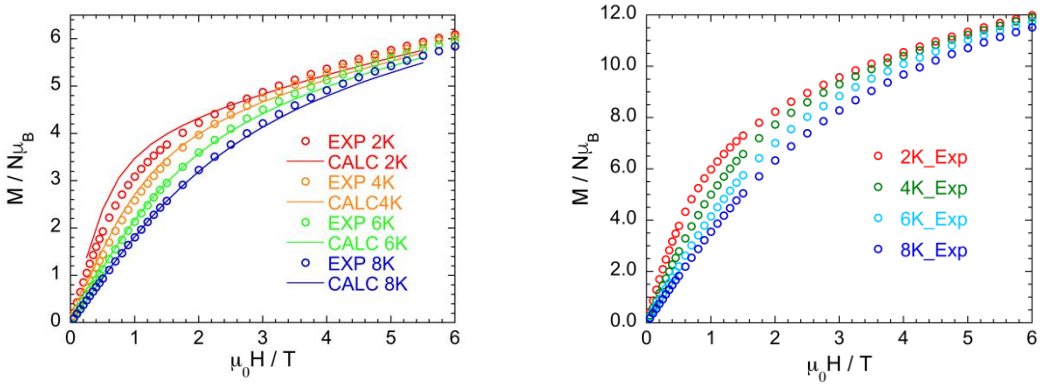

Figure 4.12. Magnetization *vs.* $\mu_0 H$ at variable temperatures for complexes **4-3** (left, (○ (exp), — (calculated)) and **4-8** (right).

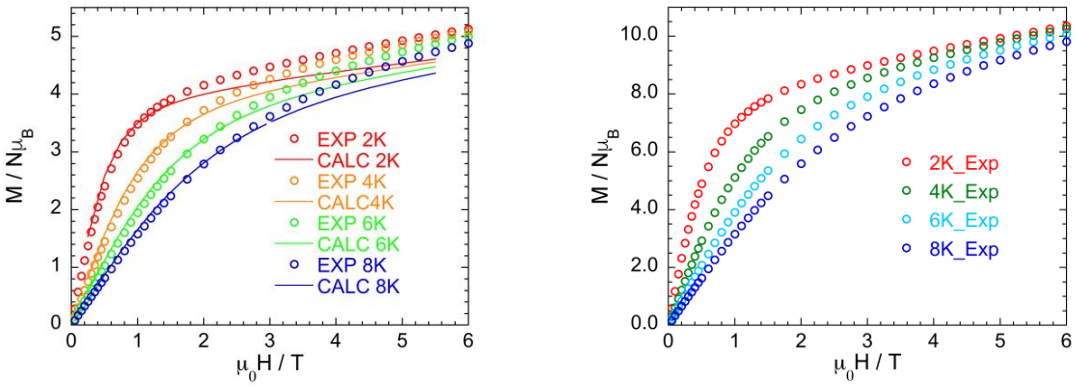

Figure 4.13. Magnetization *vs.* $\mu_0 H$ at variable temperatures for complexes **4-4** (left, (○ (exp), — (calculated)) and **4-9** (right).

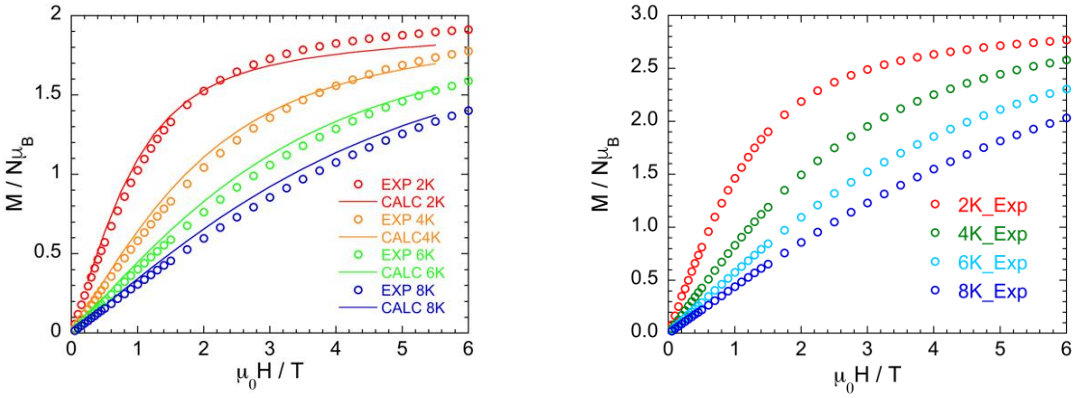

Figure 4.14. Magnetization *vs.* $\mu_0 H$ at variable temperatures for complexes **4-5** (left, (○ (exp), — (calculated)) and **4-10** (right).

4.3.3.3 Alternating current magnetic susceptibility studies

Relevant ac data can be found from Figure 4.15 to Figure 4.38. Some magnetic parameters extracted for these complexes also can be found in Table 4.15 and Table 4.16.

Field optimization experiments revealed that the Tb^{III}- and Ho^{III}-containing complexes (**4-1**, **4-3**, **4-6**, and **4-8**) do not display slow relaxation of their magnetization in the frequency range studied. The other complexes do show magnetic relaxation, and their dynamic magnetic properties are similar. We, thus, describe the Dy^{III} complexes **4-2** and **4-7** in more details.

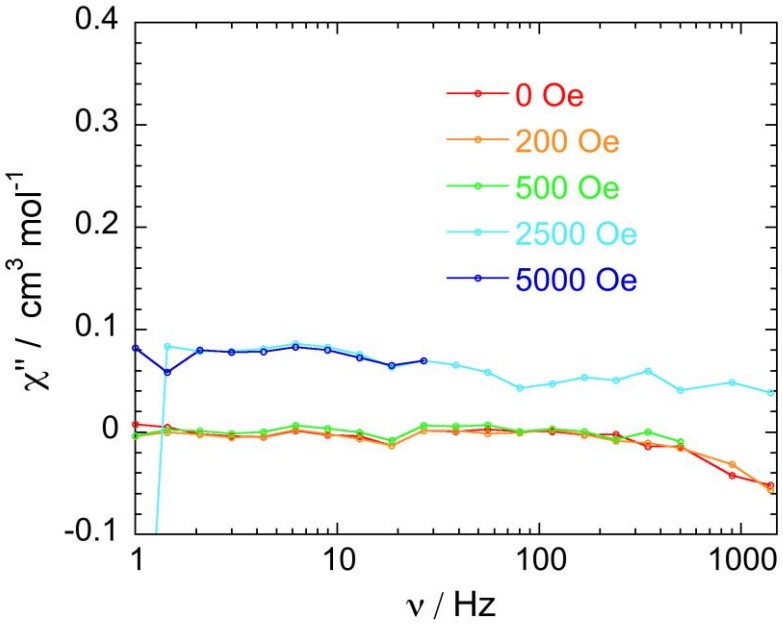

Figure 4.15. Out-of-phase susceptibility measurements at 2 K with a frequency range from 1 to 1500 Hz under various applied dc fields for complex **4-1**.

Complex 4-2

Under zero dc magnetic field, there is no out-of-phase signal (Figure 4.16 left) for complex **4-2**. Field optimization experiment was studied at T = 2 K with an applied dc field range 0 – 4000 Oe (Figure 4.16 left), which reveals that the optimum applied dc field is between 600 and 1600 Oe (Figure 4.16 right). A static dc magnetic field of 800 Oe where the maximum of χ'' is the largest was thus chosen. The maximum in the frequency-dependent ac susceptibility χ'' plot complex **4-2** shifts towards low frequency upon cooling down (Figure 4.17 right). The ac data were fitted using the generalized Debye model[45, 46] which allows plotting the Cole-Cole curves in the temperature range 1.83 – 6.00 K (Figure 4.18) and extracting the relaxation times (τ) and their distribution (α) for each temperature (Table 4.15). Fitting high temperature linear part of the ln(τ) = f(1/T) plot (Figure 4.19) leads to an effective energy barrier U_{eff} of 23.5 K (16.3 cm^{-1}) and τ_0 is 5.1 × 10^{-6} s.

The same studies were carried out on all the complexes and the data were analyzed similarly when an out-of-phase was observed. The Er^{III}- and Yb^{III}-containing complexes show a slow relaxation of their magnetization but with rather short relaxation times in the order of 10^{-3} s (Table 4.15). Apart from the Dy^{III} complex, the α values are below 0.13

indicating weak distribution of relaxation times.

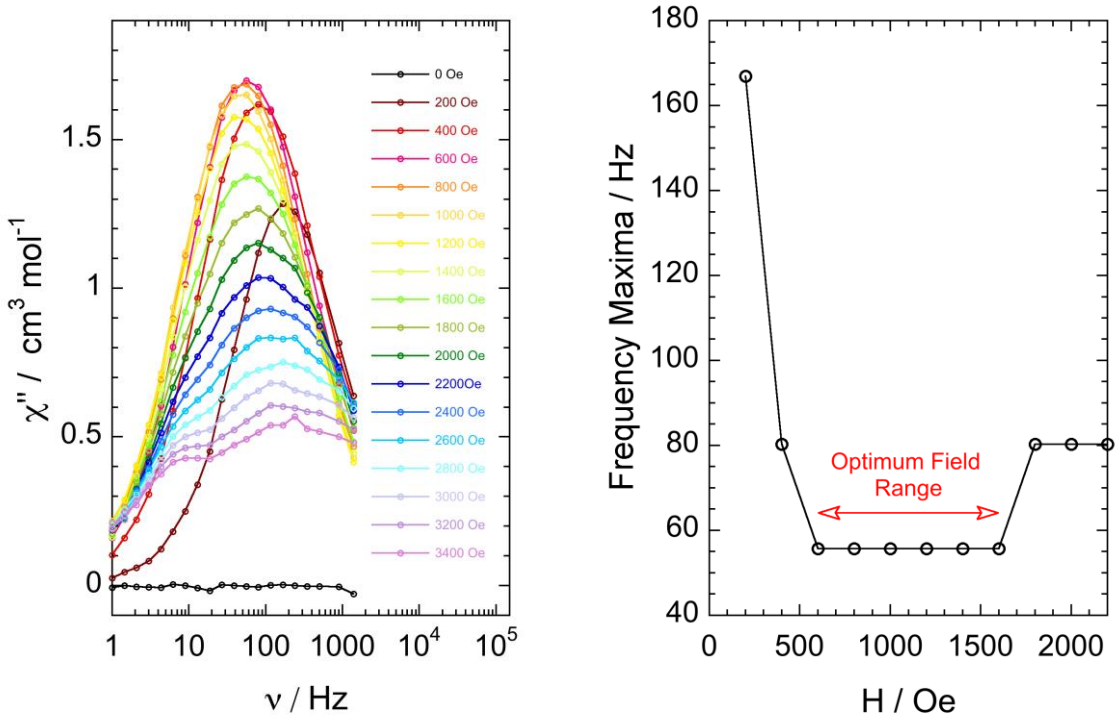

Figure 4.16. Out-of-phase susceptibility measurements at 2 K with a frequency range from 1 to 1500 Hz under various applied dc fields (left) and plot of frequency maxima *vs.* applied dc fields (right) for complex **4-2**.

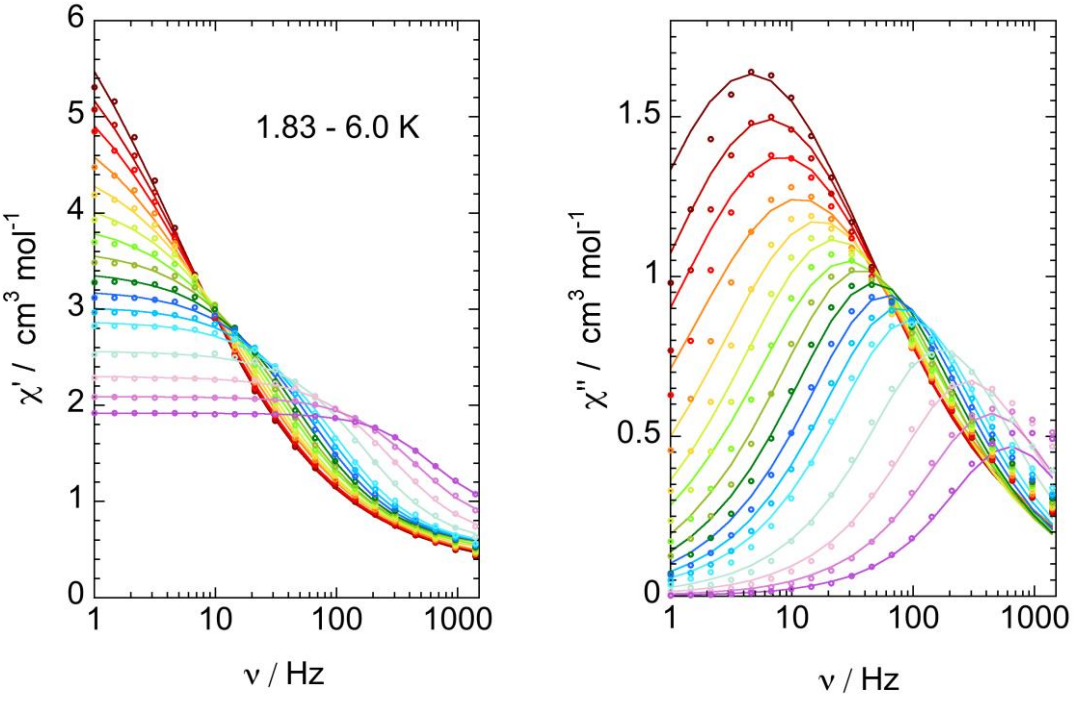

Figure 4.17. Frequency dependent in-phase and out-of-phase ac magnetic susceptibilities (○ (exp), — (fit)) for complex **4-2** under an applied dc field of 800 Oe.

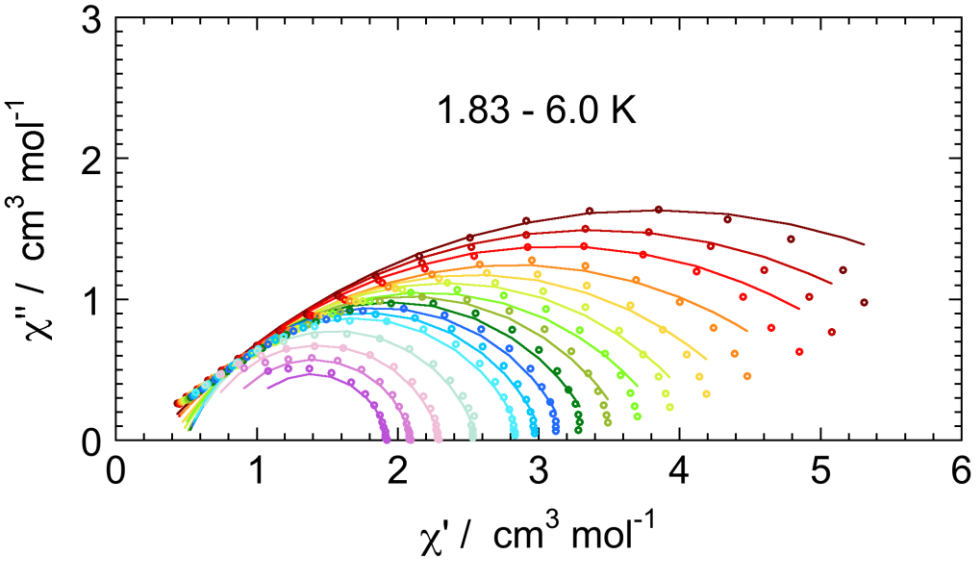

Figure 4.18. Cole-Cole plots (○ (exp), — (fit)) for complex **4-2** under an applied dc field of 800 Oe.

Table 4.15 Cole-Cole fit parameters under an applied dc magnetic field of 800 Oe for complexes **4-2**, **4-4**, **4-5** and 1600 Oe for complex **4-10**.

Complexes	Temperature	χ_0	χ_∞	α	τ
4-2	1.80 K	7.3715623120	0.2686045410	0.4512059977	0.0345974083
	2.00 K	6.4814403340	0.3089439370	0.4269622774	0.0244206240
	2.20 K	5.9401790524	0.3122588766	0.4210129682	0.0191558392
	2.40 K	5.3397954270	0.3114469653	0.4151132503	0.0138392142
	2.60 K	4.6976342809	0.3882302184	0.3648431316	0.0094565169
	2.80 K	4.2640135092	0.4362628505	0.3278258357	0.0070763999
	3.00 K	3.9741389034	0.4257512876	0.3198949549	0.0054761439
	3.20 K	3.6571358890	0.4804435348	0.2718303693	0.0042742802
	3.40 K	3.4120180120	0.4956241707	0.2463723815	0.0033400814
	3.60 K	3.2130307527	0.5017288394	0.2267547123	0.0026322871
	3.80 K	3.0379401190	0.5029850199	0.2110417098	0.0020844570
	4.00 K	2.8809990096	0.5063160740	0.1976078467	0.0016593327
	4.50 K	2.5658615668	0.5284316456	0.1708103160	0.0009451760
	5.00 K	2.3006862319	0.5764657221	0.1549205354	0.0005492242
	5.50 K	2.0913612940	0.7128434078	0.1180783799	0.0003629330
	6.00 K	1.9186976124	0.8642993986	0.0744750290	0.0002555999
4-4	1.80 K	5.246359500	0.509306666	0.069418757	0.000725573
	2.00 K	4.828949695	0.514724596	0.064713062	0.000554802
	2.25 K	4.401117411	0.319238518	0.081133564	0.000354693
	2.50 K	3.939165626	0.549190723	0.046797677	0.000235646
	2.75 K	3.599151792	0.524775910	0.040044402	0.000139016
	3.00 K	3.309192143	0.887428649	0.010494654	0.000090964
4-5	1.80 K	0.732841294	0.087366787	0.132129062	0.001328243
	2.00 K	0.676361900	0.076723937	0.140391227	0.001114053
	2.25 K	0.611314735	0.073106913	0.142138468	0.000906361
	2.50 K	0.545311215	0.073001031	0.126190966	0.000704428
	2.75 K	0.493856466	0.069672110	0.106973767	0.000554664
	3.00 K	0.452461524	0.062211002	0.093184978	0.000429613
	3.50 K	0.387982098	0.078783812	0.043587003	0.000284483
	4.00 K	0.340255366	0.082906982	0.031116781	0.000169384
	4.50 K	0.303558438	0.044139011	0.048186186	0.000084583
4-10	1.83 K	1.3761444145	0.1856151509	0.0704753841	0.0007213603
	2.00 K	1.2587022823	0.1640470156	0.0736783452	0.0005804930
	2.20 K	1.1680647782	0.1403343000	0.0785754368	0.0004670721
	2.40 K	1.0704416325	0.1404842438	0.0677893276	0.0003841142
	2.60 K	0.9910088599	0.1260679706	0.0611074190	0.0003073685
	2.80 K	0.9256948506	0.1159009546	0.0545641964	0.0002534283
	3.00 K	0.8673328560	0.1088076887	0.0488150007	0.0002090351
	3.30 K	0.7934558610	0.1026582624	0.0391474495	0.0001587682
	3.60 K	0.7325852531	0.0455409645	0.0603367351	0.0001106628
	4.00 K	0.6640367143	0.0403498440	0.0502831465	0.0000798682

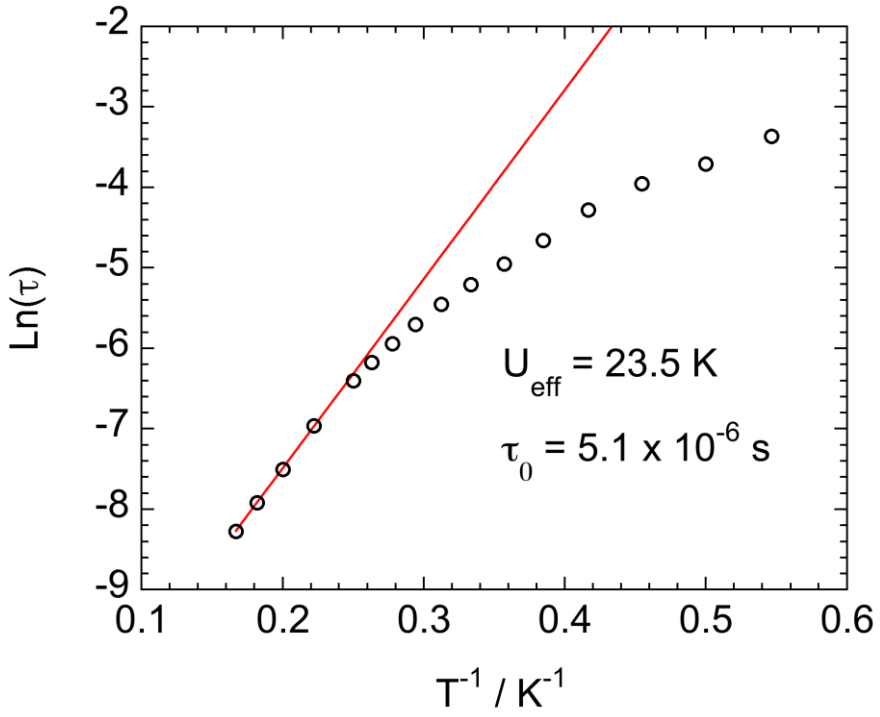

Figure 4.19. ln(τ) = f(1/T) plot (○ (exp), — (linear fit)) for the relaxation processes for complex **4-2** under an applied dc field of 800 Oe.

Table 4.16. Magnetic parameters for complexes **4-1** to **4-10**.

Complexes	**4-2**	**4-4**	**4-5**	**4-7**	**4-9**	**4-10**
[a] *OFR*	600 – 1600	800 – 1000	800 – 1200	—	—	1800 – 2200
[b] TF	800	800	800	800	1800	2200
[c] U_{eff}	16.3	9.9	13.1	—	—	9.0
[d] τ_0	5.1×10^{-6}	7.8×10^{-7}	1.4×10^{-6}	—	—	3.1×10^{-6}

[a] Optimum Field Range in Ørsted (Oe); [b] Test Field in Ørsted (Oe); [c] effective energy barriers in wavenumbers (cm^{-1}). [d] pre-exponential factor in seconds (s).

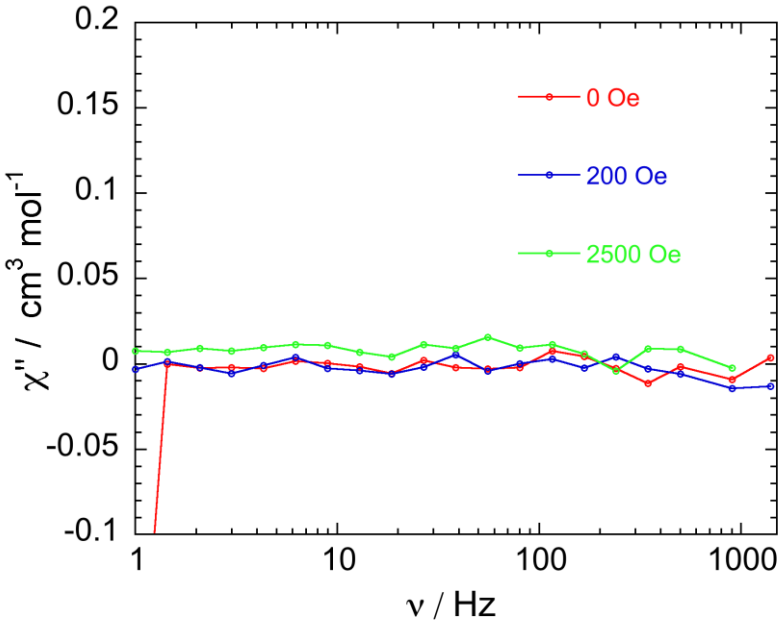

Figure 4.20. Out-of-phase susceptibility measurements at 2 K with a frequency range from 1 to 1500 Hz under various applied dc fields for complex **4-3**.

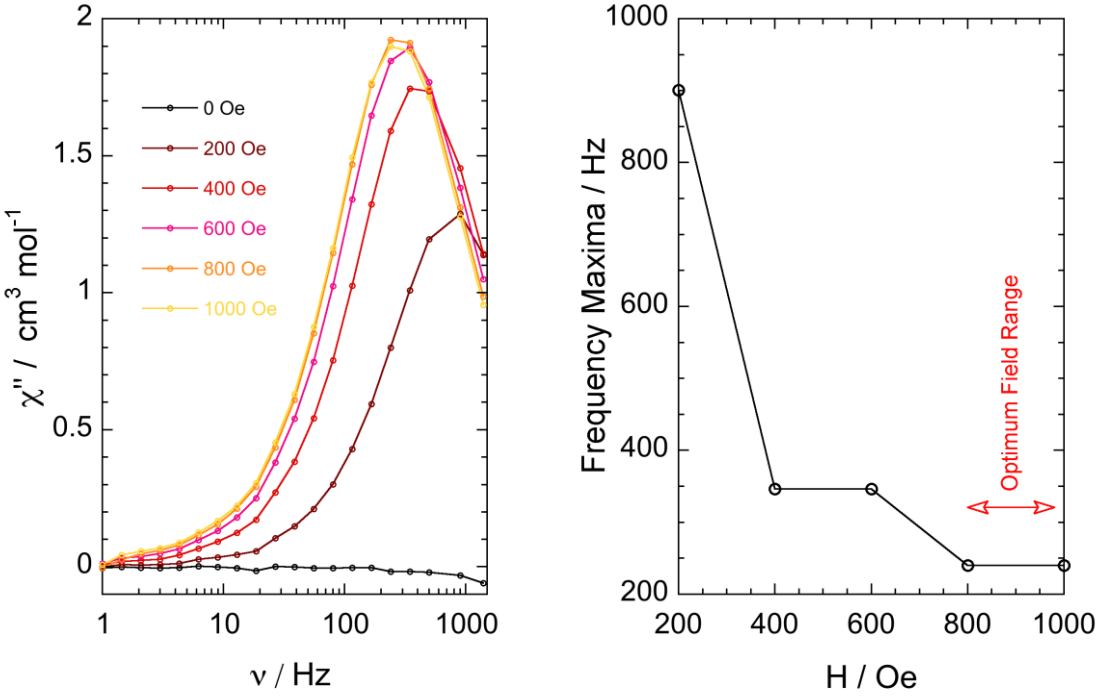

Figure 4.21. Out-of-phase susceptibility measurements at 2 K with a frequency range from 1 to 1500 Hz under various applied dc fields (left) and plot of frequency maxima *vs.* applied dc fields (right) for complex **4-4**.

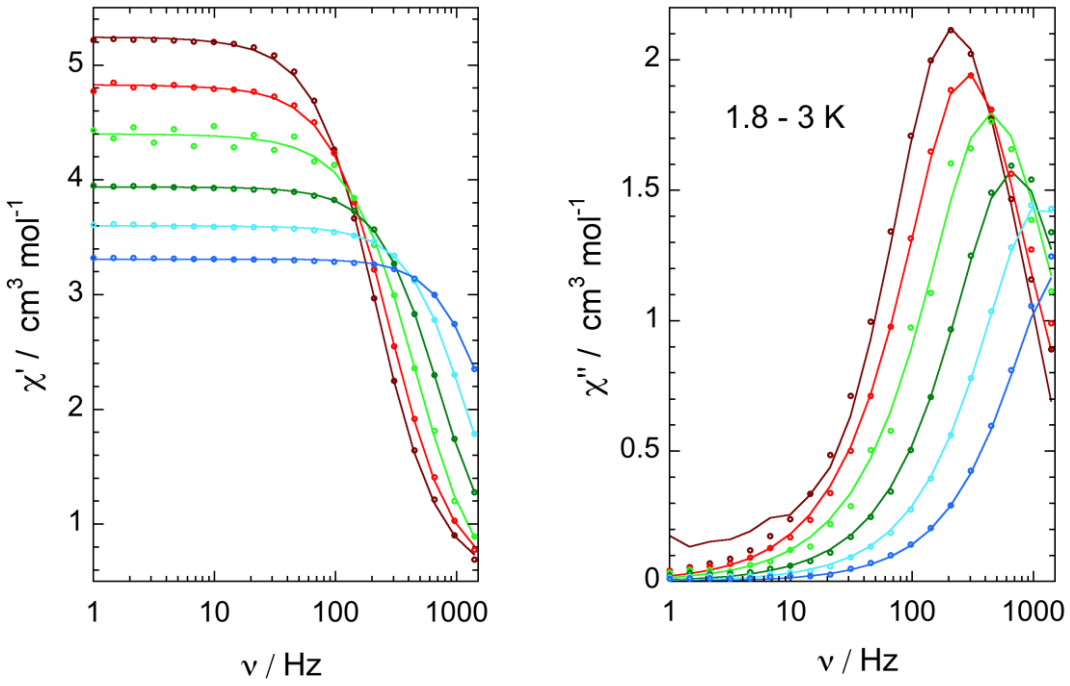

Figure 4.22. Frequency dependent in-phase and out-of-phase ac magnetic susceptibilities (○ (exp), — (fit)) for complex **4-4** under an applied dc field of 800 Oe.

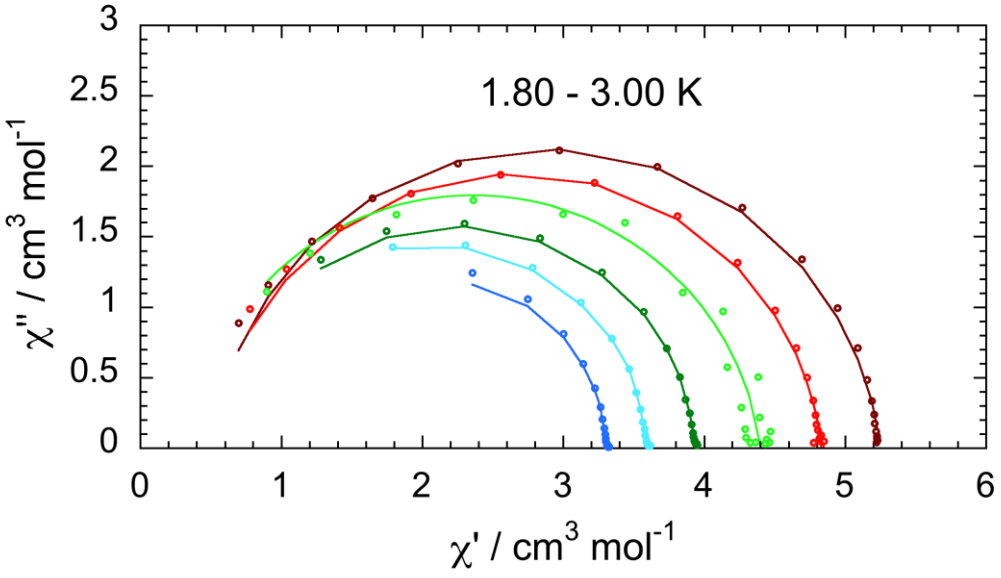

Figure 4.23. Cole-Cole plots (○ (exp), — (fit)) for complex **4-4** under an applied dc field of 800 Oe.

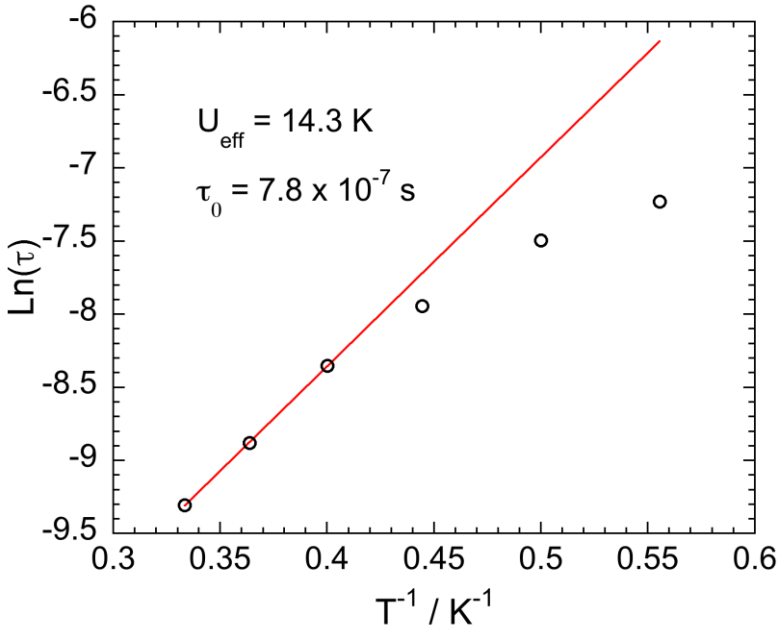

Figure 4.24. ln(τ) = f(1/T) plot (○ (exp), — (linear fit)) for the relaxation processes for complex **4-4** under an applied dc field of 800 Oe.

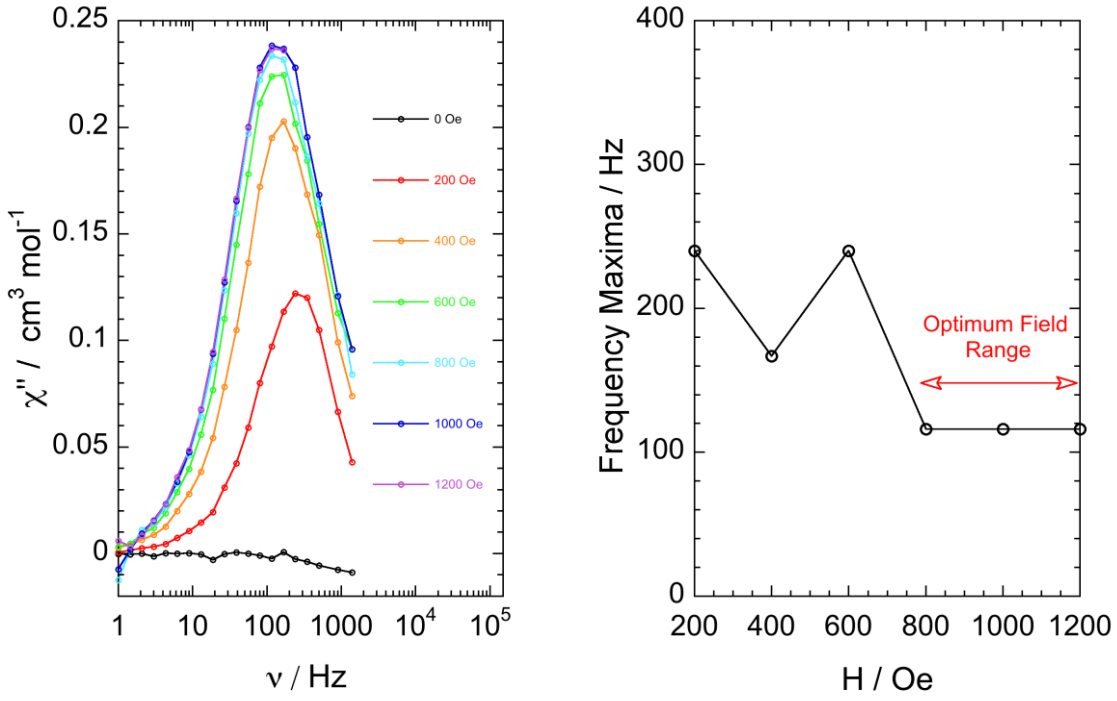

Figure 4.25. Out-of-phase susceptibility measurements at 2 K with a frequency range from 1 to 1500 Hz under various applied dc fields (left) and plot of frequency maxima *vs.* applied dc fields (right) for complex **4-5**.

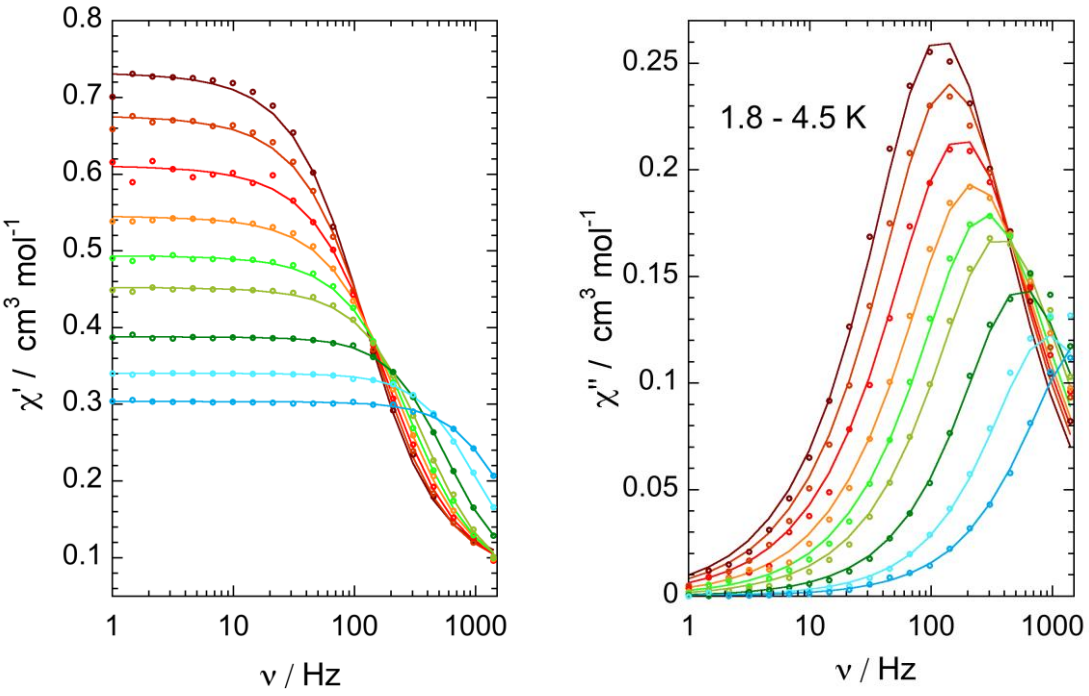

Figure 4.26. Frequency dependent in-phase and out-of-phase ac magnetic susceptibilities (○ (exp), — (fit)) for complex **4-5** under an applied dc field of 800 Oe.

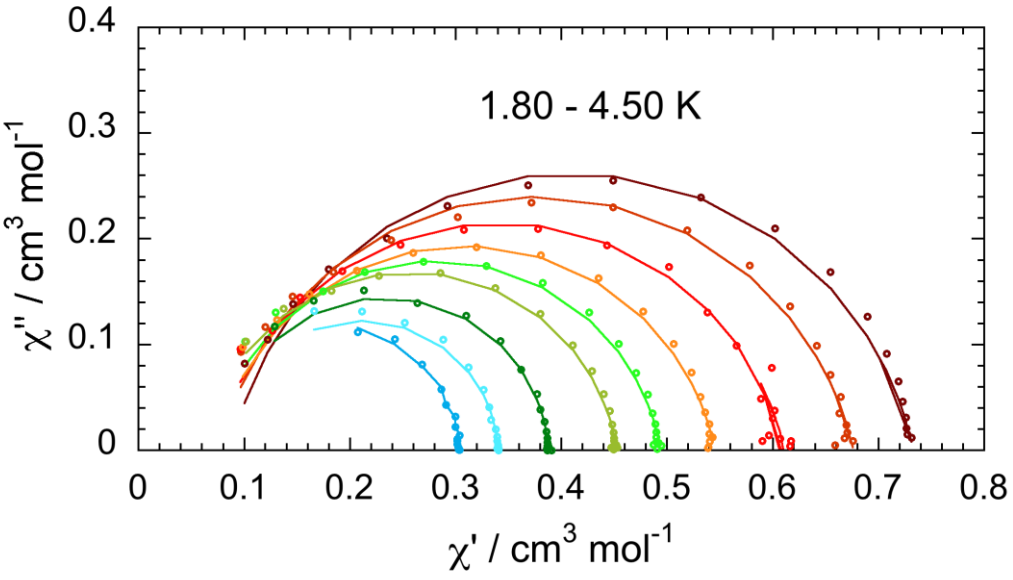

Figure 4.27. Cole-Cole plots (○ (exp), — (fit)) for complex **4-5** under an applied dc field of 800 Oe.

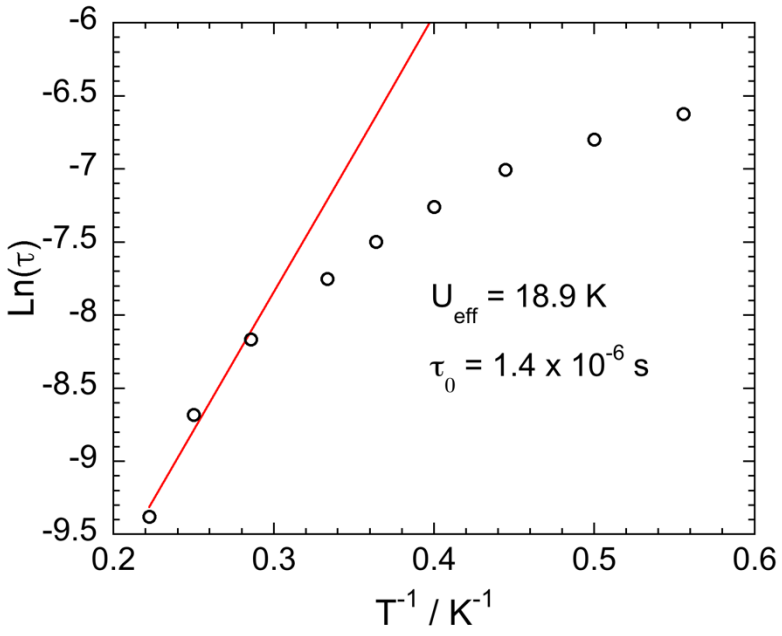

Figure 4.28. ln(τ) = f(1/T) plot (○ (exp), — (linear fit)) for the relaxation processes for complex **4-5** under an applied dc field of 800 Oe.

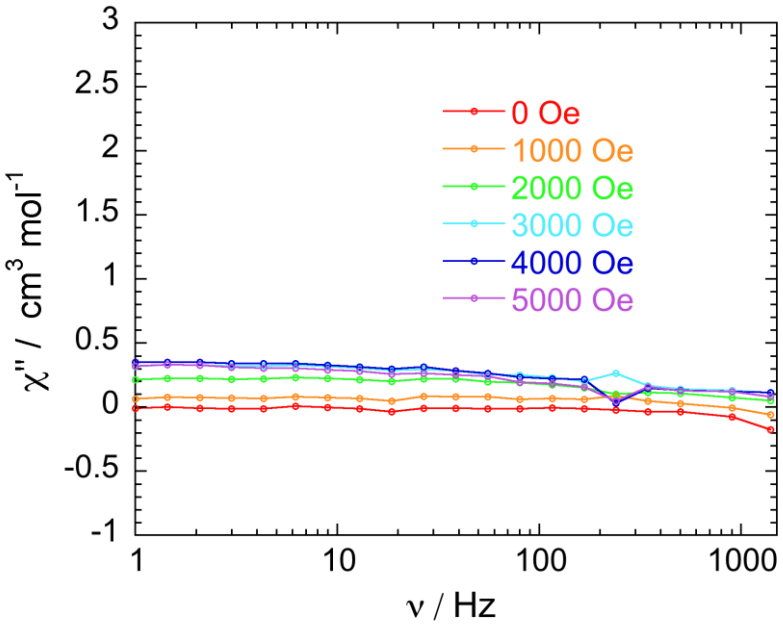

Figure 4.29. Out-of-phase susceptibility measurements at 2 K with a frequency range from 1 to 1500 Hz under various applied dc fields for complex **4-6**.

Complex 4-7

Field optimization for complex **2-7** was performed at T = 2 K with an applied dc field in the range 0 – 1200 Oe (Figure 4.30), but the maxima of the frequency-dependent ac susceptibility plots cannot be observed, below 1500 Hz (Figure 4.30). However, the largest value of χ'' is observed when the dc field is equal to 800 Oe. The frequency dependent ac data were thus performed in the temperature range 1.8 – 6 K for this value of the dc magnetic field (Figure 4.31). It is worth noting that the relaxation of this complex (**4-7**, Dy^{III}) is faster than the mononuclear one (**4-2**, Dy^{III}), probably due small differences in the coordination sphere of the two compounds. The situation is the same for the Er^{III} (**4-4** and **4-9**) and the Yb^{III} (**4-5** and **4-10**) complexes. It was possible to extract the relaxation times for the Yb^{III} complex **4-10** (Figure 4.35, Figure 4.36, Figure 4.37 and Figure 4.38) and the comparison with those of the mononuclear complex are given in Table 4.15 and Table 4.16.

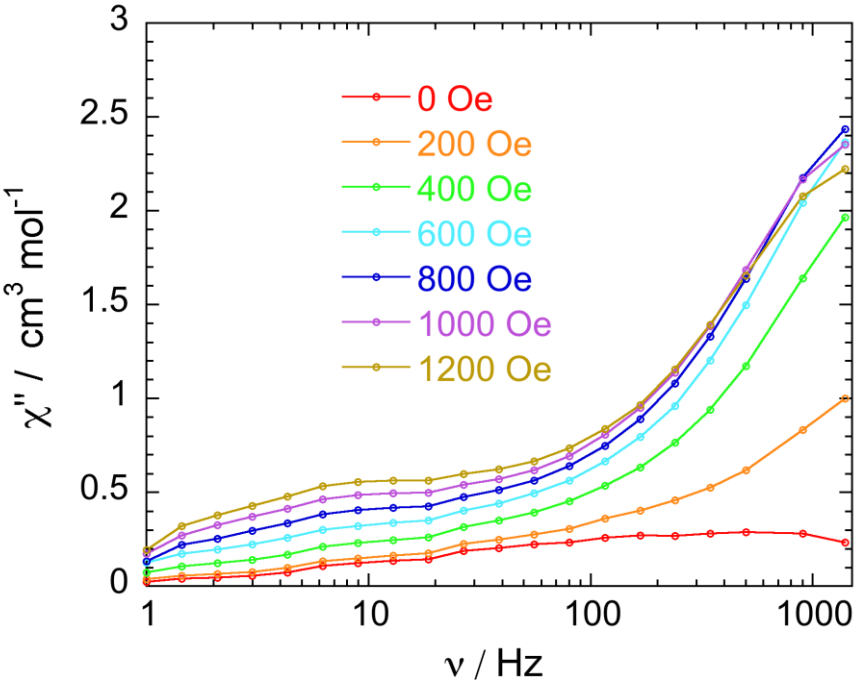

Figure 4.30. Out-of-phase susceptibility measurements at 2 K with a frequency range from 1 to 1500 Hz under various applied dc fields for complex **4-7**.

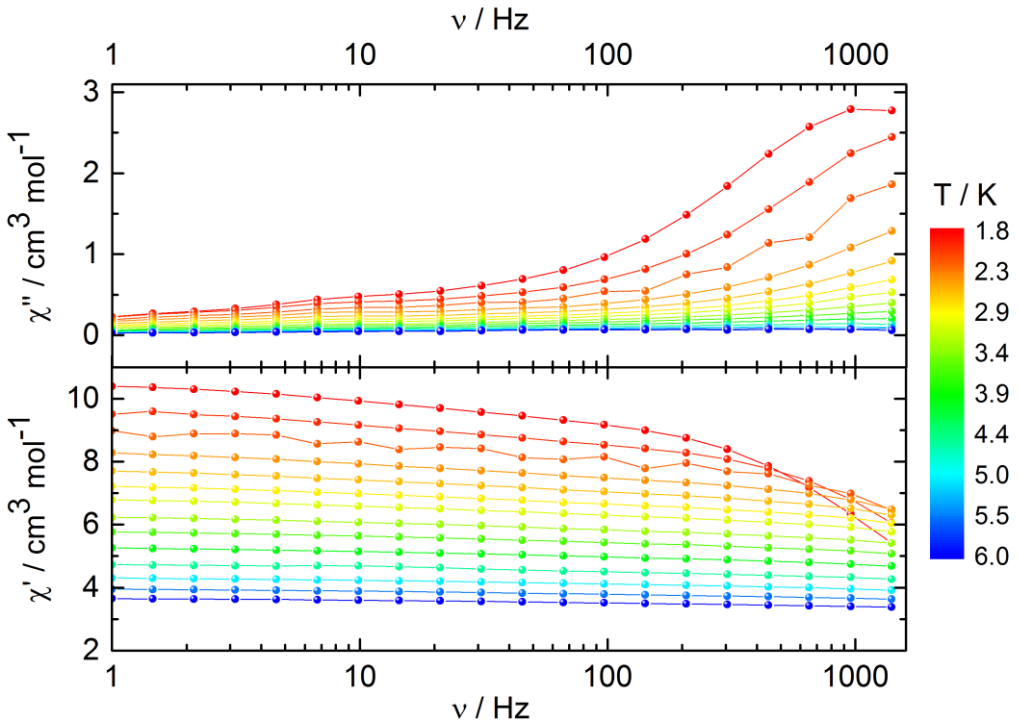

Figure 4.31. Frequency dependent in-phase and out-of-phase ac magnetic susceptibilities for complex **4-7** under an applied dc field of 800 Oe.

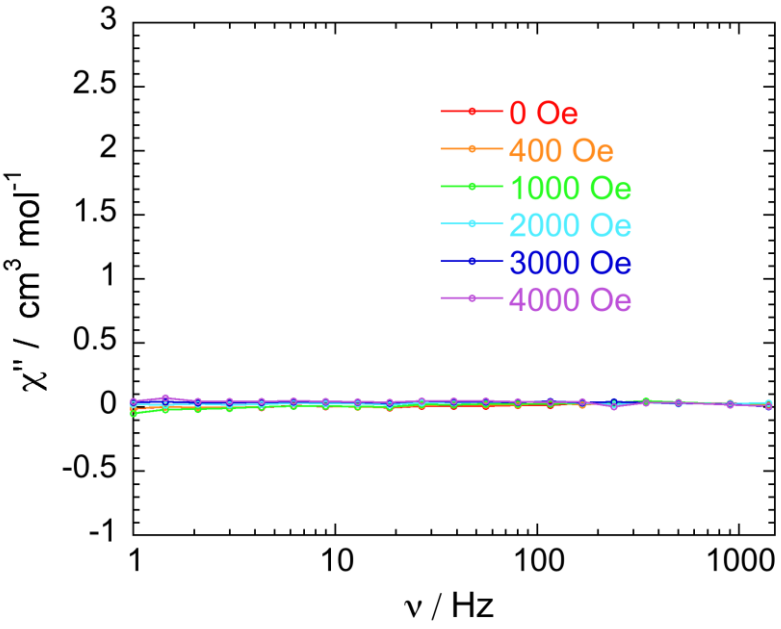

Figure 4.32. Out-of-phase susceptibility measurements at 2 K with a frequency range from 1 to 1500 Hz under various applied dc fields for complex **4-8**.

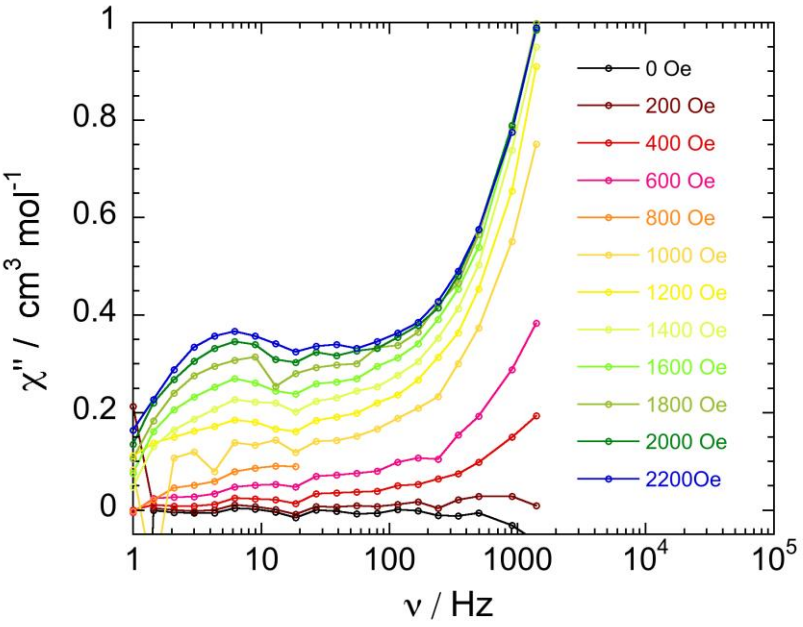

Figure 4.33. Out-of-phase susceptibility measurements at 2 K with a frequency range from 1 to 1500 Hz under various applied dc fields for complex **4-9**.

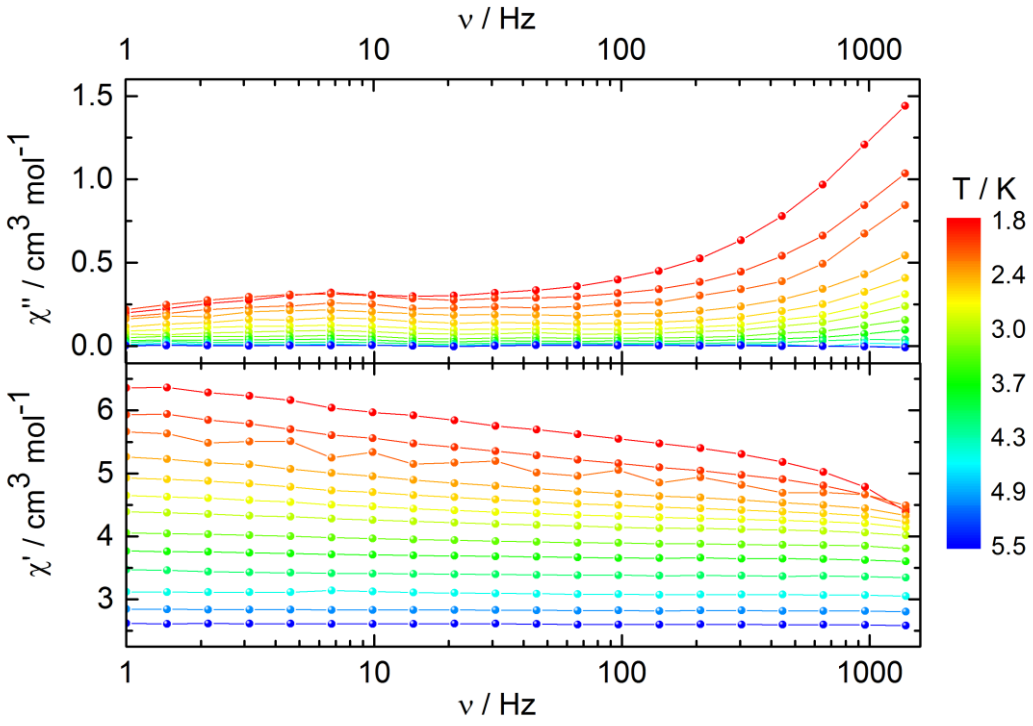

Figure 4.34. Frequency dependent in-phase and out-of-phase ac magnetic susceptibilities for complex **4-9** under an applied dc field of 1800 Oe.

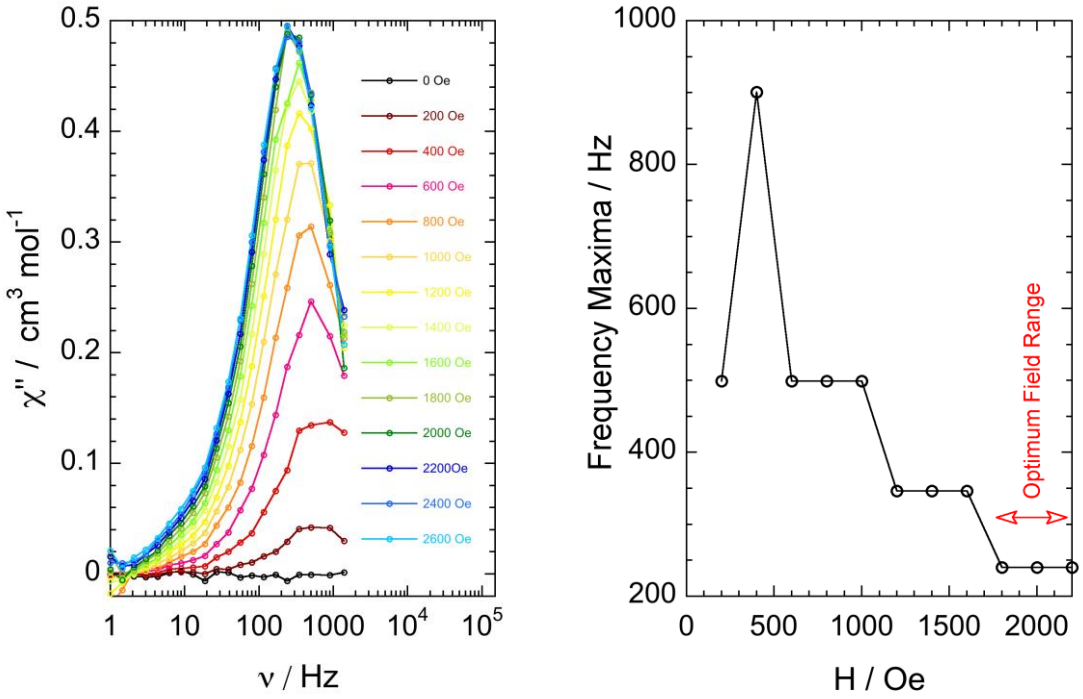

Figure 4.35. Out-of-phase susceptibility measurements at 2 K with a frequency range from 1 to 1500 Hz under various applied dc fields (left) and plot of frequency maxima *vs.* applied dc fields (right) for complex **4-10**.

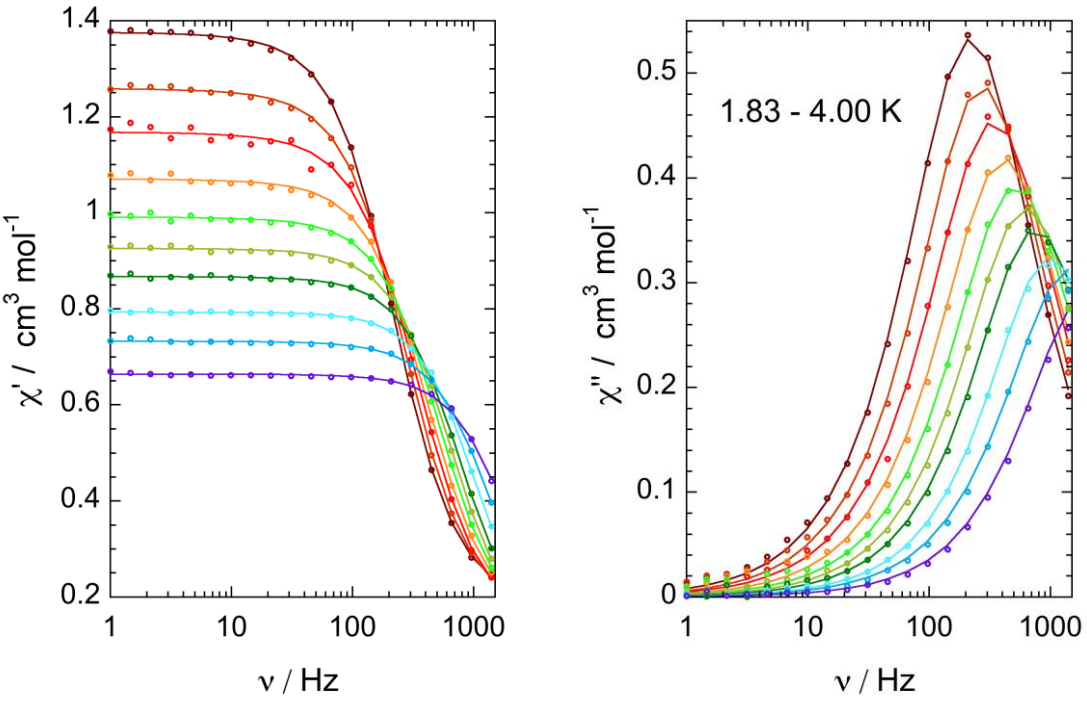

Figure 4.36. Frequency dependent in-phase and out-of-phase ac magnetic susceptibilities (○ (exp), — (fit)) for complex **4-10** under an applied dc field of 2200 Oe.

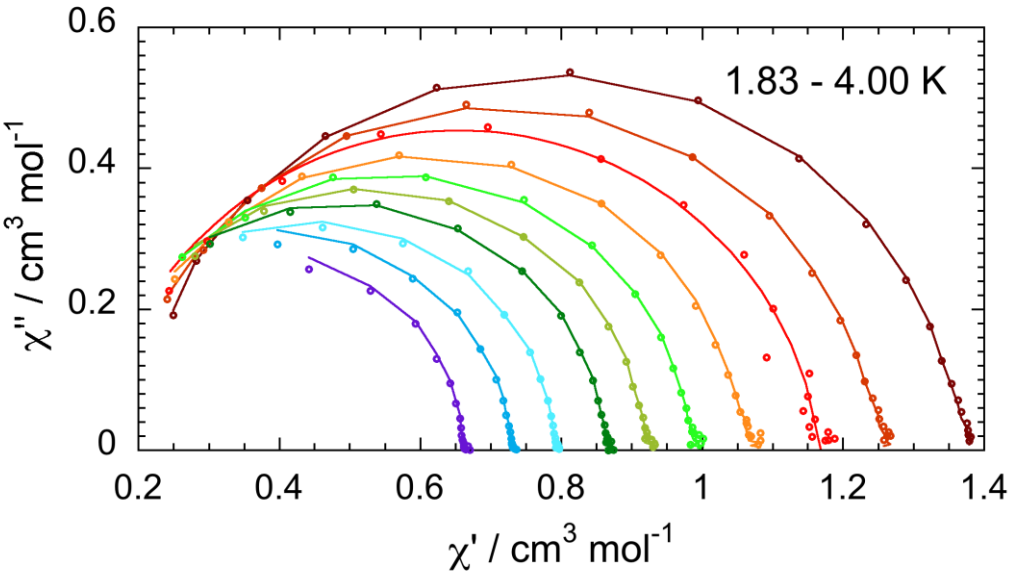

Figure 4.37. Cole-Cole plots (○ (exp), — (fit)) for complex **4-10** under an applied dc field of 2200 Oe.

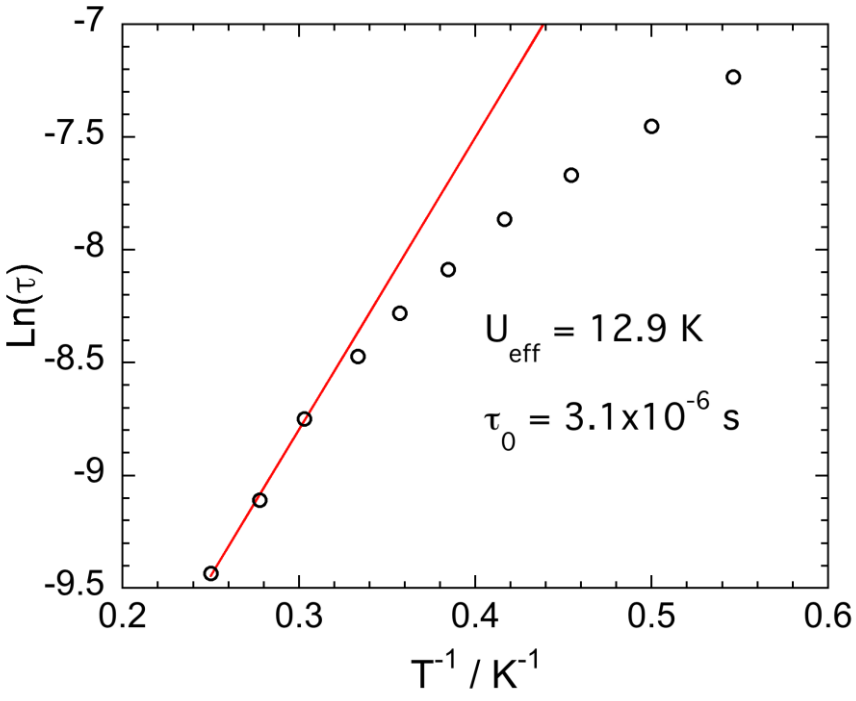

Figure 4.38. ln(τ) = f(1/T) plot (○ (exp), — (linear fit)) for the relaxation processes for complex **4-10** under an applied dc field of 2200 Oe.

4.4 Theoretical Calculations

Complexes 4-1 to 4-5

Calculations are performed within the crystallographic geometry using the MOLCAS 8.0 suite of programs[47]. Solvent molecules were not considered in the calculations. All atoms except the Ga^{III} ones are described with all electron basis sets ANO-RCC[48, 49], Ln^{III} atoms with TZP quality, the O in the first coordination sphere with TZP, N and other O atoms with DZP quality and other atoms with DZ quality. Ga^{III} atoms are described by Dolg ECP with 3 valence electrons[50]. First, a multistate CASSCF (Complete Active Space Self Consistent Field) calculation is performed[51] with an active space of n electrons in the 7 4*f* orbitals for a Ln^{III} of configuration $4f^n$. Spin-orbit coupling is evaluated as a state interaction between the CASSCF wave functions using the RASSI (Restricted Active Space State Interaction) code.[52] Spin-Orbit integrals are evaluated within the AMFI approximation[53]. The calculation of all the properties is implemented in a local program: *g* factors are calculated according to the reference[54] even in the case of non-degenerate states and magnetic susceptibility according to reference[55].

The calculations carried out on the mononuclear complexes allow determining the nature of the ground state, the associate g_i values and the energy spectrum of the $^{2S+1}L_J$ manifold split by the crystal field of the ligands. It is also possible to determine the orientation of the *g*-tensor with respect to the molecular frame. The calculated energy spectrum of the 5 complexes is given in Table 4.17. The calculated magnetic data calculated from these energy spectra are not in good agreement with the experimental ones, apart for the Ho^{III} complex. However, a fairly good agreement could be obtained by rescaling the energy spectra of the Dy^{III} and the Yb^{III} complexes as shown in Table 4.18. For Tb^{III}, only the energy of the first level was reduced from 5.9 to 1.5 cm^{-1} in order to better reproduce the magnetization data. For the Er^{III} complex, a mere rescale does not allow obtaining a good agreement for the magnetization curves at all temperatures; the magnetization values at high field are less saturated than the experimental ones (Figure 4.13). The fact that the magnetization is less saturated is usually due to the presence of several excited states close to the ground one with energy differences that are poorly reproduced by calculations. There is no clear reason why calculations give results not compatible with the experimental data, even after increasing the dimension of the CAS. Figure 4.39 depicts the energy spectra before rescaling of the data.

Table 4.17. Energy spectrum for the 5 mononuclear complexes **4-1** to **4-5** before rescaling.

Energies / cm^{-1}				
Tb	**Dy**	**Ho**	**Er**	**Yb**
0	0	0	0	0
5.894	0	1.053	0	0
28.806	56.028	22.312	42.633	97.998
58.063	56.028	34.828	42.633	97.998
68.277	72.493	41.376	50.247	237.041
129.943	72.493	46.226	50.247	237.041
134.673	104.617	52.311	75.454	303.718
194.045	104.617	96.442	75.454	303.718
194.866	145.232	155.92	156.887	
252.493	145.232	167.553	156.887	
253.124	162.348	184.258	201.879	
352.617	162.348	187.952	201.879	
352.713	178.219	191.137	224.263	
	178.219	192.844	224.263	
	411.224	196.416	258.11	
	411.224	247.27	258.11	
		247.879		

Table 4.18. Energy spectrum for the 5 mononuclear complexes **4-1** to **4-5** after rescaling. The rescaled states are highlighted in red.

Rescaled energies / cm^{-1}				
Tb	**Dy**	**Ho**	**Er**	**Yb**
0	0	0	0	0
1.5	0	1.053	0	0
28.806	33.6168	22.312	42.633	117.5976
58.063	33.6168	34.828	42.633	117.5976
68.277	43.4958	41.376	50.247	284.4492
129.943	43.4958	46.226	50.247	284.4492
134.673	62.7702	52.311	75.454	364.4616
194.045	62.7702	96.442	75.454	364.4616
194.866	87.1392	155.92	156.887	
252.493	87.1392	167.553	156.887	
253.124	97.4088	184.258	201.879	
352.617	97.4088	187.952	201.879	
352.713	106.9314	191.137	224.263	
	106.9314	192.844	224.263	
	246.7344	196.416	258.11	
	246.7344	247.27	258.11	
		247.879		

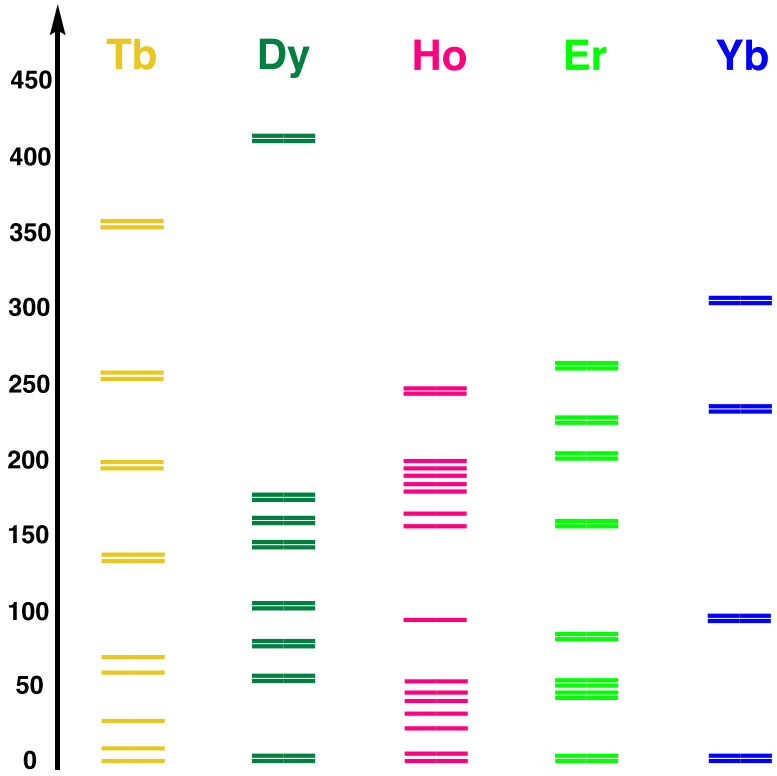

Figure 4.39. Energy spectrum for the 5 mononuclear complexes before rescaling of the data.

The energy spectra of the non-Kramers ions (Tb^{III} and Ho^{III}) show a lift of degeneracy of the $\pm m_J$ sub-levels due to the distortion of the complexes from the strict D_{4d} symmetry. Only the two low-lying levels are relatively close with an energy difference of 1.5 and 1.05 cm^{-1} for Tb^{III} and Ho^{III}, respectively. This is in full agreement with an absence of slow relaxation of the magnetization for these two complexes.

For the Kramers ions (Dy^{III}, Er^{III} and Yb^{III}), the energy difference between ground Kramers doublet and the first excited ones are equal to 33.6, 42.6 and 118 cm^{-1} respectively, which is compatible with the observation of a slow relaxation of the magnetization if the ground m_J sub-levels are pure and had axial anisotropy (large values). We already know from the simple examination of the data of the non-Kramers ions that the ground sub-levels are not pure, this should also be the case for the Kramers ones. The composition of the sub-levels determined form calculations show that for Dy^{III}, the first Kramers doublet (KD) had 90% weight of the $m_J = \pm 15/2$ sub-levels. While for Er^{III}, the first KD has only 45% weight of the ±15/2, 20% of the ±13/2 and 23% of the ± 11/2 m_J sub-levels (and less contribution from other sub-levels). For Yb^{III}, the weight for the ground KD is 73% and 15% for the $m_J = \pm 7/2$ and ±3/2 respectively. These compositions are in line with a rather Ising-type magnetic anisotropy for the Dy^{III} and the Yb^{III} complexes, while the Er^{III} complex has a less Ising-type

character. This simple qualitative analysis is in agreement with the ac data where a blocking of the magnetization was observed at 2 K for these complexes but with rather fast relaxation times.

The values of the components of the *g* tensors were determined for the Dy^{III} and the Yb^{III} complexes (Table 4.19). It was also done for the Er^{III}, but because calculations do not fairly reproduce the magnetic data we will not comment further on this complex. For the two compounds, the anisotropy of the ground levels is rather of the Ising-type even though there are weak components in the other two directions. This is in line with observation of blocking of the magnetization for these two compounds but with a rather small barrier.

The orientation of the principal components of *g*-tensor for the Dy^{III} and the Yb^{III} complexes relatively to the molecular frame are depicted in Figure 4.40. The principal *g*-tensor axes are not oriented along the pseudo four-fold axis of the molecules. This is the result of the structural distortion from the strict square antiprism D_{4d} symmetry. A more detailed analysis is necessary in order to relate the nature of the distortion to the nature of ground state and the axial anisotropy.

Table 4.19. Values of the *g*-tensor components for the Dy^{III} and Yb^{III} complexes

Complexes	g_1	g_2	g_3
$DyGa_4shi_4$	18.92	0.18	0.56
$YbGa_4shi_4$	6.77	0.7	0.92

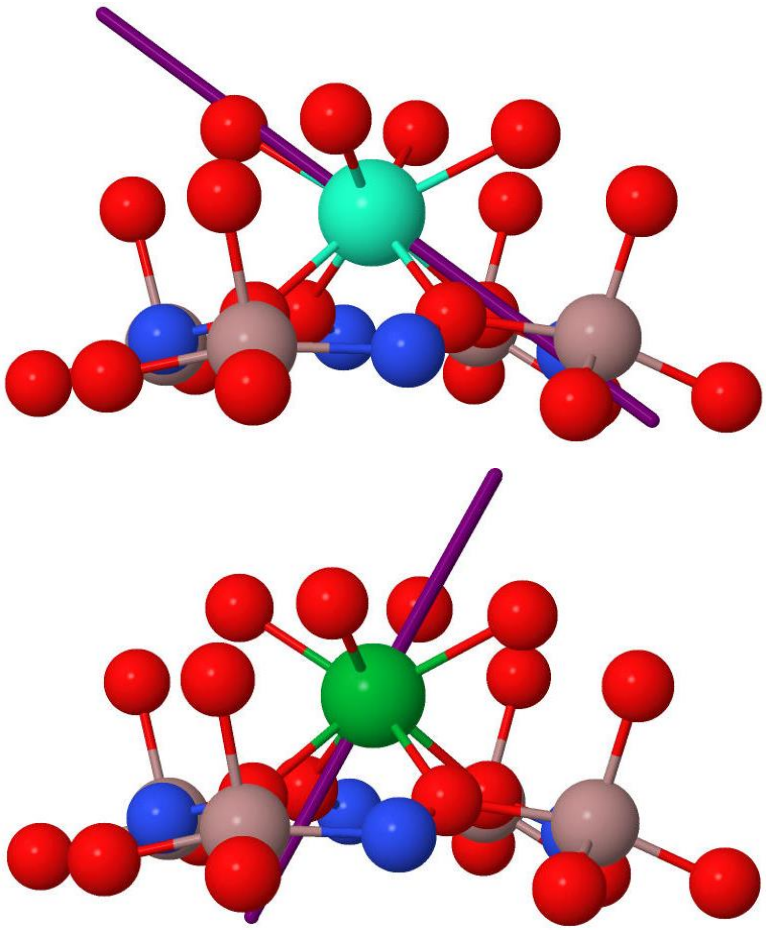

Figure 4.40. The anisotropy (violet stick) of calculation for complexes **4-2** (top) and **4-5** (bottom), Dy – cyan; Yb – green; Ga – tan; O – red; N – blue; C, H atoms and solvent molecules coordinated to Ga^{III} were omitted for clarity.

4.5 Luminescence Studies

The interest in lanthanide-containing complexes is also due to their optical behavior and the potential applications of their luminescence for imaging.[56-63] Luminescence studies allow determining the energy spectra of the low-lying sub-levels, thus providing experimental data that can be compared to theoretical calculations. Such studies have already been carried out by several groups on Yb^{III} complexes.[64, 65] But more data on different complexes are necessary to get better insight in the correspondence between experimental and theoretical energy spectra. We have measured the luminescence spectrum of the Yb^{III} complexes **4-5** and **4-10** (Figure 4.41) at 77 K. It is worth noting that the emission spectra of the two complexes are similar but not identical highlighting the difference in the energy spectra of their $\pm m_J$ sub-levels due to the small differences in their structure. Seven emission bands can be observed, while only 4 are due to the emission from the ground sub-level ($m_J = \pm 5/2$) of the first excited $^2F_{5/2}$ state to the four $m_J = \pm 1/2$, $\pm 3/2$, $\pm 5/2$ and $\pm 7/2$ sub-levels of the ground $^2F_{7/2}$ state. The

other bands are due to emission from the m_J = ±3/2 and ±1/2 sub-levels of the excited $^2F_{5/2}$ state. In order to determine the energy of the ground ±m_J sub-levels, it is necessary to perform an unambiguous assignment of the bands. Temperature dependent spectra must be measured in order to do so. We are working in this direction for a series of other highly symmetrical Yb^{III}-containing complexes.

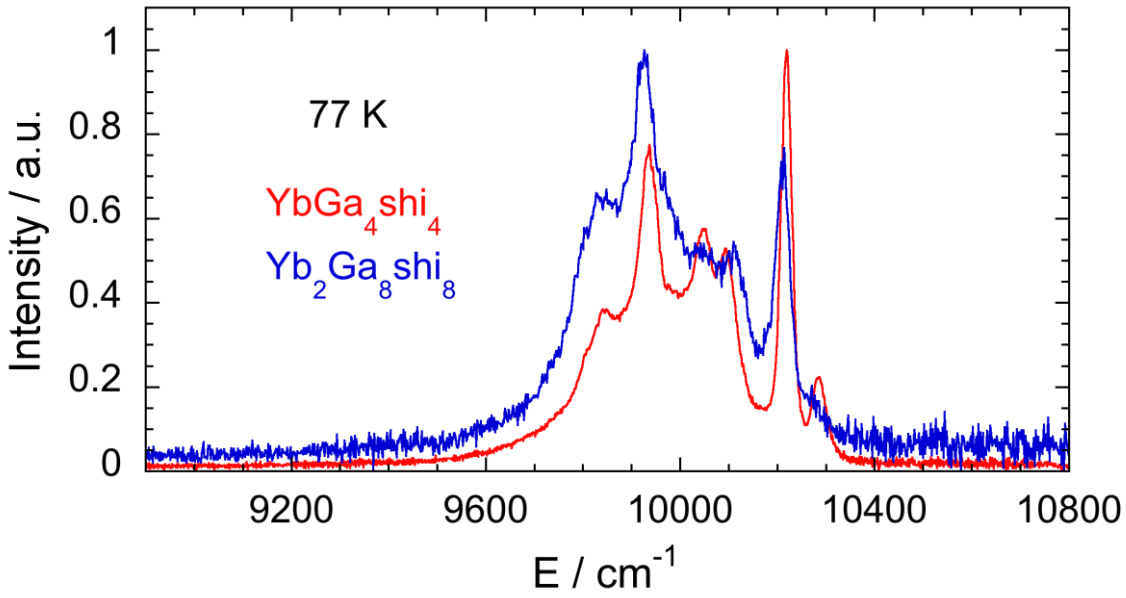

Figure 4.41. The luminescence spectrum for complexes **4-5** and **4-10** at 77 K.

4.6 Summary and Conclusions

Using the MC synthetic approach, we have structurally and magnetically characterized five mononuclear half-sandwich Ga^{III}/Ln^{III} MC complexes (**4-1** to **4-5**). The half-sandwich complexes possess benzoate ligands on one side of the complex bridging the central lanthanide ion to the four peripheral Ga^{III}, thus stabilizing the MC structure. Replacing benzoate by isophtalate that have an angle of 120° between its carboxylate groups allows linking two half-sandwich molecules and obtaining the sandwiched binuclear species (**4-6** to **4-10**). The coordination sphere around the lanthanide ions is very close to a square antiprism. The SHAPE analysis for the complexes reveals a slightly elongated and distorted antiprism geometry. Magnetic studies showed that the $Dy^{III}/Er^{III}/Yb^{III}$ species (**$LnGa_4shi_4$** and **$Ln_2Ga_8shi_8$**) display a slow relaxation of the magnetization below 4 K with rather fast relaxation times and small energy barrier to the reorientation of their magnetization. The *ab initio* calculations confirm the moderate SMM behavior and show that even though the Dy^{III} and the Yb^{III} complexes possess magnetic anisotropy close to the Ising-type, the orientation

of the principal *g*-tensor component is not aligned along the pseudo four-fold axis of the complex. The slight structural distortion from the strict D_{4d} symmetry has, thus, a major effect on the anisotropy behavior and thus on the magnetic relaxation. The effect of the distortion is easily revealed when examining the energy spectra of the non-Kramers ions (Tb^{III} and Ho^{III} derivatives) where no degenerate sub-levels are observed. The first two sublevels are separated by about 1.5 cm^{-1} precluding the occurrence of blocking of the magnetization as observed experimentally. These results highlight the crucial influence of symmetry on the dynamic magnetic behavior of lanthanide-containing mononuclear complexes.

4.7 References

1. R. Sessoli, H. L. Tsai, A. R. Schake, S. Wang, J. B. Vincent, K. Folting, D. Gatteschi, G. Christou and D. N. Hendrickson, *Journal of the American Chemical Society*, 1993, **115**, 1804-1816.
2. R. Sessoli, D. Gatteschi, A. Caneschi and M. A. Novak, *Nature*, 1993, **365**, 141-143.
3. A. Caneschi, D. Gatteschi, R. Sessoli, A. L. Barra, L. C. Brunel and M. Guillot, *Journal of the American Chemical Society*, 1991, **113**, 5873-5874.
4. L. Bogani and W. Wernsdorfer, *Nature Materials*, 2008, **7**, 179-186.
5. D. Gatteschi, R. Sessoli and J. Villain, *Molecular Nanomagnets*, Oxford University Press, New York, 2006.
6. A. M. Ako, I. J. Hewitt, V. Mereacre, R. Clérac, W. Wernsdorfer, C. E. Anson and A. K. Powell, *Angewandte Chemie*, 2006, **118**, 5048-5051.
7. F. Shao, B. Cahier, N. Guihery, E. Riviere, R. Guillot, A.-L. Barra, Y. Lan, W. Wernsdorfer, V. E. Campbell and T. Mallah, *Chemical Communications*, 2015, **51**, 16475-16478.
8. X.-Y. Wang, C. Avendano and K. R. Dunbar, *Chemical Society Reviews*, 2011, **40**, 3213-3238.
9. J. D. Rinehart, M. Fang, W. J. Evans and J. R. Long, *Nature Chemistry*, 2011, **3**, 538-542.
10. R. J. Blagg, L. Ungur, F. Tuna, J. Speak, P. Comar, D. Collison, W. Wernsdorfer, E. J. L. McInnes, L. F. Chibotaru and R. E. P. Winpenny, *Nature Chemistry*, 2013, **5**, 673-678.
11. N. Ishikawa, M. Sugita, T. Ishikawa, S.-y. Koshihara and Y. Kaizu, *Journal of the*

American Chemical Society, 2003, **125**, 8694-8695.

12. N. Ishikawa, M. Sugita, T. Ishikawa, S.-y. Koshihara and Y. Kaizu, *The Journal of Physical Chemistry B*, 2004, **108**, 11265-11271.
13. N. Ishikawa, M. Sugita, T. Okubo, N. Tanaka, T. Iino and Y. Kaizu, *Inorganic Chemistry*, 2003, **42**, 2440-2446.
14. J. Liu, Y. C. Chen, J. L. Liu, V. Vieru, L. Ungur, J. H. Jia, L. F. Chibotaru, Y. Lan, W. Wernsdorfer, S. Gao, X. M. Chen and M. L. Tong, *Journal of the American Chemical Society*, 2016, **138**, 5441-5450.
15. Y.-S. Ding, N. F. Chilton, R. E. P. Winpenny and Y.-Z. Zheng, *Angewandte Chemie International Edition*, 2016, **55**, 16071-16074.
16. L. Sorace, C. Benelli and D. Gatteschi, *Chemical Society Reviews*, 2011, **40**, 3092-3104.
17. D. N. Woodruff, R. E. P. Winpenny and R. A. Layfield, *Chemical Reviews*, 2013, **113**, 5110-5148.
18. J. D. Rinehart and J. R. Long, *Chemical Science*, 2011, **2**, 2078-2085.
19. Y.-S. Meng, S.-D. Jiang, B.-W. Wang and S. Gao, *Accounts of Chemical Research*, 2016, **49**, 2381-2389.
20. J. J. Baldovi, Y. Duan, C. Bustos, S. Cardona-Serra, P. Gouzerh, R. Villanneau, G. Gontard, J. M. Clemente-Juan, A. Gaita-Arino, C. Gimenez-Saiz, A. Proust and E. Coronado, *Dalton Transactions*, 2016, **45**, 16653-16660.
21. M. J. Martínez-Pérez, S. Cardona-Serra, C. Schlegel, F. Moro, P. J. Alonso, H. Prima-García, J. M. Clemente-Juan, M. Evangelisti, A. Gaita-Ariño, J. Sesé, J. van Slageren, E. Coronado and F. Luis, *Physical Review Letters*, 2012, **108**, 247213.
22. S. Ghosh, S. Datta, L. Friend, S. Cardona-Serra, A. Gaita-Arino, E. Coronado and S. Hill, *Dalton Transactions*, 2012, **41**, 13697-13704.
23. M. A. AlDamen, S. Cardona-Serra, J. M. Clemente-Juan, E. Coronado, A. Gaita-Ariño, C. Martí-Gastaldo, F. Luis and O. Montero, *Inorganic Chemistry*, 2009, **48**, 3467-3479.
24. M. A. AlDamen, J. M. Clemente-Juan, E. Coronado, C. Martí-Gastaldo and A. Gaita-Ariño, *Journal of the American Chemical Society*, 2008, **130**, 8874-8875.
25. M. S. Lah, M. L. Kirk, W. Hatfield and V. L. Pecoraro, *Journal of the Chemical Society, Chemical Communications*, 1989, DOI: 10.1039/C39890001606, 1606-1608.
26. M. S. Lah and V. L. Pecoraro, *Journal of the American Chemical Society*, 1989, **111**,

7258-7259.

27. V. L. Pecoraro, *Inorganica Chimica Acta*, 1989, **155**, 171-173.
28. C. M. Zaleski, S. Tricard, E. C. Depperman, W. Wernsdorfer, T. Mallah, M. L. Kirk and V. L. Pecoraro, *Inorganic Chemistry*, 2011, **50**, 11348-11352.
29. C. M. Zaleski, E. C. Depperman, J. W. Kampf, M. L. Kirk and V. L. Pecoraro, *Inorganic Chemistry*, 2006, **45**, 10022-10024.
30. J. Jankolovits, J. W. Kampf and V. L. Pecoraro, *Inorganic Chemistry*, 2014, **53**, 7534-7546.
31. A. Deb, T. T. Boron, M. Itou, Y. Sakurai, T. Mallah, V. L. Pecoraro and J. E. Penner-Hahn, *Journal of the American Chemical Society*, 2014, **136**, 4889-4892.
32. T. T. Boron, J. W. Kampf and V. L. Pecoraro, *Inorganic Chemistry*, 2010, **49**, 9104-9106.
33. C. M. Zaleski, J. W. Kampf, T. Mallah, M. L. Kirk and V. L. Pecoraro, *Inorganic Chemistry*, 2007, **46**, 1954-1956.
34. G. Mezei, C. M. Zaleski and V. L. Pecoraro, *Chemical Reviews*, 2007, **107**, 4933-5003.
35. C. M. Zaleski, E. C. Depperman, C. Dendrinou-Samara, M. Alexiou, J. W. Kampf, D. P. Kessissoglou, M. L. Kirk and V. L. Pecoraro, *Journal of the American Chemical Society*, 2005, **127**, 12862-12872.
36. C. Dendrinou-Samara, M. Alexiou, C. M. Zaleski, J. W. Kampf, M. L. Kirk, D. P. Kessissoglou and V. L. Pecoraro, *Angewandte Chemie International Edition*, 2003, **42**, 3763-3766.
37. C. Y. Chow, S. V. Eliseeva, E. R. Trivedi, T. N. Nguyen, J. W. Kampf, S. Petoud and V. L. Pecoraro, *Journal of the American Chemical Society*, 2016, **138**, 5100-5109.
38. S. Alvarez, P. Alemany, D. Casanova, J. Cirera, M. Llunell and D. Avnir, *Coordination Chemistry Reviews*, 2005, **249**, 1693-1708.
39. D. Casanova, M. Llunell, P. Alemany and S. Alvarez, *Chemistry – A European Journal*, 2005, **11**, 1479-1494.
40. K. Katoh, Y. Yoshida, M. Yamashita, H. Miyasaka, B. K. Breedlove, T. Kajiwara, S. Takaishi, N. Ishikawa, H. Isshiki, Y. F. Zhang, T. Komeda, M. Yamagishi and J. Takeya, *Journal of the American Chemical Society*, 2009, **131**, 9967-9976.
41. C. Loosli, S. X. Liu, A. Neels, G. Labat and S. Decurtins, in *Zeitschrift für Kristallographie - New Crystal Structures*, 2006, vol. 221, p. 135.

42. B. R. Gibney, H. Wang, J. W. Kampf and V. L. Pecoraro, *Inorganic Chemistry*, 1996, **35**, 6184-6193.
43. D. P. Kessissoglou, J. J. Bodwin, J. Kampf, C. Dendrinou-Samara and V. L. Pecoraro, *Inorganica Chimica Acta*, 2002, **331**, 73-80.
44. E. L. Muetterties and L. J. Guggenberger, *Journal of the American Chemical Society*, 1974, **96**, 1748-1756.
45. K. S. Cole and R. H. Cole, *The Journal of Chemical Physics*, 1941, **9**, 341-351.
46. H. Miyasaka, R. Clérac, K. Mizushima, K.-i. Sugiura, M. Yamashita, W. Wernsdorfer and C. Coulon, *Inorganic Chemistry*, 2003, **42**, 8203-8213.
47. F. Aquilante, J. Autschbach, R. K. Carlson, L. F. Chibotaru, M. G. Delcey, L. De Vico, I. Fdez. Galván, N. Ferré, L. M. Frutos, L. Gagliardi, M. Garavelli, A. Giussani, C. E. Hoyer, G. Li Manni, H. Lischka, D. Ma, P. Å. Malmqvist, T. Müller, A. Nenov, M. Olivucci, T. B. Pedersen, D. Peng, F. Plasser, B. Pritchard, M. Reiher, I. Rivalta, I. Schapiro, J. Segarra-Martí, M. Stenrup, D. G. Truhlar, L. Ungur, A. Valentini, S. Vancoillie, V. Veryazov, V. P. Vysotskiy, O. Weingart, F. Zapata and R. Lindh, *Journal of Computational Chemistry*, 2016, **37**, 506-541.
48. B. O. Roos, R. Lindh, P.-Å. Malmqvist, V. Veryazov, P.-O. Widmark and A. C. Borin, *The Journal of Physical Chemistry A*, 2008, **112**, 11431-11435.
49. B. O. Roos, R. Lindh, P.-Å. Malmqvist, V. Veryazov and P.-O. Widmark, *The Journal of Physical Chemistry A*, 2004, **108**, 2851-2858.
50. A. Bergner, M. Dolg, W. Küchle, H. Stoll and H. Preuß, *Molecular Physics*, 1993, **80**, 1431-1441.
51. B. O. Roos, P. R. Taylor and P. E. M. Si÷gbahn, *Chemical Physics*, 1980, **48**, 157-173.
52. P. Å. Malmqvist, B. O. Roos and B. Schimmelpfennig, *Chemical Physics Letters*, 2002, **357**, 230-240.
53. B. A. Heß, C. M. Marian, U. Wahlgren and O. Gropen, *Chemical Physics Letters*, 1996, **251**, 365-371.
54. H. Bolvin, *ChemPhysChem*, 2006, **7**, 1575-1589.
55. S. Vancoillie, L. Rulíšek, F. Neese and K. Pierloot, *The Journal of Physical Chemistry A*, 2009, **113**, 6149-6157.
56. E. R. Trivedi, S. V. Eliseeva, J. Jankolovits, M. M. Olmstead, S. Petoud and V. L. Pecoraro, *Journal of the American Chemical Society*, 2014, **136**, 1526-1534.
57. A. D'Aléo, F. Pointillart, L. Ouahab, C. Andraud and O. Maury, *Coordination*

Chemistry Reviews, 2012, **256**, 1604-1620.

58. J. Jankolovits, C. M. Andolina, J. W. Kampf, K. N. Raymond and V. L. Pecoraro, *Angewandte Chemie International Edition*, 2011, **50**, 9660-9664.
59. S. V. Eliseeva and J.-C. G. Bunzli, *Chemical Society Reviews*, 2010, **39**, 189-227.
60. R. M. Duke, E. B. Veale, F. M. Pfeffer, P. E. Kruger and T. Gunnlaugsson, *Chemical Society Reviews*, 2010, **39**, 3936-3953.
61. J.-C. G. Bünzli and S. V. Eliseeva, *Journal of Rare Earths*, 2010, **28**, 824-842.
62. J.-C. G. Bünzli, *Chemical Reviews*, 2010, **110**, 2729-2755.
63. E. G. Moore, A. P. S. Samuel and K. N. Raymond, *Accounts of Chemical Research*, 2009, **42**, 542-552.
64. Q.-W. Li, J.-L. Liu, J.-H. Jia, Y.-C. Chen, J. Liu, L.-F. Wang and M.-L. Tong, *Chemical Communications*, 2015, **51**, 10291-10294.
65. F. Pointillart, J. Jung, R. Berraud-Pache, B. Le Guennic, V. Dorcet, S. Golhen, O. Cador, O. Maury, Y. Guyot, S. Decurtins, S.-X. Liu and L. Ouahab, *Inorganic Chemistry*, 2015, **54**, 5384-5397.

CHAPTER 5 Single Molecule Magnet Behavior in Dy^{III}[12-$MC_{Ga^{III}nha}$-4] Complexes

5.1 Introduction

This chapter will focus on the synthesis and characterization of two Dy^{III}[12-$MC_{Ga^{III}nha}$-4] complexes (**5-1**: $[Dy_2Ga_8(C_{11}H_6NO_3)_8(C_6H_5CO_2)_8(CH_3OH)_4Na_2]\cdot(H_2O)_8$ and **5-2**: $[Dy_2Ga_8(C_{11}H_6NO_3)_8(C_6H_4C_2O_4)_4(C_5H_5N)_8]\cdot(C_5H_6N)_2\cdot(CH_3OH)\cdot(C_5H_5N)_2)$ based on the ligand 3-hydroxy-2-naphthohydroxamic acid (H_3nha) which are similar to the complexes in Chapter 4.

5.2 Experimental Section

5.2.1 Syntheses

All starting materials were obtained commercially and were used without further purification unless otherwise stated.

3-hydroxy-2-naphthohydroxamic acid: H_3nha

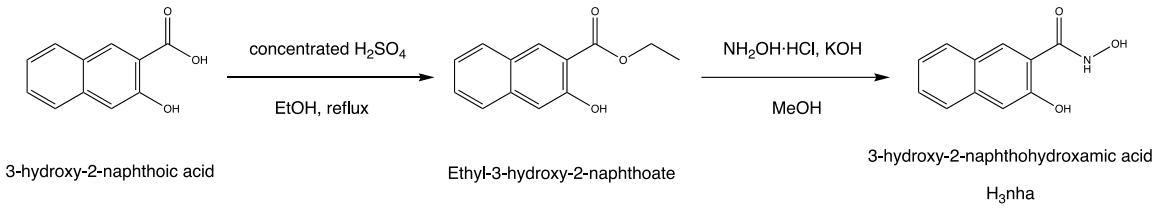

Scheme 5.1. Synthesis of 3-hydroxy-2-naphthohydroxamic acid.

3-hydroxy-2-naphthoic acid (18.8 g, 100 mmol) was refluxed in 500 mL of absolute ethanol with 5 mL concentrated sulfuric acid for 18 hours. Periodic water removal was achieved via a Dean-Stark trap (8 × 15 mL). The resulting solution was cooled to room temperature and solvent was removed by flash evaporation. Ethyl-3-hydroxy-2-naphthoate crystallized during this process. Recrystallization from methanol gave 54.0 g (62.5% yield) of ethyl 3-hydroxy-2-naphthoate. Condensation of Ethyl-3-hydroxy-2-naphthoate (24.5 g, 115 mmol) with hydroxylamine hydrochloride (15.98 g, 230 mmol) and KOH (19.3 g, 345 mmol) in 300 mL of methanol yielded the potassium salt of 3-hydroxy-2-naphthohydroxamic acid.

This salt was dissolved in 1.25 M acetic acid in CH_3OH and crystallized to yield 18.7 g of H_3nha (46% yield based on ester). ^{1}H-NMR (CD_3OD, 300MHz): δ 7.12(s,1H), 7.21(t, J = 7.4 Hz, 1H), 7.37(t, J = 7.4 Hz, 1H), 7.58(d, J = 8.3 Hz, 1H), 7.75(d, J = 8.3 Hz, 1H) and 8.29(s,1H). ^{13}C-NMR (CD_3OD) δ 111.8, 121.0, 123.8, 126.5, 128.2, 128.4, 129.5, 129.7, 137.6, 157.4, 167.5. Mass spectroscopic molecular weight calculated for $C_{11}H_9NO_3$:203.0582, observed 203.0580 m/e.

$[Dy_2Ga_8(C_{11}H_6NO_3)_8(C_6H_5CO_2)_8(CH_3OH)_4Na_2]\cdot(H_2O)_8$ (5-1)

H_3nha (203.1 mg, 1.0 mmol), $Dy(NO_3)_3\cdot 5H_2O$ (109.7 mg, 0.25 mmol), and $Ga(NO_3)_3\cdot xH_2O$ (255.7 mg, 1.0 mmol) were dissolved in 40 mL of methanol. Sodium benzoate (576.4 mg, 4.0 mmol) was added to the solution and stirred overnight. A light-yellow precipitate was formed, it was filtered, washed with methanol for several times, and dried in vacuum at room temperature. Yield, 45.6%, 235 mg. X-ray quality crystals were obtained by vapor diffusion of methyl tert-butyl ether into an MeOH/DCM (v/v 1:1) solution of complex **5-1**. Elem Anal. Calcd: C, 52.72; H, 3.18; N, 6.79. Found: C, 52.26; H, 3.34; N, 7.09. Single-crystal unit cell: Monoclinic, space group $P2_1/c$, a = 14.3157(12) Å, b = 16.9523(14) Å, c = 36.063(3) Å, α = 90°, β = 97.236(2)°, γ = 90°, V = 8682.2(13) Å^3.

$[Dy_2Ga_8(C_{11}H_6NO_3)_8(C_6H_4C_2O_4)_4(C_5H_5N)_8]\cdot(C_5H_6N)_2\cdot(CH_3OH)\cdot(C_5H_5N)_2$ (5-2)

H_3nha (40.6 mg, 0.2 mmol), $Dy(OTf)_3$ (30.5 mg, 0.05 mmol), isophthalic acid (68.4 mg, 0.4 mmol) and $Ga(OTf)_3$ (103.4 mg, 0.2 mmol) were dissolved in 4 mL of methanol, 2 mL of peydine was added and the solution was stood. The square block crystals of complex **5-2** was formed for 3 weeks. Yield, 21.3%, 22 mg. Elem Anal. Calcd: C, 52.72; H, 3.18; N, 6.79. Found: C, 52.26; H, 3.34; N, 7.09. Single-crystal unit cell: Monoclinic, space group P–1, a = 16.2671(5) Å, b = 21.0276(6) Å, c = 30.7190(10) Å, α = 97.303(2)°, β = 102.284(2)°, γ = 102.8470(10)°, V = 9840.9(5) Å^3.

5.2.2 Physical Measurements

Unless otherwise stated, all starting materials were obtained commercially and were used without further purification. General procedures, X-ray Crystallography, Magnetic Measurements are aforementioned in Chapter 2.

5.3 Results and Discussion

5.3.1 Syntheses

The one pot reaction H_3nha, $Ga(NO_3)_3{\cdot}xH_2O$, and sodium benzoate with $Dy(NO_3)_3{\cdot}5H_2O$ in CH_3OH afforded an MC that adopts the 12-MC-4 topology, which negatively charged and bridged by two sodium cations (Scheme 5.2).

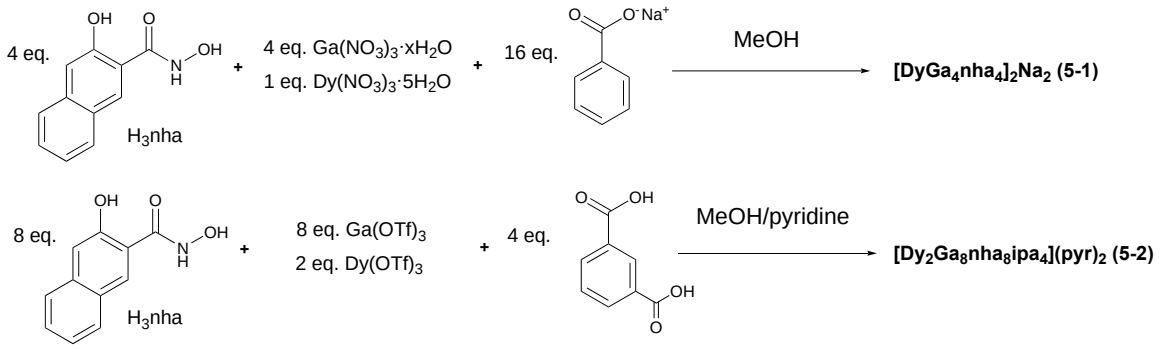

Scheme 5.2. Synthesis of complexes **5-1** and **5-2**.

The one pot reaction H_3nha, $Ga(OTf)_3$, isopathalic acid, and sodium bicarbonate with $Dy(OTf)_3$ in in CH_3OH/pyridine mixture afforded an MC that adopts the sandwich 12-MC-4 topology, and the negative charge of which is counter-balanced by two pyridinium cations (Scheme 5.2).

5.3.2 Description of Structures

Complex 5-1

Single crystal X-ray analysis of complex **5-1** (Figure 5.1) revealed that the monolanthanide MC complexes have distorted square antiprism geometry, as noted in Table 5.1, which crystallizes in the monoclinic $P2_1/c$ space group and it is similar to the complex **4-2** in the chapter 4. However, for complex **5-1**, the two [12-$MC_{Ga^{III}}$-4] rings were charged and bridged by two sodium(I) cations linked to two methanol molecules and four nha^{3-} ligands (Figure 5.1 left). Additionally, each [12-$MC_{Ga^{III}}$-4] ring has two coordination forms, 68% of complex **5-1(i)** and 32% of complex **5-1(ii)** (Figure 5.2). Therefore, one complex (**5-1(i)**) will be described in more detail, the four organic ligands nha^{3-} and bridges Ga^{III} ions forming a [12-$MC_{Ga^{III}}$-4] ring with –[Ga–N–O]– as the repeat unit. Four Ga^{III} ions are five-coordinated with nha^{3-} ligands and benzoate ligands. While the two neighbor Ga^{III} ions of them are bridged two Na^{I} ions via the oxygen from nha^{3-} ligands. The central Dy^{III} ion is bridged to

the [12-$MC_{Ga^{III}}$-4] ring by four benzoates and four nha^{3-} ligands. The four hydroximate oxygen atoms (O_{MC}) presents a planar square, while the four oxygen atoms (O_{Bz}) of benzoate serve as another square, and adopts an eight-coordinated square antiprism geometry (quasi-double deck structure, Figure 5.1), which was also confirmed by the continued shape measurements (CShM) SHAPE[1, 2] analysis, like complex **4-2** in chapter 4 and the results are listed in Table 5.6. The smaller value means the closer coordination geometry to the ideal model. Regarding the lanthanide inner coordination sphere, the skew angle (ϕ) through the coordinating oxygen atoms (O1A, O2A, O3A, O4A and O5A, O6A, O7A, O8A) are very slightly twisted (44.98°, 44.58° 45.91° and 45.67°) with respect to each other (Table 5.2) and to the ideal D_{4d} symmetry (ϕ = 45°). The different tables (Table 5.3) and figures (Figure 5.1) below give the information on the structural parameters and show that the local coordination sphere is similar to the related complexes with the shi^{3-} ligand described in chapter 4. At last, the analysis of the packing arrangement reveals that sodium(I) bridged molecules are arranged parallel to each other (Figure 5.3).

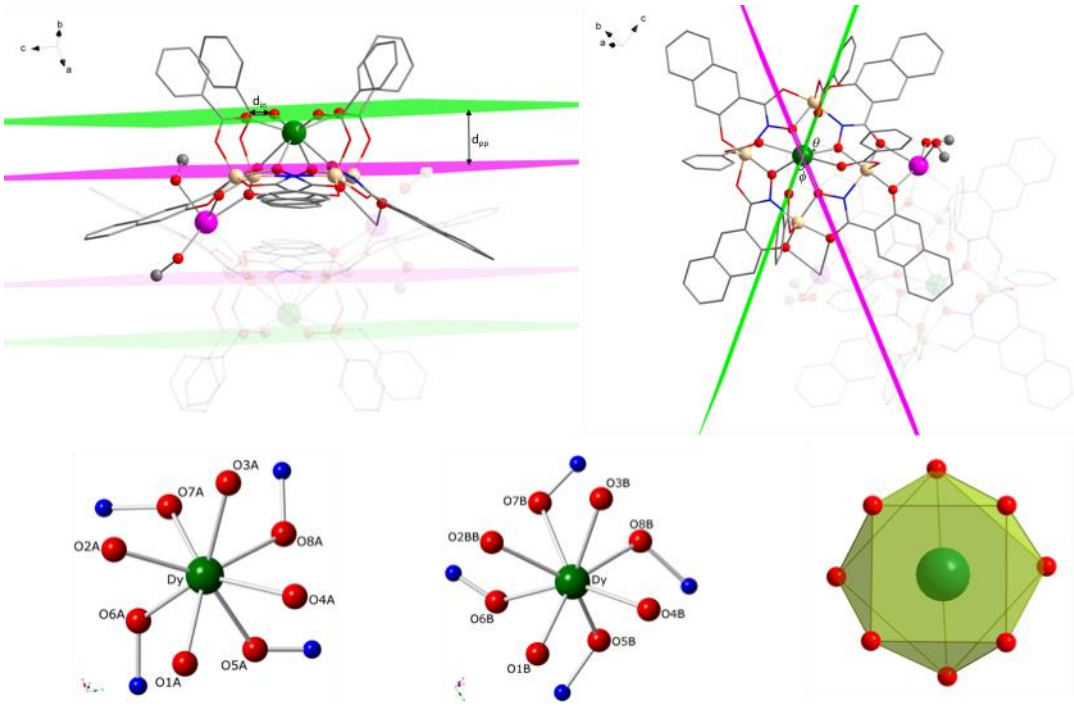

Figure 5.1. Molecular structure of complex **5-1** obtained from X-ray diffraction: (top left) side-view perspective showing d_{in} and d_{pp}; (top right) top-down view showing ϕ and θ structural features of the [12-$MC_{Ga^{III}}$-4] core; (bottom) square-antiprismatic coordination geometry around the central Dy^{III} ion. Dy – green; Ga – tan; Na – Pink; O – red; N – blue; C – grey; H atoms and solvent molecules coordinated to Ga^{III} were omitted for clarity.

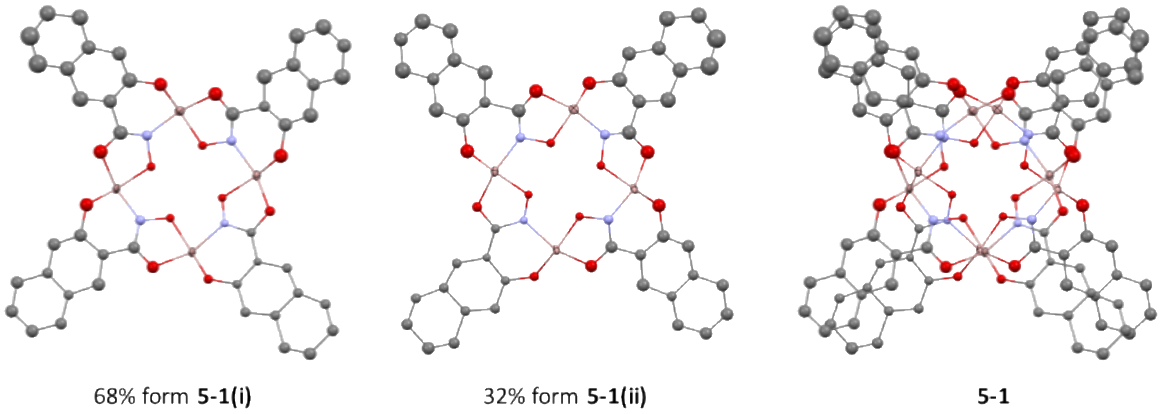

Figure 5.2. Molecular structure of complex **5-1** obtained from X-ray diffraction: (left) form complex **5-1(i)** and (middle) form complex **5-1(ii)**. (right) overlap view of form complex **5-1(i)** and complex **5-1(ii)**. Ga – tan; O – red; N – blue; C – grey; H atoms and solvent molecules coordinated to Ga^{III} were omitted for clarity.

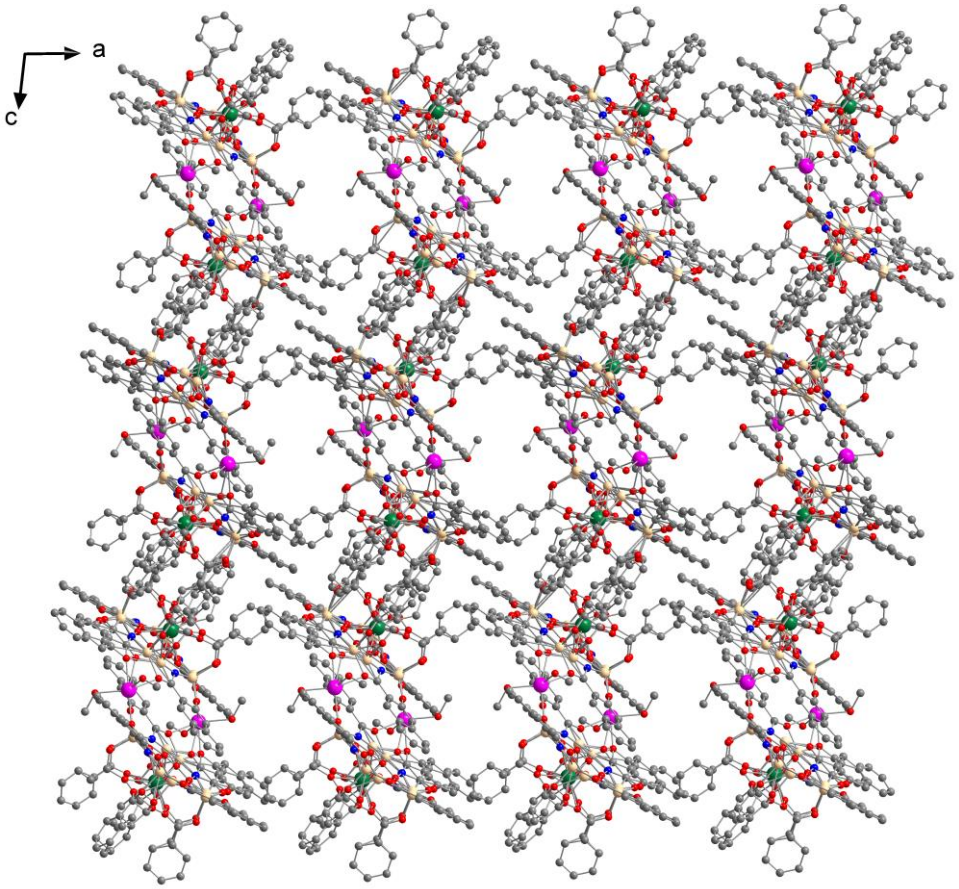

Figure 5.3. The packing arrangement of complex **5-1**. Dy – green; Ga – tan; Na – Pink; O – red; N – blue; C – grey; H atoms and solvent molecules coordinated to Ga^{III} were omitted for clarity.

Complex 5-2

Single crystal X-ray analysis of complex **5-2**(Figure 5.4) revealed that the binuclear lanthanide MC crystallizes in the triclinic *P*–1 space group (Table 5.1). The four organic ligands nha^{3-} and bridges Ga^{III} ions form a [12-$MC_{Ga^{III}}$-4] ring with –[Ga–N–O]– as the repeat unit. Four Ga^{III} ions are six-coordinated with nha^{3-} ligands, isophthalate ligands and one pyridine molecule. It is worth noting that one nha^{3-} ligand is different from other three; it is nearly perpendicular to the [12-$MC_{Ga^{III}}$-4] ring, which is different from the **$Ln_2Ga_8shi_8$** complexes in Chapter 4; the pyridine molecules and the hydroximate ligands exchanged their position because of the steric hindrance. Another difference is that in complex **5-2**, the two [12-$MC_{Ga^{III}}$-4] rings are not symmetric, we noted as complex **5-2(i)** and complex **5-2(ii)** for each. The third difference is that the four Ga^{III} ions are crystallographically equivalent, meanwhile, the negative charge of the 12-MC-4 metallacrowns are balanced by two pyridinium cations, not the sodium cations. At last, the analysis of the packing arrangement reveals that the binuclear bridged molecules are arranged parallel to each other (Figure 5.5).

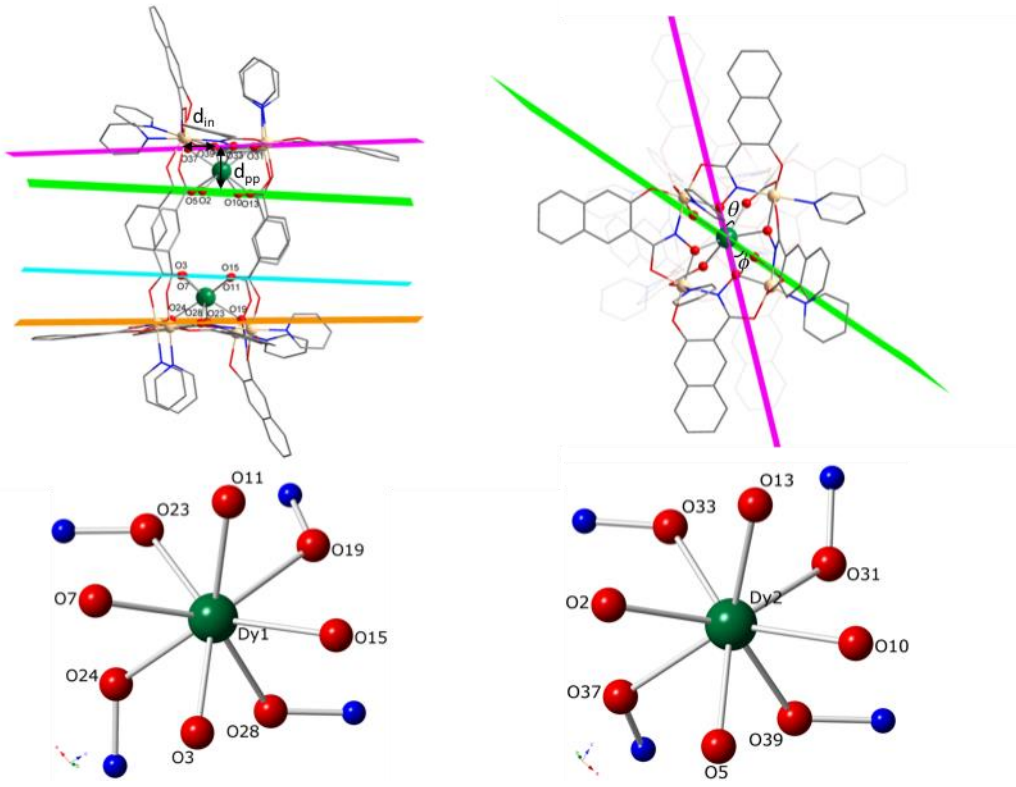

Figure 5.4. Molecular structure of complex **5-2** obtained from X-ray diffraction: (top left) side-view perspective showing d_{in} and d_{pp}; and (top right) top-down view showing ϕ and θ structural features of the [12-$MC_{Ga^{III}}$-4] core; (bottom) square-antiprismatic coordination geometry around the central Dy^{III} ion. Dy – green; Ga – tan; O – red; N – blue; C – grey; H atoms and solvent molecules coordinated to Ga^{III} were omitted for clarity.

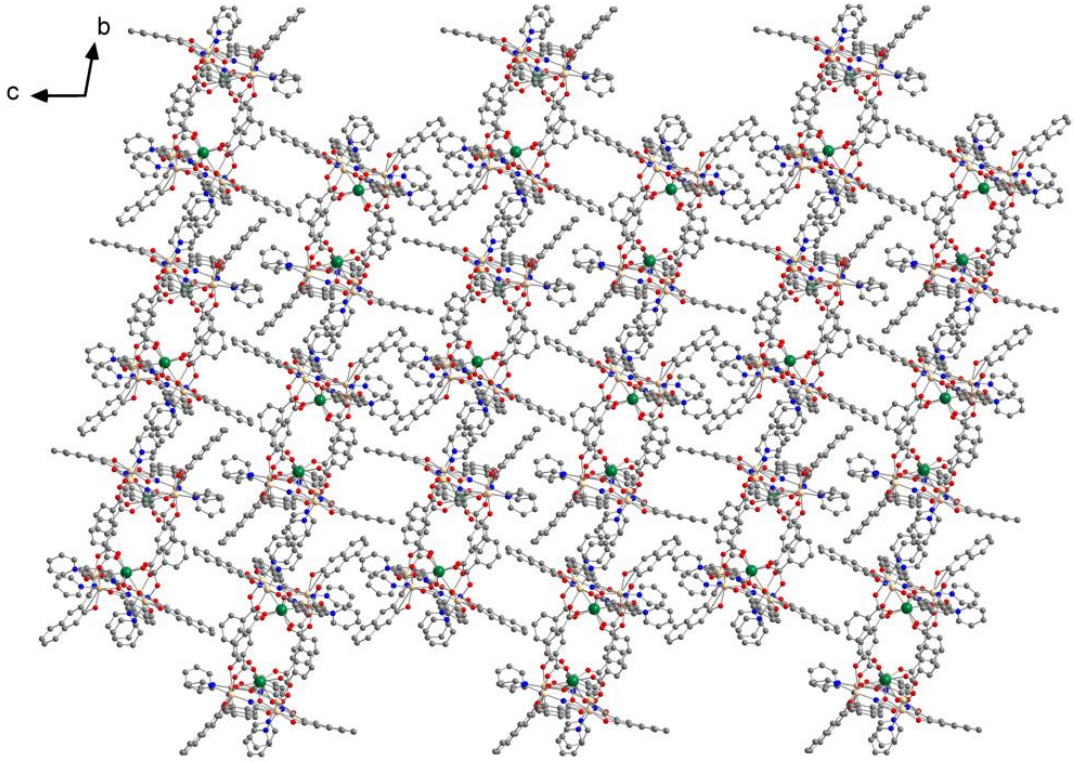

Figure 5.5. The packing arrangement of complex **5-2**. Dy – green; Ga – tan; O – red; N – blue; C – grey; H atoms and solvent molecules coordinated to Ga^{III} were omitted for clarity.

Table 5.1. Crystallographic data structure refinement for complexes **5-1** and **5-2**.

Complexes	**5-1**	**5-2**
formula	$Dy_2Ga_8C_{158}H_{138}N_8O_{51}Na_2$	$Dy_4Ga_{16}C_{370}H_{208}N_{41}O_{89}$
M_r	3893.58	8417.28
cryst syst	Monoclinic	Triclinic
space group	$P2_1/c$	$P\bar{1}$
a, Å	14.3157 (12)	16.2671(5)
b, Å	16.9523(14)	21.0276(6)
c, Å	36.063(3)	30.7190(10)
α, deg	90	97.303(2)
β, deg	97.236(2)	102.284(2)
γ, deg	90	102.8470(10)
cell volume, $Å^3$	8682.2(13)	9840.9(5)
Z	4	1
T, K	100(2)	100(2)
F_{000}	5248	4187
μ, mm^{-1}	4.250	1.825
θ range, deg	2.1–30.7	1.0–30.6
reflns collected	192276	248204
reflns unique	26708	59850
R_{int}	0.0918	0.0546
R_1	0.1356	0.0781
wR_2 (all data)	0.3468	0.2699
GOF	1.096	0.818
largest diff. peak and hole ($e \cdot Å^{-3}$)	3.40, −2.27	9.49, −2.03

Table 5.2. Characteristic parameters (θ, ϕ) of a square anti-prism geometry for complexes **5-1** and **5-2**.

Angle / °	**5-1(i)**		**5-1(ii)**		**5-2(i)**		**5-1(ii)**		**Ideal D_{4d}**[3, 4]
θ1	O1A	61.18	O1B	66.29	O3	57.98	O2	59.81	57.23
θ2	O2A	64.42	O2BB	55.56	O7	58.93	O5	57.89	57.23
θ3	O3A	60.63	O3B	57.26	O11	58.12	O10	57.63	57.23
θ4	O4A	58.70	O4B	67.63	O15	59.88	O13	58.18	57.23
θ5	O5A	51.33	O5B	55.86	O19	59.57	O31	51.93	57.23
θ6	O6A	55.73	O6B	53.87	O23	51.47	O33	52.89	57.23
θ7	O7A	52.84	O7B	43.95	O24	55.56	O37	60.05	57.23
θ8	O8A	51.06	O8B	51.16	O28	51.63	O39	51.51	57.23
ϕ1	O1A	44.98	O1B	47.93	O3	47.12	O2	48.26	45
ϕ2	O2A	44.58	O2BB	44.27	O7	43.28	O5	42.05	45
ϕ3	O3A	45.91	O3B	45.58	O11	41.23	O10	41.37	45
ϕ4	O4A	45.67	O4B	48.61	O15	47.57	O13	49.03	45

Table 5.3. Structural parameters of a square anti-prism geometry for complexes **5-1** and **5-2**.

Complexes	Ln–O_{ave} [a] / Å	MAD_{ϕ} [b] / °	d_{in} [c] / Å	d_{pp} [d] / Å	d_{pp}/d_{in} [e]
5-1(i)	2.317	0.505	2.741	2.513	0.917
5-1(ii)	2.332	1.963	2.734	2.541	0.929
5-2(i)	2.342	2.545	2.768	2.571	0.929
5-2(ii)	2.348	3.468	2.760	2.605	0.944

[a] The average values for bond lengths of Ln–O; [b] MAD = mean absolute deviation, skew angle ϕ for the ideal D_{4d} ligand field symmetry is 45°; [c] d_{in} means the average distance between the four neighboring atoms placed in each square; [d] d_{pp} means the distance between two centroids from the upper and lower planes respectively; [e] d_{pp}/d_{in} is 0.841 for the ideal square antiprism.[3, 5]

Table 5.4. Lanthanide center bonds with oxygen for complexes **5-1** and **5-2**.

5-1(i)		**5-1(ii)**		**5-2(i)**		**5-1(ii)**	
Dy–O1A	2.319	Dy–O1B	2.194	Dy1–O3	2.286	Dy2–O2	2.369
Dy–O2A	2.285	Dy–O2BB	2.477	Dy1–O7	2.340	Dy2–O5	2.318
Dy–O3A	2.341	Dy–O3B	2.380	Dy1–O11	2.295	Dy2–O10	2.334
Dy–O4A	2.355	Dy–O4B	2.204	Dy1–O15	2.375	Dy2–O13	2.300
Dy–O5A	2.349	Dy–O5B	2.154	Dy1–O19	2.412	Dy2–O31	2.417
Dy–O6A	2.243	Dy–O6B	2.327	Dy1–O23	2.322	Dy2–O33	2.325
Dy–O7A	2.278	Dy–O7B	2.534	Dy1–O24	2.357	Dy2–O37	2.399
Dy–O8A	2.368	Dy–O8B	2.386	Dy1–O28	2.351	Dy2–O39	2.320
$Dy–O_{ave}$	2.317	$Dy–O_{ave}$	2.332	$Dy1–O_{ave}$	2.342	$Dy2–O_{ave}$	2.348

Table 5.5. The distance between the four neighboring atoms placed in each square for complexes **5-1** and **5-2**.

5-1(i)		**5-1(ii)**		**5-2(i)**		**5-1(ii)**	
O1A–O2A	2.945	O1B–O2BB	2.893	O3–O7	2.774	O2–O5	2.871
O2A–O3A	2.891	O2BB–O3B	2.828	O7–O11	2.773	O5–O10	2.755
O3A–O4A	2.887	O3B–O4B	2.903	O11–O15	2.862	O10–O13	2.749
O4A–O1A	2.807	O4B–O1B	2.866	O15–O3	2.830	O13–O2	2.852
O5A–O6A	2.623	O5B–O6B	2.624	O19–O23	2.794	O31–O33	2.622
O6A–O7A	2.598	O6B–O7B	2.600	O23–O24	2.623	O33–O37	2.858
O7A–O8A	2.574	O7B–O8B	2.576	O24–O28	2.621	O37–O39	2.835
O8A–O5A	2.605	O8B–O5B	2.580	O28–O19	2.866	O39–O31	2.539
$O–O_{ave}$	2.741	$O–O_{ave}$	2.734	$O–O_{ave}$	2.768	$O–O_{ave}$	2.760

Table 5.6. SHAPE analysis of eight-coordinated geometry for complexes **5-1** and **5-2**.

Label Symmetry	OP D_{8h}	HPY C_{7v}	HPBY D_{6h}	CU O_h	SAPR D_{4d}	TDD D_{2d}	JGBF D_{2d}	JETBPY D_{3h}	JBTP C_{2v}	BTPR C_{2v}	JSD D_{2d}	TT T_d	ETBPY D_{3h}
5-1(i)	29.785	23.377	17.733	10.506	0.413	2.666	17.271	29.172	2.738	1.598	5.512	11.324	24.684
5-1(ii)	30.452	22.790	17.240	10.206	0.614	2.624	17.087	29.375	2.602	1.528	5.346	10.954	25.173
5-2(i)	30.439	23.259	15.756	9.487	0.505	2.102	14.811	28.876	2.138	1.529	4.425	10.298	23.995
5-2(ii)	31.131	22.412	15.421	8.885	0.628	2.211	14.891	28.307	2.469	1.956	5.016	9.658	23.191

Abbreviations: OP – Octagon, HPY – Heptagonal pyramid, HBPY – Hexagonal bipyramid, CU – Cube, SAPR – Square antiprism, TDD – Triangular dodecahedron, JGBF – Johnson – Gyrobifastigium (J26), JETBPY – Johnson Elongated triangular bipyramid (J14), JBTP – Johnson Biaugmented trigonal prism (J50), BTPR – Biaugmented trigonal prism, JSD – Snub disphenoid (J84), TT – Triakis tetrahedron, ETBPY – Elongated trigonal pyramid

5.3.3 Magnetic Studies

5.3.3.1 Direct current magnetic susceptibility studies

The dc magnetic susceptibility measurements were carried out between 2 and 300 K at 1000 and 10000 Oe (Figure 5.6). At room temperature, $\chi_M T$ = 28.87 and 28.49 $cm^3mol^{-1}K$ for complexes **5-1** and **5-2**, respectively, which are in good agreement with the expected values for non-coupling binuclear Dy^{III} (S = 5/2, L = 5, $^6H_{15/2}$, g = 4/3, $\chi_M T_{free\ ion}$ = 28.34 $cm^3mol^{-1}K$) complexes. Due to the thermal depopulation of the Stark sublevels, the $\chi_M T$ values decrease at low temperatures.

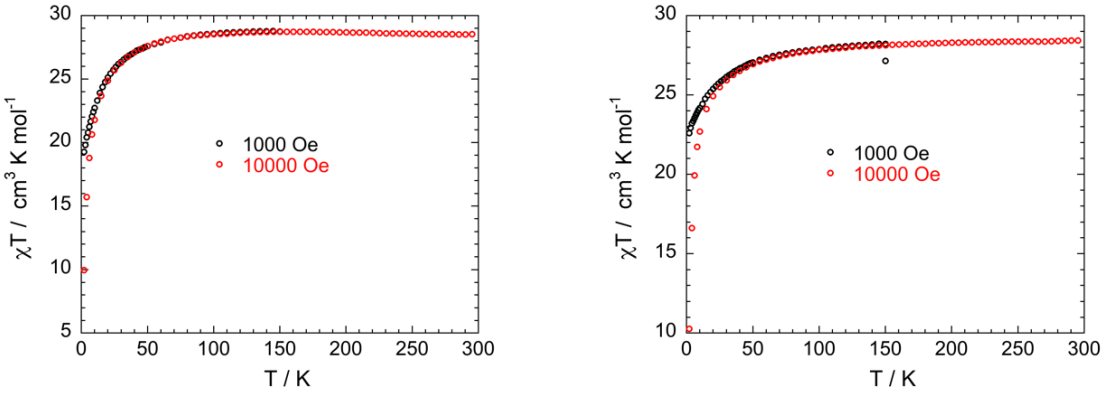

Figure 5.6. Temperature dependence of the χT product for complexes **5-1** (left) and **5-2** (right).

5.3.3.2 Magnetization versus dc magnetic field studies

The magnetization vs. the applied magnetic field M = f($\mu_0 H$) for complexes **5-1** and **5-2**, are plotted in Figure 5.7. M = f($\mu_0 H$) has the similar behavior for the two complexes. A slight difference is observed at high field where the magnetization of **5-2** is more saturated than that of **5-1**. This is probably due to a slightly larger separation in the energy spectrum of complex **5-2** in comparison to complex **5-1**.

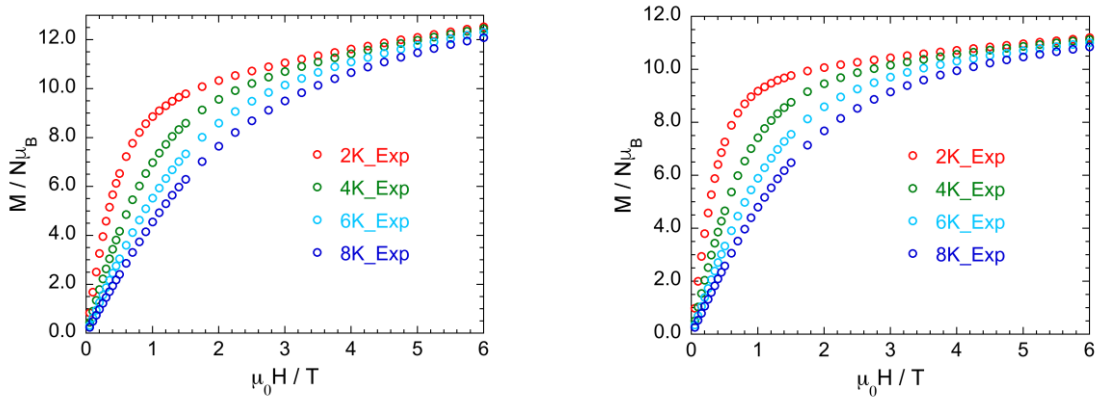

Figure 5.7. Magnetization *vs.* $\mu_0 H$ at variable temperatures for complexes **5-1** (left) and **5-2** (right).

5.3.3.3 Alternating current magnetic susceptibility studies

Complex 5-1 and 5-2

Field optimization studies were performed at T = 2 K with an applied dc field range 0 – 1200 Oe (Figure 5.8), but the maxima in the frequency-dependent ac susceptibility plot cannot be observed for **5-1**. We performed the ac measurements at different temperatures in the presence of a dc field of 1000 Oe as shown in Figure 5.9, but no further analysis could be carried out.

The field optimization experiment for complex **5-2** reveals that the optimum applied dc magnetic field is between 800 and 1000 Oe (Figure 5.10). In the presence of a dc field of 800 Oe, the maxima in the frequency-dependent ac susceptibility plots are present and a slow relaxation of its magnetization can be observed (Figure 5.11). The Cole-Cole plots at 800 Oe were obtained in the temperature range 1.83 – 6.0 K (Figure 5.12), and were fitted using a generalized Debye model[6, 7] which allows extracting the relaxation times (τ) and their distribution (α) for each temperature (Table 5.7). Fitting the linear parts of the ln(τ) = f(1/T) plot (Figure 5.13) provides the magnitude of the effective energy barriers for the reorientation of the magnetization U_{eff} that is found equal to 15.9 K (11.1 cm^{-1}) and τ_0 is 7.9 × 10^{-6} s.

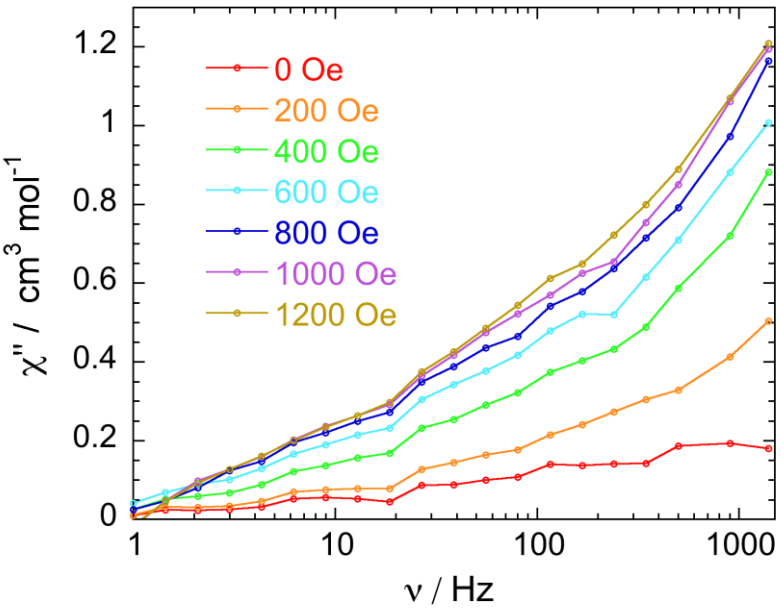

Figure 5.8. Out-of-phase susceptibility measurements at 2 K with a frequency range from 1 to 1500 Hz under various applied dc fields for complex **5-1**.

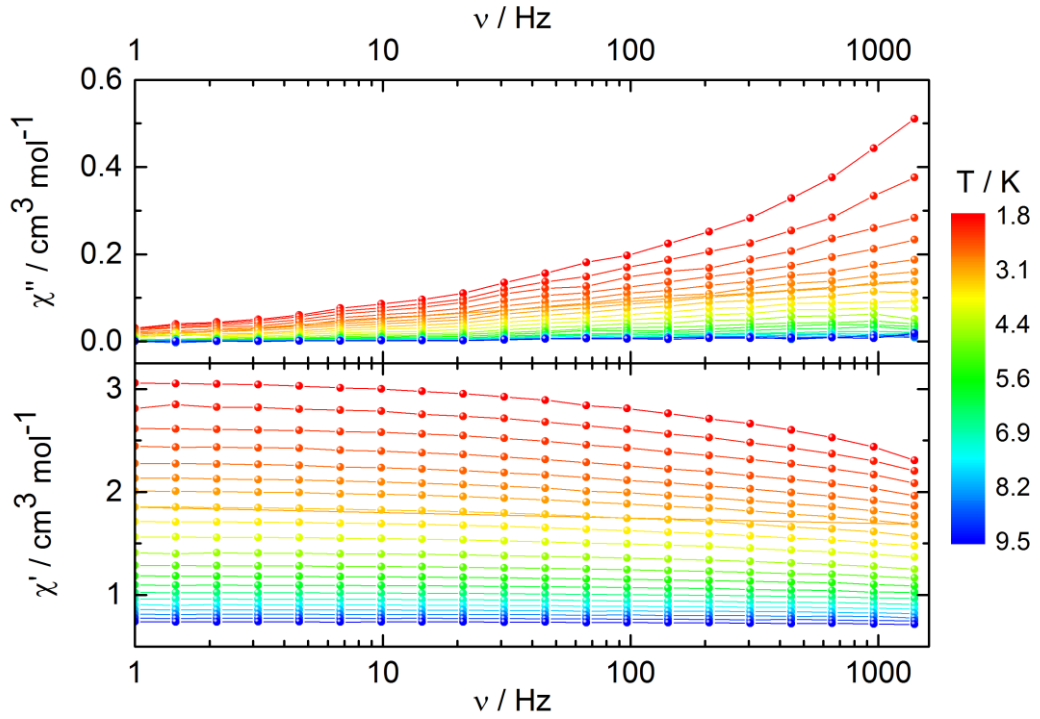

Figure 5.9. Frequency dependent out-of-phase and in-phase ac magnetic susceptibilities for complex **5-1** under an applied dc field of 1000 Oe.

Table 5.7. Cole-Cole fit parameters under an applied dc magnetic field of 800 Oe for complex **5-2**.

Complexes	Temperature	χ_0	χ_∞	α	τ
5-2	1.83 K	12.8358398375	0.1415122513	0.4933297160	0.0021718987
	2.00 K	11.8129973067	0.5234111741	0.4905791902	0.0020240115
	2.25 K	10.6651523933	0.9286091106	0.4820533827	0.0018178426
	2.50 K	9.4936093903	1.1454761880	0.4734175083	0.0014692021
	2.75 K	8.5795348872	1.4920116766	0.4527990931	0.0012775140
	3.00 K	7.8269526129	1.6673271936	0.4327960391	0.0010454363
	3.50 K	6.6828849348	2.0130447120	0.3992207783	0.0007273072
	4.00 K	5.8409713175	2.0487307439	0.3846404548	0.0004182837
	4.50 K	5.1975509957	2.2821559033	0.3610679550	0.0002939481
	5.00 K	4.6710290682	2.5238912397	0.3250024131	0.0002203042
	5.50 K	4.2603464083	2.3951282176	0.3355495468	0.0001195573
	6.00 K	3.9140735453	2.6810924691	0.3149971390	0.0001166745

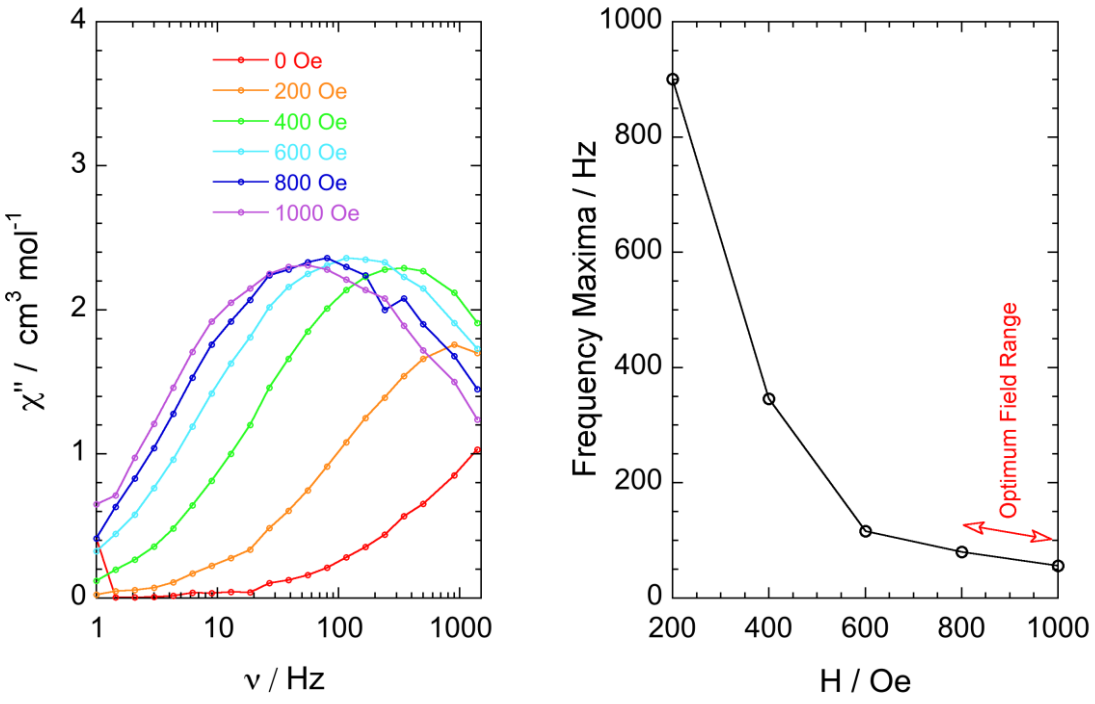

Figure 5.10. Out-of-phase susceptibility measurements at 2 K with a frequency range from 1 to 1500 Hz under various applied dc fields (left) and plot of frequency maxima *vs.* applied dc fields (right) for complex **5-2**.

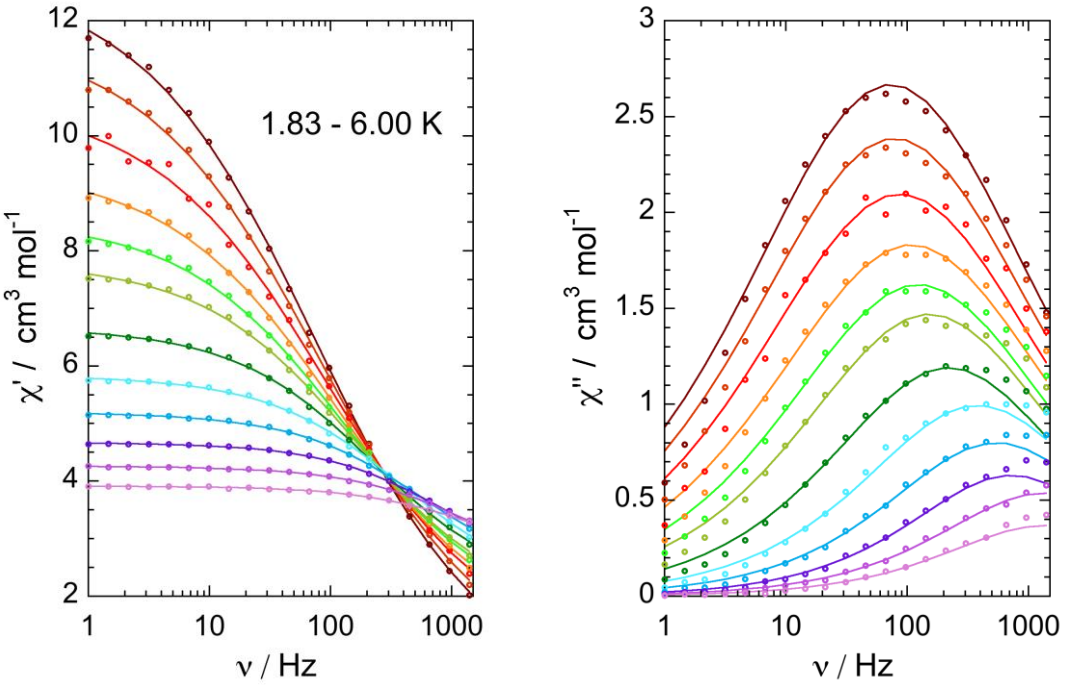

Figure 5.11. Frequency dependent in-phase and out-of-phase ac magnetic susceptibilities (○ (exp), — (fit)) for complex **5-2** under an applied dc field of 800 Oe.

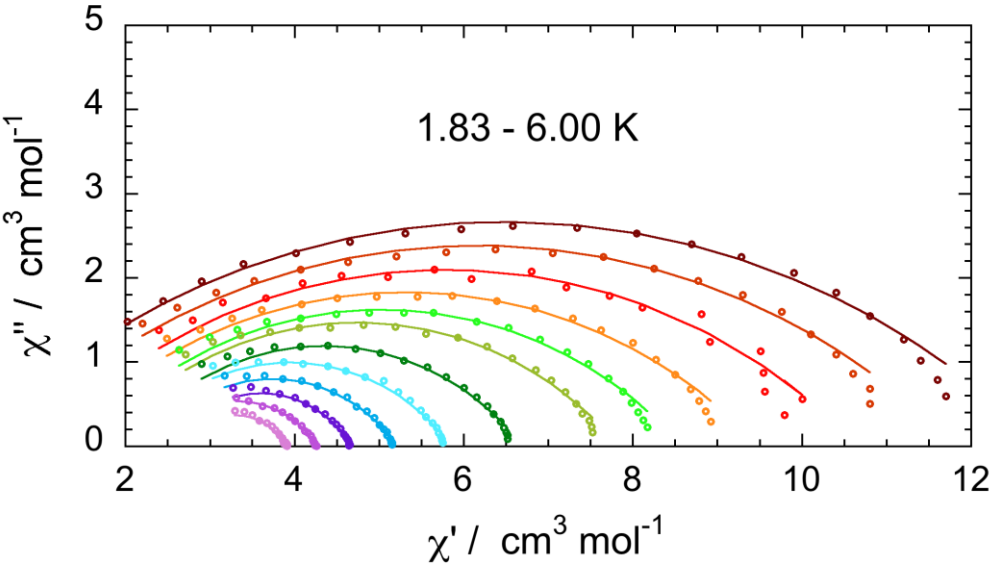

Figure 5.12. Cole-Cole plots (○ (exp), — (fit)) for complex **5-2** under an applied dc field of 800 Oe.

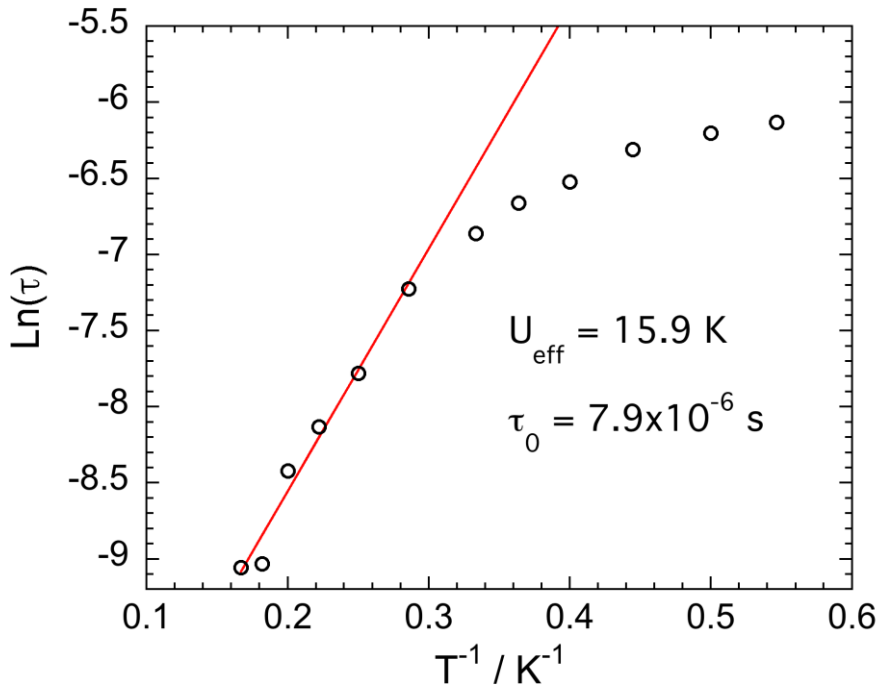

Figure 5.13. ln(τ) = f (1/T) plot (○ (exp), — (linear fit)) for the slow relaxation processes of complex **5-2**.

It is worth noting that the difference in the dynamic behavior between the two complexes can be related (at least qualitatively) to the magnetization data. Indeed, the less saturated magnetization data for **5-1** suggested that the energy separation among the low-lying $\pm m_J$ sub-levels is smaller than for **5-2** which leads to a larger mixture of the wavefunctions for the former than for the latter and thus probably to less Ising-type character for the ground state. Because of the lack of time, we did not perform *ab initio* calculations that would confirm our qualitative interpretation of the experimental data.

5.4 Summary and Conclusions

A slight difference in the local structure around the Dy^{III} ions between the two complexes may be the origin of the different dynamic behavior. Another possibility may be due to the interaction among the molecules within the crystal. It would be interesting to prepare diluted compounds and compare their behavior in order to get insight into the origin of the difference in the slow relaxation behavior of the two complexes.

5.5 References

1. S. Alvarez, P. Alemany, D. Casanova, J. Cirera, M. Llunell and D. Avnir, *Coordination Chemistry Reviews*, 2005, **249**, 1693-1708.
2. D. Casanova, M. Llunell, P. Alemany and S. Alvarez, *Chemistry – A European Journal*, 2005, **11**, 1479-1494.
3. E. L. Muetterties and L. J. Guggenberger, *Journal of the American Chemical Society*, 1974, **96**, 1748-1756.
4. M. A. AlDamen, J. M. Clemente-Juan, E. Coronado, C. Martí-Gastaldo and A. Gaita-Ariño, *Journal of the American Chemical Society*, 2008, **130**, 8874-8875.
5. M. A. AlDamen, S. Cardona-Serra, J. M. Clemente-Juan, E. Coronado, A. Gaita-Ariño, C. Martí-Gastaldo, F. Luis and O. Montero, *Inorganic Chemistry*, 2009, **48**, 3467-3479.
6. K. S. Cole and R. H. Cole, *The Journal of Chemical Physics*, 1941, **9**, 341-351.
7. H. Miyasaka, R. Clérac, K. Mizushima, K.-i. Sugiura, M. Yamashita, W. Wernsdorfer and C. Coulon, *Inorganic Chemistry*, 2003, **42**, 8203-8213.

CHAPTER 6 Conclusions and Future Directions

Understanding the relationship between geometrical and electronic structure and their impact on magnetic anisotropy is essential in the field of molecular magnetism. For molecular complexes, magnetic anisotropy is the consequence of spin-orbit coupling and low symmetry and is thus intimately linked to the number of single electrons and their distribution in different orbitals. The number of single electrons is determined by the chemical nature and the oxidation state of the metal ion, while their distribution in the different orbitals depends on both the symmetry imposed by the organic ligand and the number of electrons. For instance, for nickel(II), it is possible to have diamagnetic square planar complexes, five-coordinated trigonal bipyramidal or square pyramidal complexes and octahedral complexes depending on both the nature of the organic ligands and electronic configuration of the Ni^{II} ion.[1-4] The synthetic chemist is able, making the right choice, to privilege one of these geometries and eventually symmetries, thus influencing the magnetic anisotropy of the final complex.[3] However, once the geometry (or the symmetry) is fixed, subtle changes in the local structure of the coordination sphere impacts the nature and the magnitude of magnetic anisotropy. Again, if we take the example of Ni^{II} complexes, it is well understood that axially distorted six-coordinated complexes may present Ising-type of XY anisotropy depending on the compression or the elongation along the four-fold axis of the complex.[2]

In this work, we focused on cobalt(II) that possesses three single electrons and examined the case of five-coordinated trigonal bipyramidal (Figure 6.1) complexes with the objective of understanding and then tuning the magnitude of the Ising-type anisotropy already discovered in this type of complexes.[5] The flexibility of the organic ligand in the generic complex depicted in Figure 6.1, which allows examining the chemical effect of the axial ligand X and the peripheral ones Y. We demonstrated that for long Co–Y peripheral bonds and short Co–X axial bond leads to Ising-type anisotropy with larger magnitude than in the case of short Co–Y and long Co–X bond lengths.[6, 7] We were able, using *ab initio* calculations, to link these structural features to the energy scheme of the d orbital and thus present a qualitative magneto-structural correlation in this type of complexes. A more detailed and quantitative analysis for these complexes and will be detailed in the PhD

dissertation of Benjamin Cahier. We are now working on using this knowledge in order to build binuclear complexes with Ising-type anisotropy and (weak) antiferromagnetic exchange coupling that may be relevant to field of quantum information.

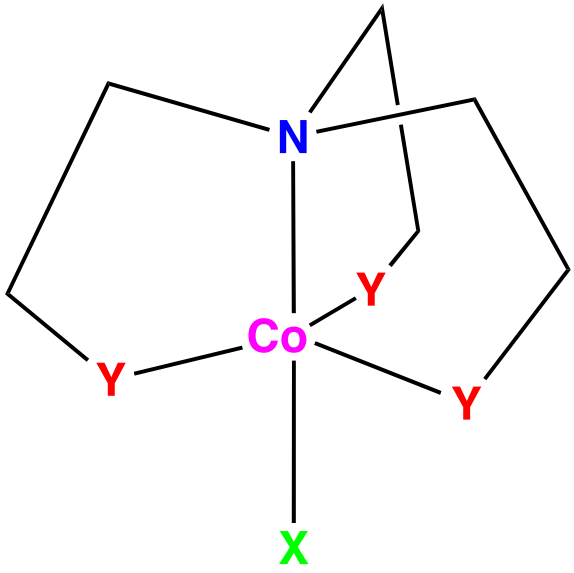

Figure 6.1. Scheme of the mononuclear trigonal bipyramidal Co^{II} complexes.

We have also studied the magnetic behavior of a series of mononuclear lanthanide complexes possessing a square antiprism geometry with a pseudo four-fold symmetry. It was already pointed out, based on a quadruple electrostatic model, that the organization of the electronic density coming from the ligands around the lanthanide(III) ions determine their magnetic anisotropy.[8] For the oblate ions (Tb^{III}, Dy^{III}, Ho^{III}), the Ising-type anisotropy ($m_J = \pm J$ sublevels with minimum energy) is obtained by minimizing the ion ligand electronic repulsion thus when the electronic density of the ligands sandwiches the metal ions. While for the prolate ions (Er^{III}, Yb^{III}), the electronic density of the ligands must lie in a plane around the metal ions in order to minimize the electronic repulsion and stabilize the $\pm m_J$ sub-levels with largest value. In the case we studied (Figure 6.2), the oxygen ligands impose a slightly elongated antiprism geometry, which is not the ideal situation for any of the lanthanide(III) ions. This is why, even though an Ising-type anisotropy is obtained, the energy separation between the ground and the excited sub-levels is not large and more importantly there is a large mixing of the wavefunctions that reflects the non-strict axial symmetry imposed by the ligands resulting from the local structural distortion. In order to obtain large Ising-type anisotropy (large separation between the ground and the excited levels and pure ground wavefunctions) for the Tb^{III} and the Dy^{III} complexes, the antiprism geometry must be

more elongated in order the minimize as much as possible the metal/ligands electronic repulsion, while for Er^{III} and Yb^{III} complexes should be more compressed. For $DyZn_{16}$ MC derivatives are under study, the ratio of d_{pp}/d_{in} is 0.723,[9] which the metallacrown structure could allow such control.[10, 11]

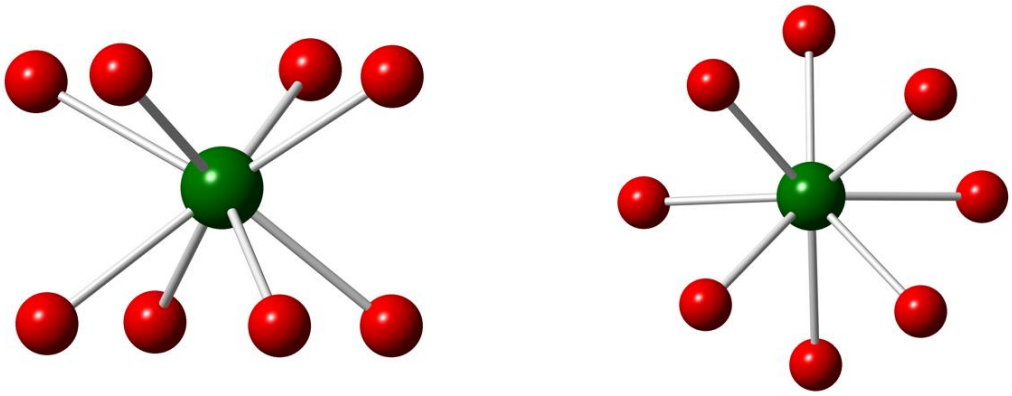

Figure 6.2. Coordination models for the Ga^{III}/Ln^{III} MC complexes. Ln – green; O – red.

References

1. G. Rogez, J. N. Rebilly, A. L. Barra, L. Sorace, G. Blondin, N. Kirchner, M. Duran, J. van Slageren, S. Parsons, L. Ricard, A. Marvilliers and T. Mallah, *Angewandte Chemie-International Edition*, 2005, **44**, 1876-1879.
2. G. Charron, E. Malkin, G. Rogez, L. J. Batchelor, S. Mazerat, R. Guillot, N. Guihéry, A.-L. Barra, T. Mallah and H. Bolvin, *Chemistry – A European Journal*, 2016, **22**, 16850-16862.
3. B. Cahier, M. Perfetti, G. Zakhia, D. Naoufal, F. El-Khatib, R. Guillot, E. Riviere, R. Sessoli, A. L. Barra, N. Guihery and T. Mallah, *Chemistry-a European Journal*, 2017, **23**, 3648-3657.
4. R. Ruamps, R. Maurice, L. Batchelor, M. Boggio-Pasqua, R. Guillot, A. L. Barra, J. Liu, E.-E. Bendeif, S. Pillet, S. Hill, T. Mallah and N. Guihéry, *Journal of the American Chemical Society*, 2013, **135**, 3017-3026.
5. R. Ruamps, L. J. Batchelor, R. Guillot, G. Zakhia, A. L. Barra, W. Wernsdorfer, N. Guihery and T. Mallah, *Chemical Science*, 2014, **5**, 3418-3424.
6. F. Shao, B. Cahier, N. Guihery, E. Riviere, R. Guillot, A.-L. Barra, Y. Lan, W. Wernsdorfer, V. E. Campbell and T. Mallah, *Chemical Communications*, 2015, **51**,

16475-16478.

7. F. Shao, B. Cahier, E. Rivière, R. Guillot, N. Guihéry, V. E. Campbell and T. Mallah, *Inorganic Chemistry*, 2017, **56**, 1104-1111.
8. J. D. Rinehart and J. R. Long, *Chemical Science*, 2011, **2**, 2078-2085.
9. J. Jankolovits, C. M. Andolina, J. W. Kampf, K. N. Raymond and V. L. Pecoraro, *Angewandte Chemie International Edition*, 2011, **50**, 9660-9664.
10. P. Happ, C. Plenk and E. Rentschler, *Coordination Chemistry Reviews*, 2015, **289–290**, 238-260.
11. M. Ostrowska, I. O. Fritsky, E. Gumienna-Kontecka and A. V. Pavlishchuk, *Coordination Chemistry Reviews*, 2016, **327–328**, 304-332.

Feng SHAO: 0000-0001-8606-8628

List of Complexes

Complexes	Formula
2-1	$[Co(Me_6tren)Cl](ClO_4)$
2-2	$[Co(Me_6tren)Cl](PF_6)$
2-3	$[Co(Me_6tren)Cl](Cl)$
2-4	$[Co(Me_6tren)Br](ClO_4)$
2-5	$[Co(Me_6tren)I](ClO_4)$
2-6	$[Co(Me_6tren)F](ClO_4)(H_2O)$
2-7	$[Zn(Me_6tren)F](ClO_4)(H_2O)$
2-8	$[Co_{0.12}Zn_{0.88}(Me_6tren)F](ClO_4)(H_2O)$
3-1	$[Co(NS_3^{iPr})Cl](BPh_4)$
3-2	$[Co(NS_3^{tBu})Cl](ClO_4)$
3-3	$[Co(NS_3^{tBu})Br](ClO_4)$
3-4	$[Co(NS_3^{tBu})NCS](ClO_4)$
4-1	$[TbGa_4(C_7H_4NO_3)4(C_6H_5CO_2)_4(C_5H_5N)(CH_3OH)]•C_5H_6N•C_5H_5N•CH_3OH$
4-2	$[DyGa_4(C_7H_4NO_3)4(C_6H_5CO_2)_4(C_5H_5N)(CH_3OH)]•C_5H_6N•C_5H_5N•CH_3OH$
4-3	$[HoGa_4(C_7H_4NO_3)4(C_6H_5CO_2)_4(C_5H_5N)(CH_3OH)]•C_5H_6N•C_5H_5N•CH_3OH$
4-4	$[ErGa_4(C_7H_4NO_3)4(C_6H_5CO_2)_4(C_5H_5N)(CH_3OH)]•C_5H_6N•C_5H_5N•CH_3OH$
4-5	$[YbGa_4(C_7H_4NO_3)4(C_6H_5CO_2)_4(C_5H_5N)(CH_3OH)]•C_5H_6N•C_5H_5N•CH_3OH$
4-6	$[Tb_2Ga_8(C_7H_4NO_3)_8(C_6H_2C_2O_4)_4(C_3H_7NO)_6Na_2]•(C_3H_7NO)•(H_2O)_2$
4-7	$[Dy_2Ga_8(C_7H_4NO_3)_8(C_6H_2C_2O_4)_4(C_3H_7NO)_6Na_2]•(C_3H_7NO)_3•(H_2O)_8$
4-8	$[Ho_2Ga_8(C_7H_4NO_3)_8(C_6H_2C_2O_4)_4(C_3H_7NO)_6Na_2]•(C_3H_7NO)_4•(H_2O)_8$
4-9	$[Er_2Ga_8(C_7H_4NO_3)_8(C_6H_2C_2O_4)_4(C_3H_7NO)_6Na_2]•(C_3H_7NO)_4•(H_2O)_6$
4-10	$[Yb_2Ga_8(C_7H_4NO_3)_8(C_6H_2C_2O_4)_4(C_3H_7NO)_6Na_2]•(C_3H_7NO)_4•(H_2O)_6$
5-1	$[Dy_2Ga_8(C_{11}H_6NO_3)_8(C_6H_5CO_2)_8(CH_3OH)_4Na_2]•(H_2O)_8$
5-2	$[Dy_2Ga_8(C_{11}H_6NO_3)_8(C_6H_4C_2O_4)_4(C_5H_5N)_8]•(C_5H_6N)_2•(CH_3OH)•(C_5H_5N)$

Feng SHAO: 0000-0001-8606-8628

Résumé En Français

Comme nous le savons, les applications sont déterminées par des propriétés, qui sont essentiellement déterminées par la structure. L'interaction entre la forme (structure moléculaire) et la fonction (propriétés physiques) peut être exploitée par le ligand, l'ion métallique, l'approche métallacrown et ainsi de suite. Les travaux de cette thèse portent sur la synthèse et l'étude du comportement magnétique de complexes mononucléaires de cobalt(II) de géométrie bipyramide trigonale et sur l'étude de complexes mononucléaires de lanthanides possédant une structure de type métallacrown.

Pour les complexes de cobalt(II), l'objectif a été de modifier l'anisotropie magnétique en modifiant la nature du ligand organique tétradenté et du ligand terminal en gardant, autant que faire se peut, la géométrie et même la symétrie des complexes. Dans le cas des complexes de métaux de transition, une anisotropie magnétique non négligeable est le résultat de l'effet conjugué du couplage spin-orbite et d'une géométrie basse. Nous avons donc focalisé sur les complexes de cobalt(II) de géométrie bipyramide trigonale (bpt). Pour ce faire, nous avons utilisé deux ligands tétradentes qui conduisent aux complexes schématisés ci-dessous :

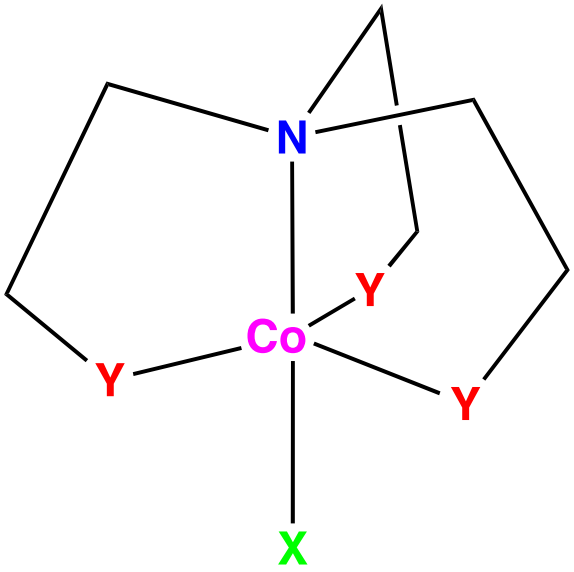

La nature tétradente du ligand organique et sa géométrie imposent des complexes avec une géométrie bpt. Le cinquième site de coordination est occupé par un ligand monodente

dont la nature électronique peut influencer l'anisotropie magnétique. De plus, les atomes Y dans le plan équatorial peuvent être des atomes d'azote ou des atomes de soufre établissant des liaisons différentes dans le plan équatorial et influençant ainsi la nature et l'amplitude de l'anisotropie magnétique. Nous avons préparé une série de complexes avec le ligand Me_6tren où Y = $N(CH_3)_2$ avec X = F^-, Cl^-, Br^- et I^-. Les complexes avec ce ligand tétradente possèdent une symétrie strictement axiale C_{3v}, à part le cas où X = F^- où la symétrie dévie légèrement. Nous avons montré (i) la présence d'un axe facile de l'aimantation colinéaire à l'axe principal de symétrie C_3, et (ii) que l'amplitude de l'anisotropie augmente en allant de X = I^- à $^-$F. Les calculs théoriques permettent de rationaliser les deux effets. La présence d'un axe de facile aimantation au sein des composés est due à la présence d'un premier état excité qui se couple à l'état fondamental par l'opérateur de spin-orbite suivant la direction z (colinéaire à l'axe de symétrie C_3) et apporte donc une forte contribution où le moment orbital est bloqué suivant l'axe z. Le remplacement du ligand I par Br^-, Cl^- et puis F^- conduit à une diminution de la longueur de la liaison Co–X qui d'une augmente la contribution de ce même état excité et d'autre diminue la contribution du deuxième état excité et renforce donc l'amplitude de l'anisotropie magnétique axiale.

Nous avons aussi étudié l'influence du changement de la nature des atomes liés au cobalt(II) dans le plan équatorial. Quand les groupes $N(CH_3)_2$ du ligand tétradente sont remplacés par les groupes S(isopropyl) ou S(terthiobuthyl), les distances Co–X deviennent plus longues. L'allongement des liaisons dans le plan équatorial conduit à un couplage plus fort avec le premier état excité qui favorise l'anisotropie axiale conduisant à une augmentation de cette anisotropie. Dans le cas de ce dernier ligand, l'analyse de l'anisotropie est plus complexe à cause de l'apparition d'une anisotropie rhombique (transverse) due à la non équivalence des longueurs des trois liaisons Co–S dans le plan équatorial. Nous avons montré que cette distorsion peut renforcer l'amplitude de la contribution axiale de l'anisotropie.

Presque tous les complexes de cobalt(II) se comportent comme des molécules-aimants avec une barrière énergétique à l'inversion de l'aimantation qui peut être liée à leur anisotropie magnétique et donc à la nature des ligands. Seulement le complexe où X = I^- ne se comporte pas comme une molécule-aimant car l'amplitude de l'anisotropie est faible conduisant à une faible barrière énergétique.

Nous avons aussi étudié l'anisotropie magnétique dans une série de complexes mononucléaires à base de lanthanides possédant la structure métallacrown. La structure

métallacrown conduit, en principe, à des complexes de symétrie relativement élevé permettant d'avoir une anisotropie quasi axiale avec une composante transverse presque nulle. L'intérêt de ces études est de pouvoir établir une corrélation entre la nature de l'ion lanthanide et l'anisotropie. Cette deuxième partie est moins aboutie que la première, mais ouvre des possibilités intéressantes car nous avons commencé à étudier les propriétés de luminescence de ces composés. L'étude de la luminescence dans les composés les plus simples (Ce^{III} et Yb^{III}) permettra de déterminer expérimentalement leur spectre d'énergie et ainsi comparer avec les résultats des modèles théoriques. J'ai commencé cette partie du travail qui sera continuée dans une autre thèse.

La thèse est composée de 6 chapitres. Le chapitre 1 présente l'état de l'art du magnétisme, des molécules-aimants (SMMs et SIMs) en se basant sur quelques exemples importants de la littérature. Le chapitre 2 se concentre sur une famille de complexes de géométrie bipyramide trigonale de formule générale $[Co(Me_6tren)X]Y$ avec le ligand axial (X) et le contre-ion (Y) induisant le comportement SMM. Dans cette série de composés, l'influence du ligand axial X sur la nature et l'amplitude de l'anisotropie magnétique a été étudiée. Nous avons montré que, pour la série des halogénures, l'anisotropie la plus forte est obtenue pour le ligand axial fluorure (F^-). L'effet du cation Y qui influence l'interaction entre les molécules et affecte légèrement le comportement d'aimant moléculaire a aussi été étudié. Au chapitre 3, on étudie l'influence du changement du ligand tétradenté. Le remplacement des trois atomes d'azote qui se trouvent en position équatoriale dans la sphère de coordination de Co par des atomes de soufre induit une augmentation des distances Co–L dans le plan équatorial qui conduit à une plus forte anisotropie. Les calculs théoriques effectués sur ces complexes permettent de rationaliser les résultats expérimentaux et surtout de prévoir les propriétés de nouveaux complexes. Les chapitres 4 et 5 concernent deux séries de SMM de structure métallacrown de formule $LnGa_4$ (Ln = Tb^{III}, Dy^{III}, Ho^{III}, Er^{III}, Yb^{III}) avec les ligands basés sur l'acide salicylhydroxamique (H_3shi) et l'acide 3-hydroxy-2-naphtohydroxamique (H_3nha). Les calculs théoriques préliminaires permettent de rationaliser la différence entre les propriétés des magnétiques dues aux différents ions lanthanide. Enfin, une conclusion générale avec des perspectives sont récapitulées au chapitre 6.

Biographical Sketch

Feng SHAO (FSh) was born in Anhui, China in 1987. He attended Anhui University in Hefei and earned his Bachelor of Natural Science degree in the major of Applied Chemistry on July 1, 2009. During his last year of undergraduate studies, FSh joined the research group of Professor Dr. QIU Ling-Guang on the project "Controlled release property of hierarchically micro- and meso-porous metal-nimesulide system for drug delivery". After graduation, he had a gap year before pursuing a master degree at Xiamen University in 2010. Under the supervision of Professor Dr. TAO Jun at the Department of Chemistry, FSh performed Synthesis, Structures, Magnetic Properties of Spin Crossover (SCO) compounds and was conferred the Master of Natural Science degree in the major of Inorganic Chemistry on June 30, 2013. Meanwhile, FSh received a PhD fellowship from the China Scholarship Council and joined the group of Distinguished Professor MALLAH Talal and Dr. CAMPBELL Victoria at the Institut de Chimie Moléculaire et des Matériaux d'Orsay, Department of Chemistry, Université Paris-Sud, Université Paris-Saclay. His doctoral research primarily focuses on engineering the magnetic anisotropy in trigonal bipyramidal cobalt(II) complexes and lanthanide-based metallacrowns. FSh has been the recipient of several awards and fellowships for his PhD research excellence, including the FP7 Marie Curie Fellowship-International Research Staff — Exchange Scheme (2015, to the group of Professor PECORARO Vincent at the University of Michigan, Ann Arbor, United States), Student Poster Prize at 15th International Conference on Molecule-Based Magnets (2016), Best Poster Prize at the 2ed Doctors' day, Department of Chemistry, Université Paris-Saclay (2016).

List of Publications

1. ***Feng Shao***, Benjamin Cahier, Eric Rivière, Régis Guillot, Nathalie Guihéry, Victoria E. Campbell and Talal Mallah, Structural Dependence of the Ising-type Magnetic Anisotropy and of the Relaxation Time in Mononuclear Trigonal Bipyramidal Co(II) Single Molecule Magnets, *Inorg. Chem.*, ***2017**, 56, 1104-1111.*
2. ***Feng Shao***, Benjamin Cahier, Nathalie Guihéry, Eric Rivière, Régis Guillot, Anne-Laure Barra, Yanhua Lan, Wolfgang Wernsdorfer, Victoria E. Campbell and Talal Mallah, Tuning the Ising-type anisotropy in trigonal bipyramidal Co(II) complexes, *Chem. Commun.*, ***2015**, 51, 16475-16478.*
3. Fatima El-Khatib, Benjamin Cahier, ***Feng Shao***, Maurici López-Jordà, Régis Guillot, Eric Rivière, Hala Hafez, Zeina Saad, Jean-Jacques Girerd, Nathalie Guihéry, and Talal Mallaha, Design and magnetic properties of a mononuclear Co(II) single molecule magnet and its antiferromagnetically coupled binuclear derivative. *Inorg.Chem.*, ***2017**, 56, 4601-4608.*
4. Feng-Lei Yang, ***Feng Shao***, Guang-Zhou Zhu, Yan-Hui Shi, Feng Gao and Xiu-Ling Li, Structures and Magnetostructural Correlation Analyses for Two Novel Hexanuclear Complexes Based on a Pentadentate Schiff Base Ligand, *ChemistrySelect* ***2017**, 2, 110–117.*
5. ***Feng Shao***, Benjamin Cahier, Eric Rivière, Régis Guillot, Nathalie Guihéry, and Talal Mallah, Relaxation Dynamics of Identical Trigonal Bipyramidal Co(II) Single Molecule Magnets. In Preparation.
6. ***Feng Shao***, Yiting Wang, Eric Rivière, Régis Guillot, Victoria E. Campbell, Talal Mallah and Vincent L. Pecoraro, Single molecule magnet behavior in Half-sandwich Ga^{3+}/Ln^{3+} Metallacrowns, In Preparation.
7. ***Feng Shao***, Yiting Wang, Eric Rivière, Régis Guillot, Victoria E. Campbell, Talal Mallah and Vincent L. Pecoraro, Single molecule magnet behavior in Sandwich Ga^{3+}/Ln^{3+} Metallacrowns, In Preparation.
8. Ted Bolon, ***Feng Shao***, Joseph Jankolovits, Eric Rivière, Hélène Bolvin, Vincent L. Pecoraro and Talal Mallah, Single molecule magnet behavior in Zn^{2+}/Ln^{3+} Metallacrowns. In Preparation.

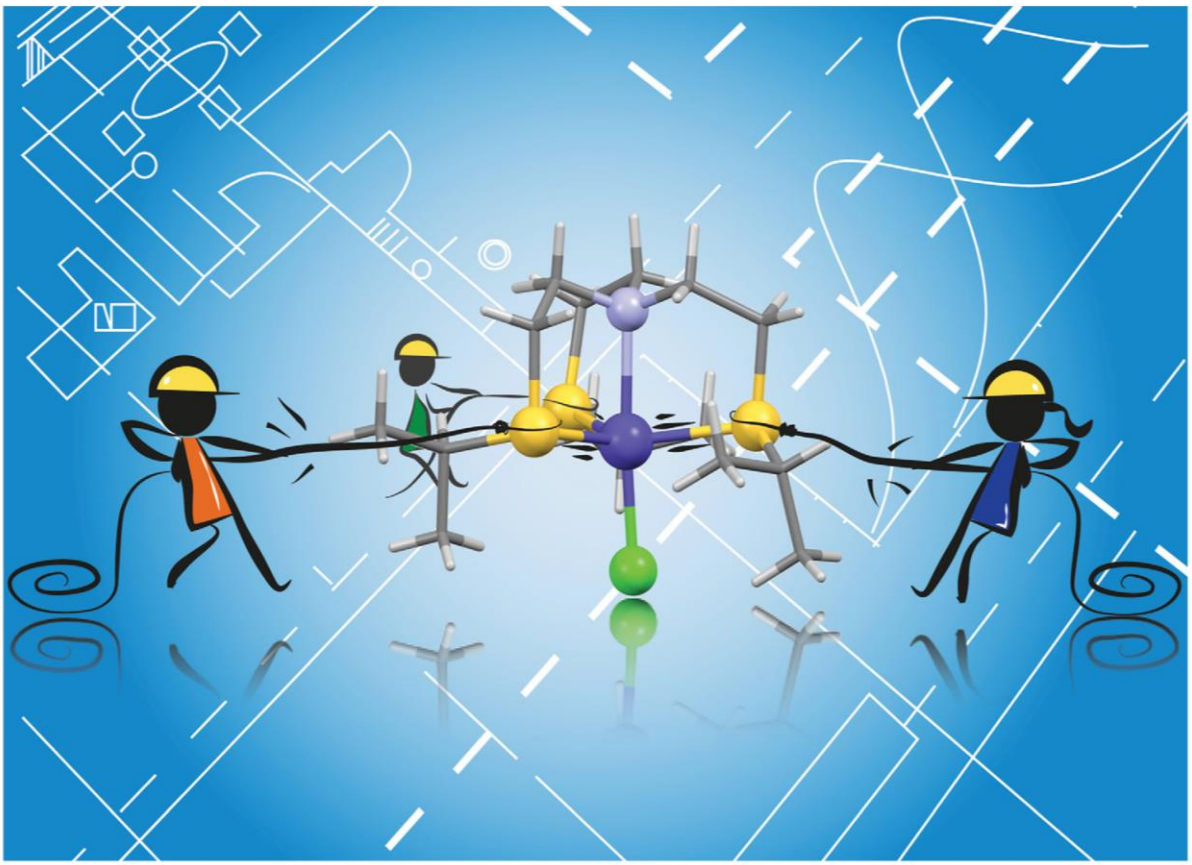

Showcasing research by F. Shao, B. Cahier, N. Guihéry, E. Rivière, R. Guillot, A.-L. Barra, Y. Lan, W. Wernsdorfer, V. E. Campbell and T. Mallah from, INCMI, Néel Institute, Universités de Toulouse, Paris-Sud, and Paris-Saclay, France.

Tuning the Ising-type anisotropy in trigonal bipyramidal Co(II) complexes

We can tune the Ising-type anisotropy in trigonal bipyramidal Co(II) complexes using simple ligand theory considerations. We used a sulfur containing ligand to synthesize a complex that had long equatorial Co–S bonds. This complex exhibits a larger anisotropy barrier and a longer relaxation time in comparison to the complex prepared with a nitrogen-containing ligand.

As featured in:

See Victoria E. Campbell, Talal Mallah *et al.*, *Chem. Commun.*, 2015, **51**, 16475.

ROYAL SOCIETY OF CHEMISTRY

www.rsc.org/chemcomm

Registered charity number: 207890

ChemComm

COMMUNICATION

View Article Online
View Journal | View Issue

Cite this: *Chem. Commun.*, 2015, **51**, 16475

Received 15th September 2015,
Accepted 28th September 2015

DOI: 10.1039/c5cc07741a

www.rsc.org/chemcomm

Tuning the Ising-type anisotropy in trigonal bipyramidal Co(II) complexes†

Feng Shao,[a] Benjamin Cahier,[a] Nathalie Guihéry,[b] Eric Rivière,[a] Régis Guillot,[a] Anne-Laure Barra,[c] Yanhua Lan,[d] Wolfgang Wernsdorfer,[d] Victoria E. Campbell*[a] and Talal Mallah*[a]

This paper demonstrates the engineering and tuning of Ising-type magnetic anisotropy in trigonal bipyramidal Co(II) complexes. Here, we predict that employing a ligand that forces a trigonal bipyramidal arrangement and has weak equatorial σ-donating atoms, increases (in absolute value) the negative zero field splitting parameter *D*. With these considerations in mind, we used a sulfur containing ligand (NS_3^{iPr}), which imposes a trigonal bipyramidal geometry to the central Co(II) ion with long equatorial Co–S bonds. The resulting complex exhibits a larger anisotropy barrier and a longer relaxation time in comparison to the complex prepared with a nitrogen containing ligand (Me_6tren).

Single molecule magnets (SMMs) have been extensively studied in the past 20 years.[1,2] The interest for these molecules lies in their magnetic bistability, which could have potential applications in quantum information.[3,4]

The first SMMs were polynuclear transition metal clusters with large zero field splitting (D) and large spin ground states (S).[1,5] More recently, research efforts have focused on building mononuclear SMMs with the intent to better control and tune the anisotropy of these systems. There are many examples in the literature of mononuclear lanthanide ion SMMs.[6–8] These complexes benefit from the large spin–orbit coupling of the f-block elements inherent to the single ion. These orbitals, however, are deeply buried beneath the valence shell, and the control of the symmetry of the molecules by the ligands is difficult in most cases. While it is not difficult to control the symmetry in transition metal ion complexes. There are few examples of mononuclear complexes that contain a single transition metal ion and display slow relaxation of the magnetization. The most notable examples are a linear Fe(I) complex, a tetrahedral Co(II) complex, and a trigonal bipyramidal Co(II) complex.[9–13]

Mononuclear complexes present clear advantages over polynuclear clusters, as they can be easily manipulated in solution and on surfaces, which is a requirement if we want to employ them as single quantum bits in quantum information applications. The interest in mononuclear transition metal SMMs stems from the possibility to more easily control their coordination geometry and in turn tune and shape their magnetic anisotropy.

Our group has previously shown that imposing a trigonal bipyramidal symmetry around Co(II) and Ni(II) cations leads to large Ising-type magnetic anisotropy (negative D value).[10] The anisotropy arises from the axial symmetry imposed by the organic ligand Me_6tren. The [Ni(Me_6tren)Cl](ClO_4) complex has a D value close to -200 cm^{-1}, due to the quasi first-order spin–orbit coupling.[10] Blocking of the magnetization was not observed because quantum tunneling is large in $S = 1$ systems, and because of the presence of a tiny transverse anisotropy due to a dynamic Jahn–Teller effect, which leads to fast relaxation of the magnetization. Slow relaxation of the magnetization and an opening of the hysteresis loop (both parameters are indicative of SMM behavior) were observed in the Co(II) analog ([Co(Me_6tren)Cl](ClO_4), $S = 3/2$), which has a strict C_{3v} symmetry, even though its anisotropy is much weaker than the isostructural Ni(II) analog. This complex exhibits an Ising-type anisotropy.[9] It was found that the zero field splitting parameter D changes when the Cl^- is replaced by Br^- (from -8.1 to -4.6 cm^{-1}, respectively). The difference in magnitude was rationalized in terms of the σ/π donating effects of the ligands. Building upon these results we designed the study reported herein.

This paper describes the rationalization behind engineering and tuning of Ising-type magnetic anisotropy in trigonal bipyramidal Co(II) complexes. We predicted that employing a ligand, which imposes a trigonal bipyramidal arrangement and has weak equatorial σ-donating atoms, increases the negative zero field splitting parameter D.

[a] *Institut de Chimie Moléculaire et des Matériaux d'Orsay, CNRS, Université Paris Sud, Université Paris Saclay, 91405 Orsay Cedex, France. E-mail: victoria.campbell@u-psud.fr, talal.mallah@u-psud.fr*
[b] *Laboratoire de Chimie et Physique Quantiques, Université de Toulouse III, 118 route de Narbonne, 31062 Toulouse, France*
[c] *Laboratoire National des Champs Magnétiques Intenses, UPR CNRS 3228, Université J. Fourier, 25, avenue des Martyrs, B.P. 166, 38042 Grenoble, France*
[d] *Insitut Néel, CNRS, Université Grenoble Alpes, 25 rue des Martyrs, 38042 Grenoble, France*

† Electronic supplementary information (ESI) available: Detail experimental procedures, spectroscopic data, single crystal X-ray data and computational details. CCDC 1061993. For ESI and crystallographic data in CIF or other electronic format see DOI: 10.1039/c5cc07741a

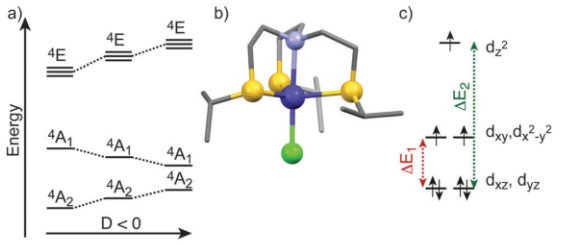

Fig. 1 (a) Schematic energy diagram of the lowest quadruplets for a trigonal bipyramidal Co(II) complex; (b) X-ray crystal structure of $[Co(NS_3^{iPr})Cl](BPh_4)$: Co = purple; C = grey; N = lilac; S = yellow; Cl = green; H atoms and counter ions were removed for clarity; (c) orbital energy diagram for a trigonal bipyramidal Co(II) complex.

We synthesized and magnetically characterized a trigonal bipyramidal Co(II) complex, which was constructed from tris-(2-(isopropylthio)ethyl)amine (NS_3^{iPr}). We show that we can tune the magnitude of D by using our design principles and that we can considerably increase D (= -23 cm^{-1} for $[Co(NS_3^{iPr})Cl](BPh_4)$ by lengthening the bonds in the equatorial plane. The magnitude of the anisotropy parameters was experimentally determined and calculated using a correlated *ab initio* method (see ESI,† for details).

From perturbative arguments it can be shown that $|D|$ is inversely proportional to the energy difference between the ground and the excited states.[14,15] As the symmetry point group of the molecule is close to C_{3v}, the rationalization of the magnitude and nature of the zero-field splitting will be performed assuming that the geometry adopts this symmetry (Fig. 1). Two quadruplet excited states, $^4A_1$, and ^4E primarily influence the main contributions to the anisotropy parameters. The first excited state $^4A_1$ is responsible for the negative value of D while ^4E brings a positive but smaller contribution.[9,13] There is another excited quadruplet state ($^4A_2$) just above the ground $^4A_2$ state but it does not contribute to D (it does not appear in the energy spectrum of Fig. 1) The appearance of a non-zero rhombic parameter E is due to the lift of degeneracy of the ^4E states as the symmetry of the complex is not exactly C_{3v}. The energy difference between the ground state $^4A_2$ and the first excited state $^4A_1$ that has a contribution to D is related to the energy difference between the (d_{xz}, d_{yz}) and ($d_{x^2-y^2}$, d_{xy}) orbitals noted ΔE_1, since the state $^4A_1$ is obtained from a single excitation involving these orbitals. At variance, the state ^4E results from excitations between (d_{xz}, d_{yz}) and the d_{z^2} orbitals (Fig. 1).[9,13] In order to increase the negative contribution to D, the $^4A_2$–$^4A_1$ energy difference (related to ΔE_1) must decrease while the $^4A_2$–^4E energy difference (related to ΔE_2) must increase (Fig. 1a and c). This effect can be achieved by designing a molecule that has longer equatorial Co–L distances (weaker equatorial σ-donating effect; L = ligand) and shorter axial Co–L bonds (larger axial σ-donating effect). These qualitative arguments only consider the σ-donating effects of the ligands, which are dominant. Increasing π-donation of the equatorial ligands will further decrease ΔE_1 and make D more negative.

Synthesis. With these parameters in mind we set out to design a ligand that would yield trigonal bipyramidal complexes with the characteristics described above. We opted for an analogue of the Me_6tren ligand. We replaced three nitrogen atoms with sulfur atoms, which are larger and result in longer Co–L bonds. The ligand NS_3^{iPr} was synthesized following a modified literature procedure.[16] The general synthesis of the complex is as follows. To a solution of NS_3^{iPr} (1 equiv.) in 1-butanol the anhydrous $CoCl_2$ salt was added (1 equiv.) to yield a purple microcrystalline solid. Air stable X-ray quality single crystals were obtained by slow evaporation of diethyl ether into a saturated ethanol/acetone (1/1) solution of $[Co(NS_3^{iPr})Cl](BPh_4)$. As expected, the ligand imposes a trigonal bipyramidal arrangement in the complexes with pseudo C_3 molecular symmetry axis. The cation structures is comprised of a central Co(II) ion surrounded by three sulfur atoms in the equatorial sites, a nitrogen and a chloride in the axial sites (Fig. 1).

As per design, here we show that it is possible to engineer the magnetic anisotropy (control of the magnitude of the spin Hamiltonian parameter D) in trigonal bipyramidal Co(II) complexes. There is a significant difference in the bond distance between $[Co(NS_3^{iPr})Cl](BPh_4)$ (Table S2, ESI†) and its Me_6tren analogue. By replacing the ligand's equatorial nitrogen atoms with sulfur atoms, the Co-equatorial atoms distance was increased by 0.245 Å from 2.152 Å (for the $[Co(Me_6tren)Cl](ClO_4)$ complex)[9] to 2.397 Å (average values at the three Co–S bonds have different lengths) for Co–N and Co–S, respectively. This elongation resulted in a slightly shorter Co–Cl bond distance in $[Co(NS_3^{iPr})Cl](BPh_4)$. These two effects in unison translated to a dramatic increase in the $|D|$ value, which went from -8.1 cm^{-1} for $[Co(Me_6tren)Cl](ClO_4)$ to -19.9 cm^{-1} for $[Co(NS_3^{iPr})Cl](BPh_4)$. It is important to note that within the crystal lattice of $[Co(NS_3^{iPr})Cl](BPh_4)$ there are two geometrically different complexes that have the same pseudo trigonal bipyramidal structure with different Co–S and Co–N bond lengths (see Table S1, ESI†). These two different isomers have different D values (-23.0, and -13.1 cm^{-1} for isomers a and b respectively, see Table S1, ESI†), as seen from the *ab initio* calculations. We can relate the differences to the geometry of the complexes, as described in more detail in the following sections.

DC magnetic data and EPR studies. Variable temperature d.c. magnetic susceptibility data were taken between 2 and 300 K and at 1000 and 10 000 Oe (Fig. S1 and S2, ESI†). The χT is constant between room temperature and 40 K, with values close to 2.4 cm^3 K mol^{-1} (Fig. S1, ESI†). Below 40 K the χT decreases indicating zero-field splitting (ZFS) of the $M_S = \pm 1/2$ and $\pm 3/2$ sublevels (magnetic anisotropy). The magnetization (M) *versus* $\mu_0 H$ (and $\mu_0 H/T$) plots (Fig. S2, ESI†) confirm the presence of magnetic anisotropy. Fitting the data using the spin Hamiltonian $H = g\beta S \cdot B + D[S_z^2 - S(S+1)/3] + E(S_x^2 - S_y^2)$ for $S = 3/2$ gives to the following values -19.9 cm^{-1}, 1.5 cm^{-1} and 2.43 for D, E, and g parameters respectively. The spin Hamiltonian parameters obtained from the fit correspond to the mean value for the two crystallographically independent molecules; it is not possible from the magnetization data to differentiate them. We have thus calculated the magnetization *vs.* field curves using the spin Hamiltonian parameters obtained from the *ab initio* calculations ($D = -23$ and -13 cm^{-1} and $E/D = 0.09$) and found that the mean curves are in very good agreement with the experimental ones (Fig. S2, ESI,† bottom). The theoretical barriers for the two independent molecules corresponding to

the energy difference between the ground $M_S = \pm 3/2$ and the excited $M_S = \pm 1/2$ Kramers doublets are thus expected to be equal to 46 and 26 cm^{-1} ($2|D|$).

In order to validate the magnetization results, we performed a powder EPR study at several frequencies, from X-band to 662 GHz, and at temperatures ranging from 5 to 40 K. Unfortunately, the quality of the recorded spectra was rather poor even at X-band frequency, perhaps due to non-resonant absorption of the microwave power by the sulfur ligand. Thus, only a few transitions could be identified and the resulting information on the magnetic anisotropy of the system is limited. At the lowest temperature, only one signal is observed at low frequencies corresponding to an effective g-value of 7.05 (Fig. S3, ESI†). With the increase of the frequency, this signal splits in two components of comparable intensity, with effective g-values of g_{1eff} = 7.14 and g_{2eff} = 6.95 respectively. These two signals originate from the ground energy level ($M_S = -3/2$) as their intensity decreases with the increase of temperature. Conversely, another signal appears at temperature larger than 5 K; it corresponds to an effective g-value of g_{3eff} = 3.18. From the rough temperature dependence performed (measurements at 5, 15, 25 and 40 K), the signal intensity goes through a maximum around 25 K with an uncertainty of ±10 K (Fig. S3, ESI† bottom). This signal, coming from an excited level, is attributed to a transition inside the $M_S = \pm 1/2$ levels because it can be followed with an effective g description. As no other signal could be surely identified, it is not possible to extract the parameters governing the magnetic anisotropy directly from the EPR spectra. Thus, we limited the analysis to checking the compatibility with the resonances expected using the values obtained from *ab initio* calculations. Fixing the g-values, according to the magnetic measurements, to $g_x = g_y = 2.2$ and $g_z = 2.4$, we find that g_{1eff} corresponds to $|E/D|$ = 0.09, close to the values obtained from the *ab initio* calculations. Conversely, for the same set of fixed g-values, g_{2eff} corresponds to $|E/D|$ = 0.18, far from the calculated values. However, both signals have comparable intensities, pointing towards signals associated to the different molecules present in the cell. Finally, the high-frequency EPR study allows determining a minimum value for the axial anisotropy parameter $|D|$, due to the absence of new signals (up to 662 GHz): $|D| > 15$ cm^{-1}.

AC studies. To probe into the relaxation dynamics, a.c. magnetic susceptibility measurements were carried out on microcrystalline samples. The compound showed frequency dependence of the out-of phase (χ'') susceptibility and slow relaxation of its magnetization (Fig. 2). For [Co(NS$_3^{iPr}$)Cl](BPh$_4$), the χ'' as a function of wave frequency signal (Fig. 2b) is broad. The χ'' and χ' and their corresponding cole–cole plots can then be deconvoluted into two series of curves (Fig. S4–S6, ESI†). The two series of curves correspond to two sets of relaxation processes: one where the relaxation is dominated by a relaxation over the energy barrier and the other where faster processes dominate. The fit of the cole–cole plots to the generalized Debye model was performed for the plots corresponding to the slower processes, which allows extracting the relaxation times (τ) and their distribution (α) for each temperature (Table S3, ESI†).[17] Fitting the linear parts of the $\ln(\tau) = f(1/T)$ plot (Fig. 3) provides the magnitude of the effective energy barriers for the reorientation of the magnetization U_{eff} that is found equal to 32 cm^{-1} (46 K).

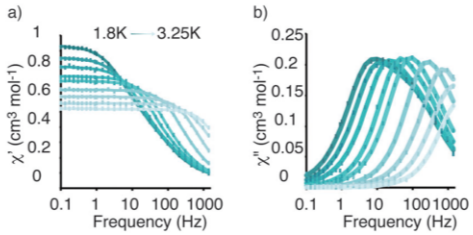

Fig. 2 A.c. magnetic susceptibility data. (a) χ', and (b) χ'' as a function of wave frequency at T = 1.8 to 3.5 K, and d.c. applied field = 2000 Oe for [Co(NS$_3^{iPr}$)Cl](BPh$_4$). The squares represent the experimental values, and the lines are the theoretical fits (see below).

Micro-SQUID magnetic data. To probe the SMM behavior of [Co(NS$_3^{iPr}$)Cl](BPh$_4$), and to gain further insight into its low temperature behavior, single crystal magnetization measurements were performed using a micro-SQUID[18] instrument at temperatures ranging from 0.03 to 5 K. The field was aligned parallel to the easy axis of magnetization by using the transverse field method.[19] Opening of the hysteresis loops were observed below T = 2 K (Fig. 4a), indicating that the complex exhibits slow relaxation of the magnetization. The effect of the quantum tunneling of the magnetization (QTM) between the $M_S = \pm 3/2$ states is evidenced by the steps at zero field. The tunnel rate is very fast because even at our fastest field sweep rate of 0.28 T s^{-1} the hysteresis loop remains closed at $\mu_0 H = 0$, which is consistent with the results of the aforementioned a.c. studies. In order to see better the slow relaxation at non-zero field, we recorded hysteresis loops starting from $\mu_0 H = 0$, at 0.03 K, and with scan rates in the range of 0.004–0.280 T s^{-1} (Fig. 4b). As soon as a small field is applied, tunneling is blocked and a large amount of molecules are in the $M_S = +3/2$ state (instead of all the molecules being in the $M_S = -3/2$ expected when upon increasing the field and in the absence of blocking) and this amount decreases slowly upon increasing the magnetic field, revealing a large SMM-type hysteresis. At higher fields, the molecules in $M_S = +3/2$ relaxes to the $M_S = -3/2$ state *via* the direct relaxation process, emitting a phonon.

Theoretical calculations. Theoretical calculations were performed to validate the experimental values of D obtained, as it is not possible to distinguish between the magnetism of the two independent molecules. We used the experimental geometries for our study. The *ab initio* calculations were done using the two-step approach implemented in the MOLCAS code (see ESI,† for details).[20–24] The values of D are reported in Table S1 (ESI†) and their

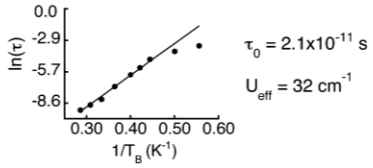

Fig. 3 $\ln(\tau) = f(1/T)$ for the slow relaxation processes of [Co(NS$_3^{iPr}$)Cl](BPh$_4$).

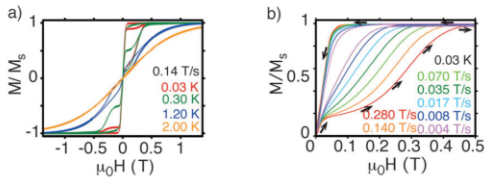

Fig. 4 (a) Magnetization *vs.* field on a single crystal of $[Co(NS_3^{iPr})Cl](BPh_4)$ at different temperatures and fixed scan rate, where M_S is the saturation magnetization. (b) First magnetization curves for different sweep rates at 0.03 K, obtained by cooling down the single crystal in zero field and then starting the hysteresis loop from zero field.

average is in perfect agreement with the experimental values obtained. It is worth noting that the difference in the calculated D values for the two isomers of $[Co(NS_3^{iPr})Cl](BPh_4)$ is mainly due to the energy difference (Table S4, ESI†) between the ground ($^4A_2$) and the first excited state ($^4A_1$). This energy difference between the states is related to the energy difference ΔE_1 between the (d_{xz}, d_{yz}) and the (d_{xy}, $d_{x^2-y^2}$) orbitals (Fig. 1). This effect translated to a weaker energy difference in complexes that have larger equatorial metal–ligand (Co–S) distances. We, therefore, obtain a larger $|D|$ value for $[Co(NS_3^{iPr})Cl]^+$ (a) than for $[Co(NS_3^{iPr})Cl]^+$ (b) (-23.0 and -13.1 cm^{-1}, respectively). In addition to their size sulfur atoms possess π-donating character that reduces the energy differences between $^4A_2$ and $^4A_1$, bringing an additional negative contribution to D. This increase of $|D|$ results in a longer relaxation time (Fig. 2) even though there is a non negligible transversal term (E) for $[Co(NS_3^{iPr})Cl](BPh_4)$.

The conclusion from this work is that we can engineer and tune the anisotropy and the barrier of the reorientation of the magnetization of trigonal bipyramidal Co(II) complexes by chemical design. Despite the presence of a transverse anisotropy term in the sulfur based complexes, the effective energy barrier U_{eff} was increased from 16 cm^{-1} $[Co(Me_6tren)Cl]^+$ to 32 cm^{-1} in the present case. The reduction of the value of the energy barrier from the theoretical one (46 cm^{-1} to corresponding the isomer with the largest $|D|$ value) is about 30%. It is usually ascribed to multiphonon processes (Raman type) that are active at high temperatures.[11] At low temperature where the micro-Squid data were recorded, the multiphonon processes are negligible.[25] At these temperatures only direct and quantum tunneling processes are active. The fast relaxation at zero field observed in the $M = f(\mu_0 H)$ loops are mainly due to the nature of the wavefunctions within the Kramers low-lying doublet. The presence of a rhombic term due to the lack of the strict axial symmetry of the complexes mixes the M_S wavefunctions ($-1/2$ with $+3/2$ and $+1/2$ with $-3/2$). The degenerate ground state Kramers doublet is not a pure $\pm 3/2$ state but has contribution from the $\pm 1/2$ wavefunctions; this mixing together with small local transverse fields (dipolar, hyperfine, *etc.*) opens a tunnel splitting within the ground state levels and is responsible for the fast quantum tunneling of the magnetization at $H = 0$.

This work is partially financed by ANR-project MolNanoSpin 13-BS10-0001-03. Y.L. and W.W. thank the EU for financial support within the FP7 FET-Proactive project MoQuaS No. 610449. We thank the collaborative program between the China Scholarship Council and Université Paris-Sud (No. 201306310014), UPS, Région Ile de France SESAME program 2012 No. 12018501, LabEx CHARM^{3}AT, and CNRS. T.M. thanks the IUF (Institut Universitaire de France) for financial support.

Notes and references

1 R. Sessoli, H. L. Tsai, A. R. Schake, S. Wang, J. B. Vincent, K. Folting, D. Gatteschi, G. Christou and D. N. Hendrickson, *J. Am. Chem. Soc.*, 1993, **115**, 1804–1816.
2 A. Caneschi, D. Gatteschi, R. Sessoli, A. L. Barra, L. C. Brunel and M. Guillot, *J. Am. Chem. Soc.*, 1991, **113**, 5873–5874.
3 L. Bogani and W. Wernsdorfer, *Nat. Mater.*, 2008, **7**, 179–186.
4 R. Sessoli, *Angew. Chem., Int. Ed.*, 2012, **51**, 43–45.
5 R. Sessoli, D. Gatteschi, A. Caneschi and M. A. Novak, *Nature*, 1993, **365**, 141–143.
6 N. Ishikawa, M. Sugita, T. Ishikawa, S.-Y. Koshihara and Y. Kaizu, *J. Am. Chem. Soc.*, 2003, **125**, 8694–8695.
7 D. N. Woodruff, R. E. P. Winpenny and R. A. Layfield, *Chem. Rev.*, 2013, 5110–5148.
8 J. D. Rinehart and J. R. Long, *Chem. Sci.*, 2011, **2**, 2078–2085.
9 R. Ruamps, L. J. Batchelor, R. Guillot, G. Zakhia, A.-L. Barra, W. Wernsdorfer, N. Guihéry and T. Mallah, *Chem. Sci.*, 2014, **5**, 3418.
10 R. Ruamps, R. Maurice, L. Batchelor, M. Boggio-Pasqua, R. Guillot, A.-L. Barra, J. Liu, E.-E. Bendeif, S. Pillet, S. Hill, T. Mallah and N. Guihéry, *J. Am. Chem. Soc.*, 2013, **135**, 3017–3026.
11 J. M. Zadrozny, D. J. Xiao, M. Atanasov, G. J. Long, F. Grandjean, F. Neese and J. R. Long, *Nat. Chem.*, 2013, **5**, 577–581.
12 J. M. Zadrozny, J. Liu, N. A. Piro, C. J. Chang, S. Hill and J. R. Long, *Chem. Commun.*, 2013, **48**, 3927.
13 D. Schweinfurth, M. G. Sommer, M. Atanasov, S. Demeshko, S. Hohloch, F. Meyer, F. Neese and B. Sarkar, *J. Am. Chem. Soc.*, 2015, **137**, 1993–2005.
14 F. E. Mabbs and D. Collison, *Electron paramagnetic resonance of d transition metal compounds*, Elsevier, 2013.
15 J. N. Rebilly, G. Charron, E. Rivière, R. Guillot, A. L. Barra, M. D. Serrano, J. van Slageren and T. Mallah, *Chem. – Eur. J.*, 2008, **14**, 1169–1177.
16 G. Fallani, R. Morassi and F. Zanobini, *Inorg. Chim. Acta*, 1975, **12**, 147–154.
17 K. S. Cole and R. H. Cole, *J. Chem. Phys.*, 1941, **9**, 341–351.
18 W. Wernsdorfer, *Supercond. Sci. Technol.*, 2009, **22**, 064013.
19 N. Ishikawa, *J. Phys. Chem. A*, 2003, **107**, 5831–5835.
20 R. Maurice, R. Bastardis, C. D. Graaf, N. Suaud, T. Mallah and N. Guihéry, *J. Chem. Theory Comput.*, 2009, **5**, 2977–2984.
21 F. Aquilante, L. De Vico, N. Ferré, G. Ghigo, P.-Å. Malmqvist, P. Neogrády, T. B. Pedersen, M. Pitoňàk, M. Reiher, B. Roos, L. Serrano-Andrés, M. Urban, V. Veryazov and R. Lindh, *J. Comput. Chem.*, 2010, **31**, 224–247.
22 B. O. Roos and P.-A. Malmqvist, *Phys. Chem. Chem. Phys.*, 2004, **6**, 2919–2927.
23 G. Karlstroem, R. Lindh, P.-A. Malmqvist, B. O. Roos, U. Ryde, V. Veryazov, P.-O. Widmark, M. Cossi, B. Schimmelpfennig, P. Neogrady and L. Seijo, *Comput. Mater. Sci.*, 2003, **28**, 222–239.
24 P. A. Malmqvist, B. O. Roos and B. Schimmelpfennig, *Chem. Phys. Lett.*, 2002, **357**, 230–240.
25 A. Abragam and B. Bleaney, *Electron paramagnetic resonance of transition ions*, Oxford University Press, 2012.

Inorganic Chemistry

Article

pubs.acs.org/IC

Structural Dependence of the Ising-type Magnetic Anisotropy and of the Relaxation Time in Mononuclear Trigonal Bipyramidal Co(II) Single Molecule Magnets

Feng Shao,[†] Benjamin Cahier,[†] Eric Rivière,[†] Régis Guillot,[†] Nathalie Guihéry,*[,‡] Victoria E. Campbell,*[,†] and Talal Mallah*[,†]

[†]Institut de Chimie Moléculaire et des Matériaux d'Orsay, CNRS, Université Paris Sud, Université Paris Saclay, 91405 Orsay Cedex, France

[‡]Laboratiore de Chimie et Physique Quantiques, Université Toulouse III, 118 route de Narbonne, 31062 Toulouse, France

Supporting Information

ABSTRACT: This paper describes the correlation between Ising-type magnetic anisotropy and structure in trigonal bipyramidal Co(II) complexes. Three sulfur-containing trigonal bipyramidal Co(II) complexes were synthesized and characterized. It was shown that we can engineer the magnitude of the Ising anisotropy using ligand field theory arguments in conjunction with structural parameters. To prepare this series of compounds, we used, on the one hand, a tetradentate ligand containing three sulfur atoms and one amine (NS_3^{tBu}) and on the other hand three different axial ligands, namely, Cl^-, Br^-, and NCS^-. The organic ligand imposes a trigonal bipyramidal arrangement with the three sulfur atoms lying in the trigonal plane with long Co−S bond distances. The magnetic properties of the compounds were measured, and ab initio calculations were used to analyze the anisotropy parameters and perform magneto-structural correlations. We demonstrate that a smaller axial zero-field splitting parameter leads to slower relaxation time when the symmetry is strictly axial, while the presence of very weak rhombicity decreases the energy barrier and speeds the relaxation of the magnetization.

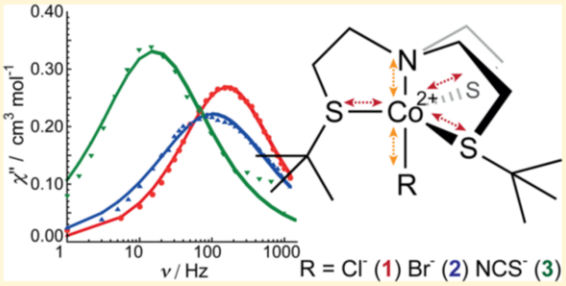

INTRODUCTION

Single molecule magnets (SMMs)[1−7] have been the focus of extensive research due to their potential as new materials for data storage and quantum computing.[8−10] SMMs exhibit a slow relaxation of their magnetization that yields a magnetic hysteresis (i.e., bistability) at low temperatures (liquid-helium range) even in the absence of an external magnetic field.[11] This bistability is due to the existence of a degenerate ground state with two components of different magnetizations ($+M_s$, $-M_s$) arising from the splitting of the M_s components of the ground spin state (S) by relativistic effects (mainly spin−orbit coupling). This property, which occurs in absence of an external magnetic field, is called zero-field splitting (ZFS). The magnitude and the nature (axial, rhombic, Ising, or planar) of the magnetic anisotropy account for the magnitude of the splitting, for the energetic ordering, and for the coupling (responsible for tunneling) of the M_s components. When the ground state has the largest M_s value, an easy axis of magnetization is present ($D < 0$), and when it has the lowest M_s value an easy plane of magnetization is present ($D > 0$). When D is negative, the energy difference between the largest and lowest M_s components (often referred to as an energy barrier) is proportional to the axial anisotropy parameter D, and the coupling between the components are proportional to the rhombic parameter E.

The first generation of SMMs were polynuclear transition metal clusters that possessed a large spin (S) ground state in addition to a large Ising-type anisotropy (D).[2,12] The classic example is the famous dodecametallic manganese-acetate family of SMMs ($Mn_{12}Ac$) that has $S = 10$ and energy barrier to the reorientation of their magnetization (U_{eff}) up to 74 K.[2,12] The efforts, however, toward increasing the total spin of these kinds of systems has yielded a decrease in the total anisotropy of the clusters.[13] For example, Brechin and Christou et al. reported a transition metal complex, which had a record barrier (U_{eff} = 86 K) but a $|D|$ parameter of 0.62 K.[14,15]

In the past decade, research efforts have focused on the synthesis of mononuclear SMMs with the idea that it is easier to control the structural requirements that lead to the anisotropy in these systems, and it is easier to manipulate these molecules in solution and on surfaces (a requirement for quantum information applications), even though some clusters (the Fe4 family) were perfectly stable in solution and successfully linked to surfaces.[16] Slow relaxation was observed

Received: August 15, 2016
Published: January 12, 2017

DOI: 10.1021/acs.inorgchem.6b01966
Inorg. Chem. 2017, 56, 1104−1111

in many single lanthanide ion complexes,[4,17−20] because they benefit from the large orbital angular momenta and large spin−orbit coupling of the f-block elements. The f orbitals, however, are deeply buried in the valence shell rendering the control of the symmetry of the molecules difficult to predict in most cases.[21] An alternative strategy is to construct mononuclear transition metal ion complexes that have the appropriate geometrical and chemical properties to display slow relaxation of the magnetization using the organic ligands to do so.[22,23] Among few mononuclear complexes based on transition metal ions,[24−32] which display slow relaxation of the magnetization notable examples, include a tetrahedral Co(II) complex,[24,32] trigonal bipyramidal Co(II) complexes,[26−28] and a linear Fe(II) complex.[25] A small opening of the magnetic hysteresis loop at zero direct-current field was first observed below 1 K,[26] and recently at 2 K,[33] for Co(II) complexes highlighting mononuclear transition metal ions as excellent SMMs.

Our group has previously studied trigonal bipyramidal symmetry around Co(II) and Ni(II) metal ions and showed that this geometry leads to Ising-type magnetic anisotropy (negative D values) that arises from the axial symmetry of the complexes imposed by the organic ligands.[26,28,34] When the organic ligand imposes a given geometry to the complex, it is possible to develop a strategy to design complexes with predictable geometries and in some cases symmetries. Such design allows analyzing the origin of the magnetic anisotropy (nature and magnitude) in a first step and in a second step preparing molecules where anisotropy can be predicted. The as-designed trigonal [Ni(Me$_6$tren)Cl](ClO$_4$) complex had an Ising-type anisotropy with a very large D value (close to −200 cm^{-1}),[34] and recently another Ni(II) trigonal complex was shown to possess even larger Ising-type anisotropy.[35] Replacing Ni(II) with Co(II) resulted in a complex that displayed slow relaxation of the magnetization and an opening of the hysteresis loop.[26] For the Co(II) complex, it was found that the ZFS parameter D changes when the Br$^-$ is replaced by Cl$^-$ (from −4.6 to −8.1 cm^{-1}, respectively). The differences in the magnitude of D were attributed to the σ/π effects of the ligands.[26] We could expand on these results and increase D by designing a molecule that has longer equatorial Co−L distances and shorter axial Co−L. By replacing the three nitrogen atoms of Me$_6$tren by sulfur atoms we considerably increased D to −23 cm^{-1}.[28]

The aim of this paper is to investigate structural and chemical effects on the magnitude of the magnetic anisotropy and the relaxation times in a series of three Co(II) compounds. We employed a sulfur-containing ligand (NS$_3^{tBu}$), which imposes a trigonal bipyramidal arrangement. We characterized their magnetic properties and analyzed two effects: (1) the influence of the Co−S bond distances and angles within each complex and among them and (2) the influence of the axial ligand (Cl$^-$, Br$^-$, or NCS$^-$ and amine).

RESULTS AND DISCUSSION

Synthesis. The ligand NS$_3^{tBu}$ was synthesized following a modified literature procedure.[36] The general synthesis of the complexes is as follows. To a solution of NS$_3^{tBu}$ (1 equiv) in 1-butanol the anhydrous Co(II) salt was added (1 equiv) to yield a microcrystalline solid. Air-stable X-ray quality single crystals were obtained by slow evaporation of diethyl ether into a saturated ethanol/acetone (1/1) solution of the complex. The complexes were characterized further by Fourier transform infrared (FT-IR) spectroscopy and electrospray ionization mass spectrometry (ESI-MS).

Structural Description. The structure of **2** was already reported.[37] We recorded a new set of data to have more accurate angles and bond distances necessary for calculations. As noted in Tables 1, S1, and S2, complexes **1** and **2** (Figures 1, S1, and S2) crystallized in the monoclinic space group $P2_1/c$, while complex **3** (Figures 1 and S3) crystallized in the cubic space group $P2_13$. The cation structure in all complexes is comprised of a central Co(II) ion surrounded by three sulfur atoms in the equatorial sites, a nitrogen, and a chloride (**1**), bromide (**2**), or NCS (**3**) ion in the axial sites. As expected, the ligand imposes a trigonal bipyramidal arrangement in the three complexes with pseudo C_3 molecular symmetry axis for **1** and **2**, while for **3**, the complex has a strict three-fold symmetry (C_{3v} point group) with equal equatorial Co−S bond distances, $\widehat{SCoS}$ angles, and perfectly linear N$_{axial}$−Co−NCS atoms. We use here, for all complexes, the C_{3v} point group notation for clarity even though the symmetry for the other complexes is lower. The bond distances for all compounds are reported in Table 1 and Table S1. Compound **2** has two crystallographically independent molecules in the asymmetric unit. The two molecules have almost the same average Co−S bond distances (2.410 and 2.412 Å), but the difference between the longest and shorter bond lengths is larger for one, noted **2a**, (0.005 Å) than for the other, noted **2b**, (0.05 Å; Tables 1 and S2). The Co−X bond distance ranges from 2.26 to ∼2.38 for X = Cl and Br, but it is much shorter when X is NCS (2.00 Å). The Co−

Table 1. Relevant Co(II)-Ligand Bond Distances and Angles and Anisotropy Parameters for Complexes 1, 2a, 2b, and 3

complex	1	2a	2b	3
space group	$P2_1/n$		$P2_1/c$	$P2_13$
d_{Co-X}[a]	2.264	2.383	2.361	2.000
d_{Co-S}[a]	2.404; 2.397; 2.389	2.412; 2.411; 2.407	2.435; 2.416; 2.385	2.380
d_{Co-S}(av)[a]	2.397	2.410	2.412	2.380
d_{Co-N}[a]	2.287	2.274	2.231	2.345
$\widehat{SCoS}$[b]	118.88	116.83	122.81	117.58
	118.6	114.07	122.28	117.58
	116.56	122.81	109.71	117.58
Δ	2.18	7.36	12.835	0
g	2.29		2.29	2.29
D_{exp}[c]	−21.4		−20.2	−11.0
D_{calc}[c]	−17.1	−18.0	−21.7	−13.8
D_{calc}(av)[c]		−19.8		
E_{calc}[c]	0.24	0.80	2.00	0.00

[a]In angstroms; (av) stands for average. [b]In degrees. [c]In inverse centimeters; (av) stands for average.

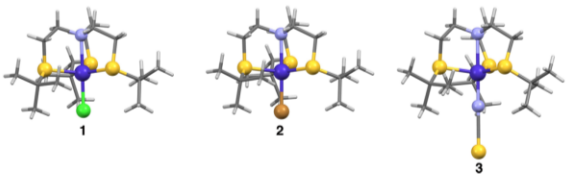

Figure 1. X-ray crystal structures of complexes **1**, **2**, and **3**: Co = purple; C = gray; N = lilac; S = yellow; Cl = green; Br = brown-orange; H = white; counterions were removed for clarity.

DOI: 10.1021/acs.inorgchem.6b01966
Inorg. Chem. 2017, 56, 1104−1111

N_{axial} bond distance is in the range of 2.287−2.345 Å and is the largest in **3**.

Magnetic Properties. *Direct-Current Magnetic Studies.* The $\chi_M T$ is constant between room temperature and 50 K with values close to 2.4 cm^3 K mol^{-1} for **1** and **2** and 2.7 cm^3 K mol^{-1} for **3** (Figures S4−S6). Below 40 K the $\chi_M T$ decreases indicating magnetic anisotropy (ZFS of the $M_s = \pm 1/2$ and $= \pm 3/2$ sublevels), which was further confirmed by the magnetization (M) versus B plots (Figure 2). The D and g parameters are reported in Table 1, and they were obtained by fitting the data using the spin Hamiltonian $H = \beta \mathbf{S}\cdot\mathbf{g}\cdot B + D[\mathbf{S}_z^2 - S(S+1)/3] + E(\mathbf{S}_x^2 - \mathbf{S}_y^2)$ for $S = 3/2$, where **g** is a tensor, **S** are the spin operators, B is the magnetic induction, and D and E are the axial and rhombic anisotropy parameters, respectively. To avoid overparameterization, the rhombic term E was not considered in the fit procedures. The fit of the $\chi_M T$ data gives a rough value of the axial parameter D (Figures S4−S6) and allows determining the g-values for the three compounds that were subsequently used to fit the field-dependent magnetization.

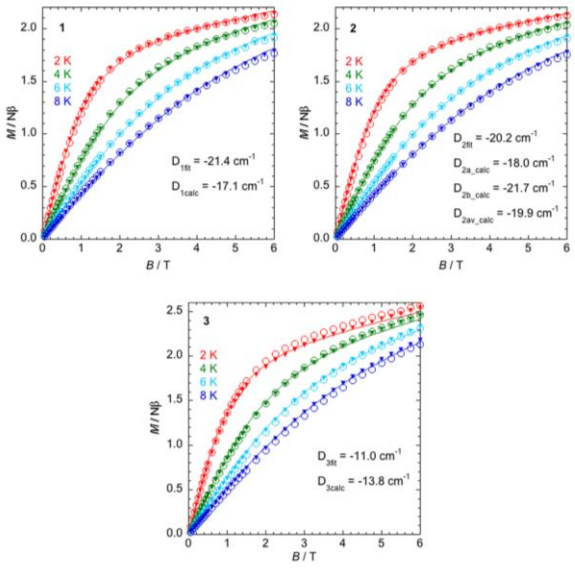

Figure 2. Field-dependent magnetization at variable temperatures; (○) experimental data; (—) theoretical fit with the best D and g parameters; (▼) average of the calculated magnetization considering D values from ab initio calculations for **1**−**3**.

It is important to stress here that because the Kramers nature of the levels ($S = 3/2$), the fit of the magnetization data is not unique, and a range of D and g values can give calculated data with reasonable agreement with experimental ones. The fit of the field-dependent magnetization data was performed by leaving free g_x ($= g_y$), g_z, and D (Table 1). It is worth noting that for **2**, where two crystallographically independent molecules are present, we calculated the magnetization for each independent molecule using the D parameters obtained from ab initio calculations (see below), made their average, and compared with the experimental data (Figure 2); the average calculated curves are in excellent agreement with the experimental data. It is possible to include the parameter E in the fit procedure, but very good agreement between calculated and experimental values can be obtained with a large range of E values. The main result is that complexes **1** and **2** have D values close to −20 cm^{-1}, and **3** has an axial anisotropy that is about half in magnitude ($D = -11$ cm^{-1}).

Alternating Current Magnetic Studies. To probe into the relaxation dynamics, we performed alternating current magnetic susceptibility measurements on microcrystalline samples of complexes **1**, **2**, and **3**. The compounds showed frequency dependence of the out-of-phase susceptibility (Figures S7−S9) and slow relaxation of their magnetization. The alternating current data in the form of Cole−Cole plots (Figures S10−S12) were fitted to the generalized Debye model that allowed to extract the relaxation times at different temperatures (τ) and their distribution (α; Table S3).[38] The comparison of the frequency-dependent out-of-phase signals at $T = 1.8$ K (Figure 3) for the three compounds shows that the relaxation time for **3** is 1 order of magnitude larger than for **1** and **2** (0.01 vs 0.001 s). The $\ln(\tau) = f(1/T_B)$ plots, where T_B is the blocking temperature for a given frequency, are depicted in Figure 4. For **1** there is no clear linear part showing that the relaxation in the 1.8−4 K temperature range has little contribution from an Orbach process and that other processes dominate such as the direct and the multiphonon Raman-like ones.[30,33,39] For **2**, the situation is similar, but it is possible to fit the high-temperature

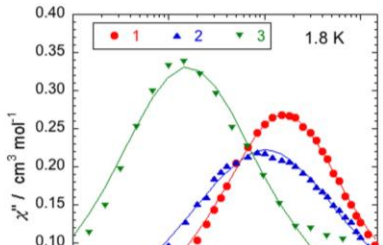

Figure 3. Experimental frequency dependence of χ'' at $T = 1.8$ with direct-current applied field = 3000, 3000, and 1600 Oe for **1** (red ●), **2** (blue ▲), and **3** (green ▼), respectively; experimental data and fit (—).

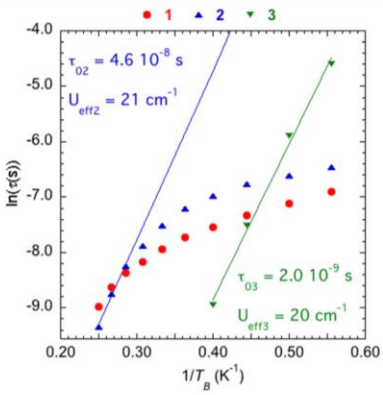

Figure 4. $\ln(\tau) = f(1/T_B)$ for **1** (red ●), **2** (blue ▲), and **3** (green ▼); experimental data and linear fit (—).

DOI: 10.1021/acs.inorgchem.6b01966
Inorg. Chem. 2017, 56, 1104−1111

data to the Arrhenius dependence of the relaxation time $\tau = \tau_0 + \exp(U_{eff}/kT)$, where U_{eff} is effective barrier to the reorientation of the magnetization and τ_0 the relaxation time at infinite temperature. For **3**, the fit of the data leads to $\tau_{02} = 2 \times 10^{-9}$ s and $U_{eff2} = 20$ cm^{-1} (Figure 4). The value of U_{eff} is the same for **2** and **3** (see Figure 4) despite the larger (in absolute value) D for the former than for the latter (−20.6 in comparison to −11.0). In addition, U_{eff} for **3** (20 cm^{-1}) is almost equal to 2|D| (22 cm^{-1}), while it is much weaker for **2** (21 cm^{-1} instead of 41.2) considering the same temperature range for the two compounds. It is important to note that since there are only few figures to fit the linear dependence of ln(τ), the extracted values of U_{eff} are only indicative. However, the difference between **3** and **2** has a physical meaning reflected in the difference of their relaxation time as seen in Figure 3.

Theoretical Calculations. Theoretical calculations were performed to rationalize the values of the ZFS parameters that were determined experimentally. As these parameters are very sensitive to the geometrical features, the theoretical study was performed using experimental geometries obtained from the X-ray crystal data. Ab initio calculations were done using the two-step Complete Active Space Self Consistent Field (CASSCF) method followed by the spin−orbit state-interaction (SO-SI)[40] method implemented in the MOLCAS code.[41] The averaged orbitals on 10 quadruplet states were optimized at the CAS(7,10)SCF level, and the wave functions used in the following analysis are the corresponding CASSCF ones. Calculations at the CASPT2 level were also performed.[42,43] However, as can be seen in the Supporting Information (Figure S13), even if the spectrum presents exactly the same features as the CASSCF spectrum and would therefore support the same analysis, the values of D (Table S4) were not improved in comparison to those obtained at the CASSCF level. All information regarding the calculations are given in Supporting Information. The method of extraction of the parameters from both the effective Hamiltonian theory[44,45] and the computed energies and wave functions has already been successfully used by our group for the determination of ZFS parameters.[46−53] The energy of the four first excited states that bring the most important contributions to the ZFS parameters are depicted in Figure 5. The values of D, for all complexes, and their average for the crystallographically different molecules of compound **2** are reported in Table 1, and they are in good agreement with the values obtained from the fit of the experimental data.

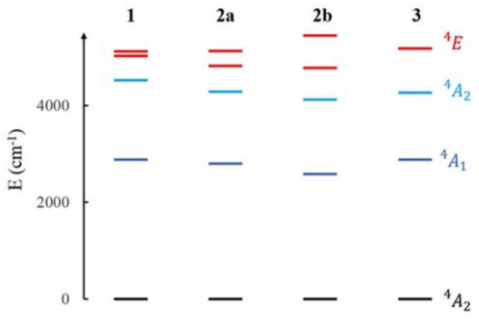

Figure 5. CAS(7,10)SCF energies of the lowest quadruplet states calculated for compounds **1**−**3**; **2a** and **2b** correspond to the two independent molecules of **2**.

Structure/Magnetism Correlation. Several effects are analyzed: (i) the influence of the Co−S bond distances and angles within each complex and among them, (ii) the influence of the axial ligand (Cl, Br, or NCS), and (iii) the angular distortions around the Co(II) ion. As from perturbative arguments, we know that |D| is inversely proportional to the energy difference between the ground and the excited states;[39,54−56] the energy of the various states is used to rationalize the nature and magnitude of the ZFS. Finally, as these energies can be related to those of the magnetic orbitals, magneto-structural correlations can be established from a ligand field analysis.

The main contribution to the anisotropy parameters is primarily due to the two quadruplet excited states, $^4A_1$ and ^4E (Figure 5). The first excited state $^4A_1$ is responsible for the negative value of D, while ^4E brings a positive but smaller contribution.[26,27] Please note that there is another excited quadruplet state ($^4A_2$ in light blue in Figure 5) just above the excited $^4A_1$ state but this state does not contribute to D. As complexes **1** and **2** do not have exactly a C_3 symmetry axis, the Co−S bond lengths and $\widehat{SCoS}$ angles are different—there is a nonzero rhombic parameter E, which is due to the lift of degeneracy of the ^4E state (Figure 5). One may notice that E increases with the splitting.

The energy difference between the ground state $^4A_2$ and the first excited state $^4A_1$ can be related to the energy difference noted $\delta\varepsilon_1$ in Figure 6, between the two lowest molecular

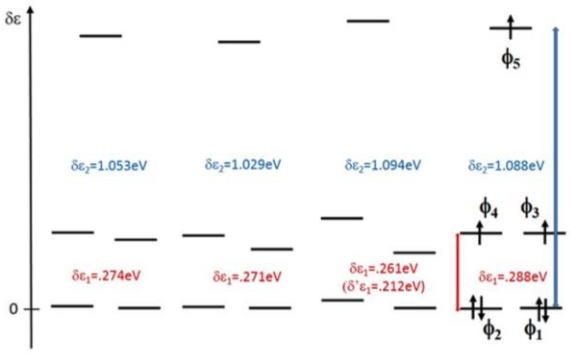

Figure 6. (left to right) Orbital CAS(7,10)SCF energy diagram calculated for complexes **1**, **2a**, **2b**, and **3** and mean energy differences between the two lowest orbitals and the two first ones ($\delta\varepsilon_1$) and between the two lowest ones and the highest one ($\delta\varepsilon_2$). $\delta'\varepsilon_1$ is the energy difference between the first and the third orbital.

orbitals (MOs) (ϕ_1 and ϕ_2) and the two first excited ones (ϕ_3 and ϕ_4), because the state $^4A_1$ is obtained from a single excitation involving these sets of orbitals. As shown in Table 2, these orbitals are linear combinations of (d_{XZ}, d_{YZ}) and ($d_{X^2-Y^2}$, d_{XY}) orbitals, with larger coefficients on the d_{XZ} and d_{YZ} orbitals in the lowest MOs and larger coefficients on the $d_{X^2-Y^2}$ and d_{XY} in the highest ones. The coefficients of the most important determinants of the first excited state wave function are listed in Table 3, showing that this state is strongly multideterminantal. As predicted by group theory (in C_{3v}), the selection rule $\Gamma_{A_2} \otimes \Gamma_{R_Z} \otimes \Gamma_{A_1} = \Gamma_{A_2} \otimes \Gamma_{A_2} \otimes \Gamma_{A_1} \supseteq \Gamma_1$ indicates that the $\hat{l}_Z\hat{s}_Z$ part of the spin−orbit operator couples the two states and that the contribution to D is negative, as ground and excited states have the same spin multiplicity.[53] The state ^4E is also strongly

DOI: 10.1021/acs.inorgchem.6b01966
Inorg. Chem. 2017, 56, 1104−1111

Table 2. Decomposition of the Magnetic CAS(7,10)SCF Orbitals on the 3d Atomic Orbitals of the Co(II)[a]

complexes	1		2a		2b		3	
AO	$d_{X^2-Y^2}$	d_{XZ}	$d_{X^2-Y^2}$	d_{XZ}	$d_{X^2-Y^2}$	d_{XZ}	$d_{X^2-Y^2}$	d_{XZ}
MO	d_{XY}	d_{YZ}	d_{XY}	d_{YZ}	d_{XY}	d_{YZ}	d_{XY}	d_{YZ}
ϕ_4	72%	28%	78%	22%	82%	18%	78%	22%
ϕ_3	72%	28%	66%	34%	52%	48%	78%	22%
ϕ_2	27%	73%	32%	68%	47%	53%	22%	78%
ϕ_1	28%	72%	24%	76%	19%	81%	22%	78%

[a]As we do not have access to the overlap matrix, the squared coefficients were renormalized by their sum and multiplied by 100 to reach 100% of contribution. The reader may see the computed coefficients in Table S5. ϕ_5 is mainly spread over d_{Z^2}.

Table 3. Weight of the Dominant Determinants in the First Excited CAS(7,10)SCF States in the Four Molecules

				
1	0.446	0.400	.072	.053
2a	0.467	0.303	0.115	.0780
2b	0.675	0.248	0.032	0.04
3	0.289	0.289	0.197	0.197

multideterminantal.[26,27] It results from excitations between the two previous sets of MOs ($\phi_1/\phi_2 \rightarrow \phi_3/\phi_4$) and between the lowest MOs and the fifth one ($\phi_1/\phi_2 \rightarrow \phi_5$ essentially d_{Z^2}) orbital. Its energy difference with the ground state can therefore also be related to the energy difference noted $\delta\varepsilon_2$ in Figure 6. The selection rule $\Gamma_E \otimes \Gamma_{R_xR_y} \otimes \Gamma_{A_1} = \Gamma_E \otimes \Gamma_E \otimes \Gamma_{A_1} \supseteq \Gamma_1$ here predicts that the $\hat{l}_+\hat{s}_- + \hat{l}_-\hat{s}_+$ part of the spin−orbit Hamiltonian now operates and that the contribution to D is positive. In summary, the $^4A_2 - {}^4A_1$ energy difference that brings a negative contribution to D is related to $\delta\varepsilon_1$, and the $^4A_2 - {}^4E$ energy difference that brings a positive contribution to D is related to $\delta\varepsilon_2$.

Let us start by analyzing the geometrical/chemical factors acting on the $\delta\varepsilon_1$ value (see Figure 6). Looking at the magnetic orbitals (the coefficients of these orbitals on the atomic ones are given in Table S5), one may see that there is an antibonding interaction between the sulfur orbitals and the Co ones mainly spread on $d_{X^2-Y^2}$ and d_{XY}. As a consequence, shorter Co−S bond lengths (see Table 1), that is, stroner equatorial σ-donating effects, induce larger $\delta\varepsilon_1$ value.[28,34] The Co−S distances decrease in the complexes ranging **2b**, **2a**, **1**, and **3**, as well as the D value in agreement with the increase of the $\delta\varepsilon_1$ value. As this contribution is the leading one, this argument rationalizes the D magnitude ordering in the four molecules.

One may note the singularity of the **2b** complex. Its first excited-state wave function has 0.675 weight (see Table 3) on a single determinant resulting from an excitation from ϕ_1 to ϕ_3. As the energy difference between these two orbitals is much smaller ($\delta\varepsilon'_1$ in Figure 6) than $\delta\varepsilon_1$ in the other molecules, the energy of the first excited state of **2b** is particularly low (see Figure 5). Further analyzing the physical content of the orbitals given in Table 2, one may see that the weight of the d_{XY} and $d_{X^2-Y^2}$ orbitals is much lower in orbital ϕ_3 in favor of d_{XZ} and d_{YZ} for that peculiar molecule. As the contribution of the former destabilizes this orbital, this effect is mainly responsible for the low energy of ϕ_3 and therefore for the small value of $\delta\varepsilon'_1$. An extra effort of rationalization requires to go back to the geometrical structure. As the closure of the $\widehat{NCoS}$ angles does not qualitatively vary between the complexes, this distortion cannot be invoked to rationalize the observed hybridization. On the contrary, looking at the $\widehat{SCoS}$ angles in the equatorial plane one may see that one of them is 109°79′, that is, much smaller than the two others (122°). As shown in Supporting Information on model calculations, this angular distortion is responsible for the qualitative change in the orbital hybridization and for the further decrease of $\delta\varepsilon'_1$.

Let us now consider the factors acting on the $\delta\varepsilon_2$ energy difference and, in particular, the axial ligand effect. Looking at the magnetic orbitals, one may see that all ϕ_5 orbitals (mainly d_{Z^2}) orbitals have components on the axial ligand orbitals. In the spectrochemical series, Br^- exerts a weaker ligand field than Cl^- itself exerting a weaker ligand field than $\underline{N}CS^-$. From this argument, one may rationalize the decrease of the $\delta\varepsilon_2$ energy difference in the three molecules ranging **3**, **1**, and **2a**. This effect is in favor of increasing positive contributions in complexes ranging **2**, **1**, and finally **3**. Despite this, as the positive contribution to D of the ^4E state is small (due to its high energy) this effect does not compensate the large negative contribution brought by the $^4A_1$ state, and the ordering of the D values is finally governed by the $\delta\varepsilon_1$ energy difference. Here again molecule **2b** shows a singularity: the $\delta\varepsilon_2$ value is particularly large, which is in favor of a smaller positive contribution to D. The analysis of the distances shows that this complex has smaller Co−N and Co−Br distances and therefore undergoes a stronger axial ligand field than the other molecules, which explains the larger $\delta\varepsilon_2$ value. These results are corroborated by the larger coefficients of the magnetic orbitals ϕ_5 on the 2s and $2p_Z$ orbitals of the nitrogen (see Table S5). Finally one may also note that orbitals ϕ_1 and ϕ_3 of **2b** have significant weights on $4p_x$ and $4p_y$ of Br^-; that is, the antibonding π-donor effect of Br^- in this molecule is stronger than in the others. In summary, in **2b** there is a synergistic effect between weaker equatorial σ-donating effects and angular distortions that decrease $\delta\varepsilon_1$ and larger axial σ-donating effects that increases $\delta\varepsilon_2$, both favoring a larger negative D value.

Concerning the rhombic parameter E, it decreases within the molecules ranging **2b**, **2a**, **1**, and **3**. This evolution can also be related to the variation of the $\widehat{SCoS}$ angles (see Table 1) that renders asymmetrical X and Y in the equatorial plane. One may see that in all complexes, two angles are similar, while one is different. The deviation between the mean value of the former and the latter, spotted by the parameter Δ, exactly follows the evolution of E. Looking at the orbitals decomposition, one may see that this distortion causes a larger contribution of the d_{XZ} in one orbital of the first set (d_{YZ} in the other) and concomitantly

DOI: 10.1021/acs.inorgchem.6b01966
Inorg. Chem. 2017, 56, 1104−1111

to a larger contribution of $d_{X^2-Y^2}$ in one orbital of the second set (d_{XY} in the other) as corroborated by the coefficients of these orbitals in the magnetic ones (Table S5). Of course the fact that E is equal to zero for **3** is due to its C_{3v} symmetry, in which X and Y are symmetrical.

CONCLUDING REMARKS

In conclusion we have shown the synthesis and characterization of three sulfur-containing trigonal bipyramidal Co(II) complexes. We show that it is possible to perform correlation between the geometrical structure of the complexes and the electronic structure of the ligands on the one hand and the magnitude of the magnetic anisotropy on the other hand. We demonstrate that, in the low-temperature range, the relaxation time of the complex with the weaker Ising type anisotropy is the slowest and that its energy barrier corresponds to what is expected if all other relaxation effects are absent. For the compounds with the weaker Ising type anisotropy parameters the relaxation is much faster. The main reason behind the "better" properties of complex **3** is the absence of the rhombic term due to the C_{3v} symmetry point group that prevents tunneling between the low-lying $\pm 3/2$ sublevels, while the ground levels of the other complexes are made from mixtures of the $\pm 3/2$ and $\pm 1/2$ wave functions allowing a pathway for quantum tunneling. Therefore, to design Co(II) complexes with slow relaxation times and large barrier to the reorientation of the magnetization one needs not only to perform large Ising type anisotropy, but the rhombic term must be strictly equal to zero. For large axial anisotropy parameters to be obtained, the D_{2d} symmetry seems to be efficient as recently demonstrated,[33] but one must succeed to avoid small distortions that deviate from the strict symmetry, which is still a challenge.

ASSOCIATED CONTENT

Supporting Information

The Supporting Information is available free of charge on the ACS Publications website at DOI: 10.1021/acs.inorgchem.6b01966.

Crystallographic data (CCDC reference numbers 1448438, 1448439, and 1448440), magnetic data, and theoretical calculations (PDF)

X-ray crystallographic information (CIF)

X-ray crystallographic information (CIF)

X-ray crystallographic information (CIF)

AUTHOR INFORMATION

Corresponding Authors

*E-mail: nathalie.guihery@irsamc.ups-tlse.fr. (N.G.)
*E-mail: victoria.campbell@u-psud.fr. (V.E.C.)
*E-mail: talal.mallah@u-psud.fr. (T.M.)

ORCID

Victoria E. Campbell: 0000-0002-6469-5759

Author Contributions

The manuscript was written through contributions of all authors. All authors have given approval to the final version of the manuscript.

Notes

The authors declare no competing financial interest.

ACKNOWLEDGMENTS

This work is partially financed by ANR-project MolQuSpin 13-BS10-0001-03. This work is supported by a public grant overseen by the French National Research Agency (ANR) as part of the "Investissements d'Avenir" program "Labex NanoSaclay" (Reference: ANR-10-LABX-0035). We thank the collaborative program between the China Scholarship Council and Université Paris-Sud (No. 201306310014), UPS, Région Ile de France SESAME program 2012 No. 12018501 and CNRS. T.M. thanks the Institut Universitaire de France for financial support.

REFERENCES

(1) Caneschi, A.; Gatteschi, D.; Sessoli, R.; Barra, A. L.; Brunel, L. C.; Guillot, M. Alternating-Current Susceptibility, High-Field Magnetization, and Millimeter Band Epr Evidence for a Ground S = 10 State in [Mn12o12(Ch3coo)16(H2o)4].2ch3cooh.4h2o. *J. Am. Chem. Soc.* **1991**, *113*, 5873−5874.

(2) Sessoli, R.; Gatteschi, D.; Caneschi, A.; Novak, M. A. Magnetic bistability in a metal-ion cluster. *Nature* **1993**, *365*, 141−143.

(3) Gatteschi, D.; Sessoli, R. Quantum tunneling of magnetization and related phenomena in molecular materials. *Angew. Chem., Int. Ed.* **2003**, *42*, 268−297.

(4) Ishikawa, N.; Sugita, M.; Ishikawa, T.; Koshihara, S.-y.; Kaizu, Y. Lanthanide Double-Decker Complexes Functioning as Magnets at the Single-Molecular Level. *J. Am. Chem. Soc.* **2003**, *125*, 8694−8695.

(5) Rebilly, J. N.; Mallah, T. Synthesis of single-molecule magnets using metallocyanates. *Single-Molecule Magnets and Related Phenomena* **2006**, *122*, 103−131.

(6) Cornia, A.; Fabretti, A. C.; Garrisi, P.; Mortalo, C.; Bonacchi, D.; Gatteschi, D.; Sessoli, R.; Sorace, L.; Wernsdorfer, W.; Barra, A. L. Energy-barrier enhancement by ligand substitution in tetrairon(III) single-molecule magnets. *Angew. Chem., Int. Ed.* **2004**, *43*, 1136−1139.

(7) Moragues-Canovas, M.; Riviere, P.; Ricard, L.; Paulsen, C.; Wernsdorfer, W.; Rajaraman, G.; Brechin, E. K.; Mallah, T. Resonant quantum tunneling in a new tetranuclear iron(III)-based single-molecule magnet. *Adv. Mater.* **2004**, *16*, 1101.

(8) Urdampilleta, M.; Klyatskaya, S.; Cleuziou, J.-P.; Ruben, M.; Wernsdorfer, W. Supramolecular spin valves. *Nat. Mater.* **2011**, *10*, 502−506.

(9) Vincent, R.; Klyatskaya, S.; Ruben, M.; Wernsdorfer, W.; Balestro, F. Electronic read-out of a single nuclear spin using a molecular spin transistor. *Nature* **2012**, *488*, 357−360.

(10) Thiele, S.; Balestro, F.; Ballou, R.; Klyatskaya, S.; Ruben, M.; Wernsdorfer, W. Electrically driven nuclear spin resonance in single-molecule magnets. *Science* **2014**, *344*, 1135−1138.

(11) Gatteschi, D.; Sessoli, R.; Villain, J. *Molecular Nanomagnets;* Oxford University Press, 2006.

(12) Sessoli, R.; Tsai, H. L.; Schake, A. R.; Wang, S.; Vincent, J. B.; Folting, K.; Gatteschi, D.; Christou, G.; Hendrickson, D. N. High-spin molecules:[Mn12O12 (O2CR) 16 (H2O) 4]. *J. Am. Chem. Soc.* **1993**, *115*, 1804−1816.

(13) Neese, F.; Solomon, E. I. Calculation of zero-field splittings, g-values, and the relativistic nephelauxetic effect in transition metal complexes. Application to high-spin ferric complexes. *Inorg. Chem.* **1998**, *37*, 6568−6582.

(14) Chakov, N. E.; Lee, S.-C.; Harter, A. G.; Kuhns, P. L.; Reyes, A. P.; Hill, S. O.; Dalal, N. S.; Wernsdorfer, W.; Abboud, K. A.; Christou, G. The Properties of the [Mn 12O 12(O 2CR) 16(H 2O) 4] Single-Molecule Magnets in Truly Axial Symmetry: [Mn 12O 12(O 2CCH 2Br) 16(H 2O) 4]·4CH 2Cl 2. *J. Am. Chem. Soc.* **2006**, *128*, 6975−6989.

(15) Milios, C. J.; Vinslava, A.; Wernsdorfer, W.; Moggach, S.; Parsons, S.; Perlepes, S. P.; Christou, G.; Brechin, E. K. A Record Anisotropy Barrier for a Single-Molecule Magnet. *J. Am. Chem. Soc.* **2007**, *129*, 2754−2755.

DOI: 10.1021/acs.inorgchem.6b01966
Inorg. Chem. 2017, 56, 1104−1111

(16) Mannini, M.; Pineider, F.; Danieli, C.; Totti, F.; Sorace, L.; Sainctavit, P.; Arrio, M. A.; Otero, E.; Joly, L.; Cezar, J. C.; Cornia, A.; Sessoli, R. Quantum tunnelling of the magnetization in a monolayer of oriented single-molecule magnets. *Nature* **2010**, *468*, 417−421.
(17) Rinehart, J. D.; Long, J. R. Exploiting single-ion anisotropy in the design of f-element single-molecule magnets. *Chem. Sci.* **2011**, *2*, 2078−2085.
(18) Woodruff, D. N.; Winpenny, R. E. P.; Layfield, R. A. Lanthanide Single-Molecule Magnets. *Chem. Rev.* **2013**, *113*, 5110−5148.
(19) Campbell, V. E.; Guillot, R.; Rivière, E.; Brun, P.-T.; Wernsdorfer, W.; Mallah, T. Subcomponent Self-Assembly of Rare-Earth Single-Molecule Magnets. *Inorg. Chem.* **2013**, *52*, 5194−5200.
(20) AlDamen, M. A.; Clemente-Juan, J. M.; Coronado, E.; Martí-Gastaldo, C.; Gaita-Ariño, A. Mononuclear Lanthanide Single-Molecule Magnets Based on Polyoxometalates. *J. Am. Chem. Soc.* **2008**, *130*, 8874−8875.
(21) Car, P.-E.; Perfetti, M.; Mannini, M.; Favre, A.; Caneschi, A.; Sessoli, R. Giant field dependence of the low temperature relaxation of the magnetization in a dysprosium(iii)−DOTA complex. *Chem. Commun.* **2011**, *47*, 3751−3753.
(22) Gomez-Coca, S.; Cremades, E.; Aliaga-Alcalde, N.; Ruiz, E. Mononuclear Single-Molecule Magnets: Tailoring the Magnetic Anisotropy of First-Row Transition-Metal Complexes. *J. Am. Chem. Soc.* **2013**, *135*, 7010−7018.
(23) Craig, G. A.; Murrie, M. 3d single-ion magnets. *Chem. Soc. Rev.* **2015**, *44*, 2135−2147.
(24) Zadrozny, J. M.; Liu, J.; Piro, N. A.; Chang, C. J.; Hill, S.; Long, J. R. Slow magnetic relaxation in a pseudotetrahedral cobalt(ii) complex with easy-plane anisotropy. *Chem. Commun.* **2012**, *48*, 3927.
(25) Zadrozny, J. M.; Xiao, D. J.; Atanasov, M.; Long, G. J.; Grandjean, F.; Neese, F.; Long, J. R. Magnetic blocking in a linear iron(I) complex. *Nat. Chem.* **2013**, *5*, 577−581.
(26) Ruamps, R.; Batchelor, L. J.; Guillot, R.; Zakhia, G.; Barra, A.-L.; Wernsdorfer, W.; Guihéry, N.; Mallah, T. Ising-type magnetic anisotropy and single molecule magnet behaviour in mononuclear trigonal bipyramidal Co(ii) complexes. *Chem. Sci.* **2014**, *5*, 3418.
(27) Schweinfurth, D.; Sommer, M. G.; Atanasov, M.; Demeshko, S.; Hohloch, S.; Meyer, F.; Neese, F.; Sarkar, B. The Ligand Field of the Azido Ligand: Insights into Bonding Parameters and Magnetic Anisotropy in a Co(II)−Azido Complex. *J. Am. Chem. Soc.* **2015**, *137*, 1993.
(28) Shao, F.; Cahier, B.; Guihéry, N.; Rivière, E.; Guillot, R.; Barra, A.-L.; Lan, Y.; Wernsdorfer, W.; Campbell, V. E.; Mallah, T. Tuning the Ising-type anisotropy in trigonal bipyramidal Co (ii) complexes. *Chem. Commun.* **2015**, *51*, 16475−16478.
(29) Brazzolotto, D.; Gennari, M.; Yu, S.; Pécaut, J.; Rouzières, M.; Clérac, R.; Orio, M.; Duboc, C. An Experimental and Theoretical Investigation on Pentacoordinated Cobalt(III) Complexes with an Intermediate S = 1 Spin State: How Halide Ligands Affect their Magnetic Anisotropy. *Chem. - Eur. J.* **2016**, *22*, 925−933.
(30) Novikov, V. V.; Pavlov, A. A.; Nelyubina, Y. V.; Boulon, M.-E.; Varzatskii, O. A.; Voloshin, Y. Z.; Winpenny, R. E. A trigonal prismatic mononuclear cobalt (II) complex showing single-molecule magnet behavior. *J. Am. Chem. Soc.* **2015**, *137*, 9792−9795.
(31) Díaz-Torres, R.; Menelaou, M.; Roubeau, O.; Sorrenti, A.; Brandariz-de-Pedro, G.; Sañudo, E. C.; Teat, S. J.; Fraxedas, J.; Ruíz, E.; Aliaga-Alcalde, N. Multiscale study of mononuclear Co IISMMs based on curcuminoid ligands. *Chem. Sci.* **2016**, *7*, 2793.
(32) Vaidya, S.; Upadhyay, A.; Singh, S. K.; Gupta, T.; Tewary, S.; Langley, S. K.; Walsh, J. P. S.; Murray, K. S.; Rajaraman, G.; Shanmugam, M. A synthetic strategy for switching the single ion anisotropy in tetrahedral Co(II) complexes. *Chem. Commun.* **2015**, *51*, 3739−3742.
(33) Rechkemmer, Y.; Breitgoff, F. D.; van der Meer, M.; Atanasov, M.; Hakl, M.; Orlita, M.; Neugebauer, P.; Neese, F.; Sarkar, B.; van Slageren, J. A four-coordinate cobalt(II) single-ion magnet with coercivity and a very high energy barrier. *Nat. Commun.* **2016**, 7.1046710.1038/ncomms10467
(34) Ruamps, R.; Maurice, R.; Batchelor, L.; Boggio-Pasqua, M.; Guillot, R.; Barra, A.-L.; Liu, J.; Bendeif, E.-E.; Pillet, S.; Hill, S.; Mallah, T.; Guihéry, N. Giant Ising-Type Magnetic Anisotropy in Trigonal Bipyramidal Ni(II) Complexes: Experiment and Theory. *J. Am. Chem. Soc.* **2013**, *135*, 3017−3026.
(35) Marriott, K. E. R.; Bhaskaran, L.; Wilson, C.; Medarde, M.; Ochsenbein, S. T.; Hill, S.; Murrie, M. Pushing the limits of magnetic anisotropy in trigonal bipyramidal Ni(II). *Chem. Sci.* **2015**, *6*, 6823−6828.
(36) Morassi, R.; Sacconi, L. *Inorg. Synth.* **1976**, *16*, 174−175.
(37) Fallani, G.; Morassi, R.; Zanobini, F. Cobalt(Ii) and Nickel(Ii) Complexes with Nitrogen-Sulfur Tripod Ligands - Crystal and Molecular-Structure of 5-Coordinate Complex Bromotris(2-Tert-Butylthioethyl)Aminecobalt(Ii) Hexafluorophosphate(Ns3br Donor Set). *Inorg. Chim. Acta* **1975**, *12*, 147−154.
(38) Cole, K. S.; Cole, R. H. Dispersion and Absorption in Dielectrics I. Alternating Current Characteristics. *J. Chem. Phys.* **1941**, *9*, 341−351.
(39) Abragam, A.; Bleaney, B. *Electron Paramagnetic Resonance of Transition Ions;* OUP: Oxford, 2012.
(40) Malmqvist, P. A.; Roos, B. O. The Casscf State Interaction Method. *Chem. Phys. Lett.* **1989**, *155*, 189−194.
(41) Aquilante, F.; Autschbach, J.; Carlson, R. K.; Chibotaru, L. F.; Delcey, M. G.; De Vico, L.; Fdez. Galvan, I.; Ferre, N.; Frutos, L. M.; Gagliardi, L.; Garavelli, M.; Giussani, A.; Hoyer, C. E.; Li Manni, G.; Lischka, H.; Ma, D. X.; Malmqvist, P. A.; Muller, T.; Nenov, A.; Olivucci, M.; Pedersen, T. B.; Peng, D. L.; Plasser, F.; Pritchard, B.; Reiher, M.; Rivalta, I.; Schapiro, I.; Segarra-Marti, J.; Stenrup, M.; Truhlar, D. G.; Ungur, L.; Valentini, A.; Vancoillie, S.; Veryazov, V.; Vysotskiy, V. P.; Weingart, O.; Zapata, F.; Lindh, R. Molcas 8: New capabilities for multiconfigurational quantum chemical calculations across the periodic table. *J. Comput. Chem.* **2016**, *37*, 506−541.
(42) Andersson, K.; Malmqvist, P. A.; Roos, B. O. 2nd-Order Perturbation-Theory with a Complete Active Space Self-Consistent Field Reference Function. *J. Chem. Phys.* **1992**, *96*, 1218−1226.
(43) Andersson, K.; Malmqvist, P. A.; Roos, B. O.; Sadlej, A. J.; Wolinski, K. 2nd-Order Perturbation-Theory with a Casscf Reference Function. *J. Phys. Chem.* **1990**, *94*, 5483−5488.
(44) Bloch, C. Sur la théorie des perturbations des états liés. *Nucl. Phys.* **1958**, *6*, 329−347.
(45) des Cloizeaux, J. Extension d'une formule de Lagrange à des problèmes de valeurs propres. *Nucl. Phys.* **1960**, *20*, 321−346.
(46) Maurice, R.; Bastardis, R.; Graaf, C. d.; Suaud, N.; Mallah, T.; Guihéry, N. Universal Theoretical Approach to Extract Anisotropic Spin Hamiltonians. *J. Chem. Theory Comput.* **2009**, *5*, 2977−2984.
(47) Maurice, R.; de Graaf, C.; Guihéry, N. Magnetic anisotropy in binuclear complexes in the weak-exchange limit: From the multispin to the giant-spin Hamiltonian. *Phys. Rev. B: Condens. Matter Mater. Phys.* **2010**, *81*.10.1103/PhysRevB.81.214427
(48) Maurice, R.; Guihery, N.; Bastardis, R.; Graaf, C. Rigorous Extraction of the Anisotropic Multispin Hamiltonian in Bimetallic Complexes from the Exact Electronic Hamiltonian. *J. Chem. Theory Comput.* **2010**, *6*, 55−65.
(49) Maurice, R.; Sivalingam, K.; Ganyushin, D.; Guihery, N.; de Graaf, C.; Neese, F. Theoretical determination of the zero-field splitting in copper acetate monohydrate. *Inorg. Chem.* **2011**, *50*, 6229−6236.
(50) Ruamps, R.; Batchelor, L. J.; Maurice, R.; Gogoi, N.; Jimenez-Lozano, P.; Guihery, N.; de Graaf, C.; Barra, A. L.; Sutter, J. P.; Mallah, T. Origin of the Magnetic Anisotropy in Heptacoordinate Ni-II and Co-II Complexes. *Chem. - Eur. J.* **2013**, *19*, 950−956.
(51) Ruamps, R.; Maurice, R.; Batchelor, L.; Boggio-Pasqua, M.; Guillot, R.; Barra, A. L.; Liu, J.; Bendeif, E.; Pillet, S.; Hill, S.; Mallah, T.; Guihery, N. Giant Ising-type magnetic anisotropy in trigonal bipyramidal Ni(II) complexes: experiment and theory. *J. Am. Chem. Soc.* **2013**, *135*, 3017−3026.
(52) Shao, F.; Cahier, B.; Guihery, N.; Riviere, E.; Guillot, R.; Barra, A. L.; Lan, Y.; Wernsdorfer, W.; Campbell, V. E.; Mallah, T. Tuning

DOI: 10.1021/acs.inorgchem.6b01966
Inorg. Chem. 2017, 56, 1104−1111

the Ising-type anisotropy in trigonal bipyramidal Co(ii) complexes. *Chem. Commun. (Cambridge, U. K.)* **2015**, *51*, 16475−16478.
(53) Cahier, B.; Maurice, R.; Bolvin, H.; Mallah, T.; Guihéry, N. Tools for Predicting the Nature and Magnitude of Magnetic Anisotropy in Transition Metal Complexes: Application to Co(II) Complexes. *Magnetochemistry* **2016**, *2*, 31.
(54) Mabbs, F. E.; Collison, D. *Electron paramagnetic resonance of d transition metal compounds;* Elsevier, 2013.
(55) Rebilly, J. N.; Charron, G.; Rivière, E.; Guillot, R.; Barra, A. L.; Serrano, M. D.; van Slageren, J.; Mallah, T. Large magnetic anisotropy in pentacoordinate NiII complexes. *Chem. - Eur. J.* **2008**, *14*, 1169−1177.
(56) Pryce, M. H. L. A Modified Perturbation Procedure for a Problem in Paramagnetism. *Proc. Phys. Soc., London, Sect. A* **1950**, *63*, 25.

DOI: 10.1021/acs.inorgchem.6b01966
Inorg. Chem. 2017, 56, 1104−1111

Inorganic Chemistry

Article

pubs.acs.org/IC

Design and Magnetic Properties of a Mononuclear Co(II) Single Molecule Magnet and Its Antiferromagnetically Coupled Binuclear Derivative

Fatima El-Khatib,[†,‡] Benjamin Cahier,[†] Feng Shao,[†] Maurici López-Jordà,[†] Régis Guillot,[†] Eric Rivière,[†] Hala Hafez,[‡] Zeinab Saad,[‡] Jean-Jacques Girerd,[†] Nathalie Guihéry,[*,§] and Talal Mallah[*,†]

[†]Institut de Chimie Moléculaire et des Matériaux d'Orsay, CNRS, Université Paris Sud, Université Paris Saclay, 91405 Orsay Cedex, France

[‡]Lebanese University, Inorganic & Environmental Chemistry Laboratory (IECL), Faculty of Sciences I, Hadath, Lebanese University, Beirut, Lebanon

[§]Laboratoire de Chimie et Physique Quantiques, Université Toulouse III, 118 route de Narbonne, 31062 Toulouse, France

Supporting Information

ABSTRACT: The preparations of related mononuclear and binuclear Co(II) complexes with a quasi-identical local C_{3v} symmetry using a cryptand organic ligand are reported. The mononuclear complex behaves as a single molecule magnet (SMM). A relatively weak antiferromagnetic exchange coupling (J) of the same order of magnitude as the local magnetic anisotropy (D) is determined experimentally and theoretically for the binuclear complex. The weak magnitude of the antiferromagnetic exchange coupling, analyzed using a combination of broken-symmetry density functional theory and wave function based calculations, is ascribed to the weak overlap between the singly occupied orbitals because of the local C_{3v} symmetry of the Co(II) ions; the organic ligand was found to contribute to the exchange coupling as the azido bridge that directly links the Co(II) ions. Calculation of the energy and wave functions of the spin states for the binuclear complex, in the general case, allows analysis of the effect of the $|J/D|$ ratio on the magnetic behavior of the binuclear complex and prediction of the optimum range of values for the complex to behave as two weakly interacting SMMs.

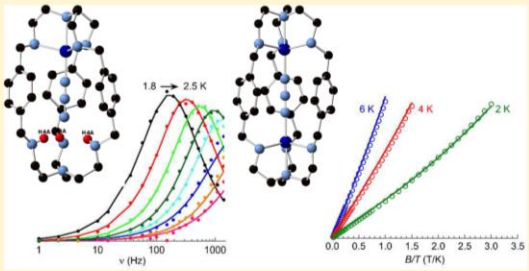

INTRODUCTION

Single molecule magnets (SMMs) are molecules that possess a slow relaxation of the magnetization below a blocking temperature T_B creating magnetic bistability associated with the individual species.[1−3] SMMs were, thus, proposed as quantum bits (q-bits) for quantum information processing.[4−6] Historically, SMMs were transition metal containing polynuclear complexes possessing a high spin ground state associated with magnetic anisotropy leading to an energy barrier to the reorientation to their magnetization. Extensive studies on these systems allowed researchers to get deep insight into their magnetic properties and behavior but revealed the difficulty in controlling their magnetic anisotropy and particularly in designing species made from two (or more) SMM molecules with the perspective of building quantum logical gates necessary for quantum information processing.[7] The presence of a weak antiferromagnetic coupling between two SMMs leads to an entangled state in a double q-bit system,[8] which is one of the several requirements for building quantum logical gates. Such difficulties are due to the polynuclear nature of the molecules: (i) magnetic anisotropy is difficult to predict; (ii) the energy barrier cannot be easily enhanced; and (iii) stability in solution is weak precluding the design of double q-bits. Mononuclear complexes based on transition metal ions have emerged during the past few years as possible substitutes to polynuclear SMM species.[9−12] The advantage of mononuclear complexes is their excellent stability in solution allowing the preparation of binuclear ones with controlled anisotropy and more importantly controlled antiferromagnetic exchange coupling. In addition, despite their low spin value, their magnetic anisotropy can be chemically designed.[9,13−15]

We report, here, the preparation of a mononuclear Co(II) complex **1** that possesses a slow relaxation of its magnetization and its binuclear derivative **2** using the bis chelating cryptand-like organic ligand 6,16,2,5-tribenzena(1,4)-1,4,8,11,14,18,23,27-octaazabicyclo[9.9.9]nonacosaphane noted L (Figure 1).

The cryptand ligand was chosen because it has two coordination sites able to accommodate Co(II) ions in a trigonal bipyramidal geometry known to induce an Ising type single ion anisotropy as in the case of the related [Co(Me$_6$tren)Cl]$^+$ complex,[11] thus ensuring the presence of two

Received: January 30, 2017
Published: April 4, 2017

DOI: 10.1021/acs.inorgchem.7b00205
Inorg. Chem. 2017, 56, 4601−4608

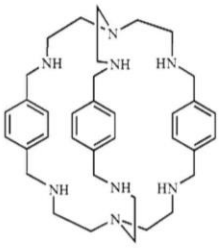

Figure 1. Schematic view of the cryptand ligand L.

Ising type Co(II) ions in the binuclear complex that may experience antiferromagnetic exchange coupling via a bridge. In order to ensure a weak exchange coupling, the azido ligand was used as a bridge because it imposes a large distance between the two metal ions. This type of cryptand ligand and the related binuclear Co(II) complexes are known in the literature, and a recent paper by Murugesu and co-workers reported similar binuclear Co(II) ones.[16−19] However, the experimental determination of the local magnetic anisotropy of the Co(II) ions belonging to the binuclear species on one hand and the preparation of a mononuclear Co(II) complex, on the other hand, with the same ligand that behave as an SMM were not reported.

■ RESULTS AND DISCUSSION

Synthesis. The synthesis of the cryptand-like ligand L in the following was carried out using the procedures reported in the literature.[18,20] The mononuclear complex **1** of formula $[Co(N_3)LH_3]Cl_4$ was obtained by a two-step procedure. First, the cryptand ligand L was protonated in solution by adding 3 molar equiv of a strong acid, and then the Co(II) and the azido salts were added (see Supporting Information). The binuclear complex $[Co(N_3)CoL]Cl_3$ was prepared by modifying a procedure reported in the literature.[17,19] Air-stable X-ray quality single crystals were obtained by diffusing the mother solutions of the complexes in ethyl acetate. The complexes were characterized by infrared spectroscopy, elemental analysis, and ESI-MS that show the presence of the molecular species in solution (see Supporting Information). The preparation of the mononuclear complex **1** using a simple procedure, reacting 1 molar equiv of L and the Co(II) salt, systematically leads to the formation of a mixture containing the targeted mononuclear complex but also the binuclear species. This was easily detected by infrared spectroscopy from the asymmetric elongation vibration of azido in the 2200 cm^{-1} region that is shifted toward high frequency in the binuclear complex (see Supporting Information). Furthermore, the preparation of heterobinuclear species containing Co(II) and the diamagnetic Zn(II) ions leads to a statistical mixture of the three compounds, namely, Co_2, CoZn, and Zn_2, precluding the formation of a compound containing exclusively the $[Co(N_3)ZnL]^{3+}$ species. To circumvent this problem, we reasoned that the protonation of the ligand may block one of the coordination sites and allow the formation of a mononuclear complex. The addition of 3 molar equiv of HCl to a solution containing 1 molar equiv of L leads to the formation of different species in solution with the amine coordination sites partially protonated. The subsequent addition of 1 molar equiv of the Co(II) salt leads to the coordination of Co(II) in only one of the coordination sites, while the other coordination site is automatically fully protonated. The mass spectrometry study shows that the mononuclear complex is almost the only species present in solution (see Supporting Information). This tentative mechanism is based on the reasonable assumption of the larger stability of Co(II) in a coordination site as compared to that of one or two protons.

Structural Description. Compound **1** crystallizes in the cubic system with the $P2_13$ space group (Table S1). Within the mononuclear cationic species $[Co(N_3)LH_3]^{4+}$ (Figure 2), the

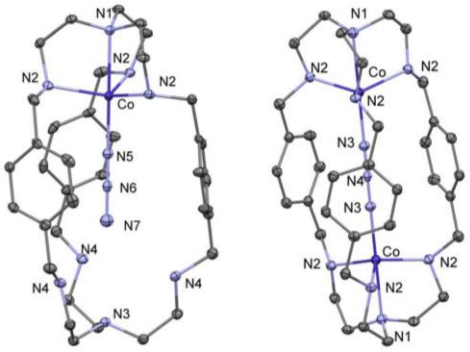

Figure 2. ORTEP drawing of the mononuclear and binuclear complexes $[Co(N_3)LH_3]^{4+}$ (left) and $[Co(N_3)CoL]^{3+}$ (right) of **1** and **2**, respectively. Thermal ellipsoids are shown at the 30% level; hydrogen atoms are omitted for clarity.

Co(II) ion is pentacoordinated with a trigonal bipyramidal (tbp) geometry and a strict C_3 symmetry (C_{3v} if one considers only the first coordination sphere) as in the parent $[Co(Me_6tren)Cl]^{2+}$ species we recently reported.[11] Compound **2** crystallizes in the trigonal system with the *R*32 space group. The binuclear cationic species $[Co(N_3)CoL]^{3+}$ (Figure 2) contains the two Co(II) ions in a tbp geometry with C_3 symmetry as for the mononuclear one. The Co atoms are displaced by 42.7 pm from the plane defined by the three equatorial nitrogen atoms. The angles and bond distances around the metal ions for the two complexes are almost identical; the only difference is for the Co−N distances in the equatorial plane of the tbp that are slightly longer for **1** than for **2** (Table 1).

Table 1. Angles and Bond Distances in the Coordination Sphere of the Metal Ions for 1 and 2

complex	Co−N_{ap} [a]	Co−$N(N_3)$	Co−N_{eq}	$N_{ap}CoN_{eq}$	$N_{ap}CoN_{ap}$
1	229.0	202.4	216.5	79.23	116.59
2	228.8	204.8	213.0	78.44	116.08

[a]Bond distances are in pm, and angles are in deg.

Magnetic Properties. *Direct Current Magnetic Studies.* For **1**, $\chi_M T$ is constant between room temperature and 30 K (2.5 cm^3 mol^{-1} K) and then drops to a value of 1.4 cm^3 mol^{-1} K at T = 2 K. For **2**, $\chi_M T$ is equal to 4.8 cm^3 mol^{-1} K corresponding to two isolated Co(II) ions ($S = {}^3/_2$ and g_{av} close to 2.3). Upon cooling, it slightly decreases to reach a value of 3.8 at T = 60 K and then drops more abruptly to 0.1 cm^3 mol^{-1} K at T = 2 K. The difference in behavior between the two complexes (Figure 3) can be qualitatively ascribed to the presence of magnetic anisotropy (zero-field splitting, ZFS, of $S = {}^3/_2$ leading to $m_s = \pm{}^3/_2$ and $\pm{}^1/_2$ sublevels with different

DOI: 10.1021/acs.inorgchem.7b00205
Inorg. Chem. 2017, 56, 4601−4608

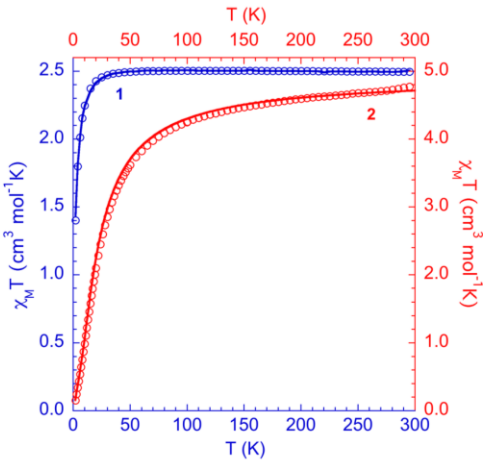

Figure 3. $\chi_M T = f(T)$ for **1** and **2**: (○) experimental data and (—) calculated data (see text).

energy) for **1** and an antiferromagnetic exchange coupling between the two Co(II) ions in **2**. The magnetizations in the form of $M = f(B/T)$ (Figure 4) are not superimposable for complex **1** indicating the presence of ZFS. For **2**, the shape of the magnetization curves is different from that of **1** and is compatible with a nonmagnetic ground state as expected from the antiferromagnetic coupling assumed from the susceptibility data. However, the magnetization at $T = 2$ K increases relatively rapidly for a nonmagnetic ground state and reaches 1 Bohr magneton at 6 T, which is compatible with the presence of a magnetic state close to the ground one. It is not possible to draw any quantitative conclusion on the presence of magnetic anisotropy and its magnitude from this qualitative analysis of the experimental data. We, thus, performed a fit of the susceptibility and the magnetization data using the PHI program,[21] and considering the spin Hamiltonians $H_1 = \beta \mathbf{S}\cdot[\mathbf{g}_1]\cdot\mathbf{B} + \mathbf{S}\cdot[\mathbf{D}_1]\cdot\mathbf{S}$ and $H_2 = \beta \mathbf{S}_{2a}\cdot[\mathbf{g}_{2a}]\cdot\mathbf{B} + \beta \mathbf{S}_{2b}\cdot[\mathbf{g}_{2b}]\cdot\mathbf{B} + \mathbf{S}_{2a}\cdot[\mathbf{D}_{2a}]\cdot\mathbf{S}_{2a} + \mathbf{S}_{2b}\cdot[\mathbf{D}_{2b}]\cdot\mathbf{S}_{2b} - J_{ab}\mathbf{S}_{2a}\cdot\mathbf{S}_{2b} + \mathbf{S}_{2a}\cdot[\mathbf{D}_{ani}]\cdot\mathbf{S}_{2b}$ for **1** and **2**, respectively (the indices a and b correspond to the Co(II) ions in the binuclear complex **2**). The x and y components of the $\mathbf{g}_{2a}$, $\mathbf{g}_{2b}$ tensors on one hand and for the $\mathbf{D}_{2a}$ and $\mathbf{D}_{2b}$ tensors, on the other hand, were considered equal and the tensors considered colinear for the two ions because **2** has D_3 (D_{3h} if only considering the Co and N atoms) symmetry; the anisotropic exchange $\boldsymbol{D}_{ani}$ was neglected. The rhombic parameter of the $\boldsymbol{D}$ tensors defined as $E = |D_{xx} - D_{yy}|/2$ is thus equal to zero, and the axial parameter D is equal to $3D_{zz}/2$, assuming $D_{xx} + D_{yy} + D_{zz} = 0$. The susceptibility and magnetization data were fitted simultaneously and lead to the following parameters: for **1**, $g_{1x} = g_{1y} = 2.36$, $g_{1z} = 2.24$, and $D_1 = -7.1$ cm^{-1}, and for **2**, $g_{2x} = g_{2y} = 2.43$, $g_{2z} = 2.03$, $D_{2a} = D_{2b} = D_2 = -5.35$ cm^{-1}, and $J_{ab} = -6.6$ cm^{-1}. We have explored the interdependence of the J and D parameters and found that the susceptibility data are mainly sensitive to J_{ab}, and a wide range of D_2 values give satisfactory calculated data. The magnetization is, however, sensitive to both values and thus allows a relatively good determination of the two parameters constraining J_{ab} within a range compatible with the susceptibility data. The energy spectrum of the spin states (Table S2) of the binuclear complex, considering the spin Hamiltonian parameters obtained from fitting the experimental data and provided by the PHI package, shows that the first excited state is very close to the ground state with a separation of 1.9 cm^{-1}, while the other states are located at energies larger than about 14 cm^{-1}.

Considering colinear local **D** tensors and an isotropic J exchange term (for the calculation J_{ab} is replaced by J) for the binuclear complex **2**, it is possible to determine the exact eigenfunctions and eigenvalues that are labeled by m_s and by S (see Supporting Information for the calculation method). We found that, for some states, S is a good quantum number and thus an exact label. For the others, S is only exact in the limit of large $|J/D|$ but, with this caveat, can be retained as an approximate label (see Supporting Information Table S3 and Figure S). Figure S depicts the evolution of the spin state energy spectrum of **2** as a function of the exchange parameter J for experimental value $D = -5.35$ cm^{-1}. The ground state ($m_s = 0$) contributes poorly to the magnetization because it is correlated to the total spin value $S = 0$ (when $|J| \gg |D|$). The first excited state ($m_s = 0$, Table S3) is correlated to the total spin $S = 1$ and is, thus, magnetic when the applied magnetic field is not exactly parallel to the principle anisotropy axis. Since it is only at 1.9 cm^{-1} above the ground state, it is populated at $T = 2$ K and contributes to the magnetization. This explains the absence of an S shape in the $M = f(B/T)$ curves at low fields. There are two degenerate excited states ($m_s = \pm 1$, Table S3) located at 14.8 cm^{-1} and correlated to $S = 1$; they are expected to cross the ground state around an applied magnetic field not

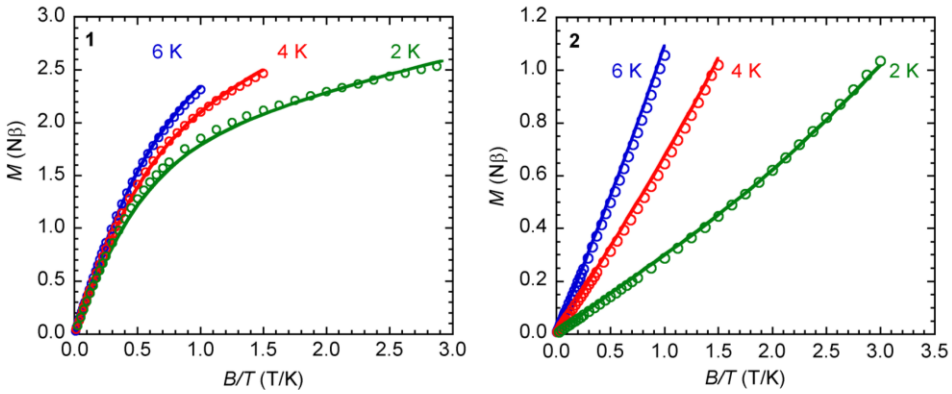

Figure 4. $M = f(B/T)$ for **1** and **2**: (○) experimental data and (—) calculated data (see text).

DOI: 10.1021/acs.inorgchem.7b00205
Inorg. Chem. 2017, 56, 4601−4608

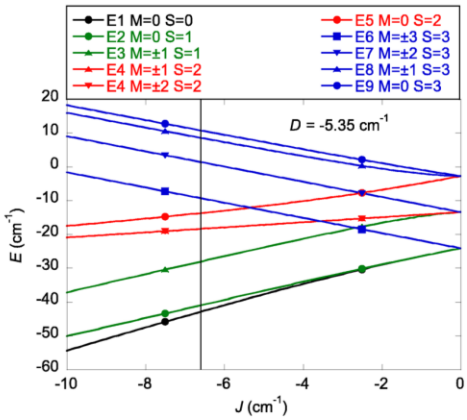

S	Calculation of D_S *using per*turbation theory[22,23]	Exact calculation of D_S for J_{ab}=-10 cm^{-1}	Exact calculation of D_S for J_{ab} = -100 cm^{-1}	Exact calculation of D_S for J_{ab} = -100 cm^{-1} if S is considered as a good quantum number
3	-2.14	-2.23	-2.15	-2.14
2	0	-1.71	-0.19	0
1	12.84	12.93	12.86	

Figure 5. (Top) Evolution of the energy states of the binuclear complex **2** with the exchange parameter J_{ab} for D_2 = −5.35 cm^{-1}; curves with the same symbols correspond to the energy states having the same M value, and those with the same color correspond to those with the same total spin S value (exact or approximate). The vertical black line indicates the energy spectrum for J_{ab} = −6.6 cm^{-1}. (Bottom) Calculated values of the ZFS parameters associated with the total spin values for different cases.

available experimentally, i.e., 15 T, which precludes the observation of an inflection point for the $M = f(B/T)$ curves in the 0−6 T experimental range. It is worth noting that the calculation allows determination of the ZFS values associated with total spin S (D_S) (Figure 5, bottom). For J equal to −10 cm^{-1}, we find that D_S values calculated using perturbation theory[22,23] are very close to those obtained with the method presented in this paper for S = 1 and S = 3. For S = 2, D_2 was found to be equal to −1.71 cm^{-1}, while calculations from perturbation theory give a value of zero. However, for large J our method gives the same results obtained from perturbation theory for the S = 2 state.

The axial parameter values D_1 and D_2 of the mononuclear and binuclear complexes, respectively, are very close as expected from their very similar coordination spheres; a more detailed analysis is performed in the theoretical section below.

Alternating Current Magnetic Studies. To probe the relaxation dynamics, we carried out alternating current (ac) magnetic susceptibility measurements on microcrystalline samples of **1**. The compound showed frequency dependence of the out-of-phase susceptibility (Figure 6 and Figure S1) and slow relaxation of its magnetization. The ac data in the form of Cole−Cole plots (Figure S2) were fitted to the generalized Debye model that allowed extracting the relaxation times at different temperatures (τ) and their distribution (α) (Table S4). The fit of the linear dependence of the ln(τ) versus $1/T$ curve leads to U_{eff} = 15 cm^{-1} and $\tau_0 = 5 \times 10^{-9}$ s, where U_{eff} is the effective energy barrier to the reorientation of the magnetization of Co(II) and τ_0 the attempt time. It is remarkable to note that the effective energy barrier is the same as the theoretical barrier $2D_1$ equal to 14.2 cm^{-1}, which means that the relaxation via an Orbach process is dominating. This is attributed to the strict axial symmetry of the complex where the transverse anisotropy is strictly equal to zero. The fact that a dc magnetic field (500 Oe) is needed to observe the slow relaxation is most probably due to dipolar intermolecular interactions that may activate quantum tunneling processes. Unfortunately, the equivalent complex with a diamagnetic ion, i.e., Zn(II), could not be prepared in order to investigate the effect of dilution. The relaxation time at T = 1.8 K extracted from the Cole−Cole plot is 10^{-3} s, while in a similar complex recently reported,[15] with only slightly larger D value (−11 cm^{-1}), the relaxation was 1 order of magnitude slower which highlights the important role of the axial anisotropy parameter on slowing the relaxation dynamics when the transverse anisotropy is absent.

Theoretical Calculations. The section aims at determining both the zero-field splitting parameters of the metal ions and the magnetic couplings between these ions. As all of these parameters are very sensitive to geometrical features, the

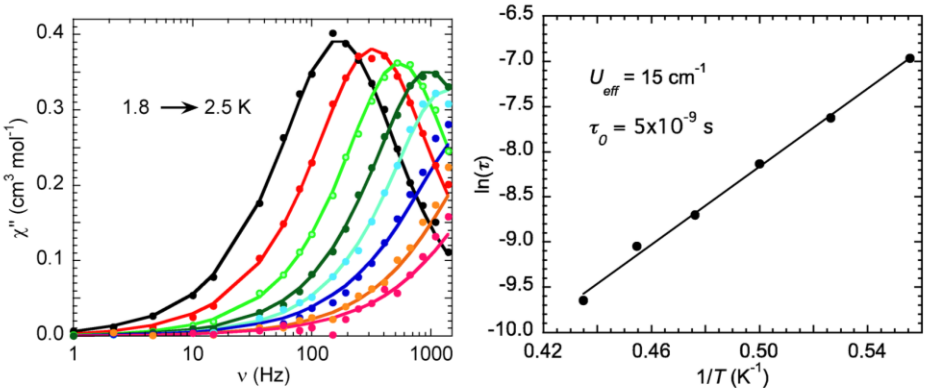

Figure 6. Frequency dependence of χ'' at variable temperatures with direct current applied field = 500 Oe (left) and ln(τ) = $f(1/T)$ (right) for **1**: experimental data (●) and fit (—).

DOI: 10.1021/acs.inorgchem.7b00205
Inorg. Chem. 2017, 56, 4601−4608

theoretical study was performed using the experimental geometries obtained from the X-ray crystal data. Two types of theoretical calculations were carried out: (i) Relativistic wave function (WF) based calculations were performed using the Molcas 8.0 package[24] in order to determine the local ZFS parameter D in **1** and **2**. ANO-RCC basis sets were used (details are given in Supporting Information).[25,26] The calculations of the ZFS parameter for the Co(II) ion in the binuclear complex were performed by replacing one of the Co(II) ions by the diamagnetic Zn(II) cation. The ZFS parameters were calculated using a two-step method. Non-dynamic correlation is taken into account at the complete active space self consistent field (CASSCF) level, and the spin−orbit coupling (SOC) is introduced in a second step using the SO-RASSI method.[27] The procedure of extraction of the ZFS parameters from the effective Hamiltonian theory[28,29] and the computed energies and wave functions has already been successfully used by our group.[11,13,15,30−32] Computational details can be found in the Supporting Information, and (ii) broken-symmetry density functional theory (DFT) calculations were performed using the GAUSSIAN package in order to evaluate the exchange coupling J_{ab} for the binuclear complex.[33] The range separated wB97XD functional[34] and a TZVP basis set[35] were used for all atoms. The broken-symmetry (BS) density functional theory (DFT) approach combined with a strategy first proposed by Noodleman is a powerful tool for the calculation of model Hamiltonian parameters.[36] While one of its main advantages over WF based methods lies in its application to larger systems, it is also particularly suited for geometry optimizations,[37,38] for the determination of subtle interactions such as double exchange,[39] and the biquadratic exchange in systems of spin $S = 1$.[40] Their performances are well-documented in several review papers.[41−45] Two broken-symmetry solutions have been computed, namely, the $m_s = 0$ one that has the local $m_s = {}^3/_2$ and $m_s = -{}^3/_2$ components on each Co(II) ion and the $m_s = 3$ solution. Assimilating the corresponding energies to those of the Ising Hamiltonian (diagonal energies of the Heisenberg Hamiltonian), the magnetic coupling J_{ab} can be extracted from the energy difference between the two solutions.

Ab Initio Calculation of the Zero-Field Splitting Parameters. The calculated ZFS parameters have almost the same value for the two complexes: $D_{1calc} = -9.22$ cm^{-1} and $D_{2calc} = -9.91$ cm^{-1}. Both Co(II) complexes adopt a local axial C_{3v} symmetry. In this symmetry point group, a mixing between the $(x^2 - y^2, xy)$ and (xz, yz) sets of orbitals occurs because they belong to the same irreducible representation (IRREP) E; such a mixing is absent for the D_{3h} symmetry[32] in which these orbitals belong to two different IRREP. The composition of the e orbitals is given in Figure 7, right. The calculations show that only a few excited electronic states are relevant to reproduce the ZFS resulting from the SOC.[11,14,32,46] Two low excited quadruplet states ($^4A_1$ and ^4E) and two highly excited doublet states ($^2A_1$ and ^2E) have a non-negligible contribution to the ZFS value (Figure 7). The first excited quadruplet $^4A_1$ is obtained by monoelectronic excitations from the lower e to the higher e orbitals (Figure 7 and Figure S3). These excitations involve the same m_l values as the two sets of e orbitals that are linear combinations of both the $(x^2 - y^2, xy)$ and (xz, yz) 3d orbitals (Figure 7). Thus, the first excited state is coupled to the ground state $^4A_2$ through the $\hat{l}_z\hat{s}_z$ part of the SOC operator stabilizing more the $m_s = \pm{}^3/_2$ components than the $m_s = \pm{}^1/_2$

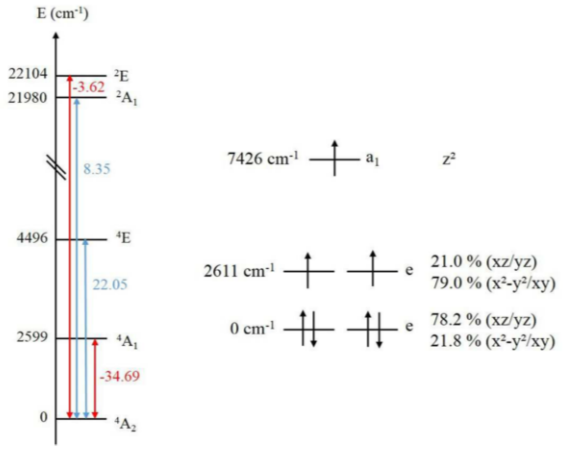

Figure 7. Calculated low energy spectrum for **1** and contributions to D_1 of each excited state (left) and 3d orbital energies and composition (right). The red arrows indicate a negative contribution to D while the blue arrows indicate a positive one.

ones and hence bringing a negative contribution to the total D_{1calc} value (Figure 7). The second excited state ^4E is obtained by several excitations (Figure S3), among them two from the lower e set of orbitals to the a_1 orbital involving a change in the m_l values (Figure S3); thus, the $\hat{l}_-\hat{s}_+ + \hat{l}_+\hat{s}_-$ part of the SOC Hamiltonian (in addition to the $\hat{l}_z\hat{s}_z$ one) now couples the ground state to the ^4E excited one leading to an overall stabilization of the $m_s = \pm{}^1/_2$ components and thus bringing a positive contribution to ZFS (Figure 7). Finally, the $^2A_1$ and ^2E excited states, respectively, contribute positively and negatively to D_{1calc}, but to a lesser extent than the quadruplets as they are higher in energy. In summary, the C_{3v} symmetry brings an overall negative contribution to D_{1calc} absent in the case of D_{3h} symmetry because the $(x^2 - y^2, xy)$ and (xz, yz) sets of orbitals belong to the same IRREP E in C_{3v}, while they belong to two different IRREP in D_{3h} precluding the coupling with the first excited state ($^4A_1$) that is mainly responsible for the negative contribution to ZFS.[32] It is worth noting that, for all the pentacoordinate Co(II) complexes that possess a C_{3v} symmetry point group (or slightly distorted C_{3v}), we found both experimentally and theoretically negative D values when the $N_{ap}CoL_{eq}$ angles are between 80° and 78°, with N_{ap} being the tertiary amine nitrogen atom and L_{eq} the atoms that are in the equatorial plane of the trigonal bipyramid that can be a nitrogen (in Me_6tren) or a sulfur (in (2-(isopropylthio)ethyl)-amine) atom for the organic ligand.[11,13,15,32] Recently, Dunbar, Ruiz, and co-workers reported a series of similar complexes using the TPMA (=tris(2-pyridylmethyl)amine) tetradentate ligand that possesses, in the equatorial plane, nitrogen atoms belonging to pyridine groups.[14] They found negative D values for all complexes except when acetonitrile is the axial ligand in trans position of the tertiary amine. The analysis of the electronic spectra of this complex revealed that the first excited state ($^4A_1$) brings a negative contribution as usual but of weaker magnitude than the other complexes so that the positive contributions dominate leading to an overall positive D value. The weaker magnitude in absolute value of the contribution of the $^4A_1$ state to the overall ZFS parameter is due not to its higher energy in the case of the axial acetonitrile ligand but probably, as mentioned by the authors, to a weaker mixing

DOI: 10.1021/acs.inorgchem.7b00205
Inorg. Chem. 2017, 56, 4601−4608

between the two sets of e orbitals that leads to a smaller SOC matrix element with the ground state. This result highlights the major role of not only the equatorial ligands,[13] but also the axial ligand in the coordination sphere of Co(II) in engineering the D values.[14,15]

For complex **2** the results (Figure S4) are similar to those of complex **1** as expected from the quasi-identical coordination sphere of the Co ion in the two complexes. However, small differences in the extent of mixing of the two sets of 3d orbitals of symmetry e are observed (see Figure 7 and Figure S3 for comparison) due to slight differences in the local structure (Table 1), but this does not affect the resulting axial anisotropy values.

Broken-Symmetry Density Functional Theory Calculations of the Exchange Coupling Parameter. The computed exchange coupling parameter J_{ab} (-8.2 cm^{-1})[36,47,48] is very close to the value extracted from the fit of the magnetic data (-6.6 cm^{-1}). The analysis of the singly occupied molecular orbitals (Figure 8) optimized for the $m_s = 0$ broken-symmetry

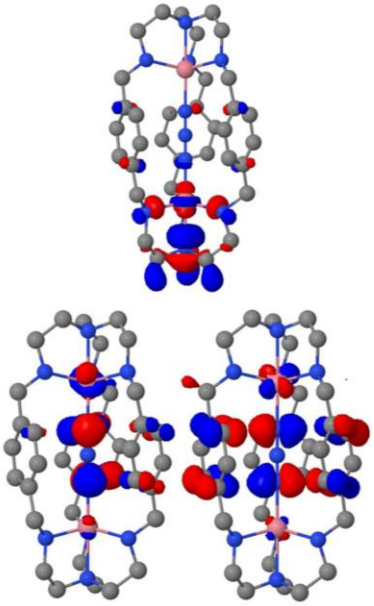

Figure 8. Singly occupied magnetic orbitals calculated for the $m_s = 0$ broken-symmetry solution.

solution provides insight into the nature (antiferromagnetic vs ferromagnetic) and magnitude of the exchange coupling. As usual in DFT and contrary to what is obtained in WF based methods, the magnetic orbitals are strongly delocalized on the ligands.[49] The highest in energy α spin orbital, mainly a $3d_{z^2}$ of symmetry a_1 (Figure 8), is localized on one of the Co(II) ions while the equivalent β spin orbital is located on the other Co(II) ion (not shown). They have no contribution on the N_3^- bridging ligand and thus should not (or weakly) contribute to the antiferromagnetic exchange coupling between the two metal ions. The absence of contribution from a N_3^- orbital is probably due to the large energy difference between the 3d orbitals and the HOMO $-$ 1 σ-type orbital of N_3^-. The other two singly occupied e orbitals are lower in energy; they possess a mixed ($x^2 - y^2$, xy) and (xz, yz) character of the metal ions (see above). They show a contribution from the HOMOs of N_3^- in addition to a contribution from the π orbitals of the benzene arms (Figure 8). This latter contribution is due to the π stacking with the benzene part and N_3^-. These two orbitals are mainly responsible for the antiferromagnetic exchange coupling between the Co(II) ions transmitted not only by the direct azido bridge but also by the benzene arms of the cryptand ligand. The weak magnitude of the coupling in the binuclear complex has two origins. First, the a_1 orbital does not really contribute to the coupling due to the lack of contribution of the N_3^- bridge orbitals. Second, the magnetic orbitals of symmetry e have only 25% contribution from the pure (xz, yz) orbitals (see Figure S4, left) that overlap with the HOMOs of N_3^-, and as the magnitude of the antiferromagnetic contribution is proportional to the overlap integral, their contribution is weak.

■ CONCLUDING REMARKS

We reported the preparation of a mononuclear Co(II) complex embedded in a cryptand-like ligand that possesses a strict C_3 symmetry and an Ising type anisotropy and presents a slow relaxation of its magnetization. The nature of the cryptand ligand that bears two coordination sites allows obtaining the binuclear associated complex with the same local C_3 symmetry for Co(II) and an antiferromagnetic exchange coupling between the metal ions. The quasi-identical coordination sphere of Co(II) in the mononuclear and the binuclear complexes permits fixing the axial ZFS parameter in a narrow range and extracting the value of the exchange coupling parameter that would have been difficult otherwise because of the interdependence of these two parameters. The exact calculation, in the general case, of the energy and the wave functions associated with the different coupled states of a binuclear Co(II) complex allows analysis of the impact of the $|J|/|D|$ ratio on the energy spectrum of the spin states. We find that, even though the ratio is close to 1, complex **2** has a behavior close to the situation of the strong exchange coupling limit. Only when $|J|/|D|$ is weaker than around 0.4 (Figure 5, top) does the binuclear compound have an energy spectrum corresponding to the weak exchange limit and behave as two weakly coupled Co(II) ions. In order to prepare such a complex with weak exchange coupling and Ising type anisotropy, one simple solution may consist of removing the direct bridge between the Co(II) ions. Indeed, DFT calculations showed a contribution coming of the benzene arms of the cryptand ligand to the antiferromagnetic coupling that may be sufficient to induce a weak interaction so that the complex could behave as two weakly antiferromagnetically coupled SMMs and thus be considered as a double q-bit system.

■ ASSOCIATED CONTENT

Supporting Information

The Supporting Information is available free of charge on the ACS Publications website at DOI: 10.1021/acs.inorgchem.7b00205.

Experimental and magnetic data and theoretical calculations (PDF)

Crystallographic information (CCDC 1521747) for compound **1** (CIF)

Crystallographic information (CCDC 1521748) for compound **2** (CIF)

DOI: 10.1021/acs.inorgchem.7b00205
Inorg. Chem. 2017, 56, 4601−4608

AUTHOR INFORMATION

Corresponding Authors

*E-mail: nathalie.guihery@irsamc.ups-tlse.fr.
*E-mail: talal.mallah@u-psud.fr.

ORCID

Feng Shao: 0000-0001-8606-8628
Talal Mallah: 0000-0002-9311-3463

Author Contributions

The manuscript was written through contributions of all authors. All authors have given approval to the final version of the manuscript.

Notes

The authors declare no competing financial interest.

ACKNOWLEDGMENTS

This work is partially financed by ANR-project MolQuSpin 13-BS10-0001-03. This work is supported by a public grant overseen by the French National Research Agency (ANR) as part of the "Investissements d'Avenir" program "Labex NanoSaclay" (reference: ANR-10-LABX-0035). We acknowledge the collaborative program between the China Scholarship Council and Université Paris-Sud (No. 201306310014), UPS, Région Ile de France SESAME program 2012 no. 12018501 and CNRS. F.E.-K. thanks the Conseil National de la Recherche Scientifique du Liban (CNRSL) (http://www.cnrs.edu.lb/) for financial support. T.M. thanks the IUF (Institut Universitaire de France) for financial support.

REFERENCES

(1) Sessoli, R.; Gatteschi, D.; Caneschi, A.; Novak, M. A. Magnetic bistability in a metal-ion cluster. *Nature* **1993**, *365*, 141−143.
(2) Sessoli, R.; Tsai, H. L.; Schake, A. R.; Wang, S.; Vincent, J. B.; Folting, K.; Gatteschi, D.; Christou, G.; Hendrickson, D. N. High-spin molecules:[Mn12O12 (O2CR) 16 (H2O) 4]. *J. Am. Chem. Soc.* **1993**, *115*, 1804−1816.
(3) Gatteschi, D.; Sessoli, R.; Villain, J. *Molecular Nanomagnets*; Oxford University Press, 2006.
(4) Leuenberger, M. N.; Loss, D. Quantum computing in molecular magnets. *Nature* **2001**, *410*, 789−793.
(5) Lehmann, J.; Gaita-Arino, A.; Coronado, E.; Loss, D. Spin qubits with electrically gated polyoxometalate molecules. *Nat. Nanotechnol.* **2007**, *2*, 312−317.
(6) Lehmann, J.; Gaita-Arino, A.; Coronado, E.; Loss, D. Quantum computing with molecular spin systems. *J. Mater. Chem.* **2009**, *19*, 1672−1677.
(7) Aromi, G.; Aguila, D.; Gamez, P.; Luis, F.; Roubeau, O. Design of magnetic coordination complexes for quantum computing. *Chem. Soc. Rev.* **2012**, *41*, 537−546.
(8) Candini, A.; Lorusso, G.; Troiani, F.; Ghirri, A.; Carretta, S.; Santini, P.; Amoretti, G.; Muryn, C.; Tuna, F.; Timco, G.; McInnes, E. J. L.; Winpenny, R. E. P.; Wernsdorfer, W.; Affronte, M. Entanglement in Supramolecular Spin Systems of Two Weakly Coupled Antiferromagnetic Rings (Purple-Cr7Ni). *Phys. Rev. Lett.* **2010**, *104*, 037203.
(9) Gomez-Coca, S.; Cremades, E.; Aliaga-Alcalde, N.; Ruiz, E. Mononuclear Single-Molecule Magnets: Tailoring the Magnetic Anisotropy of First-Row Transition-Metal Complexes. *J. Am. Chem. Soc.* **2013**, *135*, 7010−7018.
(10) Zadrozny, J. M.; Xiao, D. J.; Atanasov, M.; Long, G. J.; Grandjean, F.; Neese, F.; Long, J. R. Magnetic blocking in a linear iron(I) complex. *Nat. Chem.* **2013**, *5*, 577−581.
(11) Ruamps, R.; Batchelor, L. J.; Guillot, R.; Zakhia, G.; Barra, A. L.; Wernsdorfer, W.; Guihery, N.; Mallah, T. Ising-type magnetic anisotropy and single molecule magnet behaviour in mononuclear trigonal bipyramidal Co(II) complexes. *Chem. Sci.* **2014**, *5*, 3418−3424.
(12) Rechkemmer, Y.; Breitgoff, F. D.; van der Meer, M.; Atanasov, M.; Hakl, M.; Orlita, M.; Neugebauer, P.; Neese, F.; Sarkar, B.; van Slageren, J. A four-coordinate cobalt(II) single-ion magnet with coercivity and a very high energy barrier. *Nat. Commun.* **2016**, *7*, 10467.
(13) Shao, F.; Cahier, B.; Guihéry, N.; Rivière, E.; Guillot, R.; Barra, A.-L.; Lan, Y.; Wernsdorfer, W.; Campbell, V. E.; Mallah, T. Tuning the Ising-type anisotropy in trigonal bipyramidal Co (ii) complexes. *Chem. Commun.* **2015**, *51*, 16475−16478.
(14) Woods, T. J.; Ballesteros-Rivas, M. F.; Gómez-Coca, S.; Ruiz, E.; Dunbar, K. R. Relaxation Dynamics of Identical Trigonal Bipyramidal Cobalt Molecules with Different Local Symmetries and Packing Arrangements: Magnetostructural Correlations and ab inito Calculations. *J. Am. Chem. Soc.* **2016**, *138*, 16407−16416.
(15) Shao, F.; Cahier, B.; Rivière, E.; Guillot, R.; Guihéry, N.; Campbell, V. E.; Mallah, T. Structural Dependence of the Ising-type Magnetic Anisotropy and of the Relaxation Time in Mononuclear Trigonal Bipyramidal Co(II) Single Molecule Magnets. *Inorg. Chem.* **2017**, *56*, 1104.
(16) Menif, R.; Reibenspies, J.; Martell, A. E. Synthesis, Protonation Constants, and Copper(Ii) and Cobalt(Ii) Binding Constants of a New Octaaza Macrobicyclic Cryptand - (Mx)3(Tren)2 - Hydroxide and Carbonate Binding of the Dicopper(Ii) Cryptate and Crystal-Structures of the Cryptand and of the Carbonato-Bridged Dinuclear Copper(Ii) Cryptate. *Inorg. Chem.* **1991**, *30*, 3446−3454.
(17) Drew, M. G. B.; Hunter, J.; Marrs, D. J.; Nelson, J.; Harding, C. Cascade Complexes of an Octaaza Cryptand - Coordinated Azide with Linear M-Nnn-M Geometry. *J. Chem. Soc., Dalton Trans.* **1992**, 3235−3242.
(18) Chen, J. M.; Zhuang, X. M.; Yang, L. Z.; Jiang, L.; Feng, X. L.; Lu, T. B. Anion recognition of chloride and bromide by a rigid dicobalt(II) cryptate. *Inorg. Chem.* **2008**, *47*, 3158−3165.
(19) Caballero-Jimenez, J.; Habib, F.; Ramirez-Rosales, D.; Grande-Aztatzi, R.; Merino, G.; Korobkov, I.; Singh, M. K.; Rajaraman, G.; Reyes-Ortega, Y.; Murugesu, M. Inducing magnetic communication in caged dinuclear Co(II) systems. *Dalton Trans.* **2015**, *44*, 8649−8659.
(20) Chen, D.; Martell, A. E. The Synthesis of New Binucleating Polyaza Macrocyclic and Macrobicyclic Ligands - Dioxygen Affinities of the Cobalt Complexes. *Tetrahedron* **1991**, *47*, 6895−6902.
(21) Chilton, N. F.; Anderson, R. P.; Turner, L. D.; Soncini, A.; Murray, K. S. PHI: A powerful new program for the analysis of anisotropic monomeric and exchange-coupled polynuclear d- and f-block complexes. *J. Comput. Chem.* **2013**, *34*, 1164−1175.
(22) Bencini, A.; Gatteschi, D. *EPR of Exchange Coupled Systems*; Springer-Verlag: Berlin, 1990.
(23) Kahn, O. *Molecular Magnetism*; VCH Inc.: New York, 1993; p 142.
(24) Aquilante, F.; Autschbach, J.; Carlson, R. K.; Chibotaru, L. F.; Delcey, M. G.; De Vico, L.; Galvan, I. F.; Ferre, N.; Frutos, L. M.; Gagliardi, L.; Garavelli, M.; Giussani, A.; Hoyer, C. E.; Li Manni, G.; Lischka, H.; Ma, D. X.; Malmqvist, P. A.; Muller, T.; Nenov, A.; Olivucci, M.; Pedersen, T. B.; Peng, D. L.; Plasser, F.; Pritchard, B.; Reiher, M.; Rivalta, I.; Schapiro, I.; Segarra-Marti, J.; Stenrup, M.; Truhlar, D. G.; Ungur, L.; Valentini, A.; Vancoillie, S.; Veryazov, V.; Vysotskiy, V. P.; Weingart, O.; Zapata, F.; Lindh, R. Molcas 8: New capabilities for multiconfigurational quantum chemical calculations across the periodic table. *J. Comput. Chem.* **2016**, *37*, 506−541.
(25) Roos, B. O.; Lindh, R.; Malmqvist, P.-Å.; Veryazov, V.; Widmark, P.-O. Main Group Atoms and Dimers Studied with a New Relativistic ANO Basis Set. *J. Phys. Chem. A* **2004**, *108*, 2851−2858.
(26) Roos, B. O.; Lindh, R.; Malmqvist, P.-Å.; Veryazov, V.; Widmark, P.-O. New Relativistic ANO Basis Sets for Transition Metal Atoms. *J. Phys. Chem. A* **2005**, *109*, 6575−6579.
(27) Malmqvist, P. A.; Roos, B. O. The Casscf State Interaction Method. *Chem. Phys. Lett.* **1989**, *155*, 189−194.
(28) Bloch, C. Sur la théorie des perturbations des états liés. *Nucl. Phys.* **1958**, *6*, 329−347.

DOI: 10.1021/acs.inorgchem.7b00205
Inorg. Chem. 2017, 56, 4601−4608

(29) des Cloizeaux, J. Extension d'une formule de Lagrange à des problèmes de valeurs propres. *Nucl. Phys.* **1960**, *20*, 321−346.
(30) Maurice, R.; Bastardis, R.; Graaf, C. d.; Suaud, N.; Mallah, T.; Guihéry, N. Universal Theoretical Approach to Extract Anisotropic Spin Hamiltonians. *J. Chem. Theory Comput.* **2009**, *5*, 2977−2984.
(31) Maurice, R.; Guihery, N.; Bastardis, R.; Graaf, C. Rigorous Extraction of the Anisotropic Multispin Hamiltonian in Bimetallic Complexes from the Exact Electronic Hamiltonian. *J. Chem. Theory Comput.* **2010**, *6*, 55−65.
(32) Cahier, B.; Maurice, R.; Bolvin, H.; Mallah, T.; Guihéry, N. Tools for Predicting the Nature and Magnitude of Magnetic Anisotropy in Transition Metal Complexes: Application to Co(II) Complexes. *Magnetochemistry* **2016**, *2*, 31.
(33) Frisch, M.; Trucks, G.; Schlegel, H.; Scuseria, G.; Robb, M.; Cheeseman, J.; Scalmani, G.; Barone, V.; Mennucci, B.; Petersson, G. *Gaussian09, Revision D. 01*; Gaussian, Inc.: Wallingford, CT, 2013.
(34) Chai, J. D.; Head-Gordon, M. Long-range corrected hybrid density functionals with damped atom-atom dispersion corrections. *Phys. Chem. Chem. Phys.* **2008**, *10*, 6615−6620.
(35) Schäfer, A.; Huber, C.; Ahlrichs, R. Fully optimized contracted Gaussian basis sets of triple zeta valence quality for atoms Li to Kr. *J. Chem. Phys.* **1994**, *100*, 5829−5835.
(36) Noodleman, L. Valence Bond Description of Anti-Ferromagnetic Coupling in Transition-Metal Dimers. *J. Chem. Phys.* **1981**, *74*, 5737−5743.
(37) Malrieu, J. P.; Trinquier, G. A Recipe for Geometry Optimization of Diradicalar Singlet States from Broken-Symmetry Calculations. *J. Phys. Chem. A* **2012**, *116*, 8226−8237.
(38) Saito, T.; Thiel, W. Analytical Gradients for Density Functional Calculations with Approximate Spin Projection. *J. Phys. Chem. A* **2012**, *116*, 10864−10869.
(39) Boilleau, C.; Suaud, N.; Bastardis, R.; Guihery, N.; Malrieu, J. P. Possible use of DFT approaches for the determination of double exchange interactions. *Theor. Chem. Acc.* **2010**, *126*, 231−241.
(40) Labeguerie, P.; Boilleau, C.; Bastardis, R.; Suaud, N.; Guihery, N.; Malrieu, J. P. Is it possible to determine rigorous magnetic Hamiltonians in spin s = 1 systems from density functional theory calculations? *J. Chem. Phys.* **2008**, *129*, 154110.
(41) Illas, F.; Moreira, I. D. P. R.; Bofill, J. M.; Filatov, M. Extent and limitations of density-functional theory in describing magnetic systems. *Phys. Rev. B: Condens. Matter Mater. Phys.* **2004**, *70*, 132414.
(42) Bencini, A. Some considerations on the proper use of computational tools in transition metal chemistry. *Inorg. Chim. Acta* **2008**, *361*, 3820−3831.
(43) Cramer, C. J.; Truhlar, D. G. Density functional theory for transition metals and transition metal chemistry. *Phys. Chem. Chem. Phys.* **2009**, *11*, 10757−10816.
(44) Neese, F. Prediction of molecular properties and molecular spectroscopy with density functional theory: From fundamental theory to exchange-coupling. *Coord. Chem. Rev.* **2009**, *253*, 526−563.
(45) Swart, M. Spin states of (bio)inorganic systems: Successes and pitfalls. *Int. J. Quantum Chem.* **2013**, *113*, 2−7.
(46) Schweinfurth, D.; Sommer, M. G.; Atanasov, M.; Demeshko, S.; Hohloch, S.; Meyer, F.; Neese, F.; Sarkar, B. The Ligand Field of the Azido Ligand: Insights into Bonding Parameters and Magnetic Anisotropy in a Co(II)-Azido Complex. *J. Am. Chem. Soc.* **2015**, *137*, 1993−2005.
(47) Noodleman, L.; Norman, J. G. X-Alpha Valence Bond Theory of Weak Electronic Coupling - Application to the Low-Lying States of Mo2cl84-. *J. Chem. Phys.* **1979**, *70*, 4903−4906.
(48) Bencini, A.; Totti, F. On the importance of the biquadratic terms in exchange coupled systems: A post-HF investigation. *Inorg. Chim. Acta* **2008**, *361*, 4153−4156.
(49) Phillips, J. J.; Peralta, J. E. Magnetic Exchange Couplings from Semilocal Functionals Evaluated Nonself-Consistently on Hybrid Densities: Insights on Relative Importance of Exchange, Correlation, and Delocalization. *J. Chem. Theory Comput.* **2012**, *8*, 3147−3158.

DOI: 10.1021/acs.inorgchem.7b00205
Inorg. Chem. 2017, 56, 4601−4608

université PARIS-SACLAY
ÉCOLE DOCTORALE
Sciences chimiques : molécules, matériaux, instrumentation et biosystèmes

Titre: Ingénierie de l'anisotropie magnétique dans les complexes mononucléaires de cobalt(II) et les métallacrowns à base de lanthanides

Mots clés: Anisotropie, Levée de dégénérescence au champ nul, Molécules-Aimants; Cobalt, Lanthanide, Métallacrown

Résumé: Comme nous le savons, les applications sont déterminées par des propriétés, qui sont essentiellement déterminées par la structure. L'interaction entre la forme (structure moléculaire) et la fonction (propriétés physiques) peut être exploitée par le ligand, l'ion métallique, l'approche métallacrown et ainsi de suite. Les travaux portent sur la synthèse et l'étude du comportement magnétique de complexes mononucléaires cobalt(II) de géométrie bipyramide trigonale et sur l'étude de complexes mononucléaires de lanthanides possédant une structure de type métallacrown.

Pour les complexes de cobalt(II), l'objectif a été de modifier l'anisotropie magnétique en modifiant la nature du ligand organique tétradenté et du ligand terminal en gardant, autant que faire se peut, la géométrie et même la symétrie des complexes. Presque tous ces complexes se comportent comme des molécules-aimants avec une barrière énergétique à l'inversion de l'aimantation qui peut être liée à leur anisotropie magnétique et donc à la nature des ligands. Et les complexes métallacrown à base de lanthanides étant hautement symétriques, permet de les utiliser comme modèles pour effectuer une corrélation entre la nature de l'ion lanthanide et leurs propriétés d'aimants.

La thèse est composée de 6 chapitres. Le chapitre 1 présente l'état de l'art du magnétisme, des molécules-aimants (SMMs et SIMs), et quelques exemples importants. Le chapitre 2 se concentre sur une famille de complexes de géométrie bipyramide trigonale de formule générale [Co(Me$_6$tren)X]Y avec le ligand axial (X) et le contre-ion (Y) induisant le comportement SMM.

Dans cette série de composés, j'ai étudié l'influence du ligand axial X sur la nature et l'amplitude de l'anisotropie magnétique. J'ai montré que la série des halogénures, l'anisotropie la plus forte est obtenue pour le ligand axial fluorure (F^-). J'ai aussi étudié l'effet du cation Y qui influence l'interaction entre les molécules qui affectent le comportement d'aimant moléculaire. Au chapitre 3, on étudie l'influence du changement du ligand tétradenté. Le remplacement des trois atomes d'azote qui se trouvent en position équatoriale dans la sphère de coordination de cobalt(II) par des atomes de soufre induit une augmentation des distances Co–L dans le plan équatorial qui conduit à une plus forte anisotropie. Les calculs théoriques effectués sur ces complexes permettent de rationaliser les résultats expérimentaux et surtout de prévoir les propriétés de nouveaux complexes. Les chapitres 4 et 5 concernent deux séries de SMM 12-MC-4 basées sur LnGa$_4$ (Ln = Tb^{III}, Dy^{III}, Ho^{III}, Er^{III}, Yb^{III}) avec les ligands basés sur l'acide salicylhydroxamique (H_3shi) et l'acide 3-hydroxy-2-naphtohydroxamique (H_3nha). J'ai préparé plusieurs complexes et étudié leurs propriétés magnétiques. Les calculs théoriques permettent de rationaliser la différence entre les propriétés des magnétiques dues aux différents ions lanthanide. Enfin, une conclusion générale avec des perspectives sont récapitulées au chapitre 6.

Title: Engineering magnetic anisotropy in mononuclear cobalt(II) complexes and lanthanide-based metallacrowns

Keywords: Anisotropy, Zero-Field Splitting, Single Molecule Magnets, Cobalt, Lanthanide, Metallacrown

Abstract: As we know, the applications are determined by properties, which are essentially determined by structure. The interplay between form (molecular structure) and function (physical properties) can be exploited engineering by the ligand, the metal ion, the metallacrown approach and so on. The work focuses on the synthesis and the study of the magnetic behavior of mononuclear cobalt(II) complexes with trigonal geometry and on the study of mononuclear lanthanide complexes that possess a metallacrown structure.

For the cobalt(II) complexes, the aim was to tune the magnetic anisotropy by changing the nature of the tetradentate organic ligand and the terminal ligand. Almost all these complexes behave as Single Molecule Magnets with an energy barrier to the reversal of the magnetization that can be linked to their magnetic anisotropy and thus to the nature of the organic ligands. The lanthanide containing metallacrown complexes are highly symmetric, which allows performing a correlation between the nature of the lanthanide ion and their Single Molecule Magnet properties.

The dissertation will be composed of 6 chapters. Chapter 1 introduces the background of the magnetism, Single Molecule Magnets, Single Ion Magnets, and some important SIMs. Chapter 2 focuses on a family of trigonal bipyramidal complexes [Co(Me$_6$tren)X]Y. We show that the axial ligand affects the SMM behavior allowing us to prepare a complex with a magnetic bistability at T = 2 K. In Chapter 3, we examine the effect of changing the coordinated atoms (sulfur instead of nitrogen) in the equatorial coordination sphere of cobalt(II). We demonstrate that this slight change improves the SMM behavior. Chapter 4 and 5, which concern two series of 12-MC-4 SMMs based on LnGa$_4$ (Ln = Tb^{III}, Dy^{III}, Ho^{III}, Er^{III}, Yb^{III}) with the ligands salicylhydroxamic acid (H_3shi) and 3-hydroxy-2-naphthohydroxamic acid (H_3nha), respectively, where we correlate the nature of the lanthanide ion to its magnetic behavior using ab initio calculations. At last, the understanding gained from this dissertation research, along with future research directions will be recapitulated in Chapter 6.

Université Paris-Saclay
Espace Technologique / Immeuble Discovery
Route de l'Orme aux Merisiers RD 128 / 91190 Saint-Aubin, France